PETROLOGICAL, GEOCHEMICAL AND Sr-Nd ISOTOPIC STUDIES OF METAMORPHOSED MAFIC ROCKS IN THE WONOMINTA BLOCK, NORTHWESTERN NEW SOUTH WALES

Bo ZHOU
(B. Sc., Peking University)

A thesis submitted in fulfilment
of the requirement for the degree of
Doctor of Philosophy

Department of Geology and Geophysics
The University of Sydney

December, 1992

SUMMARY

The Wonominta Block is located in far north-western New South Wales and consists of composite stratigraphic units. This project is focused on investigation of selected mafic rocks in the lower three sequences, namely the basement, Late Proterozoic and early Cambrian, using petrological, geochemical and isotopic methods, in order to achieve a better understanding of the tectonic evolution of the region. Such an understanding of the region is relevant to understanding continental development at the broader scale but also provides a more sound basis for mineral exploration.

Field observation, petrographic and mineralogical investigations of the mafic rocks reveal a complicated metamorphic and deformation history. In general, all samples appear to have experienced burial metamorphism (*sensu lato*) to various degrees before deformation, and the metamorphism had already reached peak conditions (ca. 500 °C) when deformation occurred. The P-T calculations reveal a high geothermal gradient for the burial metamorphism and a low one for regional metamorphic processes. This resulted in anti-clockwise P-T-t paths up to upper greenschist -lower amphibolite facies for the basement sequence, lower greenschist for Late Proterozoic sequence and pumpellyite-actinolite for early Cambrian sequences.

Geochemical studies reveal MORB-like compositions for the basement mafic rocks with significant Th-enrichment and some Nb-depletion. Detailed geochemical stratigraphy also shows systematic changes within the basement sequence: from the Wilandra Inlier in the south to the northern Ponto Mine Inlier, an increasing involvement of crustal materials in magma generation has been inferred. It is also inferred that magma mixing processes had not been important in magmatic evolution due to the facts that several petrographically distinct rocks in various sequences cannot be distinguished geochemically, and that large variations in high-field-strength (HFS) element compositions generally show coherent correlations. The younger rocks (both Late Proterozoic and early Cambrian) have sodic alkaline basalt affinities with no crustal contamination observed.

To provide a chronological constraint on the Wonominta Beds, an ion microprobe zircon U-Pb study yielded a preliminary age of 525±8 Ma (2σ) for the youngest part (the Mt. Wright Volcanics), but the Nd/Sm isotope analyses on basement samples produced only a poorly defined isochron of 1.40 ± 0.24 Ga (mean standard weighted deviation (MSWD) = 0.9).

The Sr-Nd isotopic investigations indicate low initial $^{87}Sr/^{86}Sr$ ratios and positive $\varepsilon_{Nd}(T)$ values for all the analysed mafic rocks from the three sequences. For the basement samples, the initial $^{87}Sr/^{86}Sr$ ratios are various due to alteration but may range from 0.7020 to 0.7041; the $\varepsilon_{Nd}(T)$ is from 4.8 to 8.9. These results suggest that there were possibly two depleted mantle sources for the formation of the basement mafic rocks. One of the extremely depleted end-members may have been a "fossil mantle wedge" in the source region. The assimilation-fractional crystallisation (AFC) model calculation using Nd isotope compositions indicates that the contribution of crustal materials to the observed most contaminated sample could be up to 7%. In contrast, the alkaline basalts in the younger sequences, have clear primitive isotope compositions with $\varepsilon_{Nd}(T)$ about 4.7 ± 0.4 and an initial $^{87}Sr/^{86}Sr$ ratio about 0.703.

From these petrological, geochemical and isotopic studies, a new tectonic model for the evolution of the Wonominta Block is proposed. In this model, the Ponto Mine Inlier and Wilandra Inlier are proposed to comprise the basement for Late Proterozoic development, and they themselves may have developed in a back-arc basin environment during Early - Middle Proterozoic. Above the basement, the emplacement of alkaline basalts in the Late Proterozoic and Early Cambrian sequences represents the beginning of a rifting event along the cratonic margin, which led to the formation of a deep-water basin where the Early Cambrian Teltawongee beds were deposited. Regionally, the Kanmantoo Trough in South Australia would have been developed during the same tectonic event

Such a model requires a reevaluation of the tectonic boundary between the Phanerozoic Tasman Orogen and its Precambrian basement in eastern Australia. It is thus suggested that the Delamerian Foldbelt (or Delamerian - Ross Orogen to be comparable with the Tasman Orogen) represents a transitional tectonics between the Phanerozoic tectonic development and the Precambrian cratons. This transitional tectonics comprises the Adelaide Geosyncline and the Kanmantoo regime, and involved two rifting events that may have been parts of the global rifting which led to the break-up of the Proterozoic supercontinent.

DECLARATION

All results and interpretation presented in this thesis are the original work of the author except where otherwise acknowledged.

Wonominta

Wonominta is derived from an aboriginal name, referring to a place, close to the present Wonnaminta Homestead. The name means a place next to water. Different spellings exist for the same aboriginal pronunciation, such as "Wonaminta Block" (Warren, 1972; Plumb, 1979; Edwards, 1979; Preiss & Forbes, 1981; Powell *et al.*, 1982), and "Wanaminta Block" (Cook, 1982). The word, "Wonominta", on the other hand, can be traced back to the early geological literature (*e.g.*, Kenny, 1934), and is widely used in recent publications (Warris, 1967; Rose, 1968; Pogson & Scheibner, 1971; Scheibner, 1972, 1974, 1976, 1987 and 1989; Barnes, 1974; Packham & Leitch, 1974; Thomson, 1975; Webby, 1984; Leitch *et al.*, 1987; Mills, 1992). Therefore, in this thesis, "Wonominta" is used in geological applications, such as the Wonominta Block and the Wonominta Beds; while "Wonnaminta" is the local spelling for the homestead, located in the northeastern part of the region.

Table of Contents

List of Abbreviated Symbols

AFC:	assimilation and fractional crystallisation
AI:	alkali index
BHGBG:	Broken Hill Group basic gneisses
BSE:	back-scattered electron (image)
CAB:	calcalkaline basalt
CFB:	continental flood basalt
CHUR:	chondritic uniform reservoir (DePaolo & Wasserburg, 1976a)
CIS:	Centre for Isotope Studies
DM:	depleted mantle
DSDP:	deep sea drilling project
HDM:	highly depleted mantle
HFS:	high-field strength (element, such as Zr, Nb, Y and Ti)
IC:	isotope compositions
ICP:	inductively coupled plasmas
ID:	isotope dilution
INAA:	instrumental neutron activation analyses
LKT:	low-K tholeiite
LOI:	loss on ignition
MB:	metabasalt, metabasite
MD:	metadolerite
MP:	mafic porphyritic rocks
MORB:	mid-ocean ridge basalt; including N-type (normal) & E-type (enriched)
MORBN:	MORB-normalised spidergram plot
MS:	mass spectrometer/ mass spectrometry
MSWD:	mean standard weighted deviation
NDM:	normal depleted mantle
OIB:	ocean island basalt
OFB:	ocean floor basalt
PM:	primitive mantle (composition)
PMN:	PM-normalised spidergram plot
PPM:	part(s) per-million
SHRIMP:	sensitive high resolution ion microprobe
TAS:	total alkali-silica (diagram)
TIMS:	thermal ion mass spectrometer
TTZ:	Tasman Transitional Zone

PAAS: post-Archaean Australian shales

VAB:	volcanic arc basalt
WPA:	within-plate alkali basalt
WPB:	within-plate basalt, equivalent WPT + WPA
WPT:	within-plate tholeiite
XRF:	X-ray fluorescence
Ab:	albite
Ac:	actinolite
Am:	amphibole
Cb.	carbonate, normally calcite
Ch:	chlorite
Cpx:	clinopyroxene
Cz:	clinozoisite
Ep:	epidote
Hb:	hornblende
Ka:	kaersutite
Kf:	potassium feldspar
Mt:	magnetite
Mu:	muscovite
Pl:	plagioclase
Pr:	prehnite
Pm:	pumpellyite
Py:	pyroxene, normally clinopyroxene in this study, thus same as Cpx
Qz:	quartz
Tr:	tremolite

List of Figures

List of Plates

List of Tables

PREFACE & ACKNOWLEDGEMENT

Being selected to be a student in geology was originally a kind of coincidence as my initial interest was to pursue mathematics. Nonetheless I wish firstly to thank the Chinese Government who sponsored me to carry out this research studies in Australia.

Over the years, the people to whom I should express my sincere thanks are many; only a few of them are mentioned here: David Hendry, my first supervisor, who introduced me to the Wonominta geology and later on to the isotope studies that have become the most important part of the project; George Navratil for training me to learn the thin-section making techniques; Diana Benson and Clive Nockolds for electron microprobe analyses; Zou Jin and David Cockayne for TEM analyses; Ken Williams and Rolf Beck for major element, and Jim Karaolis for trace element analyses; Jeff Davies for sulphide mineral separations; and Brenda Durie for drawing up the maps from the field work. Brian Gulson, Graham Carr, Steve Craven, Karen Mizon and Mike Korsch, provided much help to accomplish the isotope investigations. John Eames of CSIRO kindly helped to analyse the REE compositions of twenty-four mafic samples and three replicate analyses for Nb by means of ICP-MS techniques. Thanks are also given to Huang Bin, a visitor to the CSIRO, who analysed some of the sulphide samples.

In the early period of this project, Dr. S. Sangameshwar of the University of Technology, Sydney, kindly allowed access to some samples collected by S. Davies during his Honours project, with the permission of the BP Minerals Company. In this collection, a rare Mn mineral, cryptomelane, was discovered in one of the gossan samples. I am also very grateful to Dr. Jon C. Claoué-Long for introducing me in a collaborative project re-evaluating the lower boundary of the Cambrian System. In this work, zircons separated from a felsic tuff sample from the Mt. Wright area were analysed on the SHRIMP in Canberra.

Special thanks are given to Dr. Kingsley Mills, my second supervisor, and to Dr. David Whitford of CSIRO who has served as my associate supervisor later in the project. The four-year-long intensive field mapping in the Wonominta Block by Kingsley and other staff members in the Department has provided the fundamental structural basis for this project, particularly for the selection of the mapping areas and interpretation of geological correlations. On the other hand, David has offered crucial support in terms of orientation in achieving the accomplishment of this thesis.

Professor Graeme Philip and Associate Professor Don Emerson, the heads of the Department during the progress of this project have kindly provided help in both resources and finance. This project was partly supported by a Departmental scholarship for three years. The isotope analysis was financially supported by the CRAE in Broken Hill and Centre for Isotope Studies (CIS), where the analyses were carried out.

Particular thanks are given to Associate Professor Robin Offler of Newcastle University who threw some light in the darkness of metamorphic petrology of low grade mafic rocks.

Drs Yadong Chen of Macquarie University, Shensu Sun of BMR in Canberra, Erwin Scheibner of NSW Geological Survey, and Songfa Liu of La Trobe University made many critical comments during the progress of the project and are greatly appreciated. A computer program by Wheatley & Rock (1988) is used to generate various spidergrams and chondrite normalised REE plots in this thesis; rest of the writing task is accomplished on a Macintosh Plus® computer and other Apple® facilities in the Department.

And last, I wish to thank my wife, Hong, for her affection, encouragement, and understanding. We were introduced to each other in a traditional Chinese way but married in a most unusual and painful experience. A month after the marriage we were separated, and had to wait for a whole year to reunite. She has sacrificed most of the precious things a normal Chinese girl would enjoy to support me during the progress of this work.

Chapter 1
Introduction

1.1. REGIONAL SETTING

The Wonominta Block covers some 200 000 km^2 in far north-western New South Wales, north of the Broken Hill Block, south of Tibooburra and west of White Cliffs (*cf.* Figure 1.1). Within this region, a major unconformity has been recognised between Middle and Late Cambrian sequences which have clearly different deformation histories across the boundary (*cf.* Wang *et al.*, 1988). This tectonic event is correlated with the Delamerian Orogeny defined in South Australia (*cf.* Preiss, 1987) and is locally known as the Mootwingee Phase (Webby, 1978). Previously, the rocks that have experienced the deformation during the Delamerian Orogeny were collectively known as the Wonominta Beds (see review in Chapter Two); recent mapping (Mills, 1992) revealed, however, that the Wonominta Beds comprise actually three composite units. They are informally defined as the "basement", "Late Proterozoic" and "early Cambrian" sequences here and equivalent to the "Ponto beds", "Kara beds" and "Teltawongee beds" of Mills (1992) respectively. The early Cambrian rocks in the southern Wonominta Block are also known as the Gnalta Group (Rose, 1968). Various mafic rocks occurring in these sequences are the subjects of the present project, in particular their geochemical, Sr-Nd isotopic characteristics and their tectonic implications.

In eastern Australia, a general tectonic boundary, the Tasman Line (Hill, 1951), has been defined between the Phanerozoic Tasman Orogen and the Precambrian cratonic basement (*cf.* Coney *et al.*, 1990). The Tasman system is a Palaeozoic to early Mesozoic orogenic belt which makes up the eastern one-third of the Australian continent, which formed a part of the Pacific margin of Gondwana. This system lies east of the Precambrian cratonic crystalline basement of Australia with a narrow fringe of deformed upper Proterozoic sedimentary sequences, locally exposed along the southwestern margin of the orogen. In this context, the Wonominta Block is situated just astride the boundary, possibly as a part of the complicated "fringe zone". However, various, sometimes contrasting tectonic models have been proposed and one of the fundamental questions is how to address the relationship between the Wonominta Block and the Tasman Line, that is whether the Wonominta Block is part of the basement, a part of the Phanerozoic foldbelts, or a part of the transitional zone separating the two major tectonic regimes.

Fig. 1.1 Geology of the Wonominta Block and the Broken Hill Block in western NSW (Mills, 1992; Fig.1). In the legend of this diagram, the dashed line marks the tectonic boundary caused by the Delamerian Orogeny during Middle - Late Cambrian. The Wonominta Beds are defined as those below the boundary and comprise three sequences. The Ponto beds (Middle Proterozoic) are known as the basement sequence and occur as a narrow belt between the Ponto Mine and Wonnaminta Homestead in the north, and between Cymbric Vale and Wilandra in the south. This sequence is correlated with the Willyama Supergroup in the Broken Hill Block. The Kara bed in the western part of the Wonominta Block is suggested to be equivalent to the Torrowangee series also in the Broken Hill Block across the Bancannia Trough; it is also known as the Late Proterozoic sequence. The Gnalta Group and the Teltawongee beds of Early-Middle Cambrian rocks are collectively referred to here as early Cambrian sequences.

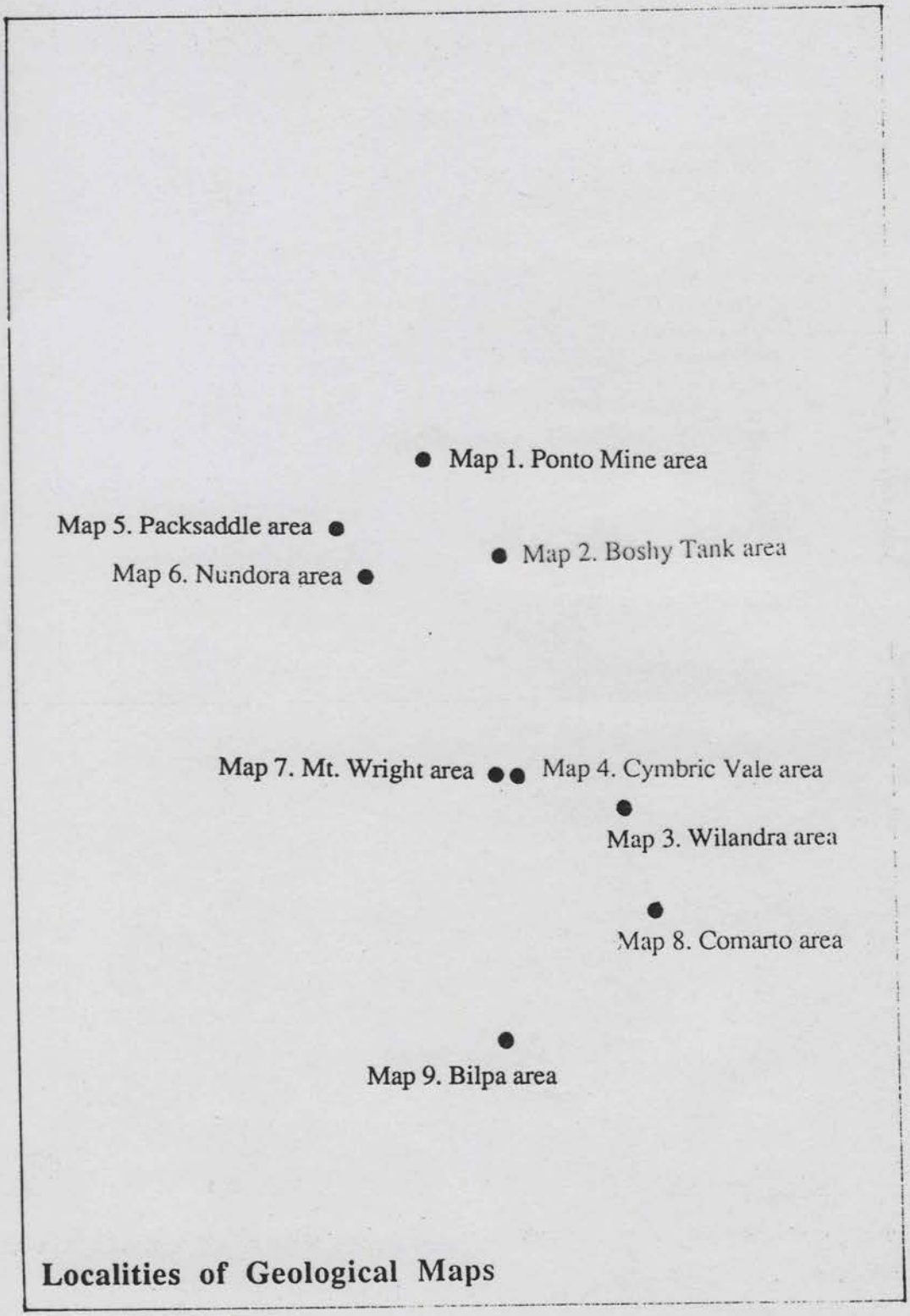

Localities of Geological Maps

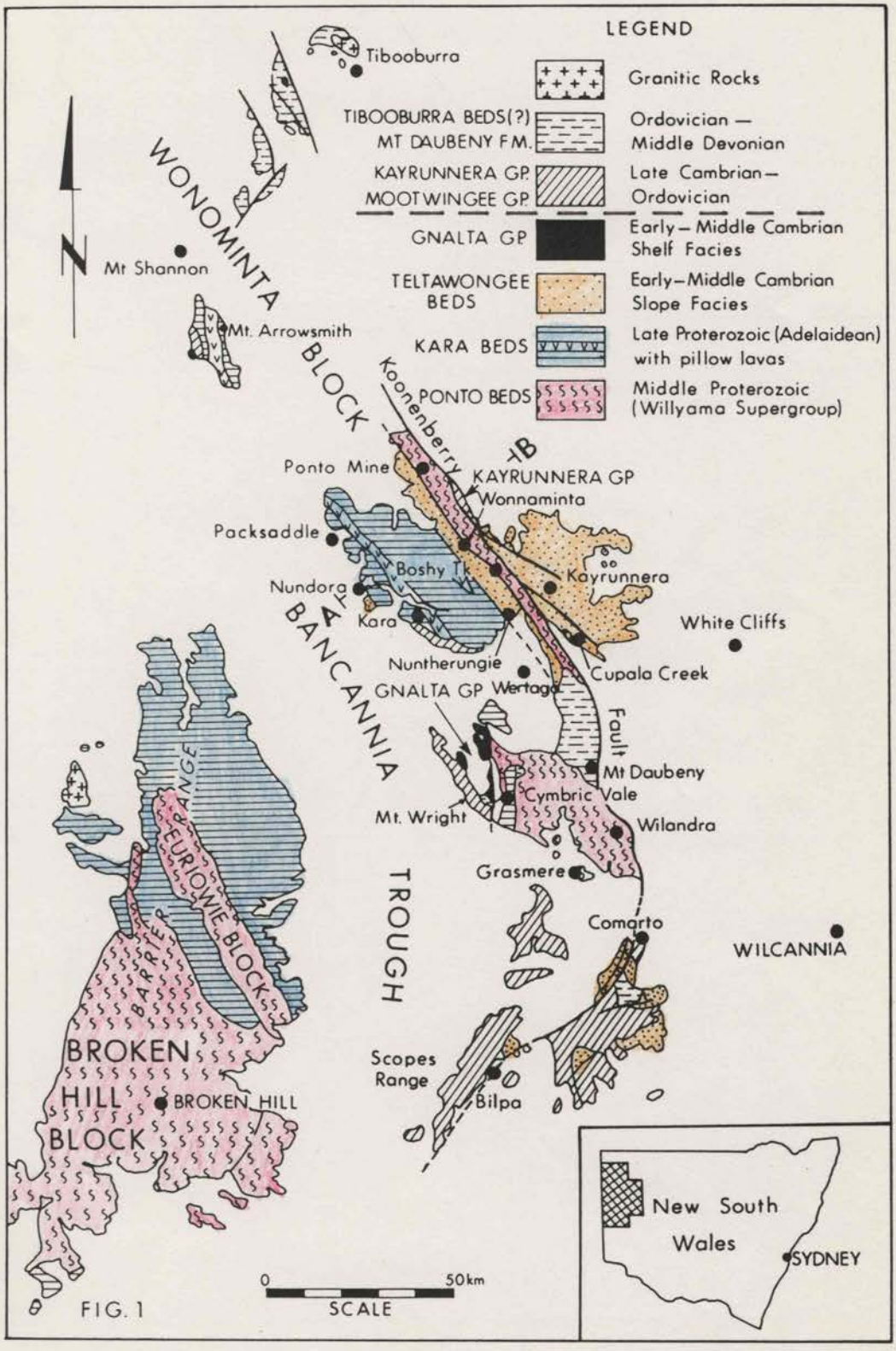
LEGEND
Granitic Rocks
TIBOOBURRA BEDS(?)
MT DAUBENY F.M.
Ordovician — Middle Devonian
KAYRUNNERA GP.
MOOTWINGEE GP.
Late Cambrian — Ordovician
GNALTA GP.
Early — Middle Cambrian Shelf Facies
TELTAWONGEE BEDS
Early — Middle Cambrian Slope Facies
KARA BEDS
Late Proterozoic (Adelaidean) with pillow lavas
PONTO BEDS
Middle Proterozoic (Willyama Supergroup)
Tibooburra
WONOMINTA BLOCK
Mt Shannon
Mt. Arrowsmith
Koonenberry FB
Ponto Mine
KAYRUNNERA GP
Wonnaminta
Packsaddle
Boshy Tk
Kayrunnera
Nundora
Kara
White Cliffs
BANCANNIA TROUGH
Nuntherungie
Cupala Creek
GNALTA GP
Wertago
Fault
Mt Daubeny
Cymbric Vale
Mt. Wright
Wilandra
Grasmere
Comarto
WILCANNIA
RAVENSWOOD EURIOWIE BLOCK
BARRIER
BROKEN HILL BLOCK
BROKEN HILL
Scopes Range
Bilpa
New South Wales
SYDNEY
0
50km
SCALE

FIG. 1

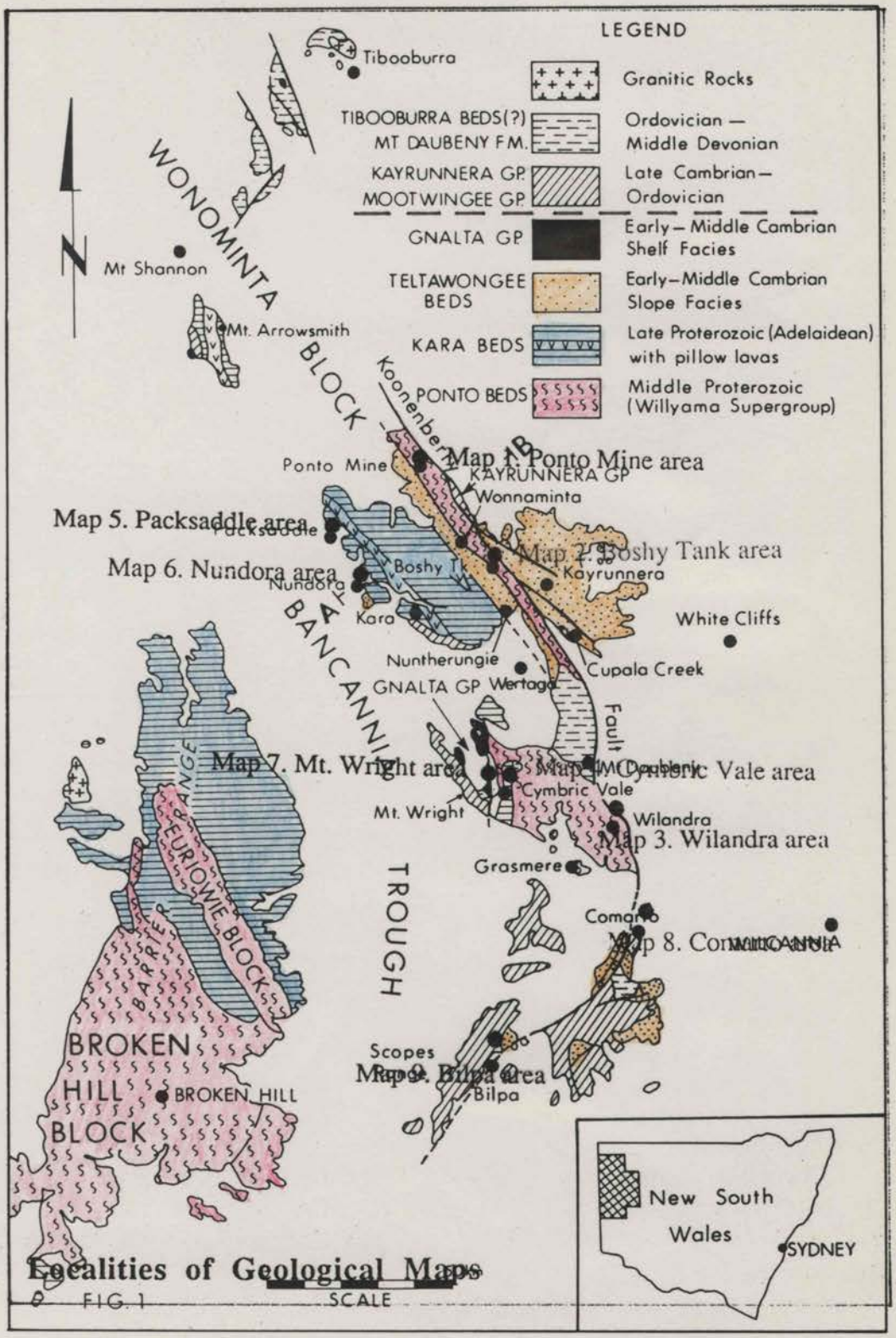
LEGEND
Granitic Rocks
TIBOOBURRA BEDS(?)
MT DAUBENY FM.
Ordovician — Middle Devonian
KAYRUNNERA GP.
MOOTWINGEE GP.
Late Cambrian — Ordovician
GNALTA GP.
Early — Middle Cambrian Shelf Facies
TELTAWONGEE BEDS
Early — Middle Cambrian Slope Facies
KARA BEDS
Late Proterozoic (Adelaidean) with pillow lavas
PONTO BEDS
Middle Proterozoic (Willyama Supergroup)
Tibooburra
WONOMINTA BLOCK
Mt Shannon
Mt. Arrowsmith
Koonenberry
BANCANNIA TROUGH
Ponto Mine
KAYRUNNERA GP
Wonnaminta
Packsaddle
Boshy Tk
Nundora
Kara
Kayrunnera
White Cliffs
Nuntherungie
Cupala Creek
GNALTA GP
Wertago
Fault
Cymbric Vale
Mt. Wright
Wilandra
Grasmere
Comaroo
BANCANNIA
Scopes
Bilpa
EURIOWIE BLOCK
BARRIER RANGE
BROKEN HILL BLOCK
BROKEN HILL
New South Wales
SYDNEY
Map 1. Ponto Mine area
Map 2. Boshy Tank area
Map 3. Wilandra area
Map 5. Packsaddle area
Map 6. Nundora area
Map 7. Mt. Wright area
Map 8. Comaroo area
Map 9. Bilpa area
Localities of Geological Maps
SCALE

FIG. 1

Understanding such a relationship helps not only to define the tectonic framework of eastern Australia, but also to explore how the continent evolved in this particular part of Gondwana. The regional geological mapping, carried out in the Department of Geology and Geophysics of The University of Sydney (Mills, 1992), provided a structural and regional geological basis for the present project. As suggested in this geological framework, the geological history of the Wonominta Beds may have extended from early Middle Proterozoic to Middle Cambrian, almost a thousand million years. Through this long period, mafic magmatism formed an essential part of the evolution of the Wonominta Block, and studies of these mafic rocks hence play a crucial role in the regional tectonic reconstruction.

1.2. AIMS OF THIS PROJECT

The ultimate aim of this study is to help to reconstruct the tectonic evolution of a region that plays an important role in understanding the evolution of the Australian continent. It is achieved by means of addressing petrological, geochemical and Sr-Nd isotope characteristics of the mafic rocks and the tectonic implications, and through the following activities:

1. To describe field occurrences of various mafic rocks within the established structural framework and to explore their primary emplacement environments.

2. To investigate relic igneous and metamorphic characters of the mafic rocks, and hence to reveal conditions of secondary processes following their emplacement.

3. To study the geochemical characteristics of the mafic rocks, their pre-metamorphic geochemical affinities and the influence of the secondary processes.

4. To establish the geochemical stratigraphy of mafic magmatism in the Wonominta Beds and to explore petrogenetic parameters of the mafic rocks.

5. To determine the emplacement ages of the mafic rocks in the Wonominta Beds using U-Pb and Sm-Nd geochronological techniques.

6. To investigate the Sr-Nd isotopic systematics of the mafic rocks and to characterise the tectonic environment of their source regions.

7. To reconstruct the tectonic setting where the mafic rocks were formed.

8. To assess the role of regional tectonics to the understanding of the evolution of the Tasman Orogen and the reconstruction of this part of Gondwana.

1.3 THESIS OUTLINE

The first part of this thesis, presented in chapters three and four following a review of the study of the Wonominta geology in Chapter Two, includes petrological studies to reveal the metamorphic history of the mafic rocks. Chapter Three contains observations of the occurrences of mafic rocks and petrography of representative samples selected in terms of freshness, variety and availability. Chapter Four presents electron microprobe studies of the mineral chemistry of the mafic rocks.

Part Two covers the geochemical investigations and the results are presented from chapters five to eight. Description of the geochemical characteristics of various mafic rocks is presented in Chapter Five for the basement , Chapter Six for the Late Proterozoic and Chapter Seven for the Cambrian samples and those with minor occurrences. The next part of the geochemical studies in Chapter Eight presents petrogenetic studies of the mafic rocks, including tectonomagmatic discrimination and petrogenetic aspects of formation of the mafic rocks.

Part Three, embodied in Chapter Nine, presents results of Sr, Rb, Nd, Sm and Pb isotopic studies. Discussions in this chapter concentrate on the characterisation of the source components and tectonic implications.

Chapter Ten presents discussions of the significance of the mafic rock studies to the regional tectonic reconstruction.

The last chapter of this thesis summarises various studies, discusses the results and makes suggestions for future studies.

Chapter 2

A REVIEW OF PREVIOUS STUDIES IN THE WONOMINTA BLOCK

This chapter is to review the available knowledge of the Wonominta Block from previous studies. Essentially, little was understood about the Wonominta geology until recently, though exploration can be traced back well into the last century when Charles Sturt and his team made an attempt to reach the heart of Australia in 1844.

The Wonominta Block is used here to refer to a region covering some 200 000 km^2 in far north-western New South Wales as shown in Figure 1.1. To the west is the Bancannia Trough, which is a north-northwestern linear feature some 50 km in width that has been defined mostly by geophysical methods (*cf.*, Webby, 1984). Southwestward of the Bancannia Trough is the Broken Hill Block. The eastern boundary of the Wonominta Block is loosely defined by the Koonenberry Fault, but significant outcrops of parts of the Wonominta Beds also occur on the eastern side of this fault.

The available knowledge of the Wonominta Block when this project commenced in 1986 may be summarised as follows. The pre-Delamerian rocks, *i.e.* the Wonominta Beds, are composed of three stratigraphic units; the basement (Early-Middle Proterozoic), late Proterozoic and early Cambrian sequences. This subdivision is based on a detailed regional mapping (Mills, 1992) and as shown in Figure 1.1, the basement sequence of the Wonominta Beds is correlated with the Willyama Supergroup in the Broken Hill Block and part of the overlying sequences are suggested to be equivalent to the Late Proterozoic Farnell Group (the upper part of the Torrowangee Series, which are correlated to the Adelaidean rocks in South Australia; *cf.*, Preiss, 1987), also in the Broken Hill Block. The youngest parts of the Wonominta Beds are of Early Cambrian to early Middle Cambrian (generally referred as early Cambrian) age. These sequences are mostly fault-bounded and there were no isotope data to constrain the age of any of these rocks.

Tectonically, the Wonominta Block is considered to comprise four stratotectonic terranes (Figure 2.1) (Leitch *et al.*, 1987), the Wertago Terrane, the Kayrunnera Terrane, the Tibooburra Terrane and the Mt. Wright Terrane. The first three of these were suggested to be probably autochthonous, forming the foundation of the block, while the last one was thought to be a suspect allochthonous terrane.

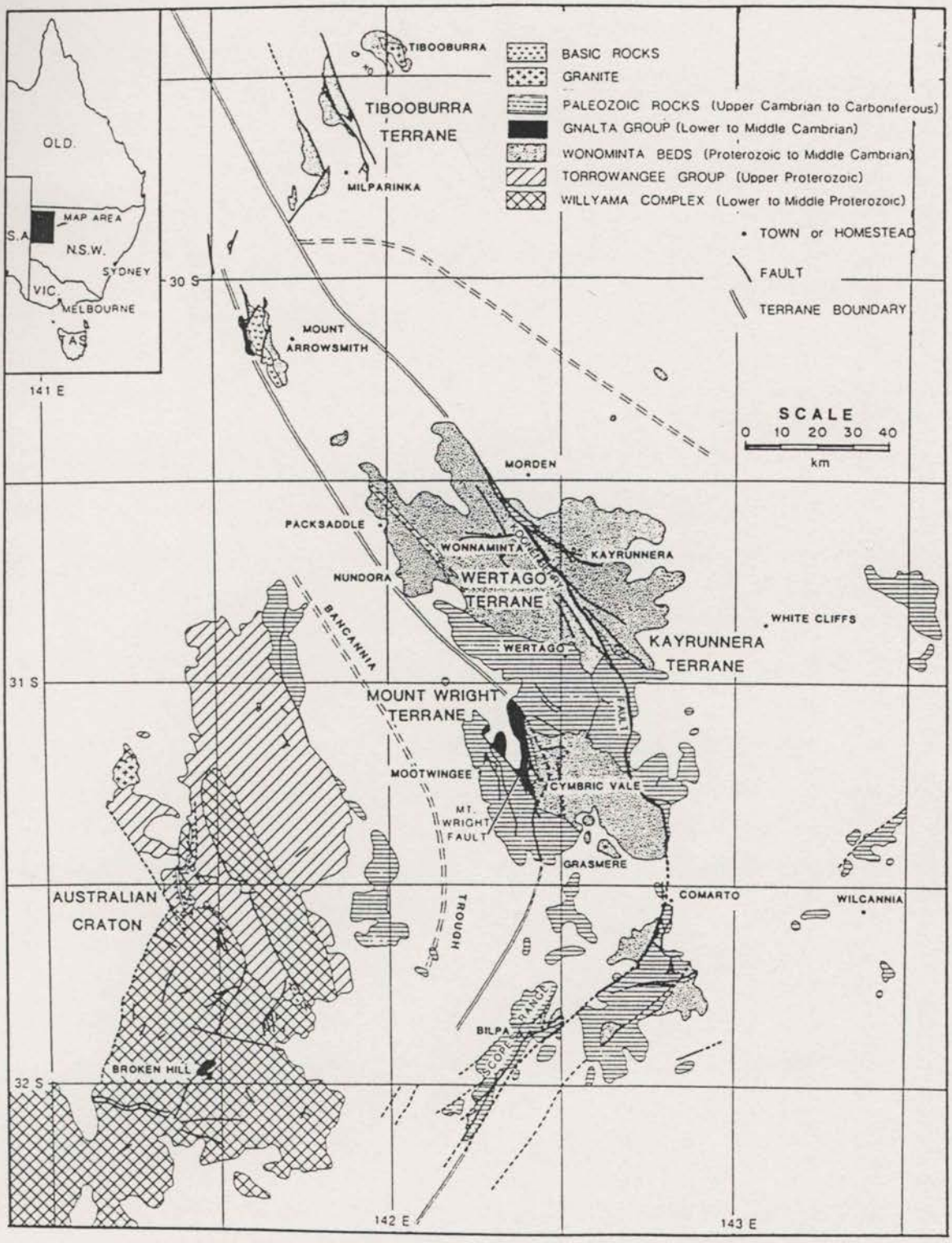

Fig. 2.1 An inferred terrane map of the Wonominta Block - Broken Hill Block in far western New south Wales (Leitch *et al.*, 1987). In this terrane map, the Wonominta Block is divided into four separate tectonic units, being the Tibooburra Terrane in the north, the Kayrunnera Terrane east of the Koonenberry Fault, the Mt. Wright Terrane west of the Mt. Wrght Fault and Wertago Terrane in between. In this scheme, the undivided Wonominta Beds is treated as a single geological unit and is not correlated with those in the Broken Hill Block..

2.1 A HISTORICAL REVIEW OF RESEARCH ON THE WONOMINTA GEOLOGY

The first work involving the Wonominta Block was published in 1849 by Charles Sturt, which was essentially a record of exploration activities five years earlier. Since then, particularly since the discovery of the Broken Hill deposits in 1883, many people, explorers, boundary riders, well sinkers, prospectors and geologists, have wandered through the region, earnestly hoping to find another big ore lode, though little significant mineralisation was discovered.

In the late nineteenth century, several geological reports on the mining activities in far western New South Wales mentioned the rocks in the Wonominta Block (Brown, 1881; Wilkinson, 1889; Jaquet, 1893). In these preliminary descriptions, the Wonominta Beds were thought to be extensions of the Willyama Complex in the Broken Hill region, and both sequences were assigned to the Early Palaeozoic.

In 1912, Douglas Mawson described some aspects of the geology in far western New South Wales. In this report he grouped the highly metamorphosed rocks in the Broken Hill Block under the name Willyama Complex, assigned to them a Precambrian age, and had the name Torrowangee Series applied to the overlying, less metamorphosed rocks, which were considered to belong to the Cambrian System, "The Torrowangee Series comprises a great thickness of slaty beds. In several localities interesting metamorphic changes have been noted in those leading to the production of phyllite and spotted slates" (p.273). This description can be applied to many rocks in the Wonominta Block.

Andrews (1922) considered the Torrowangee Series to be Precambrian. In the same report, he tentatively regarded the rocks in the Wonominta Block as equivalent to the Willyama Complex, but later (Andrews, 1926) changed his mind and suggested the rocks in the Wonominta region were equivalent to the Torrowangee Series.

Kenny (1934) was the first geologist to describe the rocks of the Wonominta Block in any significant detail. He also described the ironstones as conspicuous features; these were recently regarded as an important potential diagnostics of mineralisation in the region (*cf.*, Penny, 1985). Kenny considered all the rocks of Wonominta Block were members of the Torrowangee Series of Proterozoic age, while the Willyama Series was of Archaean age.

These ideas were virtually accepted by the following workers over almost the next forty years (*cf.* Edgeworth David, 1950; Thomson, 1963; Brunker, 1967; Packham, 1969).

In the early sixties, Brunker and Bunny (1964) spent about five weeks in the region for their compilation of the Cobham Lake 1:250 000 geological sheet as part of a regional mapping project. This work was compiled later (Brunker, 1967) as the explanatory note to the map, and it was probably the first time that any systematic work was carried out in the region.

In his Ph. D. thesis submitted in 1967, Warris gave an elegant description of Cambrian rocks in the southern part of the Wonominta Block as well as other outcrops generally in the western part of New South Wales. For the first time, he used the name "Wonominta Beds" but without definition, and regarded them generally as Precambrian rocks. He also mentioned the occurrence of mafic volcanic rocks of supposedly Cambrian age in the Mt. Wright area, which were at one stage attributed by later workers to a volcanic belt extending further north to Mt. Arrowsmith (*cf.* Brunker, 1967; Scheibner, 1974 & 1976).

In 1968, Rose of the Geological Survey of New South Wales, defined the name "Wonominta Beds" to record the Precambrian rocks in the Wonominta region and then, in the next year, he and Brunker proposed that the age of the Wonominta Beds was post-Willyama but pre-Torrowangee based on the relative degree of metamorphism and structural deformation. Rose and Brunker (1969) regarded the Wonominta Beds as equivalent to the Bijerkerno Beds, a name used for some low-grade metamorphic rocks in the Euriowie area, northeast of Broken Hill, now part of the Paragon Group of Willis *et al.* (1983). The name, "Wonominta Beds" was retained by Barnes (1974).

In 1972, Scheibner proposed the name, "Wonominta Complex" to describe the rocks in the region and then, by means of plate tectonic analysis, he considered the Wonominta Complex to be equivalent to the Willyama Complex of Broken Hill, but of lower metamorphic grade. The Wonominta Block was thought to have been separated from the continent by extensional processes during the early Cambrian and incorporated to form a small plate (microcontinent). Between the microcontinent and the cratonic basement (the Broken Hill Block and further west), the Bancannia Trough developed as a marginal sea. This model was partly retained by Edwards (1979), but was considered as highly speculative by Packham and Leitch (1974). Later, Webby

(*cf.* 1984) showed that the Bancannia Trough was not developed until Devonian time. The model was modified by the original author and the Wonominta Complex was then assigned to part of the Kanmantoo Foldbelt (Scheibner, 1989).

The name, Wonominta Block, was firstly proposed in 1974 in the form Wonominta-Tibooburra Block (Barnes, 1974), and then in 1975, as the form Wonominta Block (Rose,1975).

In the late seventies, there were two Ph. D. projects carried out in the Wonominta region. Kruse (1980) studied some Archaeocyathan faunas in limestones from Mt. Wright, which ascertained that the oldest rocks in this area are of Early Cambrian age.

Edwards (1980) carried out a study on mafic rocks at Mt. Arrowsmith in the northern part of the Wonominta Block. He also did some reconnaissance investigations of mafic rocks from various part of the region. And in a field conference in 1979, Edwards and Neef described the regional stratigraphic sequences and various igneous rocks in the Block. This work is by far the most important contribution to the igneous studies of the region.

During a two-year exploration project in the region, geologists from BP Minerals proposed again the equivalent relationship between the Wonominta Block and the Broken Hill Block (Penny, 1985). They recorded the presence of what appeared to be classical banded iron formations and explored various base metal anomalies assocaited with these ironstones.

In the mid-80s, the Wonominta Block was subdivided into several smaller structural blocks (Stevens, 1985). The Wonominta Beds were also suggested to be composite assemblages (Stevens & Raphael, 1985. p. 29).

From mid-80s, a major regional mapping project in the Wonominta region was carried out by the staff members in the Department of Geology and Geophysics, at The University of Sydney . Through this mapping endeavour, the composite features of the Wonominta Beds were, for the first time, recognised, which provided a more solid foundation for regional correlations (Mills, 1992). This work also established the biostratigraphy of the early Cambrian part of the Wonominta Beds in the northern part of the region (*e.g.* Wang *et al.*, 1989) and a better understanding of the regional tectonics, particularly the stratotectonic terrane reconstruction (Leitch *et al.*, 1987).

Geophysical investigations (*cf.* Murray *et al.*, 1989) through the Australian continent have also helped to reveal the regional structural features of the Wonominta Block. The gravity map presented in Figure 2.2 clearly shows that there are two remarkable linear features with north-northwest trends through the region. These two features can be readily correlated to the basement and late Proterozoic sequences in the region, and the positive gravity anomalies apparently result from significant occurrences of various mafic rocks in the sequences. The gravity low areas are of outcrops of early Cambrian rocks in the northern part of the region, which are largely composed of deep-water sediments.

2.2 STRATIGRAPHY AND REGIONAL CORRELATIONS

Figure 1.1 shows the distribution of various components of the Wonominta Beds and regional correlation with the rocks in the Broken Hill Block according to Mills (1992). In this synthesis, the Wonominta Beds are composed of three sequences. The oldest one, occurring as a narrow NNW trending belt along the western side of the Koonenberry Fault in the northern part of the Block, and large areas between Cymbric Vale and Moona Vale in the southern part of the Block, is assigned to the pre-Adelaidean basement and is correlated with the Willyama Supergroup in the Broken Hill Block. The northern unit is defined as the Ponto Mine Inlier and the southern one as the Wilandra Inlier. These rocks are juxtaposed against the late Proterozoic and early Cambrian sequences.

In the southern part of the region, the late Proterozoic rocks are virtually absent and the basement rocks are found everywhere juxtaposed against early Cambrian rocks with faulted contacts or unconformably overlain by younger rocks The early Cambrian rocks have been defined as the Gnalta Group in the southern part of the Wonominta Block (Rose, 1968) and the sediments are of shallow-water facies. In contrast, the equivalent rocks in the northern part of the region, known as the Teltawongee beds (Mills, 1992), are described as deep-water deposits.

In the late Middle Cambrian, the Wonominta Block underwent a major orogenic movement, locally known as the Mootwingee Movement, which is believed to be an early phase of the Delamerian Orogeny (Webby, 1978). This is a major regional tectonic boundary, and now the Wonominta Beds are defined as pre-Delamerian rocks, not only the Precambrian rocks as when the concept was firstly proposed, but also those formed during the early Cambrian.

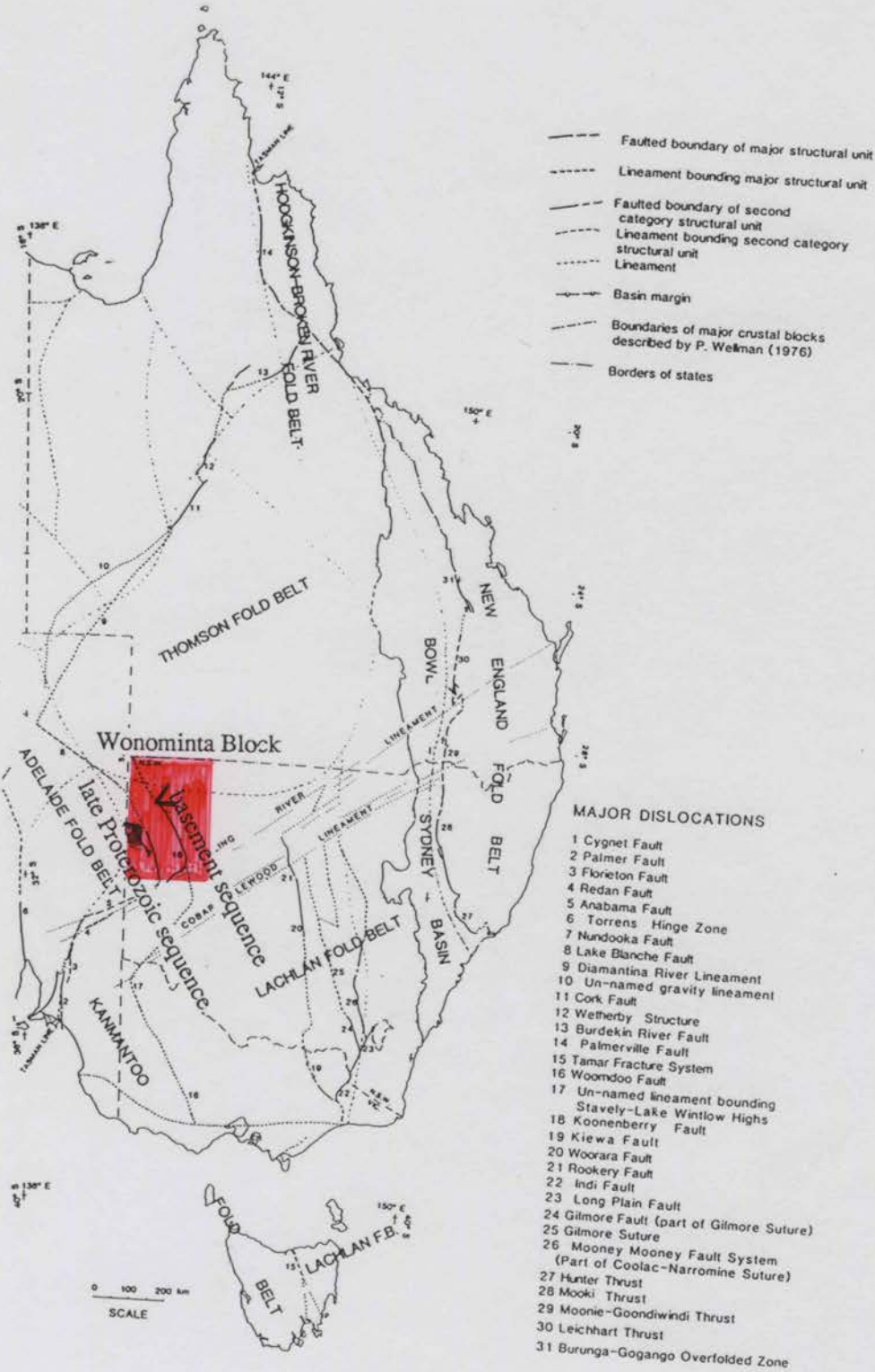
Faulted boundary of major structural unit
Lineament bounding major structural unit
Faulted boundary of second category structural unit
Lineament bounding second category structural unit
Lineament
Basin margin
Boundaries of major crustal blocks described by P. Wellman (1976)
Borders of states
HODGKINSON-BROKEN RIVER FOLD BELT
THOMSON FOLD BELT
NEW ENGLAND FOLD BELT
BOWEN BASIN
SYDNEY BASIN
LACHLAN FOLD BELT
ADELAIDE FOLD BELT
KANMANTOO
LACHLAN F.B.
Wonominta Block
Basement sequence
late Proterozoic sequence
LINEAMENT
RIVER
LEWOOD
COBAR
0 100 200 km
SCALE
MAJOR DISLOCATIONS
1 Cygnet Fault
2 Palmer Fault
3 Florieton Fault
4 Redan Fault
5 Anabama Fault
6 Torrens Hinge Zone
7 Nundooka Fault
8 Lake Blanche Fault
9 Diamantina River Lineament
10 Un-named gravity lineament
11 Cork Fault
12 Wetherby Structure
13 Burdekin River Fault
14 Palmerville Fault
15 Tamar Fracture System
16 Woomdoo Fault
17 Un-named lineament bounding Stavely-Lake Wintlow Highs
18 Koonenberry Fault
19 Kiewa Fault
20 Woorara Fault
21 Rookery Fault
22 Indi Fault
23 Long Plain Fault
24 Gilmore Fault (part of Gilmore Suture)
25 Gilmore Suture
26 Mooney Mooney Fault System (Part of Coolac-Narromine Suture)
27 Hunter Thrust
28 Mooki Thrust
29 Moonie-Goondiwindi Thrust
30 Leichhart Thrust
31 Burunga-Gogango Overfolded Zone

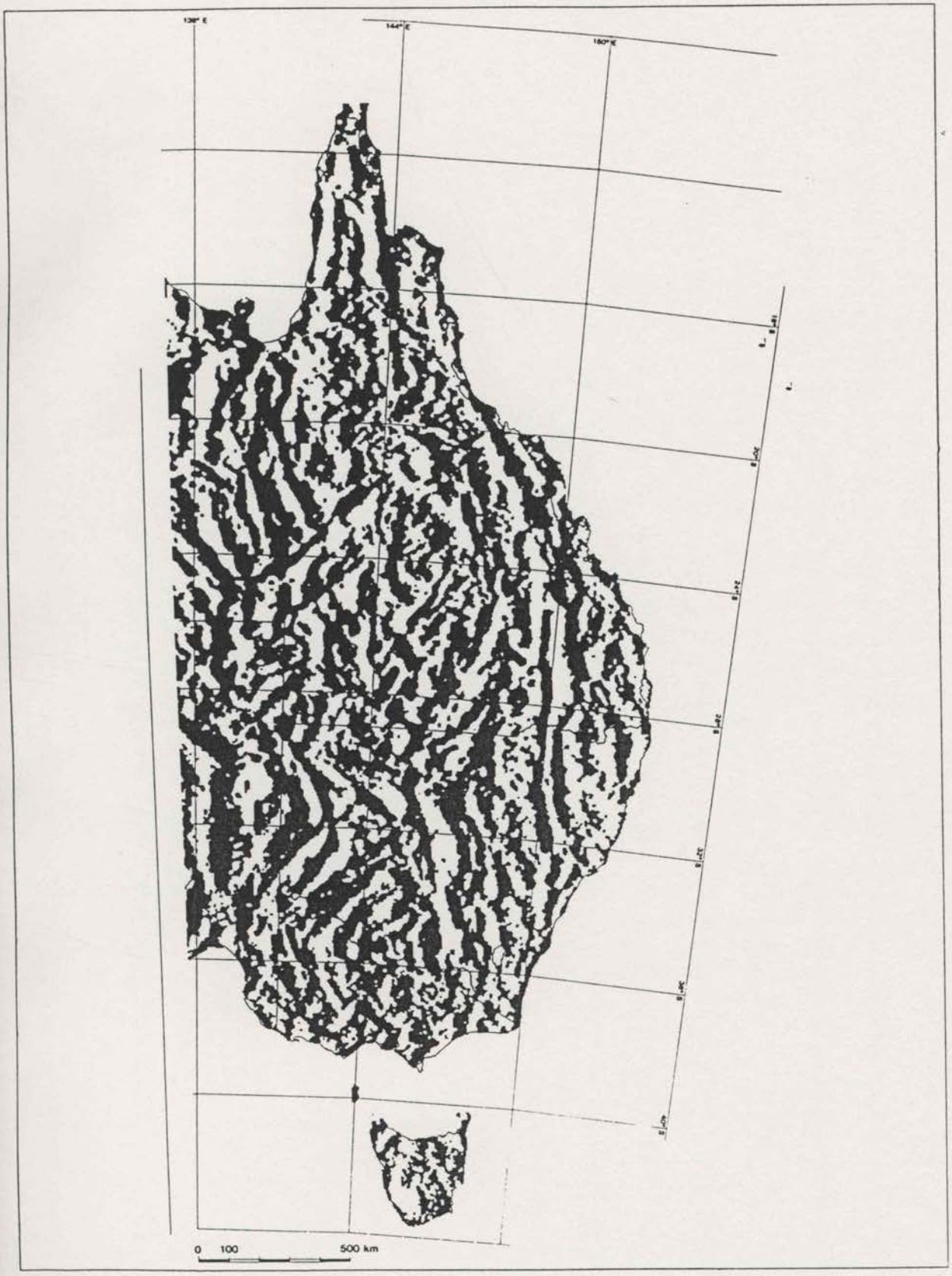

Fig. 2.2 The gravity map of eastern Australia with relatively positive domains shown in black. The position of the Wonominta Block is shown on the overleaf and is in the central western side of the map with two remarkable positive anomalies corresponding to the mafic rocks in the basement and late Proterozoic sequences respectively (Murray *et al.*, 1989).

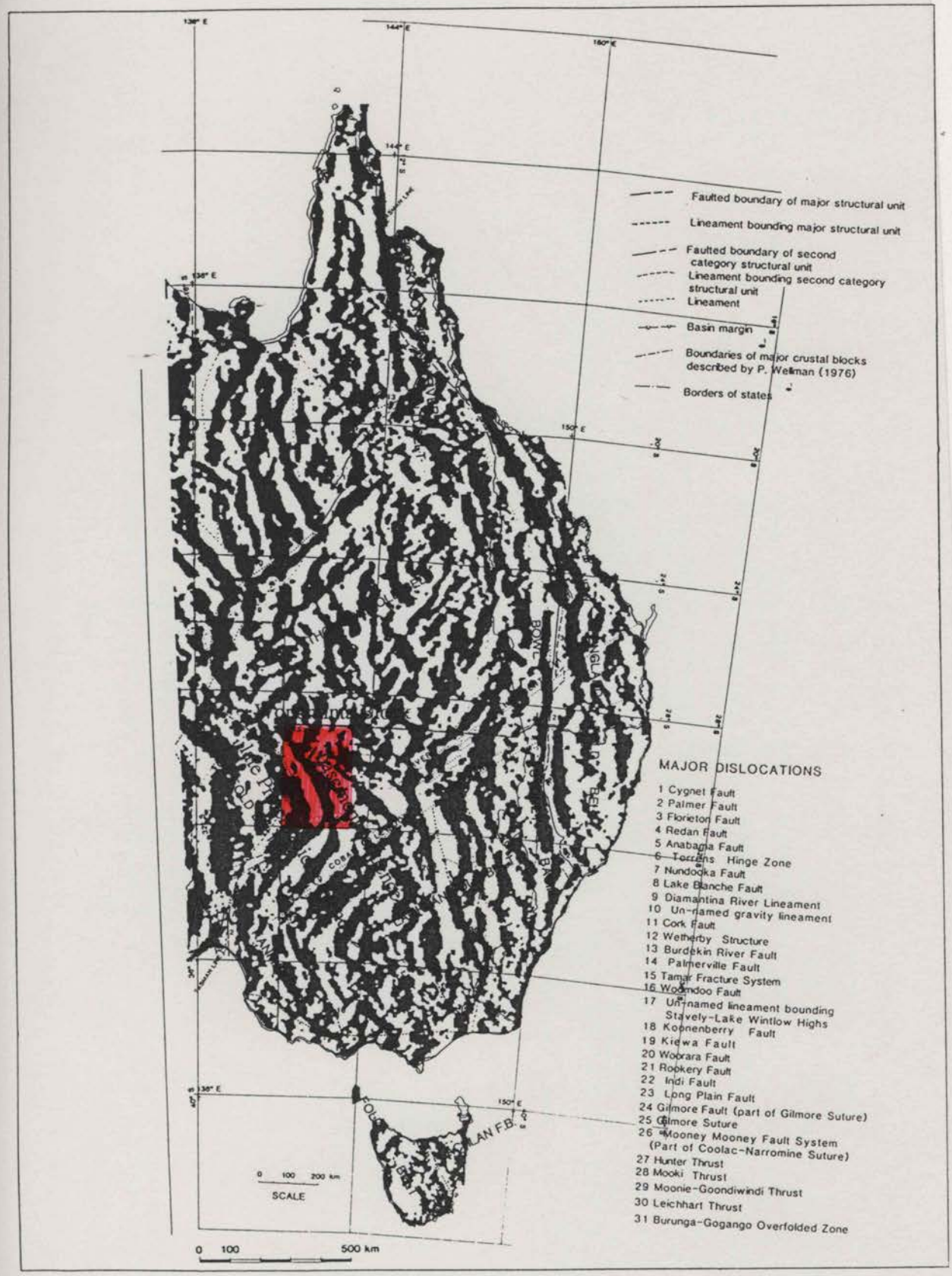

Fig. 2.2 The gravity map of eastern Australia with relatively positive domains shown in black. The position of the Wonominta Block is shown on the overleaf and is in the central western side of the map with two remarkable positive anomalies corresponding to the mafic rocks in the basement and late Proterozoic sequences respectively (Murray *et al.*, 1989).

Table 2.1. Geological Evolution of the Wonominta Beds (Mills, 1992)

Period	Orogenic event/Sequence deposited	Environment
Middle Devonian	Tabberabberan Orogeny	Tight folding with weak cleavage
Late Silurian-Early Devonian	Mt. Daubeny Formation	Fluvial/alluvial fans in intramontane basins. Current from W to SW
Early Silurian(?) (430 Ma)	Benambran Orogeny(?)	Tight folding with weak-moderate cleavage in Kayrunnera Group
Late Cambrian-Ordovician	Mootwingee-Kayrunnera Groups	Fluvial to shallow marine across White Cliffs Shelf. Current from southwest
Middle-Late Cambrian	Delamerian Orogeny (D2?)	Moderate to isoclinal folding with chlorite to biotite zone metamorphism
Early-Middle Cambrian	Gnalta Group	Shallow shelf facies with alkali basalt
Early-Middle Cambrian	Teltawongee beds	Slope and trough greywacke facies
Late Proterozoic	Kara beds	Distal shelf or rift basins with a period of local alkali basalt
Late Proterozoic	Penguin Orogeny	Unconformity at base of Torrowangee Group in Broken Hill Block
Middle Proterozoic	Olarian Orogeny (D1?)	Isoclinal folding in Ponto beds with strong cleavage and biotite to amphibolite zone metamorphism
Early-Middle Proterozoic	Ponto beds	Distal shelf or slope/basin facies with period of felsic and tholeiitic volcanism

After this tectonic event, the Mootwingee and Kayrunnera Groups were deposited in a shelf-like environment (Mills, 1992). The Mootwingee Group occurs mainly in the southern part of the region with prominent outcrops along the Scopes Range. It also occurs on the western side of the Mt. Wright area, having a faulted boundary with the Early Cambrian rocks. In the northern part of the Wonominta Block, the equivalent rocks were defined as the Kayrunnera Group (Wang *et al.*, 1989), which occurs mainly along the Koonenberry Fault north of Wonnaminta Station.

Another major post-Delamerian unit that has been described in some detail is the Mt. Daubeny Formation (Neef *et al.*, 1989). It was observed to be composed of a thick sequence lying unconformably on the basement rocks near Mt. Daubeny (Figure 1.1). Three andesitic flows were recorded in the northern part of the area (the Wertago Andesite). Early Devonian plant fossils have been found in the upper part of the sequence, though the lower part might extend into the Silurian.

The Mt. Daubeny Formation was folded during the Middle Devonian Tabberabberan Orogeny. Afterwards, the Wonominta region was again eroded to a peneplain. The stratigraphic succession in the Wonominta Block is summarised in Table 2.1.

Recent compilations of the history of the Broken Hill Block and its relationship with the Wonominta Block were also given by Stevens (1986) and Stevens *et al* . (1988). These authors discussed the history of the Broken Hill Block in terms of four tectonic stages, Precratonic stage (2300 -1490 Ma), Transitional stage (1490 - 1100 Ma), Epicratonic stage (1100 - 500 Ma), and Cratonic stage (500 Ma - present); while the major development of the Wonominta Block was suggested to be within the Proterozoic era.

2.3. DEFORMATION AND METAMORPHISM

The recent regional mapping revealed at least three stages of deformation that have influenced the basement rocks in the Wonominta Block (Mills, 1992; Table 2.1). The first major regional deformation occurred possibly during the Olarian Orogeny of Middle Proterozoic, and resulted in isoclinal folding in the basement sequence with strong cleavage. The second one occurred during the Delamerian Orogeny in the Middle - Late Cambrian, which resulted in moderate to isoclinal folding, and dominates the present structural setting of the region. Davies (1985) studied some

deformation features of metamorphic rocks in a small area south of Ponto Mine within the basement sequence. The three stages of deformation, as described by him, are summarised in Table 2.2. This work is used as a reference in relevant discussions presented in Chapter Three.

Table 2.2. Deformation characteristics of the basement sequence of the Wonominta Beds, as inferred from a local investigation in the Ponto Mine area (adapted after Davies, 1985)

Deformation	Descriptions
D3	Conjugate kinks, crenulations and fractures. NW/SE sinistral folding
D2	Tight steeply plunging isoclinal folds with 140°/150° axial planes; mega-scale refolding of F_1, wavelength 500 - 1000 m
D1	isoclinal folding; S_1 parallel S_0, now controlled by F_2

The metamorphic characteristics of mafic rocks was investigated by Edwards (1980) in the Mt. Arrowsmith area in the northern part of the Wonominta Block. Assemblages with pumpellyite, epidote, chlorite, prehnite, sphene, stilpnomelane and albite were interpreted to suggest that these rocks had undergone a pumpellyite-prehnite facies metamorphism.

2.4. MAFIC MAGMATISM

Although igneous rocks have been recorded in the Wonominta Block for a long time, most occurrences of the mafic rocks were only described briefly (*e.g.* Kenny, 1934).

While carrying out a geological reconnaissance of the Koonenberry and Tibooburra-Milparinka district, Thomson (1963) recorded an olivine rock six miles east of Nundora and dolerite at Wonnaminta Homestead, apart from similar rocks recorded by Kenny. These rocks were described again by other workers (Edwards, 1979; Edwards & Neef, 1979; Stevens & Raphael, 1985).

During the survey in 1964, Brunker and his team discovered some amygdaloidal basalts in the Nundora area. They suggested that these rocks correlate with the Mt. Arrowsmith volcanic rocks further north. In 1967, Brunker proposed a mafic volcanic belt along the western side of the Wonominta Block based on regional reconnaissance mapping. This was subsequently interpreted (*cf.* Scheibner, 1974 & 1989) to represent parts of an early Cambrian volcanic arc along the continental margin.

Edwards (1980) carried out a detailed study on the Mt. Arrowsmith igneous rocks in the northern part of the Wonominta Block, which are dominantly composed of metamorphosed mafic volcanics, together with lherzolite, amphibole-bearing microgabbro, gabbro, dolerite and syenite. He also analysed some igneous rocks in the Packsaddle, Nundora and Mt. Wright areas along the western side of the region, and in the Ponto Tank, Wonnaminta Homestead, Kayrunnera, Wertago, Grasmere and Bunker Creek areas along the eastern side at a reconnaissance level. This work revealed the alkaline features of the mafic rocks from the western side and tholeiitic features of those from the eastern side of the Wonominta Block.

Some other minor occurrences of magmatic rocks have also been recorded. These include kimberlitic outcrops at Kayrunnera (Stracke *et al*, 1977). A Permian age of emplacement for the diatreme and minimum age of 600 Ma for the formation of the garnet clinopyroxenite inclusions were determined (Stracke *et al.*, 1977; Gleadow & Edwards, 1978). Similar pipe-like outcrops have also be suggested in the southern part of the Koonenberry Range (Wilson, 1984), mainly inferred from geomagnetic analysis.

2.5 TECTONIC MODELLING

Several models have been proposed to explain the tectonic evolution of the Wonominta Block in relation to the reconstruction of eastern Australian continent. In 1972, Scheibner proposed an Early Cambrian marginal basin model. In this reconstruction, the Wonominta Block was suggested to have been separated from the Australian continent by extensional processes that formed a small plate (microcontinent). Between the microplate and the continent, the Bancannia Trough developed as a marginal sea. Similarly, Harrington (1974) proposed a model of an early Cambrian "Nebine Island Arc", which is equivalent to the modern day Japan island arc system (Figure 2.3). In this reconstruction, the Wonominta Block would have been located in

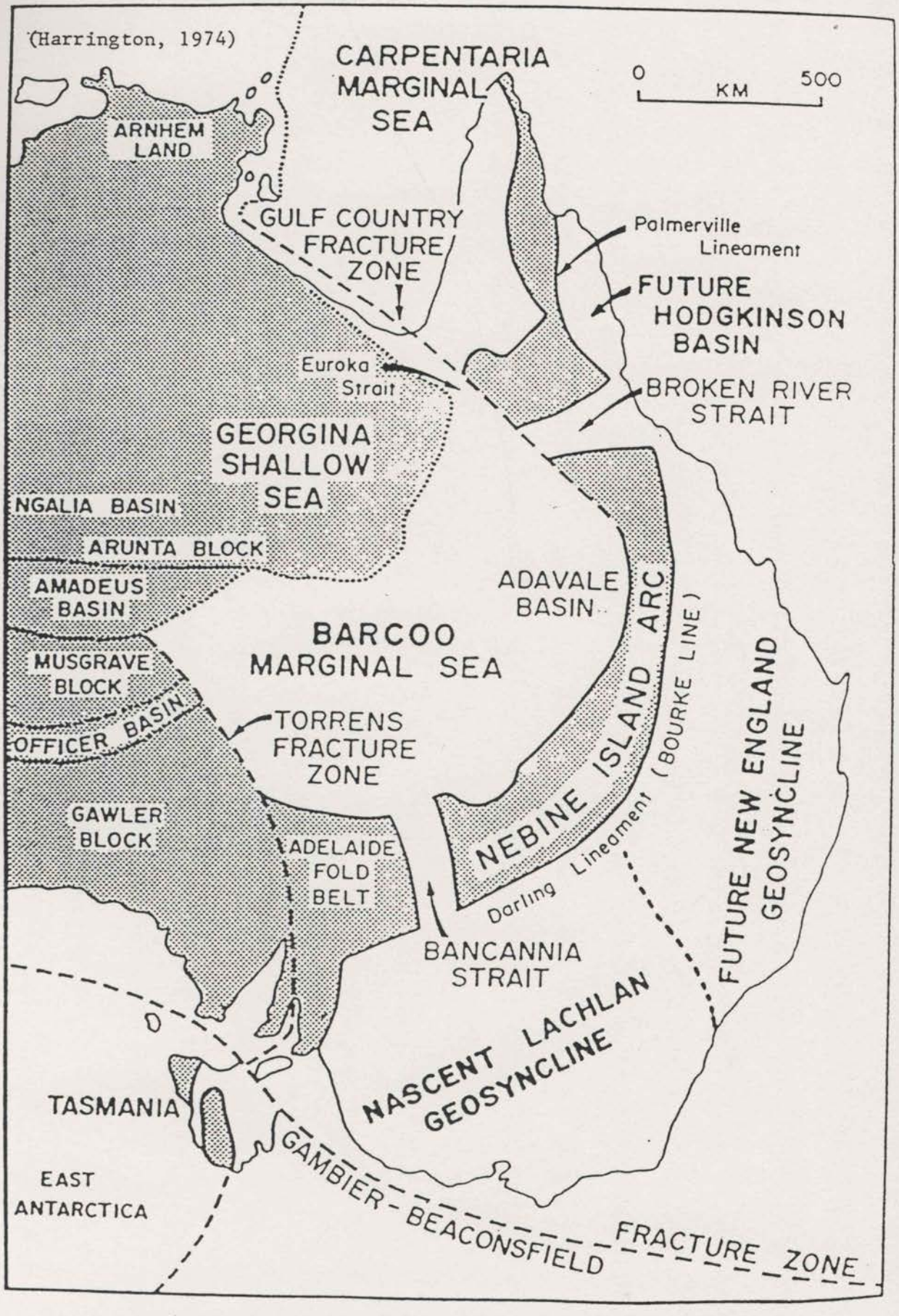

Fig. 2.3 A tectonic reconstruction of eastern Australia in the early days of plate tectonics (after Harrington, 1974). In this model, the Wonominta Block was allocated in the southwestern end of the "Nebine Island Arc", facing the Broken Hill Block (as a part of the Adelaide Fold Belt) across the "Bancannia Strait".

the southern end of the grand arc, facing the Broken Hill Block (as a part of the Adelaide Foldbelt) across the "Bancannia Strait".

In both models, the Wonominta Block would have been formed largely during the Precambrian; while the Bancannia Trough (or Strait) developed during the early Cambrian. However, subsequent work (*e.g.* Webby, 1984) showed that the Bancannia Trough was not formed until the Devonian.

The Wonominta Block has also been suggested to be a part of the cratonic basement to the Phanerozoic Tasman Orogen (*e.g.* Veevers, 1984; Powell *et al.*, 1990). In this context, this region would have been a Precambrian tectonic unit, but a part of the craton instead of small terranes away from the main continent. In other words, the Wonominta Block would have been on the western side of the Tasman Line, a major tectonic boundary in eastern Australia (Figure 2.5).

The Tasman Line was originally defined as a boundary between early Cambrian and Precambrian rocks in northern Queensland (Hill, 1951). In the original proposal, Hill pointed out that the boundary also marks the junction of an early Palaeozoic foldbelt and Precambrian cratonic basement (in other words, the stratigraphic and tectonic boundary would have coincided). The concept of the Tasman Line was developed substantially during the early seventies when the plate tectonic theory was introduced. It is now widely proposed to be the boundary between the Tasman Orogen in eastern Australia and its cratonic basement (*e.g.* Coney *et al.*, 1990)

In more recent models (*e.g.* Figure 2.4), Scheibner (1989, 1991) suggested that the Wonominta Block be part of the Kanmantoo Foldbelt, which itself is the oldest part of the Tasman Orogen. In this proposal, the Tasman Line is located somewhere between the Wonominta and the Broken Hill Blocks, probably along one of the boundaries of the Bancannia Trough; the oldest part of the Wonominta Beds would occur as inliers.

The third school of thought argues against both proposals in that the tectonic boundary should not be placed between the Kanmantoo Foldbelt and the Adelaide Foldbelt in South Australia (*e.g.* Preiss, 1987). It is pointed out that the Kanmantoo Group, which is the major component of the Kanmantoo Foldbelt, is an Early Cambrian stratigraphic extension of the Late Proterozoic Adelaidean rocks. In this context, the Tasman Line has to be used in a modified sense, that is, it would have to be located at the end of Cambrian, coinciding with the Delamerian Orogeny in South Australia.

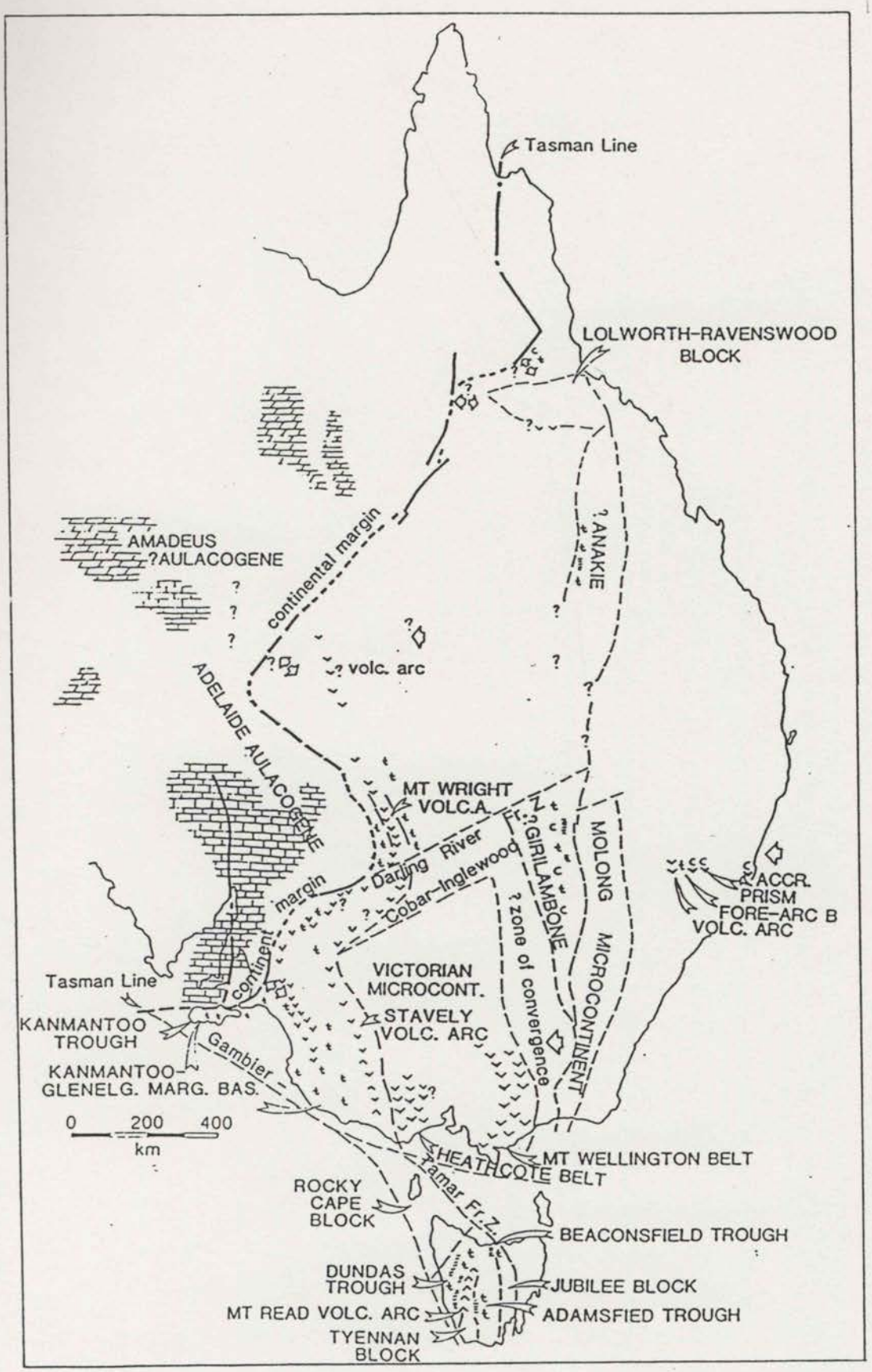

Fig. 2.4. Geology of eastern Australia (Scheibner, 1989). The Mt. Wright Volcanics in the southwestern Wonominta Block was proposed to be a part of the early Cambrian arc correlating southward to the Stavely Volcanic Arc in western Victoria and the Mt. Read Volcanic Arc in Tasmania.

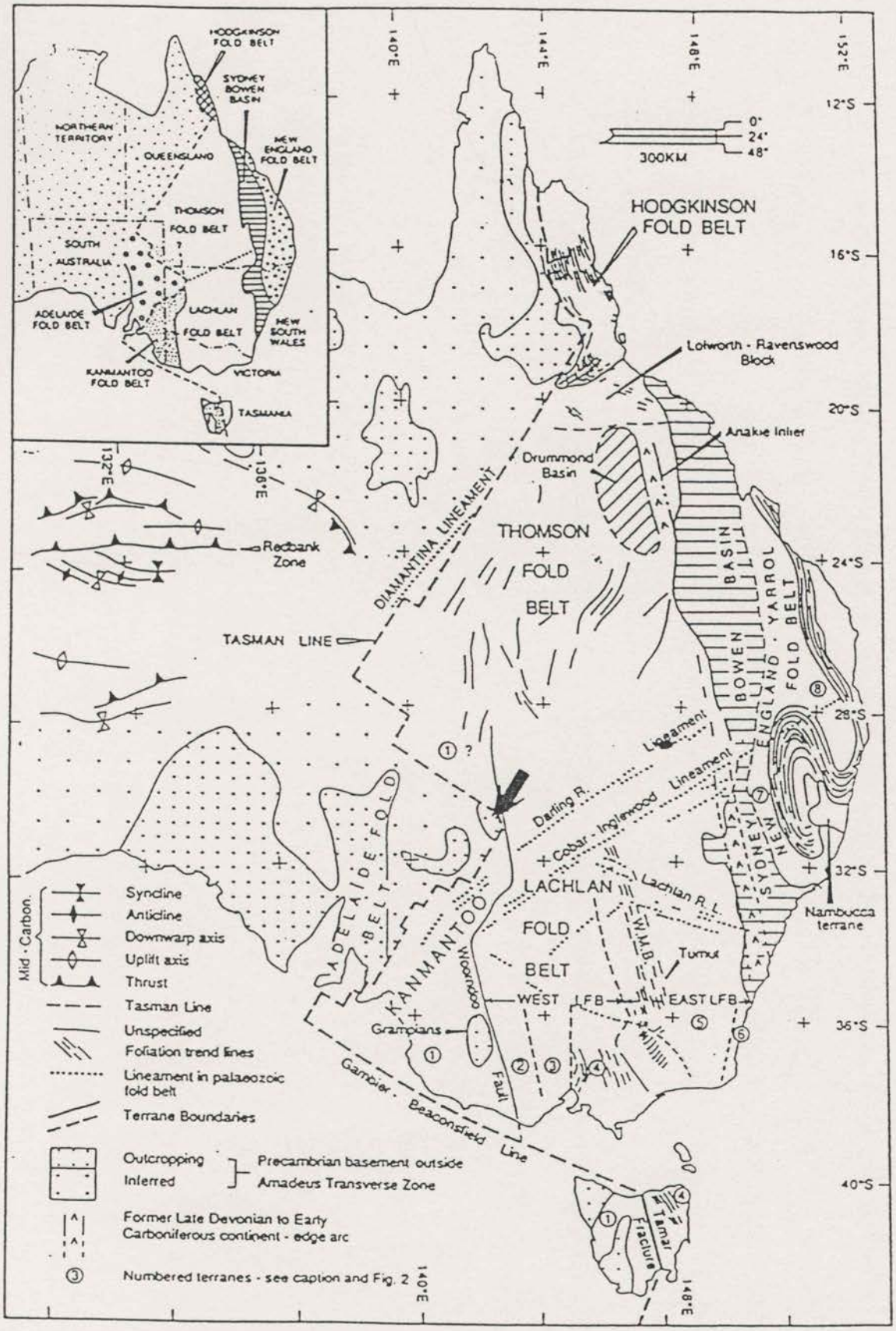

Fig. 2.5 A tectonic modelling of eastern Australia (Powell *et al.*, 1990). In this model, the Wonominta Block, as a whole, is treated as a part of the cratonic basement to the development of the Tasman Foldbelt.

As shown in Table 2.1, the Wonominta Block comprises an older basement (the Ponto beds), younger possible Adelaidean (Kara beds) and Kanmantoo-type rocks (the Teltawongee beds). Therefore, as it stands now, none of the tectonic models presently proposed can explain the unique tectonic development in the Wonominta Block without ignoring some critical facts. On one hand, the recognition of Adelaidean (the Kara beds) and pre-Adelaidean (the Ponto beds) rocks would suggest the region be part of the "basement"; on the other hand, the significant exposure of Kanmantoo-type turbidite sequences would suggest the region be part of the "Kanmantoo Foldbelt. In this sense, the Wonominta Block may be one of the key areas in understanding the evolution of the Australian continent, and possibly the evolution of Gondwana.

2.6. MINERALISATION

Many mining companies have explored the region (Table 2.3). Indeed, some small, Cu-rich ore bodies at Ponto, Koonenberry Gap, Wertago and Grasmere were mined early in this century.

The Ponto Mine is located on Morden Station, 24 km northwest of the Wonnaminta Homestead and approximately 3 km northwest of the northern prolongation of Koonenberry Mountain (Figure 1.1). It was mined in 1907, "A shaft was sunk 102 feet and a drive 50 feet long was put in on the 90 foot level, 50 tons of copper ore raised from this lode yielded 18.5% Cu" (Kenny, 1934, p. 109). No more mining activities have been recorded. According to more recent explorationists (Thomson & King, 1952; Lennon, 1967; Davy, 1972), the old workings did not reach the primary ore zone; therefore it is reasonable to infer more mineral reserve at deeper levels.

As is mentioned above, BP Minerals Australia was the last major company to carry out some exploration to evaluate the potential of lead-zinc and/or copper mineralisation in the central-northern part of the Wonominta Block. This work involved field mapping, aeromagnetic survey, percussion drilling and some geochemistry (Penny, 1985). The significance of BIFs, as an indicator of Broken Hill-type exhalative mineralisation (particularly the manganese gossan), was studied. Unfortunately, nothing of economic value was discovered. At the moment, CRAE is carrying out another major exploration project, mainly in the southern part of the Wonominta Block (Wilandra Inlier). Some lead isotope studies in this project (Chapter Nine) were done in collaboration with these activities.

company	year	area(s)	techniques	conclusions	references
Zinc Corporation	1952	Wertago	radioactivity; measurement	a little response around mine dump	Thomson & King, 1952
Kennecot Exploration Australia Pty. Ltd.	1966	Ponto	stream sediment sampling; aeromagnetics I. P.	No substantial aeromagnetic anomaly; no proximal geochemical anomaly; low but definite metal factor and resistivity anomaly.	Lennon, 1967
CRA	1971	Nuntherungie	stream sediment samping; soil auger sampling.	delineation of four major anomalies of Cu, Pb, Zn, Ni, Co, Cr and As.	Johnson & Scott, 1971
Copper & Association Minerals Exploration	1972	Ponto	mapping; magnetics; geochemistry; & in-situ leach trial	no significant anomaly located	Davy, 1972
ESSO	1976	Ponto	Barringer input E.M. survey	no significant anomaly located	Lewis, 1976
AMOCO	1981	Ponto	mapping; grab sampling; geochemistry; magnetics & gravity.	a magnetic high parallel the Ponto Gossan (400 gamma); low gravity over old mine; 4.46% Cu; 33.5 ppm Ag.	Leahey, 1981 & 1982
BP Minerals	1985	Wertago Koonenberry Wonnaminta Nuntherungie; Milpa	mapping; aeromagnetics; percussion drilling and lithogeochemistry	BIF, as an indicator of exhalative mineralisation was envisaged.	Penny, 1985

Table 2.3 Summary of modern company exploration. (revised from Davies, 1985)

Chapter 3

Mafic Rocks in the Wonominta Block: Field Occurrences & Petrographic Characteristics

3.1. INTRODUCTION

Field work was carried out in the context of the regional structure of Mills (1992). The aim was to observe the field relationship of various mafic rocks and to select representative samples for analytical studies.

Eleven local areas were selected over the entire stratigraphic range of the Wonominta Beds (Mills, 1992). These areas were selected because of the relatively good exposure of mafic rocks within their various geological settings . The location of each area and its age/stratigraphic positions is presented in Table 3.1 and on the over-leaf of Figure 1.1.

Table 3.1. Selected Areas for Field Work in the Wonominta Block

Sequence	central-northern region	southern region
Younger rocks	**Wonnaminta HS** (lamprophyre) (Wonnaminta sheet 7336)	
Cambrian	**Kayrunnera** (gabbro) (Kayrunnera sheet 7436)	**Mt. Wright area** (Nuchea sheet 7335) **Comarto area** (Bunda sheet 7434) **Bilpa** (conglomerate) (Topar sheet 7334)
late Proterozoic	**Packsaddle area** (Cobham Lake sheet 7337) **Nundora area** (Wonnaminta sheet 7336)	
Basement	Ponto Mine Inlier	Wilandra Inlier
	Ponto Mine area (Cobham Lake sheet 7337)* **Boshy Tank area** (Wonnaminta sheet 7336)	**Wilandra area** (Grasmere sheet 7435) **Cymbric Vale area** (Nuchea sheet 7335) **Bilpa area** (metabasite)

* 1:100 000 series of orthophotomaps, Central Mapping Authority of New South Wales.

3.1.1. Symbols for the Minerals in This Study

There are about thirty minerals observed in various rocks studied in the present project, and abbreviated symbols for some of the frequently used names are listed as follows:

Ab. Albite,
Ac. Actinolite,
Am. Amphibole,
Cb. Carbonate, normally calcite,
Ch. Chlorite,
Cpx Clinopyroxene,
Cz. Clinozoisite,
Ep. Epidote,
Fd. Feldspar
Hb. Hornblende,
Kf. Potassium feldspar,
Mt. Magnetite,
Mu. Muscovite,
Pl. Plagioclase,
Pr. Prehnite,
Pm. Pumpellyite,
Py. Pyroxene, normally clinopyroxene thus synonymous with Cpx,
Sp. Sphene
Qz. Quartz, and
Tr. Tremolite.

3.1.2. Petrography of Representative Metamorphosed Mafic Rocks

Metamorphosed mafic rocks studied in this project include both extrusive and intrusive varieties. The intrusive rocks include three types of metadolerites. The meta-volcanic rocks have been named spilite (Vallance, 1969 & 1974), metabasite (Cho & Liou, 1986) and metabasalt (Morris, 1988). In this study, metabasite refers to mafic extrusives without relic pyroxene, whereas metabasalt refers to those with relic pyroxene. Cleaved and massive are the two main varieties of the meta-volcanic rocks based on structural character. Other nomenclature is based Joplin (1968 &1971) and Williams *et al.* (1982).

Cleaved metabasite This type of rock is usually greyish or yellowish green with generally a fine-grained texture and distinctive foliated structure. Due to intense deformation, the rock displays well developed cleavages/foliations similar to those of surrounding phyllites (*e.g.* Plate 3.1.1). Microscopically, no relic phases can be observed; the most common assemblage is Ab+Ch±Ac±Ep±Mt±Pm. The first three phases usually define the foliation, separated by granoblastic epidote, magnetite and/or pumpellyite.

When the cleaved structure becomes transitional to a schistosity, the rock may be named **mafic schist**. The difference between cleaved metabasites and mafic schists is largely based on grain sizes with the latter showing a coarser-grained texture.

Massive metabasite/metabasalt These rocks have identical colour to the cleaved species, but are generally less deformed with various structures from pillow lavas to massive flows (Plates 3.1.3, 3,1.4, 3.1.11 & 3.1.12). Under the microscope, these samples exhibit various mineral assemblages which have been used to determine the metamorphic grades and facies. Most of the secondary minerals, however, occur as alteration products replacing primary magmatic phases.

Metadolerite IA The rock, normally green-yellow to light brown, contains relic pyroxene and displays a massive structure. In most samples, primary ophitic textures are largely preserved but alteration of magmatic phases is extensive. The common mineral phases include relic pyroxene (normally replaced by amphibole and chlorite), and minor relic plagioclase (replaced by albite) (Plate 3.2.10). Altered groundmass phases include epidote, chlorite, actinolite and pumpellyite together with albite, magnetite, carbonate and quartz. **Metadolerite IB** refers particularly to those found in the late Proterozoic sequence at Packsaddle, containing kaersutite as a relic phase; relic pyroxene may or may not be present in this rock (Plate 3.2.12). In the following texts, Metadolerite (I) will normally refer to type IA.

Metadolerite II This term refers to those metadolerites without relic pyroxene with all other characters identical to **Metadolerite (I)**.

Metadolerite III This is a metamorphosed mafic rock with distinctive porphyritic texture in hand-specimen and occurs as small outcrops in the basement sequence. The rock is generally massive, light greenish grey and show little

deformation. Under the microscope (Plate 3.2.13), no relic magmatic minerals are recognised. "Phenocrysts" of what appeared to be plagioclase in hand-specimen are composed of clinozoisite, epidote, albite and chlorite. One of the major features of this rock apart from the porphyritic texture is the presence of clinozoisite, with a xenoblastic granular texture and a distinctive anomalous ink-blue interference colour.

Metadolerites may have two kinds of occurrence in the field, small isolated intrusions and dykes within the volcanic successions. Those within the volcanic units generally have a sub-vertical dip with width no greater than two metres. Small intrusions usually have low but positive topographic relief with rounded outcrops in sedimentary or volcanic units; however, the boundaries are mostly obscured by alluvials.

Amphibolite refers to the metamorphic rock composed of hornblende, plagioclase and epidote (Plate 3.2.9). This rock was observed only in the basement sequence at Cymbric Vale in the Wilandra Inlier. It is medium to coarse grained and displays distinctive bluish-green colour; most of the rocks are massive in structure but some occurring at the margins of the outcrops suffered more intensive deformation. Under the microscope, hornblende is characterised by a blue-green pleochroism and highly refractive prisms; plagioclase is normally oligoclase to andesine in composition. The foliation is defined by both amphibole and plagioclase.

3.1.3. Common Phases of Metamorphic and Relic Magmatic Minerals

Amphiboles, observed in both metamorphosed intrusive and extrusive mafic rocks, include actinolite (yellowish green), actinolite-hornblende (green, may be with weak yellowish or greenish pleochroism) and hornblende (distinctive bluish green)[1]. Those in the matrix of the rocks (type I) normally display a needle-like or fibrous texture and light green colour. Those pseudomorphs after pyroxene phenocrysts (type II) are normally coarse-grained tabular with deeper green colours and green-yellow or green-blue pleochroism. Most of these amphiboles coexist with albite, epidote, chlorite and sometimes pumpellyite, showing characteristic assemblages of greenschist and/or prehnite-pumpellyite facies. A distinctive type of metamorphic amphibole is observed in the Cymbric Vale amphibolite in the basement sequence, with small slender prismatic crystals and bluish green colour.

---

[1] Z axial colours

The third type of amphibole occurs as relic magmatic phases in xenoliths in the Late Proterozoic sequence in the Packsaddle area and in post-D_3 lamprophyres near the Wonnaminta Homestead and in the Boshy Tank area. These idiomorphic minerals are of kaersutite composition, showing distinctive brownish colour and pleochroism.

Chlorite is a ubiquitous metamorphic phase and occurs in the groundmass, as well as in amygdales in various metamorphosed mafic rocks. The mineral has medium refractive index and is normally green or yellow in colour, all show distinctively low anomalous interference colours. In amygdales, the mineral exhibits good crystal form or a radiating texture. In the matrix, it is usually xenoblastic. Chlorite in matrix often is the one of the main phases defining the foliation. It can also occur as an alteration phase after primary pyroxene, though as a less significant component than amphibole.

Calc-silicates include epidote, clinozoisite, pumpellyite and prehnite in this study. Among these phases, epidote is ubiquitous; clinozoisite is a characteristic component in metadolerite III and may also occur with epidote in many other rocks as a minor component; pumpellyite has been recognised in samples from Comarto, Mt. Wright and Wilandra areas in the southern Wonominta Block; and prehnite occurs as a minor component in samples from the Cambrian Comarto sequence.

The common occurrence of these minerals is as patches/aggregates or discrete small grains. Microscopically, identification of these minerals may be difficult, though there are some distinctive features for each mineral, namely that epidote is characterised by its very high refractive index and birefringence; that clinozoisite is identified by its ink-blue interference colour; that pumpellyite exhibits low to medium birefringence; and that prehnite has low to medium relief and birefringence and is mostly colourless or with saussuritised texture. Electron microprobe analyses (*cf.* Chapter Four) also help to identify these minerals, particularly between epidote, pumpellyite and prehnite. Chemically, epidote contains no MgO, which is a minor component in pumpellyite; both minerals have much higher Fe contents than prehnite

Albite is the most common species of the feldspar group. This mineral usually occurs as a mosaic of xenoblastic grains, or pseudomorphs after primary plagioclase laths. Twinning is normally not developed, thus different from quartz mainly in its lower refractive index and saussuritised appearance.

Pyroxene. All relic pyroxenes observed in this study are clinopyroxene, normally displaying a pale yellow colour (some colourless), high refractive index and

tabular form; cleavages in the crystals are not well-developed, but fractures occur extensively. Along fractures and around the edge of crystals, actinolite, chlorite and sometimes calcite occur.

3.1.4. Identifying Products of Metamorphism and Metasomatism

Mineral phases recognised microscopically are classified into three categories, relic igneous, metamorphic (burial (*sensu lato*) and regional) and metasomatic.

Relic Magmatic Phases

The common relic magmatic phases in the mafic rocks are clinopyroxene and plagioclase, which generally occur as phenocrysts. Petrographic features of the relic pyroxene have been described above. Relic plagioclase tends to display well-developed and complex twinning, in contrast with the rare simple twinning in metamorphic plagioclase (typically albite in composition except those in amphibolite).

Burial Metamorphic Phases

The burial metamorphic products refer to those which replace the primary phases while preserving the primary textures. The common products of this kind include amphibole and chlorite after pyroxene, albite after plagioclase, and chlorite, epidote, amphibole, albite, pumpellyite, quartz and carbonate in primary "groundmass" and in "amygdales". However, whether the secondary phases in seemingly undeformed rocks all represent the products of alteration is questionable (see below).

Regional Metamorphic Phases

There are two types of "regional metamorphic products": the first one includes those defining the foliation; the second types refers to those filling the fractures of primary minerals and veinlets in the rocks. These phases are generally believed to have crystallised during deformation, either compressional or decompressional.

In the following presentations, the number of samples clearly representing regional metamorphism are less than that of burial metamorphism. This may be caused in part by selective sampling because highly deformed rocks usually do not have good

exposure for sample selection; it is also due to the fact that samples of burial metamorphic products show variety of mineral assemblages, whereas those of "regional products" are mineralogically more uniform.

In some cases, the burial assemblages are observed to have been deformed, whereby the foliations overprint the relic magmatic textures. This provides some evidence that burial metamorphism occurred prior to regional metamorphic processes, as would have been expected. But this also adds to the difficulty of identifying products of different secondary processes. In the field, even the least deformed massive mafic rocks are surrounded by highly deformed metasedimentary units (in particular phyllites) and this suggests stress partitioning could have occurred during deformation. In other words, the undeformed rocks could have also been influenced by the regional metamorphism. It is thus likely that some of the "alteration" phases may have actually been products of regional metamorphism though they do not display distinctive textures. This problem is relevant to the reconstruction of P-T-t paths of metamorphic histories, as presented in the next chapter.

Metasomatic Products.

Metasomatic processes are generally considered as exchanges between a system and its environment, resulting in changes of both chemical compositions and mineral assemblages. In this study, products that can be clearly attributed to a metasomatic origin include white micas in some mafic rocks; and those minerals (nepheline, aegirine, natrolite and alkaline feldspars) in nundorite within the Late Proterozoic sequence at Nundora.

In the following discussions, however, white micas are not separated from those minerals of metamorphic origin and are described according to occurrence, that is either as burial or regional products. Discussion of mineral chemistry of metasomatic products, on the other hand, are separated from those of metamorphic ones, both presented in Chapter Four.

3.2. THE BASEMENT SEQUENCE

3.2.1. Mafic rocks in the Ponto Mine area

The Ponto Mine area is located in the northeastern corner of the Wonominta Block, on the western side of the Koonenberry Fault (Figure 1.1), and has the best exposure of the basement sequence in this region. Field data are compiled in Map One.

The studied area is bounded by the Koonenberry Fault in the east and the outcrops disappear under alluvium on the western side. A strike fault, identified in the northeastern part of the area (grid 6154E, 6350N), seems to limit the occurrence of mafic rocks as there are no major outcrops further to the east. The rocks in this area have experienced three phases of deformation (see Chapter 2), and the major one is D_2, which produced in this area close-spaced cleavage and bedding, trending between 120° to 145° and dipping vertically in all rock units (Map One). The strong deformation resulted in flow-like structures for most of the meta-volcanic and meta-sedimentary (phyllitic) units. Detailed observations revealed that many lithological boundaries are actually faulted (*e.g.* Plates 3.1.1 and 3.1.2). Because of the intense deformation and the destruction of primary structures, facing directions could not be recognised; thus, establishment of a possible stratigraphic succession for the basement rocks in this local area is not possible.

Meta-greywacke, phyllite, schist and fine-grained quartzite (chert) crop out in this area. The first two are the major lithological units but their boundaries were mostly arbitrarily defined due to gradational contacts. Schists were observed only in a small area next to the Belt A volcanic association (grid 6180E, 6320N). Within the mafic rocks, carbonates are common in the form of ellipsoidal aggregates or veins. By contrast, layers of felsic rocks (quartzite) occur discontinuously in the meta-greywacke.

The ironstones are also of interest given their possible affinity to banded iron formation (BIF) (Penny, 1985). Field investigation revealed that these rocks, being dark red in colour and of solid appearance, tend to occur along strike of mafic volcanic rocks as ellipsoids and veins, though minor occurrences are also found in phyllite (Plates 3.1.6 & 3.1.7). They never extend further than about ten metres and obviously do not constitute individual stratigraphic units. Therefore, this type of rocks is probably not BIF in its normal sense.

Eight mafic volcanic units, up to 40 metres in width, were recognised in this area and

have been named Belt A to Belt H from east to west . None of them extends more than 3 km along the strike and they either disappear beneath alluvium or are cut off by faults. Texturally, five of them (A, C, D, E and H) are largely massive and the others are cleaved. In the field, however, gradation from cleaved to less cleaved (massive) rocks was observed in all eight belts. In Belt H, pillow-lavas were observed. Despite the multiple deformation suffered by these rocks, pillow structures are clearly visible with pillow lengths up to 30 cm (Plate 3.1.3).

The mineralogical compositions of representative mafic rocks from this area are summarised in Table 3.2, which also presents the selection of samples for geochemical studies. Most of the samples preserve relic magmatic textures, which are used as a framework for the presentation. Relic pyroxene (mostly replaced by actinolite-hornblende) and plagioclase (replaced by albite) are observed in both intrusive and extrusive rocks mostly as "phenocrysts", though some of the volcanic species have none of them, but consist of only "matrix" components (they may thus represent former aphyric basalts with little or no phenocrysts). Occasionally, amygdales can be observed. Those regarded as regional metamorphic assemblages occur in samples with no recognisable relic texture (mainly cleaved metabasite), or filling fractures.

Table 3.2 shows that the "matrix" of these mafic samples contains most metamorphic phases, which can be generalised as four distinctive types of alterations: Ep, Ab, Ac-Hb+Ep and Cb+Mu. The eight volcanic units can then be summarised in these four alteration types as shown in Table 3.3. From Table 3.3, it is clear that the rocks are of the same grade. Since in many samples it is observed that chlorite decreases drastically when actinolite appears, it is suggested these rocks have in general experienced upper greenschist facies metamorphism (Liou *et al.*, 1987).

Table 3.2. Petrography of various mafic rocks from the Ponto Mine area

Sample	Species	Structure	Belt	Relic	Alteration assemblage	Regional metamorphic assemblage
752106	Metadolerite II	Dyke-like, ophitic	A		[Act-Hb](40)+[Ab+Qz](40)+[Ep+Sp](15)	[Act+Ep+Qz+Cb±Ch](5)
752803	Metabasite	Massive	A		[]+[Ep+Qz+Ab](85)	[Qz+Ch](15)
752804	Metabasite	Massive	A		[]+[Ep+Qz+Ch+Ab](85)	[Qz+Cb](15)
753001	***Metabasite***	Massive	A		[]+[]+[Ep+Qz+Ch+Mt](50)	[Ep+Qz+Cz+Ch+Ac+Ab+Sp](50)
753002	Metabasalt	Massive	A		[]+[]+[Ep(60)+Qz(s)(40)]	
753106	**Metadolerite II**	Dyke-like, ophitic	A		[Act-Hb](50)+[Ab+Qz](20)+[Ep+Sp](15)	[Act+Ep+Qz+Cb±Ch](15)
760501	**Metabasite**	Cleaved	A		-	Ch(35)+Ab(35)+Sp(15)+Ep(10)+Cb(5)
753003	**Metabasite**	Massive	B		[]+[]+[Cb+Ab+Ch+Qz](90)	[Ch+Ab+Mt](10)
752304	**Metabasite**	Massive	C		[]+[]+[Ep(60)+Qz(s)(30)](90)	[Cb+Mu](10)
752305	Metabasite	Massive	C		[]+[Ab+Ep+Cb+Qz](80)	[Cb+Ch+Qz+Ep](20)
752810	**Metabasite**	Massive	C		[]+[]+[Ab+Mt+Ch+Cb+Qz](80)	[Ch+Ep+Qz](20)
752811	Metabasite	Massive	C		[]+[]+[Ab+Mt+Ch+Cb+Qz](80)	[Cb+Ch+Ep+Qz](20)
753007	**Metabasite**	Massive	C		[]+[]+[Ab+Mt+Ch](90)+[Cb+Ep](5)	[Ep](5)
753008	Metabasite	Massive	C		[]+[]+[Ab+Ch+Mt+Ep](80)+[Ep](10)	[Ep+Cb+Qz](10)
752808	**Metabasite**	Massive	D		[]+[Ab+Ac+Ep](80)	[Ac+Qz+Cb](20)
752809	Metabasite	Cleaved, 'microcrystaline'	D		[]+[]+[Ep+Ab+Qz](70)	[Qz+Ep+Ac+Cb](30)
752805	**Metabasite**	Massive	E		[]+[Ab](5)+[Ac+Ep+Qz+Mt](60)	[Ac+Ep+Ch+Qz](35)
752806	Metabasite	Massive	E		[]+[]+Ep+[Qz(s)](70)	[Ep+Ch+Mu+Cb+Qz](30)
752101	Metabasite	Cleaved	E	Pl	[]+[Ab](15)+[Mt+Ch+Ep](60)+[Ep+Ch+Qz+Cb+Sp](25)	
753013	Metabasite	Massive	E		[]+[]+[Ab+Mt+Ch](85)	[Ep+Cb](15)
753014	Metabasite	Massive	E		[]+[]+[Ab+Mt+Ch](80)	[Ep+Cb](20)
752902	Metabasite	Massive	F		[]+[]+[Ab+Ch+Ep](85)	[Cb](15)
752905	Metabasite	Massive	F		[]+[]+[Ab+Mt±Ch](70)+[Cb+Ep](5)	[Cb+Qz+Ep+Ch](25)
752907	Metabasite	Massive	F		[]+[]+[Ab+Ch+Mt](80)	[Cb+Ep](20)
752908	Metabasite	Massive	F		[]+[]+[Ab+Mt+Ch+Qz(d)+Ac](75)	[Ch+Cb+Qz+Ep](25)
752910	Metadolerite II	Dyke-like, ophitic	F	Pl	[Ac-Hb](40)+[Ab](20)+[Ep+Ab](35)	[Ac(yellow)](5)

Sample	Species	Structure	Belt	Relic	Alteration assemblage	Regional metamorphic assemblage
753010	Metadolerite II	Dyke-like, ophitic	F	Pl	[]+[]+Ab+Ch+Mt±Ep(yellow)](70)	[Cb+Qz](30)
760701	**Metabasite**	Massive	F		[]+[Ab](15)+[Ab+Ch+Sp±Ac±Ep](75)	[Cb](10)
760703	Metabasite	Massive	F		[]+[]+[Ep(30)+Cb(30)+Ch(20)+Qz(20)	
760102	**Metabasite**	Massive	G		[]+[]+[Ep+Qz+Cz](70)	[Ch+Mu±Ac](30)
760104	**Metabasite**	Massive	G		[]+[Cb]+[Cb+Mu+Ep+Mt](60)+[Cb+Ac](40)	
760201	**Metabasite**	Massive	G		[]+[]+[Ab+Ch+Mt](80)	[Cb+Qz+Ac](20)
760301	Metadolerite II	Dyke-like, ophitic	G		[Ac-Hb](40)+[Ab](35)+[Ab+Mt+Ep+Sp](20)	[Cb+Qz+Ch](5)
752201	Metabasite	Pillow lava	H		[]+[]+[Ab+Ch+Ep](90)	[Cb+Qz+Ep+Ac(yellow)+Ch](10)
752202	Metabasite	Pillow lava	H		[]+[]+[Ab+Ep+Ch](85)	[Ep+Qz±Ac](15)
752203	**Metabasite**	Pillow lava	H		[]+[]+[Ab+Ch+Ep+Cb](80)	[Ch+Qz+Mu+Cb](20)
752204	Metabasite	Pillow lava	H		[]+[]+[Cb+Ab+Ch+Ep](70)	[Cb+Qz+Mu+Ch](30)
752205	Metabasite	Pillow lava	H		[]+[]+[Cb+Ab+Ch+Ep](80)	[Cb+Qz+Mu+Ch](20)
752109	Metadolerite I	coarse grained, ophitic	M1	Py	[Ac](40)+[Ab+Cb](40)+[Ep+Mt](5)	[(Ac-Hb)+Ch](5)
752110	***Metadolerite I***	coarse grained, ophitic	M1	Py	[Ac](40)+[Ab+Ch+Ac](40)+[Ep+Cz+Sp+Mt](20)	
752111	Metadolerite I	medium grained, ophitic	M1	Py	[Ac](40)+[Ab+Ch+Ac](40)+Ep+[Cz+Sp](40)	
752001	***Metadolerite II***	Intrusive, ophitic	M2	Pl	[Ac-Hb](40)+[Ab](40)+[Cz+Ep+Ch+Qz](10)	[Ep-Ac](10)
752501	Metadolerite II	*ibid*	M2	Pl	[Ac-Hb](45)+[Ab](40)+[Ep+Sp+Mt](15)	
752301	Metadolerite II	Rim of intrusion; fine	M2		[Ac+Ep](35)+[Ab+Ac+Cz+Ep](55)+[Ch](15)	[Ac](5)
752302	***Metadolerite II***	Central intrusion; coarse	M2		[Ac](40)+[Ab+Ep+Cz](50)+[Ch+Ep+Ac](10)	
760402	***Metadolerite III***	porphyritic	M3		[]+[Ep+Ac+Ab+Cz](45)+[Ac+Ep+Cz+Mu](55)	

Key: pseudomorphous alteration after [Py]+[Pl]+[matrix]+[amygdale,optional]; (empty bracket means no mineral)

e.g. {[]+[Ep+Ac+Ab+Cz](45)+[Ac+Ep+Cz+Mu](55)} for 760402 indicates no relic pyroxene recognised nor any phases replacing it; Pl (phynocryst) replaced by (Ep+Ac+Ab+Cz); and the matrix replaced by (Ac+Ep+Cz+Mu)

Note: Minerals are presented in order of abundance; numbers in small brackets are percentages of each "component" or mineral phase (±5%

High lighted samples are those that were selected for geochemical analysis; those shown in italics were used in isotope analysis;

(s): products of static crystallisation; (d): of dynamic crystallisation;

Ponto Mine is located in Belt G.

Table 3.3. Alteration Characteristics of the Ponto Mine Mafic Rocks

Cambrian			
A small intrusive body observed:			
	Metadolerite I	Ac-Hb+Ab+Ch+Ep	(Plate 3.2.9)
Basement			
Volcanics, all metabasite:			
Belt A	Ep type	Ep+Qz+Ch	(Plate 3.2.1)
Belt B	Ab type	Ab+Ch+Cb+Ep+Mt+Qz	
Belt C	Ab type	Ab+Mt+Ch+Ep+Cb+Qz	(Plate 3.2.4)
Belt D	Ac+Ep type	Ac+Ep+Ab+Mt+Cb+Qz	
Belt E	Ac+Ep type	Ac+Ep+Ab+Mt+Cb+Qz	(Plate 3.2.2)
Belt F	Ab type	Ab+Ch+Ep	
Belt G	Ep type	Ep+Ch+Cb	
	Cb+Mu type	Cb+Mu+Ch+Mt±Ep (locally)	(Plate 3.2.5)
Belt H	Ab type	Ab+Ch+Ep+Sp	(Plate 3.2.3)
Intrusive			
	Metadolerite II	Ab+Ac+Ep+Ch	(Plate 3.2.10)
	Metadolerite III	Cz+Ep+Ab+Mt±Ac	(Plate 3.2.12)

3.2.2. Mafic rocks in the Boshy Tank area

Mafic rocks occurring in the Boshy Tank area are located at the same structural position as those of Ponto Mine, immediately to the west of the Koonenberry Fault, but further south in the basement sequence (Figure 1.1). Younger sequences of early Cambrian sandstones occur both on the western and eastern sides of the basement sequence (Map Two). Several cross-strike traverses indicated that the stratigraphic repetition is sufficiently complicated to preclude correlation of geologic boundaries between traverses. It was only by way of along-strike tracing that the distribution of mafic rocks could be mapped adequately. A comprehensive mapping of metasedimentary units is beyond the scope of the present project; nonetheless, these basement meta-sedimentary rocks appear to be identical to those observed at Ponto Mine, *i.e.*, closely-spaced cleavages (parallel to bedding) with vertical dips and dominant strikes between 120° and 145°. The plunge of F_2 fold axes is also sub-vertical (Plate 3.1.8; grid 6378E, 6050N).

Intrusive rocks form the major mafic component in this area in contrast to extrusives at Ponto Mine. Four dyke units were recognised in the field. The eastern one (Unit

One) is located immediately west of the Koonenberry Fault and has only a short extension before dying out in fault breccias at both ends. Unit Two is at the southern end with only a small extent within the studied area. Unit Three is the central dyke belt and contains the largest amount of mafic rock in this area. It extends for about five kilometres with a strike conformable to D_2 structure. The northern end of the belt is cut off by a cross-strike fault system. Further north, cleaved metabasites similar to those at Ponto Mine were observed (grid 6360E, 6070N). In the south, the dyke also dies out rapidly into a cleaved metabasite sequence (grid 6380E, 6030N). Unit Four, on the north western corner (grid 6333E, 6090N), marks the boundary between basement and Cambrian rocks; several intrusions are strung out like beads parallel to the main foliation. At the southern end of a volcanic belt in this unit, a small lamprophyre outcrop several metres in diameter was observed (grid 6332E, 6610N). Samples collected from this occurrence have suffered little deformation. On this basis it is thought to be similar to those lamprophyres seen near Wonnaminta Homestead (see below). Metadolerite III was observed in a small outcrop near the northern end of Unit Two (grid 6389E, 6025N).

Mineralogical compositions of these mafic rocks are summarised in Table 3.4. Generally, various assemblages in metadolerites (I, II and III) and in metabasite are very similar to those observed in the Ponto Mine area.

3.2.3. Mafic Rocks in the Wilandra Area

The Wilandra area is located on the eastern side of the southern Wilandra Inlier in the basement sequence (Figure 1.1). The basement mafic rocks observed in this area occur as a series of highly weathered, low-relief outcrops (Map Three).

Structurally, this area is located west of the Koonenberry Fault, where it changes its trend from SSE to SSW (Figure 1.1). The major cleavage (D_2) developed in this area strikes 070°-085° and dips vertically (Map Three). Owing to weathering and poor exposure, some outcrops are marked as "undifferentiated", which refers to those that may be either massive, cleaved or schistose in structure. Outcrops in this area are bounded by a NW-SE striking fault in the north against Upper Palaeozoic quartz sandstone. To the south, the outcrops disappear under alluvium but may extend to Grasmere (Figure.1.1), where major mineral exploration has been carried out.

A small outcrop of felsic rocks was observed within the basement sequence on the

3.4. Petrography of basement mafic samples from the Boshy Tank area.

Sample No.	Rock	Fabrics	Relics	Alteration assemblage	Regional metamorphic assemblage
762501	***Metadolerite II***	ophitic	Pl	[Ac-Hb+Mt](40)+[Ab](40)+[Ep+Sp+Qz+Ch+Cb](20)	
762602	**Lamprophyre**	porphyritic	Ka(40)	[]+[]+[Ab(35)+Mu(20)+Cb(5)±Ep]	
762603	**Metabasite**	massive		[]+[]+[Ep+Qz+Ac](70)	[Ac+Ep+Qz](30)
762604	Metabasite	massive		[]+[]+[Ep(50)+Qz(40)+Ac(10)]	
762605	**Metabasite**	massive	Pl(15)	[Ep+Qz](15)+[Ab](5)+[Ab+Ep+Mt](65)	
762606	**Metabasite**	cleaved		[]+[]+[Ep+Qz+Ab+Cz]	
762608	Metadolerite I	cleaved ophitic	Py	[Hb+Ep](60)±[Ab]+[Hb+Ep±Ch](40)	
762701	**Metadolerite II**	ophitic		[Ac-Hb](40)+[Ab](40)+[Ac+Ep+Ch+Cb](15)	[Ep+Mu](5)
762703	**Metabasite**	cleaved	Pl	[]+[Ab](10)+[Ab+Mt+Ep](70)	[Qz+Ep](20)
762704	Metabasite	deformed massive		[]+[]+[Ab+Ch+Mt±Sp](90)	[Ep+Qz](10)
762705	***Metadolerite II***	ophitic		[Ac-Hb+Ep](40)+[Ab](40)+[Ep+Sp+Ac+Ch+Qz](20)	
762706	**Metadolerite III**	porphyritic		[Ac+Ep+Cz+Mu](60)+[Ep+Ac](40)	
762803	**Metadolerite II**	deformed ophitic	Pl	[Cb+Ac-Hb](40)+[Cb+Ab(40)]+[Cb+Ep+Ch+Cz±Ab±Mt±Il](40)	

Key: pseudomorphous alteration after [Py]+[Pl]+[Matrix] (empty bracket means no mineral)

Note: Numbers in small brackets are estimated contents of the component (±5%);
Minerals in each component are presented in order of abundance and uncommon phases marked with "±"(0- 5%);
Highlighted samples are those selected for geochemical analysis and those in italics are those selected for isotope analysis.

eastern side of the area (grid 6682E, 5353N; sample 861209). Under the microscope, this rock possesses a porphyritic texture and is largely composed of albite, both as phenocrysts and in the groundmass, with minor quartz, K-feldspar and magnetite in the groundmass. This rock is probably part of the basement sequence based on its structural characters. The mafic rocks in this area are, in general, identical to those occurring in the Ponto Mine Inlier and vary from massive with minor cleaved volcanic rocks, to metadolerites with or without relic pyroxene (types I and II).

Petrographic characteristics of mafic rocks in this area are presented in Table 3.5. Relic pyroxene is observed both in intrusive (*e.g.* 861310/1, 861314) and in extrusive samples (861303). The burial assemblages include Ac+Ep and Ep+Qz types, but a Pm+Mu assemblage was also observed in some of the rocks, sometimes surrounding the Ac-Ep assemblage. Pumpellyite may occur either in matrix or in amygdales or both together with muscovite (*e.g.* Plate 3.2.7). Sometimes muscovite occurs as good sheet-like crystals and becomes a major component (*e.g.* sample 861308). In this case, the mineral assemblage is Mu+Ep+Cz±Ch±Pm (Plate 3.2.8). Regional metamorphic assemblages are observed in the mafic schist, typically with an assemblage of Ac+Ep+Cz+Mu±Ch.

From this description, it is suggested that there are at least two metamorphic events that have caused alteration of the mafic rocks in this area. The first one that caused the primary burial metamorphism may be quite similar to that observed in the Ponto Mine Inlier; while the pumpellyite assemblage represents a second (retrograde) metamorphic event, possibly during the second regional metamorphism (see also discussion below).

3.2.4. Mafic Rocks in the Cymbric Vale Area

Cymbric Vale is located in the southern part of the Wonominta Block, on the western end of the the Wilandra Inlier (Figure 1.1). Structurally, outcrops in this area are fault bounded on both the eastern and western sides (Map Four). Towards the west, occur the upper Palaeozoic quartz-sandstones. The eastern boundary is a twin fault system joined at the northern end. East of the twin faults occurs a less metamorphosed sequence (Palaeozoic; *cf.* Map Four) of chert, sandstone and carbonate rocks. The major successions disappear under alluvium to both the north and south. Most of the outcrops display cleavage with dominant N-NNE strikes and vertical dips.

The basement sequence here comprises two lithological units, mica schist and

Table 3.5. Petrographyof mafic rocks from Wilandra in the basement sequence

Sample	Rock	Fabric characters	Relics	Alteration assemblage	Regional metamorphic assemblage
861201	Metabasite	massive		[]+[]+[Ep+Qz+Cb](85)	[Ep+Qz+Cb±Mu](15)
861202	Mafic schist	cleaved			Qz+Ep+Cz+Ch+Mu±Ac
861203	**Metabasite**	massive		[]+[]+[Ep+Qz+Cz]	
861205	**Mafic schist**	**cleaved**			Ac+Ep+Cz+Sp±Qz
861206	Mafic schist	cleaved			Ac+Ep+Cz+Sp±Qz
861208	Metabasite	massive	Pl	[]+[Ab+Ep+Mu+Cb+Sp](20)+[Ch+Ep+Sp+Ab±Cz](80)	
861210	Metabasite	massive		[]+[Ab](5)+[Ep+Ac+Ab±](80)+[Cb](15)	
861211	***Metadolerite II***	***ophitic***	Pl	[Ac-Hb+Cz](40)+[Ab](40)+[Ac+Ab+Ep+Cz+Cb](20)	
861212	Metabasite	massive		[]+[Ab](15)+[Ac-Hb+Ep+Cz+Sp±Qz](65)	[Mu+Pm+Ab±Ep±Ch](20)
861301	Metadolerite III	porphyritic		[Ac+Ep+Cz+Mu]+[Ep+Ac]	
861302	**Metadolerite III**	**porphyritic**		[Ac+Ep+Cz+Mu]+[Ep+Ac]	
861303	Metabasalt	massive	Py	[Ch+Mu+Sp](30)+[]+[Mu+Ep+Cz+Sp](70)	
861304	**Metabasite**	**massive**		[Ac+Mu]+[]+[Ep+Ac+Mu+Ch]	
861305	**Metabasite**	**massive**	Pl	[]+[Ab+Mu+Cb](30)+[Ab+Cb+Mu+Ch+Ep+Cz](70)	
861306	Metabasite	massive		[]+[]+[Ep+Qz+Cz±Ch±Cb]	
861307	**Metabasite**	**deformed**		[]+[]+[Ab(40)+Mt(20)+Ch(20)](80)	[Ep+Qz+Ch](20)
861308	Metabasite	massive		[]+[Ab+Cb+Mu](10)+[Ep+Cz+Mu+Ch+Sp](90)	
861309	Metabasite	massive		[]+[]+[Ac+Ep+Cz](90)	[Cb](10)
861310	Metadolerite I	ophitic	Py	[Ac-Hb]+[Ab+Mu+Ep+Cz]+[Ac+Cz+Ep±Ch]	
861311	**Metadolerite I**	**ophitic**	Py, Pl	[Ac-Hb](30)+[Ab+Mu+Ep+Ep+Sp](40)+[Ep+Cz+Mu+Pm+Ac](30)	
861312	Metadolerite II	ophitic		[Ac-Hb](40)+[Ab+Mu+Ep+Ep+Sp](30)+[Ep+Cz+Mu+Ac](30)	
861313	Metadolerite I	ophitic	Py	[Ch+Ac]+[Ab+Cz+Ep+Mu]+[Ep+Cz+Ch±Ac]	
861314	***Metadolerite I***	***ophitic***	Py	[Ac]+[Ab+Ep+Cz]+[Ep+Cz+Ac±Ch±Sp]	
861315	**Metadolerite I**	**ophitic**	Py, Pl	[Ac±Cb](30)+[Ab](30)+[Ch+Ep+Cz+Ac](40)	
861316	**Metabasite**	**massive**		[]+[]+[Ab+Ch+Mu+Sp+Cb]	
861401	Mafic schist	cleaved			Ch+Ep+Cz+Qz+Mu
861403	Metabasite	cleaved,microcrystalline		[]+[]+[Ep+Cz±Ch±Ac±Ab]	Mu+Cz±Ep+Ch+Cb
861404	Mafic schist	cleaved			Ac+Ep+Cz+Sp±Ch
861405	Metabasite	cleaved		[]+[]+[Ep+Ac+Cz](85)+[Mu+Cz](15)	
861407	**Metadolerite II**	**ophitic**	Pl	[Ac-Hb](45)+[Ab+Ep](45)+[Ep+Sp](10)	
861408	Metabasite	porphyritic		[]+[]+[Ep+Cz+Mu](60)+[Cz+Mu+Ep](40)	
861409	Metabasite	massive		[]+[]+[Ac+Ep+Cz+Ab+Qz+Sp]	
861410	Metabasite	massive		[]+[]+[Ab+Ch+Mu+Sp+Cb]	
861601	**Metabasite**	**massive**		[]+[]+[Ac+Ep+Cz+Ab+Ch]	
861603	Metabasite	massive		[]+[Ab+Mt+Ep](25)+[Ep+Qz+Cb](60)	[Ac+Ep](15)
861604	**Metabasalt**	**massive**	Pl	[Ac+Ch]+[Ab]+[Ac+Ep+Cz+Ab+Ch]	
861605	**Metabasite**	**porphyritic**		[]+[]+[Ep+Cz+Mu](60)+[Cz+Mu+Ep](40)	
861606	Metabasite	massive		[]+[]+[Ac+Ep+Cz+Mt]	

Key: pseudomorphous alteration after [Py]+[Pl]+[matrix]+[amygdale, optional] (empty bracket means no minerals)

Note: Numbers in small brackets are estimated abundance of the component (±5%)
Minerals are shown in order of abundance with uncommon phases showns as "±" (0-5%)
Highlighted samples are those selected for geochemical analysis with those in italics selected for isotope analysis

amphibolite. Some amphibolite outcrops have schistose margins and are similar to the mafic schists, but the mineral assemblages are identical to the more massive internal portions. Massive metabasite occurs in the northern part of the area as nodules within mica schist (sample 861705) and within amphibolite (sample 861707). The mafic intrusive and related schistose rocks are bluish green and medium to coarse-grained. Under the microscope, the samples all contain a distinctive bluish green amphibole with epidote, plagioclase (andesine - oligoclase in composition) and minor quartz (Table 3.6). Most of the bluish amphiboles are prismatic and define the main foliation. Epidote is another major component and occurs mostly as granular patches. Metabasites display similar characters to those observed in the basement sequence elsewhere. There are some metadolerite samples found in small intrusions near the eastern fault zone in this area (*e.g.* 861909; *cf.* Map Four)

3.2.5. Bilpa Area

Bilpa is located in the southern end of the Wonominta Block (Figure 1.1). The late Cambrian Bilpa Conglomerate, which was the major interest of the studies in this area, has a fault-controlled wedge-like occurrence (Map Nine). Towards the north, occurs the quartz sandstone (Late Cambrian - Ordovician, see Figure 1.1), while at the southern boundary, mafic volcanic rocks of the basement sequence were observed to lie unconformably beneath it. Along the western boundary is another sequence of conglomerate, mainly composed of quartzite pebbles. Towards the east, this conglomerate disappears under alluvium. A variety of clasts were recognised in the field with mafic component comprising less than 10% (*cf.* sample list in Appendix 1). The mafic clasts are mainly metabasites with an assemblage of Ch+Ab+Ep+ Cz+Mt (Table 3.7). The mafic rocks in the basement sequence are identical to those occurring in the Ponto Mine area, and also hosts a base metal mineralisation similar to that observed at the Ponto Mine. Mineral assemblages of the mafic rocks is presented in Table 3.7.

Table 3.6. Petrography of mafic rocks from Cymbric Vale area in the basement sequence.

Sample No.	Rock	Relics	Alteration assemblage	Regional Metamorphic Assemblage
861705	**Metabasite**	Pl	[]+[]+[Ab+Mt+Qz+Sp]	
861707	**Metabasite**	Pl	]Ac+Cb](5)+[Ab](5)+[Ep+Ac+Cz±Ch](70)+[Qz+Ch](20)	
861712	Mafic schist			[Ac(50)+Ep(30)+Qz(15)±Ch]
861713	***Amphibolite***			Ep+Hb+Qz+Sp±Cz±Ch
861714	**Amphibolite**			Ep+Hb+Qz+Sp±Cz±Ch
861715	Amphibolite			Ep+Hb+Qz+Sp±Cz±Ch
861716	Mafic schist			Ep+Qz+Ch+Ac-Hb±Sp
861717	Metabasite		[]+[]+[Ep+Qz+Ch+Pl±Ac]	
861801	Mafic schist			Ac-Hb+Ep+Qz
861802	Metabasite		[]+[]+[Qz+Ep+Cb]	
861803	Mafic schist			Ep(65)+Qz(25)+Ch(5)+Cb(5)
861806	**Metabasite**		[]+[]+[Ep+Qz+Cb]	
861807	Metabasite		[]+[]+[Ep+Qz±Cb]	
861903	Metabasite	Pl	[]+[Ab](70)+[Ch+Cb+Qz](30)	
861904	Metabasite	Pl	[]+[Ab](70)+[Ch+Cb+Qz](30)	
861908	Metabasite		[]+[]+[Ep(70)+Qz(10)](80)+[Qz](20)	
861909	***Metadolerite***	Pl	[Ac+Ch](30)+[Mu+Cb](40)+[Ep+Ch+Qz+Cb+Sp](30)	
861911	**Metabasite**	Pl	[]+[Ab](70)+[Ab+Cb](30)	
861914	Mafic schist			Ac-Hb+Ep+Qz+Sp±Ch
861915	***Mafic schist***			Hb(40)+Ep(30)+Qz(30)

Key: pseudomorphous alteration after [Py]+[Pl]+[matrix] (empty bracket means no minerals)

Note: Numbers in small brackets are estimated abundance of the component (±5%)

Minerals are shown in order of abundance with uncommon phases shown as "±" (0-5%)

Highlighted samples are those selected for geochemcial analysis with those in italics selected for isotope analysis

Table 3.7. Petrography of Mafic Rocks from the Bilpa Area

Sample No.	Rock	Occurrence	Relics	Alteration assemblage	Regional metamorphic assemblage
862901	**Meta-andesite**	**conglomerate**		[]+[Ab](15)+[Ab+Qz+Ch+Ep+Cb](85)	
862909	**Metabasalt**	**basement**	Py, Pl	[Ac-Ch](15)+[Ab](15)+[Ab+Ep+Ch±Cb](60)	[Cb](10)
862910	Metabasalt	basement	Py, Pl	[Ac-Ch](10)+[Ab](15)+[Ab+Ep+Ch±Cb](60)	[Cb](15)
862914	**Metabasite**	**basement**		[Ac-Hb+Ch](15)+[Ab](20)+[Ep+Ac+Mu+Ab](65)	
862916	Metadolerite	basement	Pl, Py	[Ch+Cb]+[Ab]+[Ab+Ch±Ac]	
863012	**Metabasite**	**conglomerate**	Pl	[]+[Ab+Mu+Ep+Cz](35)+[Ab+Ep+Cz+Qz](60)	[Cb](5)
863014	Metabasite	conglomerate		[]+[]+[Ep+Qz](80)	[Qz+Cb+Ch](20)
863017	Metabasite	conglomerate		[]+[]+[Ch+Qz+Cb](70)	[Ch+Qz+Cb+Mt]30
863018	Metabasite	conglomerate			Ch+Qz+Cb±Ep

Key: Pseudomorphous alteration after [Py]+[Pl]+[matrix] (empty bracket means no minerals in the "component"

Numbers in small brakets are estimated percentage of the 'component'.

Minerals are presented in order of abundance with uncommon phases shown as "±" (0-5%)

Highlighted samples are those selected for geochemical analysis

3.3 THE LATE PROTEROZOIC SEQUENCE

3.3.1 Mafic Rocks in the Packsaddle Area

Packsaddle is located on the northwestern part of the Wonominta Block, along the Silver City Highway connecting Broken Hill to Tibooburra (Figure 1.1). The first and major deformation in this area developed structures similar in orientation to those produced during D_2 in the Ponto Mine Inlier. The cleavage strikes 130° - 145° and dips vertically (Map Five). The second deformation (equivalent to D_3) resulted in open folds with axial planes approximately normal to D_2 (Plate 3.1.9).

Within the area, four discrete outcrops containing mafic rocks with distinctive characteristics were observed. Unit One in the east, is the major volcanic unit and composed of both massive and cleaved metabasite. The cleaved samples are similar to those from Ponto Mine but more yellowish in colour (Plate 3.1.10). The outcrop can be subdivided into four belts based upon the cleaved (T) or massive (M) textures of the rocks, T_1, M_1, T_2 and M_2 from the east to the west. However, the boundaries are transitional and were marked therefore with dashed lines on the map. In the northern extension of this unit, which is beyond the study area, pillow lavas were discovered (grid 5915E, 6420N; Plate 3.1.12). Compared with those in the Ponto Mine area, the pillow lavas observed here display little deformation and are larger in size, with some pillows reaching a metre in length.

Unit Two is small and discontinuous (grid 5930E, 6200N). It is largely composed of cleaved metabasite. In the northern part of this unit, an outcrop of coarse-grained rocks occurs within the succession (grid 5929E, 6200N). Samples collected from this site are believed to be xenolithic as they display distinctive characters in terms of texture, mineralogical, geochemical and Sr-Nd isotopic compositions (*cf.* Chapters 6 & 9). Unit Three is also discontinuous and is composed of small ellipsoidal intrusions of syenite and two narrow cleaved metabasite outcrops. Unit Four in the west is the major syenite unit, which outcrops as large pink boulders. Minor carbonate rocks occur within Unit Three as lenses (grid 5947E, 6198N) and veins (grid 5946E, 6197N). The meta-sediments are largely obscured by alluvium and only those surrounding the igneous successions form recognisable outcrops.

In contrast to the basement sequence, the Late Proterozoic mafic volcanic rocks here are very fine-grained and dominated by the Ab+Ch assemblage formed during burial

(*sensu lato*) and regional metamorphism (Table 3.8). Many of these rocks have abundant amygdales filled with carbonate, quartz and minor epidote. The intrusive rocks are metadolerite IB type. The syenite is largely composed of K-feldspars (microcline and perthitic orthoclase), albite (15%), minor quartz and carbonate (Plate 3.2.17). With increasing albite content (up to 25%), samples become sodic syenite.

3.3.2. Mafic Rocks in the Nundora Area

According to Mills (1992), Nundora is located in the same structural position as Packsaddle but further south (Figure 1.1) . As with the distribution of volcanic rocks at Packsaddle, there are two volcanic and one syenite successions here; however, unlike that at Packsaddle, the major volcanic succession (Unit One) in the east is split into two parts by alluvium-obscured slates. There are also more sub-units, namely M_0, T_1, M_1, T_2, M_2 and T_3 from east to west (Map Six). While T_1, M_1, T_2 and M_2 are similar to their corresponding units at Packsaddle, M_0 is characterised by strong carbonatisation and T_3 by the appearance of greyish green nodule-like massive metabasite samples.

The petrographic characteristics of these mafic rocks, as presented in Table 3.9, are very similar to those observed in the Packsaddle area. The nodule-like samples found in T_3 have the assemblages Ep+Ac±Ch (*e.g.* 761907) or Ep+Qz (761906), which are similar to the basement samples. Geochemical analyses demonstrate that (see Chapter Six) they have identical compositions to their volcanic hosts and thus, probably are not of xenolithic origin as are the kaersutite-bearing rocks at Packsaddle.

An ultramafic outcrop was observed near the track between Nundora and Wonnaminta homesteads (grid 6074E, 6053N) and extends along a line parallel to the regional cleavage. This outcrop is suggested to be fault controlled and Edwards (1980, Figure 3.2) believed it to be the same fault on the eastern margin of the nundorite (see below). In the field, these rocks are pale green, with weathered exposures but they do not show cleavage (Plate 3.1.14). Thus, the emplacement of this outcrop is possibly post-D_3. Petrographically, this rock is mainly composed of globules of serpentine after olivine with some idiomorphic clinopyroxene, as well as some zeolitic/chloritic phases in the matrix.

Syenite occurs in the western part of the mapping area and is less widely distributed than at Packsaddle. Three small bodies were discovered, of which the largest one

Table 3.8. Petrography of mafic rocks from Packsaddle area in the late Proterozoic sequence

Sample No	Rocks	Structure	Relics	Alteration assemblage	Regional metamorphic assemblage
760801	***Metadolerite I***	***Ophitic, xenolith***	Ka, Py	[]+[]+[Ch+Ac+Ep+Cz](80)	[Qz(d)+Ac+Ep](20)
760802	Metabasite	Cleaved	Ka	[Ac+Ch](30)+[Ab](20)+[Ch+Ac+Ep+Cz]	[Qz(d)+Ac+Ep](10)
760805	***Metabasite***	***M1,Massive with vesicle***		[]+[]+[Ab+Ch+Mt+Sp](80)+[Cb+Ep](20)	
760806	***Metabasite***	***M2,Massive non-vesicle***		[]+[]+[Ab+Ch+Mt+Cb]	
760901	Metabasite	Massive		[]+[]+[Ab+Ch+Mt+Cb]	
760903	Metabasite	Massive, non-vesicles	Pl	[]+[]+[Ab+Ch±Mt](70)+[Cb](5)	[Ch](20
761001	***Metadolerite IB***	***Ophitic, xenolith***	Ka	[Ac](50)+[Ab](40)+[Cz+Sp±Ep](10)	
761002	Metadolerite II	Ophitic		[Ch](30)+[Ep](30)+[Ep+Ch+Sp](30)	[Ep+Qz](10)
761203	**Metadolerite IB**	**Ophitic**	Ka(10)	[Ac](40)+[Ab](30)+[Ac+Ab+Sp](10)	[Ep+Qz+Ch+Cb](10)
761207	Metabasite	Massive	Pl(30)	[]+[Ab](20)+[Ab+Ch+Sp±Ac](40)	[Qz(s)+Cb](10)
761301	**Metabasite**	**Pillow lava**		[]+[]+[Ab+Mt+Ch+Ep](90)+[Cb](10)	
761302	Metabasite	Pillow lava	Pl(5)	[]+[]+[Ab+Ch+Mt](80)+[Cb](15)	
761304	Metabasite	Massive			
761305	Metabasite	Massive		[]+[]+[Ab+Mt+Ch+Cb]	

Table 3.9. Petrography of mafic rocks from the Nundora area in the late Proterozoic sequence

761502	Metabasite	Cleaved		[]+[]+[Ab+Mt+Ch](85)+[Cb](15)	
761503	***Metabasite***	***Massive in tuff zone***		[]+[]+[Ep+Ac+Mt+Sp+Ab+Ch]	
761505	**Metabasite**	**Massive**		[]+[]+[Ab+Ch+Mt](80)+[Cb+Qz](20)	
761507	Metabasite	Cleaved, Spotted		[]+[]+[Ab+Ch+Mt](85)+[Cb+Qz](15)	
761508	Metabasite	Massive with vesicles		[]+[]+[Ab+Sp+Ep](80)+[Cb](20)	
761512	**Metabasite**	**Massive**		[]+[]+[Ab+Ch+Sp](85)+[Ch](15)	
761602	**Metabasite**	**Cleaved**			Ab+Ep+Ch+Sp+Qz
761809	***Metabasite***	***Cleaved***		[]+[]+[Ch+Ab++Ep+Sp](95)+[Cb](5)	
761810	Metabasite	Deformed		[]+[][Ab+Ch+Mt](90)+[Cb](10)	
761901	***Metabasite***	***Massive***	Pl	[]+[Ab](30)+[Ab+Ch+Mt](70)	
761903	Metabasite	Cleaved, spotted		[]+[]+[Ch+Ab+Mt](80)+[Cb](20)	
761906	**Metabasite**	**Cleaved**		[]+[]+[Ep+Qz+Cb+Sp](90)+[Cb+Qz](10)	
761907	**Metabasalt**	**Massive, fine-grained**	Py	[Ch±Ac](5)+[Ab](5)+[Ep+Ac+Sp](90)	
761908	**Metabasite**	**Massive, fine-grained**		[]+[]+[Ch+Ab+Sp+Mt+Cb](95)+[Cb](5)	

Key: Pseudomorphous alteration after [Py]+[Pl]+[matrix]+[amygdales, optional] (empty bracket means no mineral)
Numbers in small brackets are estimated contents of the component (±5%)
Minerals are presented in order of abundance with uncommon phases shown as "±" (0-5%)
Highlighted samples are those selected for geochemical analysis and those in italics selected for isotope analysis

(grid 6060E, 6057N) is about 200 metres long. Rocks from this intrusion display a remarkable textural zonation. The inner part is grey white, ringed by yellow and then pink zones on the outer margin (Plate 3.1.13). In thin-section, the contents of iron oxides increase from the grey to pink zones. The mineral composition is albite (30-35%) , K-feldspar (40-45%), minor biotite (5 -10%) and magnetite (5-8%). Biotite tends to co-exist with magnetite. The second outcrop of syenite (grid 6062E, 6057N) is compositionally similar to the first one but the third smaller body further south (grid 6074E, 6045N; samples 761603/04) has approximately equal amounts of albite and K-feldspar with approximately 10% biotite. These rocks do not display primary magmatic textures any more and hence are named altered syenite (see Plate 3.2.16).

Nundorite (an aegirine-nepheline rock) is another distinct rock observed in the area. It was first reported by Edwards and Neef (1979) and given its name after the local homestead. The present field study showed that this aegirine-bearing rock (grid 6063E, 6070N) occurs as a NW-trending ellipsoid up to 100 meters wide and 500 metres long and is fault bounded on the eastern side. In the field, this outcrop is divided into a western light grey and an eastern dark grey to black zone. The light unit has a crystalline appearance with bright green aegirine scattered within a light pink matrix. The matrix appears to still preserve the primary flow banding and is composed of albite, K-feldspar, natrolite and a little nepheline. The dark part shows a strong foliation and has higher contents of aegirine with a poorer crystal form. Most of the aegirine occurs as patches surrounded by feldspathic minerals and opaque components. Under the microscope (Plates 3.2.17 & 3.2.18), each patch is composed of many small crystals with identical optical orientation in a flow-like matrix banding. The matrix of dark samples is microcrystalline and has a texture identical to the volcanic tuff rocks nearby. This character suggests that the nundorite may have been originated from the felsic tuffs through alkaline metasomatic alteration.

3.4. THE CAMBRIAN SEQUENCES

3.4.1. Mafic Rocks in the Mt. Wright Area

Mount Wright is a distinctive Devonian sandstone hill in the southern part of the Wonominta Block (Figure 1.1), and is well-known for the Mt. Wright Volcanics (Brunker, 1967; Rose, 1968; Edwards, 1980; Scheibner, 1989). Structurally, the main Early Cambrian outcrops (Kruse, 1982) in this area are fault-bounded on both eastern and western sides. On the eastern side, the Mt. Wright Fault zone consists of a series of N-S trending vertical faults; the western side is also bounded by N-S trending faults. At the southwest corner of the area, a sequence of Ordovician quartz-sandstones limits the extension of the older succession. The influence of the regional deformation in this area is limited and volcanic structures are largely preserved.

Felsic and mafic rocks comprise the two distinctive associations in this area. The major occurrence of felsic rocks appears to be within a fault-controlled syncline in the northern part of the area, centred on a quartz-feldspar porphyry unit (Map Seven). In the field, these rocks are light green-yellow and massive. Under the microscope, they are seen to be fine-grained tuff composed of quartz and minor feldspars; whereas the porphyry is composed of abundant feldspar and quartz as phenocrysts, and a quartz-dominant groundmass. Zircon, tourmaline, white mica and sphene are accessory minerals.

The mafic rocks, located in the central and southern parts of the area are mostly black and massive, with undeformed amygdales. The mineral assemblages of these samples are shown in Table 3.10. Both pyroxene and plagioclase are recognised as magmatic relics (Plate 3.2.10), commonly replaced by chlorite and albite respectively. The alteration assemblage in the matrix is Ab+Ch+Mt+Ep± Qz±Cb±Pm±Sp. The amygdales and veins are filled with Cb+Qz±Ep.

Towards the south, a series of isolated, rounded hills are observed next to the mafic and felsic successions. Samples from these hills are earthy brown, massive and fine-grained. Microscopically, the rocks are largely composed of albite and K-feldspar showing a distinct trachytic texture in a brownish aphanitic groundmass with minor quartz in veins. Chemical analysis also suggested these rocks are trachytic.

Stratigraphically, these trachytic rocks were suggested to be the lowest part of a local

Table 3.10. Petrography of mafic volcanic rocks from the Early Cambrian sequence at Mt. Wright

Sample No.	Rock	Relics	Alteration assemblage	Regional metamorphic assemblage
862112	***Metabasalt***	Py	[Ch](10)+[Ab](5)+[Ab+Ch+Mt±Pm](85)	
862204	Metabasite		[]+[]+[Ab+iron oxide±Ch](85)+[Cb](10)	[Cb](5)
862205	***Metabasite***		[]+[]+[Ab+Mt±Ep]	
862217	**Metabasite**		[]+[]+[Ab+iron oxide±Ep]	
862220	Metabasite		[]+[]+[Ab+Mt+Ep]	
862221	***Metabasite***	Pl	[]+[Ab](10)+[Ab+Qz+Pr+Ch](90)	
862223	Metabasite		[]+[]+[Ab+Mt±Ep]	
862224	Metabasite		[]+[]+[Ep+Ab+Mt±Cb](85)+[Qz+Cb](15)	[Cb+Qz]
862225	***Metabasalt***	Py	[Ch](10)+[Ab](10)+[Ab+Ch+Mt±Pm](80)	
862306	Metabasite	Pl	[]+[Ab](10)+[Ab+Qz+Pr+Ch](90)	
862402	***Metabasalt***	Py	[Ch](10)+[Ab](5)+[Ab+Ch+Mt±Pm](85)	
862403	Metabasite		[]+[]+[Ab+Ch+Ep+Cb+Qz±Ac](90)+[Qz+Cb](10)	
862404	Metabasite	Pl	[]+[Ab](5)+[Ab+Mt±Ep](80)+[Ep+Cb](10)	[Ep+Cb](5)
862405	**Metabasalt**	Py	[Ch](5)+[Ab](5)+[Ab+Ch+Mt±Pm](90)	
862406	Metabasite	Pl	[]+[Ab](5)+[Ab+Ch+Mt](80)+[Cb+Ch](10)	[Cb+Ch]
862407	Metabasite		[]+[Ab]+[Ab(laths, needles)+Ch+Mt]+[Ch+Sp]	[Ch+Cb](5)

Key: Pseudomorphous alteration after [Py]+[Pl]+[matrix]+[amygdales] (empty bracket means no minerals)

Numbers in small brackets are estimated content of the component (±5%)

Minerals are presented in order of abundance with uncommon phases shown as "±" (0-5%)

Highlighted samples are those selected for geochemical analysis, with those in italics selected for isotope analysis

conformable sequence (*cf.* Rose, 1968; Kruse, 1982), overlain by the basalts (Mt. Wright Volcanics) and then by the felsic rocks (the Cymbric Vale Formation); limestones occur at the top of this sequence.

3.4.2. Mafic Rocks in the Comarto Area

The Comarto area is located in the southern part of region, north of the highway to Broken Hill (Figure 1.1). Field investigation revealed that mafic rocks in this area are composed of individual rounded pipe-like outcrops labelled from P_1 to P_{10} (Map Eight). Among them, P_9 has a faulted boundary with the others, and is characterised by carbonate nodules and carbonatised host rocks (samples 860906 to 860912). The other pipe-like outcrops were divided into three groups based on their petrological features. P_1 to P_4 are metabasalts; P_6 to P_8 are pyroclastic rocks located on the eastern side of the area; and P_5 and P_{10} are intrusive rocks of metadolerite I. There are also some other pipe-like structures inferred from aerial photographs and marked with dashed lines on the map. All samples have apparently undergone little deformation with magmatic textures largely preserved, though mineralogical alteration occurs extensively.

Petrographically (Table 3.11), samples collected from P_9 have an alteration assemblage of Cb+Ab+Mt+Qz, whereas the assemblage in P_1 to P_4 is Ep+Ch+Cz+Pm±Ac±Pr. The pyroclastic rocks from P_6 to P_8 display typical tuff-breccia textures (Plate 3.2.1f) with an alteration assemblage of Ep+Ch±Pm±Pr. Metadolerite I in P_5 and P_{10} have a Ac+Ab alteration assemblage for phynocrysts and the matrix is Ch+Ab+Sp±Pm±Pr.

The isolated pipe-like occurrences cannot be stratigraphically correlated with other mafic rocks in the region, but the presence of prehnite and pumpellyite indicates a prehnite-pumpellyite grade of alteration similar to that in the Mt. Wright area. On this basis, it is suggested that the mafic rocks in this area are possibly also of early Cambrian age, being the youngest part of the Wonominta Beds. Petrologically, the compositions of these rocks are variable. The metabasalts and metadolerites seem to be identical to those occurring in the other areas in the Wonominta Block, while the pyroclastic rocks with tuff-breccia texture are clearly unique. The significance of the pipe-like occurrences, however, is probably limited as discussed in Chapter 7.

Table 3.11. Petrography of Cambria mafic rocks from the Comarto area

Sample No.	Rock	Structure	'Pipe'	Relics	Alteration assemlage	Regional metamorphic assemblage
861016	**Metabasite**	massive	1		[Ep+Pm+Ch](10)+[Ab](20)+[Ab+Ep+Ch+Pm](70)	
861017	Metabasite	massive	1		[Pr+Ep+Ch+Qz](5)+[Ab+Ep+Ch+Pm](80)+[Ep+Cb](15)	
861001	Metabasite	massive	2		[Mu±Ep±Ch](15)+[Ab](5)+[Ep+Ab±Ep](70)+[Cb+Ep](10)	
861002	**Metabasalt**	massive	2	Pl	[]+[Ab+Mu+Ep+Ch](15)+[Ab+Ep±Qz±Cb](70)+[Cb+Ep](15)	
861003	**Metabasalt**	massive	2	Py, Pl	[Ch](15)+[Ab+Ch+Ep](10)+[Ep+Ch+Cz±Cb](75)	
861004	Metabasite	massive	2		[]+[Ab+Ep+Mu±Ch](15)+[Ab±Ch±Ep](70)+[Ep+Ch+Cb](15)	
861005	Metadolerite II	ophitic	4	Pl	[Cb+Ep+Mu](5)+[Ab](10)+[Ab+Ch±Ep](65)+[Cb+Ch](15)	
861006	Metadolerite II	ophitic	4	Pl	[Cb+Ep+Mu](5)+[Ab](10)+[Ab+Ch±Ep](50)+[Cb+Ch](20)	
861007	Metabasite	massive	4	Pl	[]+[Ab+Mu+Ep+Ch](15)+[Ab+Ep±Qz±Cb](85)+[Cb+Ep](10)	
861008	Metabasite	massive	4		[]+[Ab+Qz+Mt](15)+[Ab+Ep±Qz±Cb](85)+[Cb+Ep](10)	
861009	Metabasite	pyroclastic	5	Pl	[]+[Ab](30)+[glassy clasts+Pm+Ep±Mu±Ch](70)	
861010	**Metadolerite I**	ophitic	5	Py(25)	[Ch+Ep]+[Ab](40)+[Ch+Ab+Pm+Sp±Pr](35)	
860901	**Metabasalt**	massive	6	[Pl](5)	[Ch(yellow)](5)+[Ab+Ch](5)+[Ab+Ch](80)	[Cb](10)
860902	Metabasite	pyroclastic	6		[]+[Ab](5)+[Ab+Qz+Cb](25)+[Ch+Pm+Pr+Cb](60)	
861014	**Metabasalt**	pyroclastic	7	Py, Pl	[Ch]+[Ab]+[Ab+Qz+Ep±Cz±Ch]+[Ch+Ep+Pm]	
860904	**Metabasite**	pyroclastic	8		[]+[]+[Ch+Ab](30)+[Ch+Ab+Ep](60)	[Ep](10)
860905	Metabasite	pyroclastic	8		[]+[]+[Ch+Ab+Cb](25)+[Cb+Ab+Qz](70)	[Ep+Cb](5)
861015	**Metabasite**	pyroclastic	8		[]+[Ab](10)+[Ab+Ep+Ch+Qz](20)+[Ch+Ab+Pm+Ep](70)	[Cb](5)
860906	Metabasite	massive	9		[]+[]+[Ab+Mt](40)+[Cb](60)	
860908	Metabasite	massive	9		[]+[]+[Ab+Mt](40)+[Cb](60)	
860909	**Metabasite**	massive	9		[]+[]+[Ab+Mt+Ch+Cz+Qz](90)+[Cb](10)	
860910	Metabasite	massive	9	Pl	[]+[]+[Ab+Ep+Qz](60)+[Cb](40)	
860912	Metabasite	massive	9		[]+[]+[Ab+Mt+Ch+Cz+Qz](85)+[Cb](15)	
861011	**Metadolerite I**	ophitic	10	Py(25)	[Ch+Ep]+[Ab](40)+[Ch+Ab+Pm+Sp±Pr](35)	
861012	Metadolerite I	ophitic	10	Py(25)	[Ch+Ep]+[Ab](40)+[Ch+Ab+Pm+Sp±Pr](35)	
861013	**Metabasite**	pyroclastic	10		[]+[]+[Qz+Ch](20)+[Ch+Ep](80)	

Key: Pseodumorphous alterations after [Py]+[Pl]+[matirx]+[amygdales, optional] (empty bracket means no minerals)

Note: Minerals are presented in order of abundance ("±" for 0-5% phases); numbers in small brackets are estimated contents of the component (±5%)

Highlighted samples are those selected for geochemical analysis

3.4.3. Wonnaminta and Kayrunnera Areas

Both areas are located in the northern part of the Wonominta Block (Figure 1.1) but the former is in the basement sequence and the latter in the early Cambrian sequence. Field work in these areas was carried out only briefly.

A lamprophyre occurs to the north of Wonnaminta homestead as a cross-strike dyke cutting the basement sequence (post-D_3). The outcrop is about 20 metres wide and 400 metres long. The rocks are light earth brown in colour with massive textures. In thin-section, the rocks are composed of idiomorphic kaersutite (35 - 40%) and plagioclase (50 - 55%) with minor epidote. Some bright green epidote nodules up to 10 cm in diameter were found in the field (762413). In these nodules, epidote becomes a major component with minor plagioclase and magnetite.

The gabbro at Kayrunnera was also briefly examined for its field occurrence and petrography. In the field, the rocks have a quite extensive occurrence, having intruded into the Early Cambrian sequences. Most of the rocks are dark grey to black in colour (pyroxenes with milky white feldspars in between), and massive with little deformation. Petrographically, the gabbros are composed of pyroxene, amphibole and plagioclase together with minor sphene and magnetite. Minor amphibole surrounding the pyroxene was observed as an alteration product.

3.5. DISCUSSION: METAMORPHIC CONDITIONS

The protoliths of the metamorphosed mafic rocks observed in three sequences of the Wonominta Beds were probably both extrusive and intrusive. In the Ponto Mine Inlier, the basement outcrops in the Ponto Mine area are largely volcanic, whereas those at Boshy Tank are largely in the form of dykes, possibly indicating deeper exposure of the primary volcanic piles. In the south, the Wilandra basement mafic rocks occur as both intrusive and extrusive forms, whereas those occurring at Cymbric Vale are now amphibolite and thus it is difficult to infer their primary emplacement features. The Late Proterozoic and early Cambrian rocks are largely volcanic.

Three phases of deformation have been recognised in the basement rocks. In contrast, the Late Proterozoic and early Cambrian rocks experienced only the last two events of deformation (Davies, 1985; Mills, 1992). Throughout the whole region, however, D_2 is the major event and dominates the regional structural characteristics. However, petrographic studies revealed that most metamorphic phases appear to be of burial metamorphic origin, particularly in the massive mafic samples. Samples that can be used convincingly to construct the regional metamorphic conditions include the cleaved metabasite - mafic schist and the amphibolite with relatively minor occurrences, but it is clear from the petrographic observations that metamorphic phases in undeformed rocks are not necessarily all product of burial processes. In other words, regional products can be undeformed due to stress partitioning to sedimentary rocks.

A summary of the metamorphic facies during burial and regional metamorphism is presented in Table 3.12. On the whole, mafic rocks in all three sequences underwent only low to medium grade metamorphism. Since metamorphic reactions at such low grades are normally incomplete (Liou *et al.*, 1987), precise estimates of P-T conditions may be difficult. However, the advantage is that the records of metamorphic events can be revealed in contrast with high grade rocks, where only the peak metamorphic assemblages are preserved.

The submarine environments indicated by pillow lavas and associated marine sediments (Mills, 1992) for both basement and Late Proterozoic sequences suggest sea-water/hydrothermal alteration (ocean-floor metamorphism, Miyashiro, 1973) may have played an important role prior to burial metamorphism. As it is difficult to distinguish the two processes, both are collectively referred as burial metamorphism (*sensu lato*) (it is also possible that the two had been a continuous process that resulted in alteration of the rocks). This burial metamorphism (*sensu lato*) would have occurred prior to

Table 3.12. Metamorphic Characteristics of Mafic Rocks in the Wonominta Beds

Sequence	Burial Metamorphism	Regional Metamorphism
Basement		
Ponto Mine Inlier	upper greenschist facies Ac-Hb+Ab+Ep+Cz±Ch (ca. 500 °C)	upper greenschist facies Ac-Hb+Ab+Ep+Cz±Ch (ca. 500 °C)
Wilandra Inlier	(I) upper greenschist facies Ac-Hb+Ab+Ep+Cz±Ch (ca. 500 °C) (II) pumpellyite-actinolite facies Pm+Mu+Ac+Cb (250 - 350 °C)	upper greenschist -lower amphibolite facies Ac-Hb+Ab+Ep+Cz±Ch & Hb+Pl+Ep (500 - 550 °C)
Late Proterozoic	lower greenschist facies Ch+Ab+Mt+Ep+Ac (350 - 400 °C)	lower greenschist facies Ch+Ab+Ac+Ep+Qz+Cb (350 - 400 °C)
Cambrian	prehnite-pumpellyite facies Ab+Ch+Mt+Pm+Ac+Mu+Qz+Cb±Pr (250 - 350 °C)	? Cb+Qz±Ep (> 250 °C)

regional metamorphism, as alteration assemblages are seen to have been deformed subsequently.

To summarise earlier observations, mafic rocks in the basement sequence have experienced burial metamorphism (*sensu lato*) of upper greenschist. This is indicated by the observation of actinolite-hornblende with decreasing chlorite. The prevailing temperature of this process should be about 450 - 550 °C (Liou *et al.*, 1987). The regional metamorphism has probably reached similar or slightly higher grades as observed in cleaved metabasites, mafic schists and amphibolite (the presence of significant amount of epidote in the amphibolite suggests lower amphibolite or epidote amphibolite facies; Miyashiro, 1973). In addition, mafic samples from Wilandra area have probably experienced a second (retrograde) metamorphism of prehnite-pumpellyite facies no higher than 350 °C (Liou *et al.*, 1987).

For the late Proterozoic sequence, the assemblages of Ac+Ch+Ab, Ch+Ab+Mt±Ep and Ep+Qz suggest also a greenschist facies, but possibly of lower grade compared with those in the basement as no transition of actinolite to hornblende is observed. This would place the temperature range at 350 to 400 °C (Liou *et al.*, 1987). Again, both burial and regional processes seem to have similar metamorphic grade.

The Early Cambrian rocks are characterised by a burial metamorphism of prehnite-pumpellyite facies with temperature between 250 °C and 350 °C (Liou *et al.*, 1987), and a non-indicative assemblage (Cb+Qz+Ep) formed during regional metamorphism.

Chapter 4

Mineral Chemistry of the Mafic Rocks

4.1. INTRODUCTION

Detailed mineralogical studies using the electron microprobe techniques were undertaken and presented in this chapter. The microprobe analysis was aimed firstly at revealing compositional characteristics of various metamorphic and metasomatic phases and to obtain pressure and temperature constraints of the metamorphic processes so that a better understanding of the metamorphic history can be achieved. The second aim of the study is to determine the primary geochemical affinity of the mafic rocks from the chemistry of relic clinopyroxenes.

The metamorphic minerals analysed in this chapter include amphiboles, chlorites and Ca-Al silicates (epidote, clinozoisite, pumpellyite and prehnite). These minerals have been observed in various assemblages, and by analysing their distinct compositional variations, constraints of formation of the minerals are obtained and in turn the P-T-(t) paths for the metamorphic evolution are established. This also helps to understand the tectonic environments where the metamorphic processes may have occurred. Studies on metasomatic phases are concentrated on those observed in the nundorite (see Chapter Three) and on white micas.

4.2. STUDIES OF METAMORPHIC MINERALS

4.2.1. Amphiboles

Amphiboles from the Wonominta Block appear to have crystallised under a wide range of conditions during metamorphic processes, from low temperature (T) and low pressure (P) pumpellyite-actinolite facies to relatively higher T amphibolite facies.

Analyses of amphiboles from various localities in the Wonominta Block are presented in Tables 4.1A and B (in Appendix 3). In Table 4.1A, the calculation of structural formulae of calcic amphiboles is after Triboulet (1992) with Fe^{3+} estimates after Papike (1974) with the following procedures: (based on 23 oxygen of a formula, $A(M4)_2(M1,3)_3(M2)_2(T2)_4(T1)_4(O)_{22}(O,OH,F)_2$)

(1) Four Si in T2 site;

(2) The remaining Si and Al in T1 site with a sum of 4;

(3) The remaining Al plus Ti, Fe^{3+}, Fe^{2+}, Mn and Mg in M2 site with a sum of 2;

(4) Ca and Na in M4 site with a sum of 2;

(5) The remaining Na, K in A site with the "Vacancy" = $1 - (Na + K)_A$;

(6) $Fe^{3+} = (Al_{T1} + Na_{M4}) - ((Na + K)_A + Al_{M2} + 2Ti)$.

An iterative calculation is needed until convergence on a final Fe^{3+} is obtained.

And

(7) $(Fe^{2+}/Mg)_{M2} = (Fe^{2+}/Mg)_{M1,3} = (Fe^{2+}/Mg)_{amphibole}$.

There are some problems with this method, namely some Si-deficient amphiboles probably need part or all the Ti to fill in the T_1 site along with all Al; and some Ca-rich amphiboles have more than two units of Ca, which in turn influences the allocation of Na in M_4 and A site. Both anomalies influence the calculation of Fe^{2+}/Fe^{3+} ratio, but no correction is made here as there are no significant influence in the P-T calculations.

Following these calculations, several compositional characters can be observed: amphiboles from Nundora in the late Proterozoic sequence are low in Al and Ti; the Cambrian Comarto samples are high in Ca, which resulted in abnormal allocations to the M_4 and A sites. The Comarto samples also have no Al in M_2 due to Si deficiency in T_1. For the basement samples, most of amphiboles from the Ponto Mine Inlier (Ponto Mine and Boshy Tank areas) are low in Al_{M_2} compared with those in the

Wilandra Inlier. For those in the Wilandra Inlier, the Cymbric Vale samples are low in Ca and high in Na in M_4, compared with the unusually high Ca Wilandra samples (more than two atomic units). P-T variations are probably among the most important factors that control these compositional characteristics, as shown below.

The compositional discrimination is shown in Figure 4.1. This figure shows that most of the metamorphic amphiboles are of actinolite and actinolite-hornblende compositions: those in the hornblende field are from Comarto samples, two of which also plot as actinolite-hornblende. These analyses form two distinct compositional trends and both trends have higher Mg/Mg+Fe ratios as Si contents increase. In detail, the Comarto samples have lower Si contents than the others at the same Mg/Mg+Fe level.

The relic kaersutites (Table 4.1B) also plot in this diagram with two distinct compositional groups. Those from Packsaddle metadolerites (IB) contain less Mg compared with those from the Wonnaminta lamprophyre. The latter group displays almost constant Mg/Mg+Fe ratios over a range of Si.

Metamorphic amphiboles are known to vary in composition with metamorphic grade. An example is shown in Figure 4.2 after Laird and Albee (1981). This figure shows that most amphiboles from the basement sequence are in the biotite zone of metapelite except those from the Cymbric Vale amphibolite that fall outside the discriminant fields due to high Na/Na+Ca ratio. The Nundora samples from late Proterozoic sequence display lower grade features due to the absence of the Al component. The Cambrian Comarto samples have distinctive compositions characterised by the lower Na/Na+Ca ratios when compared to others at the same Al/Al+Si ratio.

This discrimination is in agreement with the facies analysis from petrographic studies. The basement samples have metamorphic assemblages of upper greenschist facies and their amphibole (actinolite-hornblende to hornblende) compositions suggest that the condition is equivalent to the biotite zone of metapelite, as suggested by studies on metasedimentary rocks (Mills, 1992). In contrast, samples from both Late Proterozoic early Cambrian sequences have compositions indicating a metamorphic grade lower than the biotite zone, presumably equivalent to the chlorite zone. Amphiboles from Cymbric Vale amphibolite exhibit a distinct composition with high Na/Na+Ca ratio. This character is more likely a result of higher pressure conditions, where the glaucophane component increases with relatively higher Na in M_4 (*e.g.* Miyashiro, 1973; see also Table 4.1 in Appendix 3).

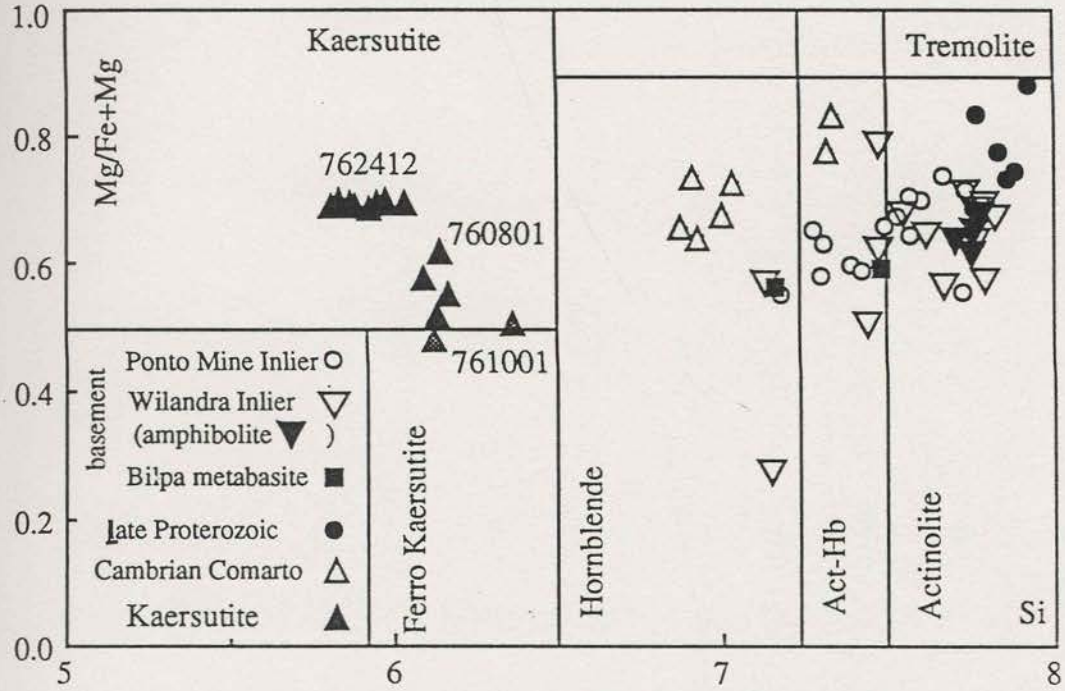

Fig. 4.1. Compositional discrimination of amphiboles from the Wonominta Block with classification after Leake (1978). The analyses can be generalised in two groups, the Ti-rich kaersutite and Ca-rich hornblende-actinolite. The kaersutites can be further divided into two compositions: those from the Wonnaminta lamprophyre have higher Mg/Mg+Fe ratios than those from late Proterozoic Packsaddle xenolithic samples. All calcic amphiboles are products of burial metamorphism except those from amphibolite in the Wilandra Inlier and plot in the hornblende-actinolite fields. They form two discrete compositional trends, both showing positive correlation between Si and Mg/Mg+Fe, but samples from Comarto have lower Si content at the same Mg/Mg+Fe level as the other samples. Amphiboles from the late Proterozoic sequence have higher Si and Mg* content compared with those from various basement localities.

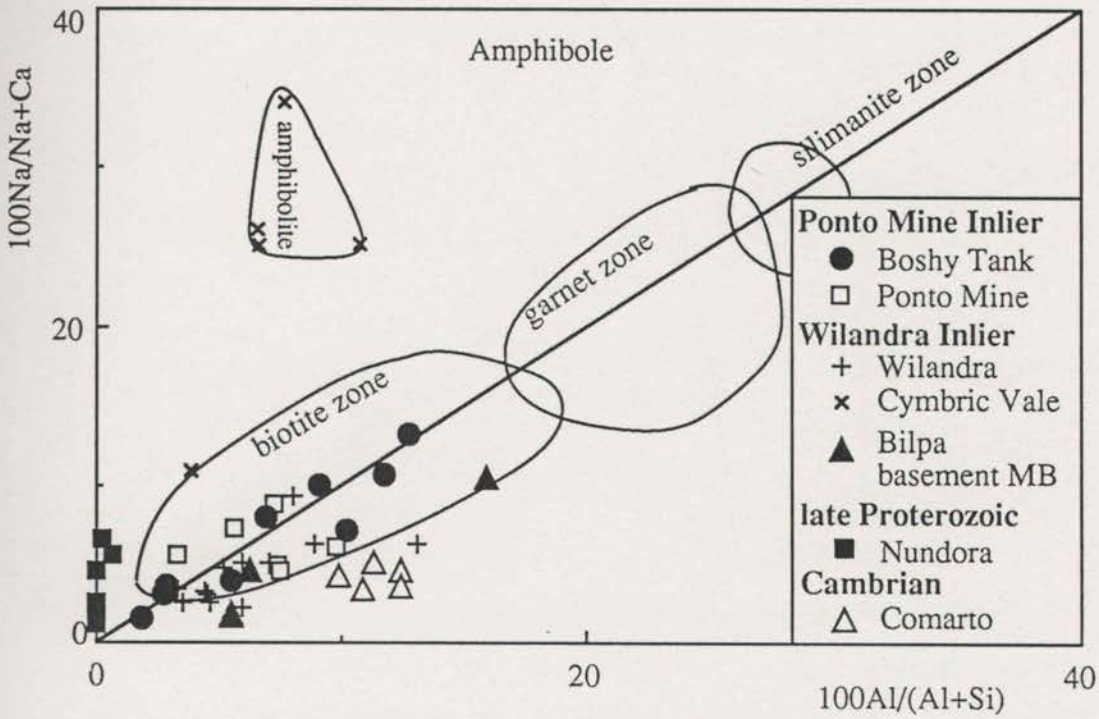

Fig. 4.2. Compositional variations of amphiboles from the Wonominta Block used to indicate metamorphic grade of the host rocks (discriminant fields after Laird & Albee, 1981). Most of the amphiboles from the Basement sequence plot in the biotite zone, except the Cymbric Vale amphibolite with high Na content. Both the Late Proterozoic and Cambrian Comarto samples plot outside the biotite zone, indicating lower grade of metamorphism.

4.2.2. Chlorite

Chemically, chlorite has a general formula of $M_{10\text{-}12}[(Si,Al)_8O_{20}](OH)_6$, of which M= Mg, Fe, Mn, Al^{VI} and Cr. The classification of chlorite has been controversial and complicated (Bayliss, 1975) due to the various substitution relationships between its components. The two major substitutions are:

$$Mg^{2+} \leftrightarrow Fe^{2+} \quad (4.1)$$

$$(Mg, Fe)^{VI} + Si^{IV} \leftrightarrow Al^{VI} + Al^{IV} \quad (4.2)$$

Analyses of chlorite from the mafic rocks are presented in Table 4.2 (Appendix 3). It can be seen from this table that Al_2O_3 ranges 15-22%, FeO 13-33% and MgO 10-26%. Mg/Mg+Fe (Mg*) ranges from 0.35 to 0.65 and high Fe species are those with yellowish colour under the microscope.

In Figure 4.3, the chlorites from the Wonominta Block are presented in two classification diagrams proposed by Hey (1954) and Bayliss (1975) respectively. Figure 4.3A shows that samples from the basement sequence with lower Si and Fe contents plot as ripidolite, and others from lower grade sequences plot in the pycnochlorite-brunsvigite fields with the same Si range as clinochlore. However, Figure 4.3B shows that the same basement samples plot in the clinochlore field and the others in the chamosite field. In his discussion of chlorite classification, Bayliss (1975) discarded all the 'species' names in Figure 4.3A except clinochlore, which is believed to be the most common species of the group. In this context, most of the chlorites analysed in this study are of clinochlore composition. This is also in agreement with Baily (1980). In Baily's classification, the compositions discussed here are between clinochlore and chamosite.

In terms of compositional variation with metamorphic conditions, Miyashiro (1973) and Moody *et al.* (1983) suggested that the Mg content in chlorite increases with progressive metamorphic grade, though Mg* numbers are also controlled by the whole rock compositions. Laird and Albee (1981) also pointed out that aluminium contents both in tetrahedral and octahedral positions increase with metamorphic grade in mafic schists. Both trends can be seen in Figure 4.3. It shows that the higher grade samples from the basement have less Si and lower Fe/(Fe+Mg) than those in the

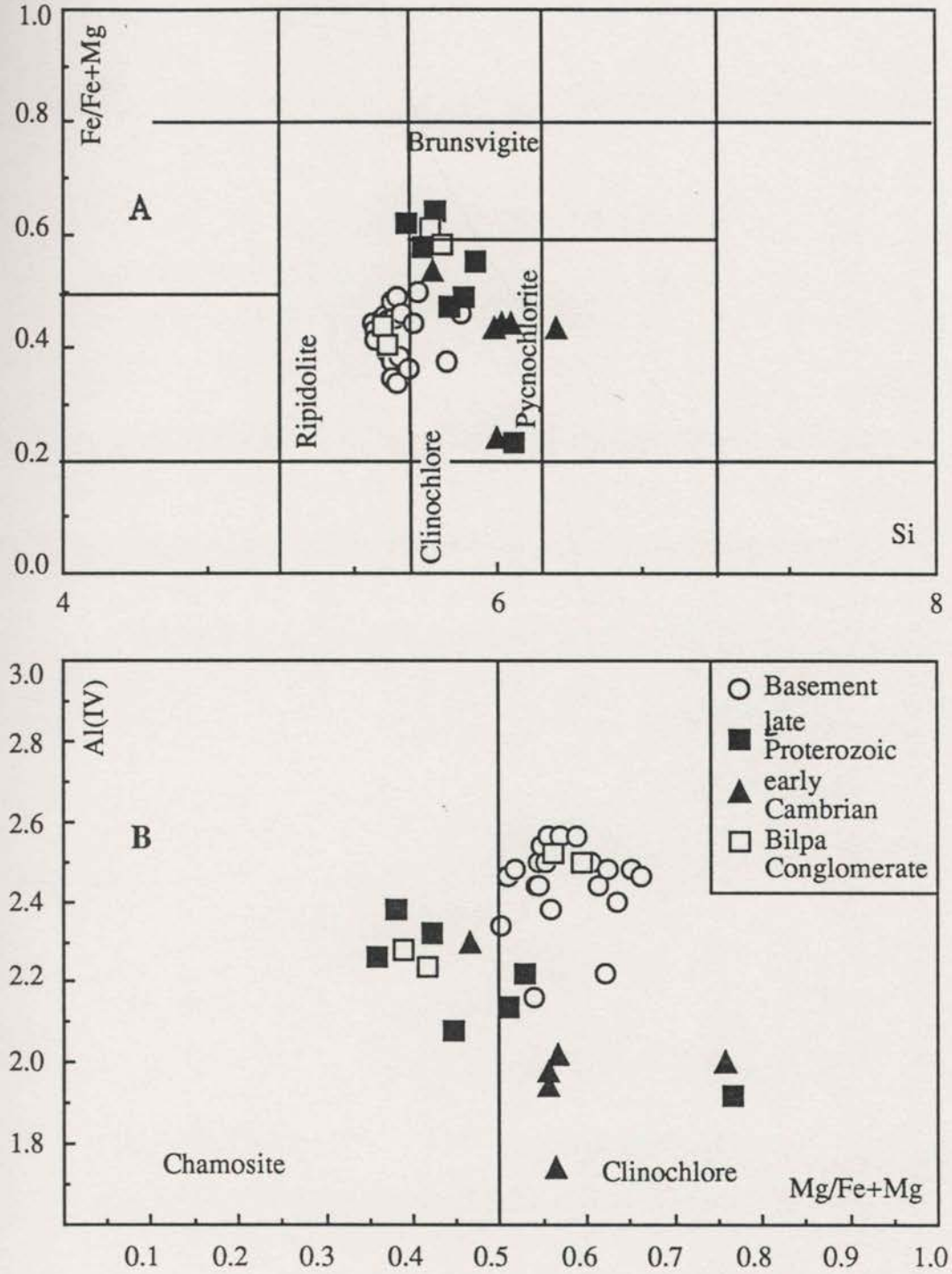

Fig. 4.3. Classification of chlorite from the Wonominta Block. In scheme A (Hey, 1954), most of the chorite in the mafic rocks from the basement sequence plot in the ripidolite field with lower Si and Fe/Fe+Mg than the others. The samples from younger sequences have brunsvigite-pycnochlorite compositions in the same Si range as clinochlore. However, in scheme B (Bayliss, 1975), the basement samples plot in the clinochlore field with higher Al and Mg, and the rest of the samples fall in both clinochlore and chamosite fields. Samples from the Bilpa area mafic clasts in the Bilpa Conglomerate appear to display two distinct compositional groups in both classifications, corresponding to those from the basement (high Mg*) and from the Bilpa Conglomerate respectively. The problem of the classification of chlorite minerals is discussed in the text.

younger sequences. Therefore, the two solid solution series may have been both dependent on P-T conditions.

Figure 4.4 displays the correlation of chlorite compositions with the metamorphic grade for mafic schist in a manner similar to that in Figure 4.2 (Laird & Albee, 1981). This figure shows that Al is approximately equally divided into tetrahedral and octahedral positions, which suggests that tschermakite substitution is dominant in the chlorites.

The above presentations suggest that the chlorite compositional variations reflect the change of metamorphic conditions, and that more Mg and Al substitute for Fe and Si as the temperature increases. Correlation between the chlorite compositions and the metamorphic grade suggests that mafic rock in the basement sequence have reached biotite zone, whereas those in the younger sequences probably only to the chlorite zone.

4.2.3. Ca-Al Silicates (Epidote Group, Prehnite & Pumpellyite)

Chemically, all the Ca-Al silicates considered here share a common formula:

$A_2B_3[SiO_4][Si_2O_7]O(OH)$
where, A = Ca, Mg, Fe^{2+} and may be substituted by minor Na and
B = Al^{3+}, Fe^{3+}

Epidote and clinozoisite form an isomorphous series with various Al/Fe ratios and without Mg. Pumpellyite contains minor Mg, whereas prehnite is characterised by minor ferrous, rather than ferric component.

Results of microprobe analyses of these minerals are presented in Table 4.3 (Appendix 3), which shows that Ca and Al are two of the major components in all species with variable amounts of Fe. Minor MgO in pumpellyite is up to 3 wt%.

Figure 4.5 presents the discrimination between total Fe and Al in these minerals. This diagram suggests that $Fe^{+3} \leftrightarrow Al^{+3}$ play a dominant role in compositional variations in epidote-clinozoisite series but to a lesser degree in pumpellyite, probably due to the presence of minor Fe^{+2} in the total Fe budget. This diagram clearly exhibits the differences of Al and Fe compositions in these minerals, which help to identify the

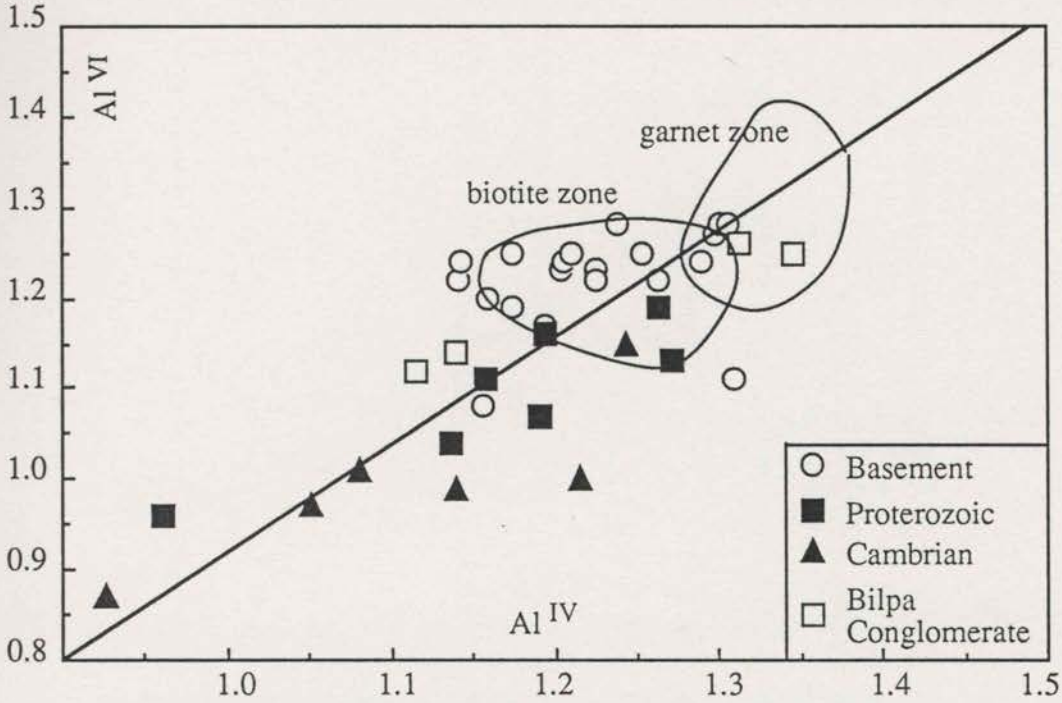

Fig. 4.4. Compositional discrimination of chlorite in the Wonominta Block. This diagram shows Al in both tetrahedral and octahedral positions in chlorite increases with metamorphic grade, and those from the basement sequence plot in the biotite zone of Laird and Albee (1981) with higher octahedral Al (some of the samples plotted in the field overlapping with garnet zone). The rest of the lower grade samples (late Proterozoic and Cambrian) plot on the lower side. This diagram, together with Fig. 4.2, clearly demonstrates different metamorphic grades experienced by mafic rocks from the three sequences of the Wonominta Beds.

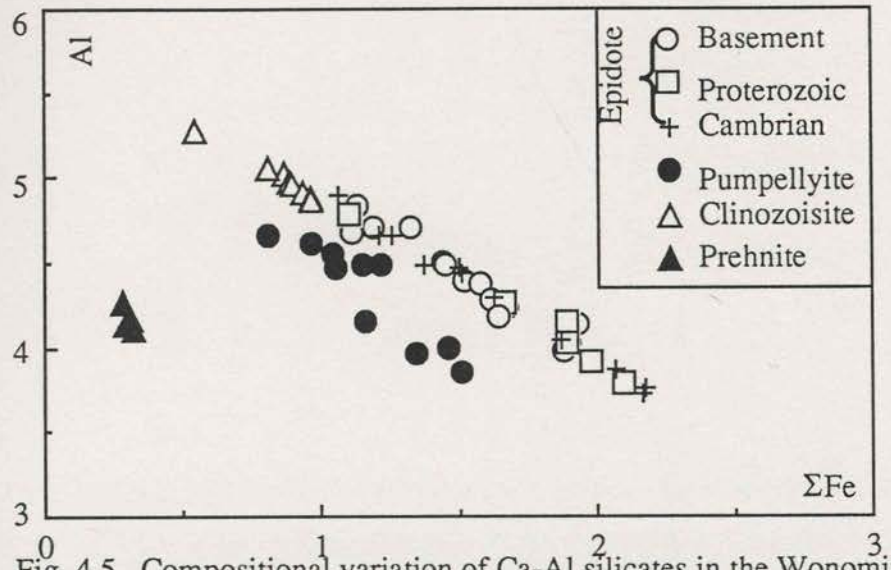

Fig. 4.5. Compositional variation of Ca-Al silicates in the Wonominta Block. The significant correlations in all three groups of the minerals suggest isomorphoic exchange between ΣFe and Al. Further, there are two compositional gaps in the epidote trend, but these exchanges do not correlate with metamorphic grades, as shown in Fig. 4.6.

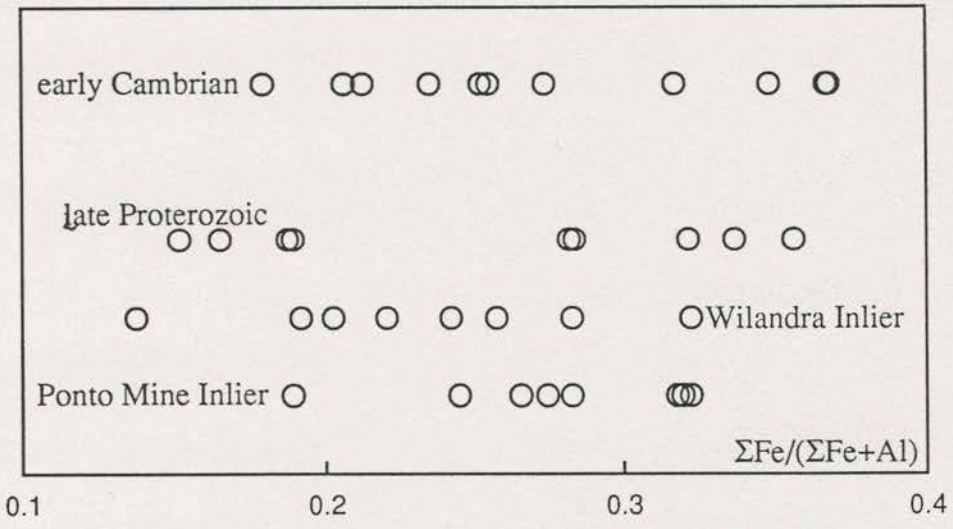

Fig. 4.6. ΣFe/(ΣFe+Al) variations in epidote against their occurrences. The diagram shows epidote in various metamorphic sequences have a wide compositional range, which does not correlate with the metamorphic grade.

minerals under the microscope. However, the compositional variation of epidote-clinozoisite series does not appears to be correlated with the metamorphic grade. To make this observation clear, $\Sigma Fe/(Al+\Sigma Fe)$ in epidote is shown in Figure 4.6 against field occurrence. It is obvious from this diagram that epidote from various occurrences have the same range of variation of $\Sigma Fe/(Al+\Sigma Fe)$ and there is no correlation between metamorphic grade and the compositional variations in epidote.

Some recent studies (Cho *et al.*, 1986; Cho & Liou, 1987; Bevin & Merriman, 1988) have shown that Fe^{3+} in epidote depends very much on f_{O_2} apart from temperature. Cho *et al.* (1986) pointed out that the amount of Fe in epidote is low in the zeolite facies, and then increases in the prehnite-pumpellyite facies; however, in the greenschist facies the iron content changes both with temperature and f_{O_2}. In the present study, epidote has been observed to coexist with various minerals that can be used to indicate the level of f_{O_2}. Detailed observation revealed that in thin sections with high Fe epidote, magnetite (and/or hematite) is generally an important accessory phase up to 10%, while in those with low Fe epidote, magnetite is generally no more than 3%, and some of the thin sections from Wilandra contain significant amounts of muscovite, in which iron is mostly in the ferrous state. This observation indicates that the epidote compositions may have been controlled mostly by the f_{O_2} of the metamorphic environment rather than temperature in the present case.

The transition between pumpellyite-actinolite facies and greenschist facies is marked by the reaction (Liou *et al.*, 1987; reaction 18):

$$\text{pumpellyite} + \text{chlorite} + \text{quartz} \leftrightarrow \text{clinozoisite} + \text{tremolite} + H_2O \qquad (4.3)$$

In this equilibrium, as the P-T increase, pumpellyite loses its minor Mg to form clinozoisite and chlorite is transformed to amphibole (adding Mg to the new phase). When amphibole is absent due to Si deficiency, Mg released from pumpellyite may enter into chlorite, which leads to the increase of Mg in chlorite as indicated in the last section.

Prehnite is a rare phase in the mafic rocks of prehnite-pumpellyite facies in this study, observed only in one sample from Comarto. Cho and Liou (1987) point out that prehnite disappears before pumpellyite when X_{CO_2} in the system is high. Considering the ubiquitous occurrence of carbonates in these mafic rocks, one of the reasons for lack of prehnite may be due to high X_{CO_2}.

4.2.4. Pressure and Temperature Constraints of Metamorphic Processes

Compositional variations observed in both amphibole and chlorite appear to correlate with metamorphic grade as discussed in the last three sections. However, it is also well known that the bulk rock compositions have a significant control over the composition of the metamorphic minerals (*cf.* Triboulet, 1992 for review). A further difficulty for P-T calculations is that most of the reactions are incomplete at these conditions, with rather limited equilibrium domains as confirmed by petrographic studies (Chapter 3). With such limitations in mind, an attempt has been made to estimate metamorphic P-T conditions from mineral chemistry. A summary of various methods used here is presented in Table 4.4.

Table 4.4. Methods used for P-T estimates in this study.

sequence	Basement		Late Proterozoic	Cambrian
facies	amphibolite	upper greenschist	lower greenschist	prehnite-pumpellyite
P	Brown (1977): Na_{M4} in Am		Cho & Liou (1988): ln $Kd_{Mg/Fe}$	
T	Blundy & Holland (1990): Am-Pl		Bevin *et al.*(1991): x values in Ch	
P-T pair	Triboulet (1992): Am-Ch-Ep assemblage			

It has been suggested that commonly at least two independent methods, if possible, should be used to calculate pressure and temperature respectively for each assemblage to obtained a range of the constraints (Liou *et al.*, 1987); but this is not always possible due to limited number of geothermometers and/or barometers available for the low grade metamorphic rocks. In the following presentations, no discrimination is made against samples representing burial (*sensu lato*) and regional metamorphic products until the final synthesis. This is because most of the methods are empirical and large errors may be introduced from selection of parameters.

4.2.4.1. Pressure (P)

Pressure has been estimated using the Mg/Fe distribution coefficients (K_D) of coexisting chlorite and actinolite (Cho & Liou, 1988). The method is suitable for the low grade samples from the late Proterozoic and Cambrian sequences. The equation is:

$$P = 10.5 \ln K_D + 0.5 (\pm 2 \text{ kbar}) \quad (4.4)$$

where $K_D = (Mg/Fe)_{Am}/(Mg/Fe)_{Ch}$ of coexisting amphibole and chlorite.

For the basement samples, Na in M_4 site is used to estimate the pressure based on an empirical relationship (Brown, 1977; Figure 10). The results are presented in Tables 4.5A, B.

4.2.4.2. Temperature (T)

The temperature has been calculated using the method of Bevin *et al.* (1991) using chlorite compositions for the Late Proterozoic and early Cambrian samples (Table 4.6A). These authors showed that the relative proportions (x) of 'pure' chlorite to the swelling component (inter-layer brucite phase) has the following relationship:

$$T = 641.02\, x - 287.18 \quad (r = 0.83) \quad (4.5)$$

$x = 1$ represents 'pure' chlorite without the swelling component. The calculation of x is after W. Wise (personal communication in Bettison & Schiffman, 1988), though descriptions in Bettison & Schiffman (1988) are rather sketchy and there are no details of the calculation at all in Bevin *et al* (1991). The procedures used here were:

1) calculate structural composition of the samples by assuming a formula of the mineral:
$(K, Na, Ca_{0.5})_{z-y}{}^{VI}[(Mg,Fe, Mn)_{6-y}Al_y]^{IV}[Si_{8-z}Al_z]O_{20}(OH)_4 * x[(Mg,Fe)_6(OH)_{12}]$;
2) calculate a proportional factor (f): $f = 16/[Al+2Si-2Ca-K]$, assuming $z<y$;
3) applying f to all components; and then calculate $z = 8-fSi$; $y=fAl-z$;
then compositions in octahedral site can be resolved:
4) $x = 6/(\Sigma(fMg, fFe)- (fMg, fFe)_{VI})$

Blundy and Holland (1990) proposed an empirical geothermometer using equilibrium reaction between amphibole and plagioclase (500 -1100 °C ± 75 °C):

$$T = (48.98 - 0.677P - Y)/(0.0429 + 0.008314 \ln K) \quad (4.6)$$

where $K = Si_{T1}/(4-Si_{T1})$; P in kbar; Y represents plagioclase non-ideality from Darken's Quadratic formalism (DQF): $Y = 0$ for $X_{Ab} > 0.5$ and

$$Y = -8.06 + 25.5\,(1- X_{Ab})^2 \text{ for } X_{Ab} < 0.5$$

This calibration is applicable only to basement samples. As most plagioclase in basement samples is pure albite, $Y = -8.06$ and (4.7) becomes:

$$T = (57.04 - 0.677P)/(0.0429 + 0.008314 \ln K) \quad (4.8)$$

For the Cymbric Vale amphibolite, the average X_{Ab} is about 0.75 from petrographic studies (andesine - oligoclase, Chapter Three), thus $Y = -6.47$ and (4.7) becomes

Table 4.5A. Pressure estimate using Mg* in coexisting Ac and Ch (Cho & Liou, 1988)

	Basement								Proterozoic		Cambrian
sample	762302	762603	762705	861210	861205	861605	861601	861304	761906		861005
	Ponto	Boshy Tank		Wilandra					Nundora		Comarto
chlorite											
Fe	4.255	3.652	4.109	4.359	4.359	3.417	4.667	4.233	2.312	4.196	4.213
Mg	5.258	6.053	5.155	5.092	5.092	5.633	4.772	5.064	7.652	5.469	5.262
Mg/Fe	1.236	1.657	1.255	1.168	1.168	1.649	1.022	1.196	3.310	1.303	1.249
amphiboles											
Fe	1.807	1.720	2.009	1.573	1.673	1.397	2.089	1.997	0.856	1.355	1.424
Mg	3.125	3.258	2.665	3.328	3.239	3.407	2.806	2.689	4.402	2.520	2.506
Mg/Fe	1.729	1.894	1.327	2.116	1.936	2.439	1.343	1.347	5.143	1.860	1.760
ln Kd	0.336	0.134	0.056	0.594	0.505	0.392	0.273	0.118	0.441	0.355	0.343
P(kbar)	4.0	1.9	1.1	6.7	5.8	4.6	3.4	1.7	5.1	4.2	4.1

Table 4.5B. Pressure estimate using Na(M4) content in amphiboles from the basement samples.

Ponto Mine Inlier																
Ponto Mine area							Boshy Tank area									
	752202			752302			762501	762603		762701	762701	762705		762706		
sample	1	2	3	1	2	3	1	2	1	2	1	2	1	2	1	2
Al (IV)	0.577	0.265	0.448	0.63	0.476	0.587	0.694	0.95	0.792	0.546	0.217	0.231	0.729	0.153	0.443	0.773
Na (M4)	0.116	0.049	0.069	0.049	0.04	0.088	0.075	0.151	0.003	0.089	0	0.037	0.024	0	0	0
P (kbar)	2.2	<2	<2	<2	<2	2	2	3	<2	2	<2	<2	<2	<2	<2	<2
general statement	approximately 2 kbar or less						0- 3 kbar, most less than 2 kbar									

Wilandra Inlier																
Wilandra area												Cymbric Vale area				
	861210		861302		861304		861311		861601		861605	861713		861714		
sample	1	2	1	2	1	2	1	2	1	2	1	1	2	1	2	2
Al (IV)	0.178	0.265	0.543	0.245	0.616	0.935	0.497	0.431	0.223	0.345	0.279	0.333	0.37	0.301	0.394	0.843
Na (M4)	0	0.116	0.007	0	0.025	0.043	0	0	0	0	0	0.502	0.685	0.425	0.455	0.419
P (kbar)	<2	2.2	<2	<2	<2	<2	<2	<2	<2	<2	<2	5.0	5.7	4.8	4.9	5.0
general statement	approximately 2 kbar or less											4.8 - 5.7 kbar				

Table 4.6A Temperature estimate using ratio (x) of swelling component in chlorite (after Bevin et al., 1991).

sequence	late Proterozoic							Cambrian									
area	Nundora							Comarto			Mt. Wright			Bilpa Conglomerate			
samples	761512		761810		761901		761906	861003	861005		862112		862402	862909		863012	
	1	2	1	2	1	2			1	2	1	2		1	2	1	2
Si	5.580	5.706	5.773	5.841	5.901	5.657	6.068	5.696	5.983	6.011	6.265	6.055	5.997	5.689	5.740	5.493	5.472
Al	4.896	4.810	4.534	4.522	4.359	4.717	3.845	4.787	4.178	4.265	3.584	4.045	4.432	4.568	4.481	5.181	5.143
Al(IV)	2.420	2.294	2.227	2.159	2.099	2.343	1.932	2.304	2.017	1.989	1.735	1.945	2.003	2.311	2.260	2.507	2.528
Al (VI)	2.476	2.516	2.307	2.363	2.260	2.374	1.913	2.483	2.161	2.276	1.849	2.100	2.429	2.257	2.221	2.674	2.615
Mg	3.537	3.296	5.035	4.774	4.244	4.015	7.652	4.326	5.469	5.262	5.631	5.376	7.001	3.743	4.028	5.428	5.174
Fe	5.753	5.871	4.486	4.605	5.284	5.492	2.312	4.965	4.196	4.213	4.344	4.299	2.210	5.886	5.620	3.693	4.057
Mn	0.040	0.032	0.028	0.026	0.048	0.055	0.057	0.056	0.041	0.042	0.047	0.091	0.069	0.066	0.073	0.057	0.062
Ca	0.032	0.027	0.038	0.007	0.027	0.018	0.023	0.037	0.036	0.040	0.060	0.050	0.075	0.029	0.039	0.027	0.011
K	0.060	0.125	0.071	0.128	0.067	0.008	0.020	0.046	0.011	0.031	0.003	0.013	0.007	0.009	0.017	0.015	0.033
z<y, f=	1.004	0.997	1.004	0.996	0.998	1.001	1.005	0.996	0.996	0.989	1.001	0.997	0.983	1.008	1.008	0.994	0.998
fSi	5.60	5.69	5.80	5.82	5.89	5.66	6.10	5.68	5.96	5.95	6.27	6.04	5.90	5.73	5.79	5.46	5.46
fAl(IV)	2.40	2.31	2.20	2.18	2.11	2.34	1.90	2.32	2.04	2.05	1.73	1.96	2.10	2.27	2.21	2.54	2.54
fAl(VI)	2.52	2.49	2.35	2.32	2.23	2.38	1.97	2.44	2.12	2.16	1.85	2.07	2.26	2.34	2.31	2.61	2.59
fMg	3.55	3.29	5.06	4.76	4.23	4.02	7.69	4.31	5.45	5.20	5.63	5.36	6.89	3.77	4.06	5.39	5.16
fFe	5.78	5.86	4.50	4.59	5.27	5.50	2.32	4.95	4.18	4.17	4.35	4.29	2.17	5.93	5.67	3.67	4.05
fMn	0.04	0.03	0.03	0.03	0.05	0.06	0.06	0.06	0.04	0.04	0.05	0.09	0.07	0.07	0.07	0.06	0.06
fCa	0.03	0.03	0.04	0.01	0.03	0.02	0.02	0.04	0.04	0.04	0.06	0.05	0.07	0.03	0.04	0.03	0.01
fK	0.06	0.12	0.07	0.13	0.07	0.01	0.02	0.05	0.01	0.03	0.00	0.01	0.01	0.01	0.02	0.01	0.03
x	0.98	0.94	0.99	0.95	0.96	0.99	1.00	0.96	0.97	0.93	0.98	0.97	0.90	1.00	1.00	0.96	0.98
T (°C)	342	318	347	321	331	349	354	328	332	309	341	334	288	354	354	325	340

Table 4.6B. Temperature estimate of basement samples (calculation after Blundy & Holland, 1990)									
sample	762305	762603	762705	861205	861210	861304	861601	861605	861714
area	Ponto Mine	Boshy Tank		Wilandra					Cymbric Vale
	amphibole (structural formula based on 23 oxygen)								
Si	7.497	7.422	7.514	7.800	7.831	7.136	7.734	7.768	7.748
P (from Cho & Liou, 1988)	4.0	1.9	1.1	5.8	6.7	1.7	3.4	4.6	-
T (°C)	648	694	676	515	490	769	571	543	-
P (from Triboulet, 1992)	7.4	7.4	7.4	7.8	7.9	7.5	7.4	7.5	7.8
T (°C)	609	629	604	495	478	696	529	513	519

$$T = (55.45 - 0.677P)/(0.0429 + 0.008314 \ln K) \quad (4.9)$$

Using (4.8) and (4.9), temperature can be estimated and the calculation is presented in Table 4.6B, where P is estimated from Table 4.5B and 4.7 respectively.

Using coexisting Am-Ch-Ep with excessive albite and quartz, Triboulet (1992) proposes an empirical geothermobarometer, estimating both P and T. This method applies to albite-bearing assemblages only, and hence to all sequences except the Cymbric Vale amphibolite. First, coefficients (ln Kd) between tremolite-edenite and (pargasite/hastingsite)- tremolite equilibria are calculated using Si_{T1}, Al^{IV}, Al^{VI}, Fe^{3+}, Fe^{2+}, Mg, Ca, Na_{M4},Na_A and A vacancy of amphiboles, Al in coexisting epidote and (Mg, Fe) in coexisting chlorite with a small BASIC computer program; then the two coefficients are plotted in a series of isopleths to determine P and T (Figure 2, Triboulet, 1992). The results are shown in Table 4.7.

4.2.4.3. Synthesis of the P-T Estimates

Table 4.8 presents synthesized P-T estimates from the above calculations. In this table, samples of burial (*sensu lato*) and regional metamorphic products are presented separately by combining the above calculations with petrographic studies.

It is clear from this table that pressure estimates following Brown (1977) are too low, though for Cymbric Vale samples, this method may provide a lower limit. The calculations using Cho and Liou's equation also yield lower values, compared with the results from Triboulet's calculations. Therefore, combining the three different P-estimates, lower and higher limits can be obtained respectively.

Most of the temperature calculations following Bevin *et al.* (1991) are in accordance with facies analysis; but some estimates from Blundy & Holland (1990) are too high for the transition of greenschist to amphibolite facies (*e.g.* Liou *et al.*, 1987), though the results for Cymbric Vale amphibolite are acceptable. Similar anomalously high-T results have also been reported recently by Mengel & Rivers (1991) with no obvious reasons. In the present case this anomaly may be explained by the fact that the assemblages studied here are at the lower limit of the application. In contrast, the temperature estimate using Triboulet's method are relatively low. By combining the two approaches, temperature ranges can be obtained for the basement samples. The temperature variations for younger sequences are estimated from Table 4.6A only.

Table 4.7 P-T estimates using coexisting Am-Ch-Ep assemblage						
sample	762705	861210	861304	861605	861714	761906
area	Boshy Tank		Wilandra		Cymbric Vale	Nundora
sequence	Ponto Mine Inlier			Wilandra Inlier		Pt(3)
	data set					
amphibole						
Si(T1)	3.271	3.375	3.065	3.721	3.606	3.768
Al(IV)	0.729	0.265	0.935	0.279	0.394	0.053
Al(VI)	0.229	0.045	0.121	0.082	0.143	0.000
Fe3+	0.213	0.201	0.453	0.112	0.600	0.000
Fe2+	1.725	1.572	1.544	1.253	1.144	0.856
Mg	2.701	3.135	2.662	3.462	3.087	4.402
Ca	1.976	1.884	1.957	2.049	1.545	2.009
Na(M4)	0.024	0.116	0.043	0.000	0.455	0.000
Na(A)	0.213	0.109	0.090	0.063	0.067	0.117
Vacancy	0.744	0.874	0.867	0.922	0.900	0.862
epidote						
Al	2.100	2.194	2.253	2.517	2.120	1.899
chlorite						
Mg	5.155	5.092	3.995	5.633	3.509	7.652
Fe	4.109	4.359	5.310	3.417	6.106	2.312
	calculations					
LnKd1	-0.5	-2.4	-1.2	-3.0	-2.6	-4.0
X(Mg)	0.61	0.67	0.63	0.73	0.73	0.84
	X(Fe3+) = 0					
LnKd2	-2.48	-6.9	-3.4	-6.9	-5.2	-15.9
T (°C)	475	353	424	352	338	321
P (kbar)	8.0	8.0	8.0	7.6	8.6	6.0
	X(Fe3+) = 0.2					
Ln Kd2	-4.1	-7.0	-3.7	-8.2	-5.4	-17.5
T (°C)	451	356	440	358	372	321
P (kbar)	6.8	7.7	7.0	7.1	6.9	6.2
	mean					
T (°C)	463	355	432	355	355	321
P (kbar)	7.4	7.9	7.5	7.4	7.8	6.1

Reference: Triboulet, 1992

Table 4.8. Synthesis of P-T Conditions of Regional and Burial Metamorphism of Mafic Rocks

sequence	Ponto Mine Inlier			Wilandra Inlier						
sample	762302/5	762603	762705	861210	861205	861605	861601	861304	861713	861714
area	Ponto	Boshy Tank		Wilandra					Cymbric Vale	
metamorphism	B	B	B	R	B	B	B	B	R	R
P(±2 kbar)(1)	4	1.9	1.1	6.7	5.8	4.6	3.4	1.7	N/A	N/A
P (kbar) (2)	≤2	≤2	≤2	≤2.2	<2	<2	<2	<2	5.0-5.7	4.8-5.0
P (kbar) (3)	(7.4)	(7.4)	7.4	7.9	(7.4)	7.5	(7.4)	7.5	-	7.8
T (°C) (4)	-	-	463	355	-	355	-	432	-	355
T (°C) (5)	(609)	(629)	604	478	(499)	513	(652)	696	534-542	519

sequence	late Proterozoic				Cambrian		
sample	761512	761810	761901	761906	861003	861005	862112
area		Nundora			Comarto		Mt Wright
metamorphism	B	B	B	R	B	B	B
P(±2 kbar)(1)	-	-	-	5.1	-	4.1-4.2	
P (kbar) (3)	-	-	-	6.1	-	N/A	N/A
T (°C) (4)	318-342	321-347	331-349	354	328	321	338
T (°C) (3)	-	-	-	321	N/A	N/A	N/A

Note: (1). After Cho & Liou (1988)
(2). After Brown (1977)
(3). After Triboulet (1992)
(4). After Bevins et al (1991)
(5). After Blundy & Holland (1990)
-: No data available; N/A: not applicable
B: burial metamorphism (sensu lato); R: regional metamorphism.

4.2.5. P-T-t Paths and Metamorphic History

The integrated estimates of P-T ranges of burial (*sensu lato*) and regional metamorphic processes is presented in Table 4.9. Using these results, anti-clockwise P-T-t paths can be constructed for basement and younger sequences respectively (Figure 4.7). This figure shows that the burial metamorphism (*sensu lato*) occurred at higher geothermal gradient (T/P) compared with that of the regional metamorphism. However, only estimates of burial (*sensu lato*) metamorphism of the Ponto Mine Inlier and that of regional metamorphism of late Proterozoic sequence yield significantly higher and lower values respectively than the average crustal geothermal gradient (25 ^{o}C/km, Turner, 1981). This may suggests that the long period of cratonic environment after the regional metamorphism during the Delamerian Orogeny (ca. 500 Ma, Preiss, 1987) have largely reset the peak metamorphic conditions. Therefore, 37 ^{o}C/km and 17 ^{o}C/km are possibly the minimum and maximum gradients for burial (*sensu lato*) and regional metamorphism respectively at the time. Alternatively, this may indicate some problems in the P-T calculations as discussed below.

The estimated upper limit of pressure for burial metamorphism appears to be too high, which would have to require, if real, an extraordinarily thick pile of deposits. Given 37 °C/km being the minimum gradient, the pressure should not be higher than 4 kbar compared with the calculated 7 kbar at 500 °C. Alternatively, some of the minerals used for the P-T calculations of burial metamorphism may have been products of regional processes. These minerals do not display significant deformation due to stress partitioning, as discussed in Chapter 3. In other words, the P-T calculations may have indirectly demonstrated that minerals of regional metamorphism do not necessarily display characteristic structures and this makes the whole exercises more complicated and less certain.

However, it can still be seen from Figure 4.7 that there is probably no significant increase in temperature during regional metamorphism, no matter if the pressure is marginally higher or significantly higher than that prevailing during burial metamorphic processes (which would depend on a better resolution of pressure calculations). This suggests that metamorphic conditions had already been at the maximum when deformation occurred. This scenario has significant tectonic implications (*cf.* Robinson, 1987) and is further discussed in Chapter 10.

maximum when deformation occurred. This scenario has significant tectonic implications (*cf.* Robinson, 1987) and is further discussed in Chapter 10.

Table 4.9. Estimated P-T conditions of Burial and Regional Metamorphism of the Wonominta Beds

		Ponto Mine Inlier	Wilandra Inlier	late Proterozoic	Cambrian
Burial Metamorphism					
Pressure	-Low	1.1	1.7	N/A	N/A
	-High	4 - 7.4	5.8 - 7.5	N/A	4.1 - 4.2
Temperature	-Low	463	432	321	309
	-High	600±75#	499-529	354	332
T/P (^{o}C/kbar)	mean	122	87	70	80
(^{o}C/km)*	mean	37	26	21	24
Regional Metamorphism					
Pressure	-Low	N/A	7.8	5.1	N/A
	-High		7.9	6.1	
Temperature	-Low	N/A	355	321	N/A
	-High		519	354	
T/P (^{o}C/kbar)	mean	N/A	82	58	N/A
(^{o}C/km)*	mean	N/A	25	17	N/A

note: * assuming 0.3 kbar/km for geothermal gradient calculations (Turner, 1981);
probably at the lower end of the range;
N/A: data not available.

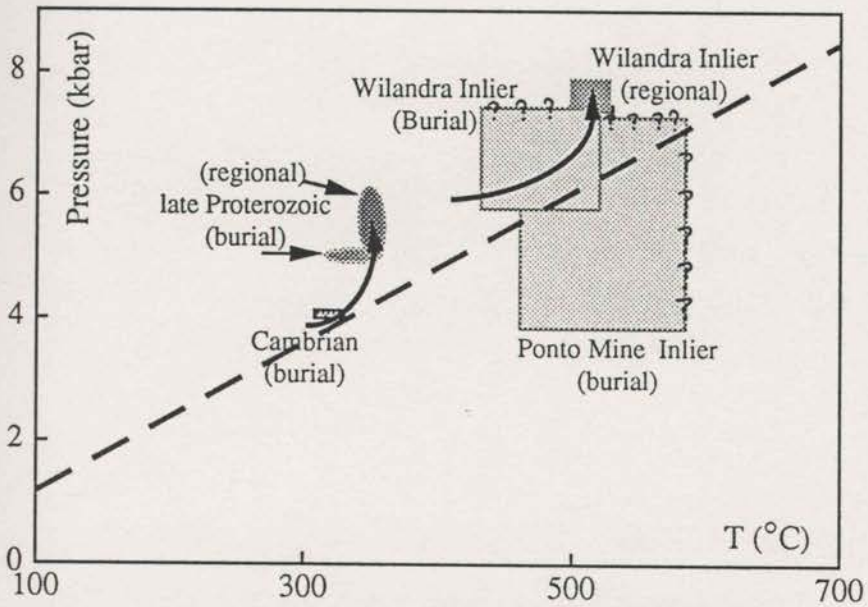

Fig. 4. 7. anti-clockwise P-T-t paths of burial/regional metamorphism for mafic rocks in the basement and late Proterozoic/Cambrian sequences of the Wonominta Beds. Dashed line shows an average continental geotherm gradient (Turner, 1981).

4.3 STUDIES OF METASOMATIC MINERALS

4.3.1.ALUMINOUS AEGIRINE.

Aegirines were observed only in nundorite from Nundora. Field observation and petrographic studies indicate that the nundorite was probably derived from the surrounding felsic tuffs in a metasomatic environment (Chapter Three). Under the microscope, most of the mineral appears in granular patches with very high relief. These patches may be divided in two groups based on their colours. The light-coloured samples show light green colour corresponding to their bright pink-green textures in hand specimen; while dark-coloured samples are dark green both in thin section and in hand specimen.

In composition, the ideal aegirine has a formula of $NaFe^{3+}Si_2O_6$, but in reality, the mineral shows a wide range of compositions and there are three major substitutions. The first one is:

$$NaFe^{3+} \leftrightarrow Ca(Mg, Fe^{2+}) \qquad (4.7)$$

which constitutes the aegirine - augite series. The second one is

$$2Fe^{3+} \leftrightarrow Fe^{2+} + Ti^{4+} \qquad (4.8)$$

The compositional end member, ($Na_2Fe^{2+}TiSi_4O_{12}$) is known as neptunite and an occurrence of the aegirine - neptunite series has been reported by Ferguson (1977). And the third one is

$$Fe^{3+} \leftrightarrow Al^{3+} \qquad (4.9)$$

which forms the aegirine-jadeite series.

Five samples of both dark (762404 and 762406/7) and light green (762402/3) species were analysed and the results are presented in Table 4.9 (Appendix 3). Chemically, all iron is treated as ferric component. It is possible to calculate the ratios of ferrous and ferric components assuming ideal structural formulae, or simply setting a ratio between these two components. But both methods are arbitrary, and there seems to be no need to do the correction in this study given the particular analytical precision. All

analyses of the mineral show virtually no Ti, Ca or Mg, and variable Fe and Al. The analyses can be divided into two groups according to the abundance of Al (Figure 4.8). The dark green minerals plot in the field of aegirine and the light green ones in the aluminous aegirine field. From this figure, it can also be seen that the dark green species contain slightly more Ca than the light ones.

Figure 4.9 presents the correlation between Fe and Al occupying the octahedral position in the mineral. Clearly the correlation is excellent, which indicates the higher content of Al is due to the substitution of Fe instead of Si by Al, that is, the chemical variations of the aegirine observed at this locality is of the Fe $\leftrightarrow$ Al series with a clear compositional gap between the two groups. This situation raises the question as to whether this mineral was formed in a high pressure environment as indicated by the presence of jadeitic component ($NaAlSi_2O_6$).

The available literature reveals that there are some disagreements about the aegirine - jadeite series. Newton and Smith (1967) showed that aegirine forms a nearly ideal solid solution with jadeite at 600 $^{\circ}$C; while Coleman and Clark (1968) presented a compositional gap between jadeite and aegirine in a natural example from the San Franciscan Formation in California. Recently, Curtis and Gittins (1979) reported both aluminous and titaniferous aegirine series from regionally metamorphosed peralkaline rocks in Central Labrador, and concluded that the omphacitic and jadeitic components do not necessarily mean a high pressure environment, but they are developed as a consequence of the low α_{Si} and high alkalinity of the rocks.

Thus, it is likely that the existence of a jadeitic component in the aegirine minerals does not indicate a high pressure, but an alkaline environment. In fact, the coexistence of nepheline minerals suggests that they were probably developed in a low pressure process. The mineral compositions were thus controlled by the compositions of host felsic tuff and alkalic fluids. From the petrographic studies presented in Chapter 3, it is clear that the darker aegirine was formed in the early stages of the alteration. As the process proceeded (or in an environment where fluids/host rock ratio are higher), the light green species grew with better crystal form. Chemically, this process involved substitution of Fe by Al, loss of all Ca and gain of Na within the mineral, as indicated by the microprobe analysis. Bulk rocks analyses, presented in Chapter 7, reveal similar processes in the whole rock system; therefore, chemical exchanges should have happened in an open system, *i.e.*, metasomatic processes.

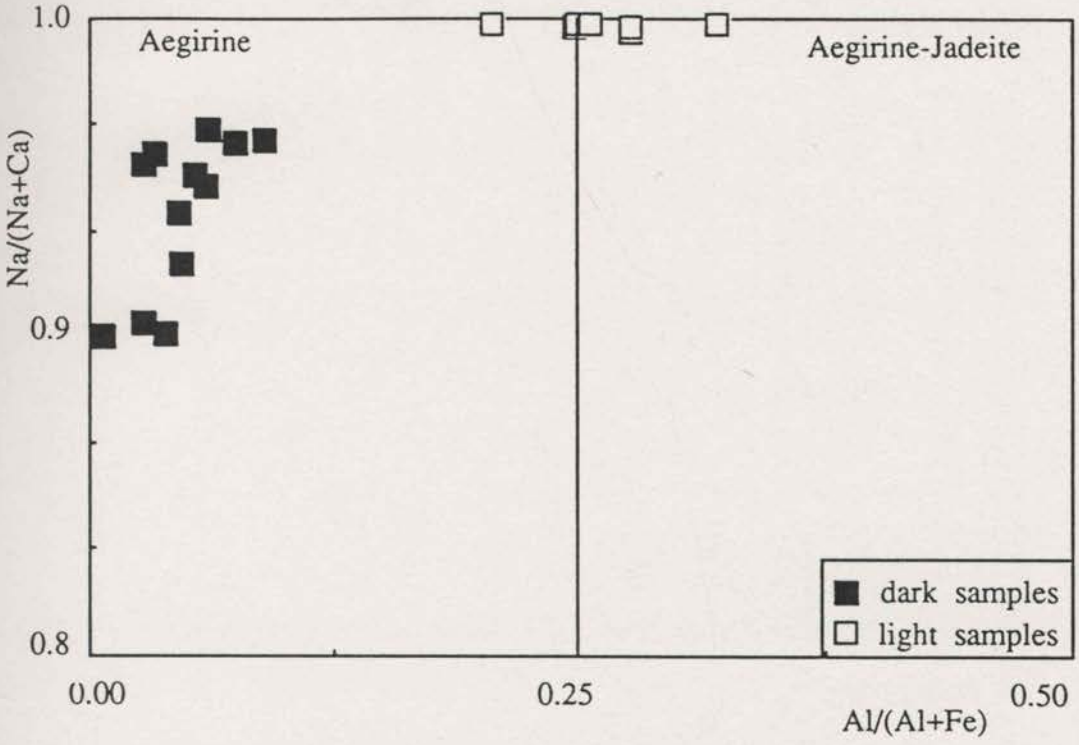

Fig.4.8. Compositional discrimination of aegirines in nundorite from the Nundora area in the Wonominta Block. The classification is after Curtis & Gittins (1978). This diagram clearly indicates aegirines from this locality form two distinctive groups corresponding to their occurrence with those from light-coloured samples plotting in the aegirine-jadeite field and those from dark-coloured samples in the aegirine field with some Na content.

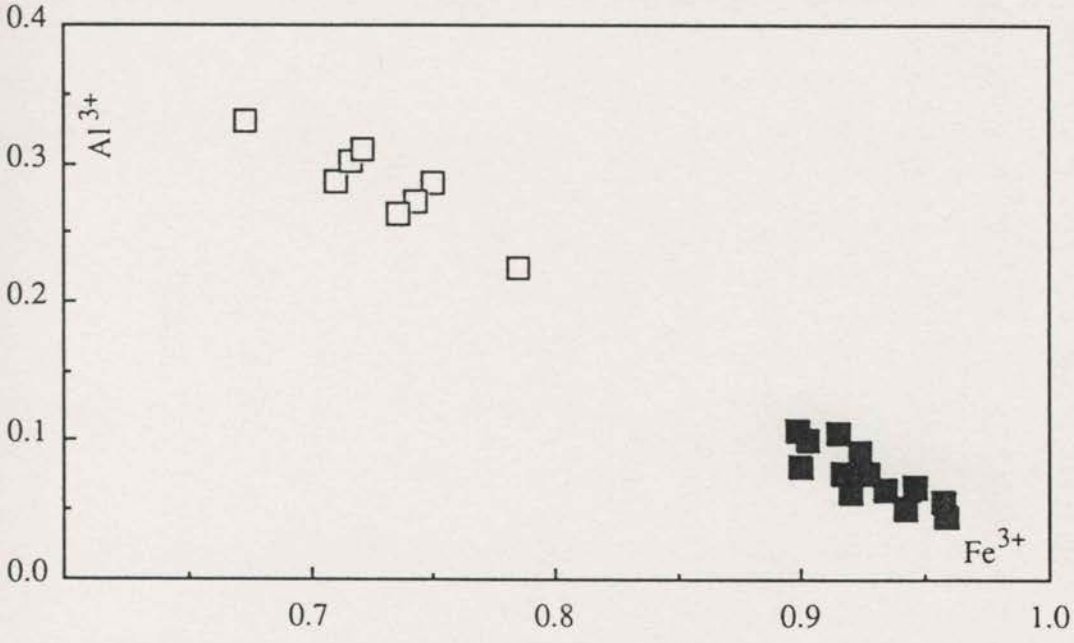

Fig.4.9 Correlation between Fe^{3+} and Al^{3+} components in octahedral position in the aegirine minerals from Nundora. Open square, light crystals; filled sqaure, dark crystals. This diagram shows a high correlation between the two components, indicating isomorphous replacement in the crystal structure.

4.3.2. Alkaline Feldspar and Feldspathoid

Feldspar minerals observed in various metamorphosed mafic samples from the Wonominta Block are dominantly albitic plagioclase. Minor potassium feldspar is observed in felsic tuff and porphyry from Mt. Wright and in sodic syenite from Packsaddle and Nundora. The feldspathoid nepheline and natrolite occur only in nundorite at Nundora together with aluminous aegirine.

Table 4.11 (in Appendix 3) presents analyses of these feldspar and feldspathoid minerals. The results also plot in Figure 4.10. Figure 4.10A shows that albite displays a rather limited range in composition while most potassium feldspars are characterised by the existence of some sodic component. In an extreme example, analyses from sample 862219 yield orthoclase, albite and anorthoclase respectively with obvious compositional gaps in between. However, in view of the high instability of anorthoclase under the conditions prevailing in these rocks, it is possible this component is an artifact resulting from analytical errors.

The feldspathoid minerals are also enriched in Na (Figure 4.10B). Two analyses of nepheline from light coloured nundorite samples yielded a ratio of 3:1 for Na:K. Natrolite analyses also display two distinct compositions corresponding to their occurrence. Analyses from dark nundorite samples contain minor K up to 1.58% in potassium oxide and those from light pinkish nundorite contain essentially no K at all.

These compositional characters suggest that the alkaline fluid that caused the alteration may have been sodic-enriched; and as the metasomatic processes proceeded, K was gradually replaced by Na.

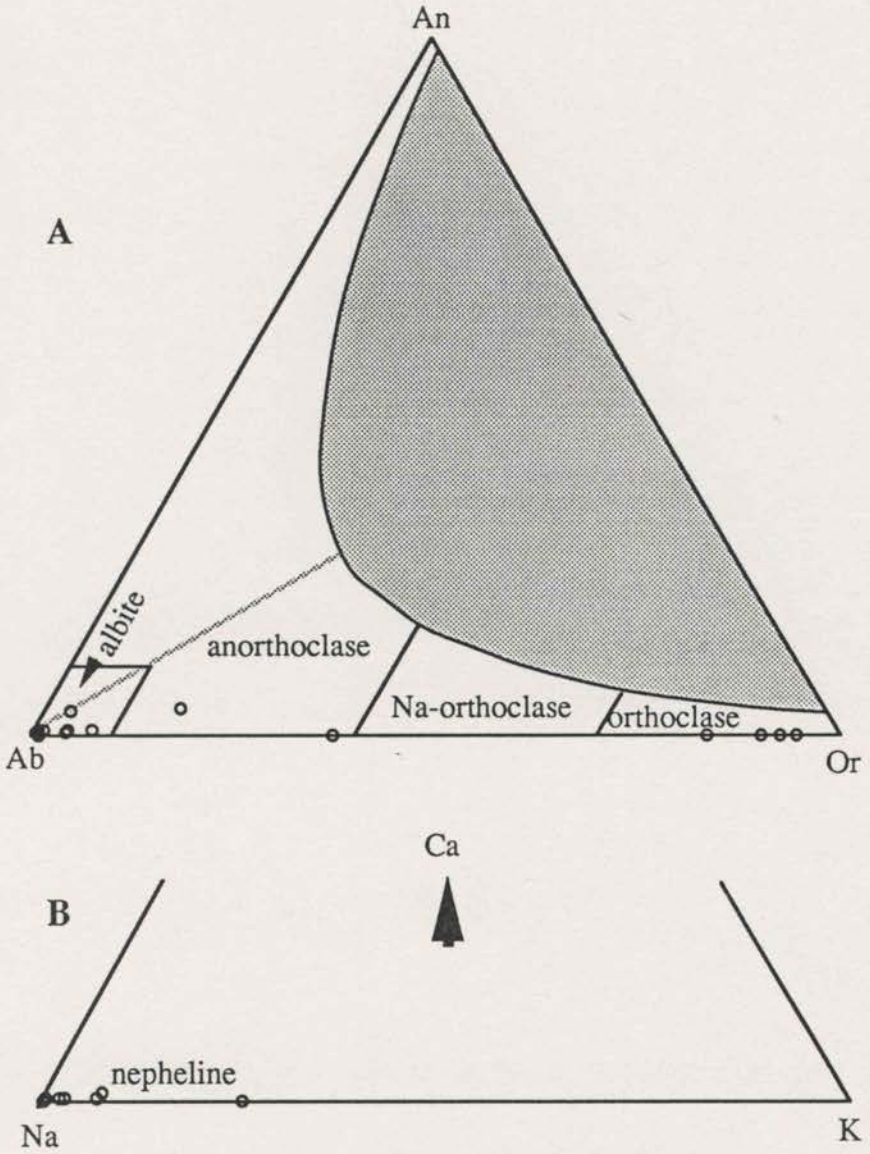

Fig. 4.10. Compositional discrimination of feldspar and feldspathoid minerals from the Wonominta Block. Fig. 4.10A shows all albitic minerals have limited compositional variation with virtually no Ca nor K; while K-feldspars contain some albite component. Some of the analyses from Mt. Wright felsic tuff samples yield anorthoclase compositions, though it appears rather unlikely to survive from alteration and weathering. All feldspathoid minerals shown in Fig. 4.10B, are sodic enriched species; even in nepheline, K is much less than Na. The analyses indicate a Na-rich environment for the formation of these minerals.

4.3.3. Micas and Tourmaline

Mica minerals recognised in the Wonominta Block are generally of two groups: white mica and biotite. The white micas have various occurrences, such as in schist (861913), in felsic tuff (762409 and 862302), in altered syenite (761603) and significantly, in metabasites (760104, 861314, 861315, 861605, 861914 and 862012). In contrast, biotite occurs mainly in limited igneous rocks (syenite and felsic tuff) as a minor phase, though it also occurs in some metasedimentary rocks in this region (Mills, 1992).

Table 4.12 (Appendix 3) and Figure 4.11 display the compositional variations of the micas. Comparatively, white mica species (Figure 4.11A) have a wide range in composition. Those in the felsic tuff samples from Mt. Wright display very high Si/Al, yielding a phengitic composition. Samples in altered syenite from Nundora display moderately high Si/Al and various Fe/Fe+Mg. Those from the felsic tuffs hosting nundorite have muscovite with very low Si/Al and no Mg at all. And white micas found in the metabasite have a low and constant in Si/Al ratio with various Fe/Fe+Mg ratios. The biotite samples are observed in syenitic intrusions and in nundorite from Nundora. All of these analyses, as shown in Figure 4.11B, have high Fe content, and all are distributed near the siderophyllite corner.

The various compositions of the mineral occurring in different rocks suggest distinctive conditions of formation, as well as the controls by bulk-rock compositions. For example, the variation of the Fe/Fe+Mg ratio in muscovites from metabasites may have been largely controlled by composition of the host rocks, whereas the constant Si/Al ratio in these minerals may suggest similar conditions of crystallisation.

Tourmaline was only recognised in one felsic tuff sample from Mt. Wright as tiny green to yellow grains in the groundmass. Analyses, however, show that there are two distinct compositions of the mineral. The green type has low Fe and high Mg; while the yellow type has high Fe, minor Mn and low Mg (Figure 4.12).

4.3.4. Metasomatic Characters of the Mafic Rocks

The rare metasomatic minerals in nundorite, such as aluminous aegirine, nepheline and natrolite indicate the peralkaline features of the alteration of felsic tuffs. Compositional analyses revealed that as the alteration proceeds, the system lost Fe and Ca, and gained

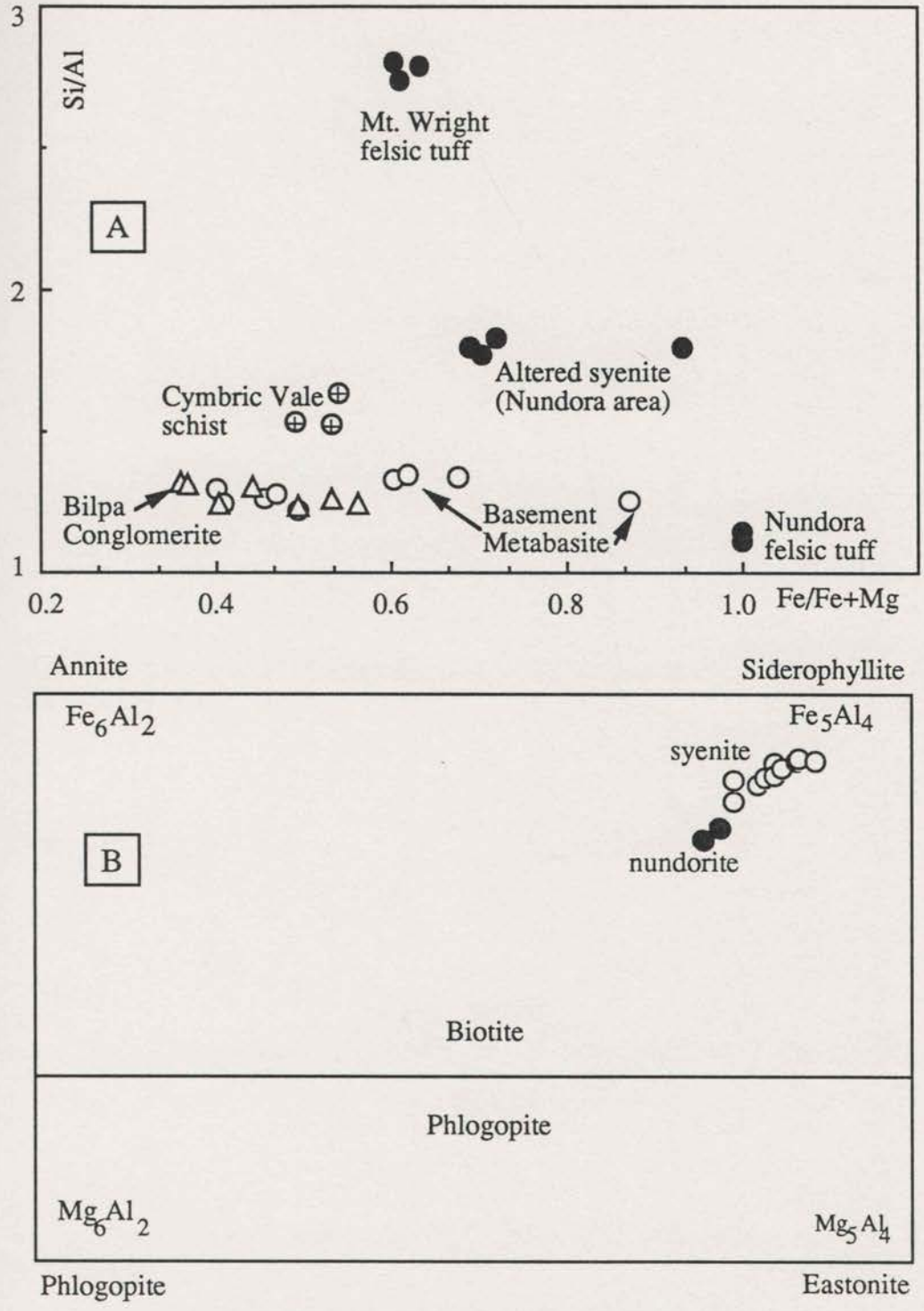

Fig. 4.11. Compositional variation of micas. Fig. 4.11A presents white micas of various origins. The diagram shows that those in the felsic tuffs from Early Cambrian Mt. Wright have a high Si/Al, thus a phengitic composition, while those from Late Proterozoic Nundora are in normal muscovite range with virtually no Mg. Micas from the Cymbric Vale schist in the basement sequence have slightly higher Si/Al than those occurring in mafic rocks, whcih also display a range of Fe/Fe+Mg. For the biotite group (Fig. 4.11B), samples from syenite and nundorite in the Nundora area are all Fe-enriched, plotting near the siderophyllite corner; in details those from nundorite are slightly enriched in Mg.

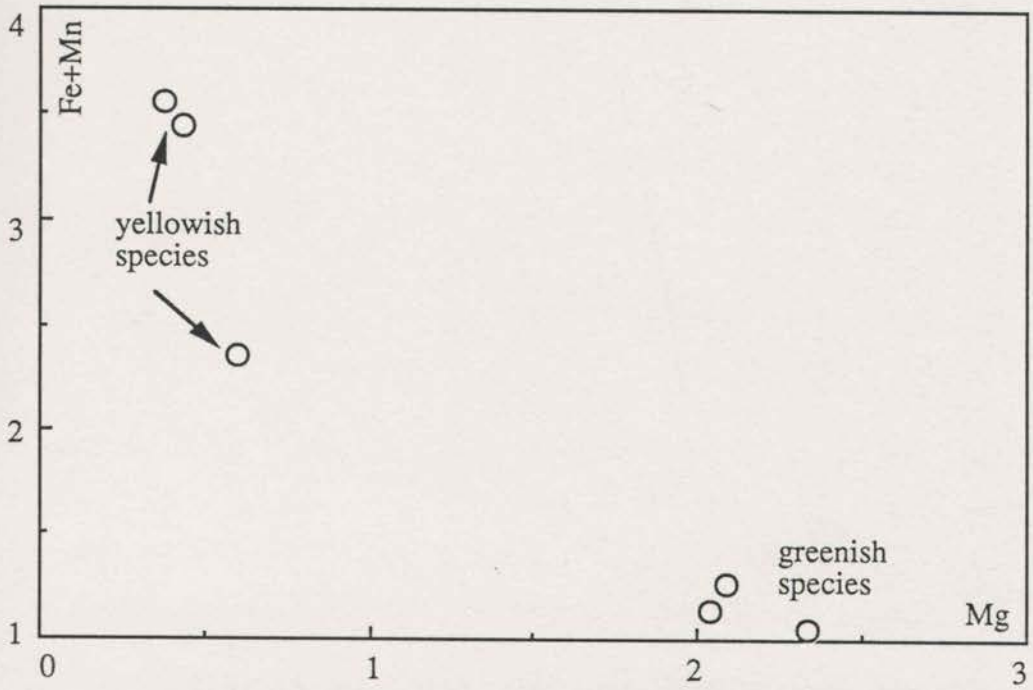

Fig. 4.12. Compositional variation of tourmalines in a Cambrian felsic tuff sample from the Mt. Wright area. Six analyses from the sample display two distinct compositions. The greenish crystals have high Mg and little Fe+Mn; while the yellowish crystals show high Fe+Mn with minor Mg. All crystals analysed here are within the range of one thin-section, and this probably implies the equilibrium domain was rather limited, or two stages of hydrothermal activity. (cations based on 31 oxygens)

Al and Na. In these processes aegirine minerals became aluminous and lost all Ca; potassium in natrolite changed from 1.5% to zero and sodic nepheline formed at a later stage. Thus, the chemical compositions of the hydrothermal fluids were probably sodic, as observed in the alteration of syenitic rocks

In contrast, secondary alteration in the southern part of the region was probably potassium-enriched and was characterised by the extensive occurrence of muscovite. Various mafic samples of mafic rocks from Wilandra, Comarto and Mt. Wright have been observed to contain muscovite; while the mineral is observed only in some samples related to the Ponto Mine mineralisation on a local scale. Microprobe analyses show that these muscovites have compositions distinct from either the Cymbric Vale schist, or the species in felsic tuffs. They are generally low in Fe and Si and high in Al, Na and K and the compositional variation may have been controlled largely by the host rock compositions.

These regional geochemical features related to secondary hydrothermal alteration obviously have important implications for mineral exploration activities. However, studies of the origin and the scale of these hydrothermal events are beyond the scope of the present project and are left for future studies.

4.4. STUDIES OF RELIC MAGMATIC PYROXENES

Pyroxenes analysed in this study occur as relic phases, such as those observed in ultramafic rocks at Nundora, in metabasalts from Mt. Wright (Cambrian), Nundora (Late Proterozoic) and Wilandra (Basement), and in metadolerite dyke from Boshy Tank, Wilandra, Cymbric Vale (Basement) and Comarto and Ponto Mine (Cambrian). The extensive occurrence of the mineral provides an opportunity for investigation of the chemical discrimination of the mineral and its petrogenetic implications.

Results of the analyses of pyroxenes are presented in Table 4.10 (Appendix 3) and Figures 4.13 to 4.15. Some of the analyses tend to give results with low totals of the structural formulae, even considering the analytical uncertainties. This implies that the secondary processes may have altered the minerals while the crystals still preserve microscopically their original identity. Plates 4.1. and 4.2 are two back-scatter electron (BSE) images of altered pyroxenes observed during the microprobe studies. In Plate 4.1, secondary phases of actinolite and chlorite are observed filling in the fractures of relic pyroxene; while in Plate 4.2, only the outline of pyroxene can be recognised, whereas the mineral is completely replaced by secondary phases (magnetite and sphene).

These observations invoked a TEM (transmitted electron microscope) study of the alteration of primary pyroxene on a sub-microscopic scale. The preliminary results revealed various alteration processes, which can qualitatively account for the deficiency of compositional analyses by microprobe. Unfortunately, a comprehensive TEM study is well beyond the scope of this project and only some preliminary observations were carried out and presented in Appendix Four.

Compositionally, all analyses show that the relic crystals are Ca-rich clinopyroxene with variable Fe and Mg. Figure 4.13 presents compositional discrimination of pyroxenes from different areas of the Wonominta Block. The basement samples (Figure 4.13A) plot as augite with wide range of composition, in particular the Cymbric Vale samples plot on the border between augite and endiopside. In contrast, the Late Proterozoic samples from Packsaddle and Nundora (including those in altered peridotite) plot within a limited range across the border between diopside and salite. Figure 4.13A also shows that large compositional variations occur within single crystal grains, almost as large as that observed between crystals in different samples; the arrow in this figure indicates the changes from core to edge in a single grain.

Plate 4.1 Alteration characters of relict pyroxene (I) The light-grey crystals with smooth surface in this BSE image are relic pyroxene, transected by dark grey elongated, somewhat fibre-like amphiboles and chlorite.

x 400; sample 762705.

Plate 4.2. Alteration of relict pyroxene (II). These BSE images present a case of complete alteration of pyroxenes. The plate-like areas outlined by the bright white small crystals (magnetite with sphene inside) are pseudomorphs of pyroxene, yet no traces of pyroxene were detected here. The smooth grey crystals are epidote, while the dark grey crystals are mostly chlorite

x 400 for the upper plate
x 800 for lower plate; sample 761503

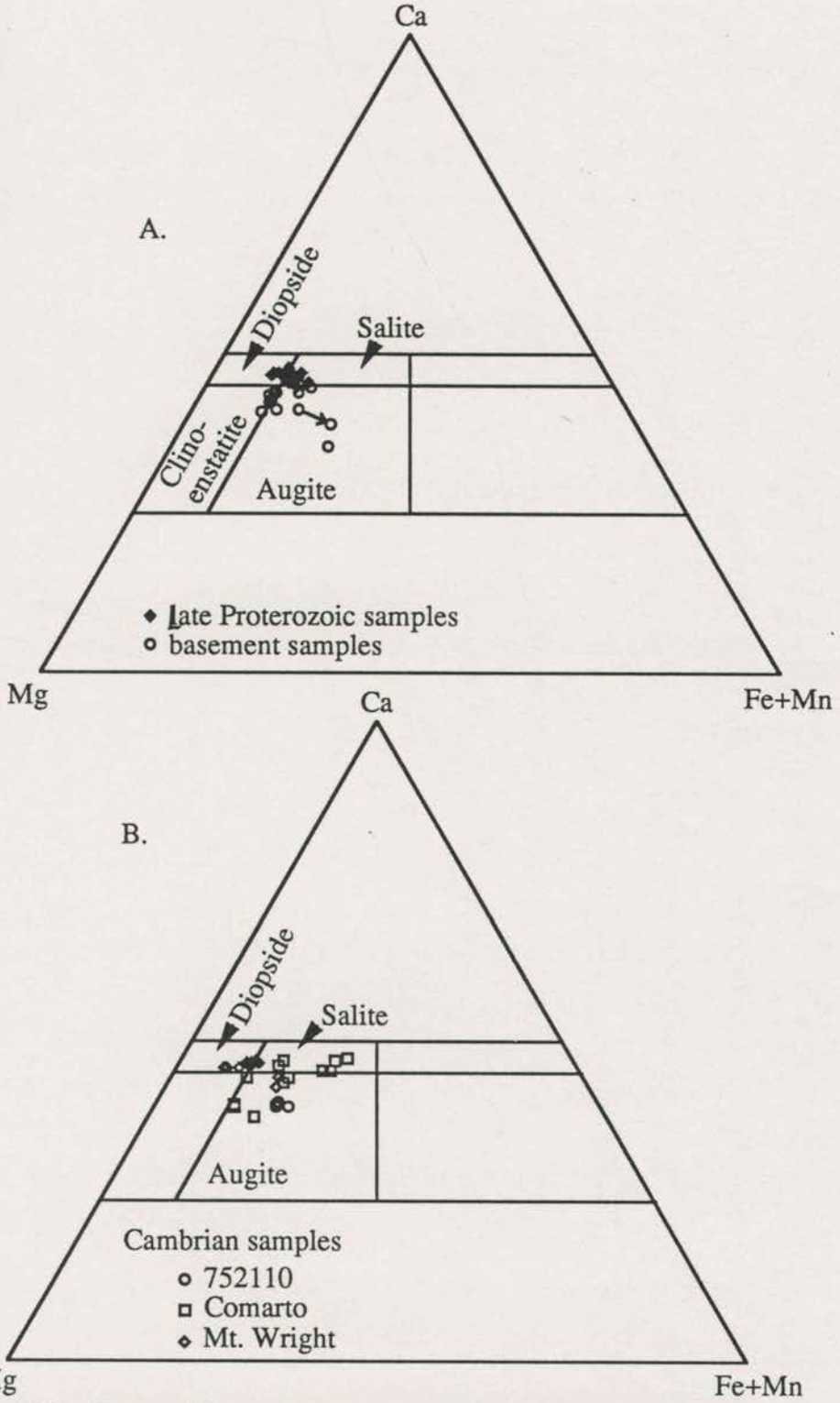

Fig. 4.13. Compositional discrimination of pyroxenes from various sequences in the Wonominta Block. Fig.4.13A presents analyses for the Precambrian sequences and the diagram shows that most of the basement samples from Wilandra and Boshy Tank have augitic compositions while pyroxenes from Nundora (late Proterozoic, including those in the peridotite) plot as diopside-salite. Compositional variation of basement samples are partly due to heterogeneity within crystal grains as indicated by the arrow. The early Cambrian samples are shown in Fig. 4.13B. Sample 752110 from the Ponto Mine area has augitic compositions; those from Mt. Wright plot in the diopside field while the Comarto samples have large compositional variations in augite - salite fields.

Figure 4.13B presents the composition of clinopyroxene from the Cambrian rocks in the Ponto Mine, Mt. Wright and Comarto areas. Those in metadolerite from Ponto Mine (752110) plot as augite; and those from Mt. Wright plot as diopside. Both groups have a rather limited variation in composition. In contrast, the Comarto samples display a wide range of composition in the augite - salite fields. These samples have a range from high to low Mg component.

The composition of relic pyroxenes persisting in the metamorphic environment has been widely used as an indicator of the primary geochemical characteristics of the whole rock as well as discrimination of tectonic environments though the correlation may be rather complicated (Nisbet & Pearce, 1977; Leterrier *et al.* ,1982). Figure 4.14 presents the geochemical discrimination of clinopyroxene samples based on the framework of Leterrier *et al.* (1982). It can been seen from Figure 4.14A that both Late Proterozoic and Early Cambrian Mt. Wright samples are discriminated as "alkalic" (those from the altered Nundora peridotite also plot in the alkalic field); while the basement samples in the 'non-alkalic' field. The Cambrian Comarto samples display a large variation with the majority plotting in the alkalic field, except the four analyses of sample 861003, which fall in the non-alkalic field. For the samples plotting in the 'non-alkalic' field, Figure 4.14B shows that analyses of sample 752110 plot in the calcalkalic field, but the Cambrian Comarto sample, 861003, is distributed on both sides of the discriminant line with small deviation from the border. Samples from the basement sequence are also distributed across both tholeiitic and calcalkalic fields, most of these points are very close to the discriminant line. In this case, the particular diagram cannot distinguish whether they are tholeiitic or calcalkalic, as the original scheme shows. In other words, this discrimination cannot distinguish the "subalkaline" pyroxenes in this study. However, as will be demonstrated in the following chapters, the discrimination between alkaline and subalkaline series yielded similar conclusion to that obtained from whole rock analysis.

Figure 4.15 is a plot of tectonomagmatic discrimination. In this figure, most of the analyses from Late Proterozoic and Cambrian Comarto/Ponto Mine samples plot in the non-orogenic field. Samples from Mt.Wright basalts and the basement sequence plot in both orogenic and non-orogenic fields. Obviously, this is an ineffective discrimination.

In the early days of this discrimination technique, it was believed that compositions of clinopyroxene may be correlated to their host lavas and the tectonic environments in which the magmas were generated (*e.g.* Kushiro, 1960; Le Bas, 1962; Verhoogen,

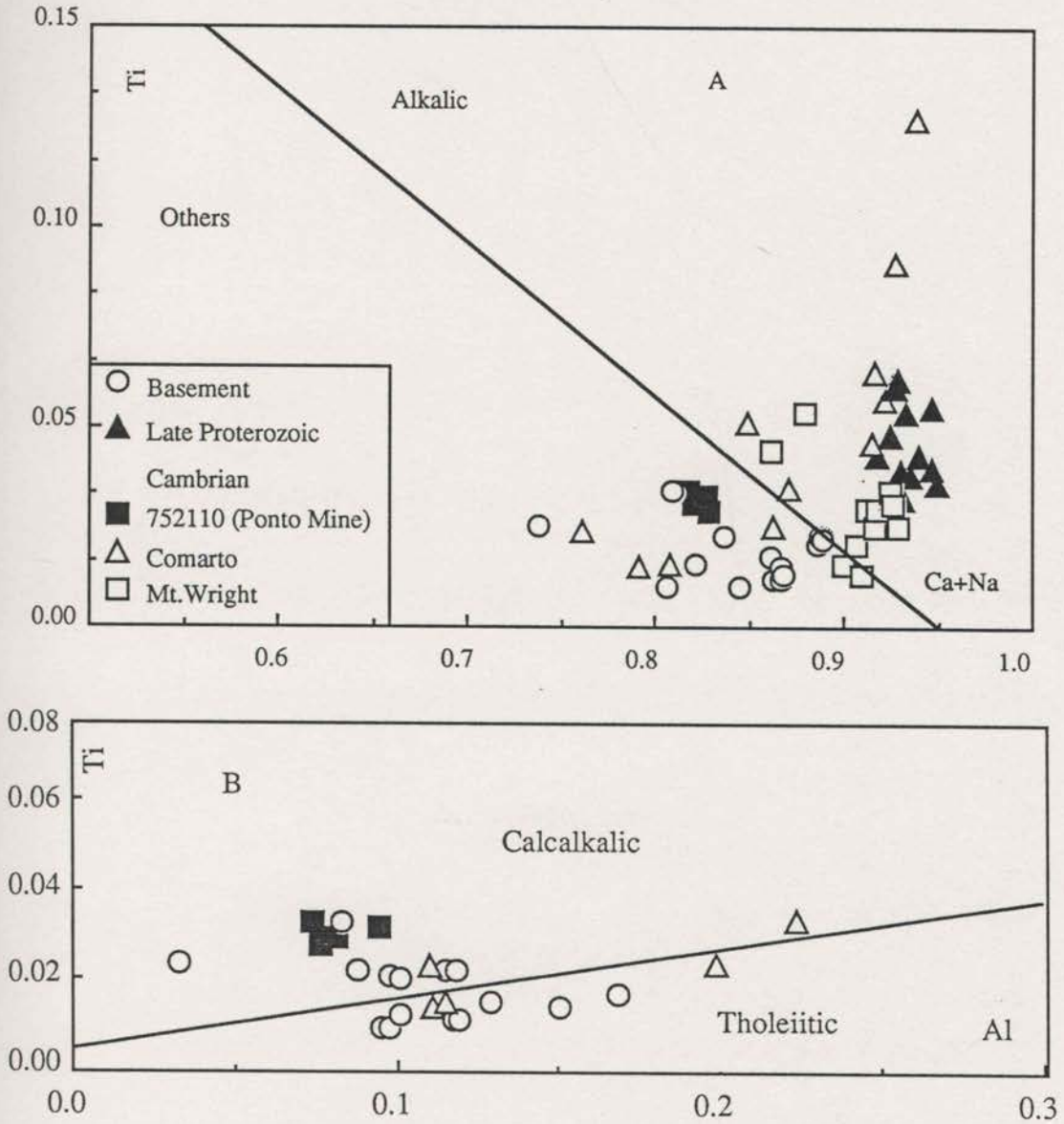

Fig. 4.14. Geochemical discrimination of mafic rocks in the Wonominta Block using microprobe analyses of relic pyroxene. The discrimination scheme is after Leterrier *et al.*. (1982). Fig. 4.14A indicates that most of the samples from Late Proterozoic and Mt. Wright (Early Cambrian) sequences may have host rocks with alkalic affinities, whereas the basement samples and the Cambrian dolerite (752110) from Ponto Mine area plot in the non-alkalic field, and most of these samples plot along the discriminant line between tholeiitic and calcalkalic associations (Fig. 4.14B). The Cambrian Comarto samples display wide ranges of composition from highly "alkalic" to "tholeiitic".

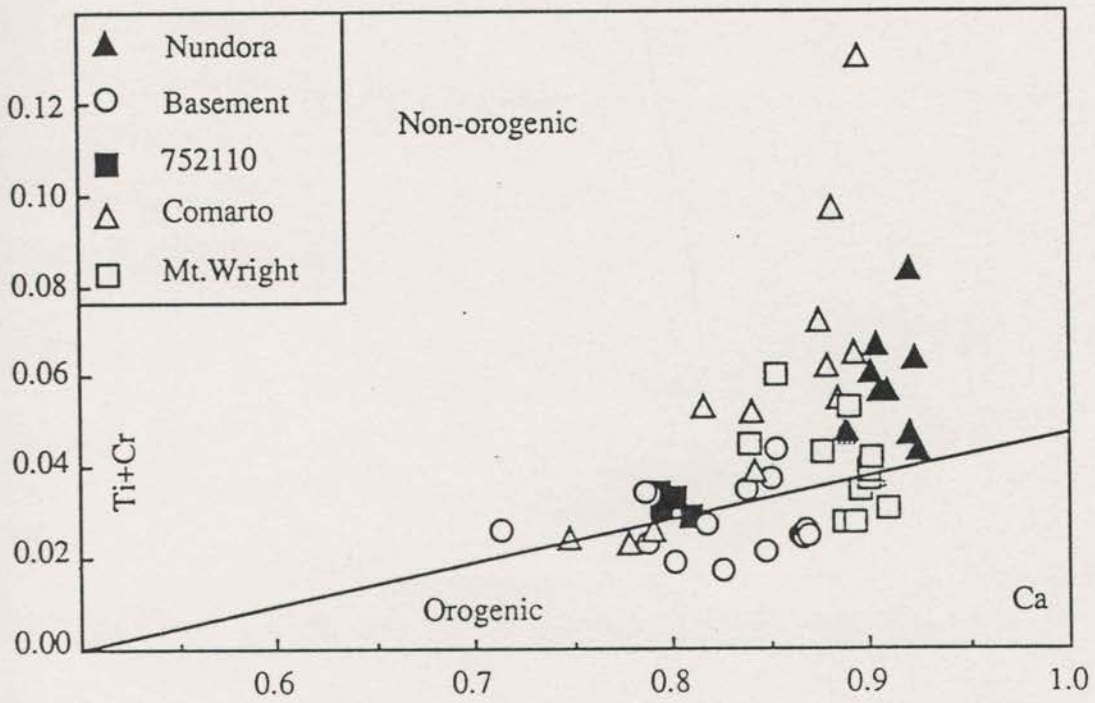

Fig. 4.15. Tectonomagmatic discrimination of mafic rocks in the Wonominta Block using microprobe analyses of relic pyroxene. In the original scheme (Leterrier *et al.*, 1982), this discrimination applys only to non-alkalic pyroxenes from Fig. 4.14. Most of the Cambrian samples (Comarto and sample 752110 from Ponto Mine area) plot in the "non-orogenic" field, but pyroxenes from the basement sequence are distributed in both "orogenic" and "non'orogenic" fields. This diagram probably has limited significance(see discussion in text).

1962). While this correlation may be valid in many cases, it does not indicate that chemically identical magmas from different tectonic environments always produce distinctive pyroxenes. Some related factors that may contribute to the compositional variations were discussed by Leterrier *et al.* (1982) when proposing their discrimination diagrams. The present study also reveals that large compositional variations may occur within samples from one local area, even within a single crystal grain, and the variation is at least not smaller than those among different grains and different areas, though the nature of the inhomogeneity (such as zoning) remain ambiguous due to secondary alterations. This variation is likely one of the reasons for the failure of tectonomagmatic discrimination using microprobe analyses of pyroxenes. The complicated circumstances indicate that it is essential to compile many strands of evidence to justify individual tectonic discrimination, and therefore application of these methods should be integrated with other methods before any conclusion can be reached. This topic is further discussed in Chapter Eight.

In summary, the discrimination using relic pyroxene suggests that the mafic rocks in the Late Proterozoic and Early Cambrian Mt. Wright sequences may have alkaline affinity and others (the Basement and Cambrian Comarto sequences) subalkaline affinity. The available discrimination schemes are ineffective to distinguish the subalkaline series, nor to carry out tectonomagmatic discriminations. Therefore, mineral chemistry of the relic magmatic pyroxenes can provide only limited, though valuable, information in terms of primary geochemical affinities of the magmas.

Chapter 5
Geochemistry of Mafic Rocks in the Basement Sequence

5.1. INTRODUCTION

Most of the mafic rocks studied in this project have been metamorphosed to various degrees and alterations are significant as described in the last two chapters. Therefore, the geochemical studies are firstly aimed at revealing primary geochemical affinities of the mafic rocks, as well as the influence of alteration. To achieve such aims, criteria of chemical immobility are discussed and examined; based on these criteria and the investigation of immobility of various components, primary geochemical characteristics and the changes introduced during alteration can be established. Most petrochemical classifications use major element compositions, from CIPW calculations (Cross, Iddings, Pirsson & Washington, 1902) to recently devised total alkali-silica (TAS) diagrams (Le Bas *et al.*,1986); but these components are often mobilised during secondary processes and thus may not reflect their primary characteristics (*cf* Morris, 1988a & b, and references therein). The geochemical discrimination can also be achieved using trace elements. Since the major components used to discriminate different magma series, in principle, control their allied trace elements, the behaviour of these trace elements would be expected to be similar to that of the major ones in magmatic processes. The latter approach has gained more attention in recent years (*e.g.* Winchester and Floyd, 1977) and exhibits particular significance for metamorphosed rocks due to the immobility of these components.

The second aim of the geochemical studies is to constrain petrogenetic processes of the mafic magmatism, such as influences of partial melting, fractionation and assimilation, and tectonomagmatic discrimination, whereby certain rocks are regarded as products of a specific tectonic environment. This method was pioneered by Pearce and Cann (1973). Many other diagrams have been published since (*e.g.* Pearce, 1979 &1982; Pearce & Norry, 1979; Wood *et al.*, 1979a; Meschede, 1986). Even the most recent method, application of spidergrams (*e.g.* Sun *et al*, 1979; Sun & McDonough, 1989; Pearce, 1983; Thompson *et al.*, 1983 & 1984), as commented on by Weaver (1987), embodies the same methodology.

5.2. SAMPLE SELECTION

Fifty-two samples were selected from four local areas of the basement sequence. The sample selection, presented in Table 5.1, is based on variety, representativeness as shown in Tables 3.2 to 3.6, and freshness of the rocks. Given that there is a broad correlation between the number of analyses and the outcrop areas, the data are considered to be broadly representative of the overall geochemistry of the sequence.

Table 5.1. Sample Selection from the Basement Sequence for Geochemical Analyses

Region	Area	Number of samples selected for each rock type						
		MB	MD(I)	MD(II)	MD(III)	AM	others	total
Ponto Mine	Ponto Mine	13		3	1			17
Inlier	Boshy Tank	4		4	1			9
Wilandra	Wilandra	9	3	2	1		1	16
Inlier	Cymbric Vale	4		1		3	2	10
Total		30	3	10	3	3	3	52

Note: MB, metabasite/metabasalt; MD, metadolerite (three types); AM, amphibolite; others include one mica schist from Cymbric Vale and two felsic tuff samples.

The results of analysis are shown in Table 5.2 in Appendix 6 along with the analytical parameters. Major element concentrations used in various discriminant diagrams, are normalised to 100% after discarding the LOI. Thus, compositional ranges presented in the following diagrams may not match the values in the table.

5.2.1. Criteria of Immobility

Immobility is one of the most important assumptions in geochemical study of the metamorphosed mafic rocks, since to make the correlations of the present-day compositions with their magmatic characteristics, one has to demonstrate that the particular elements used in the study have been "immobile", that is they were not "changed" during the secondary processes. A quantitative method can be used to judge the immobility of elements by means of a mass-balance calculation (Gresens,

1967; Bartley, 1986). The calculation considers the amounts of elements that enter or depart from an initial rock volume (which is often poorly constrained), and thus indicates whether or not an element has been mobile in this particular process. However, according to the criteria of immobility in this model, an immobile element is the one that does not move with respect to such things as vesicles, lithologic contacts and so forth. Even if an element is immobile in this sense, it may nonetheless change its concentration during metamorphism because concentration reflects only the amount of an element relative to all others in the rock (a good example has been demonstrated by Whitford *et al.* (1989), where Al_2O_3 content varied between 5 and 25% from initially about 16% in a cogenetic series while remained as "immobile"). Thus, this ideal method does not necessarily have practical application in investigating primary geochemical compositions. In methodology, this is really an interesting case. The so-called immobile element is actually not immobile as if it is ideally immobile, its concentration will be nonetheless changed due to the movements of other components.

Thus, application of the so-called immobile trace elements to any discrimination scheme should be based upon a practical assumption that these components still reflect their primary identities but not that they are not transferable at all. Some authors have suggested if two elements show a good correlation in samples of cogenetic suite, they can be treated as 'immobile' (Winchester & Floyd, 1977). Some even used regression analysis to quantify the correlation (*e.g.* Mengel *et al.*, 1987). However the cut-off value in the latter approach is mathematical or arbitrary, but not geochemical.

In the present study, most of the samples have larger than 2% LOI, some much higher (they are preserved in the discussions largely due to representativeness of particular type of rocks observed in the field). This would be a clear indication of alteration of the rocks. Therefore, a practical approach is adopted in the investigation of immobility, *i.e.*, if a pair of elements in the samples show a "significant" correlation, the elements are considered to be "immobile" on the basis that these samples have been identified to be a co-magmatic, though determination of the "significance" is somewhat arbitrary. The results are presented in Figures 5.2.1 and 5.2.2 for the basement samples. The significant correlations between HFS elements in these samples are clearly evident, whereas both LILE and Ga and Sc (both are compatible elements) exhibit scattered patterns. These features suggest that the HFS elements (Zr, Ti, Y and Nb) may have been immobile, while others (Rb, Sr, Ga and Sc) mobile during secondary processes. Ga also appears to retain some primary features particularly in the Wilandra samples, whereas relatively poor correlation between Zr and Nb is largely due to the poor analytical qualities as discussed in Section 5.7

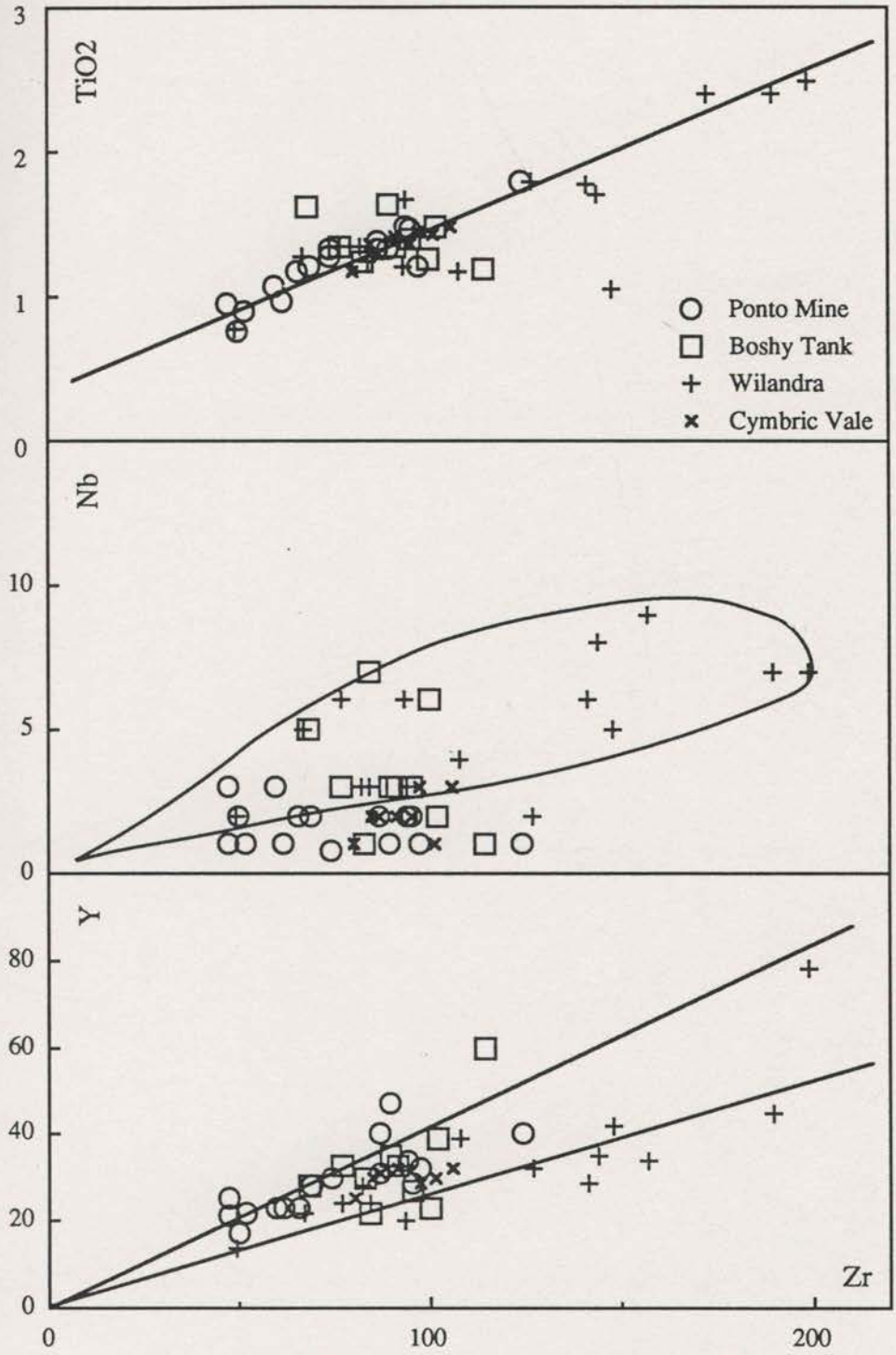

Fig. 5.2.1. Binary compositional plot of basement samples (I): the HFS compositions. Generally, significant correlations can be observed in all three chosen pairs, though Zr-Nb plot appears to be less certain largely due to poor analytical qualities. Besides, samples from north (Ponto Mine and Boshy Tank) appear to have different Y/Zr ratios from those from south (Wilandra and Cymbric Vale), possibly indicating source heterogeneities (cf Chapter 8).

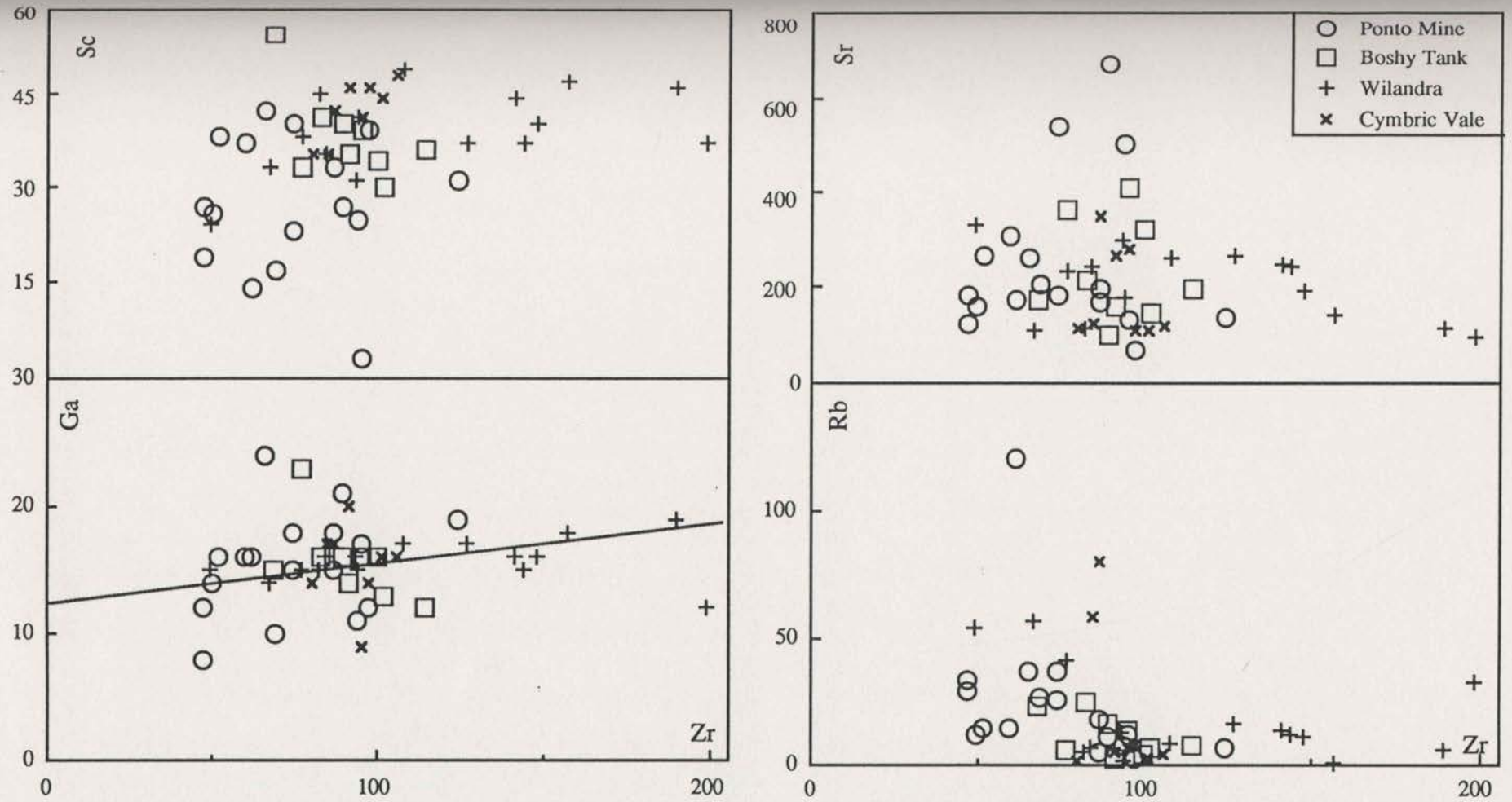

Fig. 5.2.2. Binary compositional plot of the basement mafic samples (II): LILE (Rb and Sr) and compatible elements (Ga and Sc). In contrast with the HFS element plot, the samples display considerable scatters in all these diagrams, suggesting mobility of the components. On the Zr-Ga plot, the Wilandra samples appear to show some correlation, which projects back on the Ga axis. This appear to suggest relatively immobile and more conpatible features of Ga than Zr in the Wilandra samples (*cf* Chapter 8).

5.3. GEOCHEMICAL CHARACTERISTICS OF BASEMENT MAFIC ROCKS FROM THE PONTO MINE AREA

The seventeen samples selected from all eight volcanic units in the basement sequence in this area (*cf.* Chapter Three) include thirteen metabasites (752203, 752304, 752805, 752808, 752810, 753001, 753003, 753007, 760102, 760104, 760201, 760501 and 760701) and four metadolerites (type II: 752001, 752302 and 753106; type III, 760402) (see also Tables 3.2, 5.1 and 5.2). In the following discussion, an attempt has been made to characterise the geochemical features of these samples, and to identify, if any, correlations between petrographic groupings, field sequences and petrochemical series in order to build up a basis for petrogenetic studies. The investigations are based on discriminant diagrams of major and/or trace element compositions with a clear emphasis on the possible influence of secondary processes.

5.3.1. Primary Geochemical Affinity: the Nb/Y - Zr/TiO_2 Plot

Winchester and Floyd (1977) proposed a Nb/Y versus Zr/TiO_2 diagram to discriminate magmatic series. Since then, various authors have tested this method. It appears that the statistically obtained discriminant boundaries vary slightly with different approaches, but a value of Nb/Y of 0.7 is generally used to separate alkaline and subalkaline series (*cf.* Condie, 1989). Because these components may have behaved as immobile components during secondary processes as demonstrated above (with the exception of Nb, which will be discussed later on), the discrimination may reveal the primary geochemical affinities of the mafic rocks.

Figure 5.3.1 presents the discrimination of Nb/Y versus Zr/TiO_2 plot of the samples from the Ponto Mine area. All the samples plot in the subalkaline basalt field and appear to have a constant Zr/TiO_2 with a range of Nb/Y, but this trend may be an artefact because of poor analytical quality of Nb -- samples with low Nb/Y ratios all have seemingly low Nb content. In this context, those with relatively higher Nb ($\geq$ 3 ppm) may provide a better estimate of the primary Nb/Y ratios of the samples

Even considering the analytical uncertainty, this diagram clearly reveals the subalkaline basaltic affinity of the primary compositions of the mafic rocks from the basement sequence in the Ponto Mine area.

5.3.2. Major Element Geochemistry

With respect to analyses of major element compositions, several samples yielded very high LOI contents, which can be attributed mostly to the presence of carbonates (*cf.* Chapter Three): 14.35% LOI in the sole Belt B sample (753003); 11.62% in the cleaved metabasite (760501); 9.45% in the pillow lava (752203) and 5.61- 9.16% in the Ponto Mine-related metabasites (760102, 760104, 760201). The high LOI in these samples influences significantly their chemical characteristics as presented below.

Figure 5.3.2 presents the TAS plot (classification after Le Bas *et al.*, 1986) of basement mafic samples from the Ponto Mine area. The division between alkaline and subalkaline series is after Macdonald & Katsura (1964). Most samples plot in the basalt field with SiO_2 between 45-53% (normalised to LOI-free status; all other major element contents are also normalised values). Two of the high SiO_2 metabasites (752203 & 753003) also have very high LOI, but the third one (752808) has 56.17% SiO_2 but not particularly high LOI. It plots in the basaltic andesite field.

Also in this diagram, the samples display three distinct trends in terms of Na_2O+K_2O versus SiO_2 ratios. The two metabasites located close to the mine (760104 and 760201) have the highest alkaline component; another metabasite (760701) has a slightly lower TA/Si ratio. The intermediate TA/Si group includes all four metadolerites and metabasites from Belt A (753001, 753007 and 760401), which are closely related to the intrusive samples. Rest of the metabasites have the lowest alkaline level. Only samples with high TA/S plot in the alkaline field.

These trends clearly indicate the compositional changes during secondary processes. From petrographic studies, it has been recognised that the intrusive rocks appeared to have preserved more primary textures. It is reasonable, thus, to postulate that these intrusive rocks might have preserved more primary geochemical characteristics than their volcanic counterparts. If the compositional trend of the intrusive samples is used as a reference (which is also similar to that revealed by immobile component discrimination as shown in Figure 5.3.1), some of the metabasites would be depleted in (Na_2O+K_2O), implying loss of these components, while others related to the mines are enriched in the alkalic components, probably due to hydrothermal processes (particularly the enrichment of K_2O in sample 760104). Thus, the TAS diagram is used here not only to indicate the sub-alkaline basaltic affinities of the primary magmatism, but also to reveal the alteration processes. As shown in Figure 5.3.2, the two arrays may indicate the depletion and enrichment of the alkalic components

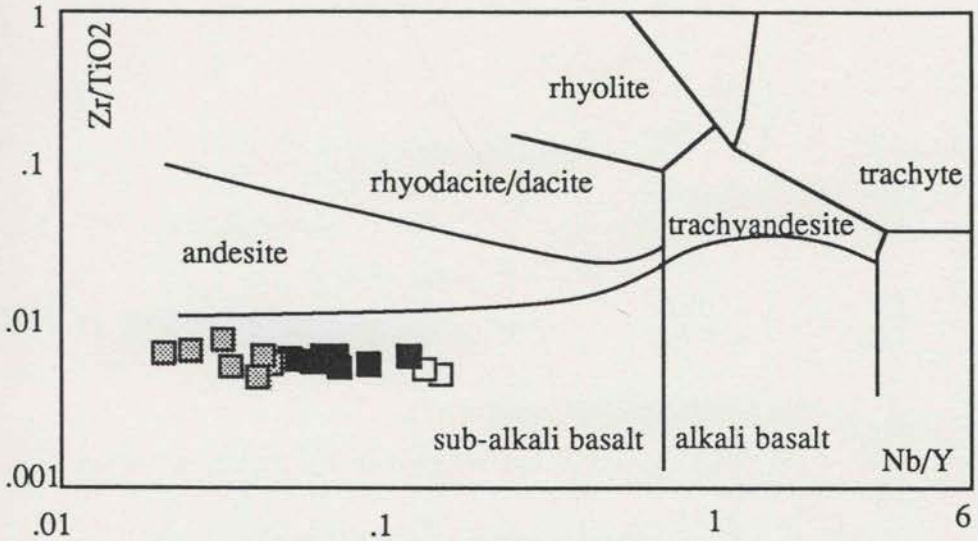

Fig. 5.3.1. Zr/TiO2-Nb/Y plot (Winchester & Floyd, 1977) of basement samples from the Ponto Mine area. The diagram shows that these samples plot in the field of sub-alkaline basalt with nearly constant Zr/TiO2 and a range of Nb/Y. Dotted squares, samples with 1 ppm Nb or less; filled squares, 2 ppm Nb samples; and open squares, 3 ppm or more Nb.

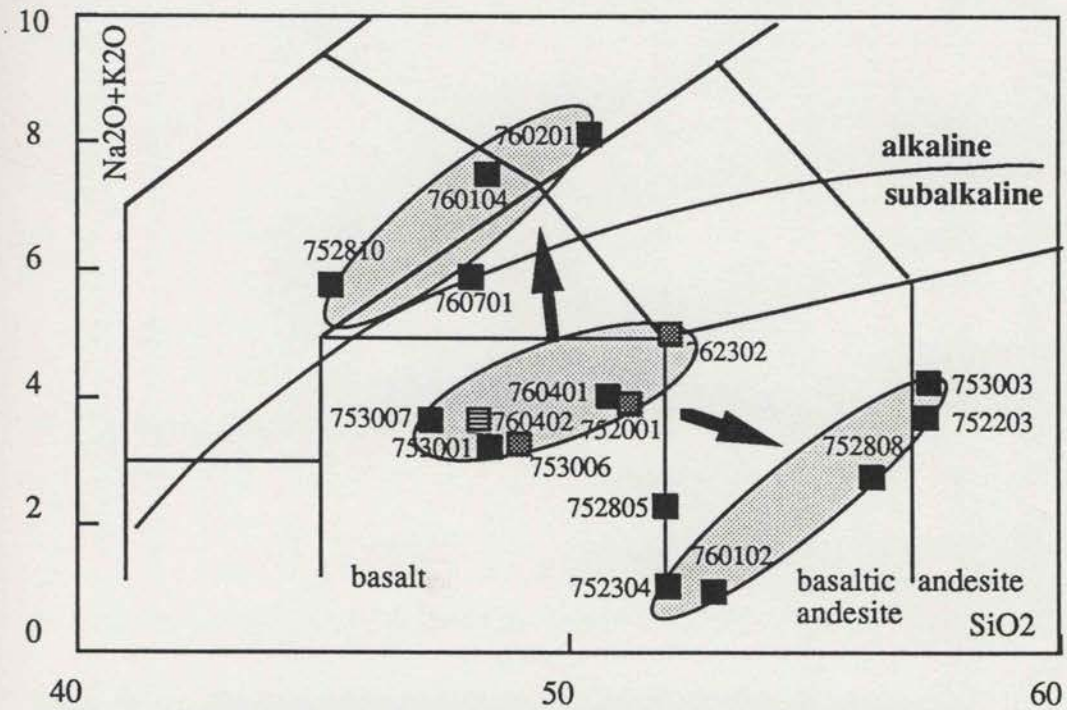

Fig. 5.3.2. TAS diagram of basement samples from the Ponto Mine area. Filled square, metabasites; dot square, metadolerite (II); striped square, metadolerite (III). This disgram shows that most of the basement mafic samples plot in the subalkaline basalt field. Samples with high alkali components are related to the Ponto Mine. Arrays in this diagram indicate possible trends of alteration.

respectively during the alteration.

In order to discriminate the subalkaline samples, the alkaline index (A.I.) against Al_2O_3 plot is used (classification after Middlemost, 1975). The alkaline index is defined as a ratio of alkalic components against silica contents in rocks, *i.e.*

$$A.I. = (Na_2O+K_2O)/0.17(SiO_2-43)$$

Figure 5.3.3 is a plot of A.I. against Al_2O_3 of the "subalkaline" samples from Figure 5.3.2. Most of the samples fall in the tholeiitic field, or close to the discriminant boundary, except sample 753001 in the calcalkalic field. In addition, the AFM diagram was also tested as a discrimination method in the early stage of the investigation. In this diagram, the subalkaline samples plot in a dispersed pattern in both tholeiitic and calcalkalic fields. Discrimination of samples from other areas also yielded similar unfavourable results. It is thus believed that due to the alterations, the AFM diagram does not provide useful information in discriminating primary magmatic associations and was consequently abandoned.

The A.I. versus Al_2O_3 diagram (Figure 5.3.3) indicates the possible tholeiitic features of these samples. For the three high Al_2O_3 samples, 760104 is within the ore body sequence of the Ponto Mine, thus significant hydrothermal influences would be anticipated; 760402 is a metadolerite (III), occurring near the Koonenberry Fault; and 753001 is from the major volcanic sequence with massive flow appearance. The high Al_2O_3 in these samples appear to be exceptional and probably do not reflect primary features. In other words, the concentration of Al_2O_3 in these samples may have been changed during mobilisation of other components, though Al_2O_3 itself may have been immobile as discussed in the last section.

Discrimination of major element compositions clearly indicates the influences of secondary processes. However to some extent, these compositions may still be used to indicate their primary geochemical affinities, in particular the TAS diagram. Besides, as demonstrated here, the TAS diagram may also be useful in revealing compositional changes during secondary processes.

5.3.3. REE Geochemistry

Four representative metabasites were selected to analyse their rare earth element (REE)

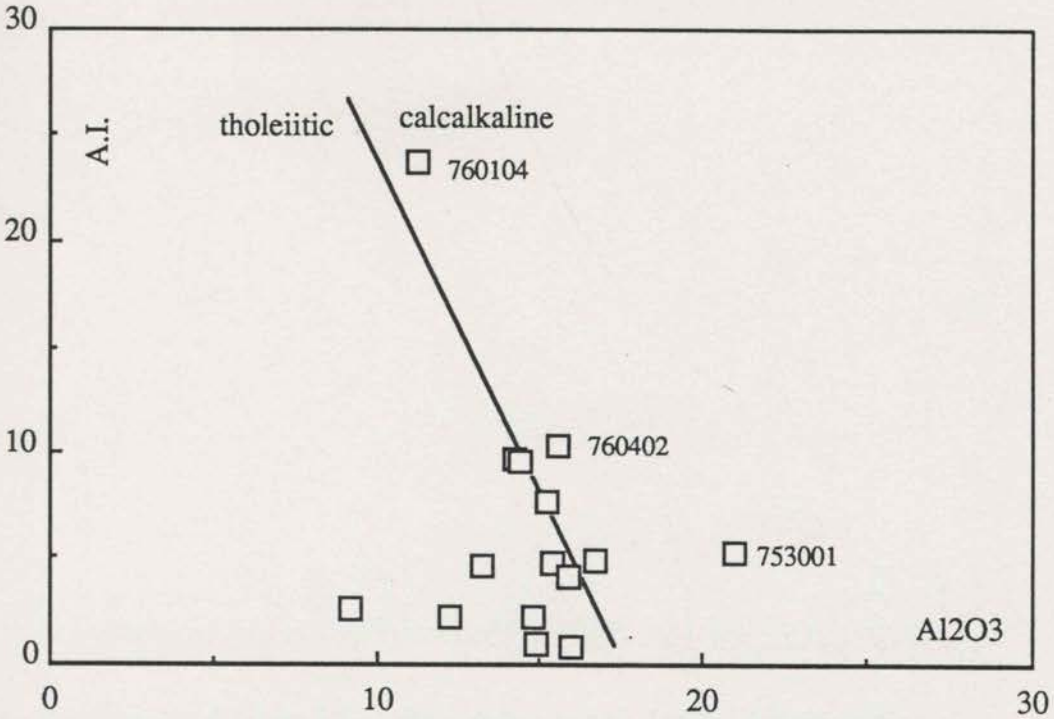

Fig. 5.3.3. Discrimination of basement samples from the Ponto Mine area using the alkali index (AI). Most of the samples plot in the tholeiitic field or lie close to the discriminant boundary with one exception, 753001, having high Al2O3 contents. Conclusions drawn from Figs. 5.3.2 and 5.3.3 are generally in agreement with those from Fig. 5.3.1 using immobile components. This suggests that these two diagrams are still useful in petrochemical studies in the present study, even though significant alterations have occurred.

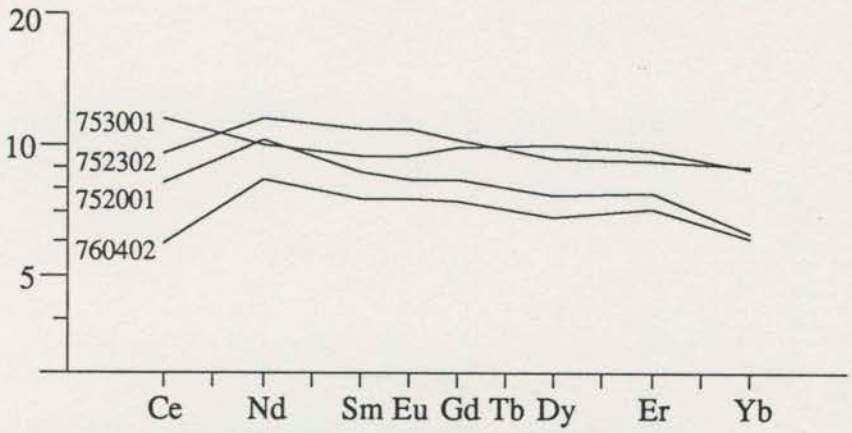

Fig. 5.3.4. Chondrite-normalised REE compositions of representative basement mafic samples in the Ponto Mine area. This figure shows that the samples in general have a flat pattern with Ce-depletion, except sample 753001which shows a slight LREE enrichment. Sample 760402 (metadolerite III) has the lowest REE abundance, even lower than a normal MORB at about ten times chondrite level.

Table 5.3. Rare Earth Element Compositions of the Representative Mafic Samples from the Wonominta Block.

sequence	area	sample	rock	Ce	Nd	Sm	Eu	Gd	Dy	Er	Yb
		752001	MD(II)	7.06	6.51	1.77	0.64	2.29	2.62	1.75	1.39
	Ponto Mine	752302	MD(II)	8.31	7.29	2.21	0.84	2.85	3.21	2.07	1.96
		753001	MB	10.0	6.33	1.93	0.73	2.74	3.42	2.19	1.94
		760402	MD(III)	5.12	5.22	1.54	0.58	2.06	2.35	1.60	1.34
basement	Boshy	762501	MD(II)	9.34	10.3	3.35	1.24	4.92	5.82	3.62	3.47
	Tank	762705	MD(I)	8.64	9.06	2.90	1.07	3.98	4.61	2.91	2.80
		861211	MD(II)	17.4	17.4	5.16	1.73	6.86	7.35	4.36	4.29
	Wilandra	861314	MD(I)	17.4	15.0	4.55	1.41	6.11	6.76	4.11	3.99
		861713	AM	7.57	8.81	2.83	1.08	3.93	4.46	2.70	2.59
	Cymbric	861909	MB	9.76	10.3	3.12	1.06	4.25	4.89	2.92	2.89
	Vale	861915	AM	8.02	8.99	2.89	1.08	3.87	4.51	2.72	2.67
		760801	MD(I)	14.3	9.71	2.22	0.81	2.45	1.83	0.79	0.58
	Packsaddle	760805	MB	38.4	27.5	5.85	1.9	5.7	4.5	2.4	2.0
		760806	MB	49.9	31.5	6.59	2.15	6.61	5.44	2.76	2.01
late		761301	MB	63.5	36.3	8.13	2.61	7.95	6.16	2.97	2.31
Proterozoic											
	Nundora	761503	MB	54.5	30.2	6.35	2.12	6.58	5.24	2.90	2.07
		761809	MB	64.9	39.6	8.37	2.75	8.42	6.51	3.15	2.20
		761901	MB	84.0	52.1	10.7	3.41	9.73	6.92	3.13	2.49
	Ponto Mine	752110	MD(I)	24.5	18.3	4.67	1.73	5.50	5.25	2.86	2.44
		862112	MB	29.7	18.4	4.14	1.47	4.59	3.90	2.00	1.63
		862205	MB	62.9	34.6	6.84	2.34	6.95	5.19	2.53	2.02
Cambrian	Mt. Wright	862221	TA	103	58.8	12.6	3.78	12.8	10.7	5.48	4.42
		862225	MB	19.6	11.5	2.27	0.77	2.16	1.87	1.00	0.79
		862402	MB	63.2	36.6	7.53	2.73	7.19	6.02	2.91	2.30

Note: MD, metadolerite; MB, metabasite/metabasalt; AM, amphibolite; TA, trachyandesite. Aboundance shown in ppm.

compositions. These analyses are presented in Table 5.3 and Figure 5.3.4.

In Figure 5.3.4, the plots are normalised to average chondrite compositions (Nakamura, 1974). This figure shows that three of the four samples have a flat chondrite-normalised pattern with a clear Ce-depletion. The fourth sample (753001) is characterised by a slight light REE enrichment. There are no significant Eu anomalies.

5.3.4. Spidergrams

"Spidergrams" (Thompson *et al.*, 1983), also known as primitive mantle normalizing diagrams (PMN) (Sun *et al.*, 1979; Wood *et al.*, 1979b; Thompson *et al.*, 1983 & 1984), represent an extreme of the approach of plotting REE abundances relative to a normalising standard. The advantage is that multiple elements are examined; thus it should intuitively provide more information. After eliminating analytical errors, the troughs, peaks and the pattern itself in the diagrams all provide useful information.

There have been several different approaches since Sun *et al.* (1979) normalised the analyses to chondrite composition. Following the same scheme, Thompson *et al.* (1983 &1984) set up the systematics of the method with minor differences in the ordering of the elements used in their diagrams, and named this type of plot a 'spidergram', though the original authors preferred the name PMN diagram (Sun & McDonough, 1989). Wood *et al* (1979b) used a "primordial mantle composition" as the normalising standard to investigate the depletion/enrichment processes of magmas; whereas Pearce (1983) normalised the compositions to a N-type MORB to characterise differences between basalts and the normal MORB. Recently, a primitive mantle composition was proposed by the original authors (Sun & McDonough, 1989) as a normalising standard.

It appears that chondrite-normalised and similar schemes are set up in the order of increasing incompatibility of elements in environments where oceanic basalts are produced, so average MORB would display a flat pattern with depletion of highly incompatible elements (*e.g.* Rb and K). Because the order of incompatibility of the elements varies significantly in rocks from different environments, this approach is very useful in evaluating the variability of possible mantle processes in magma genesis. On the other hand, MORB-normalised patterns are useful in investigating continental basalts and in identifying contributions of different components to the magmas (Pearce, 1983). This treatment is of particular relevance for metamorphosed

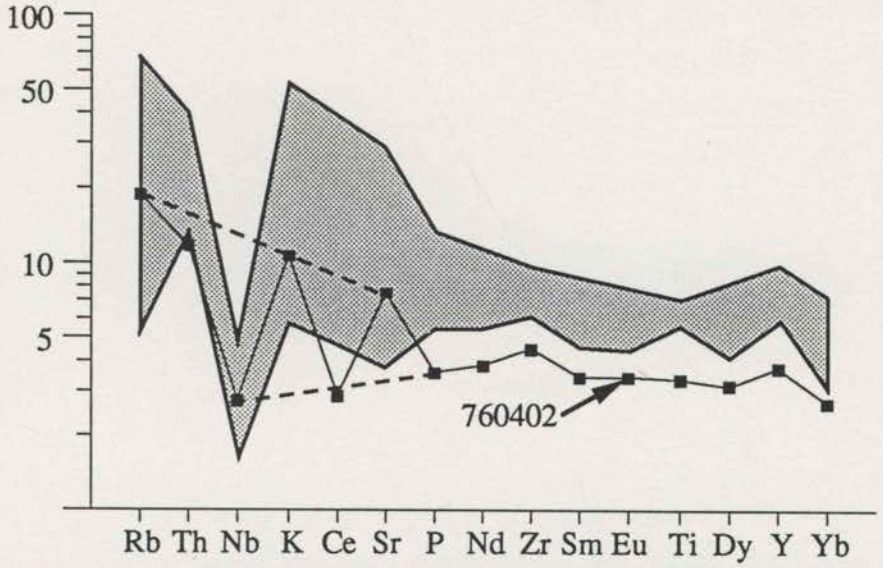

Fig. 5.3.5. The PMN plot (Sun & McDonough, 1989) of samples from the Ponto Mine area. Essentially, the samples display a flat, MORB-like pattern for most of the elements but with significant Nb depletion and K, Th and Rb enrichments. The metadolerite (III) (760402) is the most depleted sample in the group and the two dashed lines indicate enrichment and depletion respectively.

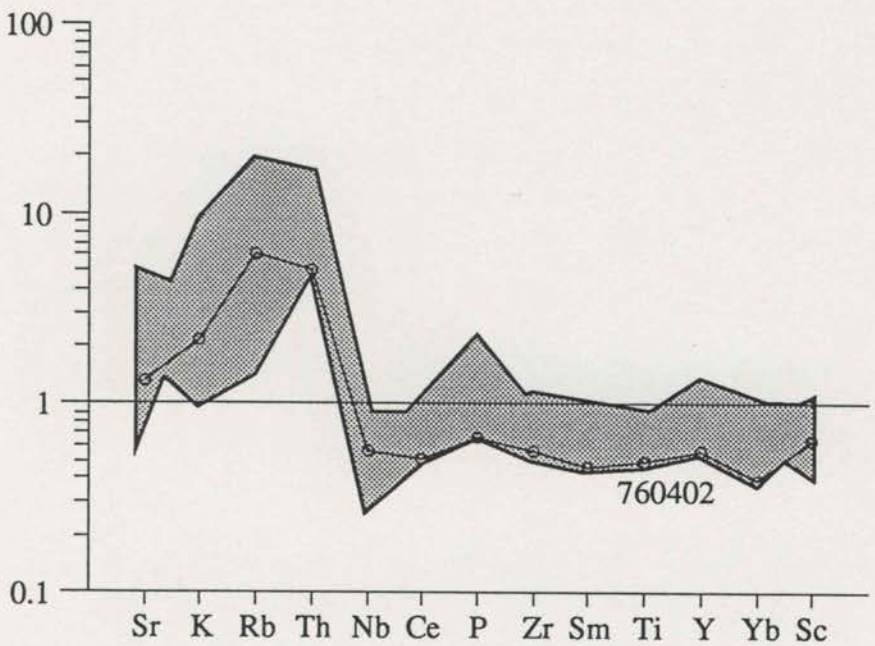

Fig. 5.3.6. The MORBN plot (Pearce, 1983) of basement samples from the Ponto Mine area. This diagram shows that these samples have significant MORB-like features but with Nb depletion and Th, Rb and K enrichments. Sample 760402 is the most depleted one in the group.

samples, as in this method, the generally mobile elements (K, Rb and Sr) are placed in the left side of the diagram and the immobile components on the right side in an order of incompatibility, which results in a clear pattern for comparison.

In this study, both primitive mantle normalised and MORB normalised diagrams are adopted. The first is named a PMN diagram and the second a MORBN diagram. The term 'spidergram' is used for general reference. Because K, Rb and Sr are probably mobilised components in the investigated samples as demonstrated earlier, the characteristics of these components are not emphasised. The mobility of these elements may also cause some difficulties in the interpretation of PMN diagrams as changes in these elements will vary the pattern of the diagrams.

The spidergrams of the selected samples from Ponto Mine are presented in Figures 5.3.5 and 5.3.6. The range of variation of most samples are shown as shaded areas in the diagrams, except 760402 (metadolerite III) shown explicitly. It appears that this sample has the lowest abundance of elements but an identical pattern to the others. In both diagrams, samples display a flat pattern with lesser contents for most components compared to normal MORB's (or less than ten times primitive mantle composition). In both diagrams, Nb displays a large negative anomaly, while Rb, K and Sr are generally enriched compared with the other elements. A minor Y anomaly also occurs in both diagrams, while a P anomaly can be seen only in the MORBN spidergram. Considering the mobility of Sr, Rb and K in these samples, it is obviously easier to observe the primary features in MORBN than in PMN diagrams. The dashed lines in Figure 5.3.5 display possible effects of alterations on the samples: the one through Sr, K Th to Rb indicate the secondary enrichment due to alteration (or crustal contamination, Pearce, 1983); while the one through P, Ce to Nb indicate a trend without these alteration/contamination (depletion of primary origin ?).

5.3.6. Discussion

The geochemical discriminations examined in this section revealed that most of the major components (Na, K, Mg, Fe and Ca) were mobile during metamorphism. However, variation of secondary mineral assemblages in these samples do not contribute significantly to the variation of their chemical compositions. This would suggest that the metamorphic processes, on the whole, may have not significantly changed the primary compositions to the extent that they are no longer recognisable. In other words, the range of the mobilisation may have not been much larger than the

sizes of the collected samples. Therefore in spite of the mobility, both TAS and A.I.-Al_2O_3 plots yield similar results to the HFS element discriminations for most samples. Among the trace elements, Sr and Rb were probably mobile but the discrimination cannot determine the mobility/immobility of Nb due to poor analytical quality, nor that of Sc and Ga as both are compatible components (see also discussion in Chapter 8).

In terms of primary geochemical compositions, the mafic samples have clear affinity with tholeiitic series or MORB, but with a significantly enriched Th and a depleted Nb, which may be explained as an indicator of crustal contamination (Saunders & Tarney, 1984; James *et al.*, 1987), although the quality of Nb analysis may be a problem.

The metadolerite (III) (760402) shows a distinct composition with low Fe_2O_3, HFS contents and relatively high MgO (6.07%), and may represent the most primitive sample in this magmatic series from depleted mantle source(s).

5.4. GEOCHEMICAL CHARACTERISTICS OF BASEMENT MAFIC ROCKS FROM THE BOSHY TANK AREA

The samples selected from this area for geochemical analysis include five metadolerites (four type IIs: 762501, 762701, 762705 and 762803, and one type III: 762706), and four metabasites (762603, 762605, 762606, 762703) from both northern and southern sides of the dyke successions.

5.4.1 Primary Geochemical Affinity

Figure 5.4.1 presents the plot of Nb/Y versus Zr/TiO_2 of these samples. This diagram shows that all samples plot in the subalkaline basalt field. Like those at Ponto Mine, these samples display a constant Zr/TiO_2 ratio and a wide range of Nb/Y, which may be caused largely by poor Nb analysis.

5.4.2 Major Element Geochemistry

In the TAS diagram (Figure 5.4.2), the samples plot in the subalkaline basalt field with relatively limited variation, except one of the metabasites (762703) with high SiO_2 in the basaltic andesite field. However, on the Al_2O_3 versus A.I. diagram (Figure 5.4.3), they plot in both the tholeiitic and calcalkaline fields. The four high Al_2O_3 samples are 762606, 762701, 762706, 762803, which are of all three petrographic groups.

This diagram indicates that the Al_2O_3 contents in these samples may no longer be indicative of their primary magmatic characteristics.

5.4.3. The REE Geochemistry

Two metadolerites (II) were selected to analyse their REE compositions and the results are shown in Table 5.3 and Figure 5.4.4. Both samples have a flat pattern with a clear Ce-depletion, like most of the Ponto Mine samples. However, both samples display a minor Eu anomaly.

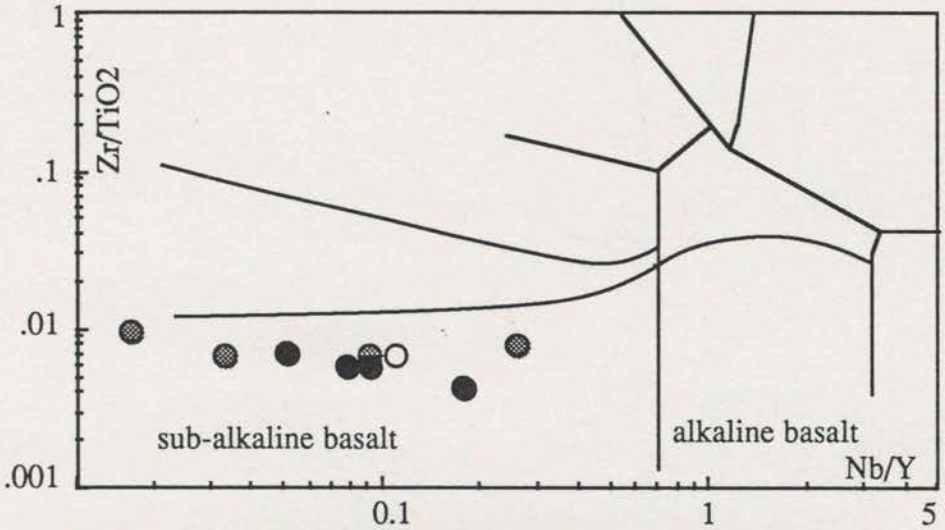

Fig. 5.4.1. Nb/Y - Zr/TiO2 diagram of mafic samples from the Boshy Tank area. Filled circles, metabasites; open circles, metadolerite (I) and dotted circles, metadolerite (II). All samples exhbit features of subalkaline basalts.

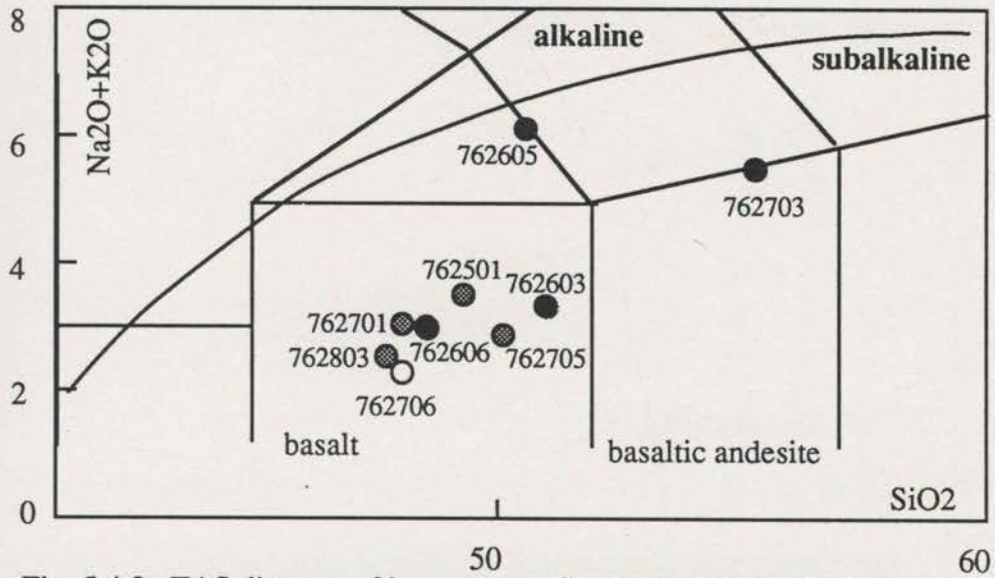

Fig. 5.4.2. TAS diagram of basement mafic samples from the Boshy Tank area. Filled circles, metabasites; open circles, metadolerite (I); dotted circles, metadolerite (II). Like those in the Ponto Mine area, the samples plot in the subalkaline basaltic clan.

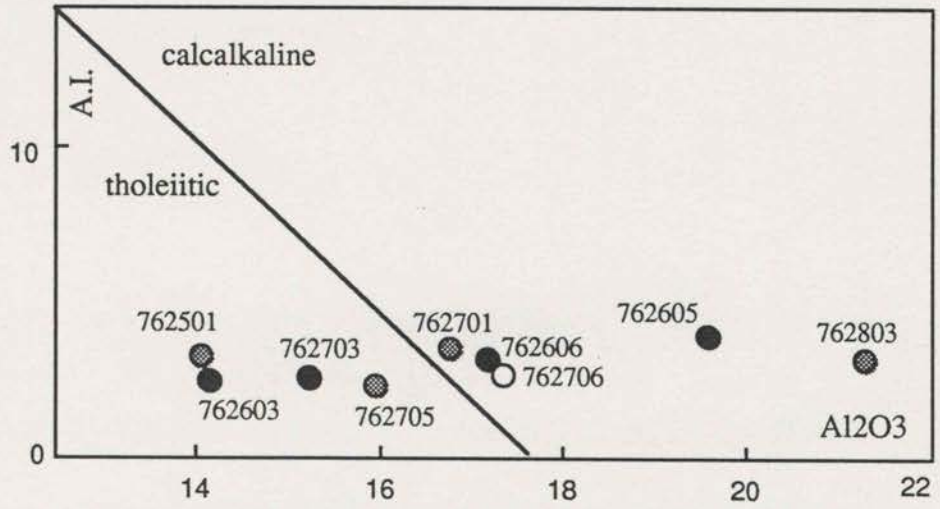

Fig. 5.4.3. Al2O3 - A.I. diagram of basement mafic samles from the Boshy Tank area. Filled circles, metabasites; open circles, metadolerite (I); dotted circles, metadolerite (II). Unlike the Ponto Mine samples, the patterns revealed (both tholeiitic and calcalkaline) probably do not resemble primary geochemical characters but alteration of the rocks. This non-discrimination is largely due to the anomalously high Al2O3.

5.4.4. Spidergram

Figure 5.4.5 is a MORBN diagram of these Boshy Tank samples. In general, these samples display flat patterns around the MORB level, with secondary but remarkable features of Nb depletion and Th enrichment. Some samples also show small peaks at P and Y, but the Y enrichment is largely due to high Y content in one sample 762701 (60 ppm).

This diagram shows that the samples are MORB like in most of their relatively immobile compositions, with secondary yet significant variations, in particular, Th enrichment and Nb depletion. The anomalously high Y in sample 762701 may possibly be an analytical error. Unfortunately this problem could not be solved by re-analyse this particular sample due to limited resources available.

Combining the discrimination results presented above, it can be said that the Boshy Tank basement samples are MORB-like with a flat chondrite normalised REE pattern, but with Th-enrichment and Nb-depletion. The small Eu anomaly in the two analysed metadolerites may suggest plagioclase fractionation in the magmatic processes (see discussion in Chapter 8), or mobilisation of the component during secondary processes. These features are rather similar to those observed in the Ponto Mine basement samples.

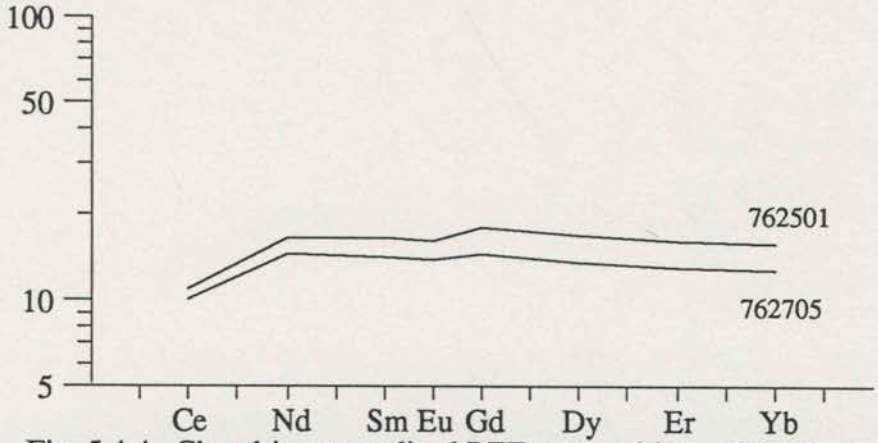

Fig. 5.4.4. Chondrite-normalised REE compositions of the Boshy Tank basement samples. The two selected representative samples (metadolerites (I) & (II)) both show a flat pattern with Ce-depletion.

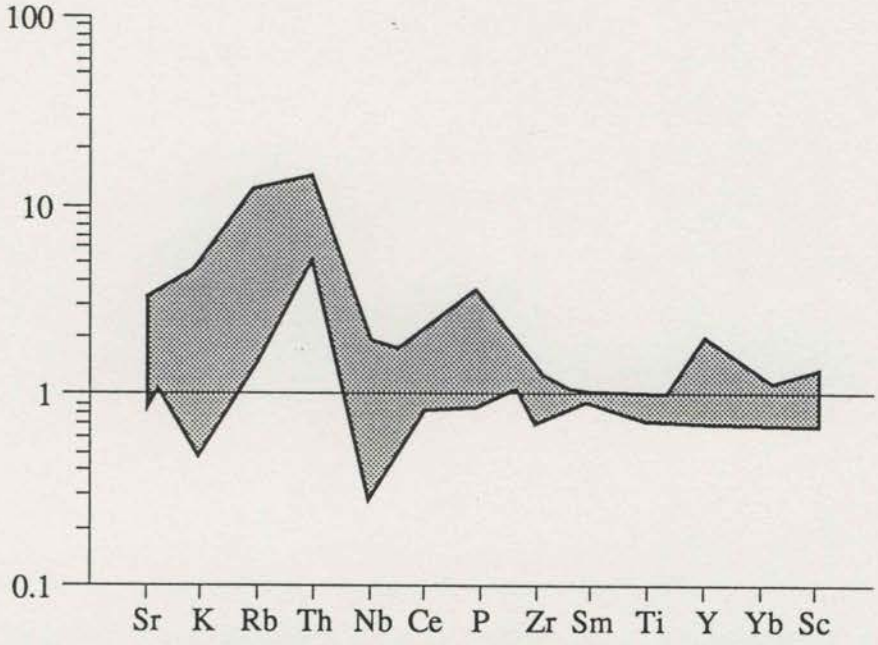

Fig. 5.4.5. The MORBN plot of the Boshy Tank basement samples. The samples are generally MORB like for most of their component except various enrichments of Th, Rb, K and Sr.

5.5. GEOCHEMICAL CHARACTERISTICS OF MAFIC ROCKS FROM THE WILANDRA AREA

Sixteen samples are selected from the basement sequence in this area, with one felsic tuff (861209), eight metabasites (861203, 861205, 861304, 861305, 861307, 861316, 861601, 861604 and 861605), six metadolerites (three type Is: 861311, 861314, 861315; two type IIs, 861211, 861407; and one type III: 861302).

5.5.1. Primary Geochemical Affinity

Figure 5.5.1 shows that all of the samples plot as subalkaline basalt, except one in the andesite field with a slightly higher Zr/TiO_2 ratio than the others. Again, the Zr/TiO_2 variations of the samples are limited, but with a range of Nb/Y.

5.5.2. Major Element Geochemistry

On the TAS diagram (Figure 5.5.2), most samples plot in the subalkaline basalt field with limited variation. There are also two exceptions having higher SiO_2: one (861307) is also higher in alkaline content (7.53% Na_2O+K_2O) and the other (861314) has the same level of alkaline component as the others. Sample 861307 is also characterised by very low MgO (0.96%).

The Al_2O_3 versus A.I. diagram (Figure 5.5.3) displays that these samples have a scattered pattern in both tholeiitic and calcalkalic fields, as do those from the Boshy Tank area.

5.5.3. REE Geochemistry

Two intrusive samples (metadolerite types I (861314) and II (861211) respectively) were selected from the Wilandra area to analyse their REE compositions. The results are shown in Table 5.3 and Figure 5.5.4, which shows that the two representative samples all have very similar compositions. Both have generally a flat pattern and show both Ce and Eu depletions.

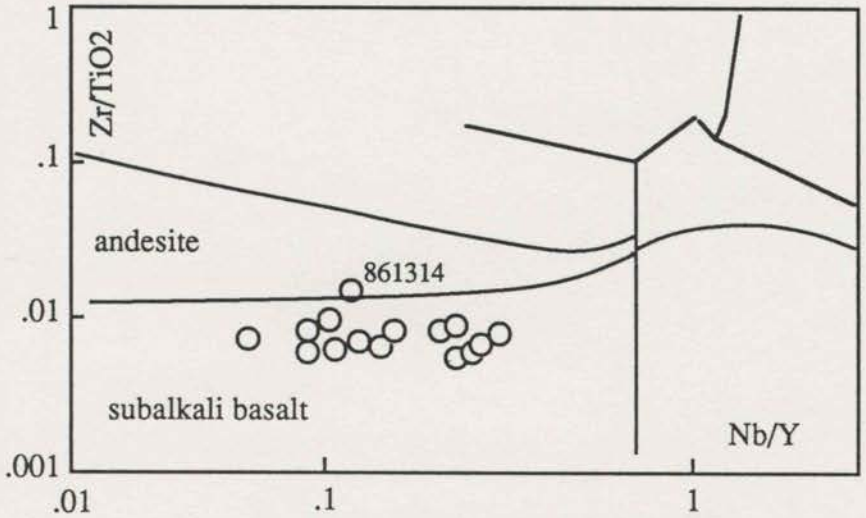

Fig. 5.5.1. Nb/Y versus Zr/TiO2 diagram of the Wilandra basement mafic samples, which all plot in the subalkali basalt field, except sample 861314 across the border in andesite with slightly higher Zr/TiO2 ratio.

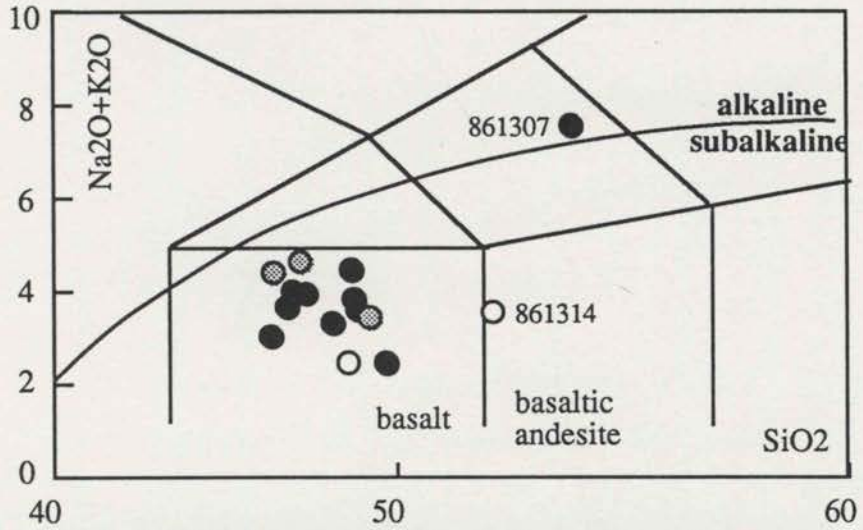

Fig. 5.5.2. TAS diagram of Wilandra basement mafic samples. Filled circles, metabasite/metabasalt; open circles, metadolerite (I); dotted circles, metadolerite (II). This diagram shows that most samples are in the basalt field.

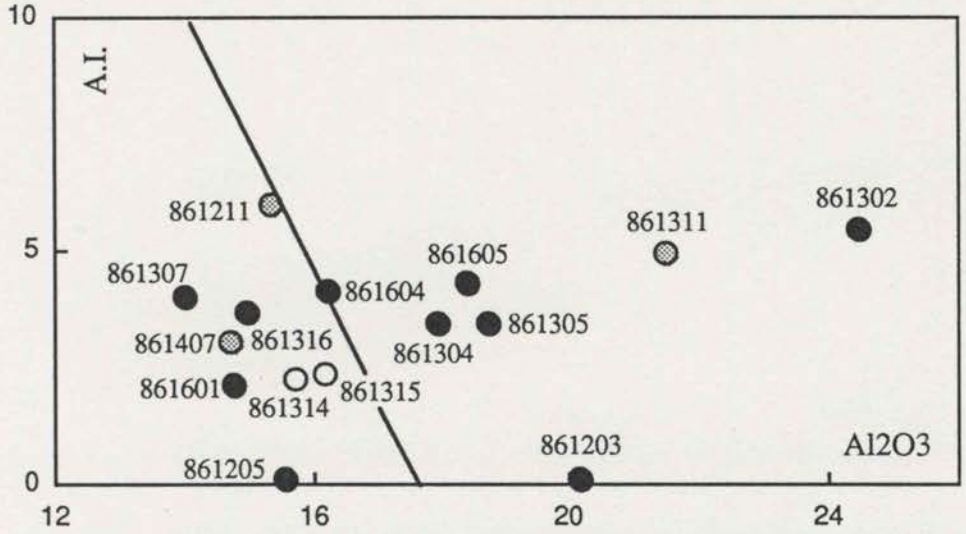

Fig. 5.5.3. Al2O3 versus A.I. plot of the Wilandra basement mafic samples. Filled circles, metabasite/metabasalt; open circles, metadolerite (I); dotted circles, metadolerite (II). Samples plot in both tholeiitic and calcalkaline fields, which probably do not represent the priamry geochemical features, as shown in Fig. 5.5 l.

5.5.4. Spidergrams

Figure 5.5.5 is a MORBN plot of these Wilandra basement mafic samples . Most of them display identical patterns with a slight increase from Sc to Nb and a sharp increase at Th; the Rb and K are also at a high level. The general variation of the selected elements is about eight fold, but K has much larger variation. Three of the samples are explicated individually. The first one (861604) has high Y content; the second (861316) has the lowest abundance in most of the components and the third one (861407) is characterised by very low Rb and K.

This diagram shows that the mafic samples from the Wilandra area have MORB-like contents for most of the elements, but are distinct from MORBs with enriched Th, Rb and K, and a slight increasing pattern for some samples in the group. Significantly, the Nb depletion observed in samples from the Ponto Mine and Boshy Tank areas is not obvious here.

These discrimination diagrams revealed that the Wilandra basement mafic samples may have primary compositional affinities with MORB with a flat chondrite normalised REE pattern, but with Th-enrichment. These features are similar to those observed in samples from the Ponto Mine Inlier (Ponto Mine and Boshy Tank), but a distinctive feature is that the Wilandra samples exhibit no Nb-depletion.

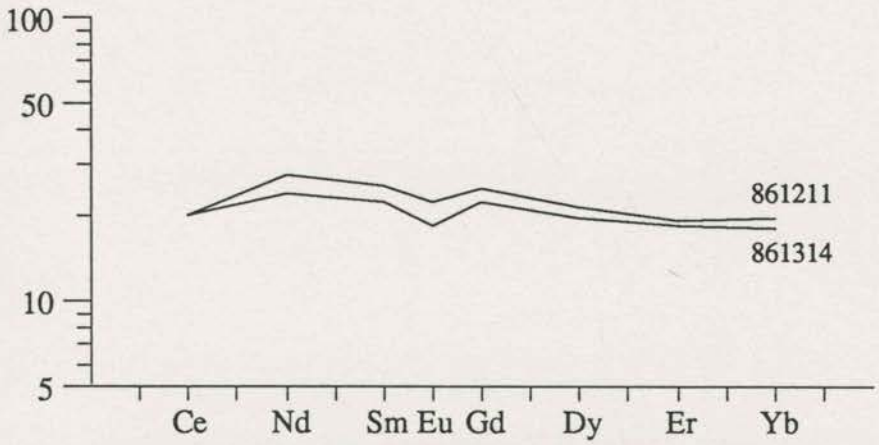

Fig. 5.5.4. Chondrite-normalised REE plot of the Wilandra samples. The two metadolerites (types I & II) have generally flat patterns with small Eu and Ce depletions.

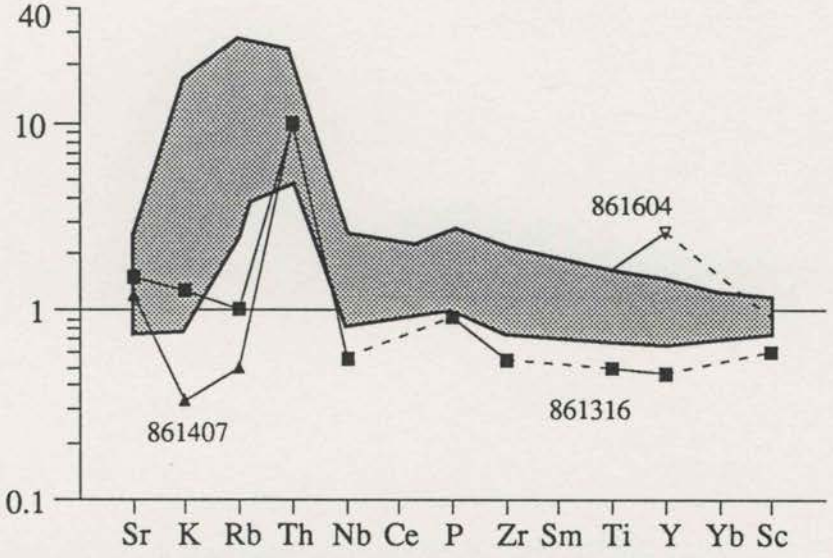

Fig. 5.5.5. The MORBN spidergram of the Wilandra mafic samples, which are MORB-like except for enriched Th, K and Rb. Nb depletion, observed in the Ponto Mine Inlier is absent here. Samples with distinct compositions are shown explictly.

5.6. GEOCHEMICAL CHARACTERISTICS OF MAFIC ROCKS FROM THE CYMBRIC VALE AREA

Samples selected in this area include two amphibolites (861713, 861714), one metadolerite (861909) and one mafic schist ((861915, amphibolite in composition), four metabasites (861705, 861707, 861806 and 861911), one mica schist (861913) and one felsic tuff (861906).

5.6.1. Primary Geochemical Affinity

Figure 5.6.1 presents the Nb/Y versus Zr/TiO_2 variation of the mafic samples. This diagram shows that the samples plot in the subalkaline basalt field though a metabasite (861911) with high Nb/Y and Zr/TiO_2, plots close to the border with andesite. Shown in this diagram are also representatives of the Broken Hill Group basic gneisses (James *et al.*, 1987). Apparently these two groups of rocks have different HFS element compositions.

5.6.2. Major Element Geochemistry

On the TAS diagram (Figure 5.6.2), all of the mafic samples plot in the subalkaline field. While the majority are basaltic, there are three metabasites plotting at the higher SiO_2 end. The highest-SiO_2 one (861911) plots in the andesite field.

On the A.I. versus Al_2O_3 diagram (Fig.5.6.3), most of the samples plot in the tholeiitic field except two of the metabasites (861707 and 861911) with higher Al_2O_3.

This two diagrams suggests metabasites suffered more compositional changes during alterations than metadolerite and amphibolite.

5.6.3. REE Geochemistry

Three samples were analysed from the Cymbric Vale area for their REE compositions. The results are shown in Table 5.6 and Figure 5.6.4, which shows that the three samples have very similar compositions with a generally flat pattern and Ce-depletion. The metadolerite II (861909) shows a small Eu-depletion. The other two samples

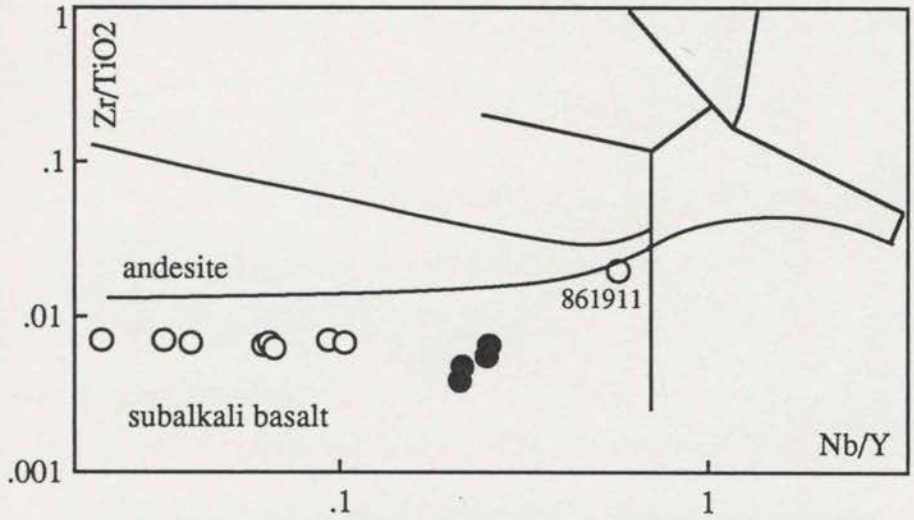

Fig. 5.6.1. Nb/Y vs Zr/TiO2 plot of the Cymbric Vale mafic samples (open circles), which all plot as subalkali basalt. For comparison, the Broken Hill Group basic gneisses (filled circles) are also show in this diagram: the difference in Nb/Y between the two groups is obvious.

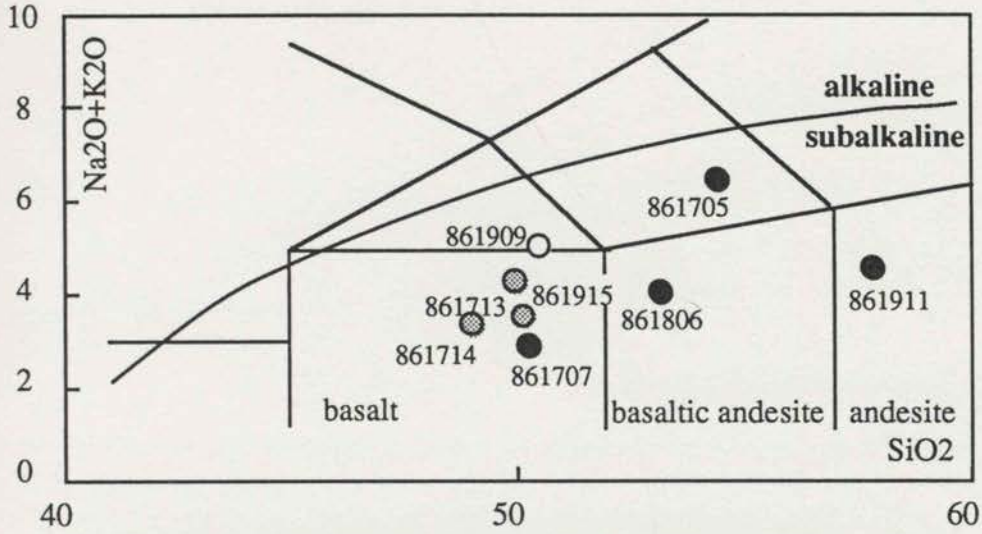

Fig. 5.6.2. TAS plot of the Cymbric Vale basement mafic samples. Filled circles, metabasites; dotted circles, amphibolite and open circle, metadolerite. Although the samples are mostly basaltic, they also show variations in both silica and alkali components.

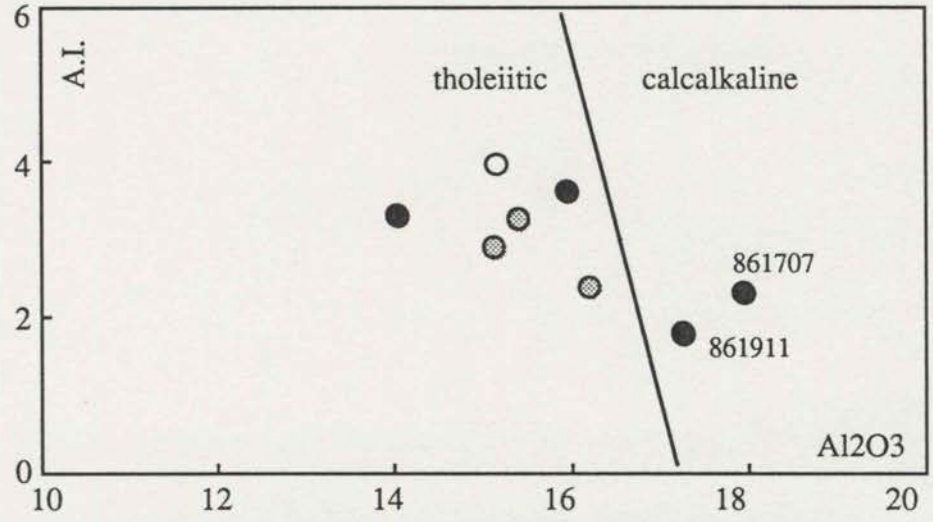

Fig. 5.6.3. Al2O3 versus A.I. diagram of the Cymbric Vale samples. Legends as Figure 5.6.2. Again some samples plot in the calcalkaline fields, probably not indicative for the primary geochemical compositions as revealved in Fig. 5.6.1.

(861713, metabasite and 861915, amphibolite) has a slightly lower REE content and no Eu anomaly. All three samples display Ce-depletion.

5.6.4. Spidergrams

Figure 5.6.5 is a MORBN plot of the selected mafic samples from the Cymbric Vale area. Clearly, these samples display a flat pattern for most of the immobile elements and have MORB values from Sc to Ce (some samples also have MORB value for Nb). The enrichment of Th is significant (4 to 20 times) and Nb depletion occurs in some of the samples. It is also noted that those with the least depleted Nb, are most enriched in Th and the one with most depletion of Nb is the least enriched in Th. The metadolerite (861909) is samples shown individually, as it is characterised by Rb and K enrichment.

Therefore, it appears that most of the mafic samples from this area may have primary affinities with tholeiitic series and have MORB-like compositions regardless of their petrographic characters. On the spidergram, the samples exhibit both Th-enrichment and Nb-depletion, similar to samples from the Ponto Mine Inlier in the north, but different from the Wilandra samples.

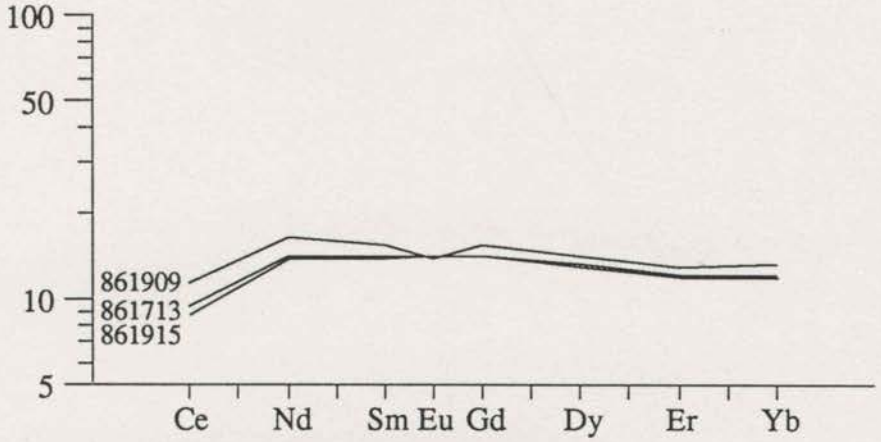

Fig. 5.6.4. Chondrite-normalised REE plot of representative Cymbric Vale samples. All show a flat pattern of ten times chondrite values, with Ce depletion. The metabasite (861909) also shows minor Eu depletion.

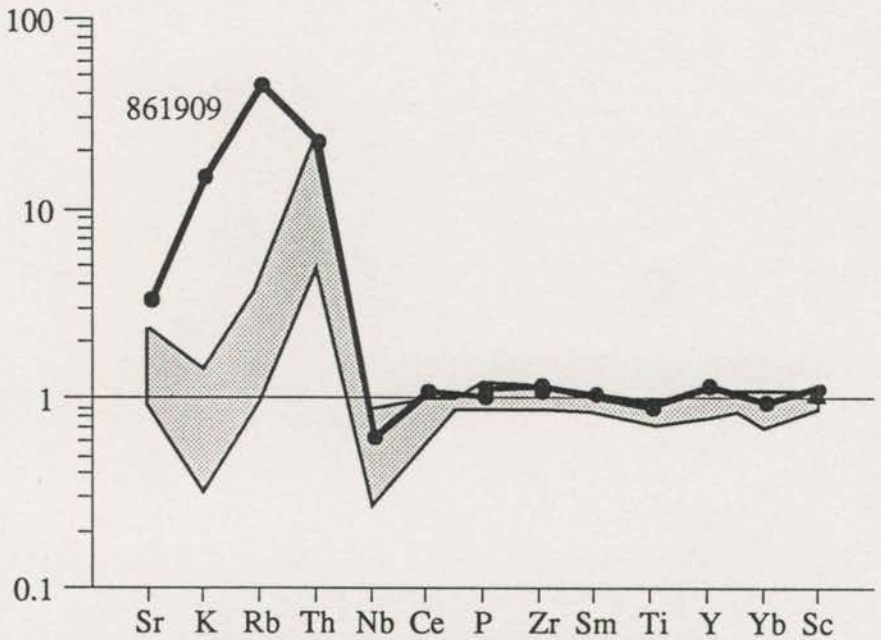

Fig. 5.6.5. MORBN plot of the Cymbric Vale mafic samples, which are mostly MORB-like with Th-enrichment. Sample 861909 (metabasite) is also enriched in Rb and K; while 861705 has an anomalously high Y.

5.7. GEOCHEMICAL STRATIGRAPHY OF BASEMENT MAFIC SAMPLES.

From the above presentations, it is obvious that mafic rocks in the basement sequence of the Wonominta Block display composite geochemical characteristics as well as complex behaviour during secondary processes. Most of the major elements may have been mobilised during alteration, such as Na, K, Mg, Fe and Ca, and Sr, Rb Ga and Sc in the trace element group, whereas the HFS group were largely immobile. An uncertainty is that the poor analytical quality of Nb.

In regard to the primary geochemical affinities, most of the samples belong to the subalkaline series as shown in Figures 5.7.1 and 5.7.2. The compositional field of the Ponto Mine samples in Figure 5.7.1 includes only those samples with moderate TA/S ratios, as the other two trends are considered to be of secondary origin as discussed in section 5.3. Figure 5.7.2 shows that all the samples have rather constant Zr/TiO_2 ratios (about 0.01). The Cymbric Vale samples have the lowest mean Nb/Y value and the most limited variation. However, compositional variations from different areas on both diagrams generally overlap in both diagrams, and are clearly distinctive from those in the Late Proterozoic sequence, shown here for comparison and further discussed below.

The MORBN diagrams (Figure.5.7.3) display roughly identical patterns, characterised by low abundances of HFS (Yb to Nb) and the enrichment of LILE components (Th to K). Although K, Rb and Sr may have been mobile components during secondary processes, Th-enrichment is likely a primary feature. However, even the flat part of the pattern, in detail, shows significant differences for samples from different localities. The Ponto Mine samples are the most depleted with the absolute abundance of individual components less than those of MORB. Both the Cymbric Vale and Boshy Tank samples are roughly on the same level as the MORB. And all three areas have samples showing remarkable Nb depletions. In contrast the Wilandra samples are the most enriched with virtually no Nb depletion.

As presented in Appendix 6, Nb analyses using XRF techniques are not necessarily reliable when approaching its analytical limit (1 ppm). However, even allowing for analytical difficulties, it can still be seen, through a statistical treatment, that the basement mafic samples from the Ponto Mine area have lower Nb abundance than those in the Boshy Tank area, which are lower than those from Wilandra area (Figure 5.7.4), this would certainly bear crucial significance in terms of tectonic implications.

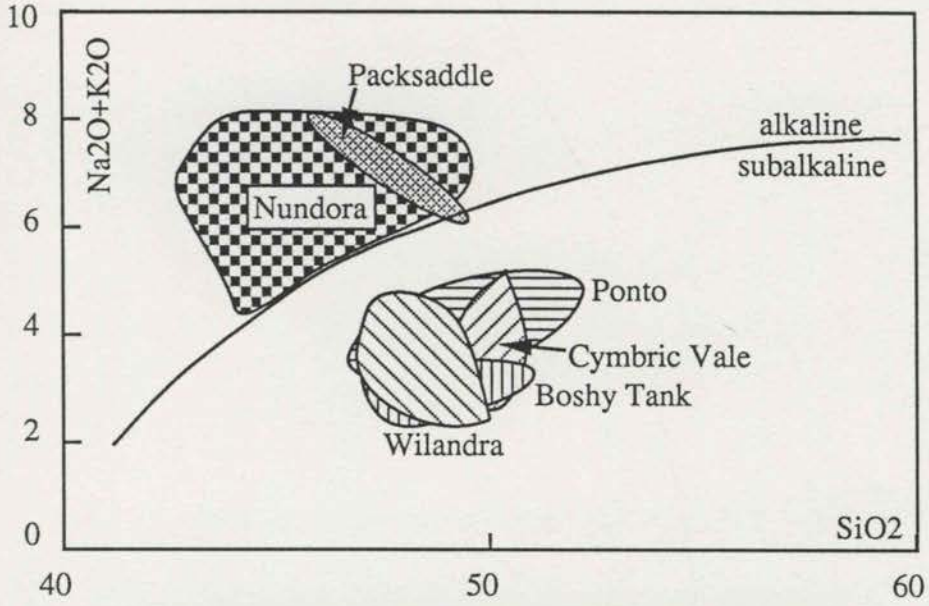

Fig. 5.7.1. The TAS plot of mafic samples from the Precambrian sequences in the Wonominta Block. Samples with obvious alterated compositions are not included in this diagram. This diagram clearly shows the geochemical difference between the basement (subalkaline) and late Proterozoic (alkaline) sequences, a conclusion similar to that drawn from discrimination disgram using immobile components as shown in Fig. 5.7.2.

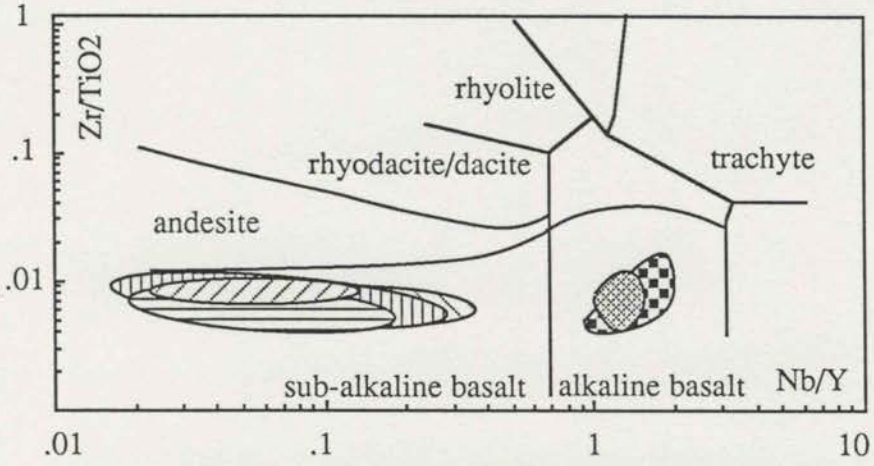

Fig. 5.7.2. Nb/Y versus Zr/TiO2 plot of mafic samples from the Precambrian sequences in the Wonominta Block. Legend as Fig. 5.7.1. All basement samples plot as subalkaline basalt, while the late Proterozoic samples are alkaline basalt.

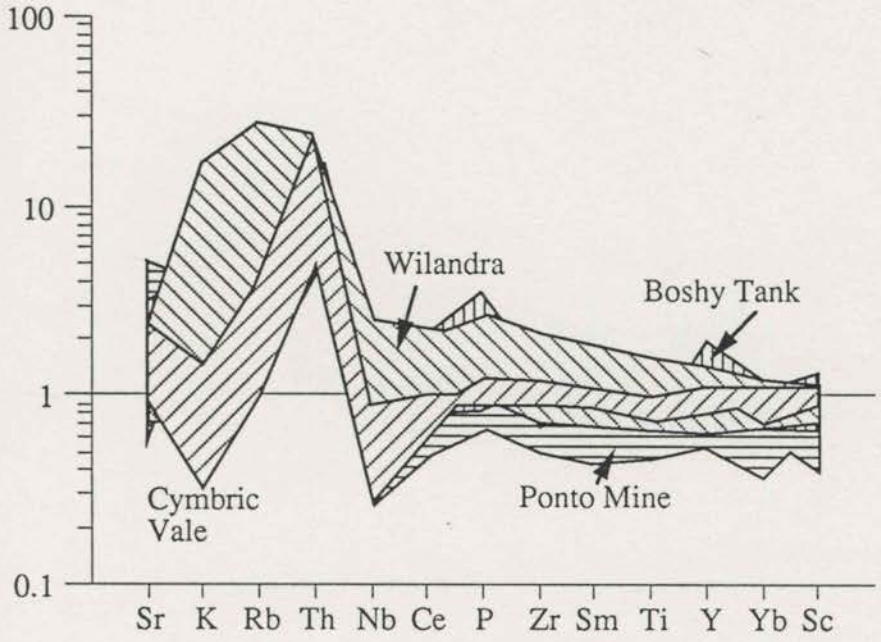

Fig. 5.7.3. The MORBN plot of the basement samples in the Wonominta Block. Samples from Ponto Mine, Boshy Tank and Cymbric Vale are MORB-like with significant Nb-depletion and Th, Rb and K-enrichment; while the Wilandra samples shows no Nb depletion and a slight increase from Sc to Nb.

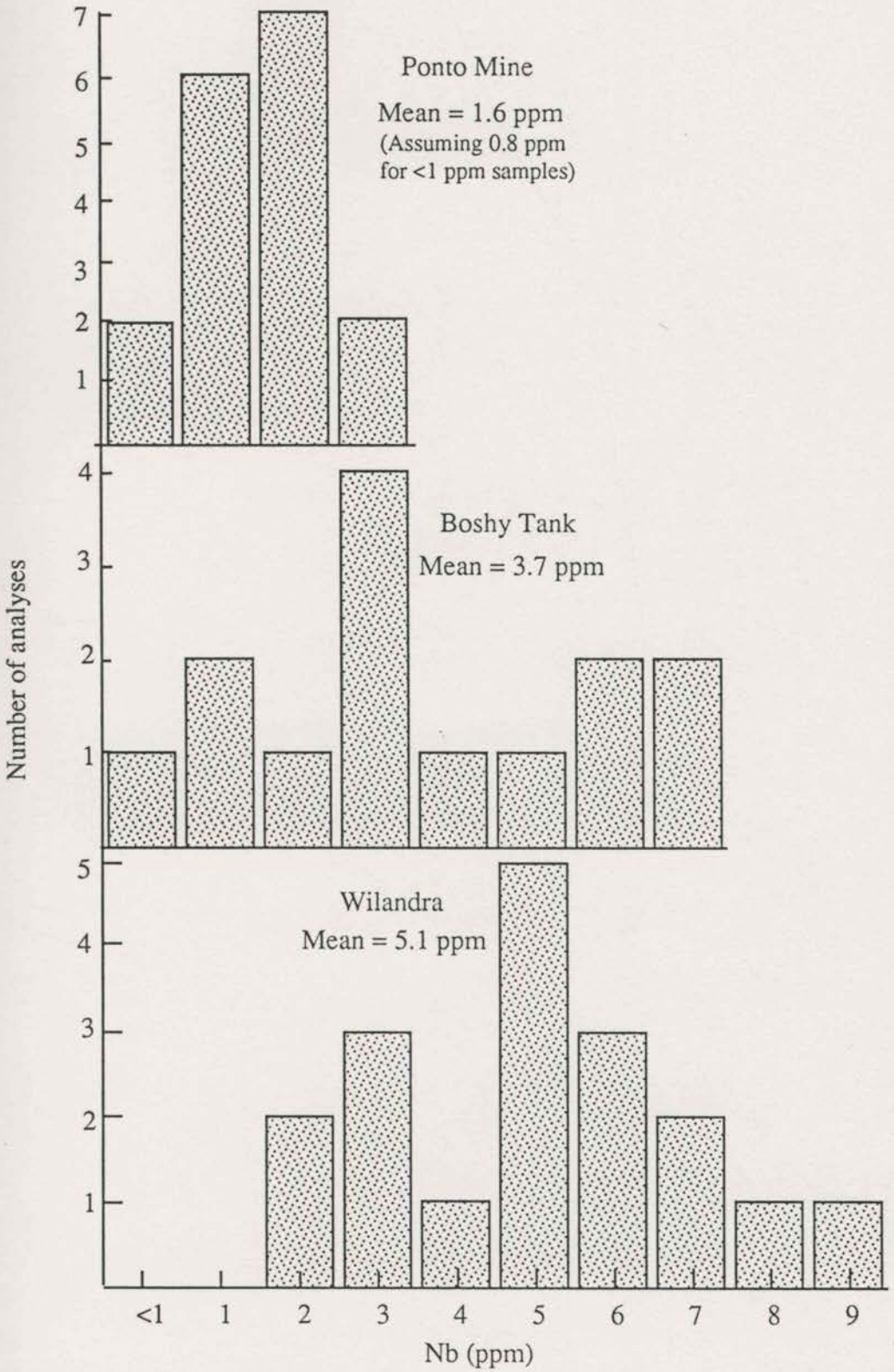

Fig. 5.7.4. Distribution of Nb concentration in the basement mafic rocks. This statistical treatment indicates that the average Nb content is obviously lower in samples in the Ponto Mine Inlier compared to those in the Wilandra Inlier, though each individual analysis may not be of good quality.

Chapter 6

Geochemistry of Mafic Rocks in the late Proterozoic Sequence

6.1. SAMPLE SELECTION

Twenty-seven samples were selected from the Packsaddle and Nundora areas of the late Proterozoic sequence for their major and trace element compositions. The sample selection is presented in Tables 3.8, 3.9 and 6.1. The Packsaddle collection includes three metabasites representing pillow lava (761301) and massive flow (760805 from M1; 760806 from M2) respectively, along with three kaersutite-bearing metadolerites (type I, 760801, 761001 and 761203) and one syenite (761204). In the Nundora collection, the nine volcanic samples include three cleaved (761602, 761809 and 761906) and six massive species (761503 (nodular mass in cleaved zone), 761505, 761512, 761901 (relic plagioclase-bearing), 761907 (relic pyroxene-bearing) and 761908 (fine-grained)). Among other samples selected, altered peridotite is represented by 761801, syenite by 761603 and nundorite and related rocks by nine samples (762401 to 762409). The last group represents a major endeavour to investigate the metasomatic processes involved in the formation of this unusual aegirine-nepheline rock. Results for both the syenite and nundorite are discussed in Chapter Seven.

Table 6.1. Sample Selection of late Proterozoic Mafic Rocks

area	MD(I)	MB	syenite	nundorite	peridotite	total
Packsaddle	3	3	1			7
Nundora		9	1	9	1	20
TOTAL	3	12	2	9	1	27

The analytical results are presented collectively in Table 6.2 in Appendix 6. Major element concentrations, used in the various discriminant diagrams, are normalised to volatile-free status, like those for the basement samples.

6.2. GEOCHEMICAL CHARACTERISTICS OF MAFIC SAMPLES FROM THE PACKSADDLE AREA

6.2.1. Major and Trace Element Geochemistry

In terms of major element compositions, all analysed mafic samples from this area fall in the basaltic clan with SiO_2 between 46 and 50%. These samples have the normalised compositional ranges of TiO_2 (1.59-3.99%), Al_2O_3 (11.86-19.53%), ΣFe_2O_3 (9.32-13.86%), MgO (2.85-7.60%), CaO (4.55-10.12%), Na_2O (3.00-6.85%) and K_2O (0.57-1.92%). On the TAS diagram (Figure 6.2.1), they plot in two groups, four (one metadolerite and three metabasites) in the alkaline field and the other two metadolerites in the subalkaline basalt field. The two subalkaline samples both have about 15% Al_2O_3, and thus belong to the tholeiitic association, if their present Al_2O_3 chemistry preserves primary characteristics.

The Nb/Y versus Zr/TiO_2 diagram (Figure 6.2.2) yields similar results, *i.e.*, four in alkaline basalt field and two metadolerites in the field of subalkaline basalt .

Figure 6.2.3 shows the variations of Zr against TiO_2, Sr, Nb, Y, Rb, Sc and Ga of these samples, which show three compositional groups in terms of Zr content. Two of the metabasites and one metadolerite are characterised by high Zr, Ti and Nb; the metadolerite (760801) has low Zr, Ti, Y and Sc, very high Sr (1280 ppm), relatively high Rb, Nb and Ga; and the second metadolerite (761001) sample falls in between along with the third metabasite. No obvious correlations are observed due to limited numbers of analyses.

6.2.2. REE Geochemistry

For the REE analyses, four samples were selected from this area, which included three metabasites and one metadolerite (760801). The results are presented in Table 5.3 and Figure 6.2.4, which show that all have similar compositional patterns with a clear and significant LREE enrichment, in contrast with the flat pattern observed for the basement samples. In terms of REE abundance, the four selected samples fall into two compositional groups: the metadolerite (760801) has lower REE content compared with the metabasites. Both groups show no Eu anomaly.

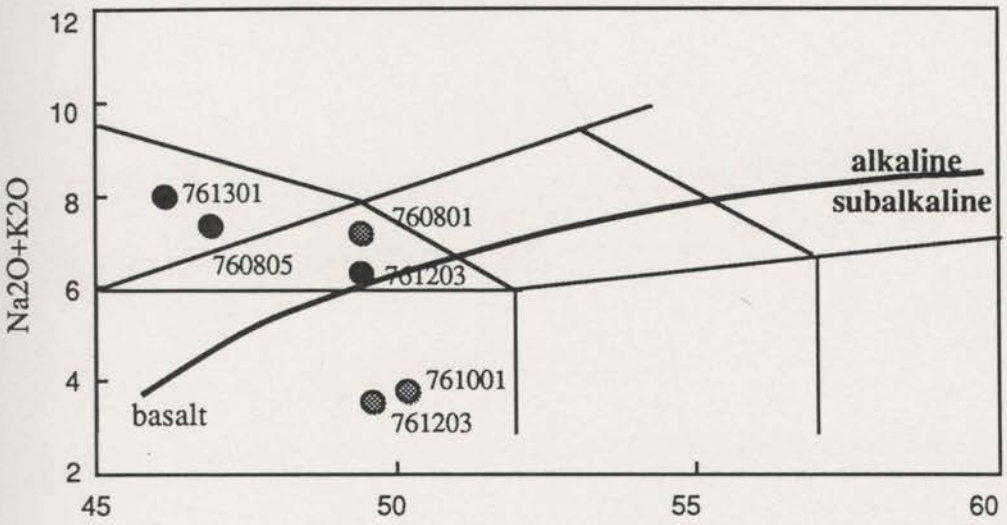

Fig. 6.2.1. TAS plot of the late Proterozoic samples from the Packsaddle area. Filled circles, metabasites; dotted circles, metadolerites. The six samples plot in two groups though both fall in the basalt clan: two of the intrusive samples in the subalkaline and the others in the alkaline fields.

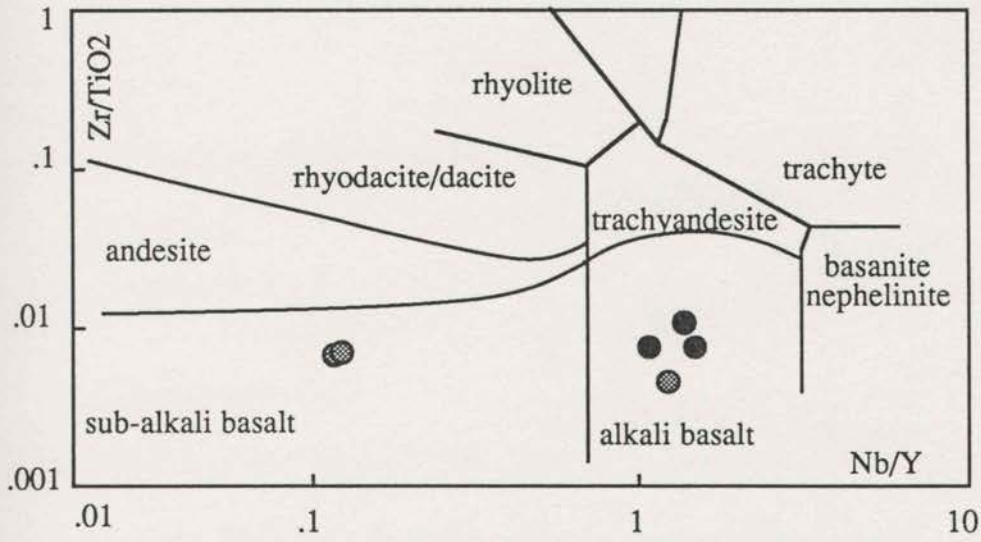

Fig. 6.2.2. Nb/Y - Zr/TiO2 plot of late Proterozoic samples from the Packsaddle area. Filled circles, metabasites; dotted circles, metadolerites. Like Fig. 6.2.1, the samples plot as both alkaline and subalkaline basalts.

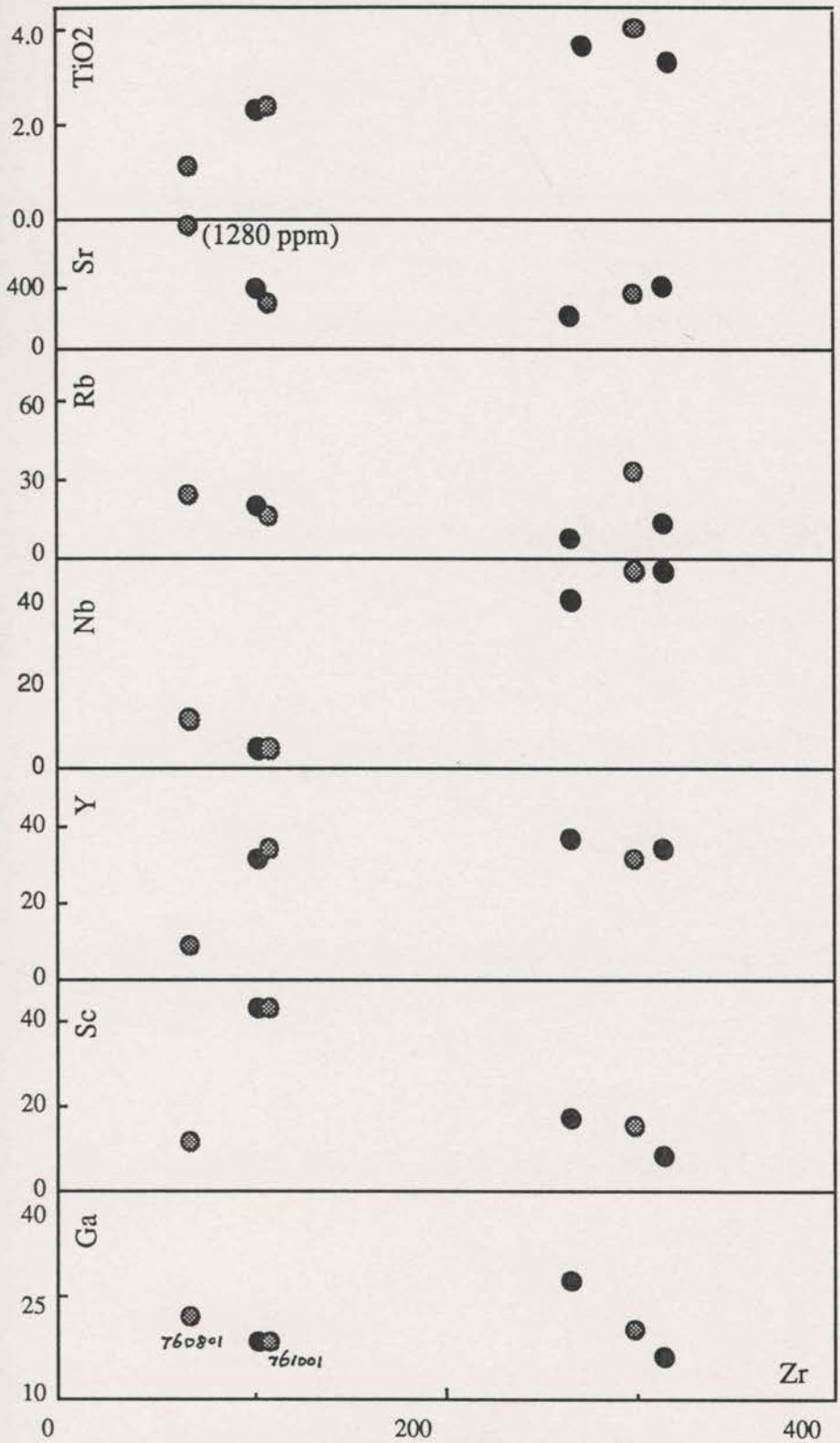

Fig. 6.2.3. Binary compositional variations of the mafic samples from the Packsaddle area. Filled circles, metabasites; dotted circles, metadolerites. Partly due to limited number of samples analysed, the presented elements do not in general show significant correlations, except parhaps for Zr-TiO2 and Zr-Nb.

6.2.3. Spidergram

Figure 6.2.5 presents the PMN plot of the selected mafic samples from the Packsaddle area. This diagram shows three distinctive patterns. The metabasites display a pattern of increase from Sc to Th with troughs at Sr, K and Rb. The two metadolerites (761001 and 761203) are characterised by a slower increasing pattern from Y to Rb with a significant Nb depletion. And the third metadolerite (760801) has lower abundance for most of the elements, except enrichments of Ti, Sr and K. Apart from these three peaks, this sample also displays a relatively smoothly increasing pattern from the right to the left of the diagram.

This diagram reveals complicated compositional patterns for the Packsaddle samples, which probably suggest different origins for the rocks they represent. In other words, if the metabasites are taken as the volcanic hosts, the three metadolerites may represent two distinctive xenoliths enclosed in the volcanic sequences: 761001/761203 being a depleted basement-type (Nb-depletion) and 760801 a primitive type. The Ti-enrichment in 760801 is probably reflected the by presence of kaersutite in the rocks and Sr, Rb-enrichments can be explained as alteration products, which resulted in depletion of the components in the volcanic host rocks.

The compositional characters of the volcanic sequence in the Packsaddle area are typical of intra-plate volcanism, with high Nb/Y (thus alkaline), LREE-enriched and increasing patterns from Yb to Rb in the spidergram.

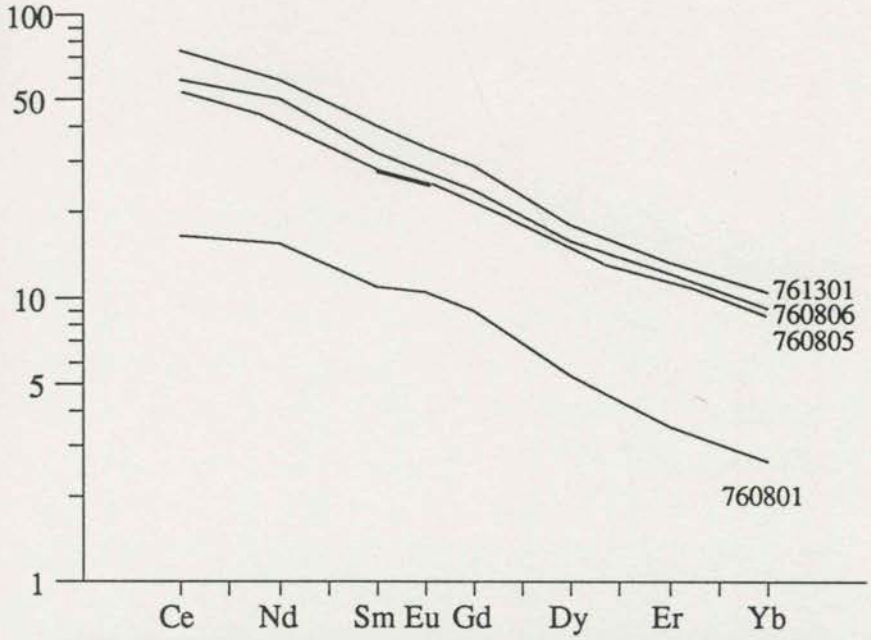

Fig. 6.2.4. Chondrite-normalised REE compositional plot of the late Proterozoic Packsaddle samples. All presented samples show significant enrichment from heavy (Yb) to light (Ce) REE, yet with large variations in abundance. The kaersutite-bearing xenolith (760801) has the lowest REE content of the group.

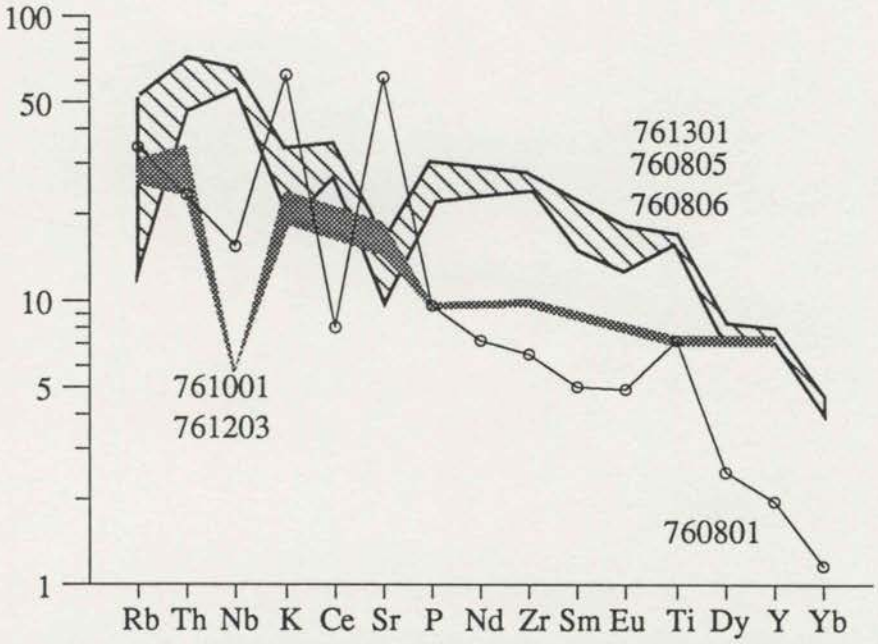

Fig. 6.2.5. The PMN plot of late Proterozoic Packsaddle mafic samples. These samples display three distinctive patterns. Sample 760801 has the lowest content for most elements and shows an increasing pattern from right to left with high K, Sr and Ti. The metabasites (760805, 760806 and 761303) display similar patterns at a higher abundance level, and the third group, 761001 and 761203 shows a flat pattern with a significant Nb depletion, similar to some basement samples.

6.3. GEOCHEMICAL CHARACTERISTICS OF MAFIC ROCKS FROM THE NUNDORA AREA

6.3.1. Major and Trace Element Geochemistry

Among the analysed samples, the altered peridotite (serpentinite) is a typical ultrabasic rock with low SiO_2 (42.75%, normalised value), high MgO (28.43%) and Fe_2O_3 (16.66%), low Al_2O_3 (5.68%), CaO (6.2%) and alkaline components (0.25%). The high LOI (11.05%) indicates that the relatively high SiO_2 is possibly the result of the normalising process. All the metabasites (massive or cleaved) are also low in SiO_2 (43-52%), with generally high TiO_2 (1.93-4.37%), high alkalic components (up to 8% and dominated by sodium component), and ranges of MgO (2.27-7.04%), Al_2O_3 (12.48-18.07%) and $\sum Fe_2O_3$ (7.4-16.47%). Two of the three cleaved metabasites have high LOI (761906, 7.44% and 761809, 9.33%), but some massive metabasites also have high LOI, such as 761505 (10.55% LOI). It appears though that the high LOI does not change the discrimination results significantly (*cf.* Figures 6.3.1, 6.3.2).

Figure 6.3.1 presents the TAS diagram of the samples. The diagram shows that all the mafic samples, except 761906 and 761907 (both are massive metabasite within the cleaved metabasite units) and the peridotite (761801), plot in the alkaline field. Samples 761906 and 761907 plot in the subalkaline field with various SiO_2 values and relatively high LOI. The peridotite sample plots at the bottom left corner of the diagram.

In contrast, the Nb/Y vs Zr/TiO_2 plot (Figure 6.3.2) shows that mafic samples plot in the alkali basalt field with rather limited variations. Further, the samples appears to show a positive correlation between Nb/Y and Zr/TiO_2 in contrast to the relationship of constant Zr/TiO_2 with a range of Nb/Y, observed for the previous groups in the basement sequence.

The binary compositional plots are shown in Figure 6.3.3. In this diagram, significant positive correlations are observed between Zr and Nb, Y and Ti; however, for Zr-Ti, this correlation exists only for samples with less than 300 ppm Zr. From an apex at 300 ppm Zr (761512), the samples with higher Zr (761602, 761809, 761901 and 761908) demonstrate a negative correlation between Zr and TiO_2. Ga in these samples varies about 20 ppm over the range of Zr (the peridotite sample, 761801, has

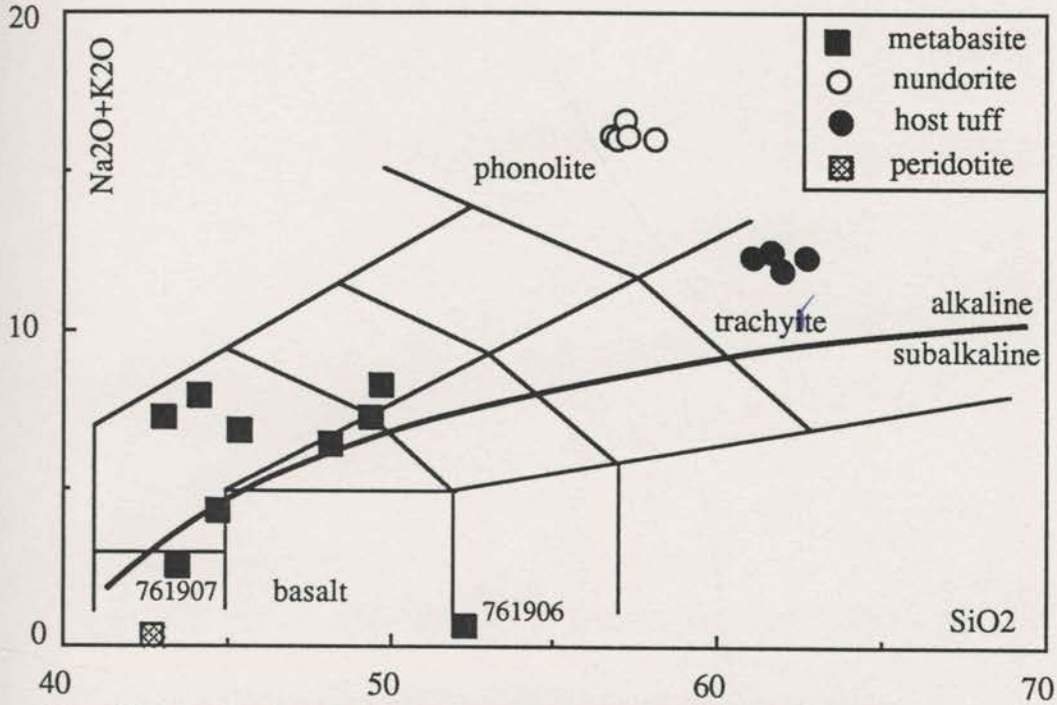

Fig. 6.3.1. TAS plot of the Nundora samples. The mafic samples are generally in the basalt clan and mostly in the alkaline field except the nodules (761906 & 761907) and the peridotite in the subalkaline field. Nundorite and host felsic tuff samples also show alkaline features.

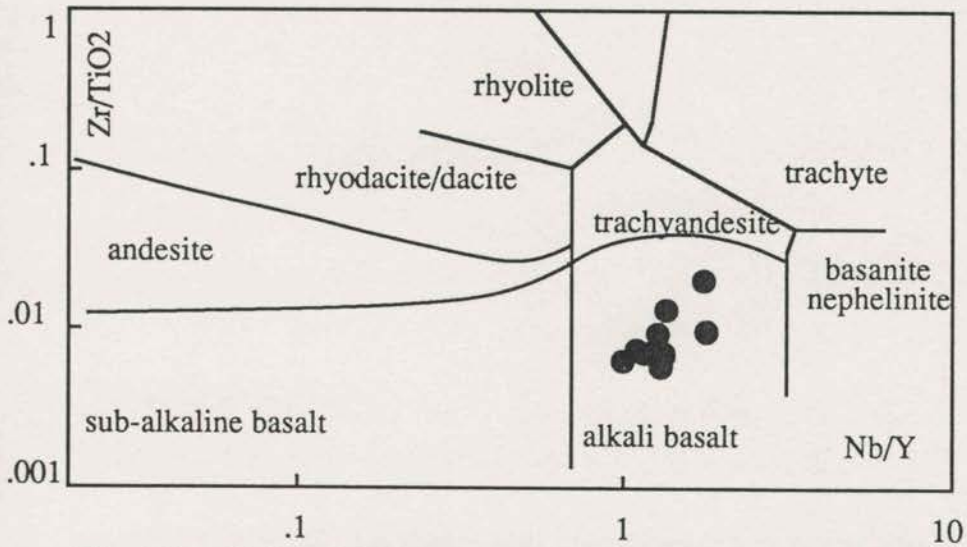

Fig. 6.3.2. Nb/Y - Zr/TiO2 plot of mafic samples from the Nundora area. All the samples plot as alkali basalt with limited variations.

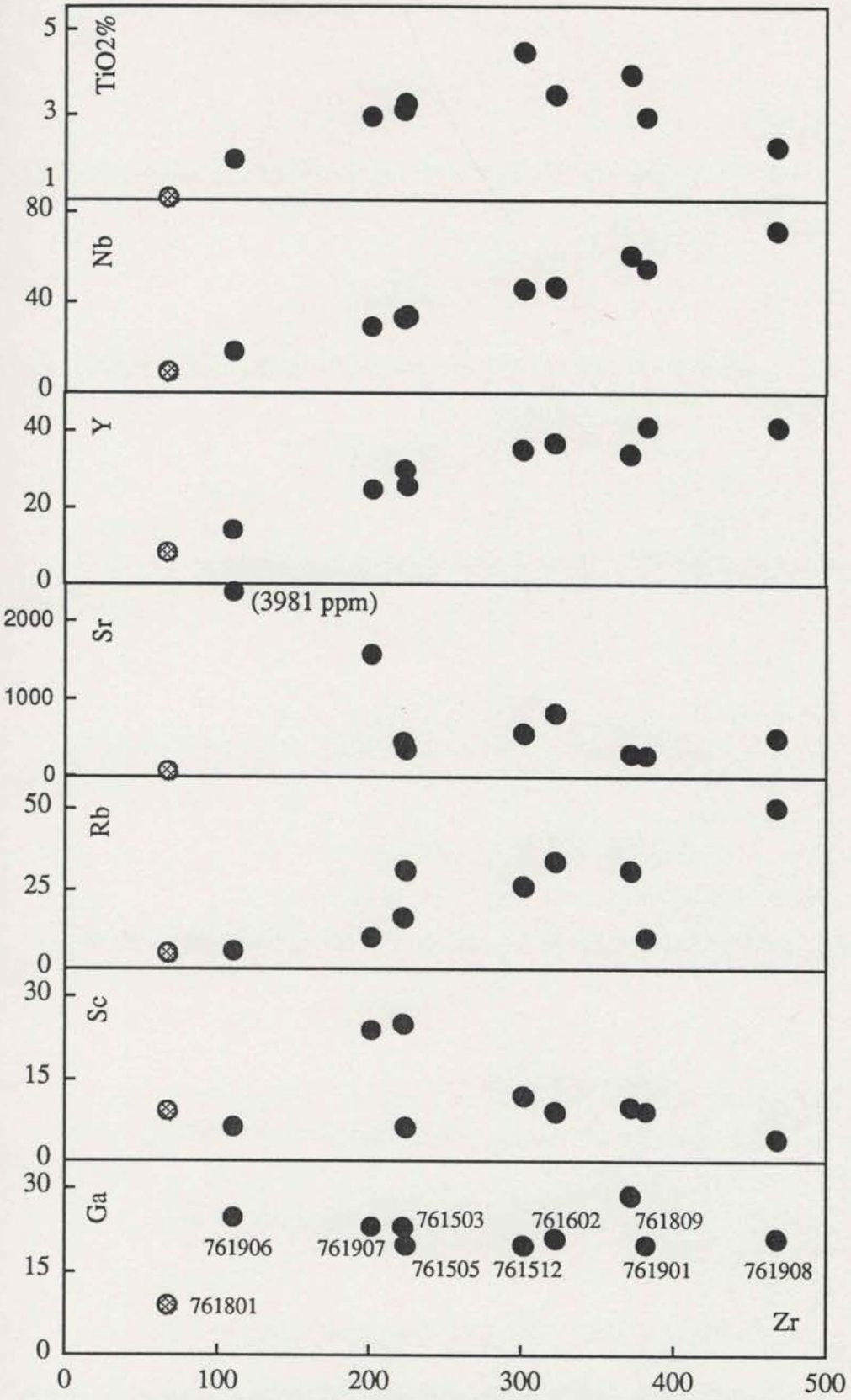

Fig. 6.3.3. Binary variations of trace and minor elements of the Nundora mafic samples. Filled circles, metabasites; crossed circle, peridotite. Significant correlations can be seen between Zr-Y, Zr-Nb and Zr-TiO2 (positive with those less than 300 ppm Zr and negative with more than 300 ppm Zr). Ga shows almost a constant level within the range of Zr.

significant low Ga content at the low Zr level). And the relationship between Zr and Sc, Rb and Sr is dispersed.

The significant correlation between Zr and Nb in these samples clearly demonstrate, with relatively reliable Nb analysis, the immobility of Nb during secondary processes. However, the two contrary correlations between Zr and TiO_2 may have to be explained using relevant petrogenetic models (Chapter Eight).

6.3.2. REE Geochemistry

Three samples selected from this area include both cleaved (761809) and massive (761503 & 761901) metabasites. The results are shown in Table 5.3 and Figure 6.3.4, which shows a clear and significant LREE-enriched pattern and all three samples have very similar compositions without Eu-anomaly. The compositional range is limited.

6.3.4. Spidergram

Figure 6.3.4 displays a PMN diagram of the mafic samples from the Nundora area. Most of the samples show a relatively smooth pattern with an increase from right to the left with peaks at P. The peridotite, 761801, has a distinct pattern from the others. Although the increasing pattern from Y to P, then from Nb to Th, is similar to the pattern of the main sequence, the absolute abundances of the elements are much lower and there is a significant depletion for Sr and K.

Although having lower alkali component as shown in Figure 6.3.1, the two nodule samples (761906 and 761907) display similar compositions to the volcanic host (thus not explicitly illustrated in all other diagrams). In this context, they are not considered xenolithic as are those from Packsaddle.

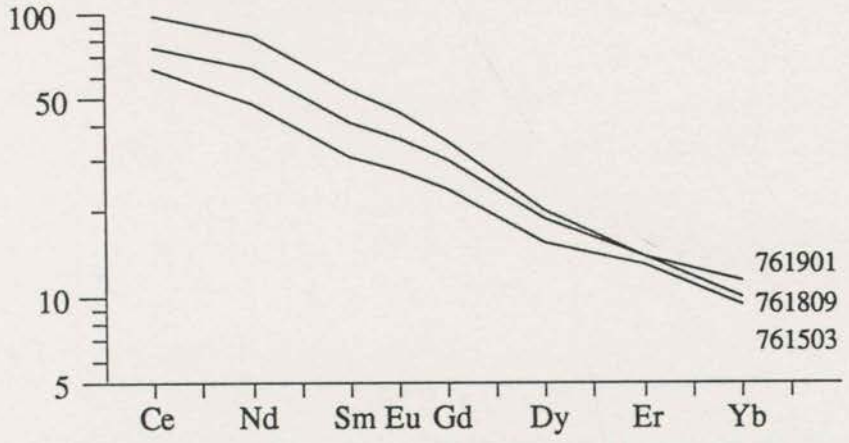

Fig. 6.3.4. Chondrite-normalised REE compositional plot of the representative metabasites from Nundora. All three samples display LREE enriched patterns with limited variations in abundance.

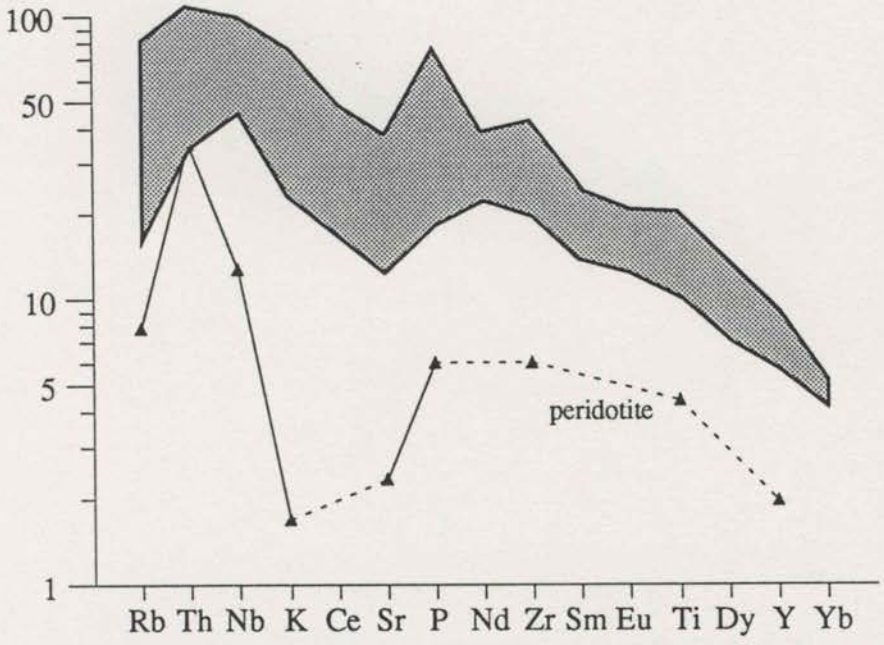

Fig. 6.3.5. The PMN plot of the Nundora mafic rocks. Samples display an increasing pattern from Yb to Th with minor P-enrichment and Rb-depletion. The peridotitic samples has much lower contents for most of the components -- both seemingly high Nb and Th may not be real due to analytical problem.

6.4. MAFIC ROCKS IN THE LATE PROTEROZOIC SEQUENCE

The mafic rocks in the late Proterozoic sequence, collected in the Packsaddle and Nundora areas, are characterised by two contrasting groups; the main mafic volcanic sequence and the xenolithic intrusive samples. All the volcanic samples from this sequence display affinities with alkaline basalt, while the intrusive rocks present various, distinctive characters as xenoliths from their volcanic host.

Figure 5.7.1 presents an integrated TAS diagram of these late Proterozoic samples together with those from the basement sequence. This diagram shows the compositional ranges of these two areas overlap totally with each other, though the Packsaddle samples exhibit limited variations, presumably due to limited number of analyses.

In Figure 5.7.2, the same pattern repeats with even smaller variations. Further, in contrast to basement samples , the younger ones display correlations between Nb/Y and Zr/TiO2. The two subalkaline xenoliths are not plotted in either diagram, but it is obvious that they would plot within the ranges of basement samples, if comparing with Figures 6.2.1 and 6.2.2.

In the PMN diagram (Figure 6.4.1), the volcanics from both Packsaddle and Nundora define identical dome-like patterns peaked at Th; while the xenoliths present distinctive patterns. Two of them form a pattern similar to those of the basement rocks. The third one (760801) shows a similar pattern to that of Nundora peridotite (761801). The patterns for 760801 and 761801 are at lower abundance levels. The peridotite also has very low Sr and K, but both these components are enriched in 760801. This diagram clearly shows the diverse origin of the intrusive rocks in the sequence.

In general, the geochemical discriminations indicate that the mafic volcanic rocks in the late Proterozoic sequence are alkali basalt. Samples from Packsaddle and Nundora do not show as much spatial variation as observed in the basement rocks, and their compositions are generally overlapping. However, the intrusive samples in the volcanic sequence display various features in both the alkaline and subalkaline fields. Some of them are rather similar to the basement rocks; while others appear to be residue of the volcanic magmatism, carrying lower abundances of incompatible components, but generally having patterns similar to those of their host rocks.

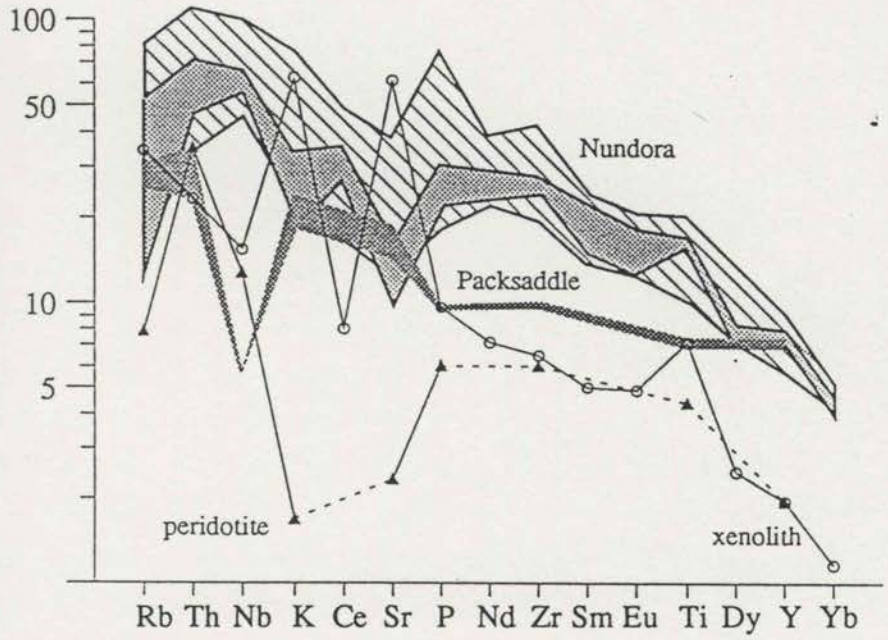

Fig. 6.4.1. The PMN plot of the Late Proterozoic mafic samples in the Wonominta Block. Compared with the basement samples, these samples display rather complex patterns. Most of metabasites from both Nundora and Packsaddle display an increasing pattern from Yb to Th, typical of "within plate basalt"; however, some of the Packsaddle intrusive samples have different patterns: sample 760801, a kaersutite-bearing xenolith, has very low contents of most of the elements, though displaying a similar pattern to the volcanics. Another two xenoliths display a flat pattern with noticeable Nb depletion, which is similar to that seen for basement samples.

Chapter 7
Geochemistry of Cambrian Mafic Rocks

7.1. SAMPLE SELECTION

Forty-six samples are selected from various outcrops of the Cambrian sequences. Sample selection is presented in Tables 3.9, 3.10 and 7.1. In the Mt. Wright area, twenty-one samples were analysed ranging from mafic (four metabasalts, 862112, 862225, 862402 and 862405; two metabasites, 862205 and 862217), intermediate (three trachytic andesite - trachyte, 862218, 862221, 862222) to felsic samples (five tuffs, 862206, 862214, MW-1 to MW-3; seven porphyries, 862101, 862103, 862110, 862304, 862501, 862504 and 862506). In the Comarto area, the selected samples are mainly metabasalts and metabasites, including both massive (860901, 860909, 861002, 861003 and 861616) and pyroclastic species (860904, 861013, 861014 and 861015) along with two metadolerites (I) (861010 and 861011). In the Bilpa area, two mafic samples are selected from basement outcrops (862909 and 862914) and mafic clasts of the Bilpa Conglomerate (862901 and 863012) respectively; they are presented in one section so that comparison can be made. One sample is selected to represent the Ponto Mine metadolerite (862110) and Kayrunnera gabbro (762904) respectively. Three samples are selected from the Wonnaminta lamprophyre, a fined-grained (762410), a coarse-grained (762412) and an epidote-nodule (762413). A lamprophyre is selected from the Boshy Tank area (762602).

Table 7.1. Sample Selections from Various Cambrian Sequences

	mafic		trachytic	felsic			
area	MB	MD(I)	andesitic	tuff	porphyry	others	total
Mt. Wright	6		3	5	7		21
Comarto	9	2					11
Bilpa:							8
basement	2						
Conglomerate	1		1	3		1(granite)	
Ponto Mine metadolerite						1	1
Kayrunnera gabbro						1	1
Wonnaminta lamprophyre						3	3
Boshy Tank lamprophyre						1	1
TOTAL	18	2	4	8	7	7	46

7.2. GEOCHEMICAL CHARACTERISTICS OF MAFIC ROCKS FROM THE MT. WRIGHT AREA

7.2.1. Major and Trace Element Geochemistry

All metabasite samples are in the basaltic clan with SiO_2 between 43.99-51.87% (normalised values). The intermediate samples have SiO_2 between 55.36 and 67.68%. On the TAS diagram (Figure 7.2.1), all these samples plot in the alkaline field with a positive correlation between the alkali components and SiO_2. Two of the intermediate samples have very high alkalic components and plot in the "trachyte" field.

In the Nb/Y - Zr/TiO_2 diagram (Figure 7.2.2), metabasites and the low-SiO_2 intermediate sample (862221) plot in the alkaline basalt field; the other two high-SiO_2 intermediate samples plot in the field of rhyolite next to the border with trachyandesite.

These two diagrams reveal ~~rather composite~~ unique geochemical compositions for the iron oxide-stained samples from several monotonous small hills in the southern part of the Mt. Wright area, in contrast with the clear affinity of alkaline basalt for the mafic rocks. Both diagrams indicate two distinctive compositions: one is similar to the basaltic samples and the other is trachytic with high Zr (about 1000 ppm) and alkalic components, and low MgO (< 1%) contents.

The distinctive compositions of these two samples are even clearer in the binary discriminations diagram (Figure 7.2.3): with high Zr, Nb, Y and Ga, and low in Ti, Sc, Rb and Sr. This diagram presents significant positive correlations between Zr versus Y and Zr versus Nb between all the mafic samples. Correlations between Zr vs TiO_2 and Zr vs Ga shows a typical reversed "V" pattern. In contrast, Zr vs Sc and Zr vs Rb present negative correlations among the basic samples. Only the Zr vs Sr plot shows a dispersed pattern.

The characteristic compositions of these intermediate samples in this area suggest that they may represent the fractionated end products of mafic magmatism in this region. In other words, the two groups of rocks with distinct petrographic characteristics are suggested to be co-magmatic, representing a series of igneous rocks with different degrees of fractionation.

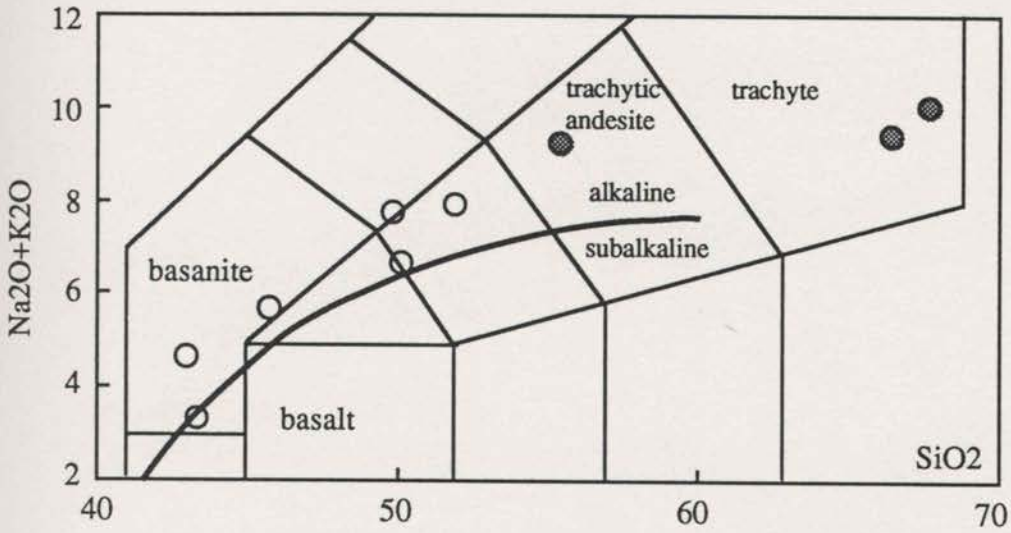

Fig. 7.2.1. TAS plot of mafic samples from the Mt. Wright area. Most of the samples plot in the basaltic clan of the alkaline field and show a positive correlation between silica and alkalic components, but two of the andesitic samples plot in the trachyite field.

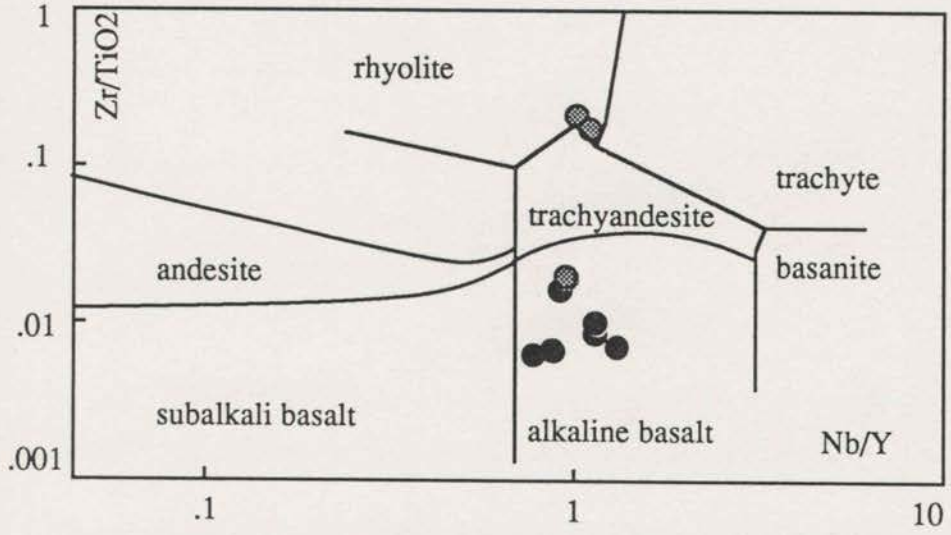

Fig. 7.2.2. Nb/Y - Zr/TiO2 plot of the Cambrian Mt. Wright mafic samples. Filled circles, basalts; dotted circles, andesitic-trachytic. This diagram shows most samples plot as alkali basalt, while two of the andesitic samples plot in the rhyolite field bordering with trachytic fields.

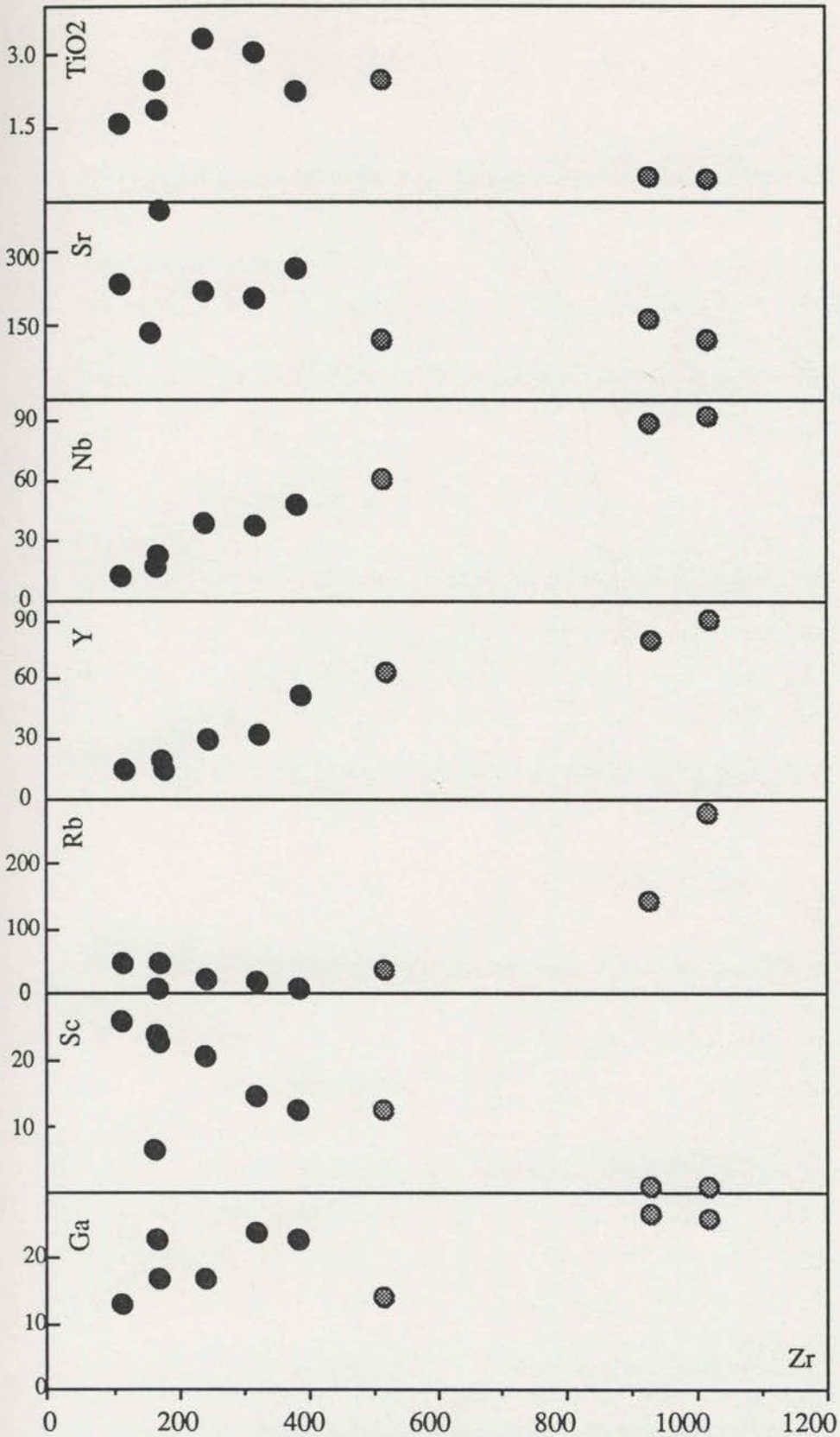

Fig. 7.2.3. Binary variations of trace and minor components of mafic samples from the Mt. Wright area. Filled circles, basalt; dotted circles, trachytic andesites. In this diagram, the two high Zr samples (trachyte) show distinct compositions in most plots. Among the others, positive correlation can be seen between Zr-Y and Zr-Nb; Zr-TiO2 and Zr-Ga display a reversed "V" shape correlation, while Zr-Sc, and less significantly Zr-Rb, present examples of negative correlations.

7.2.2. The REE Geochemistry

Five samples were selected from this area for their REE analyses. This selection includes four basalts and one of the low silica intermediate samples. The results are shown in Table 5.3 and Figure 7.2.4, which shows that all five samples have similar LREE-enriched patterns, but with various concentrations. The intermediate sample, 862221, has the highest REE contents, about five times as much as the lowest REE sample (862225) and exhibits a clear Eu-depletion. This figure also revealed that the high REE basalt (86205) has a clear Eu-enrichment; the other three low-REE basalt have slight positive Eu anomalies.

The large compositional variation may be at least partly due to fractional crystallisation processes, particularly for the high-REE samples. If the observed features are primary, the existence of Eu-depletion is an indication of plagioclase fractionation for the trachytic sample; but the Eu-enrichment in the basaltic samples would suggest the presence of plagioclase cumulate. Therefore, the local magmatic processes might have been rather complicated. The large variations of REE contents in these samples may also indicate the influence of alteration processes (Whitford *et al.*, 1988), which may have, on the other hand, largely obscured the primary compositions.

7.2.3. Spidergram

Figure 7.2.5 presents the PMN spidergram of the basaltic samples from the Mt. Wright area. In this plot, the increasing pattern from left to right is decorated with remarkable depletions of Rb, Sr and K. The dashed lines in the diagram indicate the trends without these depletions.

The increasing pattern shown in this diagram is identical to that of alkaline basalts from the late Proterozoic sequence. However, they also present distinctive depletions of Sr, Rb and K, although this is somewhat similar to the Packsaddle metabasites (*cf.* Figure 6.4.1). Since these components may have been mobilised during secondary processes, the Mt. Wright basalts must have had a different alteration history, if they have identical primary geochemical characteristics to those from the late Proterozoic sequence. The removal of the alkali elements suggests circulation of hydrothermal fluids and hence also possible leaching of metals, which may have provided the source materials for the mineralisation observed in the nearby felsic rocks. Therefore, these depletions may have an important implication for mineral exploration.

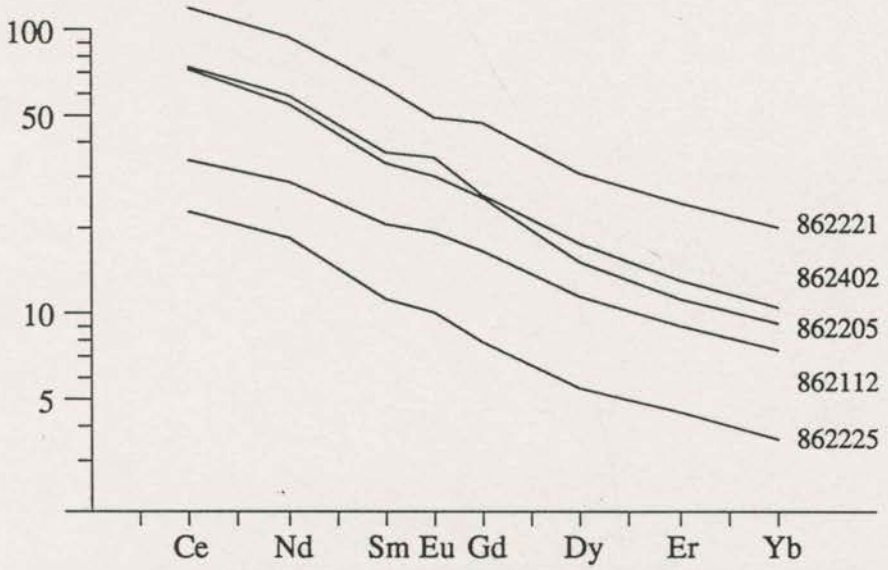

Fig. 7.2.4. Chondrite-normalised REE compositional plot of the representative Cambrian Mt. Wright basalts. Although the samples show similar LREE-enriched patterns, they have large variations in the level of REE abundance.

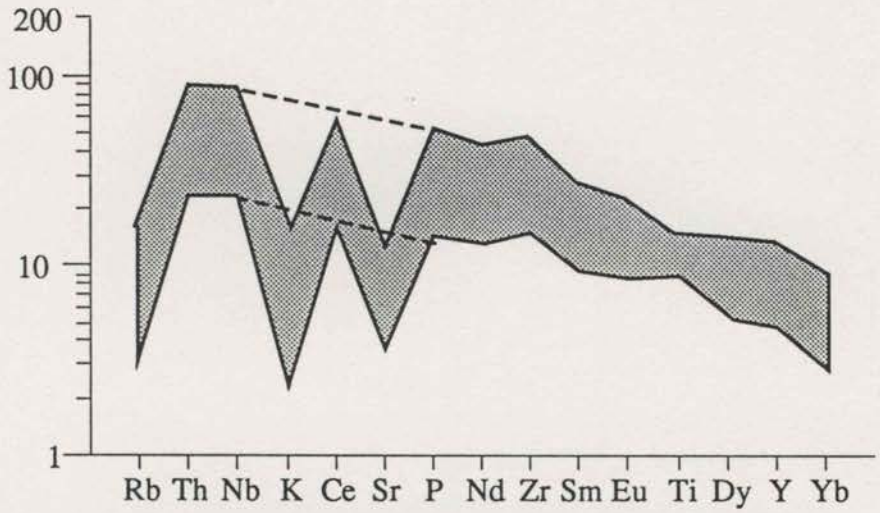

Fig. 7.2.5. The PMN plot of the Mt. Wright basalts, showing an increasing pattern from Yb to Th, similar to that of the late Proterozoic metabasites, but with remarkable Sr, K and Rb depletions. The dashed lines indicate patterns without these depletions.

7.3. GEOCHEMICAL CHARACTERISTICS OF MAFIC ROCKS FROM THE COMARTO AREA

7.3.1. Major and Trace Element Geochemistry

In terms of major element chemistry, all of the samples fall in the basalt clan with SiO_2 between 44.41 and 51.92% (normalised values). All four pyroclastic metabasites and the two metadolerites have low-K features (<0.3% K_2O). These compositional characteristics are clearly not kimberlitic, which otherwise would be K-enriched and would have lower SiO_2.

In the TAS diagram (Figure 7.3.1), all samples plot in the subalkaline field and the variation in SiO_2 in the samples resulted in a dispersed pattern. Figure 7.3.2 shows that most of the samples plot in the tholeiitic field, but there are three samples (860901, 861002 and 861015) in the calcalkaline field with a range of A.I. (4 to 16), at about 17% Al_2O_3.

The binary variation of trace and minor elements of these samples is shown in Figure 7.3.3. In this diagram, sample 861015 appears to be distinct with its low Zr. The other samples display significant positive correlations between Zr versus Y, Nb and TiO_2; and there are two groups in the Zr-Rb variation, four of the samples have relatively high Rb (about 8 ppm) and the other five have low Rb (2 to 4 ppm). The Sr, Ga and Sc versus Zr correlations appear to be dispersed.

The Nb/Y versus Zr/TiO_2 diagram of the Comarto samples is presented in Figure 7.3.4. In this diagram, all samples plot as subalkaline basalt. Also variations of both Nb/Y and Zr/Ti are limited, except for 861016 (metabasite) with a slightly lower Nb/Y.

In general, the primary composition of these Comarto samples may have affinities with subalkaline basalt. The calcalkaline features of some of them may be due to alterations, which resulted in changes in alkaline components, whereas Al_2O_3 remained relatively immobile as shown in Figure 7.3.2. These distinctive alteration features are clearly different from those observed in the basement samples, where Al_2O_3 may also have been seemingly "mobilised" during alterations while alkali components are at low level (*cf.* Figure 5.4.2).

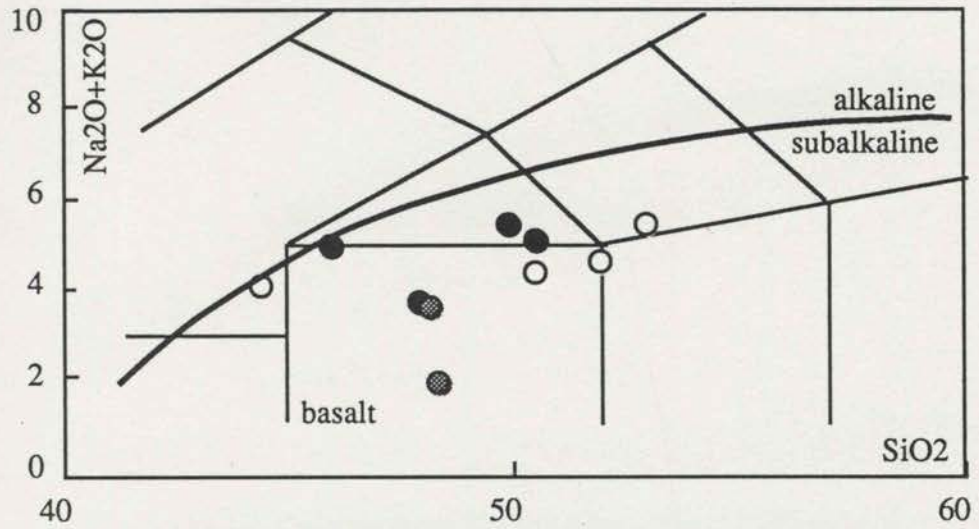

Fig. 7.3.1. TAS plot of the Comarto mafic samples. Filled circles, metabasites; open circles, metabasite with pyroclastic textures; dotted circles, metadolerite. All the samples plot in the subalkaline field, generally of basaltic clan.

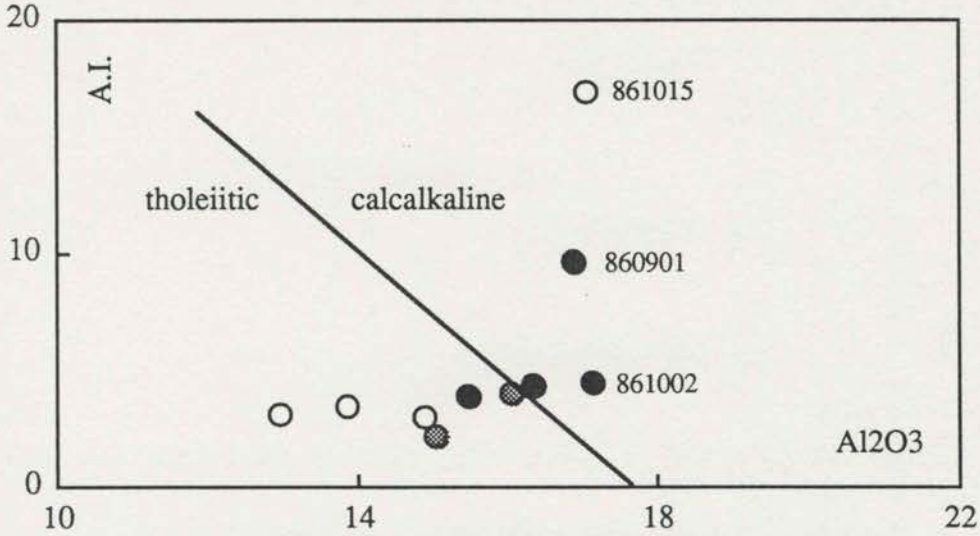

Fig. 7.3.2. Al2O3 vesus A.I. plot of mafic samples from the Comarto area. Filled circles, MB; open circles, pyroclastic; dotted circles, EP. Samples plot in both tholeiitic and calcalkaline fields and this provides another non-discriminant example, like some of the basement samples. However, unlike the basement samples, there is a large variation of alkali components, rather than Al2O3.

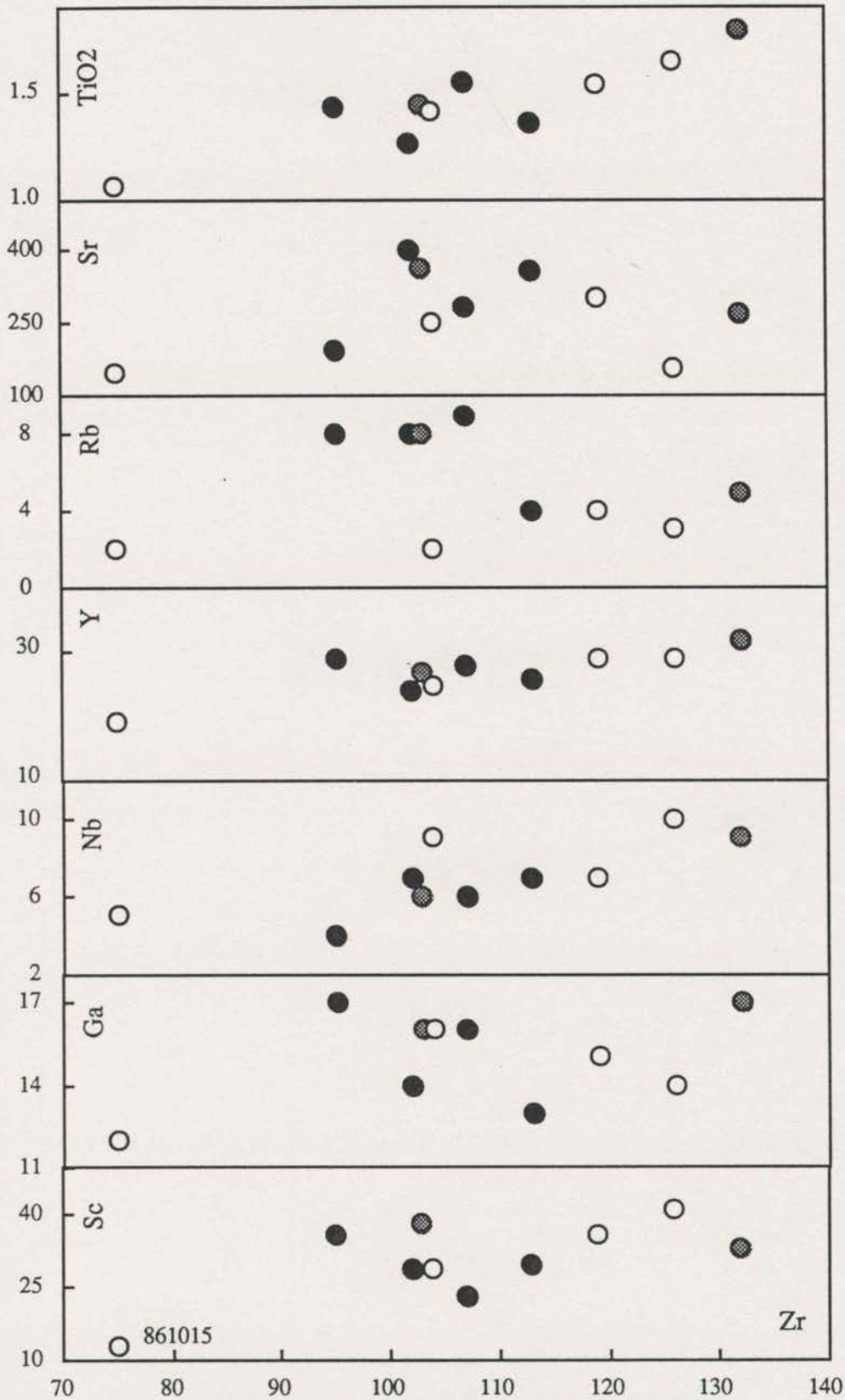

Fig. 7.3.3. Binary variations of trace and minor components of mafic samples from the Comarto area. Filled circles, metabasites; open circles, metabasites with pyroclastic textures; dotted circles, metadolerites. Good positive correlations are observed between Zr-TiO2, Zr-Y and Zr-Nb, while other pairs show dispersed patterns.

7.3.2. Spidergrams

Figure 7.3.5 is a MORBN diagram of the Comarto samples. The diagram displays a slightly increasing pattern from Sc to K as shown by the dashed line; it also shows significant Th and P enrichments and K depletion for some samples. The K variation in these samples is larger than those of the other components.

If the K depletion is assumed to be of secondary origin as discussed above, the Th and P enrichment would be hard to explain using the same assumption. Like those in the basement sequence, Th-enrichment could be an indicator of the contribution of crustal materials to the magmatism; while the slightly increasing pattern is certainly distinct from those of the basement sequence. Therefore, even though the Comarto samples have some similarities to the basement samples, such as Th-enrichment, K-depletion and about the same level as MORB's, the distinctive MORBN pattern suggests different origins.

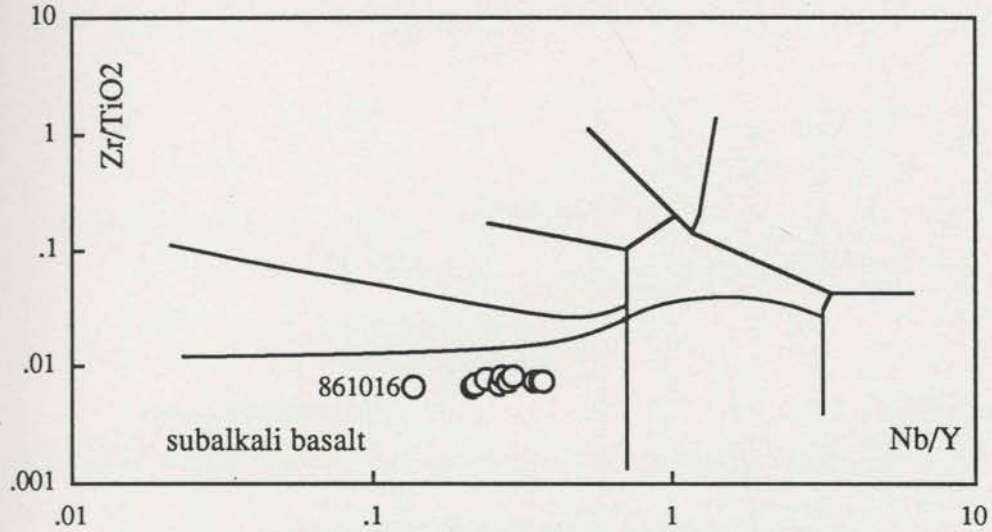

Fig. 7.3.4. Nb/Y versus Zr/TiO2 plot of mafic samples from the Comarto area. The samples all plot in the subalkali basalt field with relatively limited variations.

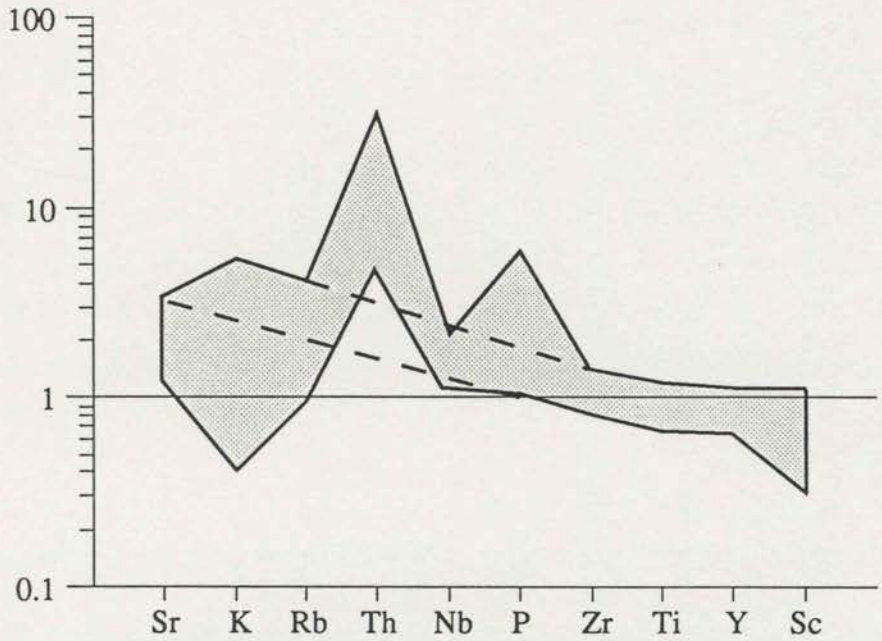

Fig. 7.3.5. The MORBN plot of mafic samples from the Comarto area. The dashed lines projects an "ideal" pattern without the enrichments of P and Th, and depletion of K. This pattern, though similar to MORB, has a slight increase from Sc to K, which is different to the basement samples.

7.4. GEOCHEMISTRY OF CAMBRIAN ROCKS

This section also includes samples from the Kayrunnera gabbro (762904) and the Ponto Mine dolerite (752110), apart from those discussed in the last two sections.

Figure 7.4.1 is an integrated TAS plot of the various Cambrian mafic samples. This diagram shows that only the Mt. Wright basalts are of alkaline association, whereas others are all subalkaline. In comparison, the Ponto Mine dolerite has Nb/Y higher than that of the Comarto samples and the Kayrunnera gabbro. Interestingly, the Zr/TiO_2 ratios of these samples show very limited variation.

Figure 7.4.2 is a PMN plot of the Cambrian samples. The samples in this figure display an increasing pattern from the right to the left side of the diagram with some small but distinctive variations. As has discussed above, the Mt. Wright basalts display deep Sr and K troughs that dominate the pattern; while only the K-trough in the Comarto pattern. Also in the Comarto plot, the high Th is a rather smooth extension along the trend from Zr to P and to Th and this trend is almost parallel to that seen in the Mt. Wright basalts. Therefore, samples from both areas should be derived from a "within plate" environment, though the elemental abundances are different. The Ponto Mine dolerite also displays a similar pattern but with different anomalies, namely, the small peaks at Ti, Sr and Nb. Much of the pattern of the Kayrunnera gabbro is shown in dashed line because of lack of REE analysis. In this latter plot, Y, Ti, Zr, P, K and Th are on a lower level, about ten times primitive mantle abundance; and Sr, Rb and Nb are on an elevated level. Both Ponto Mine dolerite and Kayrunnera gabbro display trends showing slight increases from right to left. Besides, these samples appear to have relatively high Nb (7 ppm) and low Th (<1 ppm), which are distinct from most samples discussed above. However, the representativeness could be a problem as only one sample of each was analysed.

In summary, the various Cambrian mafic rocks in the Wonominta Block are all characterised as being the result of intra-plate magmatism, though they exhibit complex compositions. The Mt. Wright basalts are alkaline, and the others are subalkaline. Regionally, the Mt. Wright basalts are similar to the late Proterozoic mafic rocks, as shown in the last chapter, the only remarkable difference is their depletions of Sr, K and Rb that could well be a secondary feature. Therefore, the alkaline basaltic rocks from late Proterozoic and early Cambrian Mt. Wright may have very similar primary geochemistry.

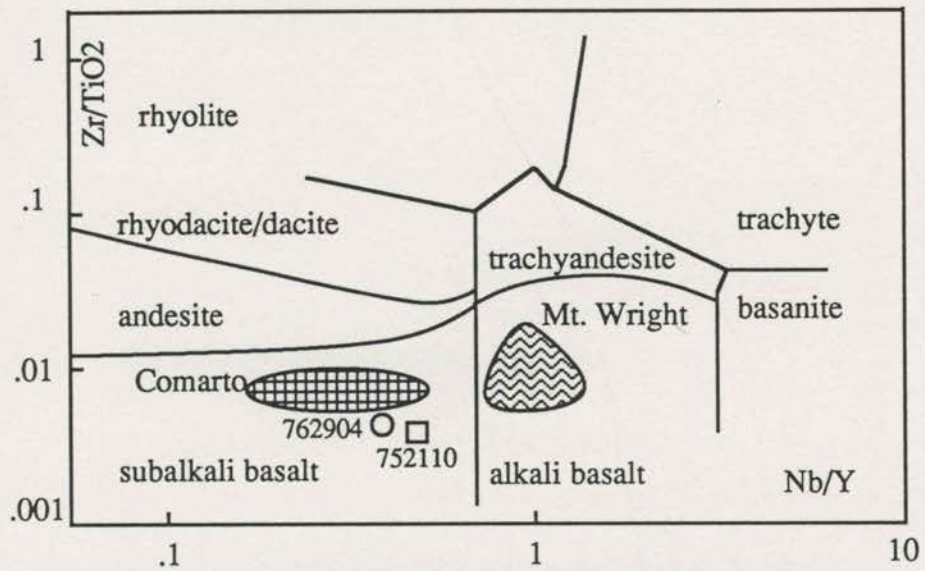

Fig. 7.4.1. Nb/Y-Zr/TiO2 plot of the Cambrian mafic rocks in the Wonominta Block. This diagram summarises the geochemical characteristics of various Cambrian samples, that is alkaline for Mt. Wright basalts, subalkaline for Comarto, Ponto Mine (752110) and Kayrunnera gabbro (762904) samples.

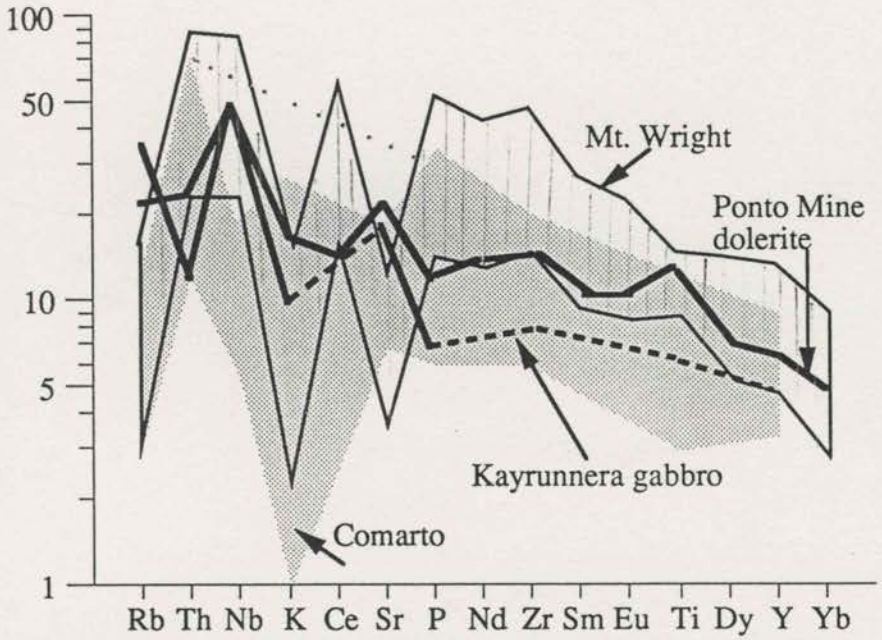

Fig. 7.4.2. The PMN plot of the Cambrian mafic rocks in the Wonominta Block. All the samples display various enrichments from Yb to Th, decorated with some depletions, Sr for Mt. Wright basalts, K for Comarto metabasalts and Kayrunnera gabbro.

7.5. GEOCHEMICAL CHARACTERISTICS OF SAMPLES OF MINOR OCCURRENCES

Samples discussed in this section include mafic clasts of the Bilpa Conglomerate (862901 and 862911), its basement mafic rocks (862909 and 862914) for comparison, lamprophyre from Wonnaminta (762410, 762412 and 762413 is an epidote-nodule in the lamprophyre) and Boshy Tank (762602); nundorite (762401 to 762409); syenite (761204 and 761603) and various felsic rocks from Wilandra, Cymbric Vale and Mt. Wright (see below).

7.5.1 Bilpa Conglomerates & Wonnaminta Lamprophyres

Figure 7.5.1 is a TAS diagram of the mafic components of the Bilpa Conglomerate and the Wonnaminta lamprophyre samples. For comparison, the lamprophyre sample from Boshy Tank is also shown in the diagram. The samples plot along the discriminant boundary of alkalinity and generally in the basaltic clan; the epidote nodule (762413) is depleted in SiO_2 (42%).

However, in the Nb/Y versus Zr/TiO_2 diagram (Figure 7.5.2), samples exhibit distinctive different characters. The lamprophyre samples plot in the alkaline basaltic field. In particular, the fine (762410) and coarse-grained (762412) samples do not show much difference at all, while the epidote nodule is more enriched in both Nb/Y and Zr/TiO_2 and plots on the corner between alkaline basalt, basanite and trachyandesite. In contrast, all Bilpa samples plot in the subalkaline fields. The two basement samples plot in the subalkaline basalt field; while the clast samples plot from basalt to dacite with only one of them in the basalt field, as observed in the TAS diagram. The clast samples show a negative correlation between Nb/Y and Zr/TiO_2. None of the felsic samples plot in the rhyolite field, though some of them have more than 70% SiO_2.

In the PMN diagram, the mafic samples from the basement and the mafic clast (Figure 7.5.3) show distinctive compositional patterns. The basement samples have average abundances of ten times those of primitive mantle concentrations, but display a remarkably irregular pattern. The sole basaltic clast also exhibits an irregular pattern with a significant enrichment of Th and Rb.

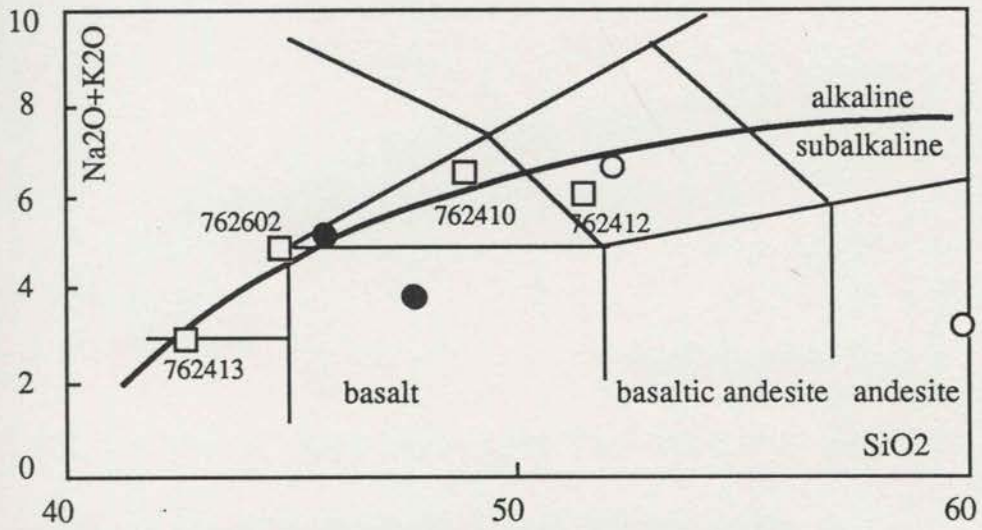

Fig.7.5.1 The TAS plot of mafic components of the Bilpa Conglomerate (open circles), basement samples in the Bilpa area (filled circles) and lamprophyre (squares) samples from Wonnaminta and Boshy Tank (762602) areas. All samples are distributed along the discriminant boundary between alkaline and subalkaline, and in the basaltic clan except the high silca clast from the conglomerate.

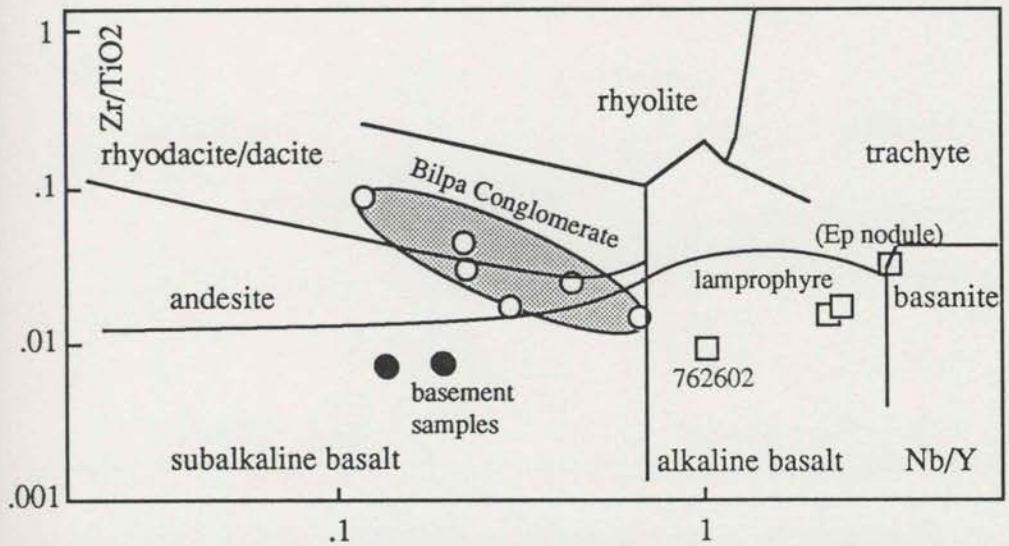

Fig. 7.5.2. Nb/Y versus Zr/TiO2 plot of Bilpa samples and lamprophyre from Wonnaminta and Boshy Tank (762602) areas. Various clasts from tyhe Bilpa Conglomerate plot in the subalkaline field, ranging from basalt to dacite; the basement samples also fall in the subalkaline basalt field but with lower Zr/TiO2 ratios. The lamprophyre samples fall in the alkaline basalt field.

In contrast, the three true lamprophyres from Wonnaminta and Boshy Tank display a smooth increasing pattern from Sc to Rb, with very similar compositions (Figure 7.5.4). The epidote nodule, though having a generally similar pattern, displays significant depletion in Ti, P and Sc, and enrichment in Sr and Th.

The smooth increasing pattern suggests that the alkaline magmas may have been products of intra-plate environment and emplaced with little crustal contamination. The identical compositions of coarse-grained and fine-grained different part of the dyke suggest fractional crystallisation was not important either. In contrast, the epidote nodules in the dykes show fractionated characters, suggesting the removal of many major as well as trace components already from the magma. The extremely high Sr in these rocks can be explained as due to the dominant presence of epidote, in which Ca is an essential component.

In general, these diagrams indicate the basic alkaline features of the lamprophyre samples and the distinctive geochemical features of the mafic component of the Bilpa Conglomerate compared with basement samples in the area. In other words, the igneous portion of the Bilpa Conglomerate may display a wide range of compositions but the local basement sequence may have played a limited role as a source for the clasts.

7.5.2 Felsic Rocks in the Wonominta Block

Most of the felsic rocks observed in the Wonominta Block are tuff-like with limited occurrence; at the only major outcrop in the Mt. Wright area they are composed of both porphyritic and tuff-like rocks. The discussion of felsic rocks in this section also includes the syenite from Packsaddle and Nundora areas. In all, twenty-nine various felsic samples were analysed. These include two syenite samples (761204 & 761603) from Packsaddle and Nundora respectively; tuff-like felsic samples from Wilandra and Cymbric Vale (861209 and 861906); seven porphyry (862101, 862103, 862110, 862304, 862501, 862504 and 862506) and five felsic tuff samples (862206, 862214 and MW-1 to MW-3) from Mt. Wright; four felsic clast of the Bilpa Conglomerate, including one granitic sample (862902, 863004, 863011 and 863009).

In the TAS diagram (Figure 7.5.5), these felsic samples generally plot in the dacite-rhyolite fields, showing a negative correlation between the two components. The mineralised tuffs from Mt. Wright are particularly enriched in SiO_2, partly because the

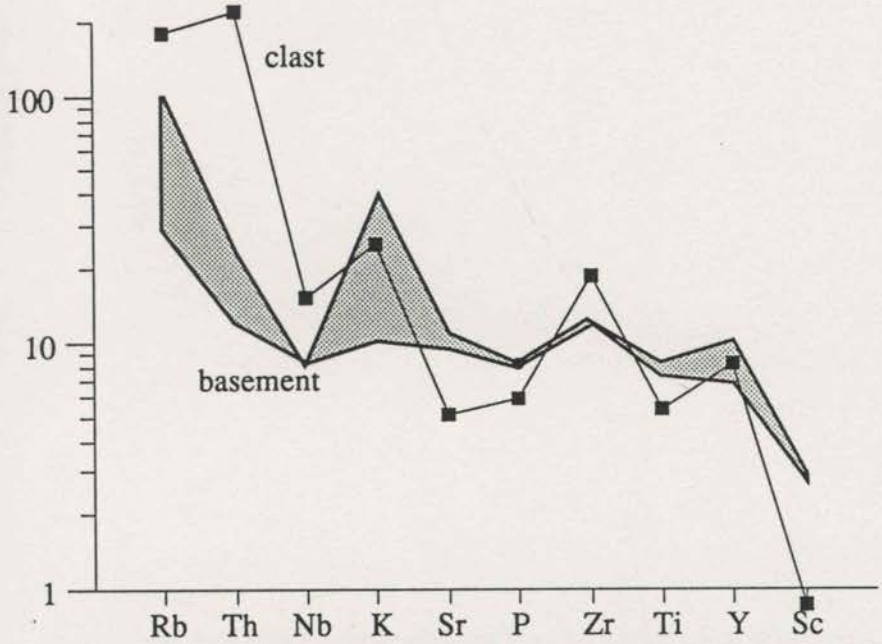

Fig. 7.5.3. The PMN plot of basaltic samples from Bilpa area. Samples from the basement sequence have their abundances about ten times of that of the primitive mantle, typical of MORB-like rocks, yet they also show significant variations of K and Rb. In comparison, the sole basaltic clast sample has higher Zr, Rb and Th, and very low Sc. On the whole, both groups show irregular patterns.

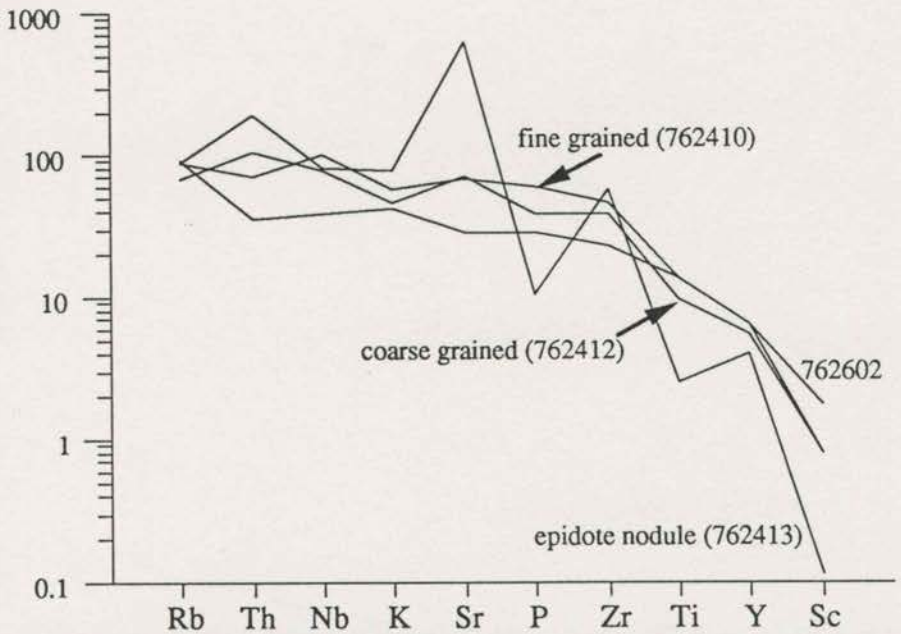

Fig. 7.5.4 The PMN plot of lamprophyres and epidote nodule from the Wonnaminta and Boshy Tank areas. The two lamprophyre samples from Wonnaminta with different grain-sizes show identical increasing patterns from Sc to Rb. The Boshy Tank lamprophyre also displays a similar pattern, which is typical of "within plate basalt". Although the pattern for Ep nodule is on the whole similar to the hosting lamprophyre, noticeable depletions of Ti and P and enrichment of Sr also exist.

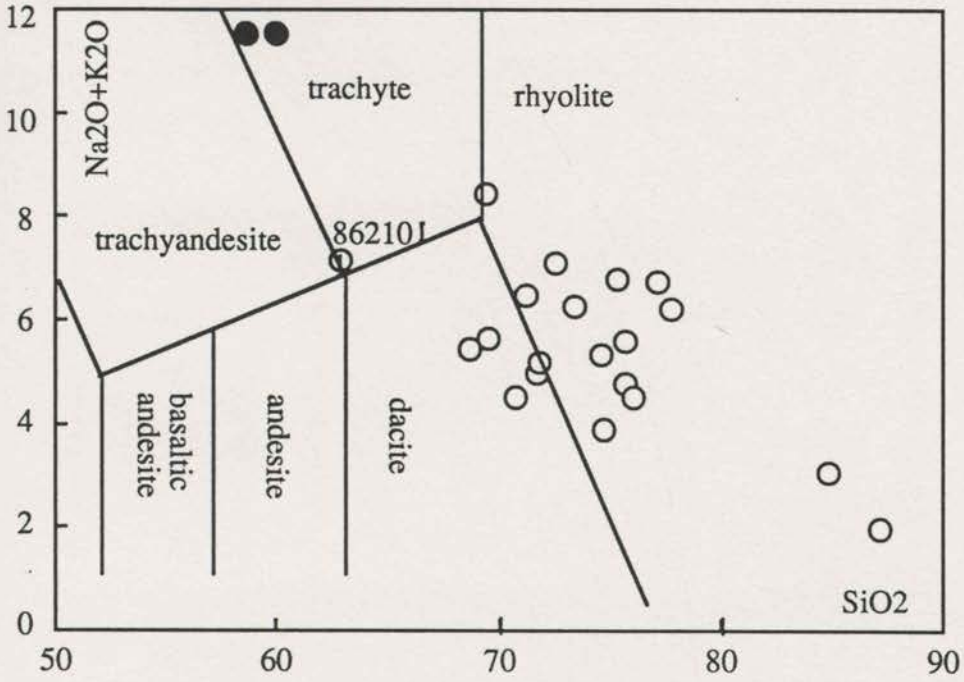

Fig. 7.5.5. The TAS plot of felsic rocks in the Wonominta Block. In terms of silica content, most of the sample plot in the dacite-rhyolite fields with one exception (862101) from the Mt. Wright area. The syenitic samples (filled circles) display their high alkali contents.

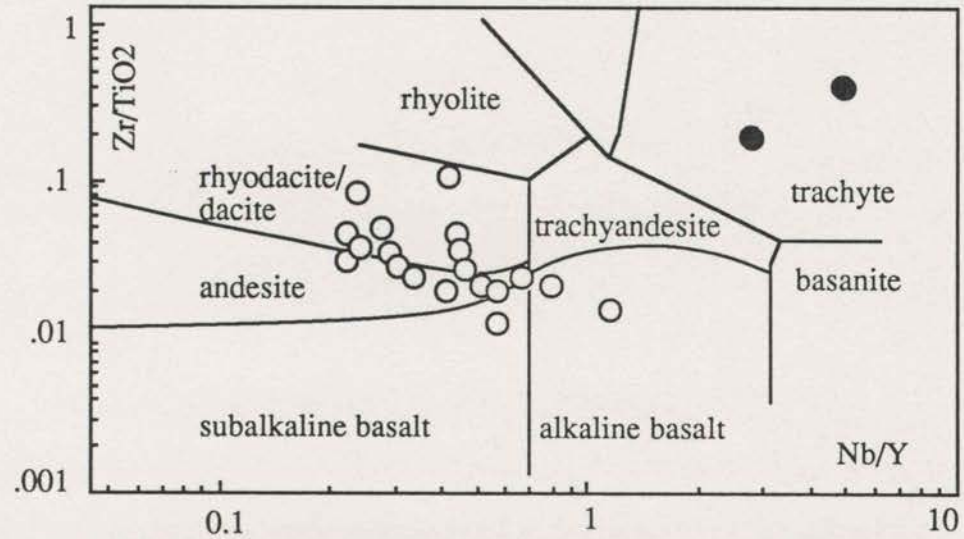

Fig. 7.5.6. Nb/Y versus Zr/TiO2 plot of felsic rocks in the Wonominta Block. This diagram shows that none of the samples plots actually in the rhyolite field with some of them even in the alkali basalt field. All syenites (filled circles) plot in the trachyte field.

unknown amounts of base metal components were treated as part of the "volatiles" in the normalisation calculations. A Mt. Wright porphyry sample, 862101, plots on the border between trachyte and trachyandesite fields, with lower SiO_2 than the others. However, the Nb/Y versus Zr/TiO_2 diagram (Figure 7.5.6) reveals that most samples are in the andesite and dacite fields, with lower Zr/TiO_2 ratios than that of rhyolite. Thus, these samples are generally named as felsic rocks instead of rhyolitic tuffs or porphyries, which are the recommended terms (Le Maitre, 1989). In both diagrams, the two syenite samples plot in the trachyte - a volcanic equivalent to the syenite - field.

7.5.3. Geochemical Characters of Nundorite

The nundorite occurs in an elongated and narrow belt. It is considered to be of metasomatic origin (*cf.* Chapter Three). In the central part of the outcrop, the rocks are indeed igneous-looking with a massive and mostly coarse-grained texture. Towards the margins of the outcrop, the rocks become tuff-like, suggesting the origin of these igneous-looking rocks. The samples selected for geochemical studies include four felsic tuff-like species (762401, 762405, 762408 and 762409), two light-coloured nundorites (762403 and 762404; *cf.* Plate 3.2.17) and three dark-coloured nundorites (762402, 762406 and 762407; *cf.* Plate 3.2.18).

In the TAS diagram (Figure 6.3.1), the four tuff-like samples plot in the trachyte field similar to the syenite, while the true nundorite samples are in the phonolite field with lower SiO_2 and higher alkali components than their precursors. These compositional variations also suggest that the metasomatic processes involve the removal of silica and the introduction of alkali components, particularly sodium (potassium actually decreased from 5.5-6.0% to 4.8-5.0%; see Table 6.2).

Figure 6.3.1 reveals that the nundorite might have been derived from tuff-like components with syenitic compositions; whereas the nundorites themselves are phonolitic. The compositional difference between nundorites and their suggested precursor way indicate the removal of Si, K, P and Sr and introduction of Na, Fe in the formation of the rocks. Al in the processes may also have been removed, though this trend is not as obvious as that of the other components. In all of the samples, Zr contents are extremely high, between 2313 to 2752 ppm, and potentially the rock may be suitable for U-Pb dating analysis on any zircons embodied.

Chapter 8.

Petrogenetic Studies of mafic rocks in the Wonominta Beds

8.1. TECTONOMAGMATIC DISCRIMINATIONS

One of the important aspects of petrogenetic studies is tectonomagmatic discrimination using HFS element compositions. This method has been proved to be very useful in many cases and has gained wide application in the past twenty years. However, there are also many strands of evidence arguing against the application of this method (e.g., Prestvik, 1982; Arculus, 1987).

Figure 8.1.1 shows two of the most widely used discrimination schemes proposed by Pearce & Cann (1973) and Meschede (1986) (data source in Table 8.1). In the Pearce & Cann's scheme (Figure 8.1.1b), basalts from "within plate environments", such as continental flood basalt (exemplified by Karoo high-Ti basalts) and ocean island basalts (OIB) plot on the low-Y side while those from plate margins on the high-Y side. The second group includes arc basalts and mid-ocean ridge basalts (MORBs). The Karoo low-Ti basalts are considered to have "oceanic" signatures (MORB-like) (Duncan *et al.*, 1990) and plot between the two typical groups. Meschede's scheme (Figure 8.1.1a) was constructed mainly to discriminate different types of MORBs and OIB based on their different Nb contents, but it may have difficulty to distinguish arc basalt from the others. However, combining the two schemes, discrimination of mafic rocks from most tectonic environments can be, presumably, achieved.

In these two discrimination schemes, Ti, Y, Zr, and Nb are the components used, primarily because their compositional variations are controlled, presumably mostly, by source heterogeneity (*e.g.*, Wood *et al.*, 1979a). Another preamble would have to be that variations between different environments are larger than those within each.

During the early days of development of the plate tectonic theory, it was noted that different magmatic types or volcanic suites occur characteristically in certain tectonic environments and within each domain, particularly oceanic, compositions of the rocks are generally homogeneous (*cf.* Gilluly, 1971). With the accumulation of geochemical

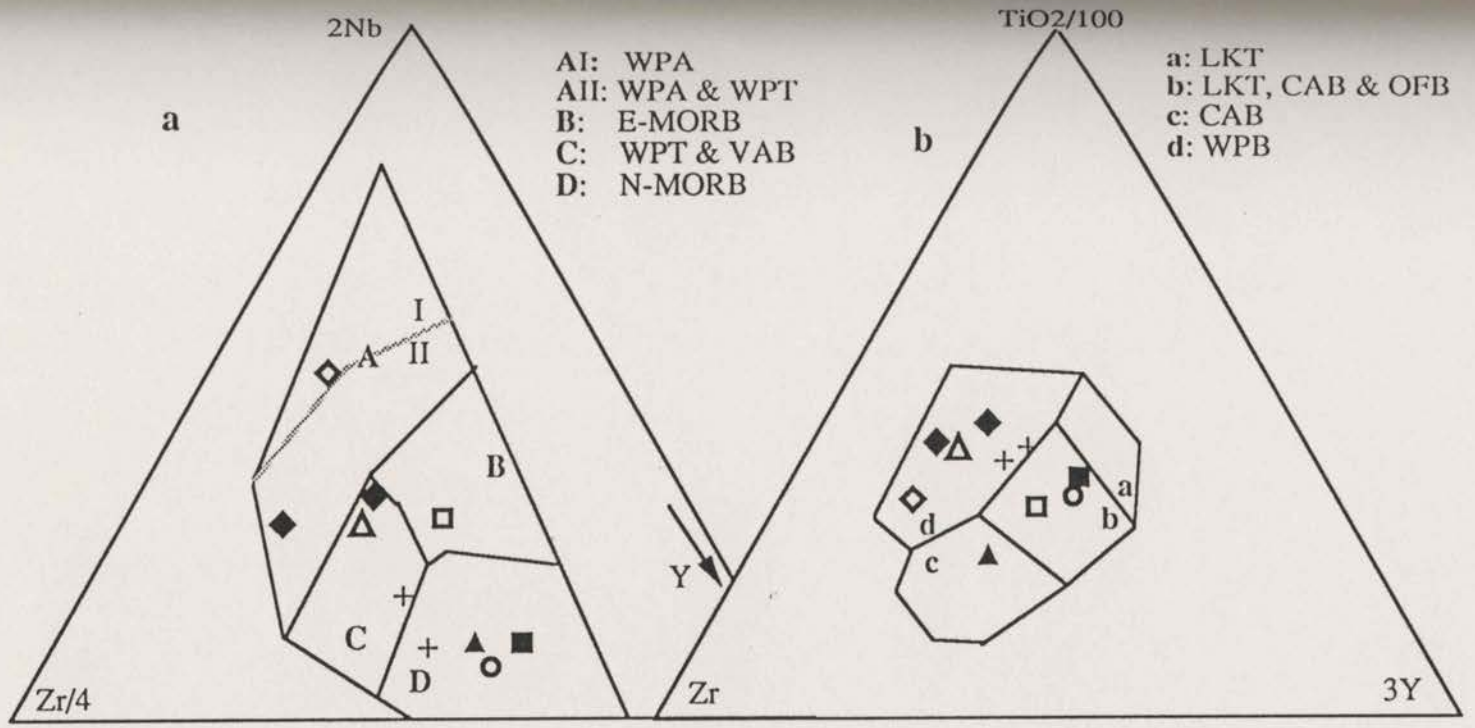

Fig.8.1.1. Schematics of tectonomagmatic discriminations (a: Meschede, 1986; b: Pearce & Cann, 1973). ○N-type MORB; □ E-type MORB; ◇ ocean island basalts; ■ island arc tholeiite; ▲ island arc calc-alkaline basalts; △ within plate tholeiite; ◆ Karoo high-Ti type basalt; + Karoo low-Ti type basalt. For data source see Table 8.1
WPB: 'within plate basalt, including ocean island and/or continental basalt, equivalent to **WPT+WPA**. **CAB**: calc-alkaline basalt. **LKT**: low-potassium tholeiitic. **OFB**: ocean floor basalt, equivalent to **N-MORB + E-MORB**. **WPT**: within plate tholeiitic. **WPA:** within plate alkaline basalt. **VAB**: volcanic arc basalt, equivalent to **CAB+LKT**. **N-MORB**: normal type mid-ocean ridge basalt. **E-MORB**: enriched mid-ocean ridge basalt.

Table 8.1. Element concentrations in primitive mantle, N-type & E-type MORBs, ocean island basalts (OIB), within plate and island arc basalts.

	Primitive Mantle*	N-type MORB*	E-type MORB*	OIB*	within plate# tholeiitic	within plate# alkalic	island arc# tholeiitic	island arc# calcalkalic
Ba	6.989	6.30	57	350	100	380	110	300
Ce	1.775	7.50	15.0	80.0	31.3	72	3.7	23
Gd	0.596	3.68	2.97	7.62	-	-	-	-
Er	0.480	2.97	2.31	2.62	-	-	-	-
Eu	0.168	1.02	0.91	3.00	-	-	-	-
Hf	0.309	2.05	2.03	7.80	-	-	-	-
Ho	0.164	1.01	0.790	1.06	-	-	-	-
K	250	600	2100	12000	4151	9600	3240	86400
La	0.687	2.50	6.30	37.0	(9)	35	1.3	10
Lu	0.074	0.455	0.354	0.300	-	-	-	-
Nb	0.713	2.33	8.30	48.0	13	53	0.7	1.4
Nd	1.354	7.30	9.00	38.5	(19)	35	3.4	13
Pb	0.185	0.30	0.60	3.20	-	-	-	-
P	95	510	620	2700	-	-	-	-
Rb	0.635	0.56	5.04	31.0	7.5	22	4.6	14
Sm	0.444	2.63	2.60	10.0	5.35	13	1.2	2.9
Sr	21.1	90	155	660	290	800	200	550
Ta	0.041	0.132	0.47	2.70	-	-	-	-
Th	0.085	0.120	0.60	4.00	-	3.4	0.25	1.1
Ti	1300	7600	6000	17200	13369	20000	3000	4650
U	0.021	0.047	0.18	1.02	-	1.1	0.10	0.36
Y	4.55	28	22	29	26	30	12	15
Yb	0.493	3.05	2.37	2.16	-	-	-	-
Zr	11.2	74	73	280	149	220	130	22

Data sources: * Sun & McDonough (1989)
Sun (1980)

analyses of various rocks, particularly during the Deep Sea Drilling Project (DSDP), heterogeneities were revealed and the mantle sources are now believed to be heterogeneous on various scales (*cf.*, Sun & McDonough, 1989). Recently, the importance of small fractions of melt in the upper mantle environment has attracted much attention (O'Nions & McKenzie, 1988; McKenzie, 1989) as a means of addressing these various compositional heterogeneities. Therefore, even though compositions of these elements are controlled by their source materials, complicated processes within source regions indicate that variations among different tectonic regions are not necessarily larger than those within one tectonic unit. Obviously, it is not practical to determine the tectonic settings of certain mafic rocks solely by these discriminant diagrams.

However, these diagrams are the results of a large amount of work from various environments and in many cases, nevertheless, they have been proved to be successful. The problem is how to deal with those 'exceptions'.

8.1.1. The Basement Sequence

Tectonomagmatic discriminations of basement samples are presented in Figure 8.1.2 and 8.1.3.

In the TiO_2/100-Zr-3Y diagram (Figure 8.1.2), the Ponto Mine samples plot largely in the LKT field, with some crossing the border into the WPB field except one (760402) in the LKT/VAB/CAB field. In the original proposal (Pearce & Cann, 1973), when samples are in this latter field, another discrimination has to be carried out using the Ti-Zr-Sr plot. However, because of the mobility of Sr, this discrimination cannot be reliable here and was thus not proceeded with.

The Boshy Tank samples plot in a scattered pattern. Sample 762703 (metadolerite) falls outside the discriminant fields due to relatively high TiO_2. Another metadolerite, 762701, is on the very right-hand corner of the LKT/CAB/OFB field due to its very high Y, while the third one (762803) is on the other side of the discriminant fields due to its low Y. The rest of the samples have limited variations but plot in both the WPB and LKT fields.

Most of the samples from the Wilandra area plot in the WPB field, while three of them (861307, 861314 and 861605) fall in the VAB/LKT field. And most of the Cymbric

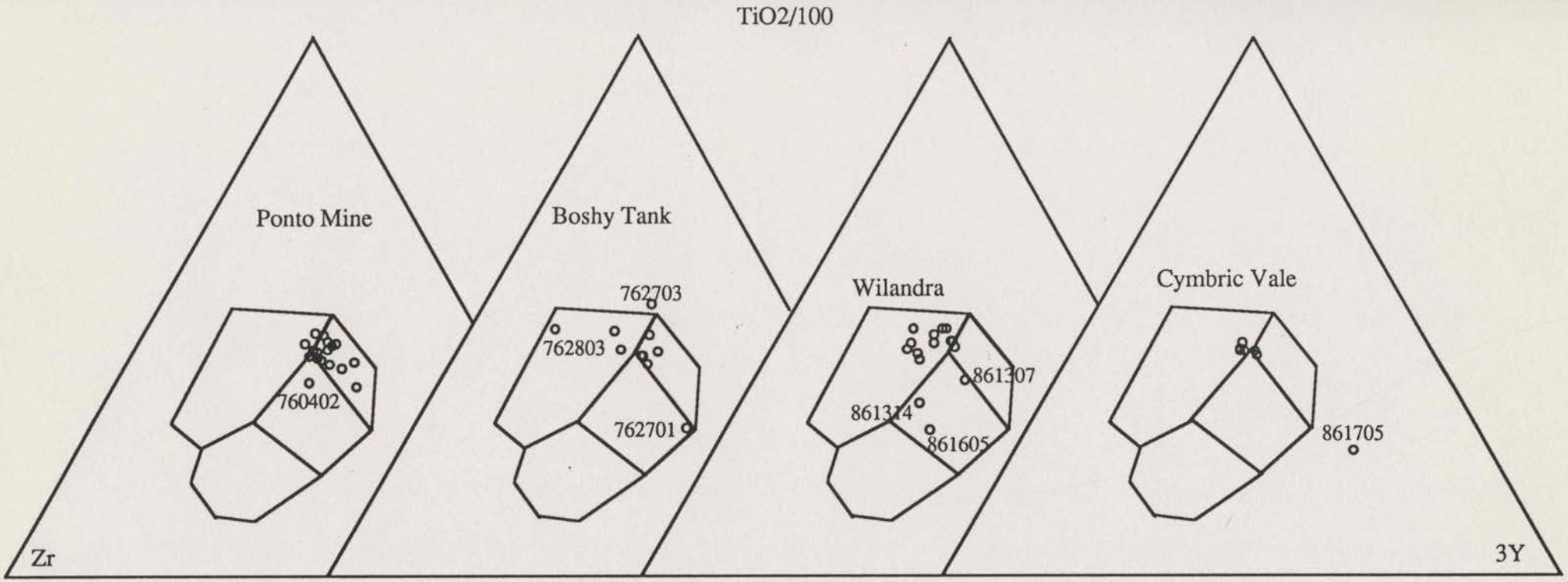

Fig. 8.1.2. TiO2/100-Zr-3Y diagram of mafic samples from the basement sequence in the Wonominta Block. In this diagram, samples from different localities show distinctive characters. The Ponto Mine samples in the LKT, while Boshy Tank and Cymbric Vale samples in both LKT and WPB fields, though the latter group has limited variations. The Wilandra samples mainly plot in the WPB field.

Vale samples plot in a rather limited area right across the border between the WPB and LKT fields. There is also an exception (sample 861705), which plots well away from the discriminant lines due to very high concentration of Y (88 ppm).

In the 2Nb-Zr/4-Y diagram (Figure 8.1.3), most samples from the Ponto Mine, Boshy Tank and Cymbric Vale areas plot in the N-MORB field. In contrast, the Wilandra samples plot in a dispersed pattern across the N-type MORB and the WPT/VAB fields. Two of the Wilandra samples (861314 and 861605) plot next to the border with E-MORB (enriched type).

Combining these two sets of discrimination diagrams, it can be said that most of the samples from the Ponto Mine Inlier (Ponto Mine and Boshy Tank) share characters with those from plate boundary environments, such as arc basalts and/or N-MORB (normal type). In contrast, samples from Wilandra Inlier present a complicated picture. While some of the Wilandra samples may be from a "within plate environment", other samples from both Wilandra and Cymbric Vale have N-MORB characters. There are apparently some exceptions in terms of individual analysis among the populations; therefore, the conclusions are reached here in a "statistical approach" and the minor "abnormal" analyses are considered insignificant for the purpose of tectonomagmatic discrimination, but probably more significant in revealing complicated magmatic processes in the sources as well as during migration and/or emplacement. The petrogenetic aspect will be dealt with in section 8.2. Another possibility is analytical errors, such as the very high Y content (88 ppm in 861705).

8.1.2. The late Proterozoic Sequence

The tectonomagmatic discriminations of the late Proterozoic mafic samples are presented in Figures 8.1.4 and 8.1.5.

In Figure 8.1.4, the mafic samples from Packsaddle plot in two compositional groups, though both lie in the WPB field. Two of the xenoliths (761001 and 761203) plot near the boundary with LKT/CAB. The third xenolith (760801) falls outside the discriminant fields, but can be considered to lie along the same trend as the three metabasites. For Nundora samples, all can be considered as plotting in the WPB field, though variations are significant and some lie beyond the field already.

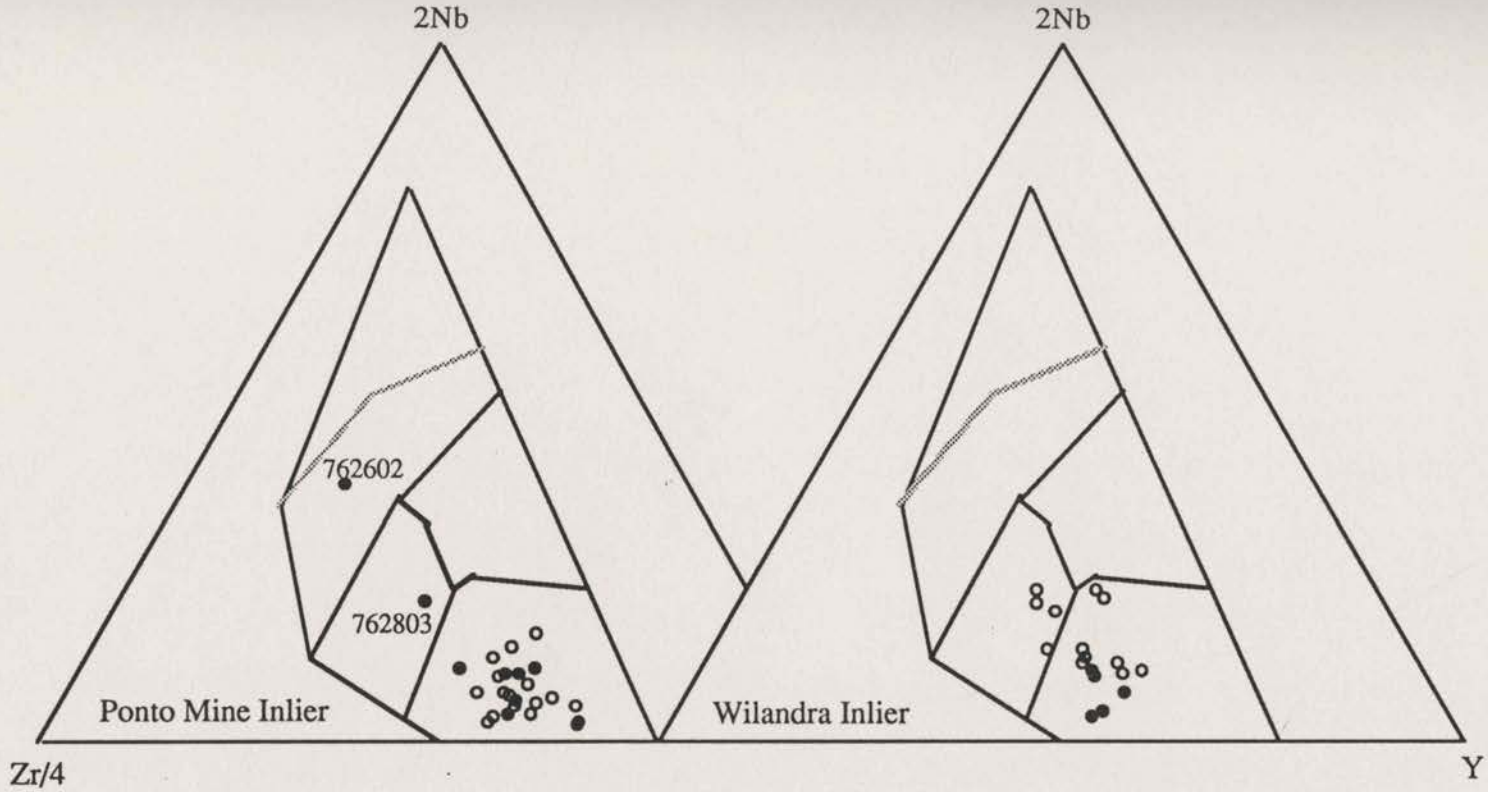

Fig. 8.1.3. 2Nb-Zr/4-Y diagram of mafic samples from the basement sequence in the Wonominta Block. In the Ponto Mine Inlier, open circles are samples from Ponto Mine and filled circles from Boshy Tank areas. Open circles in the Wilandra Inlier refer to samples from Wilandra and filled circles for Cymbric Vale. Most of the samples plot in the N-MORB field with some exceptions from Boshy Tank and Wilandra areas.

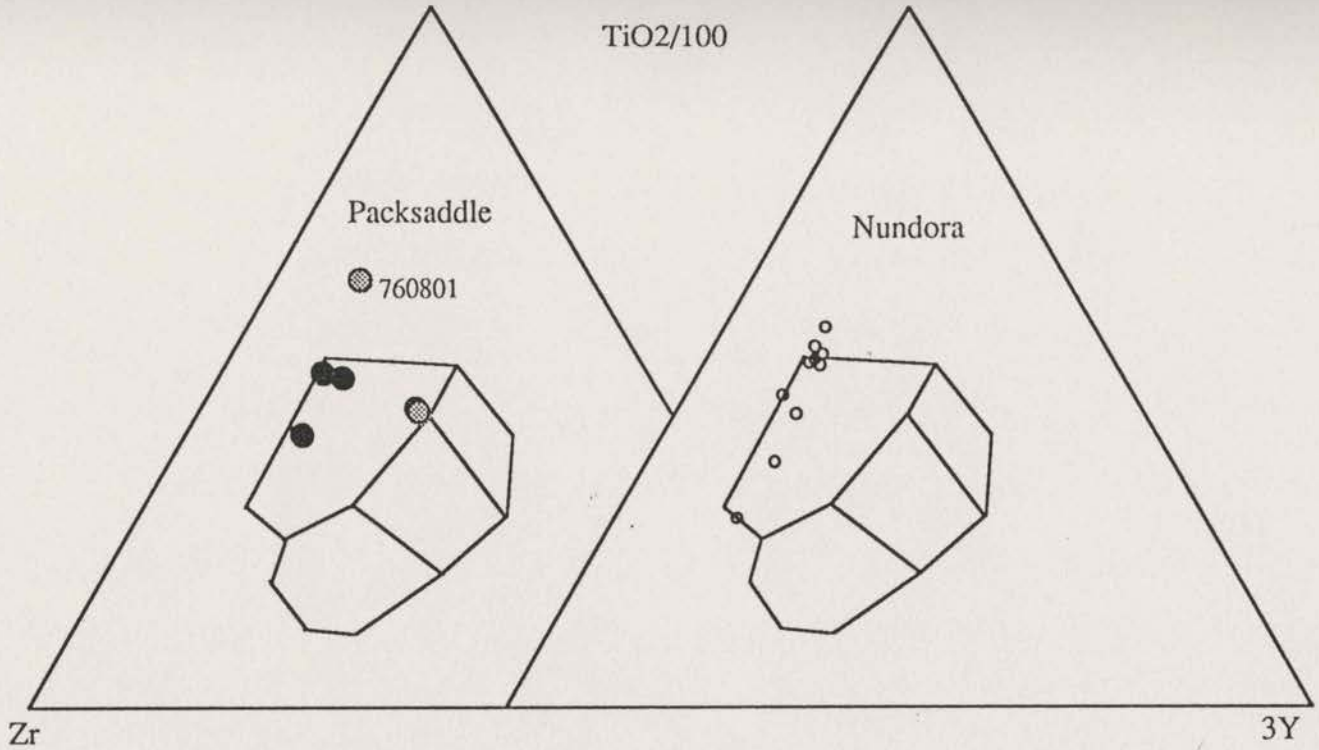

Fig. 8.1.4. TiO2/100-Zr-3Y diagram of mafic samples from the late Proterozoic sequence in the Wonominta Block. Filled circles, MB; dotted circles, MD(II). All the samples plot in the WPB field, but those from Packsaddle form two distinct compositional groups with different Y ratios.

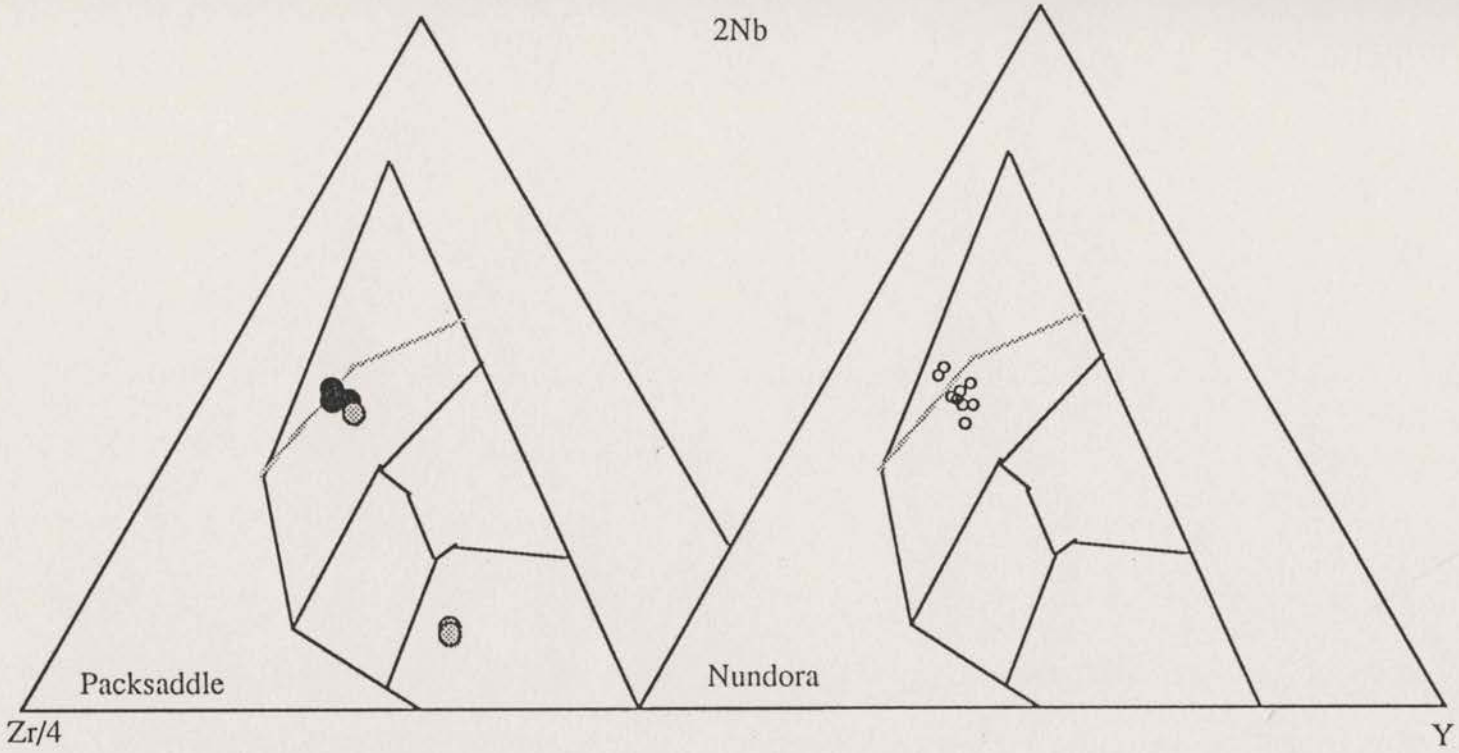

Fig. 8.1.5. 2Nb-Zr/4-Y diagram of the late Proterozoic mafic samples. Filled circles, MB; dotted circles, MD(II). Most of the samples plot in the WPB field, as Fig. 8.1.4, but two of the EPs from Packsddle plot in the N-MORB field, similar to the basement samples.

On the 2Nb-Zr/4-Y diagram (Figure 8.1.5), All metabasites from Packsaddle and Nundora plus one xenolith (760801) plot in the WPB field, while the other two xenolith samples from Packsaddle fall in the N-MORB field.

These two diagrams indicates that the alkaline basalts in the late Proterozoic sequence would have been derived from a within-plate environment; in contrast, the xenolith samples display different characters, some probably inherited from early magmatic activities, such as those observed in the basement sequence.

8.1.3. The Cambrian Rocks

The samples from the Cambrian sequences in the Wonominta Block include those from Mt. Wright, Comarto, the Ponto Mine dolerite (752110) and the Kayrunnera gabbro (762904).

In the TiO_2/100-Zr-3Y diagram (Figure 8.1.6), the Mt Wright samples plot in two distinctive areas. The basaltic samples are relatively low in Zr and form a linear trend at constant Y level. The andesitic-trachytic samples are relatively enriched in Zr plotting near the Zr-side border of the discrimination field. This diagram clearly indicates the influence of magmatic processes in the discrimination. However, both groups still plot in the WPB field, along with the Comarto samples, Ponto Mine dolerite and Kayrunnera gabbro. The last group of samples also display features transitional to "oceanic" basalts, hence are somewhat similar to the low-Ti Karoo basalts.

However, only the basaltic samples from Mt. Wright plot indisputably in the WPB field in the 2Nb-Zr/4-Y diagram (Figure 8.1.7); the other three groups fall in the WPT/VAB, largely due to their low Nb content. These features are also similar to the Karoo low-Ti basalts.

These two diagrams show that the mafic samples from various Cambrian rocks bear many of the features of intra-plate volcanism, though the Meschede's scheme presented another case of non-discrimination due to built-in deficiencies.

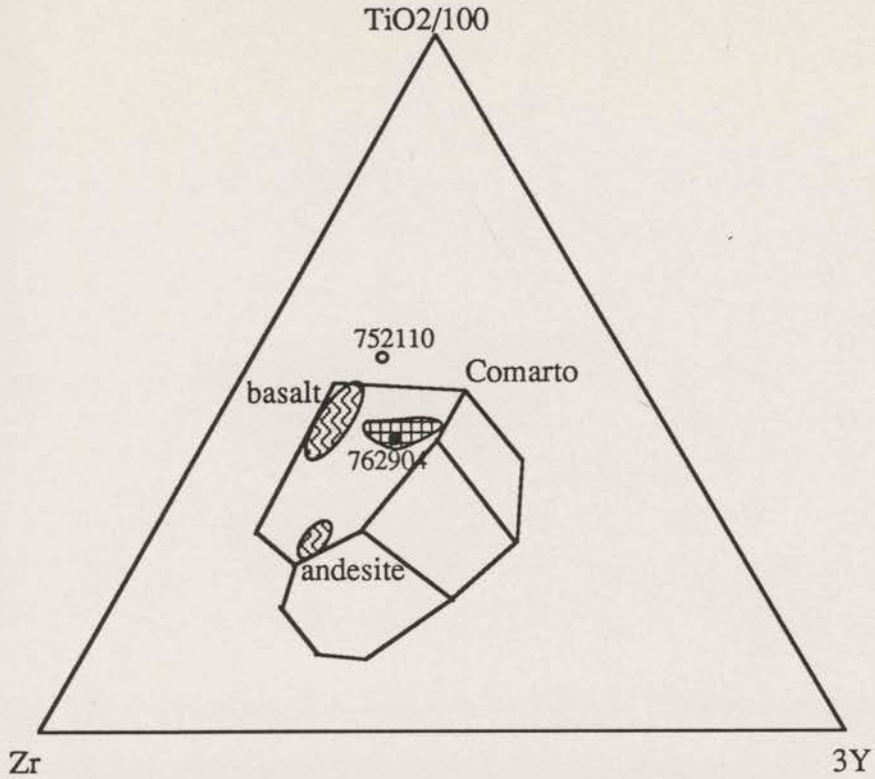

Fig. 8.1.6. TiO2/100-Zr-3Y diagram of the Cambrian mafic rocks in the Wonominta Block. The samples invariably plot in the WPB field with two distinct compositional groups for samples from Mt. Wright (basic and intermediate).

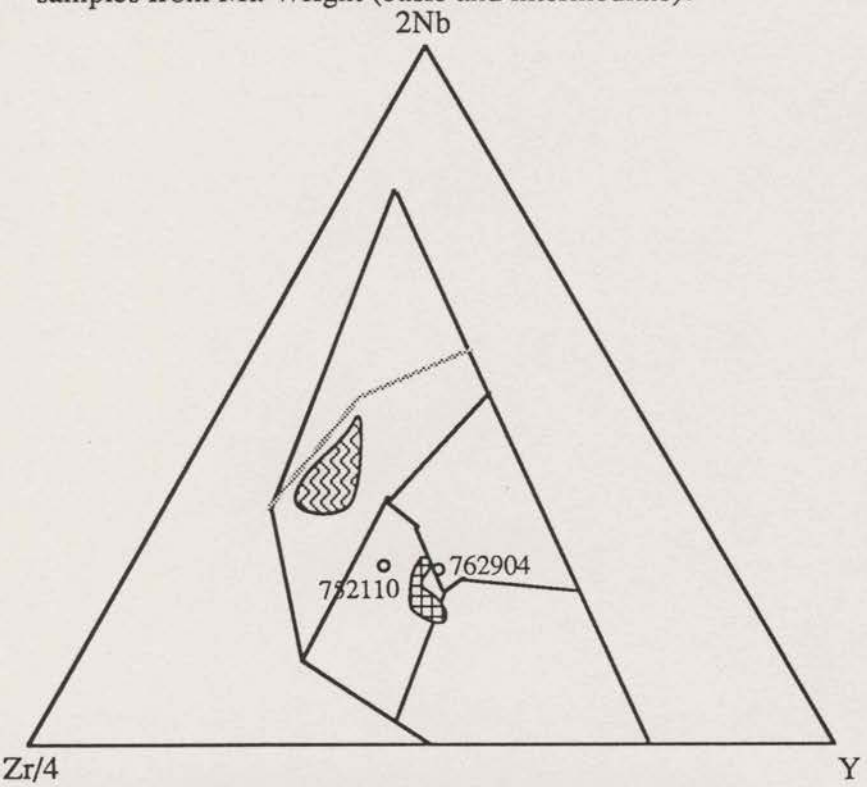

Fig. 8.1.7. 2Nb-Zr/4-Y diagram of the Cambrian mafic rocks in the Wonominta Block. Legend as Fig. 8.1.6. Only the Mt. Wright samples plot in the WPB field, while others in the field of WPT/VAB due to lower Nb proportion.

8.1.4. Discussion

From the above presentations, it is obvious that without very critical examination, tectonomagmatic discrimination would have a limited role in terms of the tectonic reconstruction here. In some cases, magmatic processes may have a significant influence on the compositional changes, which would completely disguise the real source characters. As has been emphasised by the original authors (Pearce & Cann, 1973), only the most primitive samples should be used in the exercise in order to minimise the magmatic influence; however, for the metamorphosed samples, it is sometimes difficult to assess magmatic fractionation due to secondary alterations, though the Mt. Wright andesitic-trachytic samples provided a clear case for the fractionated samples being influenced by the magmatic processes.

Nonetheless, these exercises showed that the samples from different sequences have distinct characters in terms of tectonomagmatic discrimination. The basement samples in the Ponto Mine Inlier have compositions similar to those of N-MORB; while samples from the Wilandra samples display characters from N-MORB to intra-plate volcanism. The alkaline basalts from both late Proterozoic and Early Cambrian sequences have compositions identical to those of intra-plate volcanism. And the subalkaline rocks from other Cambrian sequences (Comarto, Ponto Mine and Kayrunnera) exhibit transitional characters between typical intra-plate and plate boundary volcanism, similar to the low-Ti Karoo basalts.

8.2. PETROGENETIC STUDIES

The petrogenetic discussions presented in this section are aimed at describing physio-chemical conditions and processes of the formation of various mafic rocks in the Wonominta Beds using forward and reverse modellings (Hanson, 1989). In forward modelling, a primordial composition is presumed, then various partial melting and fractional crystallisation models are calculated to obtain theoretical results, which are then compared with the actual analyses to see if the presumed primordial composition and processes could be responsible for the real rocks. In reverse modelling, the calculations start from real rocks to determine what processes are responsible for the observed geochemical features. By means of forward modelling, the thermodynamic processes responsible for various typical magmatic rocks have been characterised comprehensively (*e.g.*, Ringwood, 1975). In contrast, petrogenetic examination of a particular group of rocks benefits mostly from the reverse modelling.

The primary mantle compositions are considered to be high in MgO and relatively low in FeO due to the mantle-core fractionation. Thus the mafic magmas generated from the mantle sources would be expected to be high in MgO and low in FeO when these magmas had not be fractionated significantly; when the magmas had undergone extensive fractionation, they would have low MgO. For this reason, the MgO contents in the basaltic rocks, in practice, are used as a general indicator of the degree of fractionation from their primary magmas. However, in metamorphic rocks, the primary geochemical features are obscured by secondary processes; thus many of the components are no longer usable, such as most of the major components and the LIL elements (Cs, Rb, Sr, K and Ba). Among the more useful elements, known as the immobile components, many of them are not available by means of routine XRF techniques, for example Ta, Hf, U. Thus, the only useful elements available to the present project are Zr, Y, Ti, and some Nb. In addition, the following discussion will also integrate the REE analyses of representative samples.

8.2.1. Some principles of petrogenetic modelling

Partial Melting

For equilibrium melting, the concentration of a given element i in the melt (C_{li}) relative to its concentration in the source rocks (C_{0i}), from which the melt is generated, can be obtained by the following equation (Schilling, 1966):

$$C_{li}/C_{0i} = 1/[(1-F)D_i + F] \quad (8.1)$$

where F is the fraction of the melt; and
D_i is the bulk distribution coefficient.

Because this is an equilibrium process, C_{li} is dependent only on the bulk distribution coefficient for the minerals in the residue at the time of melt removal. In practice, it is the concentration of the element in the aphyric groundmass of volcanic rocks, but for the metamorphosed rocks, this groundmass is no longer available. Also, because the distribution coefficients for Zr, Y, Ti and Nb in most of the minerals are much less than one (Table 8.2), equation 4.14.1 can be approximated as

$$C_{li}/C_{0i} = 1/F \quad (8.2)$$

Apparently, for a pair of elements within a particular rock system, there is a relationship:

$$C_{li}/C_{lj} = C_{0i}/C_{0j} \quad (8.3)$$

This equation can explain the linear relationship observed in the binary compositional discrimination diagrams discussed previously. The slope of the line is positive and equal to the ratio of the abundances of the two elements in the source, and the intercept is the origin.

Fractional Crystallisation

For fractional crystallisation processes, the concentration of a given element in the remaining melt (C_{li}) relative to that in the initial melt (C_{0i}) is given by Neumann *et al.* (1954):

$$C_{li}/C_{0i} = F^{(Di-1)} \quad (8.4)$$

Again, for the incompatible elements, *i.e.*, whose D_i is much less than one (Table 8.2), equation 4.14.4 becomes by approximation:

$$C_{li}/C_{0i} = 1/F \quad (8.5)$$

This is the same relationship as that for incompatible components in the partial melting processes, hence it can also explain the linear relationship for a pair of incompatible elements. Thus unfortunately, the observed linear relationship does not indicate any particular processes that may be responsible for the formation of the rocks. In practice, the observed compositional variations are usually contributed by both processes, and it is particularly important to identify the relative contribution of the two processes. From equations 8.1 and 8.4, it can be obtained that when one of the two elements has a distribution coefficient greater than one, contributions of the partial melting and fractional crystallisation will be different and it is possible to distinguish them. This is shown in Figure 8.2.1 (after Hanson, 1989).

In Figure 8.2.1, element Y is a compatible element with a rock/melt distribution coefficient of 5 (that is most of the component will be in the solid phase during magmatic processes); while element X is an incompatible element with the distribution coefficient much less than 1. During the partial melting process, element Y shows a slightly increasing trend as the melt fraction increases, while element X shows a sharp decrease in the melt at the same time (*i.e.* most of the component would be rapidly concentrated in the melt and then reduce its concentration as melting fraction increases). In contrast, during the fractional crystallisation (FC) process, element Y would be rapidly concentrated in the crystallised phases, thus depleting in the melt phase, while element X shows only a slight decrease in concentration in the melt until a very late stage of the FC process.

8.2.2. Zr, Y, Ti and Zr in petrogenetic modelling

Presentations in this section are after Pearce and Norry (1979). As discussed above, Zr, Y, Ti and Nb are the only available components from XRF analysis useful in the petrogenetic discussion of metamorphosed igneous rocks, and in general, all four elements are incompatible in the basaltic system (Table 8.2). Pearce and Norry (1979) illustrated the expected variation (forward modelling) of these elements in different fractional crystallisation processes and these are shown in Figure 8.2.2. It is clear from these diagrams that the fractional crystallisation of minerals in the basaltic system (involving olivine, clinopyroxene, orthopyroxene and plagioclase as major phases), will generally result in positive linear correlations between these four components; however, crystal fractionation of magnetite (and probably also ilmenite) will lead to a decrease of Ti at a relatively high Zr level as observed in the Mt. Wright basaltic samples.

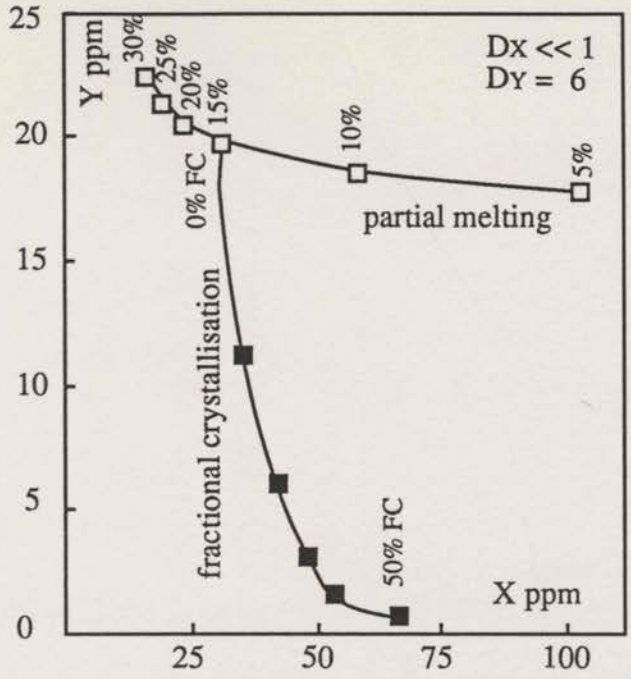

Fig. 8.2.1. Calculated scatter plot using the partial melting and fractional crystallisation modellings (After Hanson, 1989; Figs. 2D & 3D). This diagram shows the compositional variation of elements X and Y in the melting phase. Dx and Dy refer to the rock/melt distribution coefficients of X and Y of bulk rocks. In this model, the fractional crystallisation starts from a 15% partial melt from a source with 10 ppm X and 100 ppm Y.

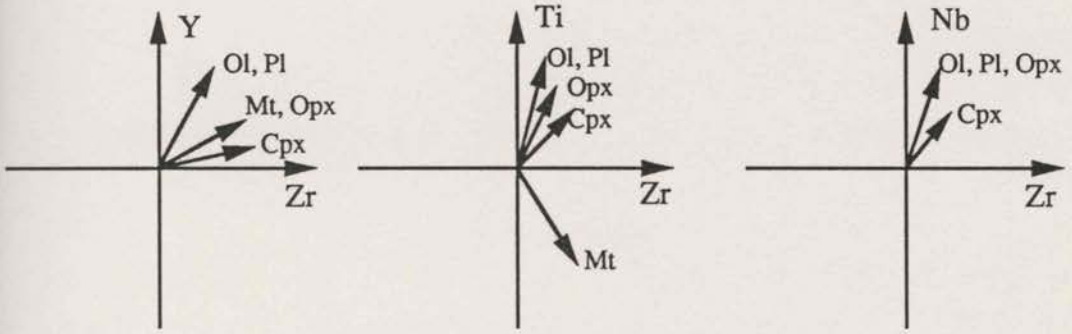

Fig. 8.2.2. Modelled fractionation trends on Y-Zr, Ti-Zr and Nb-Zr diagrams. (after Pearce & Norry, 1979). These diagrams indicate when a particular mineral in the basaltic system fractionates from the magma, how the compositional trend evolves for the residue magmatic system, that is, in most cases, the fractionation will result in a positive linear correlation between the components. However, when magnetite is involved in the fractionation, it will lead to a negative correlation between Zr and Ti. This character has been observed in samples from Nundora (Fig. 6.3.3) and Mt. Wright (Fig. 7.2.3).

Table 8.2. Distribution coefficients of Ti, Zr, Y and Nb in basaltic system.

	olivine	Cpx	Opx	plagioclase	hornblende	garnet	
Ti	0.02	0.3	0.1	0.04	1.5	0.3	
Zr	0.01	0.1	0.03	0.01	0.5	0.3	After
Y	0.01	0.5	0.2	0.03	1.0	2.0	Hanson
Nb	0.01	0.1	0.15	0.01	0.8	(0.1)	(1989)

8.2.3. Partial Melting versus Fractional Crystallisation

Figure 8.2.3 is a compilation of some of the binary compositional discriminations of samples from the basement, late Proterozoic and early Cambrian sequences in the Wonominta Beds. Basically, the five binary plots can be divided into three groups; Zr-Nb and Zr-Y plots present simple positive correlations with different slopes for different rocks; Zr-TiO_2 and Zr-Ga display two different linear correlations, with the low-Zr (less than 300 ppm) samples having positive, and high-Zr samples negative correlations; and Zr-Sc shows a negative exponential correlation.

In the Zr-Nb and Zr-Y plots, ranges of compositional variation are wide and coherent, which suggests that there were no specific minerals containing these elements involved in the crystallisation processes (*i.e.* the components are not saturated). The different linear correlations all pass through the origin, indicating Zr, Nb and Y are equally incompatible, and thus the discriminations cannot identify which processes are responsible for the compositional character from the discussions above. However, the different slopes of the linear correlations imply distinctive compositions of the sources. The mantle source(s) of the basement rocks would have lower Nb/Zr (thus depleted in Nb) and higher Y/Zr than those of the younger rocks, thus bearing some MORB-like signatures (Pearce & Norry, 1979). In this context, the higher Ti/Zr ratio in samples from the Ponto Mine Inlier than those in the Wilandra Inlier, as shown in Figure 5.2.1, suggest that the mantle source(s) in the north may have been more depleted than in the south. In contrast. the Mt. Wright samples display similar Nb/Zr and Y/Zr ratios to those samples from Nundora. This suggests that the sources of these samples have identical HFS compositions.

In both Zr-TiO_2 and Zr-Ga plots, the positive linear correlations reflect distinctive source characters as suggested by the Zr-Nb and Zr-Y variation. However, while the

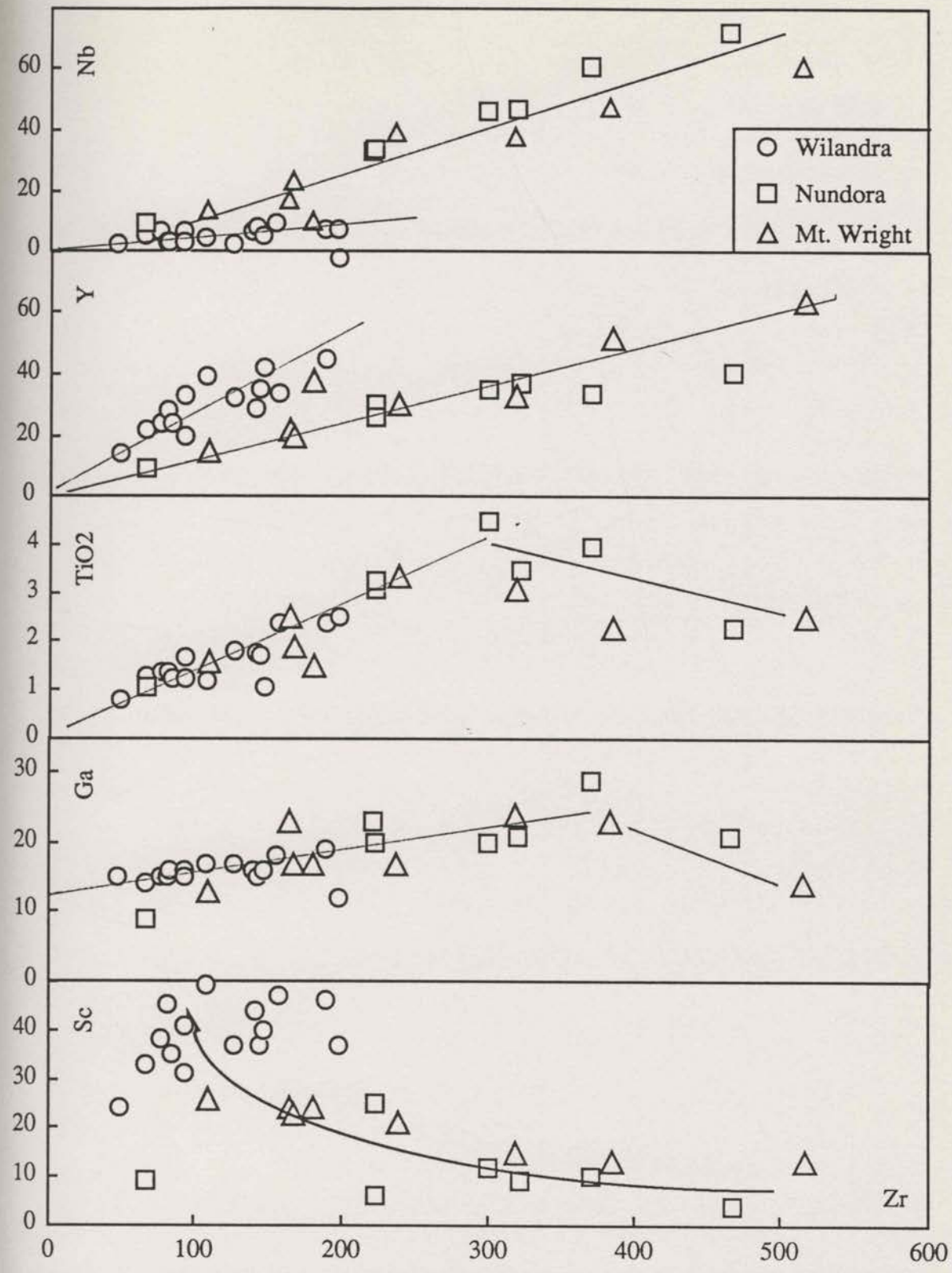

Fig. 8.2.3. Some binary compositional variations of mafic samples in the Wonominta Beds used for petrogenetic modellings. Following Pearce & Norry (1979) and Hanson (1989), the compositional plots shown here (positive correlation trends through the origin) suggest that Zr, Nb, Y and Ti have relatively comparable incompatibility; while Ga are less incompatible than Zr with the correlation intercepting its axis. In comparison, Sc behaves as a compatible component (Di>1), resulting in a negative correlation on the Zr-Sc plot, which also suggests a large degree of fractional crystallisation (approx. 50%) for the basement tholeiites, while alkaline basalts from both late Proterozoic (Nundora) and Cambrian (Mt. Wright) sequences were involved in no more than 30% fractionation, if Hanson's model is followed, with a starting point of 15% partial melting.

Zr-TiO_2 trend passes through the origin, the correlation trend between Zr and Ga intercepts the Ga axis, suggesting that Zr is more incompatible (or less compatible) than Ga. In both plots, the slope of the correlations are roughly identical for samples from different sequences, and this probably means that the sources of the various rocks have similar Zr/Ti and Zr/Ga ratios.

In contrast to the Zr-Nb and Zr-Y variation, the Ti and Ga contents in the samples decrease with Zr when Zr is above 300 ppm. This suggests that, at relatively high levels of Ti and Ga, the magmatic processes involved the crystallisation of minerals containing Ti and Ga (*e.g.* ilmenite), and removal of these phases make significant contributions to the observed compositional variation.

The Zr-Sc plot indicates that Sc is a compatible element in the magmatic systems, and the modelling suggests (from Figure 8.2.1) that the magmas in the younger sequences involved various but generally low degree of partial melting, while the basement samples would have involved large degreepartial melting.

In summary, the petrogenetic modelling using various immobile elements suggests that the basement rocks have source(s) with lower Nb/Zr, higher Y/Zr, and roughly the same Ti/Zr and Ga/Zr as those of the younger rocks. Both the Late Proterozoic and Early Cambrian Mt. Wright rocks have sources with identical HFS compositions. This modelling also reveals that fractional crystallisation has a significant influence on Ti and Ga variations at high Zr level. In general, the basement rocks may have been derived from magmas of large degree of partial melting, whereas, younger rocks from magmas of small degree of partial melting.

8.2.4. Rare Earth Elements in Petrogenetic Modelling

The REE in mafic rocks can all be considered as incompatible components, but the values of their distribution coefficients for any particular mineral vary systematically with atomic number and the shape of the coefficient patterns differs from one mineral to another (*e.g.* Figure 8.2.4, after Hanson, 1989). Thus, each mineral involved in the magmatic processes leaves its own signatures on the REE pattern of the rock. Using the reverse modelling, it is usually possible to identify specific minerals which participated in the magmatic processes.

Figure 8.2.4 presents mineral/melt REE distribution coefficient patterns (after Hanson, 1989) for plagioclase, clinopyroxene, orthopyroxene, olivine and garnet in the basaltic system. This diagram shows the olivine/melt distribution coefficients have a pattern slowly increasing from LREE to HREE at very low level. This suggests that olivine is not capable of producing significant REE fractionation during magmatic processes (that is, little REE will be incorporated in the olivine minerals). For plagioclase the pattern drops constantly from LREE to HREE except for Eu. This mineral has a much higher Eu distribution coefficient than the others, which means that a significant proportion of Eu will be retained in the plagioclase residue, producing a melt with a negative Eu anomaly; it also means when plagioclase fractionates from the melt, the residue magmas will be depleted in Eu.

Compositional variation in pyroxene can significantly change the mineral/melt coefficients. For the low-Ca orthopyroxene, the pattern slopes upwards from LREE to HREE but the LREE part has a steeper slope than that of the HREE. Again, values for all elements are at such low level that little REE fractionation is expected during partial melting of the low-Ca pyroxene. For the high-Ca clinopyroxene, the pattern slopes upwards from Ce to Sm, then fairly flat from Gd to Yb. The absolute values are higher than for the other minerals listed above, particularly for HREE. Thus, magmatic processes involving high-Ca pyroxene would result in significant REE fractionation, particularly HREE.

Garnet normally occurs as a minor phase in the mantle source rocks for the basaltic system. This mineral has a pattern similar to that of olivine, increasing from LREE to HREE, but at much higher level. Therefore, a partial melt of a source containing even small amount of residual garnet would be significantly LREE-enriched.

8.2.5. REE Compositions in the Basement Mafic Rocks

As presented previously, the mafic rocks in the basement sequence have a flat REE compositional pattern with Ce-depletion, with or without Eu anomaly.

Among the twelve samples from the Basement sequence, the two Wilandra samples (861211 & 861713) with higher REE concentrations display some Eu depletion, while the low-REE samples do not show such a feature. In order to investigate if these characters reflect their sources or the magmatic processes, the samples are normalised

to 760402, which has the lowest REE concentrations (thus the most primitive and close to source composition) in the group. The results are shown in Figure 8.2.5.

In Figure 8.2.5, the basement samples can be divided into high-REE and low-REE groups. Samples in the high-REE group (861211, 861314, 762501 and 861909) have various Eu depletion, and compared with Figure 8.2.3, the samples are derived from melts, from which plagioclase has been fractionated to generate the Eu depletion either through the fractional crystallisation or partial melting (plagioclase occurs as residue) relative to the most primitive compositions. The low-REE group (752001, 753001, 762705, 861915 and 861713) shows no Eu depletion, indicating plagioclase has not been fractionated in the magmatic processes relatively; however, sample 752302 in the low-REE group shows a little positive Eu anomaly, suggesting the fractionation of clinopyroxene from melt in the magmatic processes. Some of the samples (752302, 753001 & 861314) display a Ce positive anomaly, which can also be explained by the removal of high-Ca pyroxene. Alternatively, the Ce-anomaly could have been due to secondary alterations (*cf* discussion in Chapter Five).

Also in the low-REE group, sample 752001 has slight HREE depletion relative to LREE. The slight HREE-depletion has been also observed in the chondrite-normalised plot ; thus this feature might indeed represent a minor garnet involvement during the magmatic processes. The negative Er anomaly cannot be readily explained by the involvement of any known major minerals in the basaltic system and thus may reflect a distinctive source. Alternatively, it may imply analytical problems.

In general, the modelling shows various minerals may have been involved in the magmatic processes to produce the observed REE compositional characteristics of samples from the basement sequence. Compared with the most depleted sample in the sequence, the high-REE samples had involved plagioclase fractionation; while clinopyroxene fractionation may have been involved in both high- and low-REE samples. And the low-REE samples (in particular, sample 752001) could have undergone a partial melting involving minor garnet, which resulted in a weak LREE-enriched pattern.

8.2.6. REE Compositions in the late Proterozoic Mafic Rocks

The mafic volcanic samples from the Late Proterozoic sequence display a LREE-enriched pattern, typical of alkali basalt from intra-plate environments. The

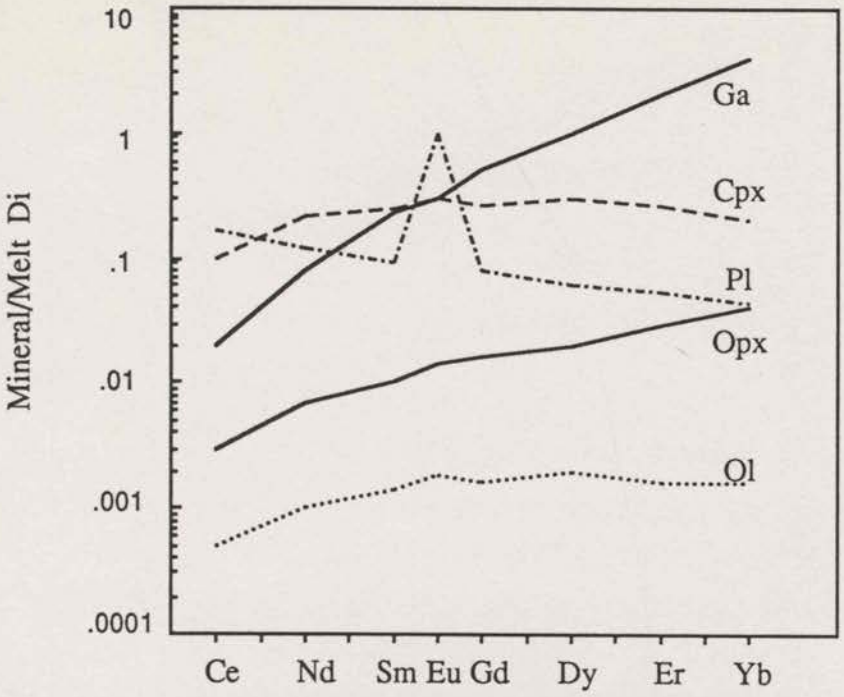

Fig. 8.2.4. Mineral /melt distribution coefficients for garnet (Ga), clinopyroxene (Cpx), orthopyroxene (Opx), olivine (Ol) and plagioclase (Pl) used for petrogenetic modellings (after Hanson, 1989).

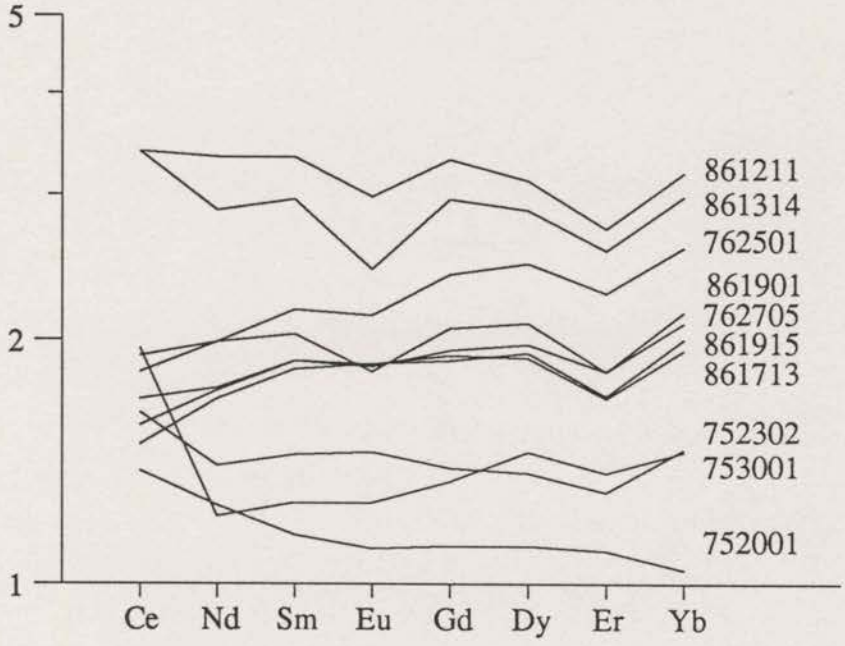

Fig. 8.2.5. rock/rock normalised REE compositions of the basement mafic samples, which are normalised to 760402, the most primitive sample analysed in the sequence. Assuming all elements are immobile during secondary processes, the Eu negative anomalies in 861211 and 861314 would suggest removal of plagioclase during fractional crystallisation, compared with the observed most primitive samples; while the LREE depleted pattern in 762501 might indicate the involvement of Ga in the formation of the melts (Hanson, 1989).

preliminary modelling suggests that the samples had undergone various but low degrees of fractionation of the melt. In Figure 8.2.6, samples are normalised to the low-REE sample (760806). This diagram presents relatively small variation of both enriched and depleted (xenolithic samples) REE compositions, but the patterns are quite variable. Most of the volcanic rocks have a relatively flat pattern and on the same level as normalising parameters in 760806, but these samples show various LREE enrichment, which could be the result of clinopyroxene fractionation (or removal of the mineral from melt as residue).

The xenolithic samples have lower REE concentrations and different patterns. Sample 760805 has a "U" pattern with increasing in both LREE and HREE, suggesting the fractionation of both plagioclase and clinopyroxene (or garnet); while the dome-like patterns of 760801 appear to suggest a cumulate origin relative to the former sample.

8.2.7. REE Compositions in Cambrian Mafic Rocks

The Mt. Wright basalts are of alkali association, similar to those in the Late Proterozoic sequence. Various discrimination diagrams indicate these two groups of rocks share many similarities in geochemical composition, and probably identical source rocks.

In the rock to rock plot (Figure 8.2.7; normalised to sample 862225), the high-REE sample (862221) has significant Eu depletion, suggesting the fractionation of plagioclase from the melt relative to the most primitive compositions, and the LREE depletion in 862112 may be explained as the removal of plagioclase. Sample 862402 displays a positive Eu anomaly, implying the fractionation of clinopyroxene. However, sample 862205 has a remarkable positive Gd anomaly, which is not observed in any other samples, thus it may be an analytical problem. Compared with the Mt. Wright basalt, the Ponto Mine dolerite displays remarkable LREE depletion, and a slight Eu depletion. These characters suggest the involvement of both plagioclase and garnet in the magmatic processes.

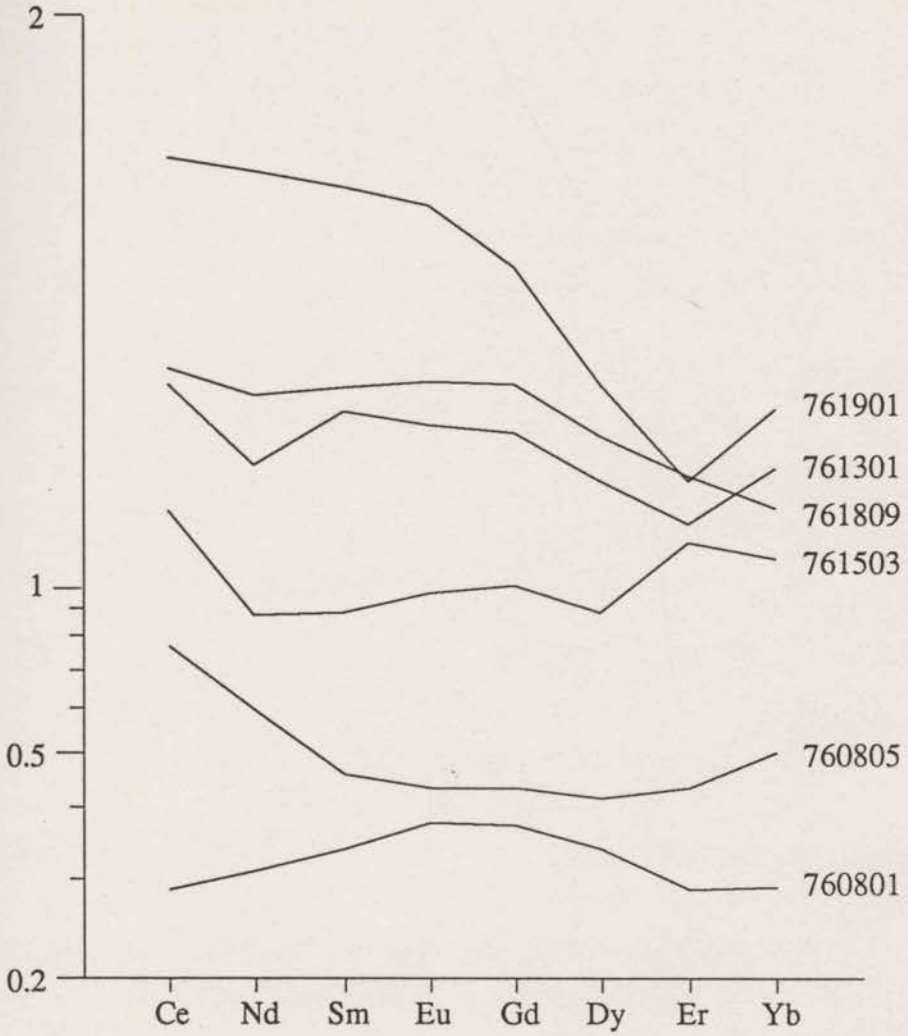

Fig. 8.2.6. Rock/rock (normalised to sample 760806) REE plot of mafic rocks from the late Proterozoic sequence. Following Hanson's (1989) treatment, the pattern of 760801 would suggest possible removal of clinopyroxene relative to the denominator and removal of Ga (or as residue) in 761901 for its LREE enriched pattern. However, the patterns of other samples suggest simple systems may not be able to explain the observed patterns.

8.3. Nb GEOCHEMISTRY AND CRUSTAL CONTAMINATION

As indicated in the previous modelling, many geochemical characters independent of magmatic processes can be explained by both source heterogeneities (various Y/Zr, Nb/Zr ratios) and crustal contamination (Th-enrichment) via AFC processes; thus, distinguishing these two different processes is crucial for petrogenetic investigations. Several studies have suggested the particular geochemical features of Nb may help to resolve this problem (Hofmann, 1986; Meschede, 1986; Sun & McDonough, 1989; Myers & Breitkopf, 1989).

Principally, Nb tends to concentrate in the liquid part in any partial melting and/or fractional crystallisation process because of its incompatibility. Thus, MORB sources would be depleted in Nb compared with OIB's, which is the basis for Meschede's diagram (1986) (see Section 8.1).

However, it is still a controversial issue whether or not Nb in VAB is more depleted than in MORBs. Recently, a new opinion has emerged that the HFS depletion (particularly Nb) in arc basalt is actually a result of the normalizing treatment, and the concentrations of Nb in MORB and VAB are indistinguishable. Woodhead (1989) suggests that the observed Nb depletion in spidergrams is due firstly, to inappropriate normalization; and secondly, to the enrichment of other components, a process similar to what has been discussed about the immobility of elements previously.

But most specialists in this field suggest that there is a significant difference in Nb contents between VAB and MORB, simply because the source rocks for VAB (subducted oceanic slabs) had been partially melted previously to produce MORB, and should promote more depleted features than the sources for MORB (*e.g.* McCulloch & Gamble, 1991). Statistics appear to support this model (*e.g.* Hawkesworth *et al.*, 1991). However, in detail, this process happens only when the new melts were generated from the particular part of the subducted slab. If the partial melting process involves the overlain altered MORB-like rocks, the magmas should be more enriched in HFS elements than those in MORBs because of the incompatible features. And overall, the mass balance of the oceanic evolution indicates the VAB sources may well be identical to those of the MORBs. Recently, McCulloch and Gamble (1989) proposed a model to explain the depletion of Nb in oceanic VAB. In this model, the depleted features of the mantle wedge, which is supposed to be the source of the VAB, is due to the magmatic activity along the back-arc spreading ridges.

Still, fundamental differences have been recognised between the two groups of volcanic rocks; for example, the LIL/HFS ratios in VAB are much higher than those in MORBs. Several models have been proposed but generally it is agreed the high LIL contents in VAB represent the contribution of sediments (Pearce, 1983; Hawkesworth *et al.*, 1991). And if Rb, K and Sr are not reliable to identify such processes due to secondary alterations, Th-enrichment is usually a diagnostic feature for such contributions (Saunders & Tarney, 1984).

As discussed above, samples from the basement sequence in the Wonominta Block display various degrees of Nb depletion in discrimination diagrams, and a transition in Nb concentrations is observed from little or no depletion in the spidergram for the southern part of the sequence (Wilandra Inlier), to significant depletion in the northern part of the sequence (Ponto Mine Inlier), even considering the analytical uncertainties (*cf.* Figure 5.7.4). All of these various Nb depletions are accompanied by constant enrichment in Th and relatively high Ti, Zr and Y. The decoupling between Nb and (Ti, Zr), that is, the coexistence of depleted Nb and normally high Ti and Zr, appears to suggest that these rocks were not derived from an arc, or arc-like environment.

There are two possible explanations to the decoupling phenomenon. The first one is that the difference reflects the source heterogeneity of the rocks. In this case, the mafic rocks in the Ponto Mine Inlier would really have an unusual source(s), with most of the trace elements bearing MORB features except for the Nb-bearing VAB features.

And secondly, the difference implies the different contribution of crustal materials to the magmas. In other words, the least Nb-depleted samples from Wilandra represent the least-contaminated rocks; and the Ponto Mine samples, having the most depleted Nb concentration, may be considered as the rocks most contaminated by crustal materials. Figure 8.2.8 is a plot to emphasise the crustal contamination in the magmatic process after Lightfoot & Naldrett (1989). This figure clearly suggests that the mafic rocks in the Ponto Mine Inlier involved more crustal materials in the magmatic evolution than those in the Wilandra Inlier.

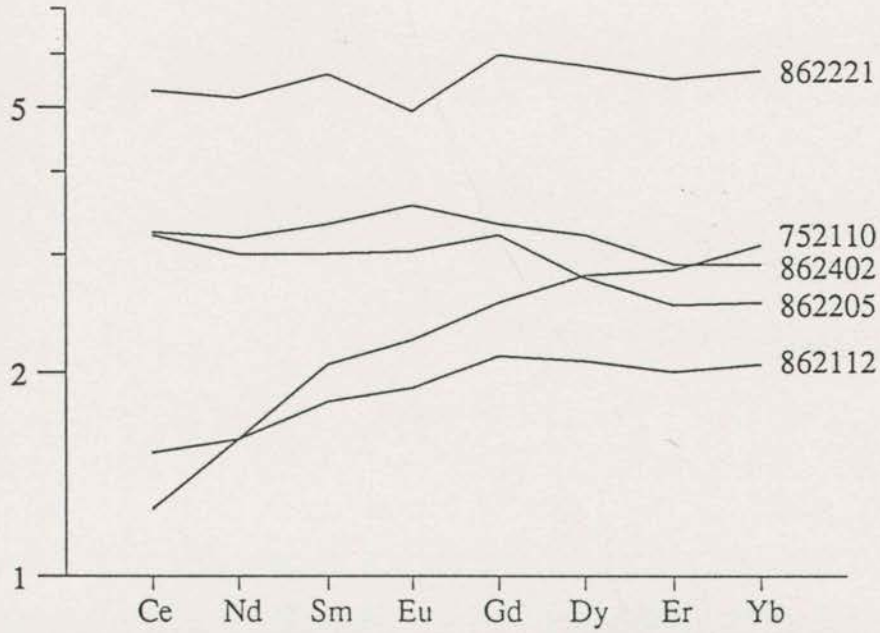

Fig. 8.2.7. Rock/rock (normalised to sample 862225) REE plot of Cambrian Mt. Wright and Ponto Mine (752110) samples. Again, the Eu depletion in samples 862221 would suggest the influence of Pl fractionation. However, the most remarkable feature is the LREE depletion of sample 752110, and less significantly for 862112. It would suggest Ga occurred as residue in the formation of alkali basalt but not for 752110 (*i.e.*, if normalised to 752110, all would display strong LREE enrichment).

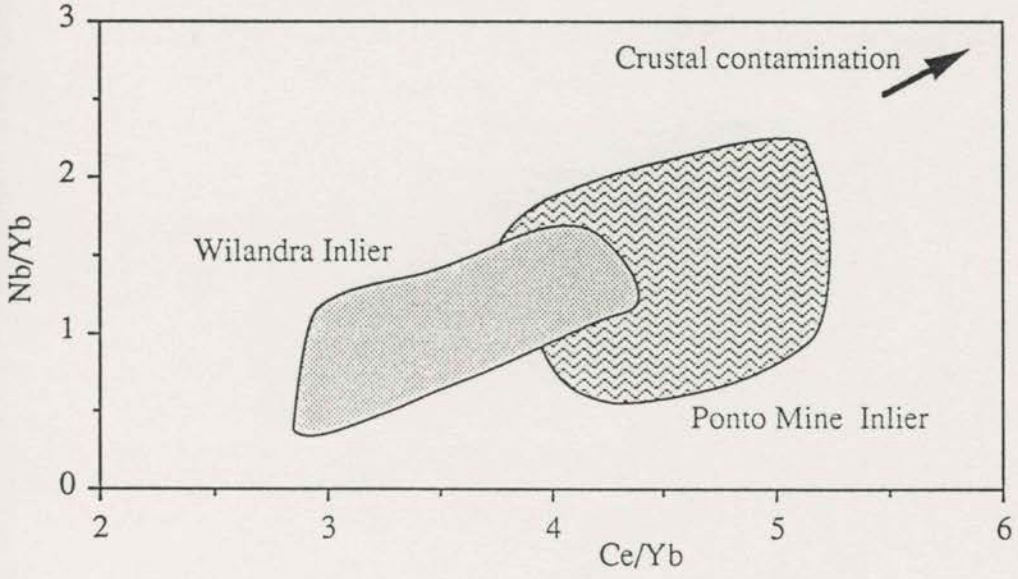

Fig.8.2.8. Ce/Yb versus Nb/Yb plot of basement mafic samples in the Wonominta Block. This diagram shows that samples from the Ponto Mine Inlier have higher Ce/Yb ratio, which may indicate moreinvolvement of crustal materials than those from Wilandra Inlier, following Lightfoot & Naldrett (1989).

Chapter 9

Rb/Sr, Sm/Nd and U-Pb Isotope Studies

9.1. INTRODUCTION

The isotope study in the present project has been to provide both geochronological and petrogenetic constraints of the mafic rocks in order to achieve a better understanding of the evolution of mafic magmatism in the Wonominta Block. The Sm/Nd, Rb/Sr and U-Pb isotope systematics were used in the geochronological study. As a relatively new means of geochronological method, Sm/Nd technique has had significant development over the last two decades particularly for rocks that have experienced multiple metamorphism. Principally, ^{147}Sm decays exponentially to ^{143}Nd by an α-process as a radioactive isotope, thus, like other radioactive systems used in geochronology, there is an equation:

$$[^{143}Nd/^{144}Nd]_t = [^{147}Sm/^{144}Nd]_t(e^{\lambda t} -1) + [^{143}Nd/^{144}Nd]_0 \qquad (9.1)$$

where λ is the decay constant ($\lambda = 6.54 \times 10^{-12}$ year^{-1}), "0" refer to the initial state and "t" the present state, also the age of the radiometric decaying processes. Based upon this isochron equation, ages of rocks can be calculated either using bulk-rocks or mineral separates, though the latter can normally yield more precise ages (DePaolo, 1988). One of the major limitations of this system is its low decay constant, which means limited application to Phanerozoic rocks. Thus, although there were some applications on Phanerozoic rocks (*e.g.* Griffin & Bruckner, 1978; Jacobsen & Wasserburg, 1979; McCulloch *et al.*, 1980), the Nd/Sm system has been largely used for Precambrian rocks. Recently, the U-Pb zircon analysis by ion microprobe (Compston *et al.*, 1984, 1992) have achieved such a great success that it has replaced the Nd/Sm technique in many geological applications. In contrast, the Rb/Sr system has very limited significance, as shown below, for the metamorphosed rocks.

The petrogenetic studies using Nd/Sm and Rb/Sr isotope systematics in the present project concentrate largely on the characterisation of mantle sources and on identification of influences of magmatic versus secondary processes in the observed present-day isotope compositions. The commencement of the use of Nd isotope techniques in petrogenetic studies occurred when the correlations between Sm/Nd and Rb/Sr in many oceanic rocks were discovered (DePaolo & Wasserburg, 1976a;

O'Nions *et al.*, 1977). As shown in Figure 9.1.1, most oceanic basalts plot along a line, named the Mantle Array (DePaolo & Wasserburg, 1976a), where MORBs plot on the upper left hand corner on the $^{143}Nd/^{144}Nd$ vs $^{87}Sr/^{86}Sr$ plot, whereas the continental rocks are on the other end with with large variations. When rocks are altered, their $^{143}Nd/^{144}Nd$ ratios may not be changed but $^{87}Sr/^{86}Sr$ will be raised. This pattern established a cornerstone for characterisation of source environment for various mafic rocks. With more isotopic studies, many of the mafic rocks have been recognised to have Nd-Sr isotope compositions away from the mantle array and many proposals have been suggested (*cf.* Worner *et al.*, 1986.). It now has been widely recognised that characterisation in terms of two component mixing (mantle source vs crust) cannot account for the various and complicated compositions observed in nature; thus models involving multiple source components have been developed. One of the mostly acknowledged models, involving four end members, was proposed by Zindler and Hart (1986). Quantitative modelling of the mixing ideas has also been developed (Schilling, 1991).

The Nd/Sm isotopic studies have also played an important role in the investigation of the secular evolution of the earth's history. Initially, it was recognised that most of the initial Nd isotope ratios of Archaean rocks were very similar to the chondritic reservoir (CHUR) at the time of their formation (DePaolo & Wasserburg ,1976a, b; Hamilton *et al.*, 1977, 1979a, b). In contrast, the younger rocks exhibit significant variations in initial $^{143}Nd/^{144}Nd$ ratios (Jacobsen & Wasserburg, 1979; Allegré & Othman,1980), and in general mantle-derived rocks tend to have higher ratios than CHUR, implying that their source had a higher Sm/Nd ratio (*i.e.* depleted); whereas crustal rocks have lower Sm/Nd ratios. Thus, DePaolo and Wasserburg (1976b) proposed the concept of Model Nd (T^{Nd}) ages as an expression of how long the crustal terranes may have had their materials separated from the mantle sources (see Appendix 8).

Applying these isotope techniques, various samples have been selected from the Wonominta Block (Table 9.1.1) to study the history of mafic magmatism. Most of the basement samples selected are of intrusive origin for obvious reasons of less alteration than the volcanics (*cf.* Chapters 5); in contrast, volcanic rocks were selected for the younger sequences (both late Proterozoic at Packsaddle and Nundora, and Early Cambrian at Mt. Wright). One xenolith was also selected from Packsaddle. One mica schist from Cymbric Vale is selected to represent the local "crustal component". One felsic tuff from Mt. Wright was selected to carry out the U-Pb dating work on zircons. And the sulphide samples from two drill cores from the Grasmere Prospect within the basement sequence are for Pb isotope studies.

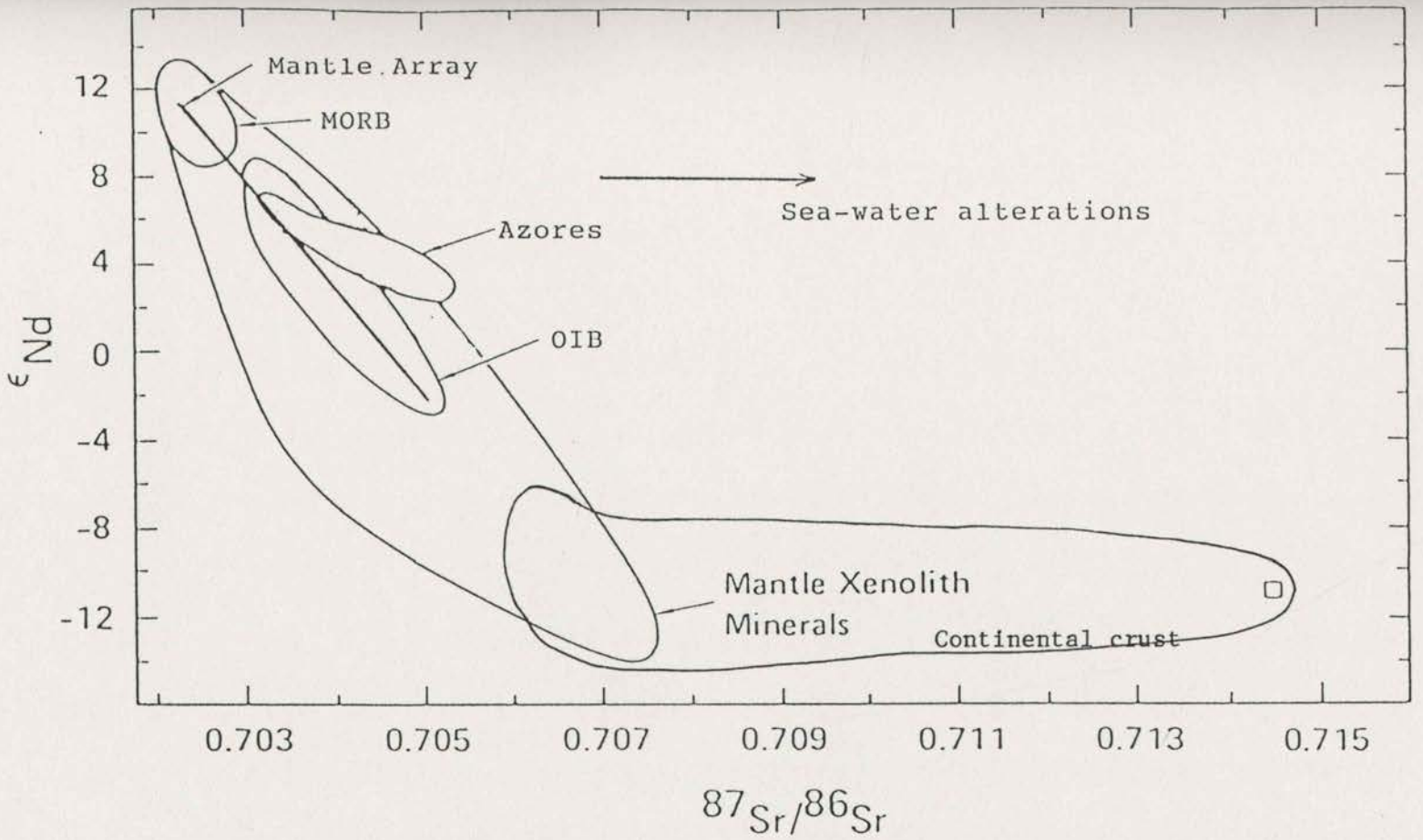

Fig. 9.1.1. Neodymium and strontium isotopic co-variation of typical oceanic basalts and mantle xenoliths, and trend of alteration on strontium isotope compositions. (After O'Nions et al.,1977)

Table 9.1.1. Sample Selection for Isotope Studies				
sequence area	sample	sample description	isotope analysed	method
	752001	metadolerite (II)	Sr-Nd-Sm	bulk rock
Ponto Mine	752302	metadolerite (II)	Sr-Nd-Sm	bulk rock
	753001	MB (massive)	Sr-Nd-Sm	bulk rock
	760402	metadolerite (III)	Sr-Nd-Sm	bulk rock
Boshy	762501	metadolerite (II)	Sr-Nd-Sm	bulk rock
Tank	762705	metadolerite (I)	Sr-Nd-Sm	bulk rock
basement				
	861209	felsic tuff	Sr-Nd-Sm	bulk rock
	861211	metadolerite (II)	Sr-Nd-Sm	bulk rock
Wilandra	861314	metadolerite (I)	Sr-Nd-Sm	bulk rock
	861713	amphibolite	Sr-Nd-Sm	bulk rock
Cymbric	861909	metadolerite (II)	Sr-Nd-Sm	bulk rock
Vale	861913	mica schist *		bulk rock
	861915	amphibolite	Sr-Nd-Sm	bulk rock
Grasmere	GR1	metasediment	Pb	mineral separates
	GR2	metasediment	Pb	mineral separates
	760801	metadolerite (I)	Sr-Nd-Sm	bulk rock
Packsaddle	760805	metabasite (massive)	Sr-Nd-Sm	bulk rock
	760806	metabasite (massive)	Sr-Nd-Sm	bulk rock
late	761301	metabasite(pillow lava)	Sr-Nd-Sm	bulk rock
Proterozoic				
Nundora	761503	metabasite (massive)	Sr-Nd-Sm	bulk rock
	761809	metabasite (massive)	Sr-Nd-Sm	bulk rock
	761901	metabasite (massive)	Sr-Nd-Sm	bulk rock
Ponto Mine	752110	metadolerite (I)	Sr-Nd-Sm	bulk rock
Cambrian	862107	felsic tuff	U-Th-Pb	zircons
	862112	metabasalt (massive)	Sr-Nd-Sm	bulk rock
	862205	metabasalt (massive)	Sr-Nd-Sm	bulk rock
Mt. Wright	862221	trachyandesite	Sr-Nd-Sm	bulk rock
	862225	metabasalt (massive)	Sr-Nd-Sm	bulk rock
	862402	metabasalt (massive)	Sr-Nd-Sm	bulk rock

* Subsequent analyses of further sedimentary rocks from the basement have revealed similar Nd/Sm isotope compositions to the sample, particularly the T_{DM} ages, ranging from 1760 – 1860 Ma

9.2. A SHRIMP U-Pb ISOTOPIC STUDY ON ZIRCONS FROM THE FELSIC TUFFS IN THE MT. WRIGHT AREA

As a part of a collaborative study of re-evaluating the lower boundary of the Cambrian System (*e.g.* Compston *et al.*, 1992), one of the felsic tuff samples (862107) was selected from the Mt. Wright area to have zircons separated and analysed for U-Pb isotopic compositions using the SHRIMP (I) in the Research School of Earth Sciences at the Australian National University in Canberra.

Before this particular work started, thin-sections of these tuff samples had been investigated using both the optical microscope and electron microprobe. These studies revealed the common occurrence of the mineral. The characteristic textural features suggested that the zircons were probably of primary origin and not inherited from older materials, and that the crystals would be ideal for geochronological dating.

As discussed in the previous chapters, the biostratigraphy has shown that the Cymbric Vale Formation lies within the earliest Cambrian (Kruse, 1982). The combination of the primary zircons and biostratigraphic age control provides an ideal candidate for dating the Cambrian-Precambrian boundary.

In a preliminary analysis (analytical procedures are same as those described in Compston *et al.*, 1992; also in Appendix 6), the selected zircon samples were analysed for two days, which resulted in about 30 individual data sets of ratios for the standard and samples respectively. A follow-up analysis has also been carried out but a systematic difference was observed due to changes of the machine conditions. This means that the two sets of results are not comparable. A new session of analysis has been planned and the final result is still in preparation (Claoué-Long *et al.*, in preparation). Although the mean age is not expected to change significantly, the quoted analytical precision does.

The preliminary result is presented in Figure 9.2.1. At this preliminary stage, the age is preferred to be 525 ± 8 Ma (2σ). This age provides a basis for the Nd-Sr isotopic modelling for alkaline rocks from both the Mt. Wright and Packsaddle-Nundora areas in the following sections. However, the significance of this age for the re-evaluation of the lower boundary of the Cambrian System, that is, the Cambrian-Precambrian boundary should be at 530 - 540 Ma rather than 570 Ma (Compston *et al.*, 1992), is beyond the scope of this project .

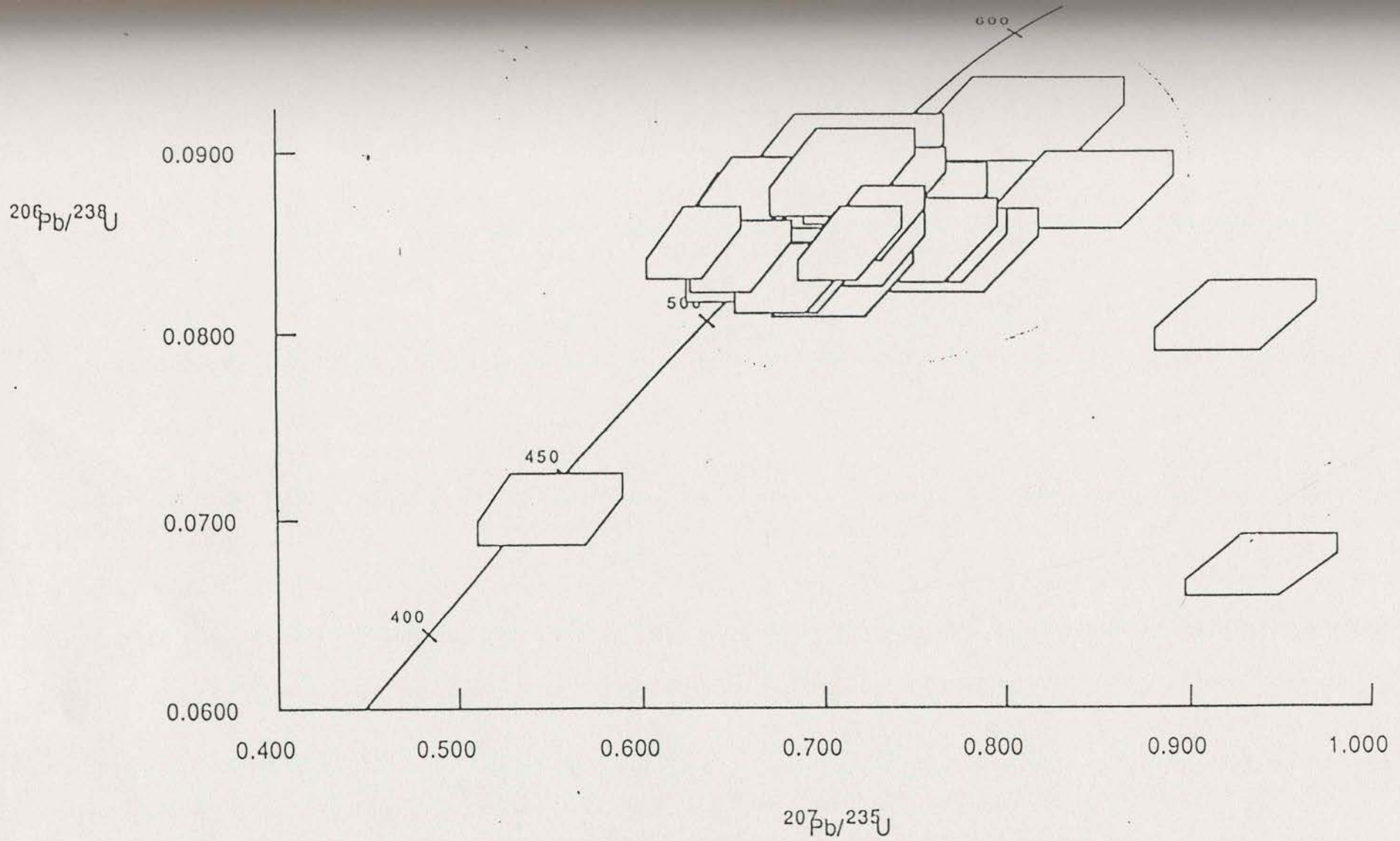

Fig. 9.2.1. $^{207}Pb/^{235}U$ vs $^{206}Pb/^{238}U$ plot of the SHRIMP zircon analysis. This sample was selected from a felsic tuff in the Mt. Wright area. The preliminary results yielded a date of 525 ± 8 Ma (2σ), which is believed to be the emplacement age.

9.3. Sr-Rb ISOTOPE CHARACTERISTICS

9.3.1. Data Presentation

The Sr-Rb isotope analyses of the selected samples from the Wonominta Block are presented in Table 9.3.1. In this table, the Rb/Sr isotopic ratios are calculated from the XRF Rb and Sr analyses (*cf.* Chapters 5 to 7). The precision of the results should be better than 5% (Norrish & Chappell, 1975), though for some low Rb samples, the error may be higher. The $^{87}Sr/^{86}Sr$ ratios are determined from the direct machine measurement, corrected for mass fractionation to $^{86}Sr/^{88}Sr = 0.1194$, and the external precision is obtained from repeated analysis of the NBS SRM 987 standard, quoted as $^{87}Sr/^{86}Sr = 0.710247 \pm 0.000015$ (N=24) during the period of analysis (see also Appendix 6).

9.3.2. The Results

The results of the Rb/Sr isotopic analyses in Table 9.3.1 clearly show that samples from different sequences of the Wonominta Beds have distinctive Sr isotopic compositions.

9.3.2.1. The Basement Sequence

The Rb/Sr isotopic compositions of the basement samples is shown in Figure 9.3.1. It is obvious from this diagram that the mafic samples display wide ranges in both $^{87}Sr/^{86}Sr$ and $^{87}Rb/^{86}Sr$ ratios. The felsic rock from Wilandra (861209) has the second lowest $^{87}Sr/^{86}Sr$ ratio of 0.70557 and $^{87}Rb/^{86}Sr$ ratio of 0.0778.

Three out of the four Ponto Mine samples have $^{87}Sr/^{86}Sr$ ratios about 0.711 with various $^{87}Rb/^{86}Sr$ ratio from 0.137 to 0.397. The fourth one, a metadolerite (III) (760402), shows a low $^{87}Sr/^{86}Sr$ of 0.7056 and a $^{87}Rb/^{86}Sr$ of 0.172. The two dyke samples from Boshy Tank show various $^{87}Sr/^{86}Sr$ ratios (0.7071 and 0.7119 respectively) at high $^{87}Rb/^{86}Sr$ levels (0.330 to 0.435). The three Cymbric Vale samples show large variation in both $^{87}Sr/^{86}Sr$ and $^{87}Rb/^{86}Sr$ values, from low (0.7037 vs 0.0755) to high (0.7194 vs 0.652) respectively. The two dyke samples from Wilandra have intermediate $^{87}Sr/^{86}Sr$ ratios of 0.7085 and 0.7094.

Table 9.3.1. Sr isotope analysis of selected samples from the Wonominta Block						
Locality	sample	87Sr/86Sr±2sigma%	Sr	Rb	87Rb/86Sr	[87Sr/86Sr]t
	752001	0.711168 ± 0.0012	308	15	0.137	0.7084
Ponto	752302	0.711651 ± 0.0012	265	15	0.160	0.7084
Mine	753001	0.711581 ± 0.0014	263	37	0.397	0.7036
	760402	0.705581 ± 0.0012	195	12	0.172	0.7021
Boshy	762501	0.707181 ± 0.0014	103	16	0.435	0.6985
Tank	762705	0.711973 ± 0.0014	214	25	0.330	0.7054
Wilandra	861209	0.705571 ± 0.0058	108	3	0.0778	0.7040
	861211	0.708503 ± 0.0016	116	6	0.145	0.7056
	861314	0.709395 ± 0.0014	193	11	0.159	0.7062
	861713	0.703726 ± 0.0014	111	3	0.0755	0.7022
Cymbric	861909	0.719416 ± 0.0014	350	80	0.652	0.7063
Vale	861913	0.792069 ± 0.0378	38	132	10.9	-
	861915	0.706045 ± 0.0014	111	8	0.202	0.7020
	760801	0.703843 ± 0.0012	1280	22	0.0480	0.7035
Packsaddle	760805	0.704298 ± 0.0012	407	13	0.0892	0.7036
	760806	0.704051 ± 0.0014	208	8	0.107	0.7037
	761301	0.705531 ± 0.0014	355	33	0.260	0.7035
Nundora	761503	0.703923 ± 0.0010	450	16	0.0993	0.7031
	761809	0.704134 ± 0.0012	506	34	0.188	0.7027
	761901	0.704483 ± 0.0016	814	51	0.175	0.7031
	862112	0.704482 ± 0.0016	77	2	0.0726	0.7039
Mt. Wright	862205	0.705920 ± 0.0012	219	5	0.0639	0.7054
	862221	0.705267 ± 0.0014	119	8	0.188	0.7038
	862225	0.703946 ± 0.0014	323	10	0.0865	0.7035
	862402	0.704452 ± 0.0016	203	4	0.0551	0.7038
Ponto Mine	752110	0.710356 ± 0.0012	449	14	0.0879	0.7091

Note: The 87Rb/86Sr ratios are calculated from the XRF Sr and Rb data in ppm,
The initial ratios are calculated to 1400 Ma for basement samples,
and 525 Ma for the others, except for sample 752110, calculated to 500 Ma.

This compositional distribution suggests that the Rb/Sr isotopic variations do not show correlation with their occurrences.

Out of the dispersive distributions, a "best-fit" regression line yields an "errorchron" of 1.89 ± 0.11 Ga (MSWD = 3.1) with a initial ratio of 0.7015 ± 0.0002. However, this is not considered to have any geochronological significance, though the regression indicates possibly low initial ratio(s).

Alterations during regional metamorphism could be one of the major reasons for the dispersive Rb/Sr isotopic compositions. The alterations would also be expected to be responsible for some unreal initial $^{87}Sr/^{86}Sr$ ratios of samples, such as 0.698 of sample 762705 (calculated to 1.4 Ga).

9.3.2.2 The Younger Sequences

The Rb/Sr isotopic compositions of the selected samples from the Late Proterozoic Packsaddle-Nundora sequence and Early Cambrian Mt. Wright sequence are shown in Figure 9.3.2. In general, the samples have lower $^{87}Sr/^{86}Sr$ ratios and relatively low $^{87}Rb/^{86}Sr$ values compared with those in the basement.

In the Late Proterozoic sequence, the xenolith from Packsaddle has a $^{87}Sr/^{86}Sr$ ratio of 0.7038 and $^{87}Rb/^{86}Sr$ ratios of 0.048, which is at the lower end of the range of volcanic rocks. The Nundora samples have very limited variation of $^{87}Sr/^{86}Sr$ ratio from 0.7040 to 0.7044, though $^{87}Rb/^{86}Sr$ ranges from 0.099 to 0.188. The Mt. Wright samples show slightly larger $^{87}Sr/^{86}Sr$ variation, from 0.7039 to 0.7059, but generally with low $^{87}Rb/^{86}Sr$ ratios (less than 0.1). Of particular interest is that the trachytic sample (862221) does show a higher ratio, but comparable to the basalts. This would be in agreement with the observation that the intermediate samples were products of fractionation of basaltic magmas.

The Cambrian dolerite (752110) from the Ponto Mine area, has a $^{87}Sr/^{86}Sr$ ratio of 0.7104 and $^{87}Rb/^{86}Sr$ ratio of 0.088, higher than those in the Mt. Wright area. The $^{87}Sr/^{86}Sr$ value is actually comparable to the average basement samples but the $^{87}Rb/^{86}Sr$ ratio is lower.

The best fit regression yielded an apparent age of 540 ± 80 Ma (MSWD = 4.3; initial ratio = 0.7034 ± 0.0001). Again, the regression does not have real geochronological significance due to unacceptable errors.

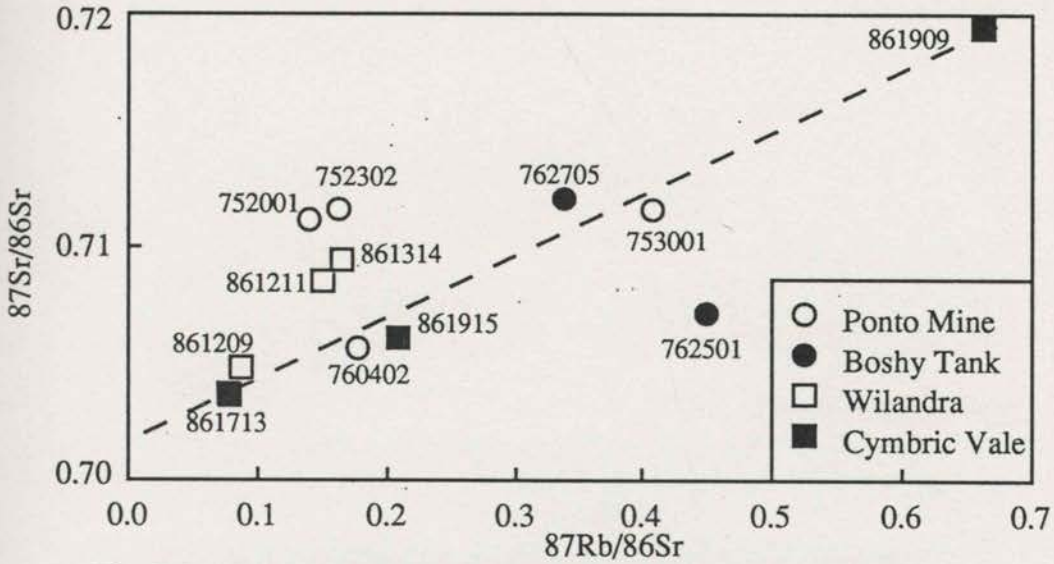

Fig. 9.3.1. Rb/Sr isotope compositions of the basement samples in the Wonominta Block. The best fit regression line of the samples yields an apparent age of 1890 ± 110 Ma with MSWD = 3.1 and initial 87Sr/86Sr ratio = 0.7015 ± 0.0002. But this age probably does not have any significance.

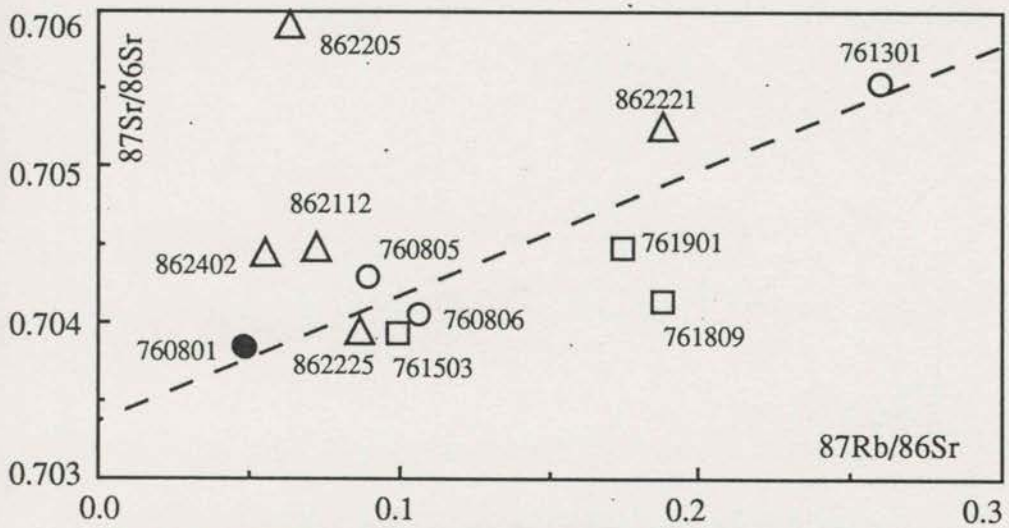

Fig. 9.3.2. Sr/Rb isotope compositions of samples from the late Proterozoic and Cambrian sequences. Circles, Packsaddle, with the xenoliths as filled symbols; squares, Nundora; triangles, Mt. Wright. The best fit regression line of the samples yielded an apparent age about 500 Ma, which might suggest that alteration of the systematics occurred mainly during the Delamerian Orogeny.

9.3.3. Discussion

The scattered Rb/Sr isotopic compositions presented here convincingly indicate that alterations had occurred to the Rb/Sr isotopic system. Since the metamorphic domain, within which the metamorphic equilibrium was achieved, was rather small as discussed in Chapter 3, the redistribution of Rb/Sr in the rocks might have been quite heterogeneous.

Nonetheless, regression exercises for both the basement and younger samples revealed low initial $^{87}Sr/^{86}Sr$ ratios, about 0.7015 for the basement rocks and 0.7030 for the alkaline basalts. This would suggest that the source of the magmas had been mantle-derived with insignificant crustal contribution. Since the alteration process would have resulted normally in higher $^{87}Sr/^{86}Sr$ ratios (O'Nions, *et al.*, 1977), this characteristic composition would suggest that the secondary processes had relatively limited influence on the primary magmatic Sr isotopic systematics, in a sense that the low initial ratio can still be recognised; but the influence of alteration is still large enough to produce errorchrons rather than isochrons. It is also clear from the above discussion that the secondary processes have had more influence on the Mt. Wright samples than on the Packsaddle-Nundora samples. This conclusion is the same as that from geochemical studies (*cf.* Chapter 6 & 7).

The ca. 500 Ma age from the regression for the alkaline basalts is in agreement with the age of the Delamerian Orogeny (*cf.* Chapter 2), a tectonic movement that would have resulted in the alteration of the Rb/Sr system. Again, the large errors of the regression means this is not the result that a conclusion can be built on.

And the Sr isotope results support the observation that the intermediate rocks in the Mt. Wright area represent products of basaltic magmas that formed the mafic sequence as they shared similar initial $^{87}Sr/^{86}Sr$ ratio(s).

9.4. Nd ISOTOPE CHARACTERISTICS

9.4.1. Data Presentation

The Nd/Sm isotope analysis is presented in Table 9.4.1.

The $^{143}Nd/^{144}Nd$ values are normalised to $^{146}Nd/^{144}Nd = 0.7219$ for the mass fractionation correction. And during the period of the present project, the CIT Nd standard is quoted as $^{143}Nd/^{144}Nd = 0.511894 \pm 0.000010$ (N=16). As shown in Table 9.4.1, the internal precision of individual machine run is generally better than the quoted external precision (see also Appendix 6).

The replicate analyses of real samples yielded an average error of 0.0020%, identical to the quoted precision of machine runs. This indicates, as for the Sr analysis, that the contribution from chemical processes to the analytical error is insignificant compared with that from machine runs.

9.4.2. The Results

The Nd/Sm isotope compositions, as shown in Table 9.4.1, display rather limited variations for each group of samples. For example, the Late Proterozoic and Early Cambrian samples have very similar Nd/Sm isotopic compositions within the quoted analytical precision. The significance of this observation is discussed further in the following sections.

9.4.2.1. Geochronological regression of basement samples

Although the mafic samples from various localities in the basement display limited variations in their $^{143}Nd/^{144}Nd$ composition, the sole felsic rock from Wilandra provided a crucial point for the regression analysis

In order to use the felsic sample for the regression, two presumptions have to be verified. Firstly, the rocks had to be formed contemporaneously and, secondly, they had the same initial $^{143}Nd/^{144}Nd$. Geological occurrence (*cf.* Chapter 3) suggests the first presumption is possibly true; and the low initial Sr isotope compositions and

Table 9.4.1. Nd/Sm isotope analyses of selected samples from the Wonominta Block.

sequence	locality	sample	143Nd/144Nd ± 2σm% present	initial	147Sm/144Nd	Nd ppm	Sm ppm	Epsilon (Nd) present	initial
Basement	Ponto Mine	752001	0.512898 ± 0.0012	0.51074	0.1992	6.92	2.28	5.1	4.6
		752302	0.512886 ± 0.0020	0.51076	0.1956	6.31	2.04	4.8	5.1
		753001	0.513008 ± 0.0018	0.51089	0.1955	5.02	1.63	7.2	7.5
		760402	0.513020 ± 0.0014	0.51097	0.1886	4.85	1.54	7.5	8.9
	Boshy Tank	762501	0.513100 ± 0.0016	0.51077	0.2143	9.13	3.23	9.0	5.9
		762705	0.513009 ± 0.0014	0.51075	0.2040	7.32	2.90	6.3	5.1
	Wilandra	861209	0.512600 ± 0.0016	0.51096	0.1507	43.0	10.7	-0.7	7.5
		861211	0.513067 ± 0.0018	0.51102	0.2041	16.1	5.16	8.4	7.1
		861314	0.512836 ± 0.0014	0.51079	0.1890	14.3	4.49	3.7	5.3
	Cymbric Vale	861713	0.513047 ± 0.0014	0.51088	0.2057	8.09	2.75	9.2	7.6
		861909	0.512843 ± 0.0016	0.51107	0.1924	10.9	3.48	10.2	4.8
		861913	0.511830 ± 0.0016	-	0.1155	13.5	2.57	-15.8	-1.2
		861915	0.513089 ± 0.0016	0.51081	0.2104	8.47	2.95	8.8	6.4
Late Proterozoic	Packsaddle	760801	0.512853 ± 0.0020	0.51234	0.1482	10.5	2.58	4.1	7.7
		760805	0.512792 ± 0.0010	0.51235	0.1286	27.5	5.85	3.0	4.6
		760806	0.512616 ± 0.0016	0.51221	0.1347	31.5	7.02	0.7	4.8
		761301	0.512661 ± 0.0014	0.51220	0.1331	36.8	8.11	0.5	4.7
	Nundora	761503	0.512672 ± 0.0014	0.51221	0.1353	29.3	6.55	0.7	4.8
		761809	0.512712 ± 0.0012	0.51227	0.1286	40.4	8.59	1.4	5.0
		761901	0.512583 ± 0.0016	0.51215	0.1263	51.2	10.7	-1.1	4.3
Cambrian	Mt. Wright	862112	0.512707 ± 0.0014	0.51221	0.1444	18.7	4.47	1.4	4.9
		862205	0.512580 ± 0.0014	0.51215	0.1251	35.6	7.36	-1.1	4.4
		862221	0.512666 ± 0.0016	0.51221	0.1336	58.2	12.9	0.6	4.8
		862225	0.512668 ± 0.0018	0.51221	0.1329	10.9	2.39	0.6	4.9
		862402	0.512672 ± 0.0016	0.51222	0.1306	37.0	7.99	0.7	5.1
	Ponto Tank	752110	0.512776 ± 0.0014	0.51225	0.1604	14.2	3.76	2.3	5.0

Note: The 143Nd/144Nd ratio is normalised to 146Nd/144Nd = 0.7219
The initial values are calculated to 1400 Ma for basement samples, 525 Ma for younger ones, except 752110, to 500 Ma.

positive $\varepsilon_{Nd}(T)$ value of the felsic sample indicate the second presumption is also likely real.

The result of this regression (Figure 9.4.1) yields an isochron of 1.40 ± 0.24 Ga (MSWD = 0.9), with an initial ratio of 0.5112 ± 0.0003. Statistically, the regression is significant since the MSWD is less than unity, given the particular analytical precision. Therefore, this result may be used to estimate the magmatic age of the formation of these igneous rocks.

However, the mean of this age is at least 200 Ma younger than the stratigraphic age (ca. 1600 Ma), postulated from geological correlations (Mills, 1992). The large error of the isochron indicates that the true age of the rocks may lie anywhere between 1640 Ma to 1160 Ma, and this range include the geological age of 1600 Ma. Thus, both ages can be considered as identical within the particular analytical precision.

The youngers samples show rather limited variations (Figure 9.4.2) and no geochronological significance can be attached.

9.4.2.2. Variation of $\varepsilon_{Nd}(T)$ Values

The initial ε_{Nd} values of the selected samples are shown in Table 9.4.1. They are calculated to 1400 Ma for the basement samples, 525 Ma for the younger samples, except the dolerite from Ponto Mine calculated to 500 Ma.

For the basement samples, there appears to be two groups of $\varepsilon_{Nd}(T)$ values; the lower around +5, and the higher around +8. The higher $\varepsilon_{Nd}(T)$ group includes 753001 and 760402 from Ponto Mine, 861209 and 861211 from Wilandra and 861713 from Cymbric Vale.

The felsic tuff sample from Wilandra (861209) in the basement sequence has a high $\varepsilon_{Nd}(T)$ value of 7.5. In contrast, the mica schist (861913) from Cymbric Vale, has a negative $\varepsilon_{Nd}(T)$ value of -1.2.

The younger mafic samples from both Late Proterozoic and Early Cambrian sequences display much more consistent $\varepsilon_{Nd}(T)$ values around 4.7±0.4 for volcanics and 7.7 for xenolith (760801).

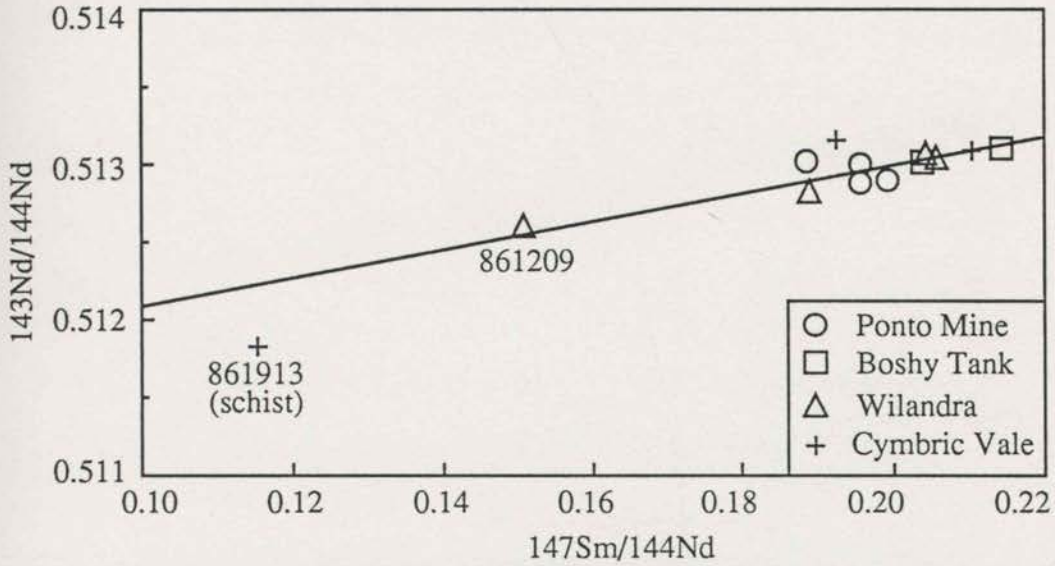

Fig. 9.4.1. Nd/Sm isotope compositions of the basement samples in the Wonominta Block. The regression through the mafic and felsic rocks yielded an age of 1.40 ± 0.24 Ga (MSWD = 0.9) with initial 143Nd/144Nd ratio = 0.5112 ± 0.0003

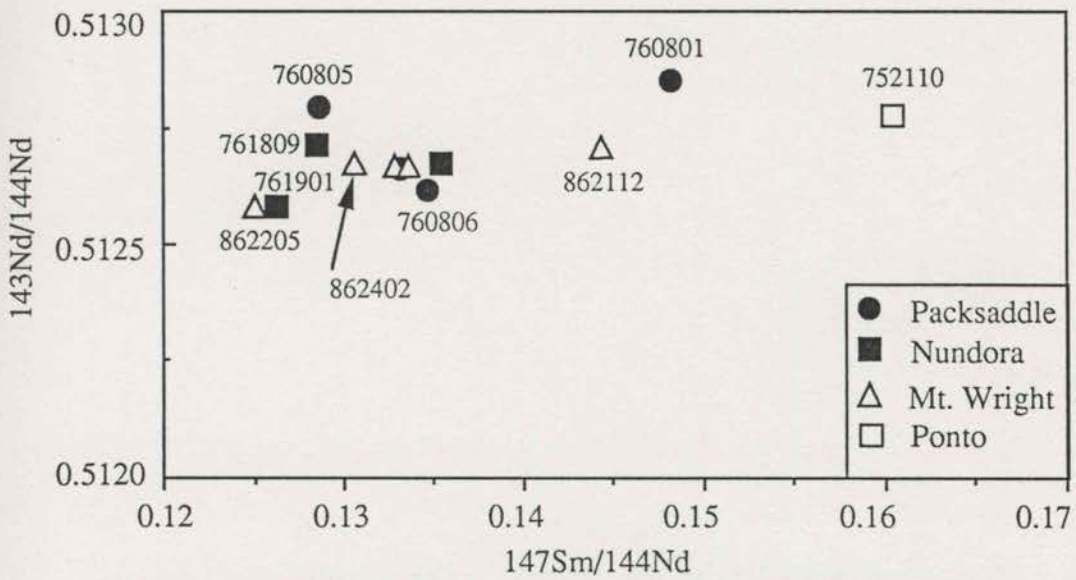

Fig. 9.4.2. Nd/Sm isotope compositions of the mafic samples from the late Proterozoic (filled symbols) and Cambrian (open symbols) sequences in the Wonominta Block.

The Cambrian dolerite from the Ponto Mine area (752110) has an $\varepsilon_{Nd}(T)$ value of 5.0. This value matches that of the alkaline basalts, as well as the lower $\varepsilon_{Nd}(T)$ group.of the basement samples.

The observed Nd/Sm isotopic compositions indicate that there is no systematic variation for the mafic rocks from different areas in all sequences.

The high $\varepsilon_{Nd}(T)$ of the felsic rock suggests it should have been the product of magmas derived from a depleted mantle without significant crustal contribution.

Since schist rocks normally would have had a fine-grained sedimentary precursor, such as shales, before metamorphism, and shales are usually ideal for estimating average crustal compositions (Taylor & McLennan, 1985), the schist sample from Cymbric Vale is used here to estimate the initial Nd isotope composition of the local crustal materials at the time of deposition in the Wonominta Block.

9.4.3. Discussion.

The Sm-Nd isotope compositions of various samples in the Wonominta Block provide several geochronological and petrogenetic constraints on the evolution of the region.

Firstly, the regression of the basement samples yielded an isochron of 1.4 ± 0.24 Ga. This age, although imprecise, is the first quantitative control of the basement sequence of the Wonominta Block. Although the age may be younger than that of the Broken Hill Group (1670-1690 Ma; Page & Laing 1990), the two sequences can still be roughly compared. It is definitely a pre-Adelaidean age (*i.e.*, older than 1000 Ma; Preiss, 1987), confirming the basement features of the oldest part of the Wonominta Beds.

And secondly, the positive $\varepsilon_{Nd}(T)$ values suggest that they have been derived from depleted upper mantle source(s) with limited crustal contamination, but the range of the ratio (4.6 - 8.9) also appear to suggest firstly the presence of different mantle sources, and secondly the crustal contamination during magmatism as further discussed below.

9.4.3.1. Model Ages (DM) of the Crustal Rocks.

Depleted mantle (DM) model ages (T_{DM}) (DePaolo, 1981a) represent the average residential age of the source materials of a particular crustal terrane. In other words, for a particular crustal terrane, T_{DM} provides a means of measurement of when the source materials for the formation of the terrane were separated from the upper mantle. Therefore, it is useful to investigate the relationship between different crustal terranes.

The representative crustal rock of the Wonominta Block used in the present project is sample 861913, a mica schist from Cymbric Vale. This rock has a model age of 1820 Ma using the formula by McCulloch (1987). This model age is about 500 Ma younger than those of the felsic gneisses in the Broken Hill Block, which have model age about 2300 Ma (*cf.* McCulloch, 1987). This age difference means that the two crustal blocks may have very different source materials, or different proportions of the same source materials, that is the Wonominta Block might have had a more juvenile sediments than the Broken Hill Block. In either case, the two blocks should have been in different environments if a contemporaneous relationship is claimed. One other possible scenario would be that the Willyama Complex had been formed in different parts of a tectonic region, where the Broken Hill Block received its sediments mostly from cratonic basement sources whereas the Wonominta Block received its source materials from much younger terranes. However, it is fully acknowledged that such correlations and reconstruction based on one sample must be tentative, more analyses of representative crustal samples are needed to substantiate or to modify the observations here.

9.5. Sr - Nd ISOTOPE SYSTEMATICS OF BASEMENT THOLEIITIC ROCKS & PETROGENETIC IMPLICATIONS

9.5.1 Sr-Nd Isotopic systematics

Figure 9.5.1 presents the plot of initial $^{87}Sr/^{86}Sr$ against $\varepsilon_{Nd(T)}$ values of the basement samples. This diagram clearly shows a correlation of the two isotopic parameters; that when initial $^{87}Sr/^{86}Sr$ ratios increase, $\varepsilon_{Nd(T)}$ of the samples decrease correspondingly.

However, there are two samples that display distinctive compositional features . Sample 762501 has an initial $^{87}Sr/^{86}Sr$ ratio of 0.6985, much too low to be real for any terrestrial samples of the time. This sample is not included in the following discussions. And sample 861915 has a lower $^{87}Sr/^{86}Sr$ ratio than the main trend at the given $\varepsilon_{Nd(T)}$ levels.

In the main trend, samples from the Ponto Mine area have both the highest $\varepsilon_{Nd(T)}$ (760402) and the lowest $\varepsilon_{Nd(T)}$ values (752001). The felsic tuff sample (861209) from the Wilandra area plots in the middle of the trend. Petrogenetically, this compositional trend can be explained using mixing between magmas from depleted mantle and local crustal materials.

In Figure 9.5.2, the crustal material is represented by the mica schist (861913) from Cymbric Vale, which has $\varepsilon_{Nd(0)}$ of -15.3 and $\varepsilon_{Nd(T)}$ of -1.2 (calculated to 1.4 Ga), and this crustal material had been separated from the depleted mantle at about 1820 Ma.

At 1.4 Ga, the mafic rocks in the basement sequence have their $\varepsilon_{Nd(T)}$ values across the depleted mantle (DM) curve, with the most depleted one well above the DM curve. Thus, the highly depleted samples should have been derived from a unique mantle source (MDM). For the other samples, those with normal depleted mantle (NDM) values, in theory, could have been derived either from a NDM source, or a mixture of MDM with crustal components. And those with $\varepsilon_{Nd(T)}$ compositions lower than NDM's appear to be likely a mixture of depleted mantle (NDM or MDM) source(s) with crustal materials. As shown in Figure 9.5.3, two of the high $\varepsilon_{Nd(T)}$ samples from the Ponto Mine Inlier appear to form a mixing trend between MDM and crustal materials; whereas, those of low $\varepsilon_{Nd(T)}$ samples in the same inlier appear to for a mixing trend between NDM and crustal materials. Therefore, there may be two

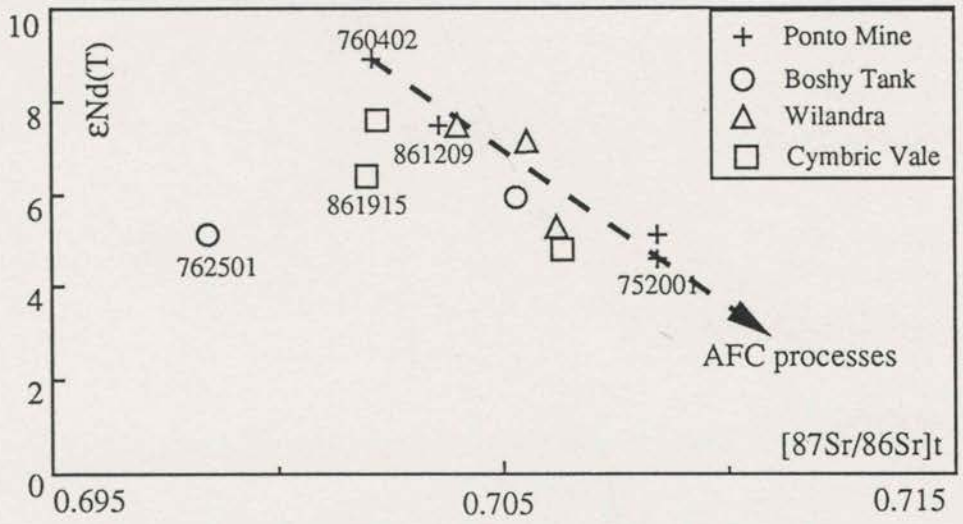

Fig. 9.5.1. Initial 87Sr/86Sr ratio against εNd(T) plot of samples from the basement sequence, showing the mixing trend of crustal contamination.

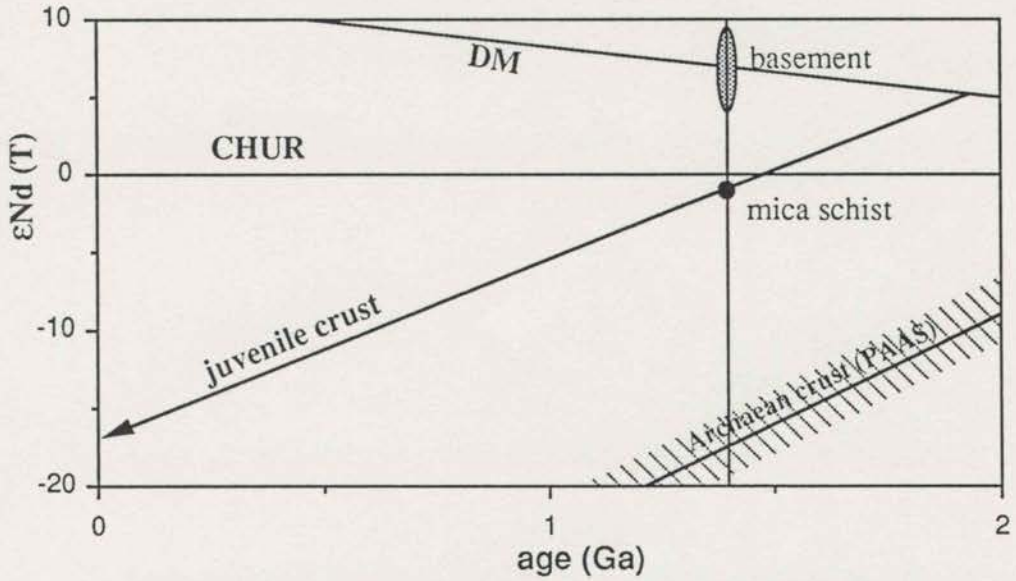

Figure. 9.5.2. The mixing model for the formation of basement samples. The model calculation shows that about 6.6% juvenile crustal materials (represented by the mica schist from Cymbric Vale) are needed to explain the observed lowest εNd(T) value of sample 752001 from Ponto Mine area. No significant Archaean crust, however, can be involved in the AFC processes to explain the observed Nd isotope character.

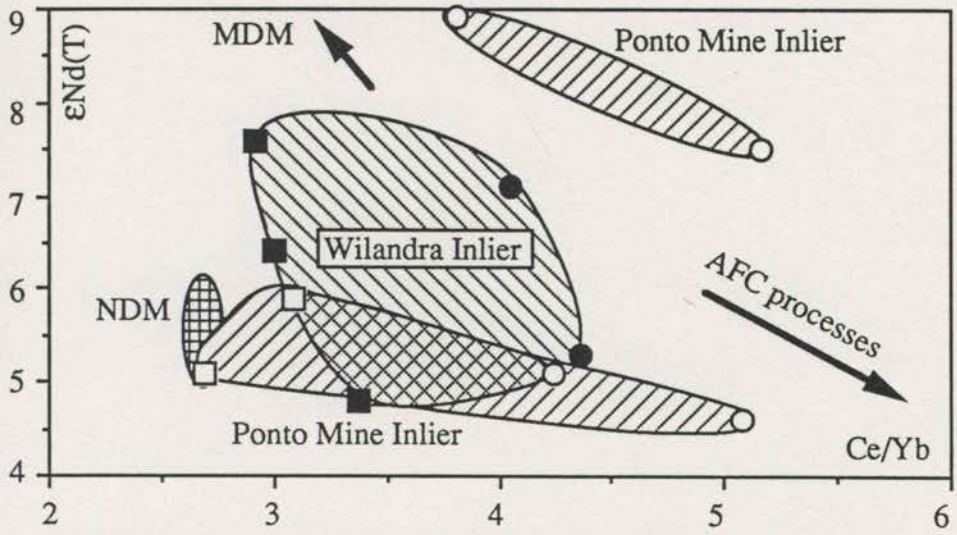

Fig.9.5.3. Ce/Yb vs εNd(T) plot of the basement samples. Open circles, Ponto Mine; filled circles, Wilandra; squares, Boshy Tank; filled squares, Cymbric Vale. This diagram shows that the observed Ce/Yb versus εNd(T) variation of the basement mafic samples cannot be explained using a simple mixing model of one upper mantle source with one crustal component; at least two distinct upper mantle sources are needed, with one being high in εNd(T) (MDM) and the other being low in εNd(T) (NDM).

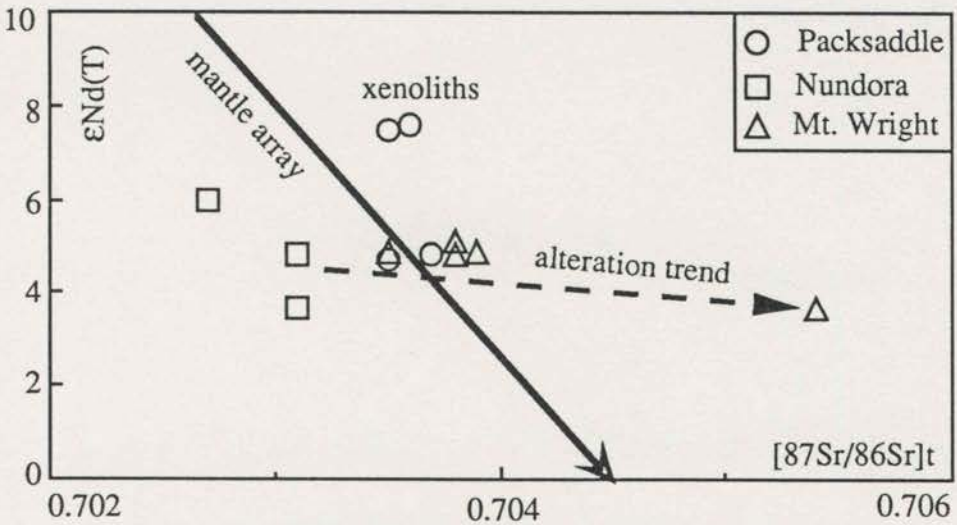

Fig.9.6.1. variation of initial 87Sr/86Sr and εNd(T) values of samples from the Late Proterozoic (Packsaddle -Nundora) sequence and the Cambrian Mt. Wright area. The mantle array is after DePaolo & Wasserburg (1976a).

different mixing processes (though both are rather simplified), and samples from the Wilandra Inlier may require all three end members, MDM, NDM and crust..

Model case one assumes that the most depleted component representing the local upper mantle source of the time had 4.85 ppm Nd and an $\varepsilon_{Nd(T)}$ of 8.9 (sample 760402). The most contaminated sample is represented by 752001, which has the least $\varepsilon_{Nd(T)}$ value of 4.6 and 6.92 ppm Nd.

Correspondingly, two model calculations are carried out to facilitate the possibility of various mixing processes. Model case one assumes a mixing between MDM and the crust, and model case two assumes that between NDM and the crust. Obviously, the crustal materials may either juvenile or old cratonic-style. Thus each model actually involves two mixing in relation to crustal end members.

Calculations of different mixing models are presented in the next two sections.

9.5.2. Quantitative Modelling One - A Simple Mixing Process

As shown in Figures 9.5.1 and 9.5.2, the observed Sm-Nd isotopic compositional variations can be explained using the simple mixing model of primary mantle-derived magmas, and crustal materials.

Following DePaolo (1988), the algebra describing the simple mixing model is given by (equation 4.4, p. 49):

$$\varepsilon_{Nd}^{m} = \{X^a[^{144}Nd]^a\varepsilon_{Nd}^{a} + (1-X^a)[^{144}Nd]^b\varepsilon_{Nd}^{b}\}/\{X^a[^{144}Nd]^a + (1-X^a)[^{144}Nd]^b \quad (9.5.1)$$

where (m) denotes the mixture of primary magma (a), and crustal materials (b), containing weight fraction of X^a and X^b (the sum of the two equals 1); the $[^{144}Nd]$ is the molar concentration of ^{144}Nd, which could be replaced by the weight concentration of total Nd with no significant loss of accuracy. Since

$$[Nd] = [142] + [143] + [144] + [145] + [146] + [148] + [150] \quad (9.5.2)$$

$$[^{144}Nd] = [Nd]/\{[142/144] + [143/144] + 1 + [145/144] + [146/144] + [148/144] + [150/144]\}$$
$$=[Nd]/\{3.68611 + [143/144]\} \quad (9.5.3)$$

From 9.5.1, X^a can be obtained by the equation:

$$X^a = \{[^{144}Nd]^b(\varepsilon_{Nd}{}^b - \varepsilon_{Nd}{}^m)\}/\{[^{144}Nd]^a(\varepsilon_{Nd}{}^m - \varepsilon_{Nd}{}^a) + [^{144}Nd]^b(\varepsilon_{Nd}{}^b - \varepsilon_{Nd}{}^m)\} \quad (9.5.4)$$

Following the discussion in section 9.5.1, for model case one,

$\varepsilon_{Nd}{}^m = 4.6$; $\varepsilon_{Nd}{}^a = 8.9$; $\varepsilon_{Nd}{}^b = -1.2$

$[^{144}Nd]^a = 4.85/(3.86811 + 0.51097) = 1.16$ (ppm)

$[^{144}Nd]^b = 13.5/(3.68611 + 0.51058) = 3.22$ (ppm)

Thus, the crustal contribution would be $1 - X^a$.

$X^a = (3.22(-1.2 - 4.6))/(1.16(4.6-8.9) + 3.22(-1.2 - 4.6))$

$= 0.79$

That is the maximum crustal contribution could have been 21%.

For model case 2,

$\varepsilon_{Nd}{}^m = 4.6$; $\varepsilon_{Nd}{}^a = 6.4$; $\varepsilon_{Nd}{}^b = -1.2$

$[^{144}Nd]^a = 8.47/(3.86811 + 0.51081) = 2.02$ (ppm)

$[^{144}Nd]^b = 13.5/(3.68611 + 0.51058) = 3.22$ (ppm)

Thus,

$X^a = (3.22(-1.2 - 4.6))/(2.02(4.6-6.4) + 3.22(-1.2 - 4.6)$

$= 0.885$

And the maximum crustal contamination using this particular model would have been 11.5%. If PAAS* is used for the modelling, the results would be less than 5% for both processes involved NDM and MDM.

*(Post-Archaean Australian shales, Taylor & McLennan, 1985)

9.5.3. Quantitative Model Two -- the AFC Process

Following this simple mixing model, the Nd elemental concentration of a mixture should fall between its two end members. However, this has not been the case for some examples in the exercise. As shown in Table 9.5.4, the Nd content in both end members (8.47 ppm for NDM (861915) and 13.5 ppm for crustal component

(861913) or 32 ppm for PAAS) of case model two are higher than that of the mixture (6.92 ppm of sample 752001, the most contaminated sample).

This observation suggests that the actual assimilation processes must have been more complicated than a simple mixing process, and involved simultaneous fractional crystallisation. In other words, the actual processes should involve both assimilation and fractional crystallisation,*i.e.*, AFC processes.

The mathematics concerned with the AFC modelling has been described by DePaolo (1981b). For the instantaneous rate of change of isotopic ratios, the differential equation can be expressed as (DePaolo, 1981b, equation 12):

$$d\varepsilon_{Nd}^{m}/dt = \mathbf{M^b/M^m}\, C^b/C^m\, (\varepsilon_{Nd}^{b} - \varepsilon_{Nd}^{m}) \qquad (9.5.5)$$

where again the (m) denotes the AFC mixture and (b) for the crustal assimilation; M for the mass of the magmas and C for the elemental concentration. The bold characters of M indicate vector variants that change instantaneously as the AFC proceeds.

Omitting all the complex transforming calculations, the results of the integration are give as:

$$\Delta\varepsilon_{Nd} = 1 - (C_m^0/C_m)F^{-z} \qquad (9.5.6)$$

where $\Delta\varepsilon_{Nd} = (\varepsilon_{Nd}^{m} - \varepsilon_{Nd}^{a})/(\varepsilon_{Nd}^{b} - \varepsilon_{Nd}^{a})$ (9.5.7)

$F = M/M_m^0$, which is equivalent to X^a in equation 9.5.1;

$Z = (r + D - 1)/(r - 1)$, $r = \mathbf{M^a/M^c}$ (9.5.8)

and D is the bulk solid/liquid partition coefficient.

For Nd, since $D << 1$ in most oceanic basaltic systems (see also discussion in Chapter 8), if the rate of assimilation is comparable to the rate of fractional crystallisation,

$Z \approx 1$, and thus

$$\Delta\varepsilon_{Nd} = 1 - (C_m^0/F \times C_m) \qquad (9.5.9)$$

From 9.5.9, it is easily obtained that:

$$F = (1 - \Delta\varepsilon_{Nd})C_m^0/C_m \qquad (9.5.10)$$

From this equation and 9.5.7, the amount of the assimilation can be calculated using the parameters presented in the last section:

For case model 1:

$$F = [1 - (4.6 - 8.9)/(-1.2 - 8.9)] (4.85/6.92) = 0.40$$

That is, a maximum of 60% of crustal contributions.

For case model 2,

$$F = [1 - (4.6 - 6.4)/(-1.2 - 6.4)] (8.47/6.92) = 0.934$$

That is, a maximum of 6.6% of crustal contamination.

As a 60% contribution of crustal materials to the formation of MORB-like rocks is geologically unlikely, the second case model with 6.6% crustal contribution, presents a much more realistic modelling. And if PAAS is used for the modelling, the results would be 42% and -13% respectively.

9.5.4. Discussion

Results of these model calculations are summarised in Table 9.5.1. These calculations provide direct constraints on the petrogenetic parameters of formation of tholeiitic rocks in the basement of the Wonominta Block.

Model (I) implies that the more depleted upper mantle source may have played a more important role than the normal DM in the formation of the most contaminated rocks; since the only region with such characteristics in a present day tectonic situation is a mantle wedge in an arc environment, a similar tectonic environment is required. In other words, the first model suggests an arc tectonic setting. In contrast, model (II) suggests the mafic rocks might have been formed in an "normal" oceanic environment, such as on a mid-ocean ridge, or in a back-arc basin, though appreciateable amount of crustal contribution in the model calculations evidently favours the latter environment.

Table 9.5.1. Model calculations of possible crustal contaminations.

	Mantle Model I (MDM)	Mantle Model II (NDM)
Simple Mixing		
with juvenile crust	*21%*	11.5%
with PAAS	6.7%	5.0%
AFC process		
with juvenile crust	*60%*	6.6%
with PAAS	*42%*	*-13%*

The simple mixing model cannot account for the observed Nd elemental abundances as discussed above, though calculations yielded reasonable results in both models. For the AFC modelling, the model involving 42-60% crustal contribution to the formation of the tholeiitic rocks is geologically unlikely, the arc model cannot be sustained by the AFC model calculations. Instead, the normal depleted mantle as the source of the rocks would require a much more realistic amount of juvenile sediments (max. 6.6%) for the observed most contaminated sample. The model calculation using PAAS compositions also yielded geologically impossible results, and this means that much of the crustal material involved in the AFC processes has to be juvenile sediments with relatively high initial ε_{Nd} compositions.

These characters favours an environment in the back-arc region, with typical "oceanic" characters yet with access of crustal materials. Although in some island arc environments (such as Java, *cf.* Vukadinovic & Nicholls, 1989), the magmas can display the observed geochemical characteristics, the AFC modelling has convincingly excluded such a possibility. The requirement of juvenile rather than old Archaean-like sediments to account for the observed Nd isotope characters means the origin of the sediments are also "oceanic", thus the emplacement of the rocks had probably been near the arc side of the basin, rather than the continental side.

Furthermore, the distinctive compositions shown in Figure 9.5.3 suggest the existence of a MDM source, though model calculation indicates the contribution cannot be significant to account for the most contaminated samples. The MDM source might have been inherited from a mantle wedge, normally in an arc environment (*e.g.* Sivell & McCulloch, 1991). In this case, if the marginal rifting had occurred along a previous subduction zone, the mantle source(s) for the formation of new magmas

would have carried some arc features The present Japan Sea could be an analogous model for the reconstruction of this particular regional tectonic setting.

In this back-arc model, the existence of a MDM component in the source regions is very similar to that recognised in central Australia in the Early Proterozoic (Sivell & McCulloch, 1991). In that case, the Nd isotope analysis was interpreted to indicate a back-arc environment in an ensialic setting, and the extremely depleted sources are suggested to represent a "fossil mantle wedge". The tectonic environment of the Wonominta region in the middle Proterozoic could have been similar to that in central Australia in the early Proterozoic.

And finally, in terms of model calculation, the important conclusion is that juvenile (with near CHUR $\varepsilon_{Nd(T)}$ values) rather than older cratonic materials are required to account for the observed most contaminated mafic rocks. This conclusion is probably irrelevant to the number of samples analysed, though more samples need to be analysed to better quantify the AFC processes.

9.6. Sr - Nd ISOTOPE SYSTEMATICS & PETROGENETIC IMPLICATIONS OF ALKALINE BASALTS

The Sr-Nd isotopic systematics of the alkaline basalt from the Packsaddle, Nundora and Mt. Wright areas are shown Figure 9.6.1.

The xenolith (760801) has higher $\varepsilon_{Nd(T)}$ values of 7.7 and low initial $^{87}Sr/^{86}Sr$ ratios of 0.7035 and plots above the volcanic rocks. Most of the basaltic samples have nearly constant $\varepsilon_{Nd(T)}$ values around 4.7 ± 0.4 and a range of initial $^{87}Sr/^{86}Sr$ ratios from 0.7031 to 0.7054.

This compositional pattern is rather distinctive from that of the basement samples, and is similar to those seen in the altered modern oceanic basalts as reviewed previously (O'Nions *et al.*, 1977). In the present case, the alteration could have occurred in either burial (*sensu lato*) or regional metamorphic processes, or both (*cf* Chapter 3).

The positive $\varepsilon_{Nd(T)}$ and low initial Sr isotope values of the alkaline basalts from both the Packsaddle-Nundora and the Mt. Wright areas indicate that they should have been derived from very similar depleted upper mantle source and there has been little crustal contribution to the magma genesis. As have been suggested from the geochemical studies (*cf.* Chapter 4), such an environment should be extensional , such as rifting, or plume-related. Furthermore, the identical $\varepsilon_{Nd(T)}$ and initial Sr isotope compositions appear to suggest that they must have been derived from very similar mantle source(s)
.

Thus, although there has been no chronological information to constrain the Late Proterozoic mafic rocks, the Nd isotope characteristics presented here strongly suggest that they should have been emplaced at a similar time to the basalts in the Mt. Wright area, *i.e.* about 525 Ma. If, as geological correlation suggested, the northern sequence had been emplaced in the Late Proterozoic, the age difference between the two sections must be small enough (<50 Ma?) for the survival of an identical upper mantle source.

The higher $\varepsilon_{Nd(T)}$ value of the xenolith suggests more depleted features, in agreement with their origin as xenoliths of the older volcanic rocks.

9.7. PRELIMINARY LEAD ISOTOPE STUDIES ON SULPHIDE SAMPLES FROM GRASMERE PROSPECT

The preliminary lead isotope studies on sulphide samples from one of the many ore bodies in the Wonominta Block were carried out to determine isotopic signatures of mineralisation in the region and to compare these with known signatures, such as those of Broken Hill. These data could be used to address problems in mineral exploration and the tectonic reconstruction of the Wonominta Block.

The sulphide samples were separated from two drill core samples (GR8 and GR9), provided by CRAE (Broken Hill) from their current drilling project at the Grasmere Prospect. The Grasmere Prospect is about 30 kilometres south of Wilandra. Geologically, the Grasmere area is located within the basement sequence and has a similar structural setting to that in the Wilandra area (Figure 1.1; Chapter Three). Although all of the small ore bodies observed on the surface during the present project are within, or closely associated with, igneous rocks of various ages, such as those at Ponto Mine, Bilpa (with mafic rocks) and Mt. Wright (felsic rocks), the sulphides from the core samples are apparently hosted by meta-greywacke.

The separated sulphides are mostly pyrite and pyrrhotite with minor chalcopyrite and sphalerite. Microscopically, pyrite shows two different textures: the coarse-grained crystals are generally cubic, while the finer-grained ones are normally allotriomorphic with patchy structures. Pyrrhotite is usually fine-grained and occurs as various allotriomorphic aggregates. In contrast, chalcopyrite occurs as interstitial phases between pyrite and pyrrhotite. Some of the chalcopyrite appears to have grown along the edge of pyrite, probably resulting from dissolution of the prior crystals. Other minor chalcopyrite is disseminated through the sediments.

These textural features suggest that there were several stages of formation of sulphides in these samples. Although the relationship between the fine- and coarse-grained pyrites is not quite clear, it appears that chalcopyrite was formed in the last stage.

The mineral separation was carried out using conventional electromagnetic methods, and most of the mineral separates used in this study have a purity better than 95%. One sample of sphalerite in a fraction of the GR9 sample was separated from chalcopyrite using a chemical method (see Appendix Six); and the influence of the chemical processing on the isotope analyses is discussed below. Analytical procedures are described in Appendix 6.

Table 9.7.1 is a compilation of the lead isotopic analysis. The lead abundances in these sulphides have a relatively limited range from 24 to 64 ppm, and it appears that high Pb samples have lower $^{206}Pb/^{204}Pb$ ratios.

The results of isotope variations are shown in Figures 9.7.1 and 9.7.2. Figure 9.7.1 shows that the sulphides have a range in $^{206}Pb/^{204}Pb$ from 17.71 to 18.62, but relatively constant ratios of both $^{208}Pb/^{204}Pb$ (37.22-37.51) and $^{207}Pb/^{204}Pb$ (15.45-15.52) except for sphalerite, which has higher $^{208}Pb/^{204}Pb$ (37.92) and $^{207}Pb/^{204}Pb$ (15.59) than the others.

A number of pyrite and pyrrhotite separates have compositions around $^{206}Pb/^{204}Pb$ 18.0, $^{207}Pb/^{204}Pb$ 15.45 and $^{208}Pb/^{204}Pb$ 37.25; while some coarse-grained pyrites have higher $^{206}Pb/^{204}Pb$ with a mean at 18.54, though the $^{207}Pb/^{204}Pb$ and $^{208}Pb/^{204}Pb$ ratios are within the range of the others. In contrast, the two chalcopyrite samples from GR8 and GR9 respectively have virtually identical $^{206}Pb/^{204}Pb$ value (18.336 vs 18.343) but slightly different $^{207}Pb/^{204}Pb$ and $^{208}Pb/^{204}Pb$. This $^{206}Pb/^{204}Pb$ value is also shared by one of the pyrrhotite samples from GR8 (18.31); and the value is higher than the main group of pyrite samples (18.0) but slightly lower than the coarse-grained pyrites (18.54).

The sphalerite from GR9 has distinctly higher $^{207}Pb/^{204}Pb$ and $^{208}Pb/^{204}Pb$ ratios than the other sulphides. This higher value, however, is attributed to possible surface lead contamination. As explained in Appendix Six, most of the sulphides were washed using dilute HCl with slight heating before digestion so that surface lead can be effectively eliminated. This method was not used in the treatment of the sphalerite/chalcopyrite sample as sphalerite is actually dissolved in dilute HCl, leaving chalcopyrite as a residue phase. Therefore, the chemically separated sphalerite probably contains some contaminating surface lead, which has resulted in the higher $^{207}Pb/^{204}Pb$ and $^{208}Pb/^{204}Pb$ ratios. An alternative explanation would be that the influence of surface lead is negligible and the primary isotope compositions are unique. Since only one of the separates from the original core samples yielded a small amount of sphalerite-chalcopyrite mixture, barely enough for a single analysis, it is impossible to do any replicate test. However, the first explanation is preferred at present; thus this sample is not considered in the following discussions.

From Figure 9.7.1, it is clear that the Grasmere sulphide samples present distinctive variation in their $^{206}Pb/^{204}Pb$ values. Two explanations are possible: The first is that

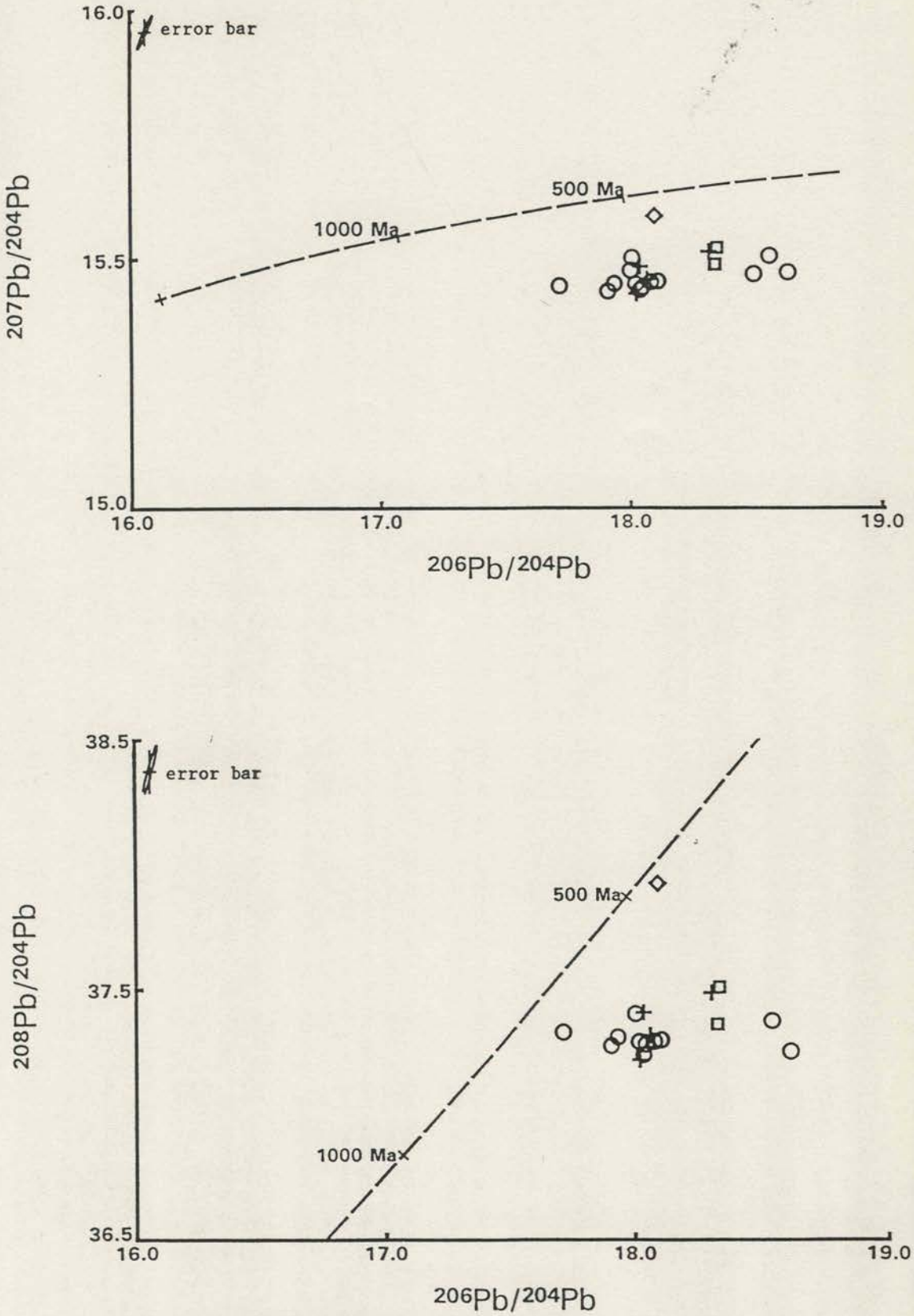

Fig.9.7.1. $^{207}Pb/^{204}Pb$ vs $^{206}Pb/^{204}Pb$ plot of sulphide samples selected from the Grasmere Prospect in the Wilandra Inlier in southern part of the Wonominta Block. This diagram presents distinctive Pb isotopic signatures for the mineralisation in this region. Circle, pyrite; square, chalcopyrite; cross, pyrrhotite; and diamond, sphalerite.

table 9.7.1. Lead isotope analyses of sulphide samples from the Grasmere Prosp

	sulphide	206/204	207/206	208/206	207/204	208/204	Pb ppm
GR-8	pyrite	17.711	0.8720	2.1077	15.444	37.329	24.3
	pyrite	17.905	0.8620	2.0818	15.434	37.275	64.0
	pyrite	17.932	0.8616	2.0806	15.450	37.309	64.1
	pyrite	18.003	0.8610	2.0776	15.501	37.403	39.2
	pyrite	18.018	0.8574	2.0696	15.449	37.290	48.6
	pyrite	18.036	0.8559	2.0648	15.437	37.241	61.0
	pyrite	18.046	0.8558	2.0659	15.444	37.281	40.9
	pyrite	18.079	0.8548	2.0628	15.454	37.293	49.8
	pyrrhotite	18.021	0.8562	2.0653	15.430	37.219	46.2
	pyrrhotite	18.035	0.8585	2.0742	15.483	37.408	56.4
	pyrrhotite	18.064	0.8558	2.0657	15.459	37.315	53.0
	pyrrhotite	18.311	0.8472	2.0472	15.513	37.486	40.4
	chalcopyrite	18.343	0.8461	2.0448	15.520	37.508	28.2
GR-9	chalcopyrite	18.336	0.8447	2.0376	15.488	37.361	N/A
	sphalerite	18.093	0.8614	2.0960	15.585	37.923	N/A
	pyrite fine	17.997	0.8599	2.0778	15.476	37.394	24.8
	pyrite fine	18.106	0.8535	2.0600	15.453	37.298	31.7
	pyrite coarse	18.489	0.8366	2.0157	15.468	37.268	33.9
	pyrite coarse	18.522	0.8358	2.0147	15.481	37.316	34.8
	pyrite coarse	18.622	0.8308	2.0004	15.471	37.251	29.9

note: N/A, not analysed.

this variation is due to *in situ* radiogenic decay of ^{238}U to ^{206}Pb (which in part can be supported by the negative correlation between Pb content and $^{206}Pb/^{204}Pb$ ratios). In this case, the values present in the sulphide at the time of formation may be approached by the value in the pyrite with the lowest $^{206}Pb/^{204}Pb$ of 17.71, and the higher values in the other samples are due to the radiogenic decay. The relatively low Pb contents of these samples would facilitate a significant change by radiogenic decay. Without U concentration data for these samples, however, it is not possible to further evaluate this explanation; and even if these data were available, one would have to assume a closed U-Pb system since the time of formation to make these calculations meaningful.

The second explanation for the isotopic variation is that of mixing with or without *in situ* radiogenic decay. The group of samples with $^{206}Pb/^{204}Pb$ values of ca. 18.0 may represent one end member of a mixed series and the other end being represented by the pyrite with $^{206}Pb/^{204}Pb$ of 17.7. Values higher than $^{206}Pb/^{204}Pb$ of 18.1, in this case, reflect *in situ* radiogenic decay. Once again, the low Pb contents of the sulphides facilitate mixing as a possible explanation for the isotope variation. If mixing (plus in situ radioactive decay) is the preferred explanation, it suggests that there are possibly at least two stages of mineralisation or remobilisation of metals during metamorphism. The older one would be represented by the sample with $^{206}Pb/^{204}Pb$ of 17.7 and the later one by the 18.0 population. As the $^{207}Pb/^{204}Pb$ and $^{208}Pb/^{204}Pb$ values for both groups are the same, a remobilisation of the mineralisation with $^{206}Pb/^{204}Pb$ of 17.7 would be the most likely explanation, rather than introduction of Pb from an external source (which may have different $^{207}Pb/^{204}Pb$ and $^{208}Pb/^{204}Pb$). Accordingly, chalcopyrite would have been formed in the later stage of the remobilisation after the cubic pyrites were crystallised.

In Figure 9.7.2, the Grasmere data are compared with other regional mineralisation. Clearly, the Grasmere samples have a different lead isotopic composition to those in Broken Hill (Gulson, 1984). They have the same range in $^{206}Pb/^{204}Pb$ with those in the Mount Read Volcanic belt in Tasmania (Gulson *et al.*, 1987), from the Cambrian Kanmantoo Trough (Gulson *et al.*, 1991) and from Cobar (G. Carr, pers. comm., 1991), but with lower $^{207}Pb/^{204}Pb$ and $^{208}Pb/^{204}Pb$ ratios. The only good match can be made with samples from Goonumbla in central New South Wales (Carr, pers. comm., 1991), which have been suggested to be of mantle-origin. The Goonumbla samples have lead isotope compositions between the fine- and coarse-grained samples from the Grasmere Prospect.

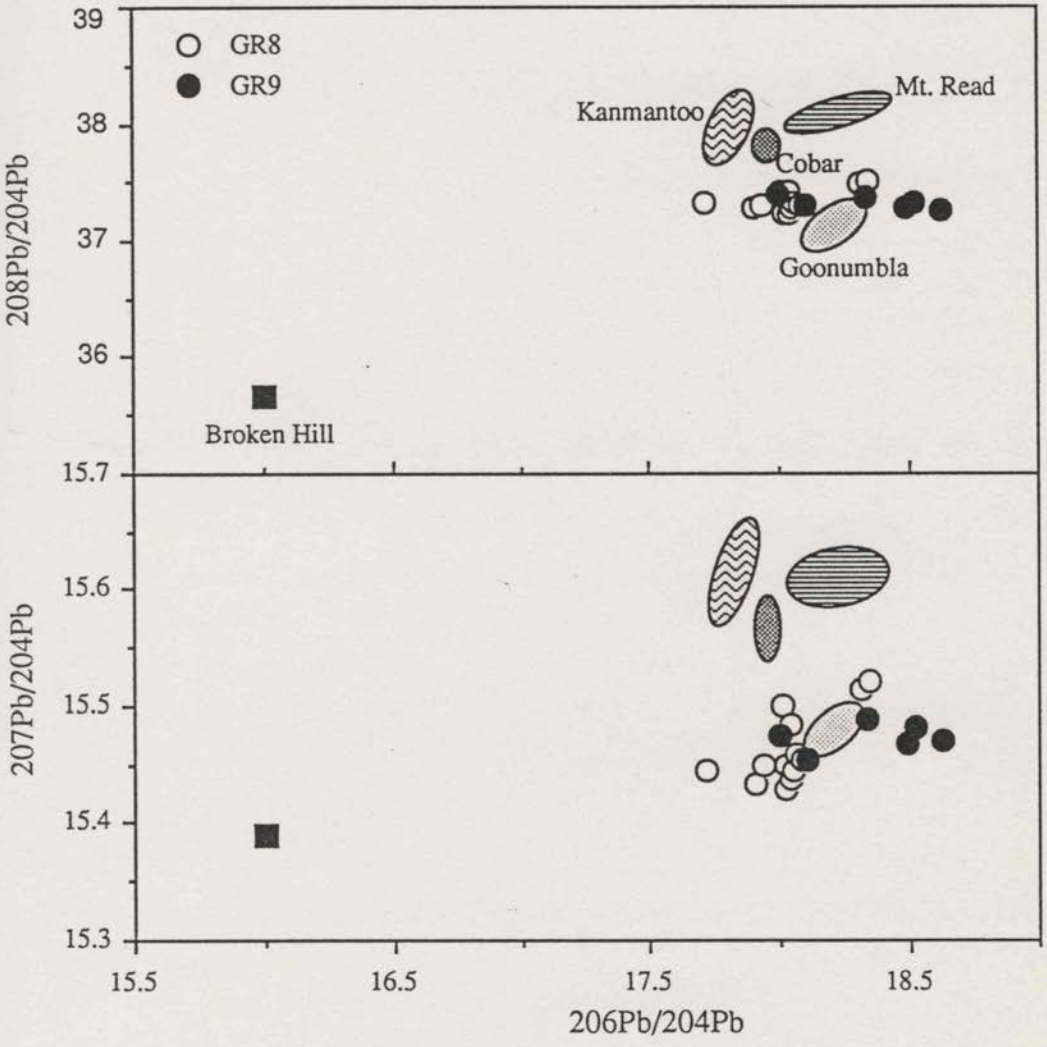

Fig. 9.7.2. Comparison of lead isotope composition of sulphide samples from various localities. (Data sources, Gulson *et al,* 1984, 1987 and CIS unpublished data).

If the sample with $^{206}Pb/^{204}Pb$ of 17.7 is assumed to have the initial values of the Grasmere mineralisation, then a calculated model age is about 500 Ma, which can be approximated for the mineralisation when the Pb was derived directly from the mantle. Alternatively, if this isotopic value is itself the result of radiogenic decay, the mineralisation may have occurred earlier, perhaps in the Proterozoic (Figure 9.7.1). Apparently, an initial ratio is crucial to resolve this problem. This particular value can be obtained by analysing any genetically related galena sample from the Grasmere area, since most of the lead in the mineral would have been formed when the galena was crystalised and the radiogenic lead would cause insignificant changes in its isotope composition. However, because of the clustering of $^{206}Pb/^{204}Pb$ values within a limited range from 17.7 to 18.0, it is highly unlikely that the Grasmere mineralisation was of the same age as Broken Hill.

The low $^{208}Pb/^{204}Pb$ and $^{207}Pb/^{204}Pb$ ratios of the Grasmere samples would suggest they had a mantle source with low Th/U ratios for the mineralisation. Therefore, the Grasmere signature appears unlikely to be comparable with that from Cobar, simply because the mantle-derived source(s) are rather unlikely for Cobar-type mineralisation.

In summary, the preliminary investigations of lead isotope compositions on sulphides from the Grasmere Prospect in the basement sequence reveal some interesting and encouraging results. First, the observed different periods of mineralisation have distinctive lead isotope compositions. The main group, including most of the fine-grained pyrite and pyrrhotite, has present-day compositions around 18.0 for $^{206}Pb/^{204}Pb$, 15.45 for $^{207}Pb/^{204}Pb$ and 37.25 for $^{208}Pb/^{204}Pb$. The lowest $^{206}Pb/^{204}Pb$ value in the group is 17.7. The coarse-grained pyrite has a mean $^{206}Pb/^{204}Pb$ ratio of 18.5, higher than the fine grain crystals but with a similar range in $^{207}Pb/^{204}Pb$ and $^{208}Pb/^{204}Pb$ ratios. One explanation for the observed Pb isotopic variation is that the signature of $^{206}Pb/^{204}Pb$ of 18.0 represents a remobilisation of Pb during regional metamorphism from earlier mineralisation (the closest $^{206}Pb/^{204}Pb$ value for this earlier event is 17.7), and the higher $^{206}Pb/^{204}Pb$ values are the results of *in situ* radiogenic decay. Regionally, the signatures of the Grasmere mineralisation are quite distinctive and the only comparable example is Goonumbla, which has been suggested to have a mantle-derived sulphide source. However, since only a limited number of samples were analysed from two drill cores, all the conclusions drawn here are tentative. It is still possible that the Grasmere samples may have an old, probably Proterozoic age of mineralisation given favourable initial ratio(s).

Chapter 10

Tectonic Implication of the Studies of Mafic Rocks

10.1 TECTONIC IMPLICATIONS

The petrological, geochemical and Sr-Nd isotopic studies of the mafic rocks provide important information on the tectonic environments of emplacement as well as subsequent secondary processes.

As revealed by petrographic studies, deformation of sequences deposited in submarine environments may have occurred in most cases after burial metamorphism (*sensu lato*). The alteration processes during burial metamorphism are characterised by high geothermal gradients (> 37 °C/km), and when the deformation occurred, metamorphism had already reached the peak conditions (*cf.* Chapter 4). These characters are very similar to those observed in the Mesozoic back-arc basin environments in South America (*cf.* Robinson, 1987).

The geochemical and Sr-Nd isotopic constraints of the basement mafic rocks require a MORB-like environment, yet with influx of crustal materials in the magma genesis. The distinctive geochemical characteristics are also typical of products of the back-arc basin environment (Saunder & Tarney, 1984).

Therefore, a back-arc basin model can best explain the observed petrological and geochemical characteristics of the mafic rocks in the basement sequence.

The alkaline basalts from both Late Proterozoic and Early Cambrian sequences resemble those from extensional environments within continental or oceanic regions, such as the Warrumbungle basalts or ocean island basalt (Figure 10.1). Considering the particular circumstance, the best candidate would be a rifting environment along the continental margin, as there is no sound evidence of substantial older rocks further east, except the basement sequence within the Wonominta region. In other words, the emplacement of the alkaline basalts represented a marginal rifting event in eastern Australia during the latest Proterozoic to earliest Cambrian time. The deep water

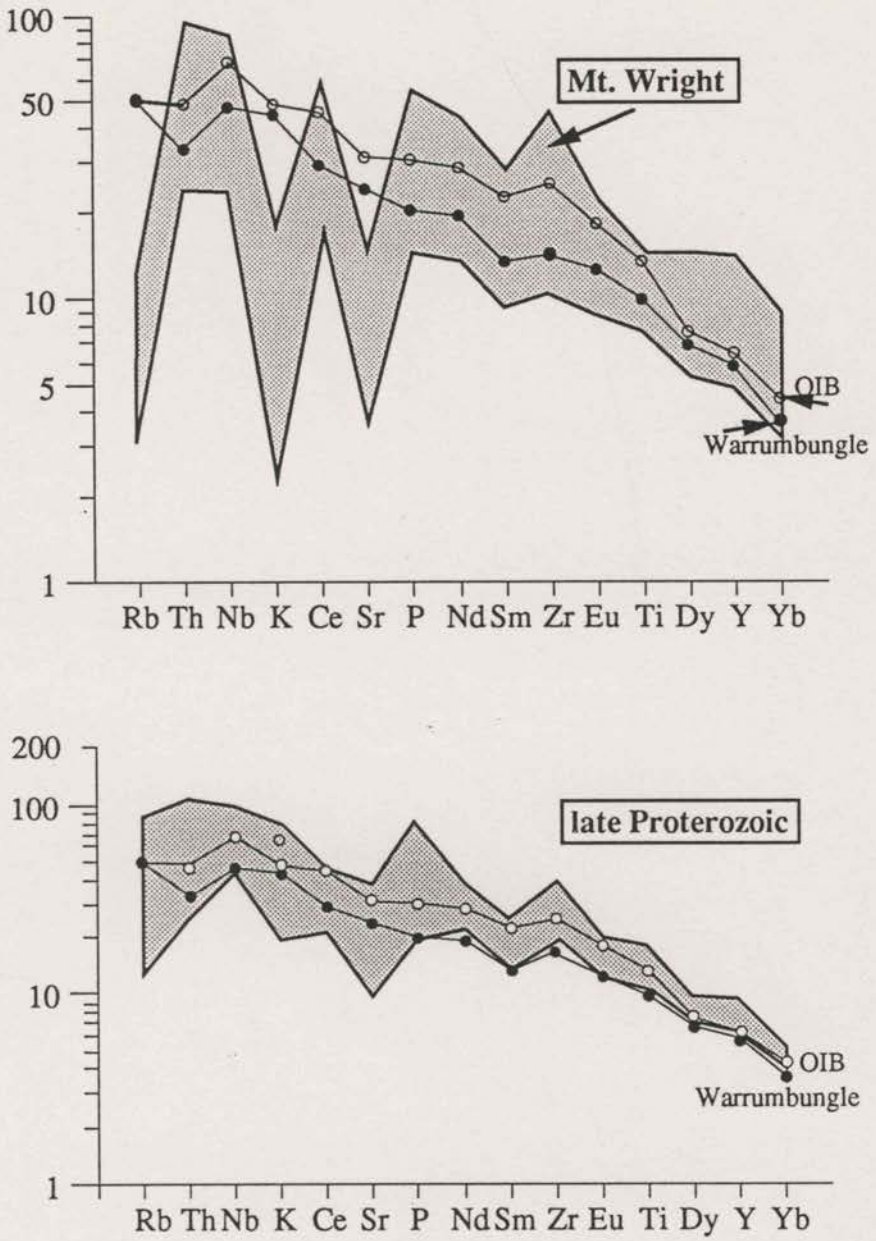

Fig. 10.1. Comparison of alkaline basalts from the late Proterozoic and Early Cambrian Mt. Wright sequences in the Wonominta Block with ocean island basalt (OIB) and the Warrumbungle basalt, a typical central volcano-type Tertiary basalt in eastern Australia (Sun *et al.*, 1989). These two diagrams clearly show that the alkaline basalts in the Wonominta Block have identical composition with samples from typical intra-plate volcanism cited here, and this has important implications for tectonic modelling.

basin derived further from this rifting event would provide an ideal environment for the deposition of the Teltawongee beds of slope and trough greywacke facies. Regionally, a similar environment developed in the Kanmantoo Trough in South Australia.

10.2. REGIONAL CORRELATIONS

10.2.1. Correlation of the Basement Sequence

As reviewed earlier, there have been several different correlations proposed for the basement sequence of the Wonominta Block, such as to the basal part of the Adelaidean rocks; to the Precambrian rocks in Tasmania; to the Kanmantoo rocks in South Australia; and the one adopted in this study, to the Willyama Supergroup in the Broken Hill Block. The preliminary Nd/Sm dating on whole rock samples presented in the last chapter, basically suggests that the basement rocks are too old to correlate with Adelaidean rocks in South Australia or in Tasmania, let alone with the younger Kanmantoo Group. This section compiles geochemical and isotopic characteristics of various mafic rocks in these regions and examines the validity of different correlations.

The mafic rocks intruding the Kanmantoo Group in South Australia are dominantly dyke or dyke-like. Comprehensive studies carried out recently (Liu, 1992 and references therein) have shown that the Kanmantoo mafic dyke rocks are essentially MORB-like (*cf.* Figure 10.2), being characterised by their low HFS element contents and high $\varepsilon Nd(T)$ values. Roughly, these rocks may be comparable to those in the basement sequence here, but many samples from the Ponto Mine Inlier have a profound Nb depletion and Th-enrichment, and unusually high $\varepsilon Nd(T)$ values. Samples from the Wilandra Inlier do not display Nb depletion but they also have the Th-enrichment, and they tend to have features of a "within plate environment". These features are clearly different from those of the Kanmantoo mafic rocks.

It has also been suggested that the basement sequence of the Wonominta Beds may be equivalent to the basal part of the Torrowangee Series (the Poolamacca Group) (Barnes, pers.comm., 1990). In this case, the basement mafic rocks might be compared to the Wilangee Basalt and its equivalent rocks in the Adelaide Geosyncline, such as the Wooltana Volcanics. According to Crawford and Hilyard (1990), the Wooltana Volcanics and similar rocks have many similarities to continental flood basalts, such as those in Parana in South America. These features are distinct from those of the basement mafic rocks in the Wonominta Block (Figure 10.2).

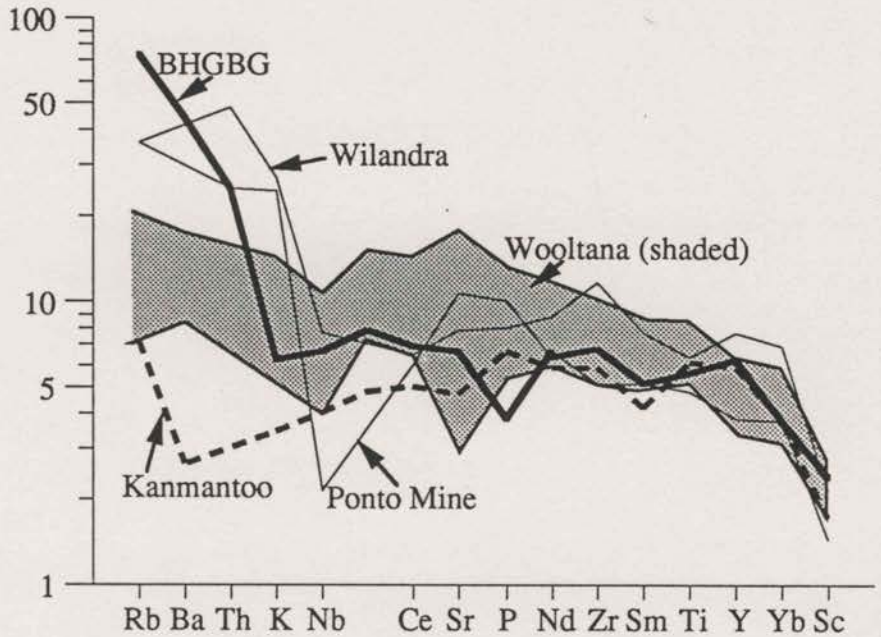

Fig. 10.2. Primitive mantle normalised plot of mafic rocks from the Wonominta (basement), Broken Hill Blocks and South Australia. This diagram shows that the only comparable samples with the basement sequence of the Wonominta Block is the Broken Hill Group basic gneiss (BHGBG) -- those from South Australia display distinctive compositions.

The basement mafic rocks have also been correlated with those in Tasmania (Scheibner, 1991). In Tasmania, similar mafic rocks have been divided into "Precambrian" and "Eo-Cambrian-Cambrian" series, separated by the 700-750 Ma Penguin Orogeny (Turner, in Burrett & Martin 1989). The "Precambrian" mafic rocks are of only minor occurrence and are probably tholeiitic but no detailed geochemical analyses are available; furthermore, these rocks have an age no greater than 1100 Ma (Raheim & Compston, 1977; in Burrett & Martin, 1989); therefore, they are not comparable to the basement sequence of the Wonominta Block. The "Eo-Cambrian-Cambrian" rocks may be temporarily compared with those in the Late Proterozoic-Early Cambrian sequences of the Wonominta Block, but they are typically boninitic (high-Mg andesite) or low-Ti tholeiitic such as those in the Dundas Trough (Brown, 1989; in Burrett & Martin, 1989) and represent a rather different tectonic environment from the alkaline basalts of the Wonominta Block. The Dundas mafic rocks are also geochemically different from those in the basement sequence of the Wonominta Block.

The Broken Hill Group basic gneisses (BHGBG) are also MORB-like with characteristic Th-enrichment (Figure 10.2). The Nb content in these rocks are on the same level as MORB's, thus there is no depletion in the MORB-normalised diagram (James *et al.*, 1987). These features appear to be rather similar to those of the Wilandra samples in the southern Wilandra Inlier as shown in Figure 10.2.

Therefore, geochemical and geochronological evidence from the mafic rocks support a correlation between the Willyama Complex in the Broken Hill Block and the basement rocks in the Wonominta Block.

10.2.2. The late Proterozoic and Early Cambrian Sequences

The late Proterozoic sequence in the Wonominta Block, known as the Kara beds, is correlated with the Farnell Group in the Broken Hill Block, and thus would be at the upper most part of the sequence, *i.e.*, the latest Proterozoic. Studies of the mafic rocks in this sequence revealed that geochemically and isotopically, they are very similar to the Mt. Wright basalt of the earliest Cambrian time. In other words, the geochemical and isotopic data require that these rocks had been coeval.

In this context, the Truro Volcanics in the northeastern part of the Mount Lofty Ranges (Forbes, *et al.*, 1972) should have comparable geochemical and isotopic characteristics to these rocks, if they are indeed correlated and in a similar tectonic environment.

10.3. TECTONIC RECONSTRUCTION

From the available geological, geochemical and isotopic information of mafic rocks, a tectonic reconstruction involving the Wonominta Block, the Broken Hill Block and the Adelaide Geosyncline in South Australia is suggested (Table 10.1).

In the basement sequence of the Wonominta Block, the emplacement of the mafic rocks may have occurred in a back-arc basin environment along the continental margin. The observation of an extremely depleted mantle component is thought to suggest the existence of a fossil mantle wedge in the source region as those observed in central Australia in early Proterozoic (Sivell & McCulloch, 1991). It is thus suggested that the continental margin might have been a subduction zone before the extension. If the Wonominta Block can be compared with the Broken Hill Block in a pre-Adelaidean time scale, the latter would have been at the continental side of the back-arc basin and the former near the arc side. This tectonic reconstruction can explain, first, the model age difference of the crustal rocks in these regions; secondly, the variation of the crustal contribution to the magma formation; and thirdly, possibly in the metamorphic grades. A precise age determination of the Wonominta basement sequence would definitely help to test this reconstruction.

The Late Proterozoic to Early Cambrian sequences in the Wonominta Block may have emplaced during a rifting event, which led to the formation of a early Cambrian marginal basin, where the Gnalta Group and Teltawongee beds were deposited in shallow shelf and deep slope-trough environments respectively. The formation of the Normanville (shelf facies) and Kanmantoo (trough facies) Groups in South Australia may have occurred during the same period (Mills, 1992).

The regional geology and geochemistry of mafic rocks in the Wonominta Block also play an important role in the reconstruction of the Gondwana supercontinent. Figure 10.3 displays a tectonic model proposed by Bradshaw *et. al.* (1985). In this model, an early Cambrian island arc in Antarctica is correlated with the low-Ti tholeiitic association in western Victoria (*cf.* Crawford, 1988), and further north with the so-called Mt. Wright Volcanic Arc. The Mt. Wright Arc model was first proposed (Scheibner, 1974) to include all the volcanic rocks on the western side of the Wonominta Block, running from Mt. Arrowsmith in the north, through Packsaddle, Nundora and down to Mt. Wright in the south. Based on the new geological framework (Mills, 1992), the model was modified so that the Mt. Wright Arc includes only the sequence in the Mt. Wright area (Scheibner, 1989). However, As have presented here, the mafic rocks in the Late

Table 10.1. Regional Correlations and Tectonic Development of a Transitional Tectonic Regime in western NSW and in South Australia.

age	Wonominta Block	Broken Hill Block	South Australia	tectonic environemt and mafic magmatism in the tectonic transitional zone
	Kayrunnera Group			
ca. 500 (Ma)	Mootwingee Group	Delamerian Orogeny		end of the transitional zone
	- - - - - - - - - -	- - - - - - - - - -	- - - - - - - - - -	Syn- &post-orogenic MORB-like dykes in Kanmantoo
	Teltawongee beds		Kanmantoo Group	Trough; Kayrunnera gabbro
525 (Ma)	Gnalta Group { Cymbric Vale Formation Mt. Wright Volcanics		Normanville Group	
				rifting --
				emplacement of alkali basalt
	Kara beds	Farnell Group		trough
Late Proterozoic		Torrowangee Group	Adelaidean series	extensional environment --
		Poolamacca Group		continental flood basalts
ca. 1000 Ma (?)	- - - - - - - - - -	- - - - - - - - - -	- - - - - - - - - -	-initiation of the transitional zone - - - - - -
ca. 1400 Ma	Ponto Mine Inlier			
	Wilandra Inlier			
1650 Ma		Willyama Supergroup		basement development (back-arc basin
			Gawler Craton	in western NSW with emplacement of
				MORB-like mafic rocks)

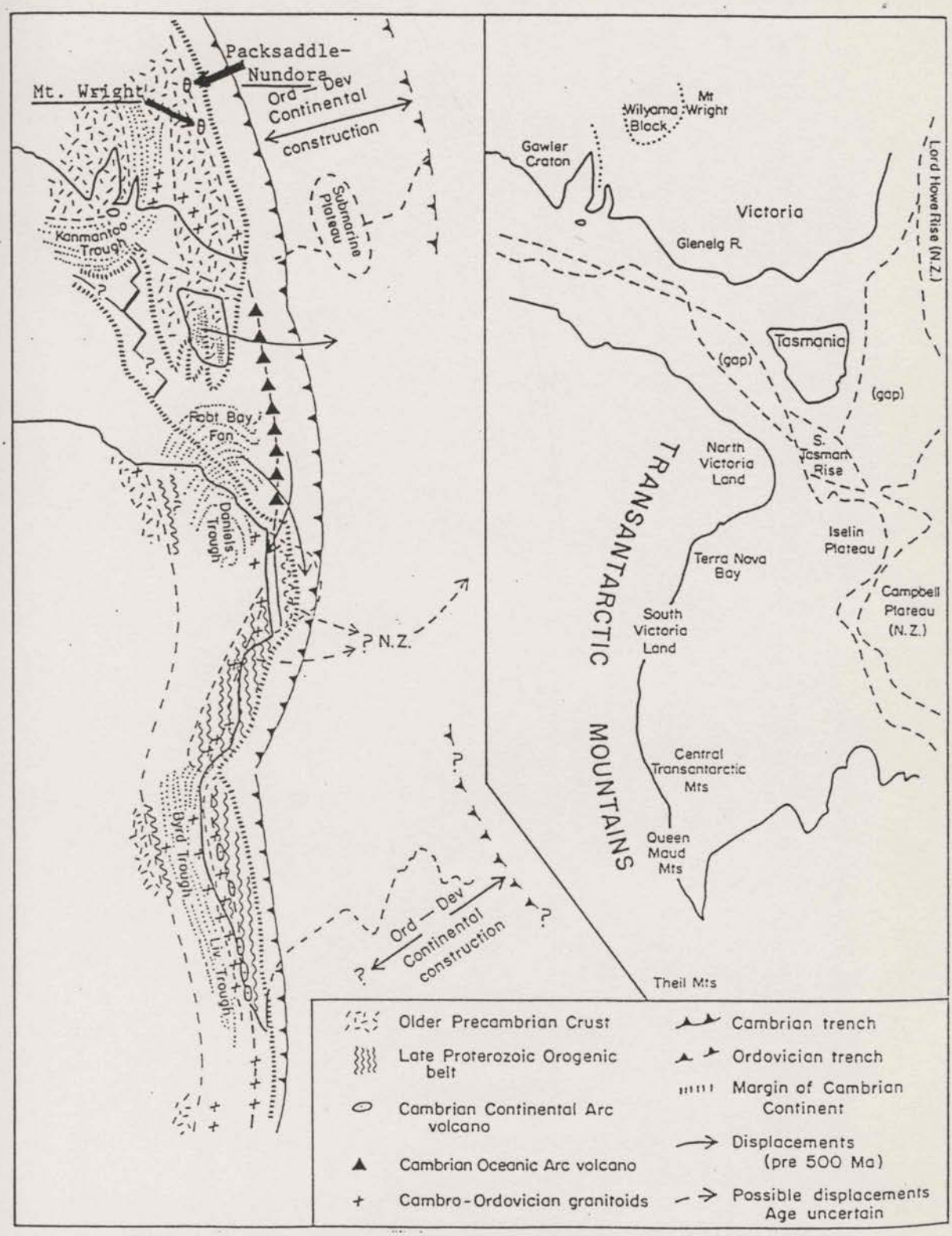

Fig. 10.3. A Gondwana reconstruction in the Early Palaeozoic (Bradshaw *et al.*, 1985). In this proposal, the volcanic rocks in the Packsaddle-Nundora and Mt. Wright areas were thought to represent a Cambrian arc along the eastern margin of Gondwana.

Proterozoic and in the Early Cambrian Mt. Wright sequences are both alkaline basalts, which are unlikely to have been derived from an arc or arc-like environment. Thus, the present prevailing models used in Gondwana reconstruction may have to be modified, at least in this particular region, in accordance with the new geological, geochemical and isotopic results. At this stage, the model proposed by Preiss (1987) is preferred (Figure 10.4) though integration with the new information is needed.

From Late Proterozoic to Early Cambrian time, eastern Australia was proposed to have been involved in two marginal rifting events (Lindsay *et al.*, 1987). According to recent radiometric work (Zhao ~~*et al.*, in prep~~.), the first rifting occurred at about 800 Ma and resulted in the initiation of Adelaide Geosyncline. The second rifting event, according the present study, should have occurred across the Precambrian-Cambrian boundary (ca. 530-540 Ma). In this context, the eastern margin of Gondwanaland could have been a rifting environment from Late the Proterozoic and developed into marginal basins in early Cambrian (whether or not the arc associations in western Victoria at the time was related to this tectonic evolution is incidental to the reconstruction here). Alternatively, as proposed by some North American geologists (*e.g.* Moores, 1991; Dalziel, 1991), these rifting events could have been a part of the "conjugate rift pair" that split Laurentia and East Antarctica-Australia from the Eocambrian supercontinent, though globally, this might have been a failed rift arm with major spreading occurring on the other side of the continent.

The products of these two rifting events have been assigned to Adelaide and Kanmantoo Foldbelts respectively (*e.g.* Coney *et al.*, 1990; Scheibner, 1989, 1991). However, both in the Wonominta -Broken Hill region and in South Australia, there is no major orogenic movement between the Late Proterozoic and Early Cambrian sequences. In Antarctica, the Ross Orogeny, as recorded in the Transantarctic Mountains, is correlated with the Cambrian - Ordovician Delamerian Orogeny in South Australia, which marks the end of the Kanmantoo Foldbelt. There is also an earlier nonmagmatic compressive event of late Precambrian (*cf.* Bradshaw *et al.*, 1985), known as the Beardmore Orogeny, which has been used to separate the Adelaide and Kanmantoo Foldbelts, though its influence is virtually absent in South Australia (Preiss, 1987). A recent study (Rowell, *et al.*, 1992) suggests that some deformation in Transantarctic Mountains previously assigned to this Beardmore event may be correlated with the Mootwingee Phase recorded in the Wonominta Block, which is an early expression of the Delamerian Orogeny. Another recent study (Pankhurst *et al.*, 1988) also put forward a case arguing that the age of the Beardmore Orogeny could be as young as 502 Ma, which is clearly in the span of the Ross/Delamerian Orogeny. If

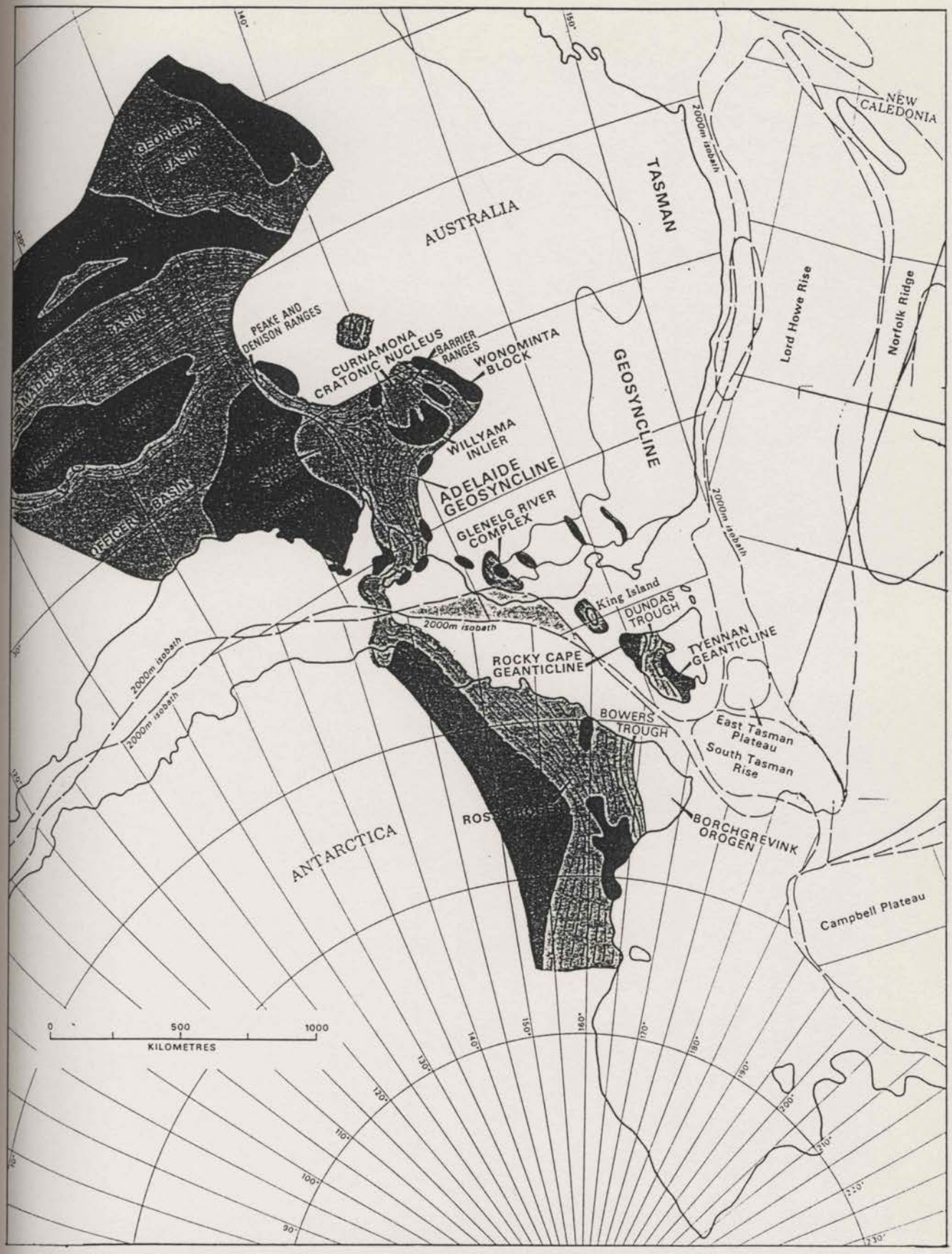

Fig. 10.4. Reconstruction of part of the Australian-Antarctic portion of Gondwana (after Preiss, 1987). Dark grey, pre-Adelaidean basement; grey, late Proterozoic-early Cambrian rocks (the Delamerian - Ross Orogen); blank, Palaeozoic and younger rocks. Note, the distribution of the three sequences in the Wonominta region needs to be changed based on Figure 1.1.

these new correlations can be substantiated, a tectonic boundary of compressive features between the Late Proterozoic and Early Cambrian sequences in southeastern Australia and in Antarctica can virtually be ruled out. The whole period represents repeated extensional movements, which may have been parts of the global rifting that ultimately led to the break-up of the Proterozoic supercontinent. In this context, the beginning of the Tasman system should have followed the Ross/Delamerian Orogeny, that is, only those features developed afterwards, can be considered to be true products of the Tasman foldbelts.

Further, these repeated rifting events are suggested to represent a transitional tectonic regime between the Tasman Orogen and its cratonic basement. Within this transitional zone, both basement rock and younger sequences occur together. If the occurrence of these sequences had regular spatial distributions, that is younging eastwards, it would not be difficult to define the position of the Tasman Line. However, the above tectonic reconstruction would almost rule out any chance of locating the position of the Tasman Line in this region, because the younger rocks occur on both east and west of the basement sequence and both have significant outcrops that cannot be ignored when constructing tectonic models.

Tectonically, this must have been a rather unusual period, when no major compressive tectonic movement was recorded for more than two hundred million years with repeated marginal riftings, if the evolution of the Adelaide Geosyncline started at about 800 millions years ago. Maybe, a new tectonic regime should be defined, such as the Delamerian Orogen (or system), rather than a transitional zone or fringe zone.

In this context, the much less known Delamerian Foldbelt (*cf.* Preiss, 1987), should probably have a significant role in this tectonic reconstruction. As shown in Figure 10.4, this foldbelt would include the Ross Orogen in Antarctica and the Adelaide Geosyncline in South Australia, and various late Proterozoic to early Cambrian developments in central and northern Australia. This tectonic regime can be considered to be transitional between the Cratonic basement and the Phanerozoic Tasman Orogen, in the sense that old basement-style inliers and younger rocks both occur within the regime. However, in itself it should be considered to represent a distinct tectonic unit in the Gondwana reconstruction.

Chapter 11
Discussion and Summary of the Wonominta Geology from Studies of Mafic Rocks

11.1. GEOCHRONOLOGICAL CONSTRAINTS ON THE WONOMINTA BEDS

11.1.1. The Basement Sequence.

The Nd-Sm isotopic studies of the bulk felsic and mafic rocks yielded a date of 1.40 ± 0.24 Ga (MSWD = 0.9). This is so-far the only geochronological constraint on the basement sequence of the Wonominta Block.

The mean of this age is younger than that of the Broken Hill Group (1670-1690 Ma; Page & Laing 1990). However, the true age could be, statistically, any where from 1160 Ma to 1640 Ma, and the older end of the range is still comparable to the age of the Broken Hill Block. Besides, although the regression yielded only an imprecise age, it still revealed the pre-Adelaidean features of the basement rocks, and is broadly comparable with the present tectonic modelling.

However technically, the present age calculation is basically a two-points regression, with the felsic rock as one end and a cluster of mafic samples as the other end. Although Sr-Nd isotopic compositions of the felsic sample suggest a co-genetic origin with the tholeiitic rocks, it is still possible that the regression represents a mixing line and the age might not carry real significance. Therefore, more precise dating work in future should be of great value for the study of the Wonominta Block.

11.1.2. The Younger Sequences

The SHRIMP U-Pb study on zircons from the Mt. Wright area has resulted in a preliminary date of 525 ± 8 Ma (2σ). Although refinement of this result is still in progress, the age determination is presented with much confidence, as further analysis would merely improve the analytical precision (thus reduce the uncertainty).

This date was obtained from the felsic rocks of the Cymbric Vale Formation in the Mt. Wright area; but together with previous biostratigraphic studies (Kruse, 1982), it is believed that the alkali basalt, stratigraphically below the felsic rocks, should also have an earliest Cambrian age.

Although there is no direct chronological control, the Sr-Nd isotopic characteristics of the alkali basalt in the Late Proterozoic (Packsaddle-Nundora) sequence clearly indicate that these rocks must have been formed at approximately the same time as those in the Mt. Wright area. If, as geological correlation suggests (Mills, 1992), the Packsaddle-Nundora sequence was formed in the Late Proterozoic, the Sr-Nd isotopic characteristics of the mafic rock presented in this project require that the formation of the volcanic rocks should be in the latest Proterozoic, that is, not much older than their counter part in the Mt. Wright area.

11.2. GEOLOGICAL CHARACTERISTICS OF MAFIC ROCKS

11.2.1. Field Occurrence

All of the basement and late Proterozoic mafic units have invariably been highly deformed and metamorphosed. In the field, depending on different responses to deformation, the mafic rocks can generally be recognised as either volcanic or intrusive in texture. There are two basic categories of volcanic mafic rocks, massive and cleaved; the latter display highly developed lamellar and fine-grained texture, somewhat similar to phyllite in the field. Among the intrusive rocks, small intrusions normally show a low positive topography and have limited outcrops with boundaries obscured by alluvials; Dyke-like rocks normally occur along with the volcanic sequences. They occur like dykes with a vertical dip, but obviously the present disposition may not be primary due to deformation and orogenic movement and some dykes may have been sills or thick flows. The occurrence of mafic porphyritic rocks in the basement sequence is distinctive and their unique geochemical and isotopic features present significant tectonic implications.

In the Ponto Mine Inlier in the central-northern part of the Wonominta Block, mafic rocks occur mainly as volcanic units (eight volcanic belts were observed) in the Ponto Mine area, while dyke-like rocks dominate the Boshy Tank area. In the Wilandra Inlier in the south, both volcanic and intrusive rocks occur in the Wilandra area and amphibolite is the main mafic species in the Cymbric Vale area, though metadolerites were also observed in thin-sections.

The Late Proterozoic mafic rocks, studied at Packsaddle and Nundora, are largely volcanic. The Early Cambrian mafic rocks observed at Mt. Wright are basaltic, preserving most of the primary magmatic textures and coexist with a pile of felsic tuffs and porphyries. The mafic rocks at Comarto, possibly of Cambrian age, have a pipe-like occurrence. Field observations revealed the rocks from these "pipes" are a mixture of pyroclasts, metabasalt and metadolerites.

From previous work, as well as some preliminary observations in this study, at least three deformation events have influenced the basement sequence; while the Late Proterozoic and Early Cambrian sequences enjoyed only the last two. Structurally, D_2, probably caused by the Delamerian Orogeny, has been the dominant deformation and is responsible for the main structural orientations, particularly in the northern part of the region.

11.2.2. Metamorphic Characteristics

The petrographic studies and analyses of mineral chemistry of the mafic rocks indicate that the basement mafic rocks in the Ponto Mine Inlier have a composite metamorphic assemblage of upper greenschist facies, equivalent to the biotite zone of metapelite. In the Wilandra Inlier, samples have primary metamorphic assemblage of upper greenschist - lower amphibolite facies but some from Wilandra have been overprinted by a retrogressive actinolite-pumpellyite facies metamorphism.

In the Late Proterozoic sequence, the metamorphic assemblage in mafic volcanic rocks is chlorite-albite, interpreted as of lower greenschist facies, presumably of chlorite zone. According to Edwards (1980), the various mafic rocks at Mt. Arrowsmith further north in the region, but probably along the same volcanic belt, apparently have an assemblage of prehnite-pumpellyite facies, indicated by the wide occurrences of both Pr and Pm. Whether these differences indicate variation in the metamorphic

history of the same volcanic belt, or compositional differences in the mafic rocks in the two areas is a question that cannot be resolved at present.

The rare minerals, such as aluminous aegirine, nepheline and natrolite in nundorite indicate the peralkaline alteration of felsic tuffs in the northern Nundora area The alkaline fluids were probably sodic, as were those which caused the alteration of syenite. In contrast, the secondary alteration in the southern part of the region was probably potassium enriched and characterised by the extensive occurrence of muscovite. At present, it is not possible, nor has it been aimed at, to define the origin and scale of the alteration processes thoroughly; however, different geochemical features of secondary alterations on the regional scale undoubtedly have important implications for exploration activities.

11.3. GEOCHEMICAL CHARACTERISTICS OF THE MAFIC ROCKS

Investigations of the influence of regional metamorphism on primary compositions of mafic rocks revealed that in most cases, Ti, Zr, Y, Nb and REE are immobile components, while most major elements such as Na, K, Fe, Ca, Mg, and Rb and Sr as trace components, are mobile to various degrees.

In the basement sequence, various mafic samples display tholeiitic features. Detailed investigations of geochemical stratigraphy revealed systematic changes within the sequence. From the Wilandra Inlier to the Ponto Mine Inlier, samples have been observed with decreasing Nb and increasing Th at relatively high Ti and Zr levels. This is interpreted to be the result of increasing involvement of crustal materials in magmatism. In the southern Wilandra Inlier, although the amphibolitic rocks at Cymbric Vale appear to be the most likely candidates petrographically for correlation with the Broken Hill Group basic gneisses (BHGBG), the geochemical compositions of these rocks are distinctive; rather, the mafic samples from Wilandra share greater similarity in geochemistry with the BHGBGs.

The mafic samples in the Late Proterozoic sequence display features of sodic alkali basalt with high LILE and HFSE concentrations and LREE-enriched patterns. The xenolithic samples show distinctive compositions of subalkaline basalt. They have lower Nb, Ti and REE abundances but higher Sc compared with their volcanic hosts,

and thus are somewhat similar to the older basement mafic rocks. Still the LREE enriched compositions suggest that they are also different from the basement rocks.

The Mt. Wright Volcanics are the most abundant magmatic rocks of early Cambrian age, and consist of a bimodal series with minor intermediate rocks as fractionated products of the mafic magmatism. The mafic rocks in this area display alkaline basalt affinity, and are identical to those in the Late Proterozoic sequence in many parameters. Still, some important differences have been observed. In particular, the Mt. Wright basalts have distinctive LILE-depleted compositions. Therefore, although these rocks might have had very similar primary compositions, they apparently experienced different histories of metamorphism . The other early Cambrian rocks, namely Comarto metabasite, Kayrunnera gabbro and Ponto metadolerite display various features typical of subalkaline basalts from intra-plate environments.

Geochemical studies also provide important constraints on the petrogenetic aspects of the formation of the rocks. The tholeiitic rocks in the basement sequence have probably undergone a large degree of partial melting with fractional crystallisation involving plagioclase and pyroxene; while the alkaline basalts have resulted from low degree of partial melting with fractional crystallisation involving plagioclase and little pyroxene. The available data can not distinguish if olivine and/or orthopyroxene had played a significant role in the petrogenetic processes.

Furthermore, the fact that various petrographically distinct rocks in both basement and late Proterozoic sequences (except the xenolithic rocks from Packsaddle) display indistinguishable geochemical compositions, and the fact that large variations in HFS compositions generally show coherent correlations suggest that magma mixing processes had not been important in petrogenesis.

In terms of source characterisation, geochemical evidence suggests that the basement rocks appear to have had MORB-like sources, yet with sigmificant and various crustal contributions. For the alkali basalts, all the features revealed by the tectonomagmatic discrimination suggest that an extensional rift-like environment would be likely for the formation of these rocks. It is unlikely that these rocks were generated in an island arc environment.

11.4. Sr-Nd ISOTOPIC CHARACTERS OF MAFIC ROCKS

The Sr-Nd studies of basement tholeiitic rocks indicate that local mixing or assimilation processes had played an important role in the formation of the rocks. The AFC model calculation suggests that a MORB-like source contaminated by up to 7% juvenile crustal materials can best explain the observed Nd isotope compositions in the most contaminated sample. Distinctive Nd isotope compositions also suggets the presence of highly depleted mantle source(s) for the formation of the basement mafic rocks.

The Sr-Nd isotopic systematics of the alkaline basalts from both the Packsaddle-Nundora and the Mt. Wright areas display different Sr-Nd isotope compositions. They have primitive and uniform Nd initial ratios and various Sr isotope compositions due to alteration. The distinctive Sr-Nd isotope composition suggest little crustal contamination involved in the formation of the rocks.

In terms of alteration history, detailed observations showed that there has probably been more disturbance to rocks from the early Cambrian Mt. Wright samples than to those from late Proterozoic sequence.

11.5. TECTONIC IMPLICATIONS OF STUDIES OF MAFIC ROCKS

From the geological framework (Mills, 1992) and the present studies of mafic rocks in the Wonominta Beds, a model of transitional tectonics has been proposed for the regional tectonic correlations. In this model, the basement sequence, comparable with the Willyama Complex in a pre-Adelaidean time scale, was developed in a back-arc basin environment, where the Wonominta Block at the time would have been located in near the arc side of the basin . This basement sequence should be considered as a part of the "Precambrian cratonic basement" in Gondwana reconstruction.

Then came the evolution of the Adelaidean system in the Late Proterozoic. The Kara beds may have developed during the latest Proterozoic time and probably continued into the earliest Cambrian time, when the Mt. Wright Volcanics were emplaced. Geochemical and Sr-Nd isotopic constraints require a relatively short period of emplacement. Tectonically, these rocks may represent the products of a marginal rift, which eventually led to the formation of the Kanmantoo Trough, an event globally related to the break-up of Gondwana supercontinent during the Pan-Africa event (Coney, *et al.*, 1990).

In this context, the Wonominta Block may have been astride ~~across~~ the Tasman Line, having started its evolution from Middle Proterozoic and finished no earlier than the Delamerian Orogeny. Therefore, this region represents a transitional tectonic regime between the Tasman system and its cratonic basement. This transitional regime may be spatially equivalent to the Delamerian Foldbelt, a combination of Kanmantoo Foldbelt and part of the Adelaide Foldbelt that deformed during the Delamerian Orogeny. It also has a similar connotation to the tectonic fringe zone as proposed by Coney *et al.*(1990).

11.6 FUTURE STUDIES

A better quantified geochronological investigation of the Precambrian sequences of the Wonominta Beds is much needed, and should benefit greatly to the understanding of the regional geology.

In order to achieve a better understanding of the history of the transitional tectonic regime across the Cambrian-Precambrian boundary, geochemical and isotopic studies of various mafic rocks should be carried out in a large regional background. In this context, a comparative study of mafic rocks from late Proterozoic to early Cambrian in Antarctica and Australia should be of great value.

Finally, the reconstruction of Gondwanaland geology in the early Cambrian should be carried out based on the new achievement of geological, geochemical and isotopic studies.

BIBLIOGRAPHY

Allegré, C.J. & Ben Othman, D. 1980. Nd-Sr isotopic relationship in granitoid rocks and continental crust development: a chemical approach to orogenesis. Nature, 286:335-342.

Andrews, E. C. 1922. The geology of the Broken Hill district. NSW Geol. Surv. Mem., 8:1-432.

Andrews, E. C. 1926. Underground water resources: Broken Hill district. NSW Dept. Mines, Ann. Rep. (1925), p. 94-98.

Arculus, R.J. 1987. The significance of source versus process in the tectonic controls of magma genesis. J. Volcano. Geotherm. Res., 32:1-12.

Bailey, S. W. 1980. Summary of recommendations of AIPEA nomenclature committee on clay minerals. Am. Mineral. 65:1-7.

Barnes, R. G. 1974. Tibooburra-Wonominta Block. In N. L. Markham & H. Basden (editors), The Mineral Deposits of New South Wales. NSW Geol. Surv., Sydney. p.93-102.

Bartley, J. M. 1986. Evaluation of REE mobility in low-grade metabasalts using mass-balance calculations. Norsk Geologisk Tidsskrift., 66:145-152.

Bayliss, P. 1975. Nomenclature of the trioctahedral chlorites. Can. Min., 13:178-180.

Belkin, H. E. & Libelo, E. L. 1987. Fibers and cylinders of cryptomelane - hollandite in Permian bedded salt, Palo Duro Basin, Texas. Am. Min., 72:1211-1224.

Bettison, L. A. & Schiffman, P. 1988. Compositional and structural variations of phyllosilicates from the Point Sal Ophiolite, California. Am. Mineral., 73:62-76.

Bevin, R. E. & Merriman, R. J. 1988. Compositional controls on coexisting prehnite-actinolite and prehnite-pumpellyite facies assemblages in the Tal y Fan metabasite intrusion, North Wales: implications for Caledonian metamorphic field gradients. J. Metamorphic Geol., 6:17-39.

Bevin, R. E., Robinson, D & Rowbotham G. 1991. Compositional variations in mafic phyllosilicates from regional low-grade metabasites and application of the chlorite geothermometer. J. Metamorphic Geol., 9:711-721.

Blundy, J. D. & Holland, T. J. B. 1990. Calcic amphibole equilibria and a new amphibole-plagioclase geothermometer. Contrib. Mineral. Petrol., 91:235-244.

Bradshaw, J. D., Weaver, S. D. & Laird, M. G. 1985. Suspect terranes and Cambrian tectonics in Northern Victoria Land, Antarctica. In D. C. Howell (editor) Tectonostratigraphic Terranes of the Circum-Pacific Region. Circum-Pacific Council for Energy and Mineral Resources. Earth Sci. Ser. 1: 467-479.

Brown, E. H. 1977. The crossite content of Ca-amphibole as a guide to pressure of metamorphism. J. Petrol., 18:53-72.

Brown, H. Y. L. 1881. Report upon the Albert Gold-field, together with a description of the geological formation of the Paroo, Wertago and Culgoa Districts, north of the Darling River. NSW Legislative Assembly, p. 1-7.

Brunker, R. L.1967. Explanatory Notes: Cobham Lake Sheet SH54-11, 1:250 000 Geological Series. NSW Geol. Surv., Sydney.

Brunker, R. L. & Bunny, M. 1964. Cobham Lake 1: 250 000 Geological Sheet. Department of Mines, NSW.

Burrett, C. F. & Martin, E. L. (eds) 1989. Geology and Mineral Resources of Tasmania. Special Publication Geol. Soc. Aust. No. 15. 574 pp.

Cho, M., Liou., J. G. & Maruyama, S. 1986. Transition from the zeolite to prehnite-pumpellyite facies in the Karmusten metabasites, Vancouver Island, British Columbia. J. Petrol., 27:467-494.

Cho, M. & Liou, J. G. 1987. Prehnite-pumpellyite to greenschist facies transition in the Karmusten metabasites, Vancouver Island, B. C. J. Petrology, 28:417-443.

Cho, M. & Liou, J. G. 1988. Pressure dependence of the Fe and Mg partitioning between actinolite and chlorite. Geol. Soc. Am., Cordilleran Section, Abstract with

Programs. P.150.

Coleman, R. G. & Clark, J. R. 1968. Pyroxenes in the blueschist facies of California. Am. J. Sci., 266:43-59.

Compston, W., Williams, I.S. & Meyer, C. 1984. U-Pb geochronology of zircons from Lunar breccia 73217 using a sensitive high mass resolution ion microprobe. J. Geophys. Res., 89:B525-B534.

Compston, W.Willams, I. S., Kirschvink, J. L., Zhang Z.-C. & Ma, G.-G.1992. Zircon U-Pb ages for the Early Cambrian time scale. J. Geol.Soci. London, 149:171-184.

Condie, K. C. 1989. Geochemical changes in basalts and andesites across the Archean-Proterozoic boundary: identification and significance. Lithos, 23:1-18.

Coney, P. J., Edwards, A., Hine, R., Morrison, F. & Windrim, D. 1990. The regional tectonics of the Tasman orogenic system, eastern Australia. J. Structural Geol., 12:519-543.

Cook, P. J. 1982. The Cambrian Palaogeography of Australia and opportunities for petroleum exploration. APEA J., 22:42-64.

Cooper, P. F., Tuckwell, K. D., Gilligan, L. B. & Meares, R. M. D. 1978. Geology of the Torrowangee and Fowlers Gap, 1:100 000 sheets 7135 and 7235. NSW Geol.Surv., Sydney.

Crawford, A. J. 1988. Cambrian. In J. G. Douglas & J. A.Ferguson (editors), Geology of Victoria. Vic. Division Geol. Soc. Aust., Melbourne, p. 37-62.

Crawford, A. J. & Hilyard, D. 1990. Geochemistry of Late Proterozoic tholeiitic flood basalts, Adelaide Geosyncline, South Australia. Geol. Soc. Aust. Spec. Publ. No. 25, p. 459-465.

Cross, W., Iddings, J. P., Pirsson, L. V. & Washington, H. S. 1902. A Quantitative Chemico-Mineralogical Classification and Nomenclature of Igneous Rocks. J. Petrol., 10:555-690

Curtis, L. W. & Gittins, J. 1979. Aluminous and titaniferous clinopyroxenes from regionally metamorposed agpaitic rocks in central Labrador. J. Petrol., 20:165-186.

Czank, M. & Liebau, F. 1980. Periodicity faults in chain silicates: a new type of planar lattice fault observed with high resolution electron microscopy. Phys. & Chem. Minerals, 6:85-93.

Dalziel, I. W. D. 1991. Pacific margins of Laurentia and east Antarctica-Australia as a conjugate rift pair: evidence and implications for an Eocambrian supercontinent. Geology, 19:598-601.

Davies, S. M. 1985. The Geology and Structure of the Ponto-Little Koonenberry Mountain Area, NSW. B.Sc.(Hons) Thesis, NSW Institute of Technology, Sydney (unpublished).

Davy, R. 1972. An appraisal of the economic prospects of the Ponto Copper Mine area, via Milpa station, NSW. Copper & Association. NSW Geol. Surv., GS1973/037 (unpublished).

DePaolo, D. J. 1981a. Nd isotopes in the Colorado Front Range and crust-mantle evolution in the Proterozoic. Nature, 291:193-196.

DePaolo, D. J. 1981b. Trace element and isotopic effects of combined wallrock assimilation and fractional crystallization. Earth Planet Sci. Lett., 53:189-202.

DePaolo, D.J. 1988. Neodymium Isotope Geochemistry: An introduction. Springer-Verlag, Berlin. 187 pp.

DePaolo, D. J. & Wasserburg, G. J. 1976a. Nd isotopic variations and petrogenetic models. Geophys. Res. Lett., 3:249-252.

DePaolo, D. J. & Wasserburg, G. J. 1976b. Inferences about magma sources and mantle structure from variations of $^{143}Nd/^{144}Nd$. Geophys. Res. Lett., 3:743-746.

Duncan, A. R., Armstrong, R. A., Erlank, A. J., Marsh, J. S. & Watkins, R. T. 1990. MORB-related dolerites associated with the final phases of Karoo flood basalt volcanism in southern Africa. In Parker, Rickwood & Tucker (eds), Mafic Dykes and Emplacement Mechanisms, Balkema, Rotterdam. p. 119-129.

Edgeworth David, T. W. 1950. The Geology of the Commonwealth of Australia. Edward Arnold & Co., London.

Edwards, A. C. 1979. Tectonic implications of the immobile trace-element geochemistry of mafic rocks bounding the Wonominta Block. J. Geol. Soc. Aust., 25:459-465.

Edwards, A. C. 1980. The Geology and Petrology of the Igneous Rocks of Mt. Arrowsmith and Related Areas of North Western New South Wales. Ph. D. thesis, W.S. & L.B. Robinson College, The University of New South Wales, Broken Hill (unpublished).

Edwards, A. C. & Neef, G. 1979. Field conference: the geology of Mt Arrowsmith, Wonominta Block, Koonenberry Gap, Kayrunnera and Wertago. NSW Geol. Surv. Report, GS1981/183 (unpublished).

Faulring, G. M., Zwickr, W. K. & Forgong, W. D. 1960. Thermal transformation and properties of cryptomelane. Am. Min., 45:946-959.

Ferguson, A. K. 1977. The natural occurrence of aegirine-neptunite solid solution. Contrib. Mineral. Petrol., 87:247-253.

Fleischer, M. & Richmond, W.E. 1943. The manganese oxide minerals: a preliminary report. Econ. Geol., 38:269-286.

Floyd, P.A. & Winchester, J. A.1978. Identification and discrimination of altered and metamorphosed volcanic rocks using immobile elements. Chem. Geol., 21:291-306.

Forbes, B. G., Coats, R. P. & Daily, B., 1972. Truro Volcanics. Q. geol. Notes, geol. Surv. South Aust., 44:1-5.

Fortey, N. J. & Michie, U. Mcl. 1878. Aegirine of possible authigenic origin in Middle Devonian sediments in Caithness, Scotland. Min. Mag., 42:439-442.

Gilluly, J. 1971. Plate tectonics and magmatic evolution. Geol. Soc. Am. Bull., 82:2383-2396.

Gleadow, A. J. W. & Edwards, A. C. 1978. Mineralogical note: fission track age of a basic inclusion from the Kayrunnera kimberlite breccia pipe. J. Geol. Soc Aust., 25:359.

Gresens, R. L. 1967. Composition-volume relationships of metasomatism. Chem. Geol., 2:47-65.

Griffin, W. L. & Bruckner, H. K. 1978. Caledonian Sm-Nd ages and a crustal origin for Norwegian eclogites. Nature, 285:319-321.

Guidotti, C. V. 1984. Micas in metamorphic rocks. In S. W. Bailey (editor), Micas. Reviews in Mineralogy, No. 13. Min. Soc. Am., Washington, DC. p. 357-468.

Gulson, B. L. 1984. Uranium-lead and lead-lead investigations of minerals from the Broken Hill lodes and mine sequence rocks. Econ. Geol., 70:476-490.

Gulson, B. L., Large, R. R. & Porritt, P. M. 1987. Base metal exploration of the Mount Read volcanics, western Tasmania: Part III. Application of lead isotopes at Elliott Bay. Econ. Geol., 82:308-327.

Gulson, B. L., Solomon, M., Vaasjoki, M. & Both, R. 1991. Geological Note: Tasman Adrift? Aust. J. Earth Sci., 38:249-250.

Hamilton, P.J., Evensen, N. M., O'Nions, R. K., Smith, H. S. & Erlank, A. J. 1979a. Sm-Nd dating of Onverwacht Group volcanics, southern Africa. Nature, 279:298-300.

Hamilton, P. J., Evensen, N. M., O'Nions, R. K. & Tarney, J. 1979b. Sm-Nd systematics of Lewisian gneisses: Implications for the origin of granulites. Nature, 277:25-28.

Hamilton, P. J., O'Nions, R. K., Evensen, N. M. 1977. Sm-Nd Dating of Archaean basic and ultrabasic volcanics. Earth Planet Sci Lett., 36:263-268.

Hanson, G. N. 1989. An approach to trace element modelling using a simple igneous system as an example. In B. R. Linpin & G. A. Mckay (editors), Geochemistry and Mineralogy of Rare Earth Elements. Min. Soc. Am., Washington, DC, p. 79-98.

Harrington, H. J. 1974. The Tasman Geosyncline in Australia. In A. K. Denmead, G. W. Tweedale & A. F. Wilson (editors). The Tasman Geosyncline: A Symposium. Geological Society of Australia, Queensland Division, Brisbane. p. 283-407.

Hawkesworth, C. J., Hergt, J. M., McDermott, F. & Ellam, R. M. 1991. Destructive margin magmatism and the contributions from the mantle wedge and subducted crust. Aust. J. Earth Sci., 38:577-594.

Hewett, D. F. & Fleischer, M. 1960. Deposits of manganese oxides. Econ. Geol., 55:1-51.

Hewett, D. F. & Olivares, R. S. 1968. High-potassium cryptomelane from Tarapaca Province, Chile. Am. Min., 53:1551-1557.

Hey, M. H. 1954. A new review of the chlorites. Min. Mag., 30:277-292.

Hill, D. 1951. Geology. In Handbook of Queensland. Australas. Assoc. Adv. Sci., Brisbane, p.13-24.

Hofmann, A. 1971, Fractionation correction for mixed-isotope spikes of Sr, K and Pb. Earth Planet. Sci. Lett., 10:397-402

Hofmann, A.W. 1986. Nb in Hawaiian magmas: Constraints on source composition and evolution. Chem. Geol., 57:17-30.

Jacobsen, S. B. & Wasserburg, G. J. 1979. Nd and Sr isotopic study of the Bay of Islands ophiolite complex and the evolution of the source of mid-ocean ridge basalts. J. Geophy. Res., 84:7429-7445.

James, S. D., Pearce, J. A. & Oliver, R. A. 1987. The geochemistry of the lower Proterozoic Willyama Complex volcanics, Broken Hill Block, New South Wales. In T. C. Pharaoh, R. D. Beckinsale & D. Rickard (editors), Geochemistry and Mineralisation of Proterozoic Volcanic Suites. Geol. Soc. Spec. Publ. No.33, p. 395-408.

Jaquet, J. B. 1893. Appendix 4A, Nuntherungie Silver-field. NSW Dept. Mines Ann. Rep. (1892), p. 138-139.

Jefferson, D. A. & Pugh, N. J. 1981. The ultrastructure of pyroxenoid chain silicates, III. Intersecting defects in a synthetic iron-manganese pyroxenoid. Acta Crystallographica, A37:281-286.

Johnson, I.R. & Scott, A.G. 1971. Final report on EL437, Nuntherungie, NSW. CRA Exploration. NSW Geol. Surv., Sydney. GS1971/658(unpublished).

Joplin, G. A. 1968. Petrography of Australian Metamorphic Rocks. Angus & Robertson, Sydney.

Joplin, G. A. 1971. Petrography of Australian Igneous Rocks. Angus & Robertson, Sydney.

Kenny, E. J. 1934. West Darling District: A geological reconnaissance with special reference to the resources of subsurface water. NSW Geol. Surv. Sydney. Mineral Resources, No. 36.

Krogh, T. E. 1973. A low contamination method for the hydrothermal decomposition of zircon and extraction of U and Pb for isotopic age determinations. Geochim. Cosmochim. Acta, 37:485-494.

Krogh, T. E. & Hurley, P. M. 1968. Strontium isotope variation and whole-rock isochron studies, Grenville Province of Ontario. J. Geophys. Res., 73:7107-7125.

Kruse, P. D. 1980. Archaeocyathan faunas of Central Australia and western New South Wales. Ph. D. thesis, The University of Sydney (unpublished).

Kruse, P. D. 1982. Archaeocyathan biostratigraphy of the Gnalta Group at Mt. Wright, New South Wales. Palaeontographica Abt. A, 177:129-212.

Kushiro, I. 1960. Si-Al relation in clinopyroxenes from igneous rocks. Am. J. Sci., 258:548-554.

Laird, J. & Albee, A. L. 1981. Pressure, temperature and time indicators in mafic schist: their application to reconstructing the polymetamorphic history of Vermont. Am. J. Sci., 281:127-175.

Leahey, T. A. 1981. Combined final and progress report: February to August, 1981.

Ponto PL's 663, 664, NSW. Amoco Minerals Australia. Report 237. NSW Geol. Surv., Sydney. GS1981/274 (unpublished).

Leahey, T. A. 1982. Final report and progress report, January to July, 1982. Grasmere EL1288, NSW. Amoco Mineral Australia. Report 314. NSW Geol. Surv., Sydney. GS1982/458 (unpublished).

Leake, B. E. 1978. Nomenclature of amphiboles. Can. Min., 16:501-521.

Le Bas, M. J. 1962. The role of aluminium in igneous clinopyroxenes with relation to their parentage. Am. J. Sci., 260:267-288.

Le Bas, M. J., Le Maitre, R.W., Streckeisen, A. & Zanettin, B. 1986. A chemical classification of volcanic rocks based on the total alkali-silica diagram. J. Petrol., 27:745-750.

Leitch, E. C, Webby, B. D., Mills, K. J. & Kolbe, P. 1987. Terranes of the Wonominta Block, far western New South Wales. In E. C. Leitch & E. Scheibner (editors), Terrane Accretion and Orogenic Belts. Am. Geophys. Union. Geodynamics Series, No.19, p. 31-37.

Le Maitre, R. W. (editor). 1989. A Classification of Igneous Rocks and Glossary of Terms. Blackwell, Oxford. 193 pp.

Lennon, I.G. 1967. Final report to Koonenberry Prospect, NSW. Kennecott Exploration (Australia). Report for Messors R. Walton & E.R. Kurray. NSW Geol. Surv., Sydney. GS1967/045 (unpublished).

Leterrier, J., Maury, R.C., Thonon, P., Girard, D. and Marchal, M. 1982. Clinopyroxene composition as a method of identification of the magmatic affinities of paleo-volcanic series. Earth Planet. Sci. Lett., 59:139-154.

Lewis, P. C. 1976. Final and six monthly report for the period ending September 20, 1976 on Ponto NSW. ESSO Exploration Aust. NSW Geol, Surv., Sydney. GS1976/146 (unpublished).

Lightfoot, P. C.& Naldrett, A. J. 1989. Assimilation and crystallisation in basic magma chambers: trace-element and Nd-isotopic variations in the Kerns sill, Nipissing

diabase province, Ontario. Can. J. Earth Sci., 26:737-754.

Lindsay, J. F., Korsch, R. J. & Wilford, J. R. 1987. Timing the breakup of a Proterozoic supercontinent: Evidence from Australian intracratonic basins. Geology, 15:1061-1064.

Liou, J. G., Maruyama, S. & Cho, M. 1987. Very low-grade metamorphism of volcanic and volcaniclastic rocks - minerals assemblages and mineral facies. In: Frey, M (editor), Low Temperature Metamorphism. Blackie, 59-113.

Liu, S.-F., 1992. Mafic Dykes and Their Tectonic Settings in the Southern Adelaide Foldbelt, South Australia. Ph. D. thesis, La Trobe University, Melbourne (unpublished).

Long, J. V. P. 1975. Electron Probe Microanalysis. In J. Zussman (Editor), Physical Methods in Determinative Mineralogy. Academic, London. p. 274-335.

Long. L. E. 1966. Isotope dilution analysis of common and radiogenic strontium using ^{84}Sr-enriched spike. Earth Planet. Sci. Lett., 1:289-292.

Macdonald, G. A. & Katsura, T. 1964. chemical composition of Hawaiian lavas. J. Petrol., 5:82-133.

Mawson, D. 1912. Geological investigation in the Broken Hill area. SA R. Soc. Mem., 2:1-273.

McCulloch, M. T. 1987. Sm-Nd isotopic constraints on the evolution of Precambrian crust in the Australia continent. In A. Kroner (editor), Proterozoic Lithospheric Evolution. Geodynamic Series 17, p. 115-130.

McCulloch, M. T. & Gamble, J. A. 1991. Geochemical and geodynamical constraints on subduction zone magmatism. Earth Planet. Sci. Lett., 102:358-374.

McCulloch, M. T., Gregory, R. T., Wasserburg, G. J. & Taylor, H. P. 1980. Sm-Nd, Rb-Sr and $^{18}O/^{16}O$ isotopic systematics in an oceanic crustal section: evidence from the Semail ophiolite. J. Geophys. Res., 86:2721.

McIntyre, J. I. & Wyatt, B. W. 1978. Contributions to the regional geology of the

Broken Hill area from geophysical data. BMR Aust. J. Geol. & Geophy., 3:265-280.

McKenzie, D. 1989. Some remarks on the movement of small melt fractions in the mantle. Earth Planet. Sci. Lett., 95:53-72.

Mengel, F. & Rivers, T. 1991. Decompression reactions and P-T conditions in high grade rocks, northern Labrador: P-T-t paths from individual samples and implications for early Proterozoic tectonic evolution. J. Petrol. 32:139-167.

Mengel, K., Borsuk, A. M., Gurbarov, A. G., Wedepohl, K. H., Baumann, A. & Hoefs, J. 1987. Origin of spilitic rocks from the southern slope of the Great Caucasus. Lithos, 20:115-133.

Meschede, M. 1986. A method of discriminating between different types of MORBs and continental tholeiites with the Nb-Zr-Y diagram. Chem. Geol., 56:207-218.

Middlemost, E. A. K. 1975. The basalt clan. Earth Sci. Rev., 11:357-364.

Mills, K. J. 1992. Geological evolution of the Wonominta Block. Tectonophysics. (in press).

Miura, H., Banerjee, H., Hariya, Y., Dasgupta, S. & Roy, S. 1987. Hollandite and cryptomelane in the manganese oxide deposits of the Sausar Group, India. Mineral. J., 13:424-433.

Miyashiro, A. 1973. Metamorphism and Metamorphic Belts. John Wiley & Sons, New York.

Moody, J. B., Meyer, D. & Jenkins, J. E. 1983. Experimental characterization of the greenschist/amphibolite boundary in mafic system. Am. J. Sci., 283:48-92.

Moore, L. J., Moody, J. R., Barnes, I. L., Gramich, J. W., Murphy, T. J., Paulsen, P. J. & Shields, W. R. 1973. Trace determination of rubidium and strontium in silicate glass standard reference materials. Anal. Chem., 45:2384-2387.

Moores, E. M. 1991. Southwest U.S.-East Antarctica (SEEAT) connection: A hypothesis. Geology, 19:425-428.

Morris, P. A. 1988a. A geochemical approach to the characterization of a hidden magmatic arc: the source of the Goonoo Goonoo Mudstone, eastern Australia. Aust. J. Earth Sci., 35:81-92.

Morris, P. A. 1988b. Petrogenesis of fore-arc metabasites from the Paleozoic of New England, Eastern Australia. Mineral. & Petrol., 38:1-16.

Murray, C. G., Scheibner, E. & Walker, R. N. 1989. Regional geological interpretation of a digital coloured residual Bouguer gravity image of eastern Australia with a wavelength cut-off of 250 km. Aust. J. Earth Sci., 36:423-449.

Myers, R. E. & Breiltkopf, J. H. 1989. Basalt geochemistry and tectonic settings: a new approach to relate tectonic and magmatic processes. Lithos, 23:53-62.

Nakamura, N. 1974. Determination of REE, Ba, Mg, Na and K in carbonaceous and ordinary chondrites. Geochim et Cosmochim Acta, 38:757-775.

Neef, G., Edwards, A. C., Bottrill, R. S., Hatty, J., Holzberger, I., Kelly, R. & Vaughan, J. 1989. The Mt. Daubeny Formation: Arenite-rich ?Late Silurian-Early Devonian (Gedinnian) strata in far western New South Wales. NSW R. Soc. J. & Proc., 122:97-106.

Neumann, H., Mead, J. & Vitaliano, C. J. 1954. Trace element variation during fractional crystallisation as calculated from the distribution law. Geochim Cosmochim Acta., 6:90-99.

Newton, R. C. & Smith, J. V. 1967. Investigations concerning the breakdown of albite at depth in the earth. J. Geol., 75:268-286.

Nisbet, E. G. & Pearce, J. A. 1977. Clinopyroxene composition in mafic lavas from different tectonic settings. Contrib. Mineral. Petrol., 63:149-160.

Norrish, K. & Chappel, B.W. 1975. X-ray fluorescence spectrometry. In J. Zussman (editor). Physical Methods in Determinative Mineralogy. Academic Press, London.

Norrish, K. & Hutton, J. T. 1969. An accurate X-ray spectrographic method for the analysis of a wide range of geological samples. Geochim. Cosmochim. Acta.,

33:431-453.

O'Nions, R. K., Hamilton, P. J. & Evensen, N. M. 1977. Variations in $^{143}Nd/^{144}Nd$ and $^{87}Sr/^{86}Sr$ ratios in oceanic basalts. Earth. Planet .Sci. Lett., 34:13-22.

O'Nions, R. K. & McKenzie, D. P. 1988. Melting and continent generation. Earth Planet. Sci. Lett. 90:449-456.

Packham, G. H. (editor).1969. The Geology of New South Wales. J. Geol. Soc. Aust. 16:1-232.

Packham, G. H. & Leitch, E. C. 1974. The role of plate tectonic theory in the interpretation of Tasman orogenic zone. In A. K. Denmead, G. W. Tweedale & A. F. Wilson (editors), The Tasman Geosyncline: A Symposium. Geol. Soc. Aust., Queensland Division, p.129-155.

Page, R. W & Laing, W. P. 1990. Depositional age of the Broken Hill group from volcanics stratigraphically equivalent to the Ag-Pb-Zn orebody. In Geol. Soc. Aust., Abstract No. 25,p. 18 - 19.

Pankhurst, R. J., Storey, B. C., Millars, I. L., Macdonald, D. I. M. & Vennum, W. R. 1988. Cambrian-Ordovician magmatism in the Thiel Mountains, Transantarctica Mountains, and implication for the Beardmore orogeny. Geology, 16:246-249.

Papike, J. J. 1974. On the chemistry of clinoamphiboles. EOS Transactions of the Geophysical Union, 55:469

Pearce, J. A. 1983. Role of the sub-continental lithosphere in magma genesis at active continental margins. In C. J. Hawkesworth & M. J. Norry (editors) Continental Basalts and Mantle Xenoliths. Shiva, Nantwich, p. 231-249.

Pearce, J. A. & Cann, J. R. 1973. Tectonic setting of basic volcanic rocks determined using trace element analyses. Earth. Planet. Sci. Lett., 19:290-300.

Pearce, J. A. & Norry, M. J. 1979. Petrogenetic implicatons of Ti, Zr, Y and Nb variations in volcanic rocks. Contrib. Mineral. Petrol., 69:33-47.

Penny, S. R. 1985. Final report for EL2431 Koonenberry, EL2437 Wonominta and EL2438 Nuntherungie. BP Minerals Australia. NSW Geol. Surv., Sydney. GS1985/298. (unpublished)

Perseil, E. A. & Pinet, M. 1976. Contribution to the study of Romanechites and cryptomelane-coronadites-hollandites, characteristics and occurrences. Contrib. Mineral. Petrol., 55:191-204.

Plumb. K. A. 1979. The tectonic evolution of Australia. Earth Sci. Rev., 14:205-249.

Pogson, D. J. & Scheibner, E. 1971. Pre-Upper Cambrian sediments east of Copper Mine Range, New South Wales. NSW Geol. Surv. Q. Notes, 3-8.

Powell, C. McA., Neef, G, Crane,D, Jell, P. A. & Percival, I. G. 1982. Significance of Late Cambrian (Idamean) fossils in the Cupala Creek Formation, northwestern NSW. Proc. Linn. Soc. NSW, 106:127-150.

Powell, C. McA, Li, Z. X., Thrup, G. A. & Schmidt, P. W. 1990. Australian Palaeozoic palaeomagnetism and tectonics - I: Tectonostratigraphic terrane constraints from the Tasman Fold Belt. J. Structural. Geol., 12:553-565.

Preiss, W. V. (compiler) 1987. The Adelaide Geosyncline. Late Proterozoic Stratigraphy, Sedimentation, Palaeontology and Tectonics. SA Dept. Mines and Energy, Bullitin 53.

Preiss, W.V. & Forbes, B.G. 1981. Stratigraphy, correlation and sedimentary history of Adelaidean (Late Proterozoic) Basin in Australia. Precambrian Res., 15:255-304.

Prestvik, T. 1982. Basic volcanic rocks and tectonic setting. A discussion of the Zr-Ti-Y discrimination diagrams and its suitability for classification purposes. Lithos, 15:241-247.

Richmond, W. E. & Fleischer, M. 1942. Cryptomelane: a new name for the commonest of the "psilomelane" minerals. Am. Min., 27:607-610.

Ried, H. 1984. Intergrowth of pyroxene and pyroxenoid; chain periodicity faults in

pyroxene. Phys. Chem. Minerals, 10:230-235.

Ried, H & Korekawa, M. 1980. Transmission electron microscopy of synthetic and natural fünferketten and siebenerketten pyroxenoids. Phys. Chem. Minerals, 5:351-365.

Ringwood, A. E. 1975. Composition and Petrology of the Earth's Mantle. McGraw-Hall, New York. 618 pp.

Robinson, D. 1987. Transition from diagenesis to metamorphism in extensional and collision settings. Geology, 15:866-869.

Roddick, J.C., Sullivan, R. W. & Dudas, F. O. 1992. Precise calibration of tracer compositions for Sm-Nd isotopic studies. Earth Planet. Sci. Lett., (in press).

Rose, G. 1968. Broken Hill Sheet Sh54-14, 1:250 000 Geological Series (preliminary edition). NSW Geol. Surv., Sydney.

Rose, G. 1975. Wonominta Block-regional geology & mineralisation. In C. L. Knight (editor), Economic Geology of Australia & Papua New Guinea. I: Metals. Australas Inst. Mineral. Metall., Parkville, Vic. p. 508-510.

Rose, G. & Brunker, R. L. 1969. The Upper Proterozoic geology of north-western NSW. Proc. Aust. Inst. Mineral. Metall., No. 229, p. 105-120.

Rowell, A. J., Rees, M. N. & Evans, K. R. 1992. Evidence of major Middle Cambriam deformation in the Ross orogen, Antarctica. Geology, 20:31-34.

Roy, S. 1981. Manganese Deposits. Academic Press, London.

Russell, R. D. 1971. The systematics of double spiking. J. Geophys. Res., 76:4949-4955.

Russell, R. D. 1977. A solution in closed form for the isotopic dilution analysis of strontium. Chem. Geol., 20:307-314.

Saunders, A. D. & Tarney, J. 1984. Geochemical characteristics of basaltic volcanism within back-arc basins. In Kokelaar, B. P. & Howell, M. F. (eds),

Marginal Basin Geology. Blackwell, Oxford. p. 59-76.

Scheibner, E. 1972. The Kanmantoo pre-cratonic province in New South Wales. NSW Geol. Sur., Sydney. Quarterly Notes, 7:1-10.

Scheibner, E. 1974. A plate tectonic model of the Palaeozoic tectonic history of NSW. J. Geol. Sci. Aust., 20:405-426.

Scheibner, E. 1976. Explanatory Notes to the Tectonic Map of New South Wales. NSW Geol. Surv., Sydney. 283pp.

Scheibner, E. 1987. Palaeozoic tectonic development of eastern Australia in relation to the Pacific region. In J.W.H. Monger & J. Francheteau(editors), Circum-Pacific Belts and Evolution of the Pacific Ocean Basin. Am. Geophy. Union, Geodynamic Series, No.18, p.133-165.

Scheibner, E. 1989. The tectonics of New south Wales in the second decade of application of the plate tectonics paradigm. NSW R. Soc. J. & Proc., 122:35-74.

Scheibner, E. (principla compiler) 1991. Broken Hill - Sydney - Tasman Sea transect: Proterozoic to Cenozoic crustal development of New South Wales, eastern Australia. Explanatory Text. NSW Geol. Survey, Sydney.

Schilling, J.-G. 1966. Rare Earth Fractionation in Hawaiian Volcanic Rocks. Ph. D. thesis. Mass. Inst. Tech. Cambridge, MA (unpublished).

Schilling, J.-G. 1991. Fluxes and excess temperatures of mantle plumes inferred from their interaction with migrating mid-ocean ridges. Nature, 352:397-403.

Sivell, W.J. & McCulloch, M. T. 1991. Neodymium isotope evidence for ultra-depleted mantle in the early Proterozoic. Science, 354:384-387.

Stevens, B. J. P. 1985. Preliminary interpretation of regional basement geology in northwestern NSW. NSW Geol. Surv. Q. Note, No. 63.

Stevens, B. J. P. 1986. Post-depositional history of the Willyama Supergroup in Broken Hill Block, NSW. Aust. J. Earth Sci., 33:73-98.

Stevens, B. J. P., Barnes, R. G., Brown, R. E., Stroud, W. J. & Willis, I. L. 1988. The Willyama Supergroup in the Broken Hill and Euriowie Blocks, New South Wales. Precam. Res., 40/41:297-327.

Stevens, B. J. P. & Raphael, N. M. 1985. Reconnaissance geology and mineral potential of the Wertago-Nuntherungie area. NSW Geol Surv. Sydney. GS1985/241 (unpublished).

Stracke, K. J., Ferguson, J. G. & Black, L. P. 1979. Structural setting of kimberlites in south-eastern Australia. Abstract Second Int. Kimberlite Conf. Sante Fe.

Sturt, C. 1849. Geology of the Barrier Range. p.127-129.

Sun, S.-S. & McDonough, W. F. 1989. Chemical and isotopic systematics of oceanic basalts: implications for mantle composition and processes. In A. D. Saunders & M. J. Norry (editors). Magmatism in the Ocean Basins. Geol. Soc. Spec. Publ, No.42, p.313-345.

Sun, S.-S., Nesbitt, R.W. & Ya Sharaskin, A. 1979. Geochemical characteristics of mid-ocean ridge basalts. Earth. Planet. Sci. Lett., 44:119-138.

Taylor, S. R. & McLennan, S. M. 1985. The Continental Crust, Its Composition and Evolution: An examination of the Geochemical Record Presented in Sedimentary Rocks. Blackwells Scientific, Oxford. 312pp.

Thompson, R. N., Morrison, M. A., Dickin, A. P. & Hendry, G.L. 1983. Continental flood basalts... Arachnids rule OK? In C. J. Hawkesworth & M. J. Norry, (editors). Continental Basalts and Mantle Xenoliths. Shiva, Nantwich, p.158-175.

Thompson, R. N., Morrison, M. A., Hendry, G. L. & Parry, S.J. 1984. An assessment of the relative roles of crust and mantle in magma genesis: an elemental approach. Phil. Trans. R. Soc. Lond., A310:549-590.

Thomson, B.P. 1963. Precambrian rock groups in the Adelaidean Geosyncline. SA Geol. Surv., Q. Geol. Note, No 9.

Thomson, B. P. & King, H. F. 1952. Geological reconnaissance of Koonenberry

and Tibooburra-Milparinka districts. The Zinc Corporation Memo, No. 239. NSW Geol. Surv., GS1952/084 (unpublished).

Triboulet, C. 1992. The (Na-Ca) amphibole-albite-chlorite-epidote-quartz geothermobarometer in the system S-A-F-M-C-N-H_2O. 1. An empirical calibration. J. Metamorphic Geol., 10:545-556.

Turner, F. J. 1981. Metamorphic Petrology: Mineralogical, Field and Tectonic Aspects (2nd ed). McGraw-Hill, New York. p.524.

Vallance, T. G. 1969. Spilite again: some consequences of the degradation of basalts. Proc. Linn. Soc. NSW, 94:8-51.

Vallance, T. G. 1974. Pyroxenes and the basalt, spilite relation. In G. C. Amstutz (editor), Spilites and Spilitic Rocks. Springer-Verlag Berlin, p. 59-70.

Veblen, D. R. 1982. Replacement of johannsenite by Mn-pyroxenoid: microstructures and mechanism of reaction (abstract). Geol. Soc. Am. Ab., 14:637.

Veblen, D. R. 1985. TEM study of pyroxene to pyroxenoid reaction. Am Min., 70:885-901.

Verhoogen, J. 1962. Distribution of titanium between silicates and oxides in igneous rocks. Am. J. Sci., 260:211-230.

Vukadinovic, D & Nicholls, I. A. 1989. The petrogenesis of island arc basalts from Gunung Slamet Volcano, Indonesia: Trace element and $^{87}Sr/^{86}Sr$ constraints. Geochim. Cosmochim. Acta, 53: 2349-2363.

Wang, Q.-M. 1989. Mineralogical Aspects of Monzonite Alteration: An Investigation by Electron Microscopy and Chemistry. Ph. D. thesis, The Australian National University (unpublished).

Wang, Q. Z., Mills, K. J., Webby, B. D. & Shergold, J. H. 1989. Upper Cambrian (Mindyallan) trilobites and stratigraphy of the Kayrunnera Group, western New South Wales. BMR J. Aust. Geol. Geophys., 11:107-118.

Warren, R. G. 1972. Metallogenic Map of Australia and Papua New Guinea. Scale

1:5,000,000. BMR, Canberra.

Warris, B. J. 1967. The Palaeozoic stratigraphy and palaeontology of north-western NSW. Ph. D. Thesis. The University of Sydney (unpublished.).

Weaver, S. D. 1987. Introduction to the symposium, geochemistry of eruption magmas - tectonic control and petrogenesis. J. Volcano. Geotherm. Res., 32:9-10.

Webby, B. D. 1978. History of the Ordovician continental and shelf margin of Australia. Geol. Soc. Aust. J., 25:41-63.

Webby, B. D. 1984. Precambrian-Cambrian trace fossils from western NSW. Aust. J. Earth. Sci., 31:427-437.

Wenk, H. R. (ed) 1978. Electron Microscopy in Mineralogy. Springer-Verlag, Berlin, p.4-14.

Wheatley, M.R.& Rock, N.M.S. 1988. Spider: A Macintosh program to generate normalised multi-element spidergrams. Am. Mineral., 73:919–921.

Whitford, D. J., Korsch, M. J., Porritt, P. M. & Craven, S. J. 1988. Rare-Earth element mobility around the volcanogenic polymetallic massive sulfide deposit at Que River, Tasmania, Australia. Chem. Geol., 68:105-119

Whitford, D. J. 1989. Geochemistry of the host rocks of the volcanogenic massive sulfide deposit at Que River, Tasmania. Econ. Geol. 84:1-21.

Wilkinson, C. S. 1889. Notes on the geology of the Barrier Ranges district, and the Mount Browne and Mount Poole Gold-fields, NSW Geol. Surv., Rec. 1:1-9.

Willis, I. L., Brown, R. E., Stroud, W. J. & Stevens, B. P. J. 1983. The Early Proterozoic Willyama Supergroup: stratigraphic subdivision and interpretation of high to low grade metamorphic rocks in the Broken Hill Block, New South Wales. Geol. Soc. Aust. J., 30:195-224.

Williams, H., Turner, F. J. & Gilbert, C. M. 1982. Petrography: an Introduction to the Study of Rocks in Thin Sections. W. H. Freeman, San, Francisco, 626pp.

Williams, K. L. 1988. Introduction to X-Ray Spectrometry: X-Ray Fluorescence and Electron Microprobe Analyses. Allen & Unwin, London.

Wilson, D. 1984. Report on an aeromagnetic survey, Bancannian North area, Sept. 1984. In S. R. Penny, Second six months report for EL2248 Milpa, 28 Dec, 1984 - 27 July, 1985. NSW Geol. Surv., GS1984/41(unpublished).

Winchester, J. A. & Floyd, P. A. 1977. Geochemical discrimination of different magma series and their differentiation products using immobile elements. Chem. Geol., 20:325-343.

Wood, D. A., Joron, J.-L. & Treuil, M. 1979a. A re-appraisal of the use of trace elements to classify and discriminate between magma series erupted in different tectonic settings. Earth. Planet. Sci. Lett., 45:326-336.

Wood, D. A., Joron, J.-L., Treuil, M., Norry, M. & Tarney, J. 1979b. Elemental and Sr isotope variations in basic lavas from Iceland and the surrounding ocean floor: the nature of mantle source inhomogeneities. Contrib. Mineral. Petrol., 70:319-339.

Woodhead, J. D. 1989. Geochemistry of the Mariana arc (western Pacific): Source composition and processes. Chem. Geol., 76:1-24.

Worner, G., Zindler, A., Staudigel, H. & Schimincke, H.-U. 1986. Sr, Nd & Pb isotope geochemistry of Tertiary and Quaternary alkaline volcanics from West Germany. Earth Planet. Sci. Lett., 79:107-119.

Zhao, J.-X., McCulloch, M. T. Korsch, R. J. & Parker, A. J. (1992). Regional correlation of ~ 800 Ma magmatic event in central-southern Australia: Evidence for a Late Proterozoic mantle plume, in preparation.

Zhou, B., Carr, G. & Gulsion, B. L. 1992. A preliminary lead isotope study on sulphide samples from Grasmere Prospect in the Wonominta Block, western NSW. In Centre for Isotope Studies, Research Report, 1991-1992, Sydney.

Zhou, B. & Mills, K.J. 1990. The geology, geochemistry and tectonic implications of metamorphosed mafic igneous rocks in the Wonominta Block, NSW. In Geol. Soc. Aust., Abstract No. 25,p. 235 - 236.

Zhou, B., Mills, K. J. & Liu, S. -F. 1990. The boundary between the Tasman Fold Belt and its basement: a reappraisal from the study of mafic rocks. Geological Society of Australia Abstract No. 26, p.7.

Zhou, B. & Mills, K. J. 1990. Multiple dyke emplacement in the Wonominta Block, western New South Wales, Australia and its tectonic significance in relation to the Tasman Line. In A. J. Parker, P. C. Rickwood & D. H. Tucker (Editors), Mafic Dyke and Emplacement Mechanisms. A.A. Balkema, Rotterdam, p.435-443.

Zhou, B., Whitford, D. J., Gulson, B. L., Mills, K. J. & Hendry, D. A. F. 1990. Isotopic studies of metamorphosed mafic rocks from the Wonominta Block western NSW: A preliminary report. In Centre for Isotope Studies, Research Report, 1988-1990, Sydney. p.116-118.

Zhou, B. & Whitford, D.J.. 1992. Geochemical and Sr-Nd isotope studies of the Mount Wright Volcanics. Aust. J. Earth Sci. (in press).

Zhou, B. & Whitford, D.J. 1992. MORB-like rocks in the basement sequence of the Wonominta Block, western NSW: Geochemical and Sr-Nd isotopic studies. In Centre for Isotope Studies, Research Report, 1991-1992, Sydney.

Zindler, A. & Hart, S. 1986. Chemical geodynamics. Ann. Rev. Earth Planet. Sci., 14:493-571.

Appendices

Appendix 1.
Sample List

Over four hundred samples of various rock types were collected during the field work, which are individually assigned a unique specimen number and a grid reference. The sample number consists of six figures that present chronological information. For example, for sample 752001, "7" stands for 1987 (hence, 8 in this position stands for 1988), "5" stands for May, "20" indicates the 20th day of the month, and "01" for the first sample collected in the day. Thus, "862222" stands for the 22nd sample collected on June 22, 1988. In this sample list, a USGD number is also given for each sample collected, representing that these samples are deposited in the collection of the Department of Geology and Geophysics, The University of Sydney.

The grid reference follows the Australian standard national grid reference (U.T.M.) as used on 1:100,000 sheet series of the Australian Map Grid in 6^0 zones. The prefix "6" in the N direction, shared in common by all specimens, is omitted. Thus, sample 752001 (grid 6148E, 6297N) has a UTM grid reference of (614800E, 6629700N). This represents a precision of ±100 metres for the location of samples in the field.

	A	B	C	D
1		Sample List		
2	Sample	USGD No.	Grid (UTM)	Sample description
3	752001	68709	6148, 6297	Metadolerite (II)
4	752002	68710	6148, 6297	Quartzite
5	752101	68711	6163, 6331	Metabasite
6	752102	68712	6163, 6331	Chert
7	752103	68713	6156, 6329	Quartzite
8	752104	68714	6156, 6329	Copper Ore
9	752106	68715	6165, 6337	Metadolerite (II)
10	752107	68716	6161, 6340	Greywacke
11	752108	68717	6163, 6338	Ironstone
12	752109	68718	6176, 6374	Metadolerite (I)
13	752110	68719	6176, 6374	Metadolerite (I)
14	752111	68720	6176, 6374	Metadolerite (I)
15	752112	68721	6176, 6374	Hornfels
16	752113	68722	6176, 6374	Hornfels
17	752114	68723	6176, 6374	Greywacke
18	752115	68724	6170, 6380	Slate
19	752116	68725	6170, 6380	Carbonate
20	752117	68726	6170, 6380	Carbonate
21	752201	68727	6124, 6371	Metabasite
22	752202	68728	6124, 6371	Metabasite
23	752203	68729	6124, 6371	Metabasite
24	752204	68730	6124, 6371	Metabasite
25	752205	68731	6124, 6371	Metabasite
26	752301	68732	6202, 6291	Metadolerite (II)
27	752302	68733	6202, 6291	Metadolerite (II)
28	752303	68734	6202, 6291	Hornfels
29	752304	68735	6202, 6291	Metabasite
30	752305	68736	6202, 6291	Metabasite
31	752306	68737	6202, 6291	Greywacke
32	752307	68738	6202, 6291	Schist
33	752308	68739	6202, 6291	Schist
34	752309	68740	6202, 6291	Schist
35	752310	68741	6202, 6291	Quartzite
36	752311	68742	6202, 6291	Sandstone
37	752312	68743	6202, 6291	Sandstone
38	752501	68744	6148, 6297	Metadolerite (II)
39	752502	68745	6145, 6300	Ironstone
40	752503	68746	6145, 6300	Ironstone
41	752801	68747	6181, 6319	Quartzite
42	752802	68748	6181, 6319	Phyllite
43	752803	68749	6183, 6317	Metabasite
44	752804	68750	6183, 6317	Metabasite
45	752805	68751	6179, 6313	Metabasite
46	752806	68752	6179, 6313	Metabasite
47	752807	68753	6179, 6313	Carbonate
48	752808	68754	6183, 6312	Metabasite
49	752809	68755	6183, 6312	Metabasite
50	752810	68756	6185, 6312	Metabasite
51	752811	68757	6185, 6312	Metabasite

	A	B	C	D
52	Sample	USGD No.	Grid (UTM)	Sample description
53	752901	68758	6181, 6319	Quartzite
54	752902	68759	6169, 6321	Metabasite
55	752903	68760	6169, 6321	Ironstone
56	752904	68761	6169, 6321	Ironstone
57	752905	68762	6169, 6321	Metabasite
58	752906	68763	6169, 6321	Carbonate
59	752907	68764	6169, 6321	Metabasite
60	752908	68765	6169, 6321	Metabasite
61	752909	68766	6169, 6321	Metadolerite (II)
62	752910	68767	6169, 6321	Metadolerite (II)
63	752911	68768	6169, 6321	Carbonate
64	753001	68769	6186, 6313	Metabasalt
65	753002	68770	6186, 6313	Metabasalt
66	753003	68771	6186, 6312	Metabasite
67	753004	68772	6186, 6312	Metabasite
68	753005	68773	6186, 6312	Metabasite
69	753006	68774	6186, 6312	Phyllite
70	753007	68775	6191, 6305	Metabasite
71	753008	68776	6191, 6305	Metabasite
72	753009	68777	6189, 6302	Metabasite
73	753010	68778	6189, 6302	Metabasite
74	753011	68779	6189, 6301	Ironstone
75	753012	68780	6189, 6301	Ironstone
76	753013	68781	6190, 6303	Metadolerite (II)
77	753014	68782	6190, 6303	Metadolerite (II)
78	753101	68783	6168, 6344	Ironstone
79	753102	68784	6154, 6347	Marble
80	753103	68785	6154, 6347	Chert
81	753104	68786	6154, 6347	Ironstone
82	753105	68787	6156, 6345	Ironstone
83	753106	68788	6164, 6337	Metadolerite (II)
84	760101	68789	6158, 6328	Ironstone
85	760102	68790	6156, 6329	Metabasite
86	760103	68791	6154, 6323	Quartzite
87	760104	68792	6157, 6330	Metabasite
88	760201	68793	6167, 6315	Metabasite
89	760301	68794	6164, 6319	Metadolerite (II)
90	760302	68795	6165, 6318	Metadolerite (II)
91	760401	68796	6195, 6323	Metadolerite (III)
92	760402	68797	6178, 6317	Metadolerite (III)
93	760403	68798	6178, 6317	Ironstone
94	760404	68799	6178, 6317	Metabasite
95	760405	68800	6178, 6317	Slate
96	760406	68801	6178, 6317	Metadolerite (II)
97	760408	68802	6178, 6317	Metadolerite (II)
98	760409	68803	6178, 6317	Phyllite
99	760410	68804	6178, 6317	Conglomerate
100	760411	68805	6178, 6317	Ironstone
101	760412	68806	6178, 6317	Greywacke
102	760413	68807	6176, 6326	Schist

	A	B	C	D
103	Sample	USGD No.	Grid (UTM)	Sample description
104	760414	68808	6174, 6321	Greywacke
105	760501	68809	6160, 6342	Metabasite
106	760502	68810	6148, 6355	Ironstone
107	760503	68811	6139, 6371	Ironstone
108	760601	68812	6192, 6328	Metadolerite (III)
109	760701	68813	6169, 6321	Metabasite
110	760702	68814	6169, 6321	Metabasite
111	760703	68815	6169, 6321	Metadolerite (II)
112	760801	68816	5960, 6189	Metadolerite (II)
113	760802	68817	5960, 6189	Metabasite
114	760803	68818	5960, 6189	Greywacke
115	760804	68819	5960, 6199	Spotted slate
116	760805	68820	5938, 6216	Metabasite
117	760806	68821	5941, 6214	Metabasite
118	760807	68822	5945, 6215	Carbonate
119	760808	68823	5945, 6200	Carbonate
120	760809	68824	5945, 6200	Quartzite
121	760901	68825	5963, 6179	Metabasite
122	760902	68826	5964, 6178	Carbonate
123	760903	68827	5965, 6177	Metabasite
124	760904	68828	5950, 6198	Carbonate
125	761001	68829	5926, 6206	Metadolerite (II)
126	761002	68830	5928, 6202	Metadolerite (II)
127	761003	68831	5926, 6205	Marble
128	761004	68832	5927, 6205	Greywacke
129	761005	68833	5927, 6205	Greywacke
130	761006	68834	5939, 6186	Quartzite
131	761008	68835	5960, 6189	Carbonate
132	761009	68836	5960, 6189	Metabasite
133	761010	68837	5960, 6189	Garnet vein
134	761201	68838	5932, 6168	Slate
135	761202	68839	5932, 6168	Quartzite
136	761203	68840	5936, 6176	Metadolerite (II)
137	761204	68841	5933, 6166	Syenite
138	761205	68842	5933, 6166	Syenite
139	761206	68843	5926, 6188	Quartzite
140	761207	68844	5954, 6189	Metabasite
141	761301	68845	5915, 6420	Metabasite
142	761302	68846	5915, 6420	Metabasite
143	761303	68847	5930, 6198	Metabasite
144	761304	68848	5948, 6198	Metabasite
145	761305	68849	5950, 6199	Metabasite
146	761306	68850	5946, 6198	Marble
147	761307	68851	5946, 6198	Carbonate
148	761308	68852	5946, 6198	Fe-oxides
149	761501	68853	6080, 6044	Metabasite
150	761502	68854	6084, 6045	Metabasite
151	761503	68855	6084, 6046	Metabasalt
152	761504	68856	6084, 6052	Marble
153	761505	68857	6080, 6058	Metabasite

	A	B	C	D
154	Sample	USGD No.	Grid (UTM)	Sample description
155	761506	68858	6082, 6057	Slate
156	761507	68859	6088, 6060	Metabasite
157	761508	68860	6089, 6061	Metabasite
158	761509	68861	6089, 6061	Hornfels
159	761510	68862	6089, 6061	Chert
160	761511	68863	6089, 6061	Chert
161	761512	68864	6089, 6061	Metabasite
162	761601	68865	6072, 6064	Carbonate
163	761602	68866	6075, 6056	Metabasite
164	761603	68867	6074, 6045	Altered syenite
165	761604	68868	6074, 6045	Altered syenite
166	761801	68869	6074, 6052	Altered peridotite
167	761802	68870	6074, 6052	Altered peridotite
168	761803	68871	6074, 6052	Altered peridotite
169	761804	68872	6074, 6052	Altered peridotite
170	761805	68873	6074, 6052	Altered peridotite
171	761806	68874	6074, 6052	Altered peridotite
172	761807	68875	6070, 6057	Greywacke
173	761808	68876	6070, 6057	Greywacke
174	761809	68877	6074, 6053	Metabasite
175	761810	68878	6074, 6053	Metabasite
176	761901	68879	6083, 6066	Metabasite
177	761903	68880	6083, 6066	Metabasite
178	761904	68881	6083, 6066	Carbonate
179	761905	68882	6086, 6065	Slate
180	761906	68883	6083, 6044	Metadolerite (I)
181	761907	68884	6085, 6048	Metadolerite (I)
182	761908	68885	6083, 6048	Metadolerite (I)
183	762001	68886	6050, 6100	Ferricrete
184	762002	68887	6059, 6057	Syenite
185	762003	68888	6059, 6057	Syenite
186	762004	68889	6059, 6057	Syenite
187	762201	68890	6084, 6055	Chert
188	762202	68891	6076, 6076	Breccia
189	762203	68892	6076, 6076	Breccia
190	762204	68893	6076, 6076	Breccia
191	762205	68894	6076, 6076	Breccia
192	762401	68895	6063, 6070	Felsic tuff
193	762402	68896	6063, 6070	Nundorite
194	762403	68897	6063, 6070	Nundorite
195	762404	68898	6063, 6070	Nundorite
196	762405	68899	6063, 6070	Felsic tuff
197	762406	68900	6063, 6070	Nundorite
198	762407	68901	6063, 6070	Nundorite
199	762408	68902	6063, 6070	Felsic Tuff
200	762409	68903	6063, 6070	Felsic Tuff
201	762410	68904	6255, 6150	Lamprophyre
202	762411	68905	6250, 6150	Lamprophyre
203	762412	68906	6250, 6150	Lamprophyre
204	762413	68907	6250, 6150	Epidote nodule

	A	B	C	D
205	Sample	USGD No.	Grid (UTM)	Sample description
206	762414	68908	6260, 6130	Gabbro
207	762501	68909	6376, 6038	Metadolerite (II)
208	762502	68910	6363, 6063	Ironstone
209	762503	68911	6363, 6063	Carbonate
210	762504	68912	6365, 6077	Breccia
211	762505	68913	6365, 6077	Breccia
212	762601	68914	6341, 6103	Greywacke
213	762602	68915	6333, 6100	Metadolerite (II)
214	762603	68916	6331, 6096	Metadolerite (II)
215	762604	68917	6331, 6095	Metadolerite (II)
216	762605	68918	6333, 6092	Metadolerite (II)
217	762606	68919	6358, 6070	Metabasite
218	762607	68920	6360, 6073	Schist
219	762608	68921	6359, 6070	Metadolerite (II)
220	762609	68922	6365, 6077	Greywacke
221	762701	68923	6381, 6050	Metadolerite (II)
222	762702	68924	6381, 6047	Schist
223	762703	68925	6379, 6026	Metabasite
224	762704	68926	6379, 6026	Metabasite
225	762705	68927	6390, 6025	Metadolerite (I)
226	762706	68928	6389, 6025	Metadolerite (III)
227	762707	68929	6393, 6033	Quartzite
228	762708	68930	6391, 6037	Quartzite
229	762709	68931	6390, 6038	Breccia
230	762710	68932	6387, 6043	Breccia
231	762801	68933	6379, 6056	Breccia
232	762802	68934	6375, 6061	Breccia
233	762803	68935	6372, 6065	Metadolerite (II)
234	762804	68936	6353, 6087	Phyllite-greywacke
235	762805	68937	6353, 6084	Chert
236	762806	68938	6383, 6058	Sandstone
237	762901	68939	6555, 6080	Sandstone
238	762902	68940	6555, 6080	Sandstone
239	762903	68941	6555, 6080	Sandstone
240	762904	68942	6500, 6050	Gabbro
241	762905	68943	6500, 6050	Hornfels
242	860901	68944	6706, 5073	Metabasalt
243	860902	68945	6706, 5073	Metabasite
244	860903	68946	6702, 5065	Qz Sandstone
245	860904	68947	6704, 5071	Metabasite
246	860905	68948	6704, 5071	Metabasite
247	860906	68949	6714, 5082	Metabasite
248	860907	68950	6714, 5082	Marble
249	860908	68951	6714, 5082	Metabasite
250	860909	68952	6714, 5082	Metabasite
251	860910	68953	6714, 5082	Metabasite
252	860911	68954	6714, 5082	Quartzite
253	860912	68955	6714, 5082	Metabasite
254	861001	68956	6711, 5083	Metabasite
255	861002	68957	6711, 5083	Metabasalt

	A	B	C	D
256	Sample	USGD No.	Grid (UTM)	Sample description
257	861003	68958	6711, 5083	Metabasalt
258	861004	68959	6711, 5083	Metabasalt
259	861005	68960	6705, 5080	Metadolerite (I)
260	861006	68961	6705, 5080	Metadolerite (I)
261	861007	68962	6703, 5078	Metabasalt
262	861008	68963	6703, 5078	Metabasalt
263	861009	68964	6701, 5075	Metabasite
264	861010	68965	6701, 5075	Metadolerite (II)
265	861011	68966	6702, 5070	Metadolerite (II)
266	861012	68967	6702, 5070	Metadolerite (I)
267	861013	68968	6703, 5071	Metabasite
268	861014	68969	6703, 5073	Metabasite
269	861015	68970	6705, 5072	Metabasite
270	861016	68971	6709, 5078	Metabasalt
271	861017	68972	6709, 5078	Metabasalt
272	861201	69973	6686, 5343	Metabasite
273	861202	69974	6686, 5343	Mafic schist
274	861203	69975	6686, 5343	Metabasite
275	861204	69976	6686, 5343	Marble
276	861205	69977	6680, 5337	Mafic schist
277	861206	69978	6680, 5337	Mafic schist
278	861207	69979	6680, 5337	Quartzite
279	861208	69980	6690, 5347	Metabasalt
280	861209	69981	6682, 5353	Felsic Tuff
281	861210	69982	6675, 5354	Metabasite
282	861211	69983	6669, 5342	Metadolerite (II)
283	861212	69984	6670, 5344	Metadolerite (II)
284	861301	69985	6668, 5347	Metadolerite (III)
285	861302	69986	6666, 5347	Metadolerite (III)
286	861303	69987	6664, 5345	Metadolerite (II)
287	861304	69988	6664, 5344	Metabasite
288	861305	69989	6664, 5344	Metabasite
289	861306	69990	6659, 5339	Metabasite
290	861307	69991	6657, 5340	Metabasite
291	861308	69992	6664, 5347	Metabasite
292	861309	69993	6672, 5355	Metabasite
293	861310	69994	6601, 5399	Metadolerite (I)
294	861311	69995	6609, 5383	Metadolerite (II)
295	861312	69996	6610, 5383	Metadolerite (II)
296	861313	69997	6623, 5376	Metadolerite (I)
297	861314	69998	6625, 5377	Metadolerite (I)
298	861315	69999	6623, 5378	Metadolerite (I)
299	861316	67000	6625, 5380	Metabasite
300	861401	67001	6647, 5357	Mafic schist
301	861402	67002	6647, 5355	Schist
302	861403	67003	6646, 5351	Metabasite
303	861404	67004	6647, 5350	Mafic schist
304	861405	67005	6646, 5350	Metabasite
305	861406	67006	6651, 5352	Calcrete
306	861407	67007	6649, 5352	Metadolerite (II)

	A	B	C	D
307	Sample	USGD No.	Grid (UTM)	Sample description
308	861408	67008	6648, 5352	Metabasite
309	861409	67009	6655, 5367	Metabasalt
310	861410	67010	6643, 5367	Metabasite
311	861601	67011	6631, 5375	Metabasite
312	861602	67012	6639, 5372	Greywacke
313	861603	67013	6633, 5379	Metabasite
314	861604	67014	6626, 5388	Metabasalt
315	861605	67015	6625, 5389	Metabasite
316	861606	67016	6632, 5377	Metabasite
317	861701	69017	6362, 5490	Schist
318	861702	69018	6364, 5491	Schist
319	861703	69019	6364, 5492	Schist
320	861704	69020	6369, 5494	Schist
321	861705	69021	6371, 5490	Metabasite
322	861706	69022	6364, 5488	Schist
323	861707	69023	6363, 5487	Metabasite
324	861708	69024	6360, 5489	Schist
325	861709	69025	6352, 5491	Qz sandstone
326	861710	69026	6355, 5487	Schist
327	861711	69027	6355, 5484	Schist
328	861712	69028	6358, 5476	Mafic schist
329	861713	69029	6365, 5488	Amphibolite
330	861714	69030	6365, 5488	Amphibolite
331	861715	69031	6365, 5488	Amphibolite
332	861716	69032	6366, 5488	Amphibolite
333	861717	69033	6366, 5488	Metabasite
334	861801	69034	6357, 5475	Mafic schist
335	861802	69035	6356, 5475	Metabasite
336	861803	69036	6356, 5475	Mafic schist
337	861804	69037	6354, 5474	Carbonatised quartzite
338	861805	69038	6353, 5475	Schist
339	861806	69039	6353, 5473	Metabasite
340	861807	69040	6353, 5469	Metabasite
341	861808	69041	6376, 5477	Chert
342	861809	69042	6380, 5477	Chert
343	861901	69043	6378, 5470	Schist
344	861902	69044	6381, 5469	Chert
345	861903	69045	6381, 5463	Metabasite
346	861904	69046	6381, 5463	Metabasite
347	861905	69047	6381, 5463	Metabasite
348	861906	69048	6381, 5463	Felsic tuff
349	861907	69049	6381, 5462	Felsic tuff
350	861908	69050	6382, 5461	Metabasite
351	861909	69051	6382, 5460	Amphibolite
352	861910	69052	6383, 5459	Chert
353	861911	69053	6383, 5459	Metabasite
354	861912	69054	6380, 5459	Schist
355	861913	69055	6365, 5458	Schist
356	861914	69056	6355, 5457	Mafic schist
357	861915	69057	6356, 5455	Mafic schist

	A	B	C	D
358	Sample	USGD No.	Grid (UTM)	Sample description
359	862101	69058	6323, 5518	Porphyry
360	862102	69059	6322, 5517	Porphyry
361	862103	69060	6320, 5517	Porphyry
362	862104	69061	6319, 5514	Porphyry
363	862105	69062	6325, 5498	Felsic tuff
364	862106	69063	6328, 5499	Felsic tuff
365	862107	69064	6332, 5498	Felsic tuff
366	862108	69065	6331, 5500	Felsic tuff
367	862109	69066	6332, 5501	Porphyry
368	862110	69067	6332, 5503	Porphyry
369	862111	69068	6328, 5505	Porphyry
370	862112	69069	6316, 5489	Metabasalt
371	862113	69070	6324, 5467	Silcrete
372	862201	69071	6336, 5443	Fe gossan
373	862202	69072	6336, 5443	Fe gossan
374	862203	69073	6336, 5443	Fe gossan
375	862204	69074	6336, 5438	Metabasite
376	862205	69075	6336, 5438	Metabasite
377	862206	69076	6336, 5438	Felsic tuff
378	862207	69077	6337, 5435	Felsic tuff
379	862209	69078	6329, 5442	Carbonate
380	862210	69079	6330, 5442	Fe gossan
381	862211	69080	6330, 5442	Fe gossan
382	862212	69081	6330, 5442	Fe gossan
383	862213	69082	6330, 5442	Fe gossan
384	862214	69083	6335, 5430	Felsic tuff
385	862215	69084	6335, 5421	Marble
386	862216	69085	6340, 5406	Felsic tuff
387	862217	69086	6339, 5404	Metabasite
388	862218	69087	6337, 5401	Trachyte
389	862219	69088	6337, 5405	Trachyandesite
390	862220	69089	6337, 5406	Metabasite
391	862221	69090	6337, 5406	Metabasite
392	862222	69091	6333, 5411	Trachyte
393	862223	69092	6327, 5428	Metabasite
394	862224	69093	6326, 5437	Metabasite
395	862225	69094	6326, 5437	Metabasalt
396	862301	69095	6320, 5486	Felsic tuff
397	862302	69096	6323, 5483	Felsic tuff
398	862303	69097	6326, 5483	Felsic tuff
399	862304	69098	6329, 5480	Porphyry
400	862305	69099	6322, 5493	Porphyry
401	862306	69100	6320, 5492	Metabasite
402	862307	69101	6324, 5489	Limestone
403	862308	69102	6330, 5486	Porphyry
404	862309	69103	6335, 5488	Porphyry
405	862401	69104	6336, 5452	Felsic tuff
406	862402	69105	6333, 5454	Metabasalt
407	862403	69106	6331, 5451	Metabasite
408	862404	69107	6330, 5450	Metabasite

Appendix 2.
Photographs of Field and Microscopic Characters of Mafic Rocks

Plate 3.1.1. An along-strike fault boundary between phyllite (left-hand side) and strongly cleaved volcanic rocks (right hand side) in the basement sequence, Ponto Mine area. The presence of this fault is indicated by a narrow negative topographic belt between the two lithological units. This kind of strike fault indicates that the seemingly "conformable" contacts between the sedimentary and volcanic units are probably tectonic in origin. The scale is indicated by the hammer in the bottom right corner. Grid reference: 6177E, 6315N

Plate 3.1.2 A cross-strike fault, indicated by emplacement of a small mafic dyke, caused the displacement of the volcanic unit in the basement sequence. A possible along-strike fault is indicated by a marble ellipsoid. The low ridge in the background is another volcanic unit. Ponto Mine area. Grid reference: 6172E, 6321N

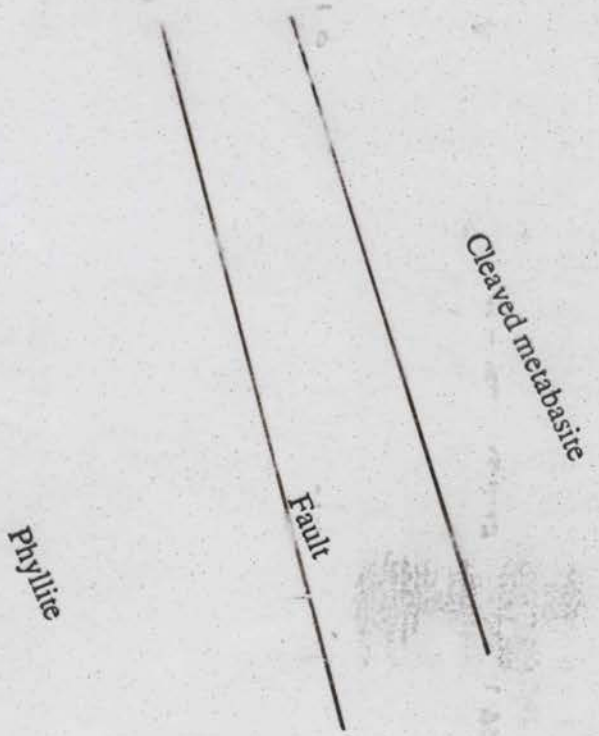
Cleaved metabasite
Fault
Phyllite

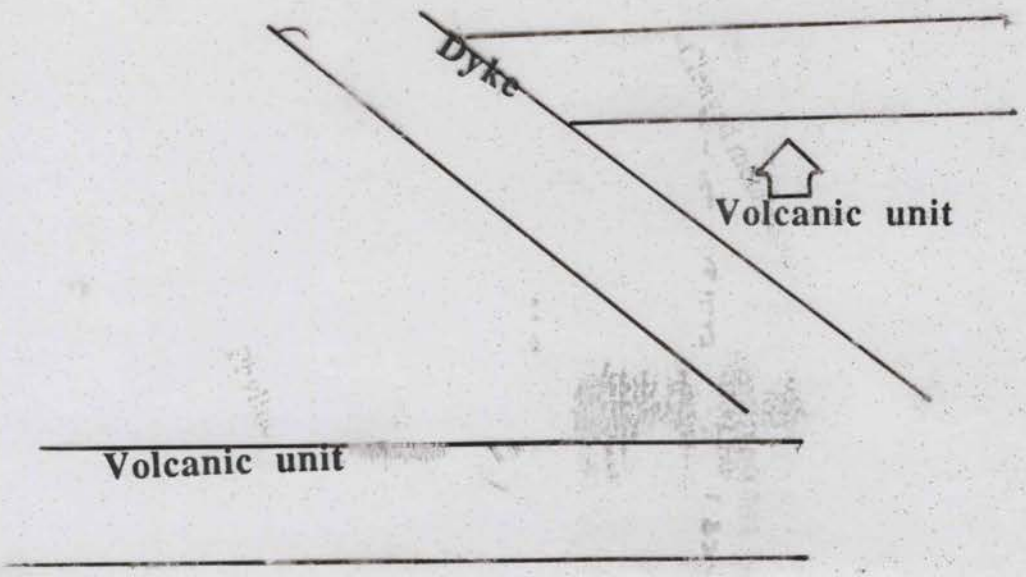
Dyke
Volcanic unit
Volcanic unit

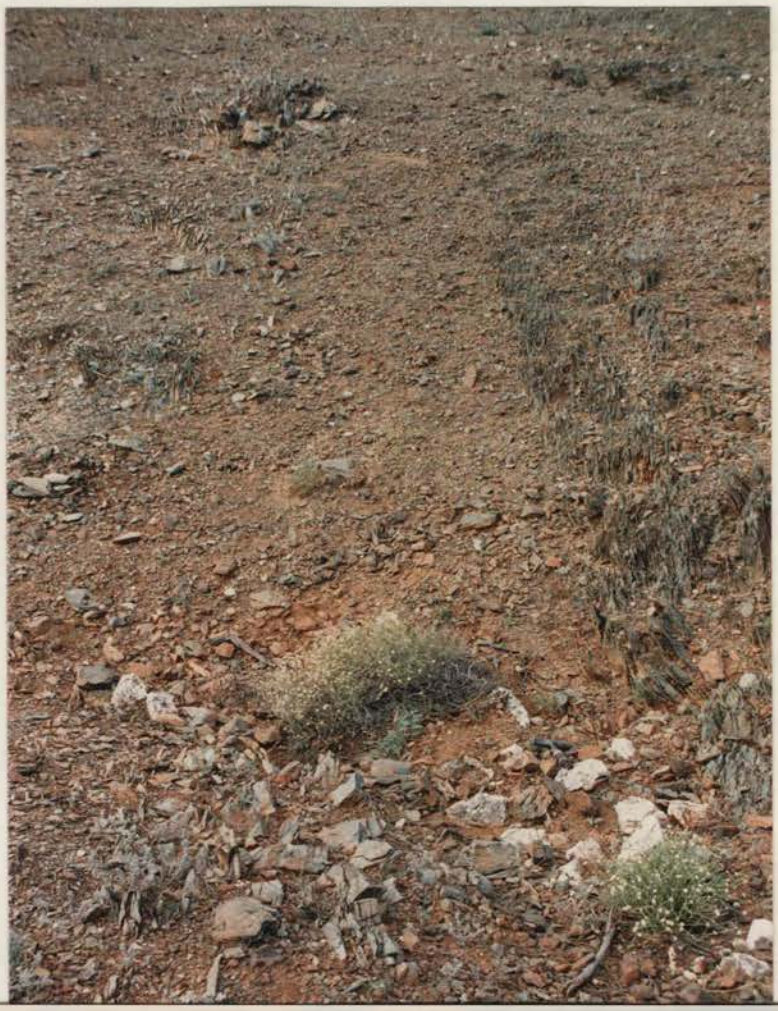

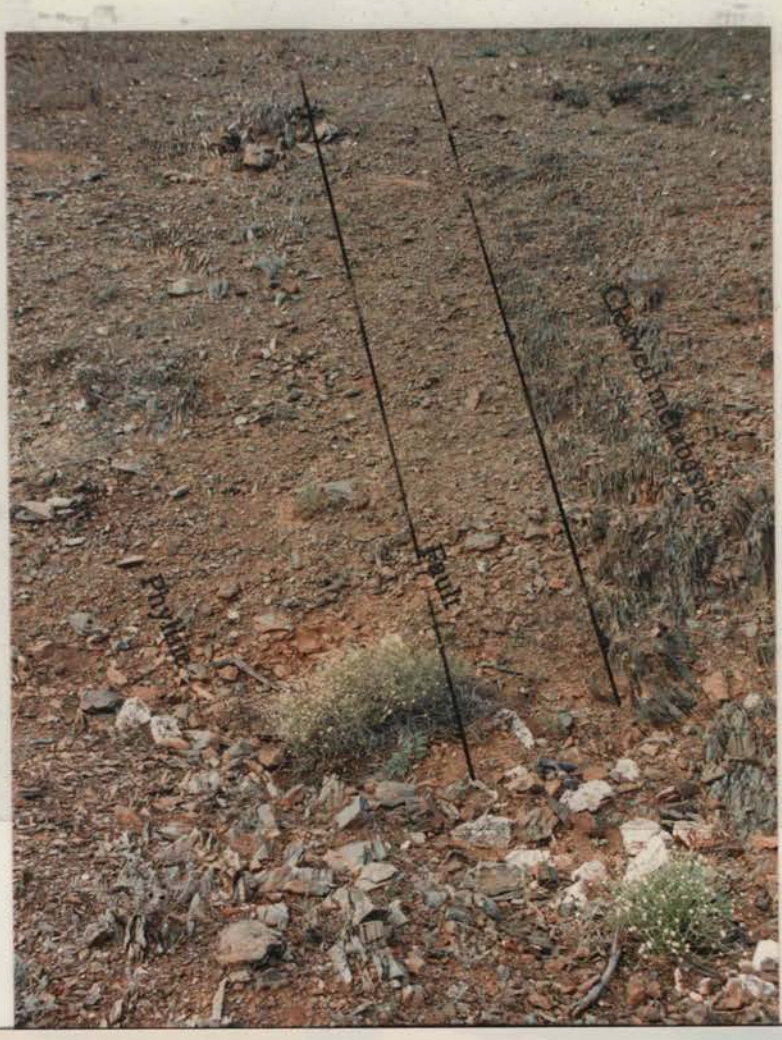
Phyllite
Fault
Chlorite metabasic


Volcanic unit
Volcanic unit

Plate 3.1.3. Pillow lavas in the basement sequence, Ponto Mine area. Although highly deformed, the pillow structure of these mafic volcanic rocks is clearly visible, with pillow length up to 30 cm. This occurrence indicates the submarine emplacement of the mafic volcanic rocks in this area. The well-developed cleavage shown with bottom part of the plate was possibly the result of D_2 deformation, which dominates the regional structural pattern. Grid reference: 6124E, 6371N

Plate 3.1.4. Massive metabasite in the basement sequence, Ponto Mine area. This plate shows the most characteristic occurrence of the mafic volcanic rocks in this area. Although sometimes the primary pillow-like structures can still be recognised as shown here, in many other cases, these rocks are exposed simply as cleaved massive boulders. The scale is shown by the hammer on central left. Grid reference: 6195E, 6298N

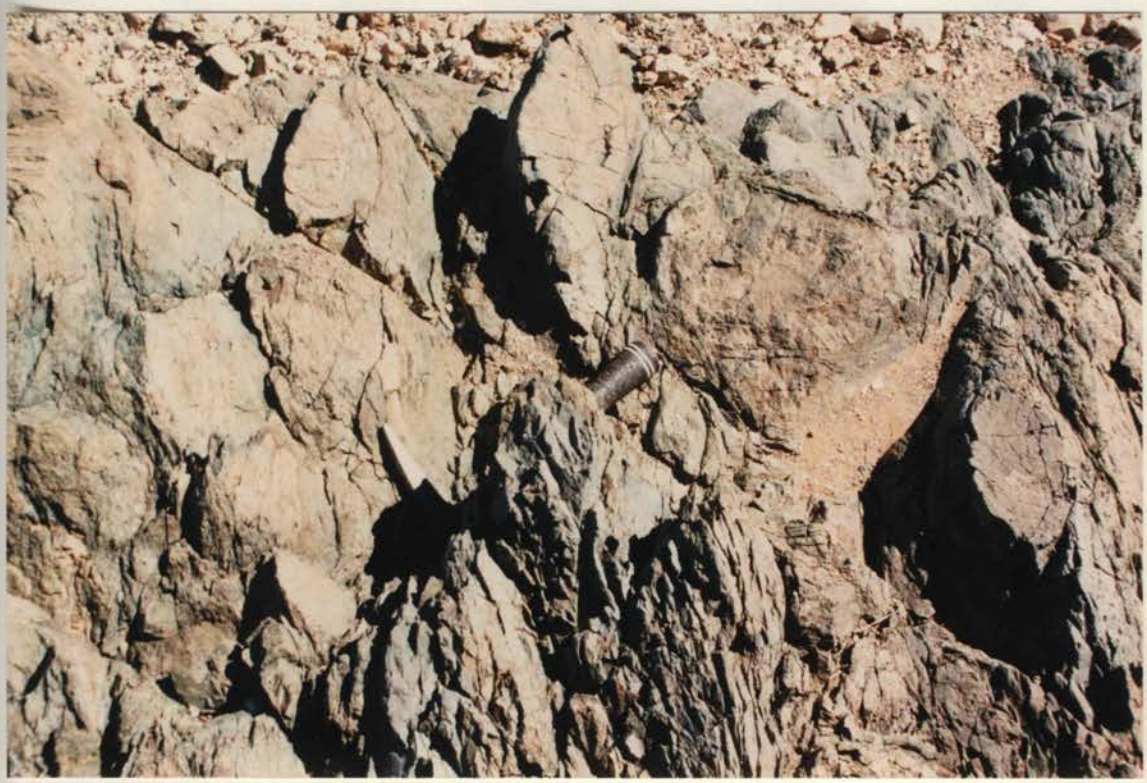

Plate 3.1.5 Carbonatised mafic volcanic rocks in the basement sequence, Ponto Mine area. This plate shows an extreme example of strongly carbonatised volcanic rock with only minor greenish mafic component left in the outcrops.

Grid reference: 6169E, 6321N

Plate 3.1.6. Ironstone coexisting with strongly cleaved volcanic rocks in the basement sequence, Ponto Mine area. The ironstone occurs as small flat ellipsoids up to 50 cm in length associated with the mafic volcanic rocks, and is not a stratigraphic unit in itself.

Grid reference: 6189E, 6301N

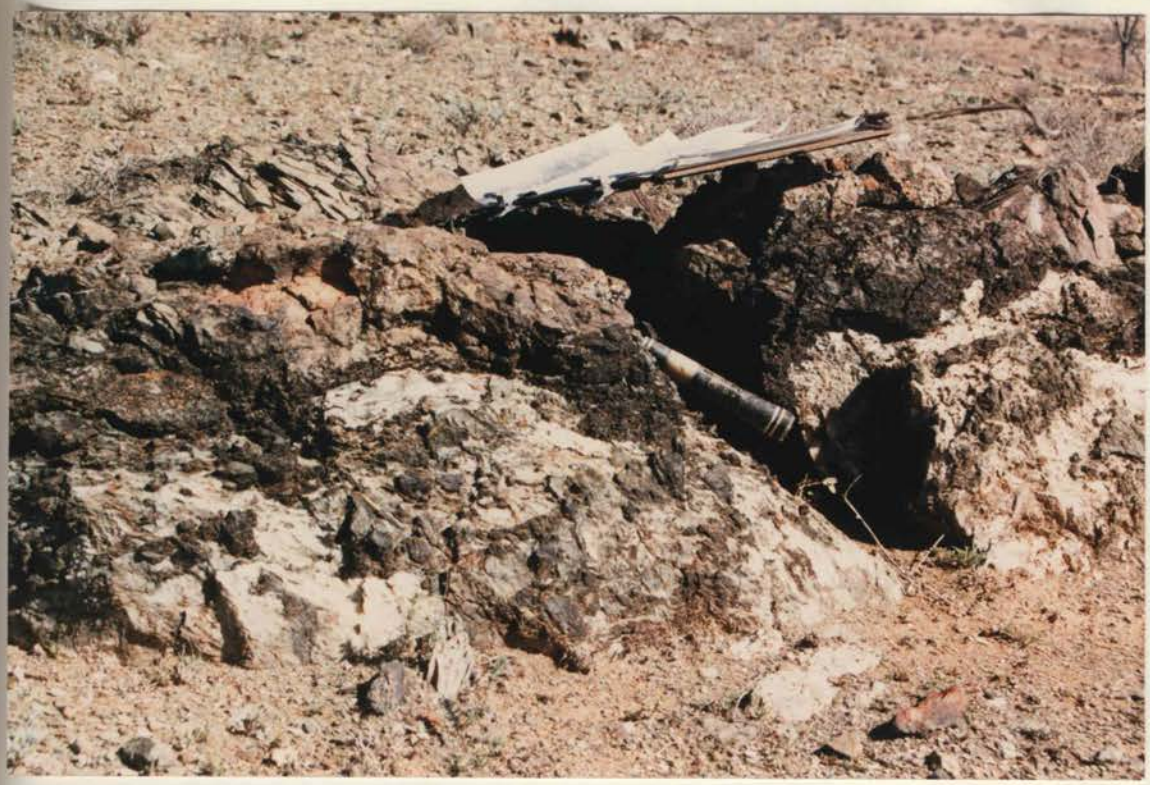

Plate 3.1.7. Ironstone lenses and quartz vein in phyllite unit in the basement sequence, Ponto Mine area. The ironstone is intercalated with the meta-sedimentary unit, not forming a stratigraphic unit in itself. Grid reference: 6176E, 6326N

Plate 3.1.8. Highly deformed meta-sedimentary units of the basement sequence near the Koonenberry Fault, Boshy Tank area. This plate shows tight steeply plunging folds that resulted from D_2 deformation, and boudins that preserve evidence of earlier deformation. The strike of the axial plane of the folds is about 140^0.

Grid reference: 6357E, 6087N

Plate 3.1.9. Late Proterozoic slates at Packsaddle, showing a pattern indicative of two deformations. The major cleavage would have resulted from the D_2 deformation with a strike about 130^0. A post-D_2 deformation developed only an open folding with its axial plane roughly normal to the D_2 cleavage, as indicated by the direction of the yellow rope. This D_3 deformation also affected the syenite in this area.

Grid reference: 5932E, 6169N

Plate 3.1.10. Strongly cleaved mafic volcanic rocks in the late Proterozoic sequence in the Packsaddle area. These mafic rocks are rather similar to those seen in the basement sequence, showing well-developed cleavages (foliations) and generally poor outcrop. In detail, however, there is a subtle difference in their greenish colours: the basement samples are greyish-green, while those shown here are yellowish-green.

Grid reference: 5950E, 6199N

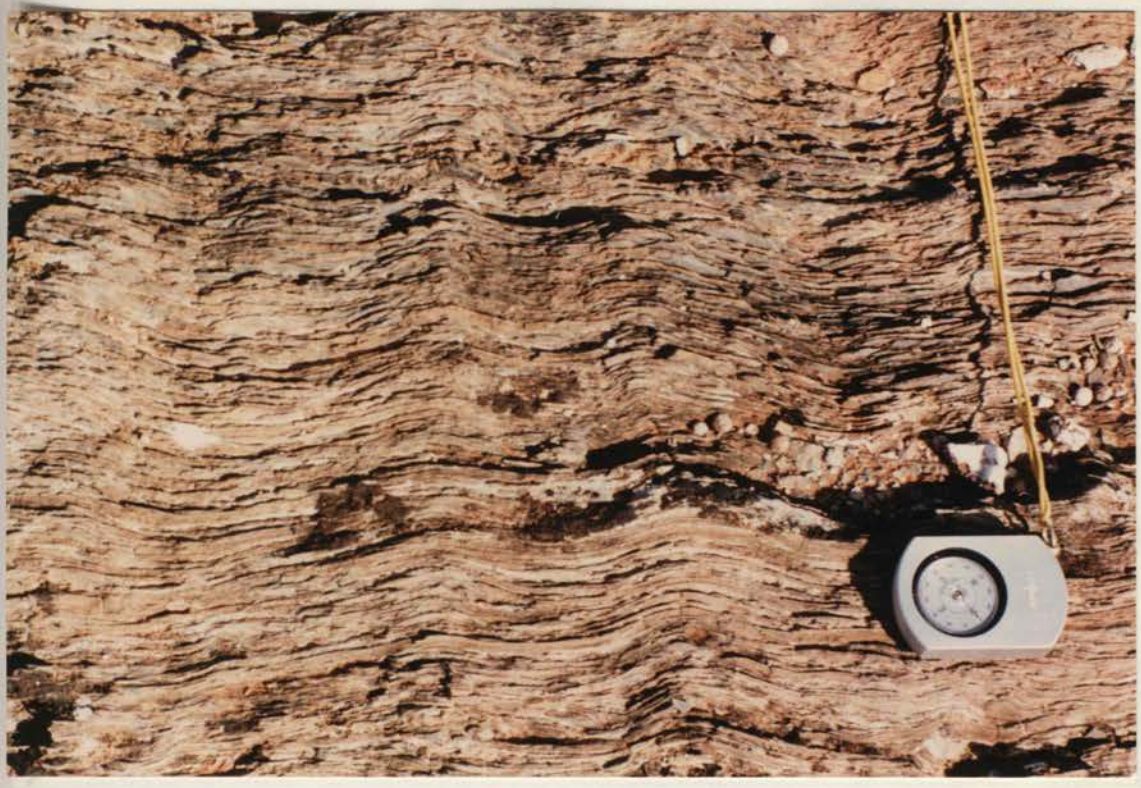

Plate 3.1.11. Cleaved pillow lavas in late Proterozoic mafic volcanic rocks in the Packsaddle area. The pillows are apparently larger than those in the basement sequence, and the intensity of deformation is not as strong as that in the basement mafic volcanic rocks. Grid reference: 5953E, 6189N

Plate 3.1.12. Pillow lavas in the late Proterozoic sequence, Packsaddle area. This plate shows an excellent example of little-deformed pillow structures of the mafic volcanic rocks in this sequence. The size of the pillows is much larger than those seen in the basement sequence, and may extend up to one metre in length.

Grid reference: 5915E, 6420N

Plate 3.1.13. Syenite at Nundora (post-D_2, pre-D_3?). This photograph shows the zoning of colours from light grey, to yellow and then pink at the bottom right part of the plate. This texture provides evidence of alteration that may have occurred in these rocks (see also Plate 3.2.16) Grid reference: 6059E, 6057N

Plate 3.1.14. Ultramafic rocks in the Nundora area (post-D_3?). The dyke-like outcrop is about 20 metres across with deeply weathered surface, greyish green colour and showing little deformation. However, deep inside the outcrop, the weathering becomes even worse, and only surface samples were collected for further studies . On the regional scale, this outcrop was suggested to be fault controlled (Edwards, 1980).
Grid reference: 6074E, 6052N

Plate 3.2.1 Metabasite, Ep type alteration **Sample 753001**

Metamorphosed massive mafic volcanic rock with fine to medium-grained texture. This type of metabasite is largely composed of xenoblastic Ep (high birefringence) and Qz (low birefringence) grains. Minor Ac and Ch occur as slender prisms that define the D_2 foliation (top and bottom right).

cross polarised light; plate width 2.5 mm

Plate 3.2.2 Metabasite, Ac-Ep type alteration **Sample 752805**

Metamorphosed massive mafic volcanic rock with fine to medium-grained texture. Compared with the Ep type, Ac-Hb (bluish green) has significantly increased with aligned textures defining the D_2 deformation in the "matrix". Ep (very high relief, yellowish) occurs mainly as xenoblastic grains or patches. Qz and Ab are of minor contents and there is virtually no Ch (less than 5%).

plain polarised light; plate width 1.0 mm

Plate 3.2.3 Metabasite, Ab-Ch type alteration **Sample 752201**

Metamorphosed massive mafic volcanic rock with fine-grained texture. This particular thin-section is cut from the interior of a pillow lava sample and hence displays no obvious aligned structure. Ab (elongated laths) and Ch (greenish) are the major components occurring as alteration products in the "matrix". Ch occurs also as xenoblastic patches filling interstices. Other phases include Ep (yellowish, very high relief), Mt (opaque) and Sp (very high refractive index, near opaque grains).

plain polarised light; plate width 1.0 mm

Plate 3.2.4 Metabasite, Ab-Mt type alteration **Sample 752810**

Metamorphosed massive mafic volcanic rock with fine to medium-grained texture. Major components are Ab after Pl (slender laths) and Mt filling the interstitial space. Others phases include Ch (greenish) surrounding the Ab laths and patches of Cb, at top of the plate.

plain polarised light; plate width 1.0 mm

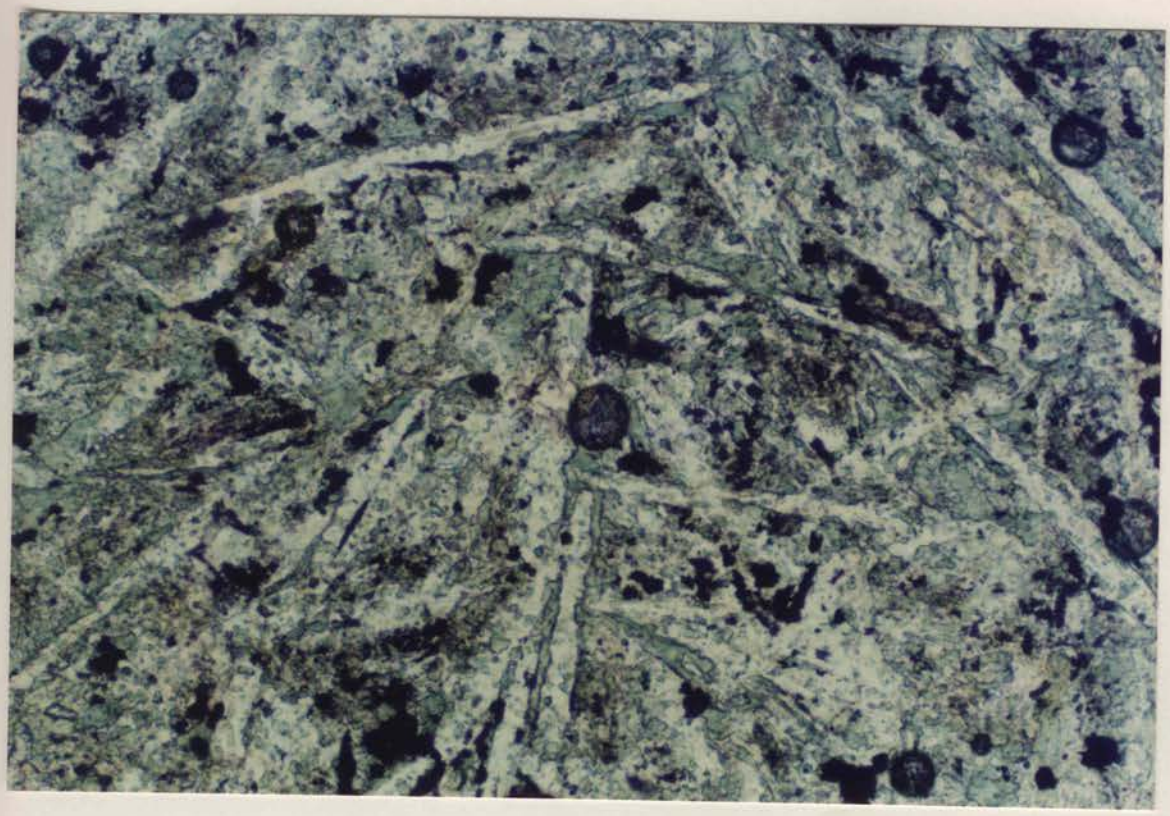

Plate 3.2.5 Metabasite, Cb-Mu type alteration **Sample 760104**

This plate illustrates the features of deeply altered (metasomatised) metabasite, which is now composed of Cb and Mu. Mu, the colourful crystals in this plate, occurs mainly as aggregates of small prismatic crystals, sometimes displaying a radiating texture in amygdales. Cb occurs as pseudomorphs after Pl in the lower left-hand side corner, as well as matrix aggregate (centre left). It represents those deeply carbonatised mafic rocks (*cf.* Plate 3.1.5)

cross polarised light; plate width 2.5 mm

Plate 3.2.6 Metabasite, Pm type (A) alteration **Sample 860902**

A medium to fine-grained metamorphosed mafic rock of black to green colour with milky white amygdales, altered phenocrysts and lapilli. The amygdales constitute about one third of the rock and may form variable patterns under the microscope. They are filled with idioblastic Ep (radiating patches on the left and around margins of amygdales), Pm (centre right , with lower birefringence), Cb (in the amygdales on the right), and minor Ch. The surrounding matrix also contains altered products, now composed of Qz (bottom), Ep (right) and Cb (top left), with minor Pm.

cross polarised light; plate 1.0 mm

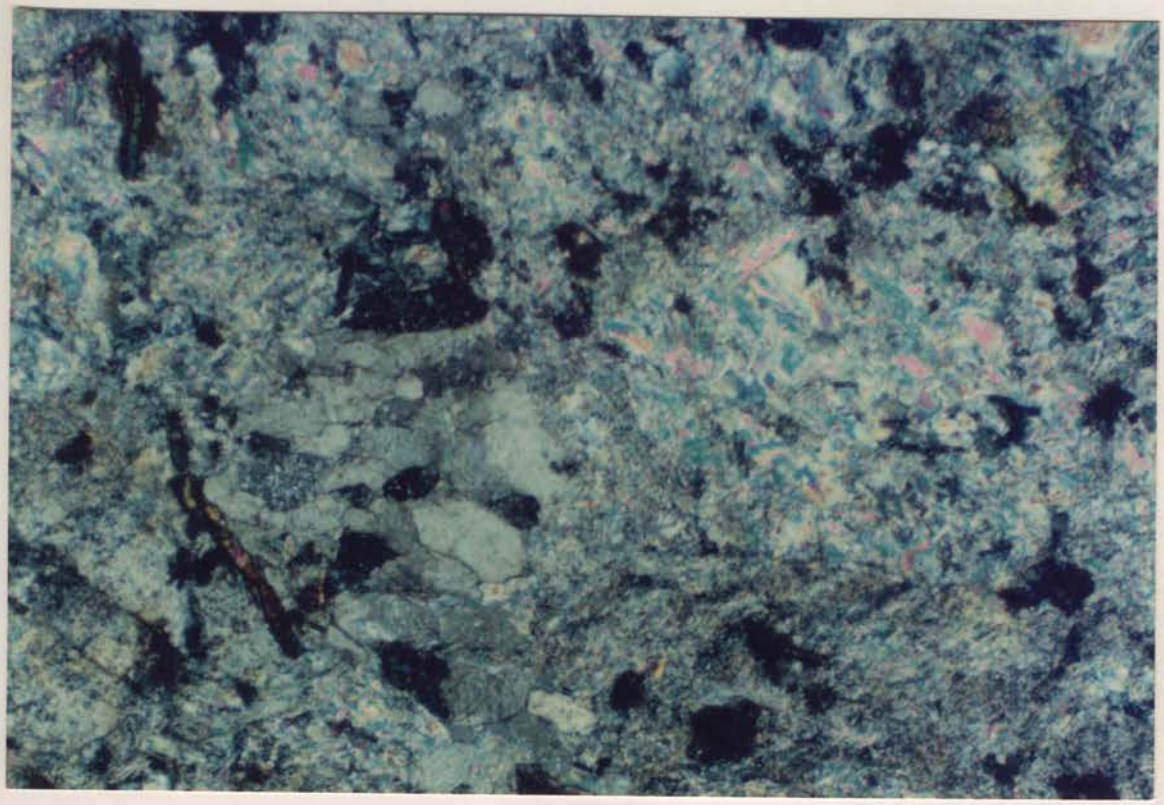

Plate 3.2.7 Metabasite, Pm type (B) alteration **Sample 861212**

A metamorphosed massive medium to coarse-grained mafic volcanic rock, which appears to comprise two metamorphic domains, a high relief and dark coloured part, and a low relief and light coloured part. Within the first domain, Ac-Hb (greenish) and Ep (yellowish) are the main components and Am plates appear to define the D_2 foliation; both Ab and Ch in this domain are less than 5%. In the second domain, Pm of relatively light green colour and medium relief coexists with Mu (small idioblastic prisms) and Cb (colourless patches with negative relief). Some of the Am-Ep patches show evidence of reactions with secondary phases along the margin of the crystals (bottom right), but the majority of them still clearly preserve their "primary" metamorphic features.

plain polarised light; plate width 1.0 mm

Plate 3.2.8 Metabasite, Mu type alteration **Sample 861308**

A metamorphosed massive fine to medium-grained mafic volcanic rock with significant occurrence of muscovite (idioblastic prisms or laths with low refractive index) and Ep (xenoblastic grains or patches of grains with very high refractive index and yellowish colour) in the "matrix". Minor mineral phases include Cb (xenoblastic plates with negative relief). There is no designable aligned texture in this rock type.

plain polarised light; plate width 1.0 mm

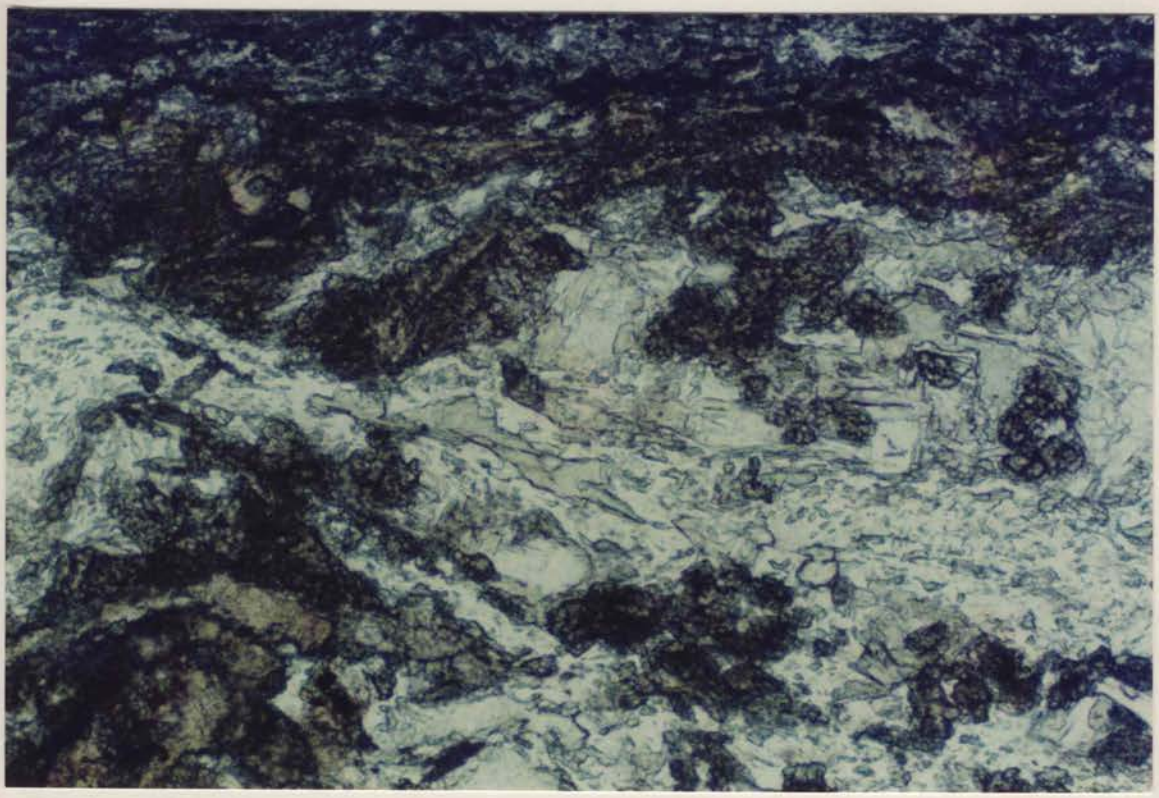

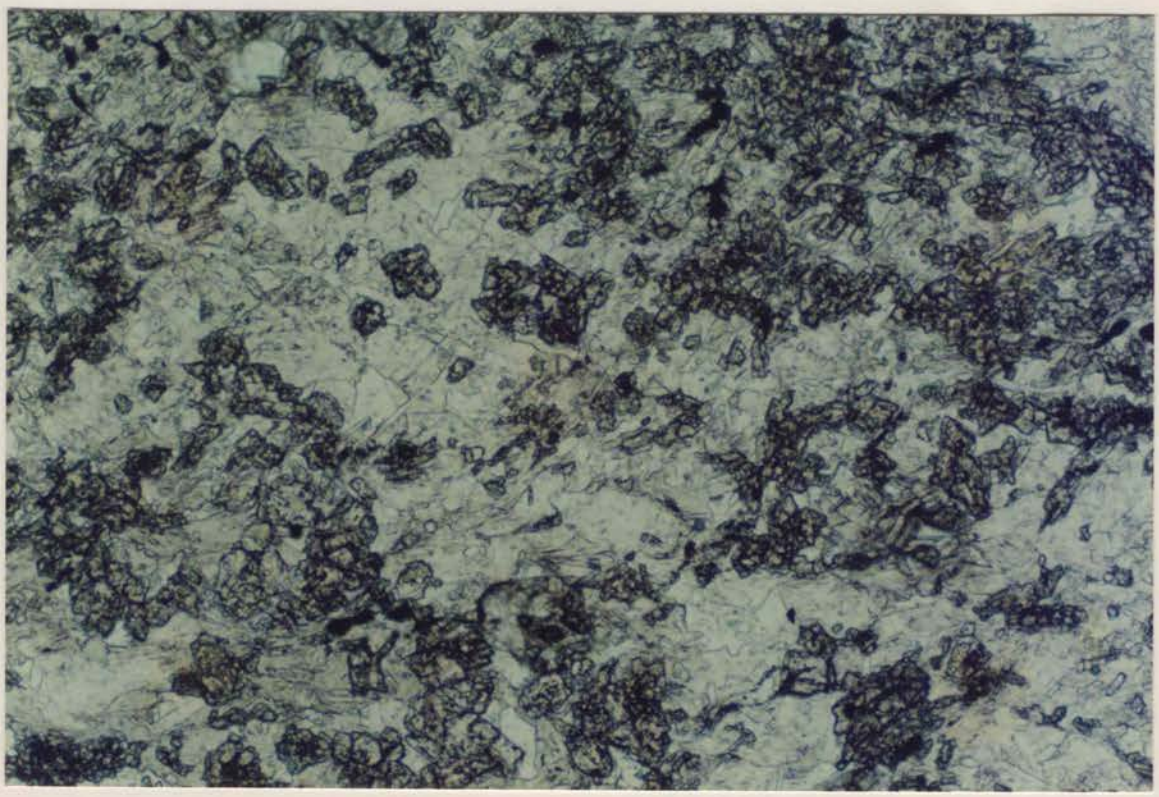

Plate 3.2.9 Amphibolite Sample 861715

A metamorphosed mafic rock composed of Hb+Ep+Pl of medium to coarse grain-size, and aligned fabrics of Hb prisms, of bluish green colour with strong pleochroism, possibly defining the D_2 foliation. Ep occurs as yellow-brown aggregates of xenoblastic grains with very high relief. Pl appears as interstitial phases due to low relief, and the composition is oligoclase-andesine.

plain polarised light; plate width 1.0 mm

Plate 3.2.10 Metadolerite I (with Py relics) Sample 752110

A metamorphosed mafic intrusive rock with ophitic texture. Py occurs as a relic phase with fractures filled with secondary minerals (mainly Ch, Ac and Cb), a light yellowish colour, very high refractive index and cleavage not developed (centre and left-hand side). Pl is quasi-idiomorphic, but albitised, (bottom right, hosting the smaller opaque grain). The matrix is composed of Ep (very high refractive index, yellowish green and xenoblastic grains; top right) and Ab (low refractive index, colourless). Ac mainly occurs as fibre-like forms within fractures of relic Py. Ch can be seen surrounding the relic Pl laths. The opaque phase is probably Mt.

plain polarised light; plate width 1.0 mm

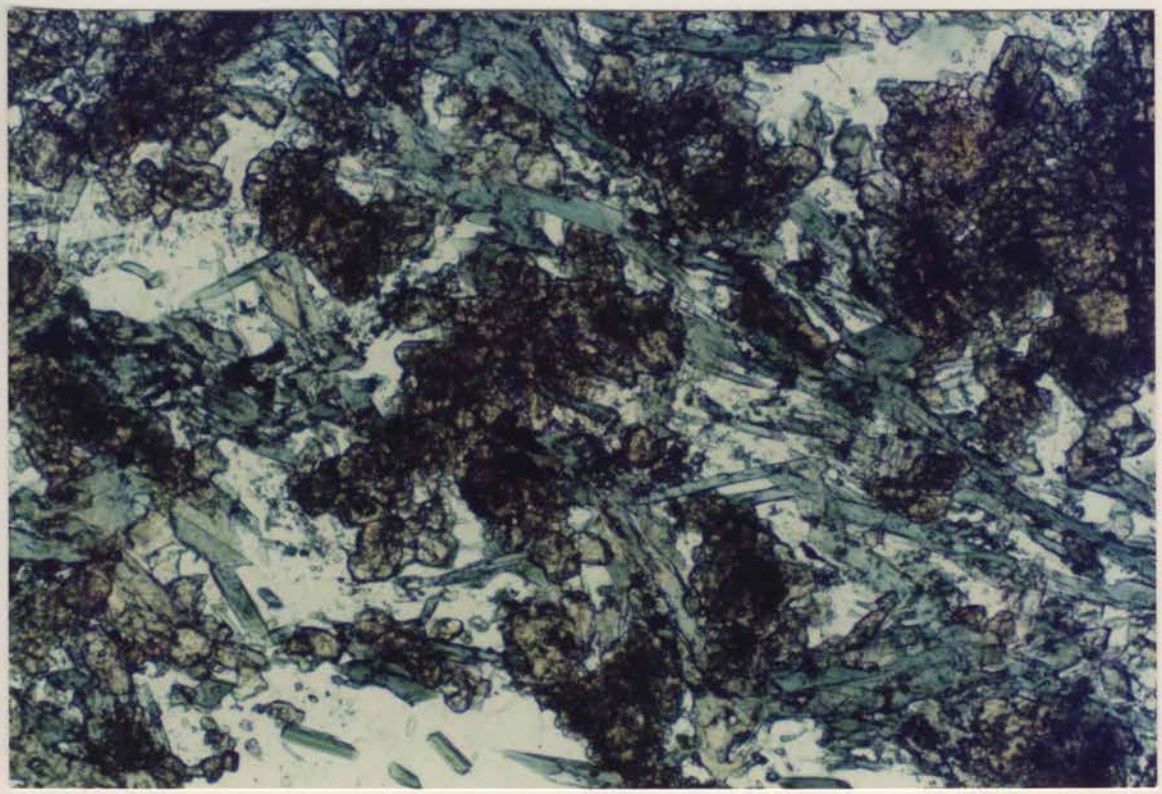

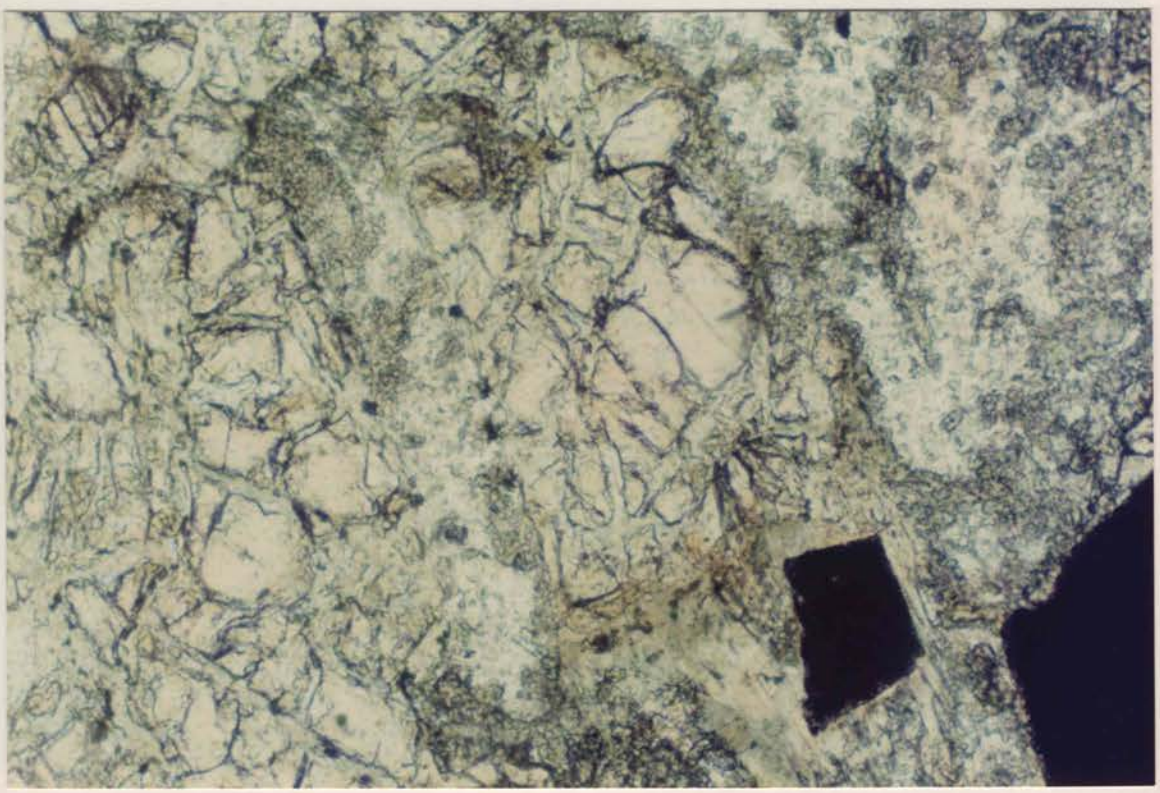

Plate 3.2.11 Metadolerite IIA (no relic Py) Sample 752106

A metamorphosed intrusive mafic rock mainly composed of Am and Ab possessing a medium to coarse-grained ophitic texture. The alteration products include Ac-Hb after Py (plate-like) and Ab after Pl. Some relic Pl with primary twins can be seen in the central part of the plate. The aligned fibrous Ac (sub-vertical, top right, and central part running into relic Pl) defines the orientation of major regional deformation (D_1 or D_2). Ep and sphene occur as minor phases (bottom right).

cross polarised light; plate width 1.0 mm

Plate 3.2.12 Metadolerite, IIB (Ka-bearing) Sample 761001

A metamorphosed Ka-bearing rock with fine to medium-grained texture. Idiomorphic kaersutite is light brown with strong pleochroism (top right), altered to form Ch, Ac and Cb in fractures. The metamorphic phases in the matrix include Ep (very high refractive index, xenoblastic grains or patches), Ch (medium to high refractive index, light green, xenoblastic grains), Ab (small colourless laths, centre and central top) and Cb (negative relief colourless patches, top left). The opaque phase is Mt.

plain polarised light; plate width 1.0 mm

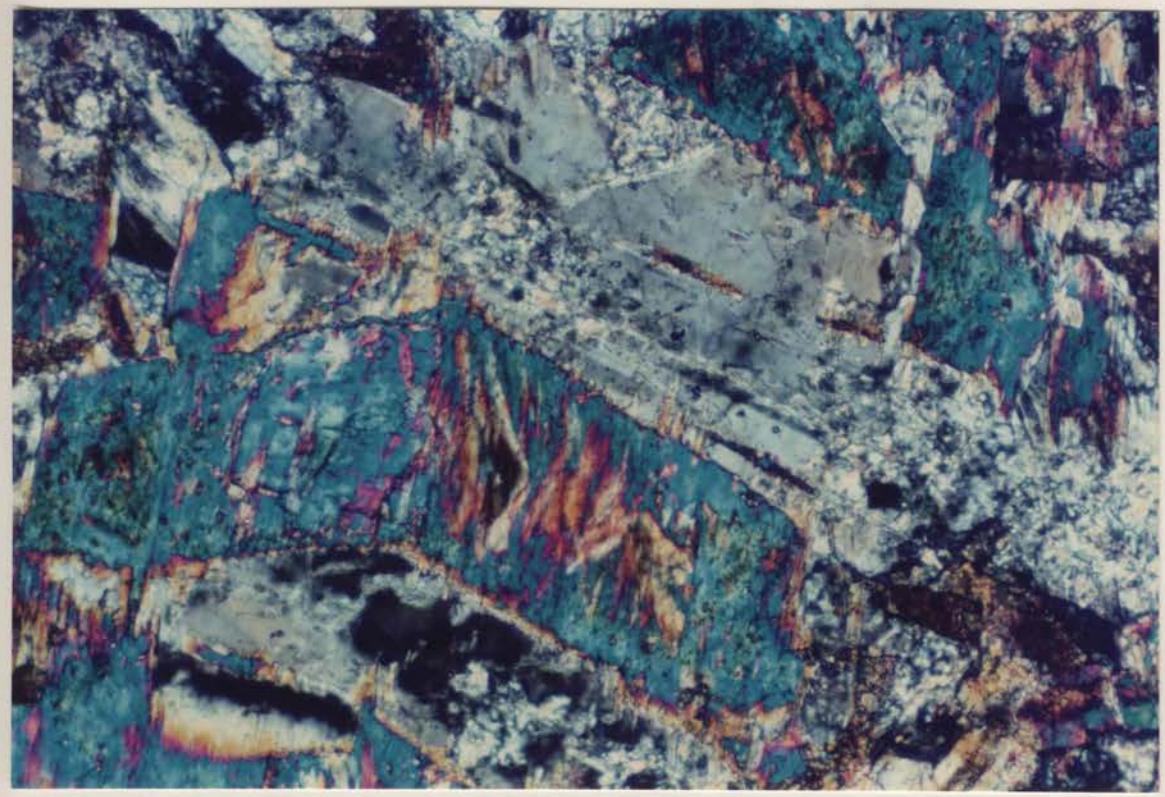

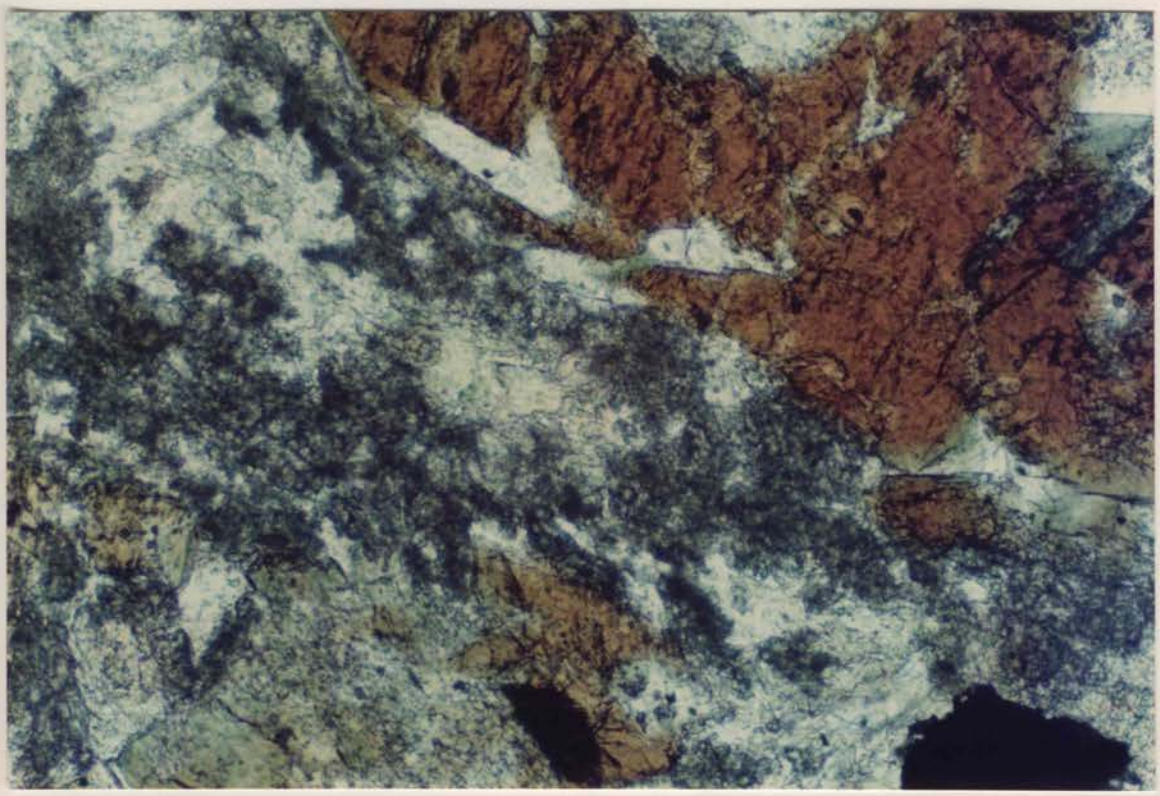

Plate 3.2.13 Metadolerite III (Porphyritic) Sample 760402

A metamorphosed mafic rock with porphyritic texture. The sample shows little deformation and light greenish grey colour. The milky white "phenocrysts" possibly represent "phenocryst feldspar". Under the microscope, however, the "phenocrysts" are composed of patches (centre and central right) of small xenoblastic Cz (ink blue), Ep (small yellowish green prisms), Cb (colourless patches) and Sp (nearly opaque). The "matrix" has a similar composition but with minor Qz (yellowish, bottom right).

cross polarised light; plate width 5.0 mm

Plate 3.2.14 Pyroclastic mafic rocks Sample 860905

The field description is breccia metabasalt. It is a fine-grained (aphanitic) greenish black rock with some remarkable "tuff-breccia" textures.

This plate presents a very characteristic "vitroclastic" texture of brownish colour, probably representing original arcuate shards of volcanic glasses. In most cases, these "arcuate shards" are altered and filled with Ch (greenish, dominant phase), Ab, Pm and some Ep. The matrix are filled with Cb, Ch and minor Pr.

plain polarised light; plate width 5.0 mm

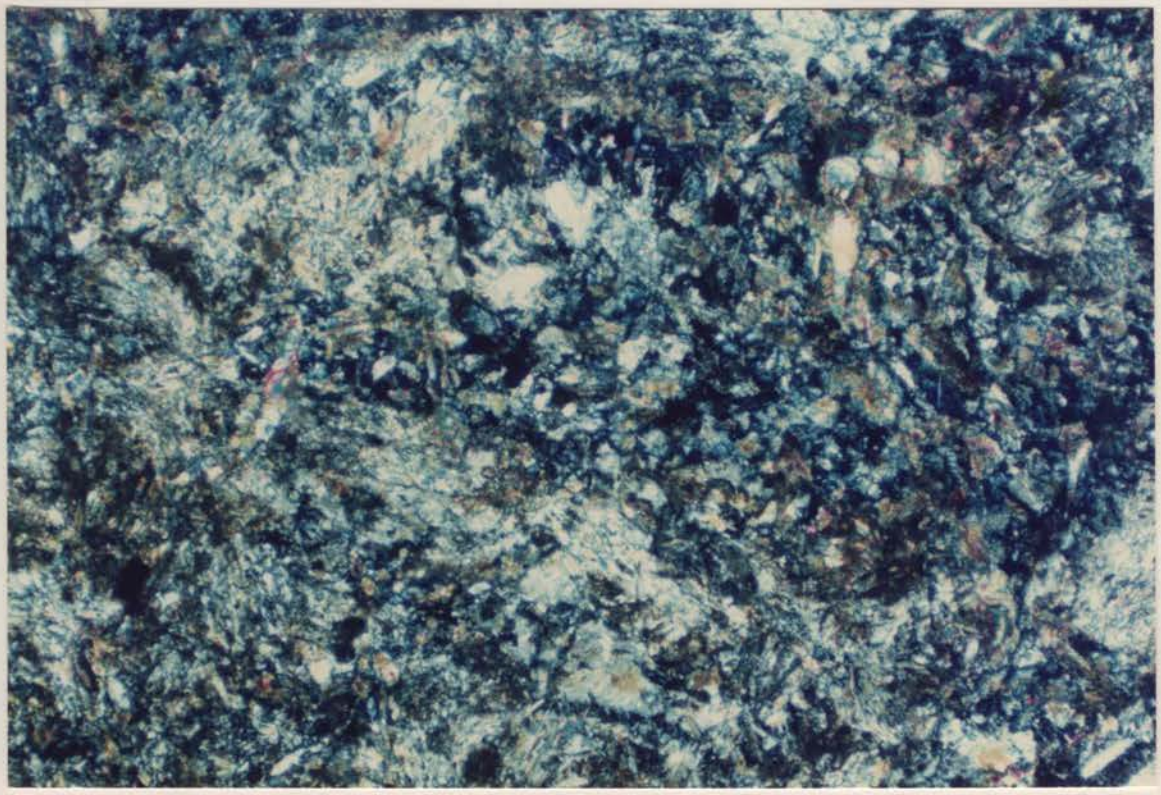

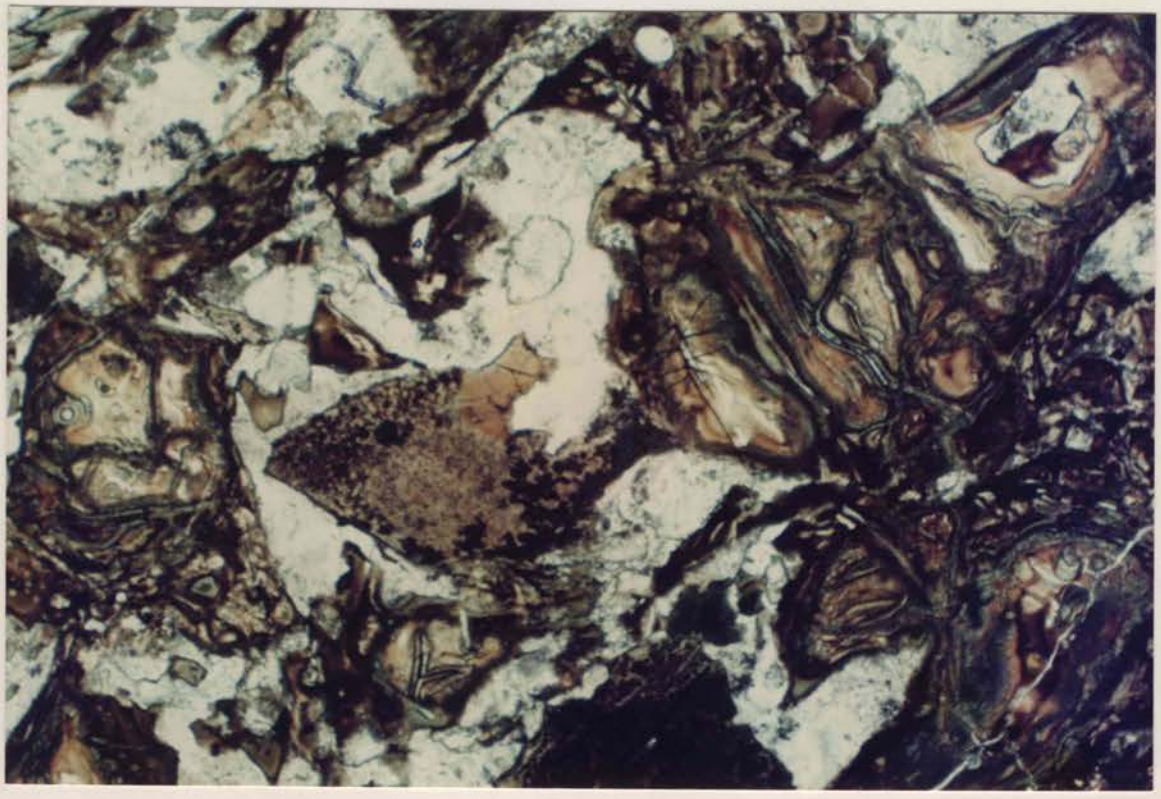

Plate 3.2.15 Syenite **Sample 761204**

An intrusive alkaline rock composed of alkaline feldspars (Kf and Ab), medium to coarse-grained texture. Under the microscope, the rock consists mainly of Kf (50-55%) and Ab (30-35%), with minor Bi, Mt and Qz. However, when alteration developed (bottom right), the content of Ab increases significantly at the expense of Kf.

cross polarised light; plate width 5.0 mm

Plate 3.2.16 Altered Syenite **Sample 761603**

This type of sample represents the highly altered syenitic rocks. When Ab increases its content due to alteration, Kf reduces its proportion correspondingly. When the two minerals are in the same proportion as observed in this plate, the rock has a mineral composition similar to monzonite. Both Ab and Kf display irregular margins of their lath-shaped crystals, which indicates alteration of the minerals. Minor phases in the samples include Bi, Mu, and Mt, mainly as patches between the feldspars.

plain polarised light; plate width 2.5 mm

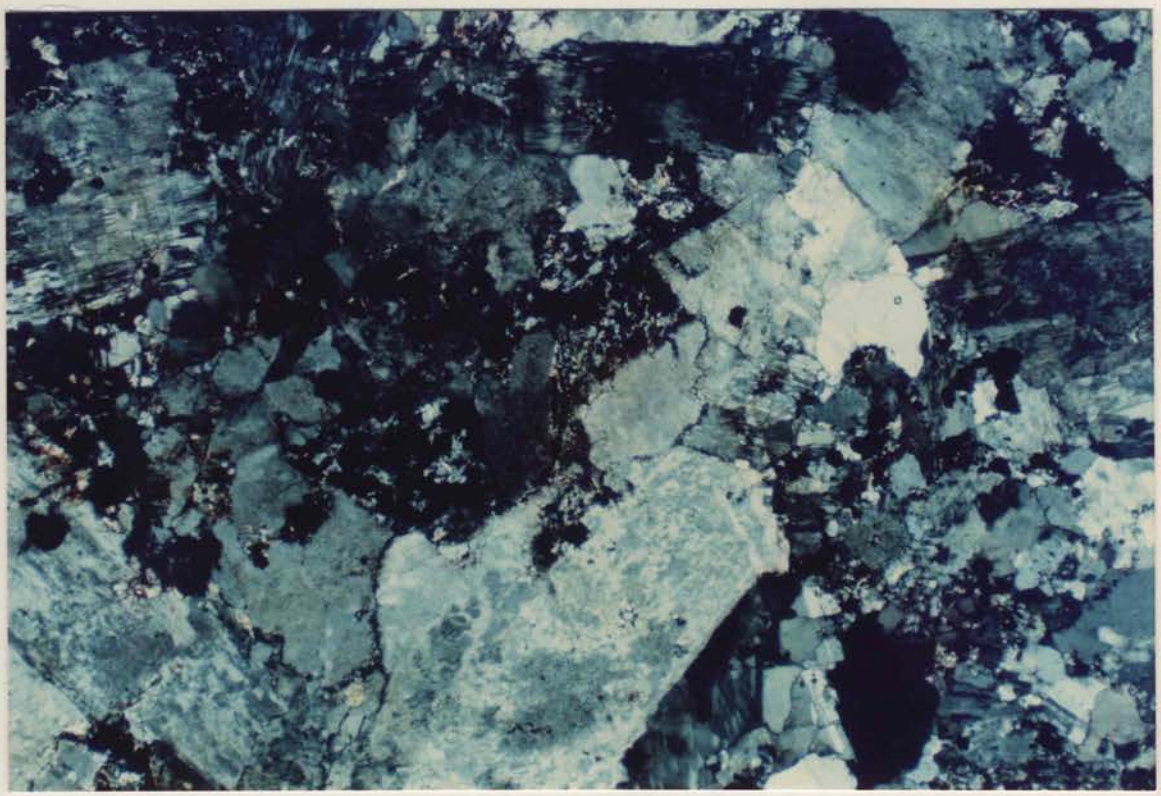

Plate 3.2.17 Nundorite. Light type Sample 762403

An coarse-grained igneous-like alkaline rock. In hand specimen, this type of rock displays impressive green-pink colours, with the aegirine being the green mineral and alkaline feldspar and feldspathoid forming the pink matrix. Under the microscope, the high-relief, dark yellow-green aegirine occurs as aggregates of small grains with same optical orientation; while the light-coloured matrix is composed of variously sized xenoblastic Ab, Kf, natrolite and nepheline.

plain polarised light; plate width 5.0 mm

Plate 3.2.18 Nundorite. Dark type Sample 762406

An coarse-grained igneous-like alkaline rock. Compared to the light type, this dark-type nundorite shows no distinctive pink-green, but grey-black colours instead. Under the microscope, the occurrence of aegirine is rather similar to that observed in the lighter samples, being composed of aggregates of small dark grains in optical continuity. The aegirine content is higher. Foliation is relatively well-developed as shown by the aligned aegirine minerals. The mineral composition of the matrix is similar to that of light-type samples, though the grain sizes are smaller.

plain polarised light; plate width 5.0 mm

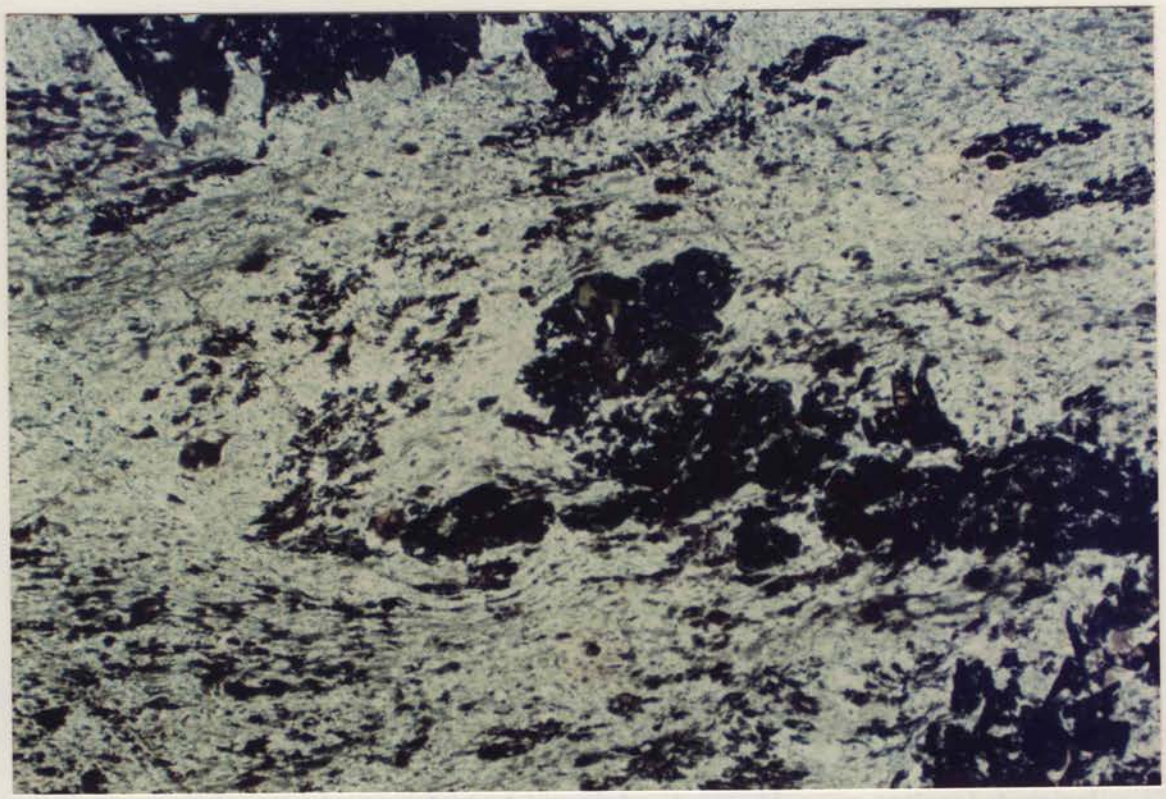

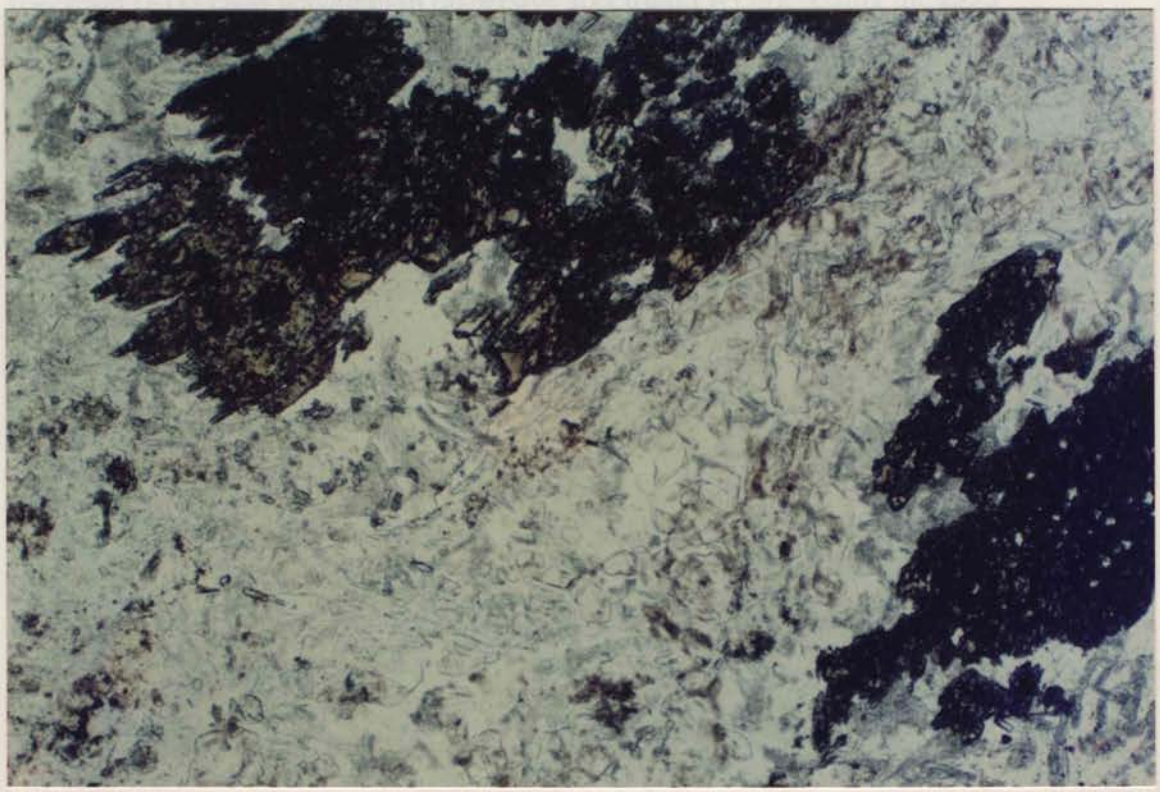

Appendix 3
Analytical Parameters of
Electron Microprobe Techniques

Mineral composition analyses were carried out using the electron microprobe techniques in this study. Principles of the technique have been discussed in detail by Long (1975) and recently by Williams (1988). A much simplified explanation is as follows.

Upon radiation by an electron beam generated by a specially designed filament, surface-polished samples will generate x-ray beams characteristic of their elemental compositions. By collecting the characteristic secondary beam with detectors, which transform the x-ray signals into electronic signals to be processed by a computer, the chemical compositions of the samples can be obtained. Since the area of irradiated samples is very small (20 μm across), this technique can reveal compositional variations within a single crystal which cannot be obtained by conventional chemical methods.

There are generally two ways of collecting the x-ray beams; energy dispersive spectrum (EDS) and wavelength dispersive spectrum (WDS). Using the EDS technique, the whole spectrum of secondary X-rays can be collected and measured simultaneously; thus, the method works efficiently but with a trade off in the precision of the analysis. The WDS technique analyses the spectrum by steps of wavelength of the beam; it takes more analytical time but with better precision of results. In the present study, a combined EDS/WDS method, which analyses Na and Mn by WDS and the other elements (Si, Al, Ti, Fe, Mg, Ca, K and Cr) by EDS, was adopted. Sodium is a difficult element to analyse by the electron microprobe due to its light atomic mass, and the WDS technique is adopted to control the quality of analytical results. The other elements are analysed relatively easily with a good quality result; WDS analysis of Mn is a requirement of calibration of the machine and also provides an internal monitor on the Si result. Therefore, the combined method achieves both good quality of results as well as relatively high efficiency.

During each analytical session, the primary electron beams are controlled by various apertures required by different minerals. Most of the silicate minerals are electron beam resistant and the beams have virtually no physical effect on the sample surface;

thus small apertures are used to focus the primary beam in limited areas to gain accurately controlled secondary beams. This method is called dot analysis. However, some minerals, like albite and feldspathoid, are not resistant to the electron beams; when radiated by the beams, the surface of the minerals are quickly burned off and hollows are generated. As the hole gets deeper, the refraction of secondary beams becomes random, which results in poor analytical results. Thus, a large aperture is used in this case, which allows electron beams to scan larger areas to disperse the energy and thus slow down the burning rate and also to obtain better controlled secondary beams as the burning surface remains flatter. This method is called the scanning method. In practice, the width of analysed area is about 20 -30 μm for the dot method and just less than 1 mm for the scanning method.

In this project, the mineral analyses using the electron microprobe technique were carried out after the petrographic studies had proceeded. Based on petrographic studies using an optical microscope, representative samples were selected; then thin-sections of these samples were prepared and polished with 1 μm grinding materials. The polished samples are coated with carbon film. After this stage, the thin section samples were stored in an oven at about 60 ^{0}C until analysed.

All analyses were carried out on a Siemens ETEC Autoprobe, at the working conditions of 15 Kv and approximately 30 nA, using a combined EDS/WDS program (with minor use of WDS method at an earlier stage). The analytical methods are essentially the same as those described by Long (1975). The machine was calibrated at the beginning of each session and accuracy was monitored during the sessions using "in-lab" standard minerals. The minerals used for standardization are:

Albite:	Na (WDS method);
Barite:	Ba;
Chromite:	Mg, Al, Cr;
Hematite:	Fe;
Orthoclase:	K;
Rhodonite:	Si, Mn (WDS method);
Rutile:	Ti;
Wollastonite:	Ca.

A3.1. A STUDY OF SUPERGENE MINERAL: CRYPTOMELANE

Cryptomelane was first named by Richmond and Fleischer (1942). Since then, few other studies have contributed to this mineral. It is considered as a product of mainly supergene processes and is the major weathering product of manganese minerals together with pyrolusite (*cf.* Roy, 1981). Recently, an occurrence in an evaporative environment was also reported (Belkin & Libelo, 1987).

Various formulae of cryptomelane have been proposed (*e.g.*, Richmond & Fleischer, 1942; Hewett & Fleischer, 1960; Roy, 1981; Belkin & Libelo, 1987). From these proposals, the formula is here generalized as: $A_{1-x}\ M_{8-x}\ O_{16}{\cdot}nH_2O$

where, A is mainly K with minor Na and Ba; when Ba is dominant, it is called hollandite. And M is mainly Mn^{4+} with minor Mn^{2+} and Fe^{3+}.

Potassium oxide in this mineral is normally in a range of 3-4% (Richmond & Fleischer, 1942) but may up to 6%. In the latter case, it is called high-K type (Hewett & Olivares, 1968). The transition between K and Ba has long been recognised (Richmond & Fleischer,1942). Recently, a complete series between cryptomelane and hollandite was studied by Miura *et al.* (1987).

During investigations of the Mn-gossan samples, collected by Davies (1985) from Little Koonenberry Gap, south of the Ponto Mine area in this study, one of the samples was found to contain some encrusting and needle-like crystals of cryptomelane. Subsequently this mineral was studied using the electron microprobe techniques.

The results of microprobe analyses of the mineral are presented in Table A3.1 with all Mn treated as Mn^{4+}. Some compositions of reference samples of the mineral are also presented in this table. It can be seen from this table that all analyses in this study show clearly that the cryptomelane here is a high-K type. Most of the analyses contain about 6% K with minor Na. Some contain minor Ba.

Plate A3.1 shows the BSE images of the occurrence of the mineral with corresponding compositional variations presented in Plate A3.2. These plates shows the "encrusting" texture of the formation of the mineral. The BSE image in Plate A3.3 presents needle-like texture of this mineral. Both textures are typical of minerals of secondary origins.

The field occurrence prescribed by Davies (1985) suggests the mineral is an end product of the manganese gossans in the supergene environment. The Mn gossans have been recognised as an important indicator of mineralisation in the Broken Hill region (Willis *et al.*, 1983); and further studies of cryptomelane-type minerals from the Broken Hill Mn gossans may help to reveal if these two Mn gossans are of the same type as far as the composition of the cryptomelane is concerned. This work may in turn help identify exploration targets.

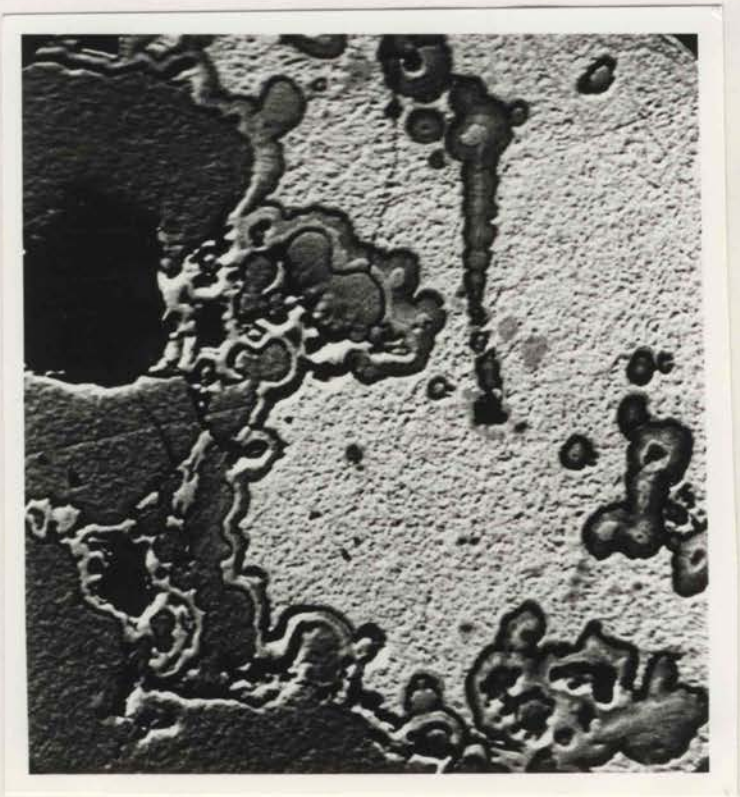

Plate A3.1 BSE image of cryptomelane crystals. The light gray area are minerals of cryptomelane, a hydrous potassium manganese oxides. This plate shows the encrusting structure of the mineral, suggesting secondary origin of the mineral.
x 400; sample SD-12.

Mn K

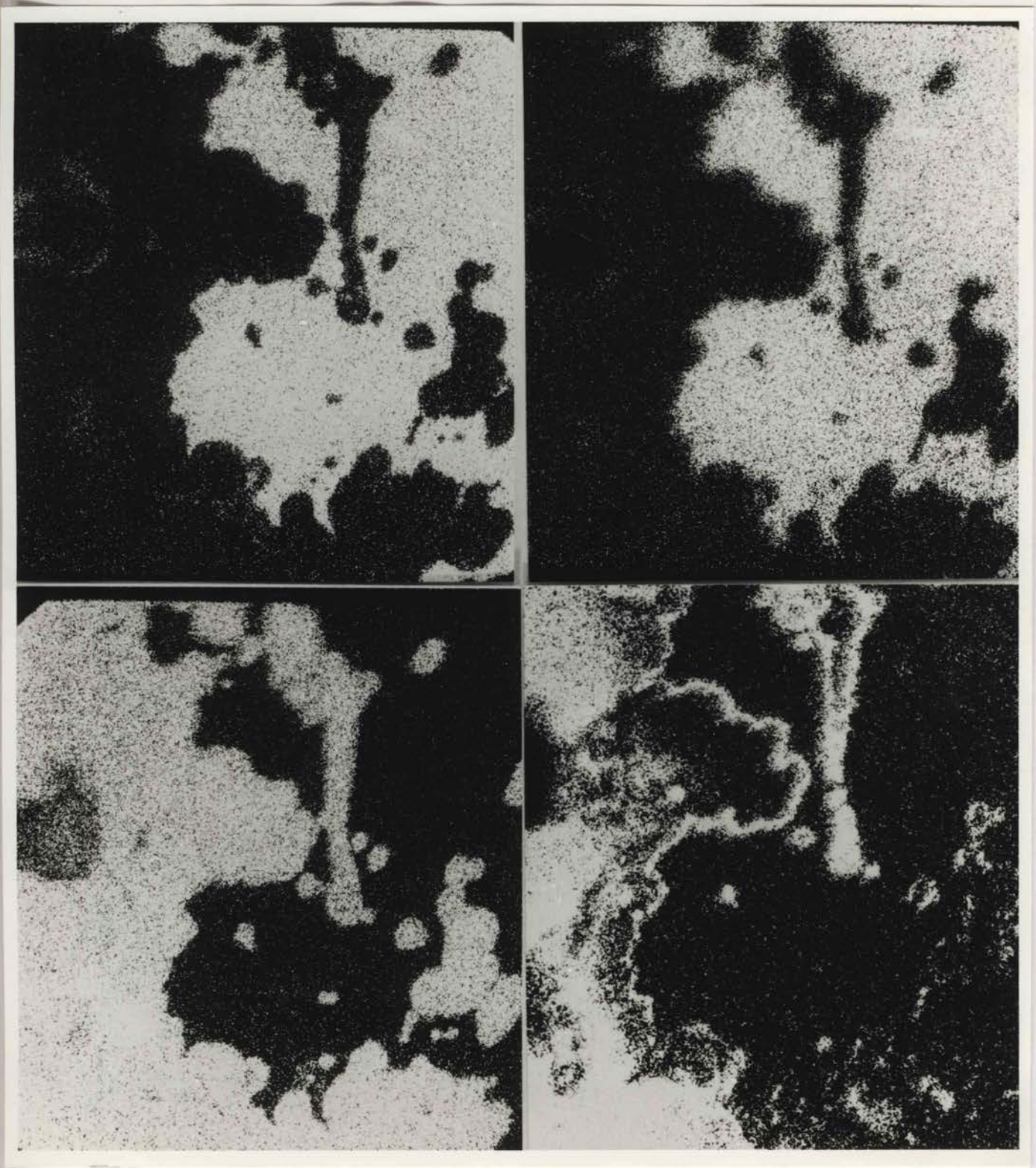

Fe Ca

Plate A3.2. Compositional vairation of cryptomelane and coexisting phases. The BSE images show tha the cryptomelane is K-and Mn-enriched, while the surrounding dark grey areas in Plate A.3 are Fe- and Ca-enriched. x 400; sample SD-12

Plate A3.3. BSE images of needle-like crystals of cryptomelane. This high magnification plate present details of the form of cryptomelane crystals with needle-like textures, growing from veins. The lower plate shows the Mn-distributions in the observed area. The compositional distribution plate helps to identify the minerals investigated. x 800; sample SD-12.

TableA3.1. Representative Microprobe Analyses of Cryptomelane.

	Sample from Ponto Mine area SD27												References		
	1	2	3	4	5	6	7	8	9	10	11	12	1	2	3
SiO2	0.02	0.01	0.05	0.07	0.00	0.17	0.01	0.02	0.11	0.16	0.08	0.00	0.00	0.05	0.00
TiO2	0.04	0.18	0.23	0.06	0.18	0.00	0.21	0.61	0.65	0.07	0.05	0.05	0.03	0.12	0.10
Al2O3	0.20	0.04	0.00	0.18	0.03	0.18	0.06	0.04	0.11	0.23	0.10	0.16	0.51	0.30	0.42
Fe2O3*	1.21	3.20	2.88	2.57	2.35	1.67	1.65	0.86	1.10	1.92	2.50	1.42	3.56	5.71	5.63
MnO2#	91.57	87.24	86.16	86.81	85.76	86.15	85.32	86.54	86.59	84.69	84.51	90.50	87.06	80.30	82.37
MnO	0.00	0.00	0.00	0.00	0.00	0.00	0.00	0.00	0.00	0.00	0.00	0.00	0.00	0.00	0.00
MgO	0.03	0.00	0.00	0.00	0.00	0.00	0.00	0.00	0.00	0.00	0.11	0.02	0.00	0.00	0.03
CaO	0.22	0.00	0.00	0.00	0.00	0.00	0.00	0.00	0.00	0.00	0.00	0.19	0.08	0.13	0.09
BaO	1.46	-	-	0.02	0.06	0.07	0.13	0.59	0.58	0.04	0.08	1.61	1.31	3.70	4.08
Na2O	0.20	0.24	0.17	0.19	0.19	0.24	0.20	0.19	0.25	0.17	0.14	0.14	1.49	1.18	0.98
K2O	3.11	6.27	6.73	6.73	6.73	6.31	6.53	5.73	5.69	6.51	6.56	5.64	6.83	4.51	4.39
total	98.06	97.18	96.22	96.63	95.30	94.79	94.11	94.58	95.08	93.79	94.13	99.73	99.56	92.30	94.01

												av. B1	C1	av.CH1
Structural formulae (Cations based on 16 oxygen)														
Si	0.002	0.001	0.006	0.009	0.000	0.022	0.001	0.003	0.014	0.021	0.010			
Ti	0.004	0.017	0.022	0.006	0.017	0.000	0.020	0.059	0.062	0.007	0.005			
Al	0.029	0.006	0.000	0.027	0.004	0.027	0.009	0.006	0.016	0.035	0.015			
Fe	0.111	0.299	0.273	0.242	0.225	0.160	0.160	0.083	0.105	0.186	0.242			
Mn4+	7.738	7.490	7.487	7.504	7.527	7.568	7.572	7.628	7.587	7.529	7.504			
Mn2+	0.000	0.000	0.000	0.000	0.000	0.000	0.000	0.000	0.000	0.000	0.000			
Mg	0.005	0.000	0.000	0.000	0.000	0.000	0.000	0.000	0.000	0.000	0.021			
Ca	0.029	0.000	0.000	0.000	0.000	0.000	0.000	0.000	0.000	0.000	0.000			
Na	0.047	0.058	0.041	0.046	0.047	0.059	0.050	0.047	0.061	0.042	0.035			
K	0.485	0.994	1.080	1.074	1.091	1.023	1.070	0.932	0.921	1.069	1.075			
Total	8.450	8.865	8.909	8.908	8.911	8.859	8.882	8.758	8.766	8.889	8.907			

*** Total treated as Fe2O3**

 # Those with no MnO contents are treated as total in MnO2

Table A3.5. Continued (2)

Reference compositions of the minerals published previously.

	4	5	6	7	8	9	10	11	12	13	14	15	16	17	18	19
SiO2	0.00	0.00	0.00	0.00	0.00	0.00	0.00	0.58	0.03	0.35	0.18	0.30	0.00	0.00	0.70	1.16
TiO2	0.14	0.01	0.06	0.03	0.00	0.19	0.05	0.01	0.00	0.00	0.00	0.00	0.00	0.00	0.00	0.00
Al2O3	0.32	0.34	0.36	0.06	0.01	0.82	0.70	0.37	0.00	1.37	0.39	0.77	0.00	3.12	0.30	0.35
Fe2O3*	6.52	3.86	6.15	5.76	9.02	3.72	3.53	0.46	0.36	4.00	0.19	1.86	0.00	0.31	0.17	0.20
MnO2#	81.30	86.52	81.68	82.68	76.68	85.05	84.09	83.13	86.54	81.75	87.09	84.20	82.40	80.40	81.34	92.00
MnO	0.00	0.00	0.00	0.00	0.00	0.00	0.00	2.08	3.92	3.50	2.49	3.30	5.80	7.77	9.76	0.00
MgO	0.02	0.01	0.01	0.01	0.00	0.00	0.02	0.05	0.00	0.02	0.07	0.08	0.00	0.00	0.00	0.00
CaO	0.06	0.06	0.05	0.06	0.44	0.07	0.03	0.27	0.30	0.28	0.00	0.05	0.00	0.37	0.00	0.00
BaO	4.46	1.47	1.64	2.96	0.00	3.60	2.97	0.13	1.04	0.00	0.00	0.08	-	-	-	1.24
Na2O	0.80	1.44	0.89	0.90	0.27	1.35	1.25	0.44	0.47	0.56	0.48	0.38	0.09	0.23	0.47	0.00
K2O	4.56	6.84	4.72	5.56	5.00	5.26	5.25	3.50	3.88	3.84	3.10	4.40	6.60	2.29	2.94	1.25
total	93.72	99.08	93.92	95.06	91.42	96.46	94.92	90.89	95.50	95.67	93.99	95.34	94.89	94.49	95.68	94.96
	av.CH2	T1	av. T2	av.T3	av. T4	av. T5	T6									

References:

1 - 10. Miura et al., 1987. The notes at the bottom show the original sample numbers and indicate that the values quoted here are the average of the analyses.

11 -14. Richmond & Fleischer, 1942

15. Faulring et al., 1960

16. Hewett & Olivares, 1968

17 - 19. Perseil & Pinet, 1976

Table 4.1A. Electron microprobe analyses of calcic amphiboles									
sequence		Basement							
area		Ponto Mine						Boshy Tank	
sample		752202			752302			762501	
		1	2	3	1	2	3	1	2
	SiO2	51.36	53.87	52.30	50.91	52.19	51.92	50.42	48.45
	TiO2	0.09	0.08	0.00	0.19	0.10	0.10	0.16	0.18
	Al2O3	3.40	1.58	2.65	4.64	3.46	3.50	4.27	5.96
	FeO#	14.01	11.38	12.26	16.16	14.28	14.23	16.25	17.73
	MnO	0.40	0.26	0.36	0.29	0.34	0.30	0.26	0.25
	MgO	15.30	17.92	16.77	13.12	14.52	15.72	13.54	12.32
	CaO	12.21	12.84	12.57	12.58	12.69	12.18	12.40	11.86
	Na2O	0.64	0.42	0.54	0.45	0.36	0.32	0.76	1.00
	K2O	0.15	0.12	0.15	0.24	0.12	0.14	0.16	0.13
	Cr2O3	0.02	0.08	0.00	0.06	0.04	0.02	0.12	0.24
	total	97.58	98.55	97.60	98.64	98.10	98.43	98.34	98.12
		Structural formulae (cations based on 23 oxygens)							
	Si	7.498	7.675	7.569	7.422	7.569	7.499	7.392	7.182
	Ti	0.010	0.009	0.000	0.021	0.011	0.011	0.018	0.020
	Al	0.585	0.265	0.452	0.798	0.592	0.596	0.738	1.042
	Fe#	1.710	1.356	1.484	1.970	1.732	1.719	1.992	2.198
	Mn	0.049	0.031	0.044	0.036	0.042	0.037	0.032	0.031
	Mg	3.329	3.805	3.617	2.851	3.139	3.384	2.959	2.722
	Ca	1.910	1.960	1.949	1.965	1.972	1.885	1.948	1.884
	Na	0.181	0.116	0.152	0.127	0.101	0.090	0.216	0.287
	K	0.028	0.022	0.028	0.045	0.022	0.026	0.030	0.025
	Cr	0.002	0.009	0.000	0.007	0.005	0.002	0.014	0.028
	Total	15.302	15.248	15.295	15.242	15.185	15.249	15.339	15.419
	Mg*	0.66	0.74	0.71	0.59	0.64	0.66	0.60	0.55
T1	Si	3.395	3.639	3.500	3.370	3.524	3.389	3.306	3.050
	Al	0.605	0.265	0.448	0.630	0.476	0.587	0.694	0.950
M2	Al	0.000	0.000	0.000	0.162	0.112	0.000	0.035	0.073
	Ti	0.010	0.009	0.000	0.021	0.011	0.011	0.017	0.020
	Fe3+	0.612	0.209	0.408	0.354	0.298	0.628	0.531	0.833
	Fe2+	0.346	0.450	0.383	0.526	0.489	0.352	0.462	0.351
	Mn	0.049	0.031	0.044	0.036	0.042	0.036	0.032	0.031
	Mg	1.035	1.484	1.277	0.921	1.064	1.074	0.924	0.687
M1,3	Fe	7.520	0.697	0.693	1.090	0.945	0.740	1.000	1.015
	Mg	2.248	2.303	2.307	1.910	2.055	2.260	2.000	1.985
M4	Ca	1.884	1.951	1.931	1.951	1.960	1.857	1.925	1.849
	Na	0.116	0.049	0.069	0.049	0.040	0.088	0.075	0.151
A	Na	0.062	0.066	0.082	0.078	0.061	0.000	0.139	0.131
	K	0.028	0.022	0.027	0.044	0.022	0.025	0.030	0.024
VACANCY		0.909	0.912	0.891	0.878	0.917	0.974	0.832	0.844

assuming all Fe in ferrious state

Mg* = Mg/(Mg+Fe#)

Fig. 4.1A. Continued (2)									
sequence		Basement							
area		Boshy Tank							
sample		762603		762701	762701	762705		762706	
		1	2	1	2	1	2	1	2
	SiO2	49.95	51.94	54.00	54.11	49.98	52.92	53.06	49.70
	TiO2	0.13	0.14	0.00	0.06	0.25	1.80	0.05	1.09
	Al2O3	5.29	3.25	1.29	1.37	5.59	0.89	2.64	4.80
	FeO#	14.79	13.43	12.06	13.09	15.86	17.04	12.41	13.41
	MnO	0.24	0.26	0.25	0.40	0.33	0.26	0.30	0.30
	MgO	14.40	15.61	17.03	16.15	12.46	12.03	16.40	14.25
	CaO	12.52	12.43	13.18	12.83	12.68	13.79	13.16	13.18
	Na2O	0.01	0.60	0.23	0.26	0.84	0.12	0.29	0.56
	K2O	0.18	0.21	0.09	0.06	0.23	0.09	0.12	0.24
	Cr2O3	0.10	0.00	0.16	0.15	0.47	0.08	0.01	0.10
	total	97.61	97.87	98.29	98.48	98.69	99.02	98.44	97.63
		Structural formulae (cations based on 23 oxygens)							
	Si	7.311	7.533	7.736	7.764	7.302	7.725	7.608	7.273
	Ti	0.014	0.015	0.000	0.006	0.027	0.198	0.005	0.120
	Al	0.913	0.556	0.218	0.232	0.963	0.153	0.446	0.828
	Fe#	1.810	1.629	1.445	1.571	1.938	2.080	1.488	1.641
	Mn	0.030	0.032	0.030	0.049	0.041	0.032	0.036	0.037
	Mg	3.142	3.374	3.636	3.454	2.713	2.617	3.505	3.108
	Ca	1.963	1.931	2.023	1.972	1.985	2.157	2.022	2.066
	Na	0.003	0.169	0.064	0.072	0.238	0.034	0.081	0.159
	K	0.034	0.039	0.016	0.011	0.043	0.017	0.022	0.045
	Cr	0.012	0.000	0.018	0.017	0.054	0.009	0.001	0.012
	Total	15.232	15.278	15.186	15.148	15.304	15.022	15.214	15.289
	Mg*	0.63	0.67	0.72	0.69	0.58	0.56	0.70	0.65
T1	Si	3.208	3.454	3.711	3.726	3.271	3.725	3.550	3.227
	Al	0.792	0.546	0.217	0.231	0.729	0.153	0.443	0.773
M2	Al	0.108	0.004	0.000	0.000	0.229	0.000	0.000	0.050
	Ti	0.014	0.015	0.000	0.006	0.027	0.198	0.005	0.119
	Fe3+	0.625	0.484	0.137	0.210	0.213	0.000	0.331	0.282
	Fe2+	0.355	0.379	0.513	0.510	0.556	0.752	0.408	0.442
	Mn	0.029	0.032	0.030	0.048	0.041	0.032	0.036	0.037
	Mg	0.928	1.101	1.420	1.287	0.870	0.946	1.227	1.005
M1,3	Fe	0.830	0.766	0.796	0.851	1.169	1.329	0.749	0.917
	Mg	2.170	2.234	2.204	2.149	1.831	1.671	2.251	2.083
M4	Ca	1.936	1.911	2.017	1.963	1.976	2.157	2.006	2.054
	Na	0.003	0.089	0.000	0.037	0.024	0.000	0.000	0.000
A	Na	0.000	0.078	0.064	0.035	0.213	0.034	0.080	0.158
	K	0.033	0.038	0.016	0.011	0.043	0.017	0.022	0.045
VACANCY		0.967	0.883	0.883	0.954	0.744	0.946	0.898	0.798

assuming all Fe in ferrious state

Mg* = Mg/(Mg+Fe#)

Table 4.1A. Continued (3).									
sequence		Basement							
area		Wilandra							
sample		861210		861302		861304		861311	
		1	2	1	2	1	2	1	2
	SiO2	52.04	51.95	49.83	52.51	49.95	48.50	52.25	51.74
	TiO2	0.01	0.04	0.47	0.03	0.14	1.24	0.08	0.04
	Al2O3	1.30	1.77	3.68	1.64	4.12	6.15	3.32	2.74
	FeO#	12.50	14.18	14.16	12.28	19.20	16.23	12.78	13.95
	MnO	0.29	0.39	0.35	0.24	0.29	0.33	0.32	0.31
	MgO	14.84	14.13	13.56	15.26	11.21	12.26	15.43	14.57
	CaO	12.50	11.81	12.43	12.94	12.47	12.54	13.14	12.87
	Na2O	0.22	0.78	0.70	0.19	0.46	0.47	0.38	0.37
	K2O	0.05	0.09	0.11	0.09	0.18	0.23	0.08	0.08
	Cr2O3	0.00	0.00	0.00	0.01	0.00	0.36	0.15	0.07
	total	93.75	95.14	95.29	95.19	98.02	98.31	97.93	96.74
		Structural formulae (cations based on 23 oxygens)							
	Si	7.831	7.769	7.477	7.777	7.444	7.136	7.552	7.613
	Ti	0.231	0.004	0.053	0.003	0.016	0.137	0.009	0.004
	Al	0.001	0.312	0.651	0.286	0.724	1.067	0.566	0.475
	Fe#	1.573	1.773	1.777	1.521	2.393	1.997	1.545	1.717
	Mn	0.037	0.049	0.044	0.030	0.037	0.041	0.039	0.039
	Mg	3.328	3.149	3.033	3.369	2.490	2.689	3.324	3.195
	Ca	2.015	1.892	1.998	2.053	1.991	1.977	2.035	2.029
	Na	0.064	0.226	0.204	0.055	0.133	0.134	0.106	0.106
	K	0.010	0.017	0.021	0.017	0.034	0.043	0.015	0.015
	Cr	0.000	0.000	0.000	0.001	0.000	0.042	0.017	0.008
	Total	15.090	15.191	15.258	15.112	15.262	15.263	15.208	15.201
	Mg*	0.68	0.64	0.63	0.69	0.51	0.57	0.68	0.65
T1	Si	3.822	3.735	3.457	3.755	3.384	3.065	3.503	3.569
	Al	0.178	0.265	0.543	0.245	0.616	0.935	0.497	0.431
M2	Al	0.052	0.045	0.106	0.040	0.102	0.121	0.065	0.041
	Ti	0.001	0.004	0.053	0.003	0.016	0.136	0.009	0.004
	Fe3+	0.049	0.201	0.121	0.127	0.368	0.453	0.294	0.262
	Fe2+	0.581	0.570	0.595	0.514	0.674	0.443	0.426	0.513
	Mn	0.037	0.049	0.044	0.030	0.036	0.041	0.039	0.038
	Mg	1.267	1.137	1.086	1.239	0.821	0.763	1.126	1.119
M1,3	Fe	0.943	1.002	1.062	0.880	1.352	1.101	0.824	0.943
	Mg	2.057	1.998	1.938	2.120	1.648	1.899	2.176	2.057
M4	Ca	2.013	1.884	1.993	2.048	1.975	1.957	2.022	2.017
	Na	0.000	0.116	0.007	0.000	0.025	0.043	0.000	0.000
A	Na	0.064	0.109	0.196	0.054	0.107	0.090	0.106	0.105
	K	0.010	0.017	0.021	0.017	0.034	0.043	0.015	0.015
VACANCY		0.926	0.874	0.783	0.929	0.859	0.867	0.880	0.880

assuming all Fe in ferrious state

Mg* = Mg/(Mg+Fe#)

Table 4.1A. Continued (4).								
sequence	Basement							
area	Wilandra				Cymbric Vale			
	861601		861605		861713		861714	
samples	1	2	1	2	1	2	1	2
SiO2	52.90	52.40	54.44	54.89	54.58	54.43	54.45	53.13
TiO2	0.07	0.06	0.03	0.03	0.09	0.11	0.05	0.03
Al2O3	1.53	2.46	2.16	2.24	3.27	3.85	2.88	3.18
FeO#	16.92	17.09	11.48	12.03	13.91	14.94	12.95	14.37
MnO	0.26	0.32	0.20	0.19	0.21	0.36	0.24	0.32
MgO	12.92	12.71	16.38	15.79	14.92	13.64	15.71	14.47
CaO	12.73	12.89	13.48	13.16	9.95	8.73	9.97	10.07
Na2O	0.24	0.35	0.23	0.19	1.95	2.52	1.55	1.88
K2O	0.07	0.20	0.08	0.09	0.12	0.18	0.12	0.18
Cr2O3	0.00	0.00	0.10	0.04	0.00	0.47	0.02	0.04
total	97.64	98.48	98.58	98.65	99.00	99.23	97.94	97.67
	Structural formulae (cations based on 23 oxygens)							
Si	7.792	7.675	7.740	7.796	7.761	7.755	7.788	7.707
Ti	0.008	0.007	0.003	0.003	0.010	0.012	0.005	0.003
Al	0.266	0.425	0.362	0.375	0.548	0.647	0.486	0.544
Fe#	2.084	2.093	1.365	1.429	1.654	1.780	1.549	1.743
Mn	0.032	0.040	0.024	0.023	0.025	0.043	0.029	0.039
Mg	2.836	2.775	3.471	3.343	3.162	2.897	3.349	3.129
Ca	2.009	2.023	2.054	2.003	1.516	1.333	1.528	1.565
Na	0.069	0.099	0.063	0.052	0.538	0.696	0.430	0.529
K	0.013	0.037	0.015	0.016	0.022	0.033	0.022	0.033
Cr	0.000	0.000	0.011	0.004	0.000	0.053	0.002	0.005
Total	15.109	15.174	15.108	15.044	15.236	15.249	15.188	15.297
Mg*	0.58	0.57	0.72	0.70	0.66	0.62	0.68	0.64
T1 Si	3.777	3.655	3.721	3.796	3.667	3.630	3.699	3.606
Al	0.223	0.345	0.279	0.204	0.333	0.370	0.301	0.394
M2 Al	0.042	0.079	0.082	0.171	0.208	0.266	0.179	0.143
Ti	0.008	0.007	0.003	0.003	0.010	0.012	0.005	0.003
Fe3+	0.084	0.117	0.112	0.000	0.558	0.734	0.514	0.600
Fe2+	0.758	0.727	0.456	0.531	0.317	0.241	0.320	0.333
Mn	0.032	0.040	0.024	0.023	0.025	0.043	0.029	0.039
Mg	1.073	1.017	1.259	1.241	0.903	0.655	1.025	0.898
M1,3 Fe	1.242	1.250	0.797	0.898	0.779	0.806	0.715	0.811
Mg	1.758	1.750	2.203	2.102	2.221	2.194	2.285	2.189
M4 Ca	2.005	2.018	2.049	2.003	1.498	1.311	1.511	1.545
Na	0.000	0.000	0.000	0.000	0.502	0.685	0.425	0.455
A Na	0.068	0.099	0.063	0.052	0.029	0.000	0.000	0.067
K	0.013	0.037	0.014	0.016	0.022	0.032	0.022	0.033
VACANCY	0.918	0.864	0.922	0.932	0.950	0.968	0.978	0.900

assuming all Fe in ferrious state

Mg* = Mg/(Mg+Fe#)

Table 4.1A. Continued (5).

sequence		Basement				Late Proterozoic			
area		Cymbric Vale		Bilpa		Nundora			
		861909		862914		761503			761907
samples		1	2	1	2	1	2	1	2
	SiO2	50.98	45.99	50.68	48.73	54.97	54.79	54.96	55.34
	TiO2	0.49	1.65	1.88	0.20	0.00	0.33	0.09	0.00
	Al2O3	1.98	4.68	2.83	7.79	0.11	0.00	0.00	0.32
	FeO#	7.25	28.00	15.40	16.47	10.82	9.77	11.44	7.29
	MnO	0.25	0.37	0.25	0.26	0.46	0.35	0.43	0.29
	MgO	15.68	6.10	12.60	12.02	18.02	18.86	17.88	21.04
	CaO	19.37	9.66	13.30	11.23	12.47	12.85	13.08	13.36
	Na2O	0.36	1.80	0.35	0.73	0.48	0.33	0.17	0.43
	K2O	0.01	0.58	0.15	0.25	0.04	0.07	0.06	0.12
	Cr2O3	0.00	0.00	0.05	0.13	0.00	0.02	0.01	0.09
	total	96.37	98.83	97.49	97.81	97.37	97.37	98.12	98.28
		Structural formulae (cations based on 23 oxygens)							
	Si	7.471	7.146	7.481	7.162	7.888	7.836	7.858	7.768
	Ti	0.054	0.193	0.209	0.022	0.000	0.035	0.010	0.000
	Al	0.342	0.857	0.493	1.350	0.019	0.000	0.000	0.053
	Fe#	0.889	3.638	1.901	2.024	1.298	1.169	1.368	0.856
	Mn	0.031	0.049	0.031	0.032	0.056	0.042	0.052	0.034
	Mg	3.425	1.413	2.772	2.633	3.854	4.021	3.810	4.402
	Ca	3.041	1.608	2.104	1.768	1.917	1.969	2.004	2.009
	Na	0.102	0.542	0.100	0.208	0.134	0.092	0.047	0.117
	K	0.002	0.115	0.028	0.047	0.007	0.013	0.011	0.021
	Cr	0.000	0.000	0.006	0.015	0.000	0.002	0.001	0.010
	Total	15.357	15.561	15.125	15.261	15.173	15.179	15.161	15.270
	Mg*	0.79	0.28	0.59	0.57	0.75	0.77	0.74	0.84
T1	Si	3.449	3.027	3.481	3.501	3.879	3.836	3.858	3.768
	Al	0.341	0.843	0.493	0.949	0.019	0.000	0.000	0.053
M2	Al	0.000	0.000	0.000	0.380	0.000	0.000	0.000	0.000
	Ti	0.054	0.190	0.209	0.022	0.000	0.035	0.010	0.000
	Fe3+	0.129	0.655	0.000	0.685	0.047	0.000	0.000	0.000
	Fe2+	0.213	0.937	1.901	0.318	0.515	0.493	0.575	0.368
	Mn	0.031	0.048	0.031	0.032	0.056	0.042	0.052	0.034
	Mg	0.960	0.436	0.993	0.614	1.585	1.697	1.603	1.890
M1,3	Fe	0.546	2.047	1.221	1.022	0.736	0.676	0.793	0.488
	Mg	2.454	0.953	1.799	0.198	2.264	2.324	2.207	2.512
M4	Ca	3.033	1.581	2.104	1.741	1.915	1.969	2.004	2.009
	Na	0.000	0.419	0.000	0.205	0.085	0.031	0.000	0.000
A	Na	0.102	0.115	0.100	0.000	0.049	0.061	0.047	0.117
	K	0.002	0.113	0.028	0.046	0.007	0.013	0.011	0.021
VACANCY		0.896	0.772	0.872	0.954	0.944	0.926	0.942	0.862

assuming all Fe in ferrious state

Mg* = Mg/(Mg+Fe#)

Table 4.1A. Continued (6).

sequence		Proterozoic	Cambrian						
area		Nundora	Comarto						
sample		761907	861003		861005		861010		
		3	1	2	1	2	1	2	3
	SiO2	57.40	51.14	51.49	46.41	46.48	48.04	47.33	46.93
	TiO2	0.05	0.85	0.53	1.98	2.11	1.22	1.80	1.75
	Al2O3	0.00	2.52	2.55	5.55	5.03	4.98	5.70	4.37
	FeO#	5.14	8.73	6.57	10.93	11.43	9.24	9.09	11.59
	MnO	0.44	0.26	0.19	0.21	0.27	0.22	0.23	0.24
	MgO	21.90	16.72	17.48	11.41	11.29	13.40	13.74	12.84
	CaO	13.31	18.71	19.53	20.85	20.42	20.58	19.95	19.20
	Na2O	0.09	0.20	0.19	0.56	0.61	0.39	0.40	0.47
	K2O	0.08	0.05	0.03	0.03	0.00	0.02	0.08	0.04
	Cr2O3	0.00	0.00	0.28	0.30	0.26	0.14	0.04	0.01
	total	98.41	99.18	98.84	98.23	97.90	98.23	98.36	97.44
		Structural formulae (cations based on 23 oxygens)							
	Si	7.925	7.318	7.335	6.878	6.923	7.028	6.908	6.995
	Ti	0.005	0.091	0.057	0.221	0.236	0.134	0.198	0.196
	Al	0.000	0.425	0.428	0.970	0.883	0.859	0.981	0.768
	Fe#	0.593	1.045	0.783	1.355	1.424	1.131	1.110	1.445
	Mn	0.051	0.031	0.023	0.026	0.034	0.027	0.028	0.030
	Mg	4.507	3.566	3.712	2.520	2.506	2.922	2.989	2.952
	Ca	1.969	2.869	2.981	3.311	3.259	3.226	3.120	3.066
	Na	0.024	0.055	0.052	0.161	0.176	0.111	0.113	0.136
	K	0.014	0.009	0.005	0.006	0.000	0.004	0.015	0.008
	Cr	0.000	0.000	0.032	0.035	0.031	0.016	0.005	0.001
	Total	15.088	15.409	15.408	15.483	15.472	15.458	15.467	15.597
	Mg*	0.88	0.77	0.83	0.65	0.64	0.72	0.73	0.67
T1	Si	3.925	3.289	3.293	2.821	2.885	2.952	2.837	2.957
	Al	0.000	0.423	0.426	0.962	0.878	0.850	0.971	0.764
M2	Al	0.000	0.000	0.000	0.000	0.000	0.000	0.000	0.000
	Ti	0.005	0.091	0.056	0.219	0.235	0.133	0.196	0.195
	Fe3+	0.000	0.177	0.255	0.359	0.233	0.471	0.453	0.231
	Fe2+	0.244	0.279	0.152	0.141	0.221	0.102	0.112	0.315
	Mn	0.051	0.031	0.023	0.026	0.034	0.027	0.028	0.030
	Mg	1.856	1.141	1.065	0.354	0.462	0.448	0.503	0.736
M1,3	Fe	0.349	0.589	0.375	0.855	0.970	0.557	0.545	0.899
	Mg	2.651	2.411	2.625	2.145	2.030	2.443	2.455	2.101
M4	Ca	1.969	2.857	2.964	3.284	3.241	3.191	3.088	3.050
	Na	0.024	0.000	0.000	0.000	0.000	0.000	0.000	0.000
A	Na	0.000	0.055	0.052	0.160	0.175	0.109	0.112	0.135
	K	0.014	0.009	0.005	0.006	0.000	0.004	0.015	0.008
VACANCY		0.986	0.936	0.942	0.835	0.825	0.887	0.873	0.857

assuming all Fe in ferrious state

Mg* = Mg/(Mg+Fe#)

Table 4.1B. Electron Microprobe Analyses of Kaersutite

	late Proterozoic - Nundora area						Wonnaminta lamprophyre								
	760801				761001		762412								
	1	2	3	4	1	2	1	2	3	4	5	6	7	8	9
SiO2	40.48	41.53	40.89	41.19	40.61	42.35	40.83	39.34	40.62	39.78	40.47	39.72	39.81	39.98	40.37
TiO2	4.51	4.30	4.76	4.98	7.41	3.32	5.22	6.26	5.12	5.97	4.81	6.15	6.08	5.59	5.65
Al2O3	11.04	10.77	11.17	10.75	9.57	9.90	11.64	12.31	11.25	11.94	11.13	12.14	11.85	11.80	11.69
FeO*	16.38	13.95	14.71	15.32	17.37	18.74	11.15	10.85	11.50	10.92	11.09	10.90	11.00	11.05	10.88
MnO	0.21	0.15	0.19	0.18	0.28	0.37	0.04	0.09	0.23	0.16	0.12	0.12	0.14	0.19	0.23
MgO	9.84	12.82	11.36	10.65	9.05	10.83	14.59	13.77	14.36	14.03	14.19	14.23	13.75	13.71	13.86
CaO	11.77	11.50	11.57	11.68	11.92	9.87	11.84	12.02	11.67	11.97	11.47	11.86	11.87	11.98	11.89
Na2O	2.70	3.17	3.21	2.66	1.93	3.04	2.98	2.91	3.08	2.91	3.43	2.82	2.99	3.01	3.06
K2O	1.01	1.00	1.08	1.09	0.33	0.26	0.46	0.53	0.44	0.52	0.52	0.54	0.50	0.43	0.47
Cr2O3	0.00	0.00	0.00	0.03	0.00	0.00	0.09	0.05	0.03	0.00	0.00	0.09	0.05	0.01	0.00
total	97.94	99.19	98.94	98.53	98.47	98.68	98.84	98.13	98.30	98.20	97.23	98.57	98.04	97.75	98.10
Structural formulae (Cations based on 23 oxygen)															
Si	6.138	6.143	6.096	6.170	6.129	6.366	5.975	5.814	5.888	5.872	6.032	5.839	5.888	5.928	5.957
Ti	0.514	0.478	0.534	0.561	0.841	0.375	0.574	0.696	0.676	0.663	0.539	0.680	0.676	0.623	0.627
Al	1.974	1.878	1.964	1.899	1.703	1.755	2.009	2.145	2.066	2.078	1.956	2.104	2.066	2.063	2.034
Fe	2.077	1.726	1.834	1.919	2.192	2.356	1.365	1.341	1.360	1.348	1.382	1.340	1.360	1.370	1.343
Mn	0.027	0.019	0.024	0.023	0.036	0.047	0.005	0.011	0.018	0.020	0.015	0.015	0.018	0.024	0.029
Mg	2.224	2.826	2.524	2.378	2.036	2.426	3.182	3.033	3.031	3.087	3.152	3.118	3.031	3.030	3.049
Ca	1.912	1.822	1.848	1.875	1.928	1.590	1.856	1.903	1.881	1.893	1.832	1.868	1.881	1.903	1.880
Na	0.794	0.909	0.928	0.773	0.565	0.886	0.846	0.834	0.875	0.833	0.991	0.804	0.857	0.865	0.876
K	0.195	0.189	0.205	0.208	0.064	0.050	0.086	0.100	0.094	0.098	0.099	0.101	0.094	0.081	0.088
Cr	0.000	0.000	0.000	0.004	0.000	0.000	0.010	0.006	0.006	0.000	0.000	0.010	0.006	0.001	0.000
Total	15.855	15.990	15.957	15.810	15.494	15.851	15.908	15.883	15.895	15.892	15.998	15.879	15.877	15.888	15.883

*: All Fe calculated as ferrous component

Table 4.2. Representative Compositions of Chlorite from the Wonominta Block analysed by Electron Microprobe.

	Basement - Ponto Mine Inlier					Basement - Wilandra Inlier										
samples	762305		762603	762605	762705	861210	861301		861304		861305		861601		861605	861707
	1	2					1	2	1	2	1	2	1	2		1
SiO2	26.95	27.02	26.61	26.52	26.55	28.04	25.37	25.75	26.53	26.61	26.41	26.63	28.02	27.14	29.14	27.49
TiO2	0.17	0.11	0.10	0.12	0.03	0.06	0.01	0.10	0.07	0.00	0.04	0.00	0.12	0.03	0.07	0.00
Al2O3	20.27	19.29	19.49	19.12	21.50	18.21	20.16	19.87	20.61	21.47	20.73	19.94	19.98	20.39	20.77	20.53
FeO*	24.99	24.33	21.09	21.35	24.04	25.05	23.25	23.40	25.71	23.40	22.58	21.83	28.11	26.99	20.65	19.13
MnO	0.31	0.26	0.31	0.27	0.38	0.35	0.44	0.50	0.34	0.37	0.33	0.28	0.43	0.41	0.32	0.41
MgO	16.89	17.30	19.61	19.12	16.92	16.42	15.87	16.34	15.55	17.45	18.09	18.87	15.88	15.73	19.10	21.04
CaO	0.09	0.12	0.10	0.07	0.06	0.33	0.01	0.04	0.02	0.05	0.11	0.14	0.09	0.09	0.15	0.07
Na2O	0.01	0.02	0.09	0.12	0.05	0.00	0.03	0.05	0.00	0.00	0.10	0.03	0.00	0.00	0.06	0.01
K2O	0.03	0.06	0.11	0.12	0.00	0.04	0.02	0.04	0.08	0.03	0.07	0.10	0.04	0.06	0.04	0.01
Cr2O3	0.09	0.02	0.00	0.00	0.07	0.09	0.00	0.02	0.04	0.00	0.07	0.26	0.03	0.30	0.14	0.00
total	89.80	88.53	87.51	86.81	89.60	88.59	85.16	86.11	88.95	89.38	88.53	88.08	92.70	91.14	90.44	88.69
Structural formulae (Cations based on 28 oxygens)																
Si	5.526	5.610	5.510	5.547	5.426	5.834	5.468	5.493	5.515	5.433	5.437	5.495	5.634	5.538	5.765	5.535
Ti	0.026	0.017	0.016	0.019	0.005	0.009	0.002	0.016	0.011	0.000	0.006	0.000	0.018	0.005	0.010	0.000
Al	4.901	4.722	4.759	4.716	5.182	4.468	5.123	4.998	5.052	5.169	5.033	4.852	4.738	4.906	4.846	4.874
Fe	4.285	4.224	3.652	3.734	4.109	4.359	4.191	4.174	4.470	3.995	3.888	3.767	4.727	4.606	3.417	3.221
Mn	0.054	0.046	0.054	0.048	0.066	0.062	0.080	0.090	0.060	0.064	0.058	0.049	0.073	0.071	0.054	0.070
Mg	5.162	5.353	6.053	5.961	5.155	5.092	5.098	5.195	4.818	5.310	5.551	5.804	4.760	4.784	5.633	6.314
Ca	0.020	0.027	0.022	0.016	0.013	0.074	0.002	0.009	0.004	0.011	0.024	0.031	0.019	0.020	0.032	0.015
Na	0.004	0.008	0.036	0.049	0.020	0.000	0.013	0.021	0.000	0.000	0.040	0.012	0.000	0.000	0.023	0.004
K	0.008	0.016	0.029	0.032	0.000	0.011	0.005	0.011	0.021	0.008	0.018	0.026	0.010	0.016	0.010	0.003
Cr	0.015	0.003	0.000	0.000	0.010	0.015	0.000	0.003	0.007	0.000	0.011	0.042	0.005	0.048	0.022	0.000
Total	20.001	20.026	20.131	20.122	19.986	19.924	19.982	20.010	19.958	19.990	20.066	20.078	19.984	19.994	19.812	20.036

*** Total Fe as FeO**

Table 4.2. Continued (2)

	Basement - Wilandra Inlier				late Proterozoic - Nundora							Cambrian -Comarto			Mt. Wright	
samples	861714	861913			761512		761810		761901		761906	861003	861005		862112	
	2		1	2	1	2	1	2	1	2			1	2	1	2
SiO2	27.59	26.92	26.91	26.30	26.10	27.35	27.82	28.45	28.00	26.84	30.78	26.73	28.50	29.27	30.38	28.74
TiO2	0.02	0.07	0.06	0.06	0.31	0.17	0.06	0.12	0.07	0.08	0.06	0.02	0.00	0.03	0.03	0.01
Al2O3	20.75	19.30	20.38	20.05	19.42	19.55	18.53	18.68	17.54	18.98	16.54	19.05	16.88	17.61	14.74	16.28
FeO*	19.75	20.22	24.59	24.74	32.18	33.65	25.85	26.82	29.98	31.16	14.02	27.86	23.90	24.53	25.19	24.40
MnO	0.30	0.22	0.77	0.69	0.22	0.18	0.16	0.15	0.27	0.31	0.34	0.31	0.23	0.24	0.27	0.51
MgO	20.81	19.74	16.29	16.64	11.10	10.60	16.28	15.60	13.51	12.78	26.04	13.62	17.48	17.19	18.32	17.12
CaO	0.27	0.09	0.07	0.03	0.14	0.12	0.17	0.03	0.12	0.08	0.11	0.16	0.16	0.18	0.27	0.22
Na2O	0.04	0.05	0.06	0.00	0.03	0.16	0.07	0.13	0.02	0.03	0.08	0.07	0.00	0.01	0.02	0.00
K2O	0.00	0.11	0.09	0.05	0.22	0.47	0.27	0.49	0.25	0.03	0.08	0.17	0.04	0.12	0.01	0.05
Cr2O3	0.04	0.11	0.00	0.05	0.01	0.01	0.00	0.00	0.00	0.00	0.05	0.02	0.09	0.00	0.00	0.00
total	89.57	86.83	89.22	88.61	89.73	92.26	89.21	90.47	89.76	90.29	88.10	88.01	87.28	89.18	89.23	87.33
Structural formulae (Cations based on 28 oxygens)																
Si	5.516	5.586	5.556	5.482	5.580	5.706	5.773	5.841	5.901	5.657	6.068	5.696	5.983	6.011	6.265	6.055
Ti	0.003	0.011	0.009	0.009	0.050	0.027	0.009	0.019	0.011	0.013	0.009	0.003	0.000	0.005	0.005	0.002
Al	4.892	4.723	4.961	4.928	4.896	4.810	4.534	4.522	4.359	4.717	3.845	4.787	4.178	4.265	3.584	4.045
Fe	3.302	3.509	4.246	4.312	5.753	5.871	4.486	4.605	5.284	5.492	2.312	4.965	4.196	4.213	4.344	4.299
Mn	0.051	0.039	0.135	0.122	0.040	0.032	0.028	0.026	0.048	0.055	0.057	0.056	0.041	0.042	0.047	0.091
Mg	6.201	6.106	5.013	5.170	3.537	3.296	5.035	4.774	4.244	4.015	7.652	4.326	5.469	5.262	5.631	5.376
Ca	0.058	0.020	0.015	0.007	0.032	0.027	0.038	0.007	0.027	0.018	0.023	0.037	0.036	0.040	0.060	0.050
Na	0.016	0.020	0.024	0.000	0.012	0.065	0.028	0.052	0.008	0.012	0.031	0.029	0.000	0.004	0.008	0.000
K	0.000	0.029	0.024	0.013	0.060	0.125	0.071	0.128	0.067	0.008	0.020	0.046	0.011	0.031	0.003	0.013
Cr	0.006	0.018	0.000	0.008	0.002	0.002	0.000	0.000	0.000	0.000	0.008	0.003	0.015	0.000	0.000	0.000
Total	20.045	20.061	19.983	20.051	19.962	19.961	20.002	19.974	19.949	19.987	20.025	19.948	19.929	19.873	19.947	19.931

*** Total Fe as FeO**

Table 4.2. Continued (3)

	Mt Wright	Bilpa Conglomerate			
samples	862402	862909		863012	
		1	2	1	2
SiO2	30.86	25.42	26.57	27.83	27.60
TiO2	0.00	0.13	0.07	0.10	0.06
Al2O3	19.34	17.31	17.59	22.26	22.00
FeO*	13.60	31.45	31.11	22.37	24.47
MnO	0.42	0.35	0.40	0.34	0.37
MgO	24.17	11.22	12.51	18.45	17.51
CaO	0.36	0.12	0.17	0.13	0.05
Na2O	0.02	0.01	0.02	0.00	0.00
K2O	0.03	0.03	0.06	0.06	0.13
Cr2O3	0.00	0.00	0.03	0.02	0.03
total	88.80	86.04	88.53	91.56	92.22
Structural formulae (Cations based on 28 oxygens)					
Si	5.997	5.689	5.740	5.493	5.472
Ti	0.000	0.022	0.011	0.015	0.009
Al	4.432	4.568	4.481	5.181	5.143
Fe	2.210	5.886	5.620	3.693	4.057
Mn	0.069	0.066	0.073	0.057	0.062
Mg	7.001	3.743	4.028	5.428	5.174
Ca	0.075	0.029	0.039	0.027	0.011
Na	0.008	0.004	0.008	0.000	0.000
K	0.007	0.009	0.017	0.015	0.033
Cr	0.000	0.000	0.005	0.003	0.005
Total	19.799	20.016	20.022	19.912	19.966

*** Total Fe as FeO**

Table 4.3. Representative Compositions of Ca-Al Silicate Minerals Analysed by Electron Microprobe.

Epidote

	Basement ssequence - Ponto Mine Inlier								Basement sequence - Wilandra Inlier							
samples	752202	752305	753001	762603	762604	762605	762701	762703	861203	861210	861302	861304	861605	861701 1	861701 2	861713
SiO2	37.02	37.75	38.87	37.97	36.63	37.59	37.74	37.25	39.03	37.94	37.92	38.38	38.68	37.81	37.04	37.90
TiO2	0.29	0.30	0.00	0.13	0.20	0.13	0.09	0.16	0.75	0.00	0.07	0.00	0.17	0.04	0.09	0.15
Al2O3	20.85	22.79	26.29	21.79	21.68	23.20	23.98	21.91	25.74	23.37	25.41	24.41	27.15	25.17	21.05	22.74
Fe2O3#	15.50	13.52	9.67	15.88	15.90	13.15	12.18	13.57	9.56	12.70	11.29	12.23	6.82	10.02	15.64	14.09
MnO	0.19	0.55	0.00	0.00	0.31	0.22	0.07	0.60	0.13	0.16	0.11	0.15	0.05	0.18	0.16	0.30
MgO	0.00	0.00	0.00	0.00	0.00	0.00	0.00	0.00	0.30	0.02	0.03	0.00	0.00	0.00	0.00	0.00
CaO	23.40	23.11	23.62	23.61	22.83	23.46	23.88	22.74	24.22	23.66	23.90	24.05	23.74	24.03	23.46	23.82
Na2O	0.07	0.02	0.00	0.01	0.04	0.01	0.00	0.00	0.12	0.00	0.01	0.02	0.00	0.00	0.00	0.06
K2O	0.01	0.07	0.02	0.00	0.08	0.01	0.00	0.02	0.03	0.00	0.00	0.04	0.00	0.02	0.04	0.09
Cr2O3	0.17	0.06	0.00	0.06	0.05	0.04	0.00	0.08	0.00	0.00	0.01	0.02	0.18	0.10	0.00	0.09
total	97.50	98.17	98.47	99.45	97.72	97.81	97.94	96.33	99.88	97.85	98.75	99.30	96.79	97.37	97.48	99.24
Structural formulae (Cations based on 25 oxygens)																
Si	5.996	6.016	6.056	6.009	5.919	6.000	5.994	6.056	6.018	6.040	5.948	6.009	6.082	6.001	5.998	5.992
Ti	0.035	0.036	0.000	0.015	0.024	0.016	0.011	0.020	0.087	0.000	0.008	0.000	0.020	0.005	0.011	0.018
Al	3.982	4.283	4.830	4.067	4.131	4.367	4.491	4.200	4.680	4.387	4.700	4.506	5.034	4.711	4.020	4.239
Fe	1.890	1.622	1.134	1.892	1.934	1.580	1.456	1.661	1.110	1.522	1.333	1.442	0.807	1.197	1.907	1.677
Mn	0.026	0.074	0.000	0.000	0.042	0.030	0.009	0.083	0.017	0.022	0.015	0.020	0.007	0.024	0.022	0.040
Mg	0.000	0.000	0.000	0.000	0.000	0.000	0.000	0.000	0.069	0.005	0.007	0.000	0.000	0.000	0.000	0.000
Ca	4.061	3.946	3.943	4.004	3.953	4.012	4.064	3.960	4.001	4.035	4.017	4.034	3.999	4.086	4.070	4.035
Na	0.022	0.006	0.000	0.003	0.013	0.003	0.000	0.000	0.036	0.000	0.003	0.006	0.000	0.000	0.000	0.018
K	0.002	0.014	0.004	0.000	0.016	0.002	0.000	0.004	0.006	0.000	0.000	0.008	0.000	0.004	0.008	0.018
Cr	0.022	0.008	0.000	0.008	0.006	0.005	0.000	0.010	0.000	0.000	0.001	0.002	0.022	0.013	0.000	0.011
Total	16.036	16.005	15.967	15.998	16.038	16.015	16.025	15.994	16.024	16.011	16.032	16.027	15.971	16.041	16.036	16.048

 # Total Fe as Fe2O3

Table 4.3. Continued (2).

Epidote

late Proterozoic -Packsaddle samples					late Proterozoic - Nundora samples				Wonnaminta lamprophyre			Comarto		Mt. Wright		
sample	760801		761001		761503		761906	762406	762412	762413		860901	861003	861005	862217	
	1	2	1	2	1	2				1	2				1	2
SiO2	37.93	38.93	38.43	38.43	37.36	37.33	36.78	37.70	36.97	37.84	37.69	37.98	37.97	37.88	36.40	36.50
TiO2	0.12	0.09	0.24	0.08	0.07	0.10	0.11	0.16	0.10	0.20	0.03	0.05	0.11	0.09	0.00	0.00
Al2O3	26.53	26.37	26.09	22.49	21.12	20.46	19.58	22.14	24.88	22.69	22.07	24.88	23.99	26.11	19.33	19.92
Fe2O3#	7.45	8.20	9.61	13.83	15.62	16.24	16.97	13.72	9.00	13.97	15.73	10.51	12.66	8.95	17.58	16.68
MnO	0.14	0.07	0.22	0.06	0.79	0.15	0.15	0.43	0.66	0.05	0.26	0.14	0.08	0.23	0.18	0.53
MgO	0.00	0.00	0.00	0.00	0.00	0.00	0.00	0.00	0.00	0.00	0.00	0.06	0.13	0.00	0.19	0.00
CaO	23.75	23.79	23.32	23.83	22.63	23.00	22.73	23.01	22.63	23.33	22.54	23.29	23.45	23.40	22.94	22.51
Na2O	0.02	0.10	0.02	0.01	0.01	0.02	0.00	0.00	0.00	0.01	0.00	0.01	0.00	0.00	0.03	0.03
K2O	0.03	0.01	0.06	0.02	0.00	0.06	0.03	0.02	0.02	0.00	0.00	0.01	0.07	0.02	0.00	0.01
Cr2O3	0.06	0.03	0.00	0.05	0.00	0.01	0.02	0.08	0.03	0.07	0.00	0.19	0.00	0.02	0.04	0.10
total	96.03	97.59	97.99	98.80	97.60	97.37	96.37	97.26	94.29	98.16	98.32	97.12	98.46	96.70	96.69	96.18
Structural formulae (Cations based on 25 oxygens)																
Si	6.039	6.100	6.026	6.080	6.037	6.054	6.049	6.065	6.037	6.026	6.018	6.037	5.999	6.014	5.990	6.013
Ti	0.014	0.011	0.028	0.010	0.009	0.012	0.014	0.019	0.012	0.024	0.004	0.006	0.013	0.011	0.000	0.000
Al	4.981	4.872	4.824	4.196	4.024	3.913	3.797	4.200	4.791	4.261	4.155	4.663	4.469	4.888	3.751	3.869
Fe	0.893	0.967	1.135	1.647	1.900	1.983	2.101	1.662	1.107	1.675	1.891	1.258	1.506	1.070	2.178	2.069
Mn	0.019	0.009	0.029	0.008	0.108	0.021	0.021	0.059	0.091	0.007	0.035	0.019	0.011	0.031	0.025	0.074
Mg	0.000	0.000	0.000	0.000	0.000	0.000	0.000	0.000	0.000	0.000	0.000	0.014	0.031	0.000	0.047	0.000
Ca	4.051	3.994	3.918	4.039	3.918	3.997	4.005	3.966	3.960	3.980	3.856	3.966	3.969	3.981	4.045	3.973
Na	0.006	0.030	0.006	0.003	0.003	0.006	0.000	0.000	0.000	0.003	0.000	0.003	0.000	0.000	0.010	0.010
K	0.006	0.002	0.012	0.004	0.000	0.012	0.006	0.004	0.004	0.000	0.000	0.002	0.014	0.004	0.000	0.002
Cr	0.008	0.004	0.000	0.006	0.000	0.001	0.003	0.010	0.004	0.009	0.000	0.024	0.000	0.003	0.005	0.013
Total	16.017	15.989	15.978	15.993	15.999	15.999	15.996	15.985	16.006	15.985	15.959	15.992	16.012	16.002	16.051	16.023

 # Total Fe as Fe2O3

Table 4.3. Continued (3).

	Epidote						Pumpellyite									
	Cambrian sequence - Mt. Wright						basement	Cambrian Comarto samples					Cambrian Mt. Wright samples			
samples	862223		862225	862901	862914		861605	860901					862225			
	1	2			1	2		1	2	3	4	5	1	2	3	4
SiO2	37.29	37.41	38.17	37.58	37.82	38.37	39.16	36.33	35.54	37.99	36.21	35.84	37.30	36.09	36.70	36.73
TiO2	0.12	0.37	0.33	0.03	0.19	0.05	0.09	0.03	0.04	0.10	0.04	0.00	0.01	0.21	0.13	0.19
Al2O3	21.40	19.59	24.08	23.61	23.04	25.05	20.40	22.72	23.17	23.23	22.95	22.44	24.10	20.13	20.01	21.12
Fe2O3#	15.56	17.84	11.62	12.63	13.66	10.22	12.51	8.50	7.63	9.39	8.24	9.56	6.54	11.61	10.67	9.31
MnO	0.12	0.72	0.50	0.13	0.01	0.11	0.22	0.09	0.09	0.14	0.11	0.11	0.73	0.20	0.17	0.29
MgO	0.22	0.49	0.00	0.00	0.00	0.00	1.88	1.73	2.08	1.50	2.18	1.44	1.77	2.22	2.82	2.67
CaO	23.66	21.49	23.58	23.74	24.08	24.23	22.58	22.09	22.79	21.05	21.77	21.29	22.73	22.42	21.72	22.46
Na2O	0.00	0.06	0.00	0.02	0.00	0.00	0.05	0.00	0.00	0.03	0.00	0.01	0.02	0.00	0.04	0.07
K2O	0.00	0.41	0.02	0.02	0.00	0.03	0.03	0.01	0.01	0.02	0.00	0.02	0.02	0.00	0.05	0.06
Cr2O3	0.00	0.05	0.06	0.03	0.01	0.01	0.01	0.17	0.00	0.00	0.00	0.07	0.15	0.00	0.00	0.09
total	98.37	98.43	98.36	97.79	98.81	98.07	96.93	91.67	91.35	93.45	91.50	90.78	93.37	92.88	92.31	92.99
Structural formulae (Cations based on 25 oxygens)																
Si	5.978	6.038	6.028	5.991	5.988	6.044	6.280	6.184	5.991	6.218	6.075	6.083	6.118	6.068	6.170	6.118
Ti	0.014	0.045	0.039	0.004	0.023	0.006	0.011	0.005	0.005	0.012	0.005	0.000	0.001	0.027	0.016	0.024
Al	4.046	3.728	4.484	4.438	4.302	4.653	3.857	4.468	4.605	4.483	4.540	4.491	4.661	3.991	3.967	4.148
Fe	1.878	2.168	1.382	1.516	1.628	1.212	1.510	1.060	0.968	1.157	1.041	1.222	0.808	1.470	1.351	1.167
Mn	0.016	0.098	0.067	0.018	0.001	0.015	0.030	0.013	0.013	0.019	0.016	0.016	0.101	0.028	0.024	0.041
Mg	0.053	0.118	0.000	0.000	0.000	0.000	0.449	0.345	0.523	0.366	0.545	0.364	0.433	0.556	0.707	0.663
Ca	4.064	3.716	3.990	4.055	4.085	4.089	3.879	3.968	4.116	3.691	3.913	3.872	3.994	4.039	3.912	4.008
Na	0.000	0.019	0.000	0.006	0.000	0.000	0.016	0.013	0.000	0.010	0.000	0.003	0.006	0.000	0.013	0.023
K	0.000	0.084	0.004	0.004	0.000	0.006	0.006	0.002	0.002	0.004	0.000	0.004	0.004	0.000	0.011	0.013
Cr	0.000	0.006	0.007	0.004	0.001	0.001	0.001	0.000	0.000	0.000	0.000	0.009	0.019	0.000	0.000	0.012
Total	16.049	16.020	16.001	16.036	16.028	16.026	16.039	16.058	16.223	15.960	16.135	16.064	16.145	16.179	16.171	16.217

 # Total Fe as Fe2O3

Table 4.3. Continued (4).

Clinozoisite						Prehnite				
basement - Boshy Tank samples						Cambrian Comarto metabasite				
samples	762705		762706			samples	Km345			
	1	2	1	2	3		1	2	3	4
SiO2	38.65	38.92	39.42	38.84	38.65	SiO2	41.98	41.31	42.73	40.25
TiO2	0.11	0.18	0.02	0.17	0.28	TiO2	0.39	0.75	0.71	1.75
Al2O3	27.35	26.47	29.08	27.08	26.77	Al2O3	21.63	21.68	22.53	20.87
Fe2O3#	7.38	8.29	4.71	7.66	8.00	FeO*	2.15	2.26	2.15	2.29
MnO	0.15	0.14	0.21	0.08	0.08	MnO	0.00	0.01	0.00	0.00
MgO	0.00	0.00	0.00	0.00	0.00	MgO	0.26	0.25	0.16	0.24
CaO	24.37	24.36	24.89	24.60	24.75	CaO	27.16	26.80	25.58	25.92
Na2O	0.02	0.01	0.00	0.00	0.00	Na2O	0.02	0.01	0.00	0.00
K2O	0.01	0.05	0.05	0.02	0.02	K2O	0.01	0.02	0.01	0.00
Cr2O3	0.06	0.13	0.00	0.00	0.00	Cr2O3	0.05	0.04	0.04	0.00
total	98.10	98.55	98.38	98.45	98.55	total	93.65	93.13	93.91	91.32
Structural formulae (Cations based on 25 oxygens)										
Si	6.021	6.055	6.066	6.035	6.014	Si	6.808	6.744	6.854	6.705
Ti	0.013	0.021	0.002	0.020	0.033	Ti	0.048	0.092	0.086	0.219
Al	5.024	4.856	5.276	4.962	4.912	Al	4.136	4.174	4.261	4.100
Fe	0.866	0.971	0.546	0.896	0.937	Fe	0.292	0.309	0.288	0.319
Mn	0.020	0.018	0.027	0.011	0.011	Mn	0.000	0.001	0.000	0.000
Mg	0.000	0.000	0.000	0.000	0.000	Mg	0.063	0.061	0.038	0.060
Ca	4.068	4.061	4.103	4.095	4.126	Ca	4.719	4.688	4.396	4.626
Na	0.006	0.003	0.000	0.000	0.000	Na	0.006	0.003	0.000	0.000
K	0.002	0.010	0.010	0.004	0.004	K	0.002	0.004	0.002	0.000
Cr	0.007	0.016	0.000	0.000	0.000	Cr	0.006	0.005	0.005	0.000
Total	16.027	16.011	16.030	16.023	16.037	Total	16.080	16.081	15.930	16.029

 # Total Fe as Fe2O3

*** Total Fe as FeO**

Tables 4.10. Representative Compositions of Pyroxenes in the Wonominta Block Analysed by Electron Microprobe.

mineral	Aegirine															
sequence	Late Proterozoic															
area	Nundora															
sample	762402 (light crystal)				762403 (light crystals)				762404 (dark crystals)				762406 (dark crystals)			
	1	2	3	4	1	2	3	4	1	2	3	4	1	2	3	4
SiO2	52.85	53.73	53.96	53.45	53.32	52.89	52.72	53.13	50.60	50.90	51.01	51.00	52.56	51.62	50.66	51.94
TiO2	0.04	0.04	0.03	0.03	0.00	0.07	0.07	0.07	0.15	0.20	0.15	0.08	0.05	0.05	0.05	0.04
Al2O3	5.11	6.58	7.66	6.14	6.89	7.06	6.54	6.03	1.03	1.84	1.43	2.26	2.34	1.27	1.10	2.06
Fe2O3#	27.92	25.60	24.27	26.53	25.75	25.79	26.82	26.34	33.17	30.94	32.29	31.87	31.73	32.74	33.01	32.16
MnO	0.01	0.00	0.00	0.00	0.03	0.01	0.03	0.03	0.39	0.48	0.30	0.23	0.18	0.37	0.41	0.22
MgO	0.09	0.04	0.07	0.04	0.02	0.24	0.14	0.20	0.22	0.16	0.04	0.00	0.04	0.07	0.11	0.05
CaO	0.05	0.07	0.04	0.04	0.09	0.07	0.08	0.06	1.99	1.34	1.08	1.30	0.93	2.35	2.41	0.92
Na2O	14.32	14.62	14.51	14.14	14.45	14.02	14.24	14.45	13.23	13.27	13.57	13.84	13.10	12.32	12.12	12.70
K2O	0.00	0.03	0.01	0.00	0.04	0.00	0.00	0.05	0.03	0.01	0.06	0.01	0.01	0.01	0.02	0.02
Cr2O3	0.02	0.00	0.03	0.01	0.00	0.00	0.00	0.00	0.00	0.02	0.00	0.00	0.00	0.00	0.01	0.00
total	100.41	100.71	100.58	100.38	100.59	100.15	100.64	100.36	100.81	99.16	99.93	100.59	100.94	100.80	99.90	100.11
	Structural formulae (Cations based on 6 oxygens)															
Si	1.977	1.985	1.984	1.985	1.974	1.965	1.959	1.978	1.942	1.967	1.963	1.948	1.983	1.968	1.955	1.979
Ti	0.001	0.001	0.001	0.001	0.000	0.002	0.002	0.002	0.004	0.006	0.004	0.002	0.001	0.001	0.001	0.001
Al	0.225	0.287	0.332	0.269	0.301	0.309	0.286	0.265	0.047	0.084	0.065	0.102	0.104	0.057	0.050	0.093
Fe	0.786	0.712	0.672	0.742	0.718	0.721	0.750	0.738	0.959	0.900	0.936	0.916	0.901	0.940	0.959	0.923
Mn	0.000	0.000	0.000	0.000	0.001	0.000	0.001	0.001	0.013	0.016	0.010	0.007	0.006	0.012	0.013	0.007
Mg	0.005	0.002	0.004	0.002	0.001	0.013	0.008	0.011	0.013	0.009	0.002	0.000	0.002	0.004	0.006	0.003
Ca	0.002	0.003	0.002	0.002	0.004	0.003	0.003	0.002	0.082	0.055	0.045	0.053	0.038	0.096	0.100	0.038
Na	1.039	1.047	1.035	1.018	1.037	1.010	1.026	1.043	0.985	0.994	1.013	1.025	0.958	0.911	0.907	0.938
K	0.000	0.001	0.000	0.000	0.002	0.000	0.000	0.002	0.001	0.000	0.003	0.000	0.000	0.000	0.001	0.001
Cr	0.001	0.000	0.001	0.000	0.000	0.000	0.000	0.000	0.000	0.001	0.000	0.000	0.000	0.000	0.000	0.000
Total	4.036	4.038	4.031	4.019	4.038	4.023	4.035	4.042	4.046	4.032	4.041	4.053	3.993	3.989	3.992	3.983

 # Total Fe as Fe2O3

Table 4.10. Continued (2)

mineral	Aegirine				mineral	Clinopyroxene									
sequence	Late Proterozoic				sequence	Basement									
area	Nundora				area	Boshy Tank			Wilandra						
samples	762407 (dark crystals)				sample	762705			861314				861604		
	1	2	3	4		1	2	3	1	2	3	4	1	2	3
SiO2	51.27	50.69	51.09	50.89	SiO2	51.57	51.38	50.23	51.18	50.76	50.34	50.84	50.71	50.91	50.86
TiO2	0.22	0.06	0.03	0.13	TiO2	0.89	0.82	1.20	0.47	0.43	0.53	0.42	0.82	0.81	0.75
Al2O3	1.68	1.39	1.49	1.72	Al2O3	0.78	2.03	1.90	2.31	2.72	3.44	2.69	2.64	2.70	2.31
Fe2O3#	31.62	32.44	31.65	31.96	FeO*	13.32	9.04	12.39	6.14	5.61	5.99	5.59	8.06	8.49	7.94
MnO	0.26	0.23	0.27	0.29	MnO	0.39	0.24	0.33	0.22	0.14	0.17	0.18	0.22	0.29	0.21
MgO	0.07	0.06	0.03	0.06	MgO	15.78	15.90	14.82	16.87	16.76	16.22	16.77	15.24	14.27	15.16
CaO	0.88	1.16	1.51	2.54	CaO	17.82	20.54	19.51	21.22	21.24	21.38	21.28	21.67	21.55	21.55
Na2O	13.35	13.44	12.87	12.71	Na2O	0.34	0.27	0.33	0.27	0.21	0.19	0.24	0.29	0.30	0.26
K2O	0.05	0.01	0.56	0.00	K2O	0.06	0.01	0.01	0.01	0.00	0.00	0.00	0.00	0.00	0.00
Cr2O3	0.01	0.00	0.01	0.01	Cr2O3	0.03	0.12	0.00	0.28	1.01	0.97	0.84	0.10	0.07	0.09
total	99.41	99.48	99.51	100.31	total	100.98	100.35	100.72	98.97	98.88	99.23	98.85	99.75	99.39	99.13
						Structural formulae (cations based on 6 oxygens)									
Si	1.975	1.961	1.974	1.951	Si	1.930	1.909	1.889	1.908	1.893	1.875	1.896	1.895	1.910	1.910
Ti	0.006	0.002	0.001	0.004	Ti	0.025	0.023	0.034	0.013	0.012	0.015	0.012	0.023	0.023	0.021
Al	0.076	0.063	0.068	0.078	Al	0.034	0.089	0.084	0.102	0.120	0.151	0.118	0.116	0.119	0.102
Fe	0.917	0.945	0.921	0.923	Fe	0.417	0.281	0.390	0.191	0.175	0.187	0.174	0.252	0.266	0.249
Mn	0.008	0.008	0.009	0.009	Mn	0.012	0.008	0.011	0.007	0.004	0.005	0.006	0.007	0.009	0.007
Mg	0.004	0.003	0.002	0.003	Mg	0.880	0.881	0.831	0.937	0.931	0.900	0.932	0.849	0.798	0.848
Ca	0.036	0.048	0.062	0.104	Ca	0.714	0.818	0.786	0.848	0.848	0.853	0.850	0.868	0.866	0.867
Na	0.997	1.008	0.964	0.945	Na	0.025	0.019	0.024	0.020	0.015	0.014	0.017	0.021	0.022	0.019
K	0.002	0.000	0.028	0.000	K	0.003	0.000	0.000	0.000	0.000	0.000	0.000	0.000	0.000	0.000
Cr	0.000	0.000	0.000	0.000	Cr	0.001	0.004	0.000	0.008	0.030	0.029	0.025	0.003	0.002	0.003
Total	4.021	4.038	4.029	4.017	Total	4.041	4.032	4.049	4.034	4.028	4.029	4.030	4.034	4.015	4.026

 # Total Fe as Fe2O3

*** Total Fe as FeO**

Table 4.10. Continued (3)

mineral	Clinopyroxene															
sequence	Basement					Late Proterozoic										
area	Cymbric Vale					Packsaddle		Nundora								
sample	861604	861909				760801		761503				761801				761907
	4	1	2	3	4	1	2	1	2	3	4	1	2	3	4	1
SiO2	50.73	50.62	52.67	52.73	51.71	50.77	49.60	48.03	49.41	49.25	48.01	49.68	47.16	50.07	50.77	48.73
TiO2	0.79	0.66	0.35	0.35	0.56	1.34	1.50	2.20	1.51	1.41	2.16	1.69	1.94	1.31	1.34	1.92
Al2O3	2.24	3.87	2.29	2.22	2.98	1.98	2.76	4.92	2.77	3.62	5.47	2.25	5.15	3.11	1.98	3.98
FeO*	7.94	5.96	6.10	5.96	7.08	8.64	7.86	6.83	6.10	5.54	7.07	7.70	5.82	5.13	8.64	7.23
MnO	0.20	0.16	0.19	0.17	0.22	0.20	0.14	0.10	0.14	0.10	0.17	0.18	0.14	0.13	0.20	0.13
MgO	15.20	16.11	17.16	17.62	16.75	14.71	14.65	14.87	15.78	15.60	14.23	15.24	14.74	16.07	14.71	14.62
CaO	21.61	21.13	21.06	20.06	20.32	22.61	21.92	22.61	22.89	23.03	22.53	22.03	22.79	23.33	22.61	22.51
Na2O	0.26	0.32	0.27	0.27	0.28	0.44	0.42	0.34	0.26	0.32	0.35	0.48	0.36	0.36	0.44	0.39
K2O	0.00	0.03	0.01	0.00	0.01	0.00	0.04	0.04	0.03	0.03	0.02	0.10	0.00	0.01	0.00	0.03
Cr2O3	0.11	0.58	0.25	0.46	0.12	0.00	0.12	0.18	0.14	0.15	0.01	0.00	0.94	0.95	0.00	0.09
total	99.08	99.44	100.35	99.84	100.03	100.69	99.01	100.12	99.03	99.05	100.02	99.35	101.04	100.47	100.69	99.63
	Structural formulae (cations based on 6 oxygens)															
Si	1.907	1.876	1.928	1.934	1.906	1.892	1.873	1.792	1.856	1.845	1.792	1.871	1.778	1.849	1.892	1.828
Ti	0.022	0.018	0.010	0.010	0.016	0.038	0.043	0.062	0.043	0.040	0.061	0.048	0.055	0.036	0.038	0.054
Al	0.099	0.169	0.099	0.096	0.130	0.087	0.123	0.216	0.123	0.160	0.241	0.100	0.229	0.135	0.087	0.176
Fe	0.250	0.185	0.187	0.183	0.218	0.269	0.248	0.213	0.192	0.174	0.221	0.243	0.183	0.158	0.269	0.227
Mn	0.006	0.005	0.006	0.005	0.007	0.006	0.004	0.003	0.004	0.003	0.005	0.006	0.004	0.004	0.006	0.004
Mg	0.852	0.890	0.936	0.963	0.920	0.817	0.824	0.827	0.884	0.871	0.792	0.855	0.828	0.885	0.817	0.817
Ca	0.870	0.839	0.826	0.788	0.802	0.903	0.887	0.904	0.921	0.924	0.901	0.889	0.920	0.923	0.903	0.905
Na	0.019	0.023	0.019	0.019	0.020	0.032	0.031	0.025	0.019	0.023	0.025	0.035	0.026	0.026	0.032	0.028
K	0.000	0.001	0.000	0.000	0.000	0.000	0.002	0.002	0.001	0.001	0.001	0.005	0.000	0.000	0.000	0.001
Cr	0.003	0.017	0.007	0.013	0.003	0.000	0.004	0.005	0.004	0.004	0.000	0.000	0.028	0.028	0.000	0.003
Total	4.028	4.023	4.018	4.011	4.022	4.044	4.039	4.049	4.047	4.045	4.039	4.052	4.051	4.044	4.044	4.043

*** Total Fe as FeO**

Table 4.10. Continued (4)

mineral	Clinopyroxene															
sequence	Late Proterozoic		Cambrian													
area	Nundora		Ponto Mine				Comarto									
sample	761907		752110				860901		861003				861005			
	2	3	1	2	3	4	1	2	1	2	3	4	1	2	3	4
SiO2	49.96	50.43	50.37	50.65	50.56	50.79	47.20	47.85	51.14	51.49	50.99	49.81	44.66	45.49	43.86	46.50
TiO2	1.40	1.15	1.17	1.09	1.02	1.19	2.01	1.62	0.85	0.53	0.57	0.88	3.09	2.17	4.29	2.06
Al2O3	2.66	3.12	2.14	1.85	1.74	1.69	5.70	5.50	2.52	2.55	2.64	4.55	5.77	5.29	5.53	4.66
FeO*	6.86	5.01	10.20	10.45	10.20	11.20	8.10	8.12	8.73	6.57	6.46	6.14	11.71	11.51	12.65	12.22
MnO	0.18	0.13	0.25	0.20	0.23	0.30	0.15	0.17	0.26	0.19	0.18	0.15	0.24	0.24	0.27	0.29
MgO	15.51	16.05	15.70	15.84	15.58	15.13	13.25	13.61	16.72	17.48	17.57	15.41	10.35	11.45	9.81	11.24
CaO	22.52	22.97	19.98	19.84	20.06	19.73	22.01	21.95	18.71	19.53	19.82	21.10	20.97	20.94	21.30	21.18
Na2O	0.37	0.31	0.35	0.34	0.28	0.34	0.40	0.41	0.20	0.19	0.23	0.30	0.59	0.56	0.55	0.64
K2O	0.08	0.03	0.00	0.05	0.00	0.00	0.01	0.02	0.05	0.03	0.05	0.02	0.04	0.01	0.03	0.05
Cr2O3	0.06	0.86	0.00	0.00	0.00	0.00	0.27	0.29	0.00	0.28	0.34	0.93	0.20	0.25	0.10	0.07
total	99.60	100.06	100.16	100.31	99.67	100.37	99.10	99.54	99.18	98.84	98.85	99.29	97.62	97.91	98.39	98.91
	Structural formulae (cations based on 6 oxygens)															
Si	1.869	1.865	1.887	1.895	1.903	1.905	1.787	1.802	1.909	1.913	1.899	1.854	1.753	1.775	1.721	1.800
Ti	0.039	0.032	0.033	0.031	0.029	0.034	0.057	0.046	0.024	0.015	0.016	0.025	0.091	0.064	0.127	0.060
Al	0.117	0.136	0.095	0.082	0.077	0.075	0.255	0.244	0.111	0.112	0.116	0.200	0.267	0.243	0.256	0.213
Fe	0.215	0.155	0.320	0.327	0.321	0.351	0.257	0.256	0.273	0.204	0.201	0.191	0.384	0.376	0.415	0.396
Mn	0.006	0.004	0.008	0.006	0.007	0.010	0.005	0.005	0.008	0.006	0.006	0.005	0.008	0.008	0.009	0.010
Mg	0.865	0.885	0.877	0.883	0.874	0.846	0.748	0.764	0.930	0.968	0.975	0.855	0.605	0.666	0.574	0.649
Ca	0.903	0.910	0.802	0.795	0.809	0.793	0.893	0.885	0.748	0.778	0.791	0.841	0.882	0.875	0.896	0.879
Na	0.027	0.022	0.025	0.025	0.020	0.025	0.029	0.030	0.014	0.014	0.017	0.022	0.045	0.042	0.042	0.048
K	0.004	0.001	0.000	0.002	0.000	0.000	0.000	0.001	0.002	0.001	0.002	0.001	0.002	0.000	0.002	0.002
Cr	0.002	0.025	0.000	0.000	0.000	0.000	0.008	0.009	0.000	0.008	0.010	0.027	0.006	0.008	0.003	0.002
Total	4.047	4.035	4.047	4.046	4.040	4.039	4.039	4.042	4.019	4.019	4.033	4.021	4.043	4.057	4.045	4.059

*** Total Fe as FeO**

Table 4.10. Continued (5)

mineral	Clinopyroxene													
sequence	Cambrian													
area	Comarto		Mt. Wright											
sample	861010		862112				862225				862405			
	1	2	1	2	3	4	1	2	3	4	1	2	3	4
SiO2	48.04	47.46	49.83	49.83	48.93	47.78	50.08	50.29	49.47	49.98	51.20	50.19	51.50	49.87
TiO2	1.22	1.80	1.17	1.20	1.54	1.88	1.09	0.88	1.06	1.07	0.58	0.75	0.47	0.91
Al2O3	4.98	5.79	3.53	3.92	3.01	4.24	3.58	3.59	4.51	3.88	3.69	4.76	3.63	4.57
FeO*	9.24	9.11	6.61	6.13	9.10	8.49	5.81	5.57	5.36	6.05	4.24	5.15	4.13	5.85
MnO	0.22	0.19	0.12	0.11	0.22	0.23	0.11	0.15	0.14	0.17	0.11	0.12	0.07	0.15
MgO	13.40	13.59	14.82	14.65	14.57	14.05	15.47	15.65	15.50	15.43	16.64	16.18	17.08	15.34
CaO	20.58	20.06	22.38	22.40	20.57	20.85	22.58	22.82	22.37	22.61	22.31	22.55	22.84	22.56
Na2O	0.39	0.43	0.34	0.35	0.30	0.37	0.35	0.28	0.30	0.25	0.33	0.27	0.24	0.28
K2O	0.02	0.02	0.06	0.06	0.03	0.02	0.05	0.04	0.00	0.08	0.02	0.03	0.04	0.01
Cr2O3	0.14	0.08	0.13	0.21	0.04	0.20	0.38	0.21	0.78	0.32	0.94	0.23	0.53	0.33
total	98.23	98.53	98.99	98.86	98.31	98.11	99.50	99.48	99.49	99.84	100.06	100.23	100.53	99.87
	Structural formulae (cations based on 6 oxygens)													
Si	1.833	1.803	1.870	1.868	1.865	1.825	1.865	1.870	1.839	1.857	1.878	1.846	1.879	1.848
Ti	0.035	0.051	0.033	0.034	0.044	0.054	0.031	0.025	0.030	0.030	0.016	0.021	0.013	0.025
Al	0.224	0.259	0.156	0.173	0.135	0.191	0.157	0.157	0.198	0.170	0.160	0.206	0.156	0.200
Fe	0.295	0.289	0.207	0.192	0.290	0.271	0.181	0.173	0.167	0.188	0.130	0.158	0.126	0.181
Mn	0.007	0.006	0.004	0.003	0.007	0.007	0.003	0.005	0.004	0.005	0.003	0.004	0.002	0.005
Mg	0.762	0.770	0.829	0.818	0.828	0.800	0.859	0.867	0.859	0.854	0.910	0.887	0.929	0.847
Ca	0.842	0.817	0.900	0.900	0.840	0.853	0.901	0.909	0.891	0.900	0.877	0.888	0.893	0.896
Na	0.029	0.032	0.025	0.025	0.022	0.027	0.025	0.020	0.022	0.018	0.023	0.019	0.017	0.020
K	0.001	0.001	0.003	0.003	0.001	0.001	0.002	0.002	0.000	0.004	0.001	0.001	0.002	0.000
Cr	0.004	0.002	0.004	0.006	0.001	0.006	0.011	0.006	0.023	0.009	0.027	0.007	0.015	0.010
Total	4.032	4.030	4.031	4.022	4.033	4.035	4.035	4.034	4.033	4.035	4.025	4.037	4.032	4.032

*** Total Fe as FeO**

Table 4.11. Representative Microprobe Analyses of Feldspar and Feldspathoids from the Wonominta Block.

mineral	Albite									Orthoclase					
area	Nundora									Mt. Wright					
sample	761603		762002	762004	762402	762408				862101		862206		862218	
	1	2				1	2	3	4	1	2	1	2	1	2
SiO2	68.77	68.36	67.09	68.32	69.23	69.34	68.85	68.13	68.52	61.03	64.69	63.46	62.57	61.24	65.47
TiO2	0.16	0.01	0.13	0.05	18.79	0.00	0.00	0.00	0.11	0.00	0.07	0.31	0.25	0.15	0.03
Al2O3	18.98	19.81	19.23	19.64	0.00	18.75	18.70	18.85	18.60	22.26	20.08	18.15	17.67	17.23	18.39
FeO*	0.13	0.17	1.06	0.01	0.01	0.11	0.00	0.03	0.10	0.37	0.18	0.19	0.00	0.13	0.11
MnO	0.02	0.03	0.00	0.03	0.01	0.00	0.00	0.03	0.00	0.10	0.01	0.00	0.02	0.00	0.00
MgO	0.00	0.00	0.00	0.00	0.00	0.00	0.00	0.00	0.00	0.17	0.00	0.15	0.00	0.00	0.00
CaO	0.10	0.07	0.14	0.10	0.00	0.02	0.13	0.13	0.06	0.76	0.71	0.00	0.00	0.00	0.19
Na2O	11.56	12.12	11.55	11.45	11.94	11.63	11.48	11.98	11.39	8.54	10.93	1.86	0.62	1.09	0.75
K2O	0.10	0.15	0.24	0.10	0.03	0.18	0.21	0.11	0.72	2.75	0.58	14.68	16.70	15.41	11.18
Cr2O3	0.00	0.00	0.00	0.01	0.00	0.00	0.00	0.11	0.00	0.00	0.00	0.00	0.00	0.00	0.00
total	99.82	100.72	99.44	99.71	100.01	100.03	99.37	99.37	99.50	95.98	97.25	98.80	97.83	95.25	96.12
Structural formulae (Cations based on 32 oxygens)															
Si	12.036	11.899	11.877	11.963	12.087	12.103	12.095	12.006	12.065	11.295	11.704	11.874	11.916	11.938	11.964
Ti	0.021	0.001	0.017	0.007	0.000	0.000	0.000	0.000	0.015	0.000	0.010	0.044	0.036	0.022	0.004
Al	3.917	4.066	4.014	4.055	3.868	3.859	3.874	3.917	3.862	4.858	4.284	4.005	3.968	3.960	3.963
Fe	0.019	0.025	0.157	0.001	0.001	0.016	0.000	0.004	0.015	0.057	0.027	0.030	0.000	0.021	0.017
Mn	0.003	0.004	0.000	0.004	0.001	0.000	0.000	0.004	0.000	0.016	0.002	0.000	0.003	0.000	0.000
Mg	0.000	0.000	0.000	0.000	0.000	0.000	0.000	0.000	0.000	0.047	0.000	0.042	0.000	0.000	0.000
Ca	0.019	0.013	0.027	0.019	0.000	0.004	0.024	0.025	0.011	0.151	0.138	0.000	0.000	0.000	0.037
Na	3.923	4.090	3.964	3.887	4.042	3.936	3.910	4.093	3.888	3.064	3.834	0.675	0.229	0.412	0.175
K	0.022	0.033	0.054	0.022	0.007	0.040	0.047	0.025	0.162	0.649	0.134	3.504	4.057	3.832	3.961
Cr	0.000	0.000	0.000	0.001	0.000	0.000	0.000	0.015	0.000	0.000	0.000	0.000	0.000	0.000	0.000
Total	19.960	20.131	20.110	19.959	20.006	19.958	19.950	20.089	20.018	20.137	20.133	20.174	20.209	20.185	20.121

*** Total treated as FeO**

Table 4.11. Continued (2).

mineral	Orthoclase			Nepheline		Natrolite									
area	Mt. Wright			Nundora		Nundora									
sample	862219			762403		762402					762403		762407		
	1	2	3	1	2	1	2	3	4	5	1	2	1	2	3
SiO2	66.95	61.07	65.56	40.64	41.88	50.35	50.73	47.28	49.51	47.36	51.11	51.71	52.08	53.29	52.64
TiO2	0.02	0.03	0.00	0.01	0.00	0.00	0.01	0.07	0.00	0.00	0.00	0.00	0.06	0.00	0.02
Al2O3	16.12	17.26	18.58	33.23	34.57	27.53	27.07	26.99	28.09	26.41	28.29	28.20	25.23	24.99	25.37
FeO*	0.33	0.23	0.23	0.00	0.00	0.09	0.04	0.07	0.00	0.90	0.00	0.50	0.47	0.02	0.00
MnO	0.00	0.01	0.01	0.04	0.00	0.00	0.00	0.00	0.01	0.00	0.00	0.01	0.10	0.00	0.01
MgO	0.03	0.00	0.08	0.00	0.00	0.04	0.00	0.00	0.00	0.00	0.02	0.02	0.00	0.00	0.00
CaO	0.00	0.00	0.19	0.00	0.01	0.00	0.00	0.15	0.08	0.09	0.01	0.00	0.09	0.07	0.34
Na2O	6.60	0.84	1.27	16.34	16.45	14.92	14.80	16.60	15.88	15.90	15.64	15.23	13.12	12.33	13.23
K2O	5.96	16.00	10.68	8.04	8.32	0.07	0.05	0.08	0.13	0.51	0.08	0.06	1.46	0.53	1.58
Cr2O3	0.00	0.01	0.00	0.03	0.00	0.00	0.00	0.00	0.00	0.00	0.01	0.00	0.04	0.00	0.00
total	96.01	95.45	96.60	98.33	101.23	93.00	92.70	91.24	93.70	91.17	95.16	95.73	92.65	91.23	93.19
Structural formulae (Cations based on 32 (20 for natrolite) oxygens)															
Si	12.387	11.921	11.943	8.074	8.066	6.140	6.196	5.957	6.029	5.995	6.103	6.136	6.385	6.533	6.405
Ti	0.003	0.004	0.000	0.001	0.000	0.000	0.001	0.007	0.000	0.000	0.000	0.000	0.006	0.000	0.002
Al	3.517	3.973	3.991	7.784	7.851	3.959	3.899	4.010	4.033	3.942	3.983	3.946	3.648	3.612	3.640
Fe	0.051	0.038	0.035	0.000	0.000	0.009	0.004	0.007	0.000	0.095	0.000	0.050	0.048	0.002	0.000
Mn	0.000	0.002	0.002	0.007	0.000	0.000	0.000	0.000	0.001	0.000	0.000	0.001	0.010	0.000	0.001
Mg	0.008	0.000	0.022	0.000	0.000	0.007	0.000	0.000	0.000	0.000	0.004	0.004	0.000	0.000	0.000
Ca	0.000	0.000	0.037	0.000	0.002	0.000	0.000	0.020	0.010	0.012	0.001	0.000	0.012	0.009	0.044
Na	2.368	0.318	0.295	6.294	6.143	3.528	3.505	4.055	3.749	3.902	3.621	3.504	3.119	2.931	3.121
K	1.407	3.984	3.772	2.037	2.044	0.011	0.008	0.013	0.020	0.082	0.012	0.009	0.228	0.083	0.245
Cr	0.000	0.002	0.000	0.005	0.000	0.000	0.000	0.000	0.000	0.000	0.001	0.000	0.004	0.000	0.000
Total	19.741	20.242	20.097	24.202	24.106	13.654	13.613	14.069	13.842	14.028	13.725	13.650	13.460	13.170	13.458

*** Total treated as FeO**

Table 4.12. Representative Microprobe Analyses of Micas and Tourmaline from the Wonominta Block.

mineral	White mica															
area	Basement - Ponto Mine			Basement - Wilandra						Basement-Cymbric Vale			Basement - Bilpa (metabasite)			
sample	760104			861304		861305			861605	861913			862914			
	1	2	3	1	2	1	2	3		1	2	3	1	2	3	4
SiO2	46.39	48.84	46.76	50.96	51.15	49.60	46.56	51.16	49.46	44.26	52.40	45.00	47.96	47.43	47.91	47.02
TiO2	0.10	0.14	0.31	0.09	0.04	0.11	0.06	0.07	0.05	0.67	0.41	0.36	0.12	0.02	0.11	0.13
Al2O3	31.37	31.09	29.47	33.83	33.58	34.54	31.70	34.43	31.33	24.48	27.24	25.03	30.73	32.42	30.88	32.24
Fe2O3*	2.15	2.62	2.98	2.12	1.97	1.66	1.87	2.07	4.03	9.34	6.46	8.15	1.97	1.66	2.03	2.11
MnO	0.00	0.00	0.02	0.01	0.01	0.03	0.03	0.06	0.03	0.34	0.00	0.07	0.01	0.01	0.01	0.05
MgO	0.16	0.87	0.92	1.21	1.50	0.86	1.37	1.25	0.97	4.90	2.77	3.64	1.77	1.24	1.77	1.09
CaO	0.00	0.00	0.00	0.00	0.00	0.00	0.00	0.00	0.00	0.00	0.00	0.00	0.00	0.00	0.00	0.00
Na2O	0.30	0.24	0.29	0.15	0.09	0.09	0.24	0.08	0.67	0.14	0.11	0.40	0.10	0.14	0.12	0.17
K2O	10.70	8.67	11.18	6.28	6.73	6.23	10.77	4.63	7.67	9.15	5.42	9.75	9.93	12.03	11.82	11.90
Cr2O3	0.00	0.00	0.00	0.00	0.00	0.05	0.07	0.00	0.00	0.00	0.04	0.01	0.00	0.00	0.00	0.00
total	91.17	92.47	91.93	94.65	95.07	93.17	92.67	93.75	94.21	93.28	94.85	92.41	92.59	94.95	94.65	94.71
Structural formulae (Cations based on 22 oxygens)																
Si	6.452	6.597	6.501	6.586	6.597	6.506	6.377	6.598	6.557	6.206	6.837	6.342	6.524	6.373	6.460	6.345
Ti	0.010	0.014	0.032	0.009	0.004	0.011	0.006	0.007	0.005	0.071	0.040	0.038	0.012	0.002	0.011	0.013
Al	5.145	4.952	4.831	5.156	5.107	5.342	5.120	5.236	4.898	4.047	4.191	4.160	4.929	5.136	4.909	5.130
Fe	0.225	0.266	0.312	0.206	0.191	0.164	0.193	0.201	0.402	0.986	0.635	0.865	0.202	0.168	0.206	0.214
Mn	0.000	0.000	0.002	0.001	0.001	0.003	0.003	0.007	0.003	0.040	0.000	0.008	0.001	0.001	0.001	0.006
Mg	0.033	0.175	0.191	0.233	0.288	0.168	0.280	0.240	0.192	1.024	0.539	0.765	0.359	0.248	0.356	0.219
Ca	0.000	0.000	0.000	0.000	0.000	0.000	0.000	0.000	0.000	0.000	0.000	0.000	0.000	0.000	0.000	0.000
Na	0.081	0.063	0.078	0.038	0.023	0.023	0.064	0.020	0.172	0.038	0.028	0.109	0.026	0.036	0.031	0.044
K	1.899	1.494	1.983	1.035	1.107	1.042	1.882	0.762	1.297	1.637	0.902	1.753	1.723	2.062	2.033	2.048
Cr	0.000	0.000	0.000	0.000	0.000	0.005	0.008	0.000	0.000	0.000	0.004	0.001	0.000	0.000	0.000	0.000
Total	13.845	13.561	13.930	13.264	13.318	13.264	13.933	13.071	13.526	14.049	13.176	14.041	13.776	14.026	14.007	14.019

*** Total Fe as Fe2O3**

Table 4.12. Continued (2).

mineral	White mica													Biotite		
area	late Proterozoic - Nundora						Cambrian - Mt. Wright			Cambrian- Bilpa Conglomerate				Nundora		
sample	761603				762409		862302			863012			762002	762003		
	1	2	3	4	1	2	1	2	3	1	2	3		1	2	3
SiO2	50.20	50.78	49.33	49.33	44.25	44.69	57.17	57.85	57.89	48.03	47.08	47.40	33.55	34.35	35.56	35.98
TiO2	0.36	0.41	0.35	0.39	0.06	0.10	0.15	0.13	0.05	0.05	0.00	0.00	2.55	2.20	1.81	2.03
Al2O3	24.10	23.97	23.34	22.91	33.74	33.24	17.37	17.92	17.53	31.34	31.75	32.22	17.77	15.36	17.04	16.53
Fe2O3*	7.31	6.54	7.21	7.87	5.44	5.42	13.23	11.38	11.59	1.80	1.84	1.31	30.64	33.88	31.36	30.07
MnO	0.09	0.01	0.02	0.01	0.15	0.20	0.04	0.06	0.04	0.02	0.03	0.05	0.11	0.06	0.03	0.02
MgO	1.56	1.49	0.27	1.54	0.00	0.00	3.86	3.68	3.80	1.16	0.82	0.52	3.60	3.11	2.36	2.61
CaO	0.00	0.00	0.00	0.00	0.00	0.00	0.00	0.00	0.00	0.00	0.00	0.00	0.00	0.00	0.00	0.00
Na2O	0.06	0.04	0.09	0.03	0.18	0.17	0.02	0.00	0.02	0.20	0.21	0.33	0.04	0.04	0.07	0.05
K2O	10.72	10.17	10.36	10.41	10.89	11.20	4.18	3.87	4.39	12.07	12.00	11.54	9.58	9.33	9.26	9.78
Cr2O3	0.00	0.00	0.08	0.05	0.04	0.00	0.00	0.04	0.00	0.00	0.00	0.00	0.09	0.00	0.04	0.00
total	94.40	93.41	91.05	92.54	94.75	95.02	96.02	94.93	95.31	94.67	93.73	93.37	97.93	98.33	97.53	97.07
Structural formulae (Cations based on 22 oxygens)																
Si	6.856	6.952	6.966	6.883	6.021	6.073	7.456	7.554	7.561	6.474	6.414	6.447	4.965	5.103	5.253	5.335
Ti	0.037	0.042	0.037	0.041	0.006	0.010	0.015	0.013	0.005	0.005	0.000	0.000	0.284	0.246	0.201	0.226
Al	3.881	3.870	3.886	3.770	5.414	5.326	2.671	2.759	2.700	4.981	5.101	5.168	3.101	2.691	2.968	2.890
Fe	0.752	0.674	0.767	0.827	0.557	0.555	1.299	1.119	1.140	0.183	0.189	0.134	3.414	3.790	3.488	3.357
Mn	0.010	0.001	0.002	0.001	0.017	0.023	0.004	0.007	0.004	0.002	0.003	0.006	0.014	0.008	0.004	0.003
Mg	0.318	0.304	0.057	0.320	0.000	0.000	0.750	0.716	0.740	0.233	0.167	0.105	0.794	0.689	0.520	0.577
Ca	0.000	0.000	0.000	0.000	0.000	0.000	0.000	0.000	0.000	0.000	0.000	0.000	0.000	0.000	0.000	0.000
Na	0.016	0.011	0.025	0.008	0.047	0.045	0.005	0.000	0.005	0.052	0.055	0.087	0.011	0.012	0.020	0.014
K	1.868	1.776	1.866	1.853	1.890	1.942	0.695	0.645	0.731	2.075	2.086	2.002	1.809	1.768	1.745	1.850
Cr	0.000	0.000	0.009	0.006	0.004	0.000	0.000	0.004	0.000	0.000	0.000	0.000	0.011	0.000	0.005	0.000
Total	13.738	13.630	13.615	13.709	13.956	13.974	12.895	12.817	12.886	14.005	14.015	13.949	14.403	14.307	14.204	14.252

*** Total Fe as Fe2O3**

Table 4.12. Continued (3).

mineral	Biotite								Tourmaline					
area	Nundora								Cambrian - Mt. Wright					
sample	762003			762004			762408		862214					
	4	5	6	1	2	3	1	2	1	2	3	4	5	6
SiO2	36.82	35.13	36.11	40.93	44.45	41.96	35.16	35.27	37.00	36.34	34.43	34.93	34.79	36.45
TiO2	0.97	1.57	2.18	1.55	0.29	0.18	0.10	0.11	0.51	0.58	0.59	0.69	0.64	0.48
Al2O3	16.90	17.36	17.60	14.85	16.32	18.85	19.74	19.68	31.42	32.06	29.00	29.84	33.92	32.36
Fe2O3*	29.69	31.27	29.73	31.37	29.15	27.40	28.27	27.50	5.78	7.24	18.51	18.28	13.20	6.54
MnO	0.02	0.05	0.01	0.00	0.07	0.01	0.64	0.60	0.00	0.03	0.85	0.85	0.11	0.05
MgO	2.86	2.10	2.55	2.17	1.93	1.86	4.41	4.84	7.53	6.74	1.15	1.35	1.90	6.58
CaO	0.00	0.00	0.00	0.00	0.00	0.00	0.00	0.00	0.25	0.62	0.15	0.10	0.35	1.16
Na2O	0.07	0.05	0.14	0.05	0.00	0.03	0.08	0.06	2.32	2.01	2.24	2.38	1.86	1.82
K2O	9.27	9.72	9.62	4.67	4.44	4.98	9.54	9.83	0.02	0.01	0.06	0.05	0.07	0.02
Cr2O3	0.02	0.01	0.00	0.00	0.00	0.00	0.08	0.00	0.16	0.07	0.00	0.00	0.00	0.22
total	96.62	97.26	97.94	95.59	96.65	95.27	98.02	97.89	84.99	85.70	86.98	88.47	86.84	85.68
Structural formulae (Cations based on 22 oxygens; 31 for tourmaline)														
Si	5.445	5.221	5.287	5.920	6.234	5.978	5.135	5.153	7.693	7.558	7.554	7.514	7.352	7.562
Ti	0.108	0.175	0.240	0.169	0.031	0.019	0.011	0.012	0.080	0.091	0.097	0.112	0.102	0.075
Al	2.947	3.042	3.039	2.533	2.699	3.167	3.399	3.390	7.704	7.862	7.502	7.569	8.452	7.916
Fe	3.306	3.499	3.277	3.416	3.078	2.939	3.108	3.025	1.005	1.259	3.396	3.288	2.333	1.135
Mn	0.003	0.006	0.001	0.000	0.008	0.001	0.079	0.074	0.000	0.005	0.158	0.155	0.020	0.009
Mg	0.630	0.465	0.557	0.468	0.403	0.395	0.960	1.054	2.334	2.089	0.376	0.433	0.598	2.035
Ca	0.000	0.000	0.000	0.000	0.000	0.000	0.000	0.000	0.056	0.138	0.035	0.023	0.079	0.258
Na	0.020	0.014	0.040	0.014	0.000	0.008	0.023	0.017	0.935	0.810	0.953	0.993	0.762	0.732
K	1.749	1.843	1.797	0.862	0.794	0.905	1.777	1.832	0.005	0.003	0.017	0.014	0.019	0.005
Cr	0.002	0.001	0.000	0.000	0.000	0.000	0.009	0.000	0.026	0.012	0.000	0.000	0.000	0.036
Total	14.210	14.266	14.238	13.382	13.247	13.412	14.501	14.557	19.838	19.827	20.088	20.101	19.717	19.763

*** Total Fe as Fe2O3**

Appendix 4
A Preliminary TEM Study of Clinopyroxenes in Metamorphic Environment

As an adjunct to the polarizing microscope and the X-ray diffractometer, the electron microscope is considered to be a very useful instrument for mineralogical study. With the optical microscope, mineralogists are able to determine the morphology and optical properties of mineral, on a scale larger than the wavelength of light. X-ray diffraction techniques can provide accurate structural determinations of minerals by averaging over thousands of unit cells based on the assumption that all cells are identical. However, it has been shown that actual crystals are not perfect and contain defects even in very small domains (Wenk, 1978). In this case, the electron microscope becomes a powerful instrument that can reveal these defects and the heterogeneity of crystals on a unit-cell scale. It is also noted that this technique may provide direct geological information, such as the cooling history of minerals and the effect of secondary processes like metamorphism and deformation. Thus the electron microscope (particularly the transmitted electron microscope; TEM) has many applications in geological research.

In this project, some preliminary studies were carried out, mainly on superstructural investigations of relic clinopyroxenes. The problem was firstly put forward during the electron microprobe analysis of the mineral (*cf.* Chapter Four). It was noted that some relict pyroxenes in the metamorphosed mafic rocks do not show a qualified structural formulae even though the sum of oxide components came out to be satisfactory. These results tend to have a low structural formulae which cannot be explained as analytical errors. Thus, it was suggested that there might be some structural defects in the minerals, though optically they still display pyroxene features. Hence, the TEM technique was proposed to investigate these pyroxenes and to ascertain the influence of metamorphism. Since similar work has been carried out in fair detail (*cf.* Wang, 1989), the investigations carried out here are only on the preliminary level and many conclusions are drawn from previous studies, in particular those by Wang (1989).

From the principle of image formation (*cf.* Verblen 1980), the picture can be explained in simple terms, that the darkness in the structure reflects the density of electrons; thus most of the black spots in the 'chains' represent the silica-oxygen tetrahedra, and the images show subtle variations from different orientations. In this context,

pyroxenes are characterized structurally by a "single chain" (plates A4.1 & A4.2); the Si-O tetrahedron constitutes a chain structure along the **C** axis and displays repetition along both **A** and **B** axes. When alteration occurs some of these chains may change their structure and become "double chains" (amphibole-type) (see plate A4.3) or "triple chains" (jimthomsonite-type) (A4.4) or even more multiple phases (Figure A4.5). In all of these cases, some $(OH)^-$ anions would replace O^{2-} in the structure, which can result in the low structural formulae. Therefore, the observation of the existence of chain-width errors under the TEM can be used as direct evidence to explain the composition problems encountered in the microprobe analyses.

The chain-width errors were firstly discovered in pyroxenoids (Czank & Liebau, 1980; Reid & Korekawa, 1980; Jefferson & Pugh, 1981) and then recognized also in natural pyroxenes (Veblen, 1982; Reid, 1984). Since then, several authors have proposed various mechanisms (*e.g.*, Veblen, 1985) for the transformation of pyroxene to the secondary products with this superstructural state, involving the laminar and bulk reactions during the transformation. Apparently, the petrogenetic discussion relates also to the studies of the metamorphic history of the rocks.

A4.1. SAMPLE-PREPARATION

Most of the relict pyroxenes in the metamorphosed mafic rocks in the present project are such fine grains that it is not practical to pick the crystal fragments by hand, even under the optical microscope. Therefore, special sample preparation techniques are needed to carry out proper investigations. The adopted sampling technique is to use a special glue which has a unique thermal property, that under room-temperature the glue can hold the rock section firmly on to the glass; while at about 100 °C, the glue will not work any more and ground slices of samples can be easily removed from the glass mounts.

In practice, the samples were cut and normal thin sections containing pyroxene were made using the special glue. Then, pyroxene crystals, particularly those showing the cross cleavages (yielding the **C** axis section) were circled under the microscope. By means of a small hand-held electronic drill, the circled pyroxene crystals are cut along with the glass, and the samples are placed on a hotplate so that the crystal slice can be removed from the glass, and placed on a copper ring after washing off the glue with acetone.

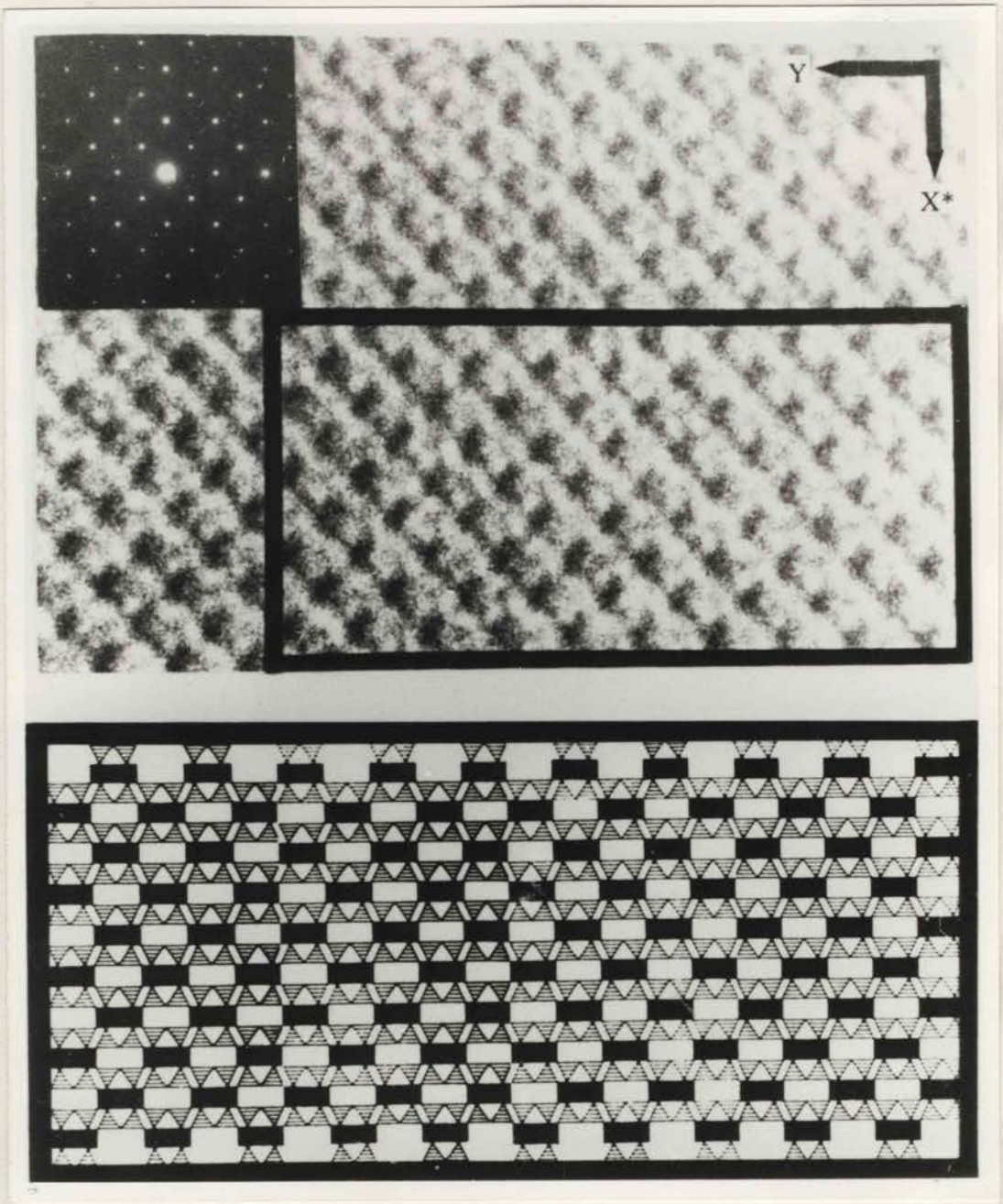

Plate A4.1. A HRTEM Z-axi image of augite (Wang, 1989). Structural interpretation and associate diffraction pattern are also shown.

Plate A4.2. A HRTEM Z-axis image of relic pyroxene from the basement sequence in the Wilandra Inlier (sample 861314; scale bar 35 Å.). This plate presents an example of perfect "single-chain" structure of the crystal.

In the final step, the crystals are ion-beam thinned to make a subtle hole and thinned areas around the the hole. The samples are now ready for investigations with TEM.

One of the problems noted during the observation sessions was that, because of the alteration of the mineral, there are often significant cracks along cleavages filled with secondary phases that are much softer than pyroxene under the ion-beam bombardment, thus the holes made by the ion beams tend to occur around these cracks rather than within the solid pyroxene crystals. This problem was resolved by carefully selecting the crystals, avoiding any obvious defects under the microscope.

Many of the early sessions on the machine was aimed at gaining skilful operation, which is essential for quickly locating the right spot and right operation for refraction. After this, the routine operations were aimed at locating any significant defects.

A4.2. SUMMARY OF PREVIOUS TEM STUDIES ON ALTERATION OF PYROXENES

This section is basically a concise summary of Wang's (1989) investigations into the alteration processes of clinopyroxenes.

In summary, the electron microscopic examinations have revealed a wide variety of secondary products formed through various mechanisms. The alteration products include mainly amphibole (Plate A4.3), jimthomsonite (Plate A4.4), chain-width disordered pyrobole (mainly two- and three- chain width mixtures) (Plate A4.5) and chlorite (Plate A4.6).

The mechanisms recognised include bulk transformation along a broad reaction front and nucleation and/or growth of narrow laminae. A step process has been observed whereby the clinopyroxenes were firstly altered to form a hydrous pyrobole zone in which single, double and triple chain laminae are mixed together; then followed by a reordering process, in which bulk amphibole replaces the highly hydrated area. This transformation is shown clearly in Plate A4.5. The formation of chlorite along the pyroxene margins, as revealed in Plate A4.6, is almost tapotactic without intermediate phases.

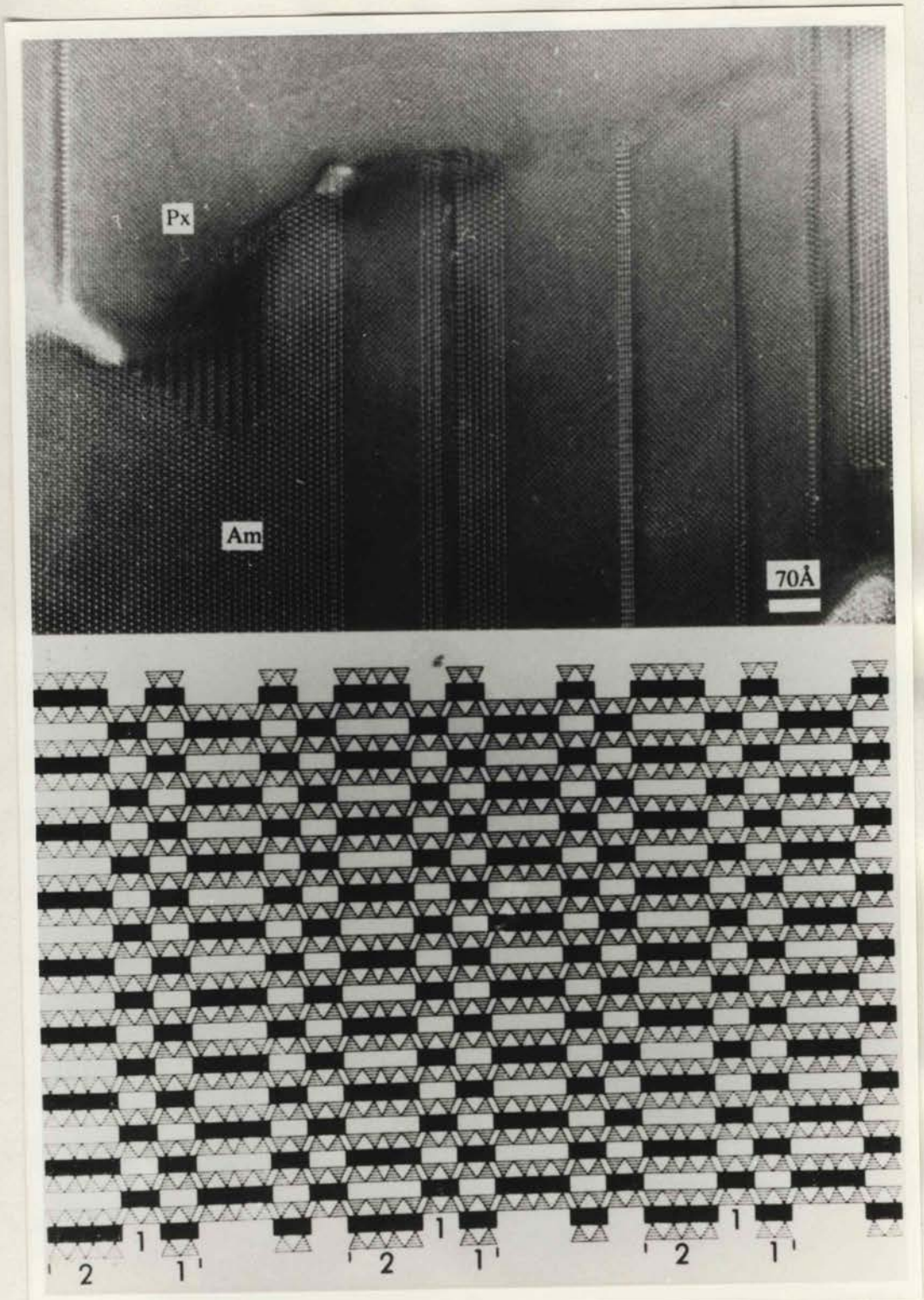

Plate A4.3. Alteration of clinopyroxene to amphiboles (Wang, 1989). This HRTEM image shows a remanant distorted region of the altered pyroxene crystals. The structural interpretation is presented in the lower part, showing the regular (2,1,1) intergrowth.

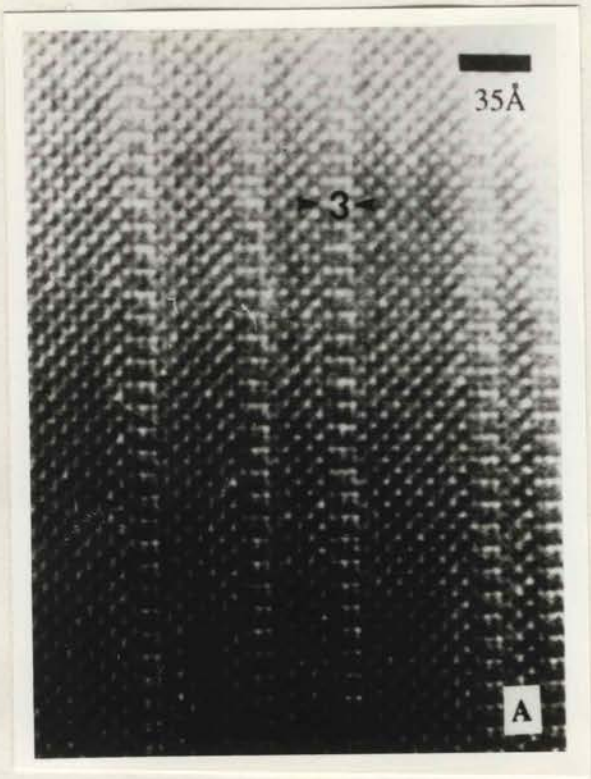

Plate A4.4. Triple chain lamellae formed in clinopyroxene as a result of alteration (Wang, 1989). This plate presents a case of single triple-chain lamella within the pyroxene structure.

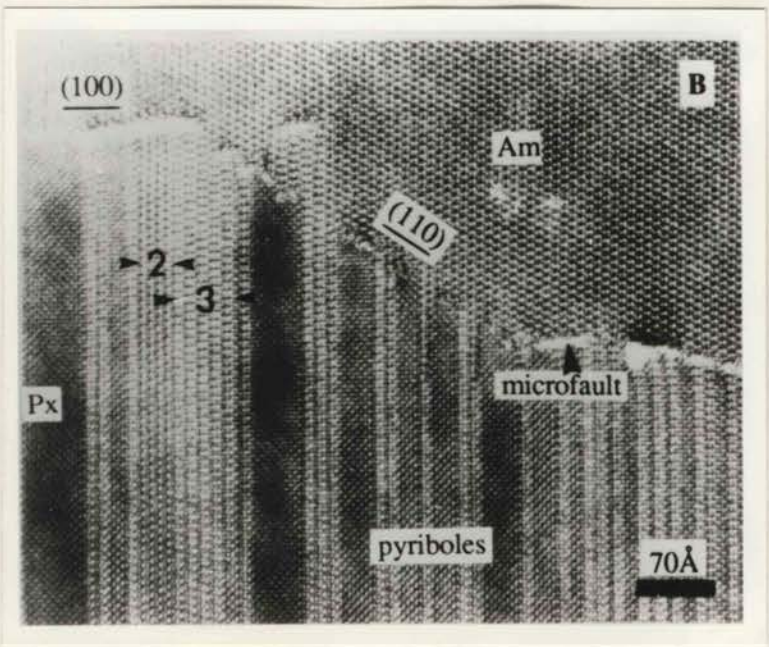

Plate A4.5. Uralitisation of clinopyroxene via pyroboles (Wang, 1989). This plate shows the intermediate phases (the pyroboles) of the alteration of pyroxenes to amphiboles.

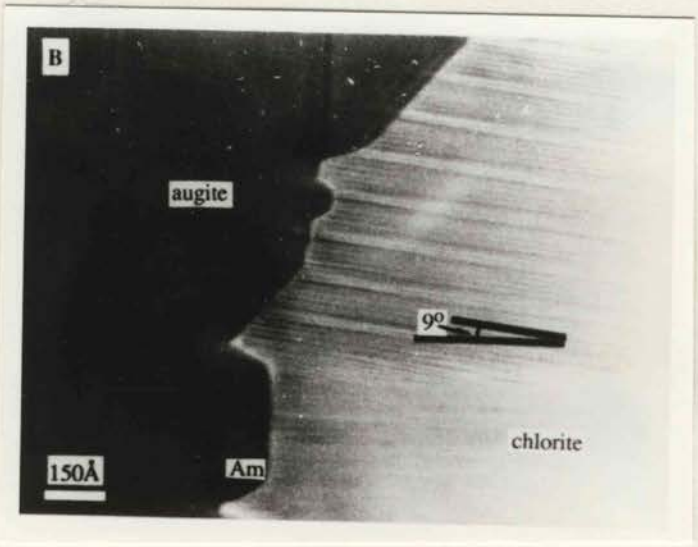

Plate A4.6. Alteration of clinopyroxenes to chlorite (Wang, 1989). This plate presents a nearly topotactic replacement of chlorite in altered augite. The Y-axis of the structure of chlorite is inclined at about 9° from that of augite.

Since the unit cells of amphibole are about 2% larger than those of pyroxenes, the transformation would also cause some dislocations and faults on a micro-scale (Plate A4.5).

A4.3. PRELIMINARY STUDIES OF THE PYROXENES IN THE WONOMINTA BEDS

Plate A4.2 is a HRTEM image of a relic clinopyroxene crystal from the Wilandra metadolerite in the basement sequence (861314) with an amplification about 4,000,000. The particular section is about normal to (001). This plate shows a perfect crystal structure of clinopyroxene, whereas the following plates present various alteration features from relic clinopyroxenes in the same sample.

Plate A4.7 provides an example of micro-dissolution of pyroxene within the crystal structure and some chain-width error, probably due to the alteration processes.

Plate A4.8 shows some micro-faults developed in the crystal structures of relic pyroxenes. Normally, these local areas in the crystal are the high-stress fields and are the ideal position for the development of secondary alteration.

However, compared with the younger samples (*cf.* Wang, 1989), the relic pyroxenes investigated here display much less superstructural defects. One of the possibilities would be that the extended duration since metamorphism might have allowed annealing of the secondary transformations, leaving few signs of intermediate phases that otherwise might be used to investigate the alteration processes.

A4.4. QUANTITATIVE APPROACH

Even if the transformation of pyroxenes has been confirmed microscopically, and this transformation will certainly influence the microprobe analyses of the relic mineral, it is still difficult to conclude that the observed microprobe analysis errors are all due to this transformation. Therefore, a quantitative approach is required to investigate if the observed errors could match those caused by the transformation (or defect). This goal can only be achieved by extensive observations under the microscope. Unfortunately, this is beyond the capability of the present project and hopefully, some future work will throw further light on the problem.

Plate A4.7. Dissolution of clinopyroxene and some chain-width errors during alteration. (Sample 861314; scale bar, 35Å).

Plate A4.8. Microfault developed within clinopyroxene lamellae. (sample 861314; scale bar, 35Å)

Appendix 5
Analytical Parameters of XRF Techniques

All the geochemical analyses of major and trace elements were carried out by means of XRF techniques in this study. The principle of this method is the same as that of electron microprobe (see Appendix 3), except that the analysed targets are 'homogenised' bulk samples (either fused glass or powder pellets) rather than individual minerals in the rocks. The determination of major element chemistry was carried out in the Department of Geology & Geophysics, The University of Sydney. Fused glasses of bulk samples were analysed on a Phillips® PW 1400 fully automated X-ray fluorescence spectrograph. Trace element analyses were carried out in the Chemical Laboratory of the NSW Department of Mineral Resources at Lidcombe. Pressed pellets of powdered bulk samples were analysed on the same type of instrument as above. Routine methods for both major and trace elements were adopted (*cf*, Norrish & Hutton, 1969), and the quality of the analyses was monitored using in-lab standards during all runs.

The major and minor (approx. 1%) elements analysed in this study include SiO_2, Al_2O_3, TiO_2, Fe_2O_3 (total iron treated as Fe_2O_3), MnO, MgO, CaO, Na_2O, K_2O and P_2O_5. Precision of the analyses is generally better than 5%. Individual volatile components (H_2O^+, H_2O^-, CO_2 and SO_2) were not analysed, but a total of all these components is presented as LOI (loss on ignition) -- the weight loss of samples after heating at 1100 ^{0}C for about one hour. Strictly speaking, the LOI is not equivalent to the sum of volatile components, as during the ignition process, all FeO in the samples will be oxidised to Fe_2O_3, gaining some extra weight. Since the geochemical studies carried out in this study are mainly aimed at revealing primary geochemical affinities of the samples and the influences of secondary processes on the primary compositions, analyses of individual volatile components were not carried out; albeit the techniques were not readily available to the present project.

Twelve trace elements at parts per million (ppm) level were analysed in this study. These components can be divided into three groups in regard to analysis; Ga, Rb, Sc, Sr, Bi, Y and Zr can be accurately measured by XRF (precision better than 10%). Nb and Th can normally be analysed by XRF without much problem, but in this study, some of the samples have low concentrations of these components, approaching to the analytical limits. And Hf, Ta and U are normally measured by techniques other than XRF; the results in this study are only qualitative.

Table A5.1 presents a comparison of Nb analysis by XRF and ICP-MS methods respectively. The results show that two of the four duplicate analyses match reasonably well but the other two show a large difference. It has been suggested that the analytical errors of Nb by XRF would lead to higher-stated values when approaching to the analytical limit (1 ppm) (*cf.* Condie, 1989), but apparently this is not the case in the present study, assuming the ICP-MS results are more accurate. This table shows that Nb analysis by XRF may or may not be accurate down to 1 ppm level and the analytical results are probably less than the real values. It is thus most unfortunate that the ICP-MS techniques were not available to the present study. However, a statistical treatment for those samples with low Nb has been presented (Chapters Five), and this should help to illustrate the particular problem encountered in the study.

Table A5.1.Comparison of Analytical Results by XRF & ICP-MS Methods

sample	752302		760805		861713		861915	
	XRF	ICP-MS	XRF	ICP-MS	XRF	ICP-MS	XRF	ICP-MS
Nb	1	1.3	1	2.9	<1	3.4	3	2.9
Hf	5	1.0	<3	1.4	5	0.8	<3	0.6
Ta	<10	0.16	<10	0.19	<10	0.21	<10	0.18

Note: all numbers are shown as ppm.

Table 5.2. Major and Trace Element Compositions of Samples from the Basement Sequence of the Wonominta Block

Ponto Mine area											
	1	2	3	4	5	6	7	8	9	10	11
	752001	752203	752302	752805	752808	752810	753001	753003	753007	753106	760102
SiO2	50.58	52.31	51.31	49.56	54.78	49.68	46.87	49.60	44.46	47.36	50.47
TiO2	1.06	1.10	0.89	1.39	1.30	1.27	1.13	0.81	1.70	1.28	1.21
Al2O3	15.65	11.18	16.49	14.13	11.79	14.20	20.29	7.94	14.34	14.83	15.19
Fe2O3	10.55	8.15	9.63	10.66	8.86	10.36	12.13	4.89	12.94	11.18	8.94
MnO	0.17	0.17	0.16	0.21	0.15	0.24	0.09	0.24	0.18	0.20	0.16
MgO	6.65	4.74	6.54	5.21	5.34	2.64	1.89	3.06	5.49	7.89	2.63
CaO	10.06	10.17	8.55	11.89	12.45	15.05	11.21	16.20	11.44	10.59	15.57
Na2O	3.60	2.59	4.60	1.92	2.58	0.84	1.80	2.83	3.33	2.72	0.32
K2O	0.28	0.82	0.36	0.31	0.15	0.17	1.33	0.85	0.15	0.47	0.62
P2O5	0.08	0.13	0.08	0.15	0.13	1.12	0.15	0.10	0.18	0.11	0.20
LOI	2.21	9.45	2.36	5.13	3.42	3.86	3.25	14.35	6.05	3.34	5.61
Total	100.89	100.81	100.97	100.56	100.95	99.43	100.14	100.87	100.26	99.97	100.92
Nb	3	1	1	2	2	2	2	1	1	<1	<1
U	2	3	<1	3	3	3	6	3	7	<1	1
Ga	16	12	16	17	15	10	24	8	19	15	18
Hf	5	<3	5	3	6	<3	<3	<3	4	<3	<3
Ta	<10	<10	<10	<10	<10	<10	<10	<10	10	<10	<10
Sc	37	39	38	33	33	17	42	19	31	40	23
Y	23	32	22	29	31	28	23	25	40	30	30
Zr	60	97	52	95	87	69	66	47	124	74	74
Sr	308	70	265	135	199	207	263	125	139	186	536
Rb	15	3	15	12	5	27	37	29	7	37	26
Th	3	<1	2	3	<1	3	3	<1	<1	<1	<1
Bi	<2	9	5	6	6	5	3	3	5	<2	4
species	MD (II)	MB	MD (II)	MB	MB	MB	MB	MB	MB	MD (II)	MB

Table 5.2. Continued (2)

	Ponto Mine area					Boshy Tank area						
	13	14	15	16	17	18	19	20	21	22	23	24
	760104	760201	760402	760501	760701	762501	762603	762605	762606	762701	762703	762705
SiO2	44.95	46.07	46.97	45.32	45.78	47.56	50.44	49.42	46.11	45.40	53.98	49.06
TiO2	0.89	1.36	0.74	0.85	1.32	1.58	1.32	1.45	1.27	1.12	1.58	1.22
Al2O3	22.75	13.03	20.68	11.79	14.83	13.56	13.98	18.86	16.31	15.84	14.86	15.62
Fe2O3	5.14	10.17	6.76	8.41	10.80	13.14	10.86	11.50	10.64	11.16	13.05	10.72
MnO	0.07	0.29	0.13	0.23	0.17	0.22	0.19	0.12	0.21	0.20	0.14	0.18
MgO	5.36	2.08	6.07	5.91	5.24	7.32	6.11	3.70	2.40	8.13	2.48	7.24
CaO	6.78	10.75	12.50	13.01	11.35	9.51	12.50	6.47	15.02	9.62	5.79	10.87
Na2O	3.68	7.24	3.26	2.89	5.14	3.05	3.22	5.38	2.77	2.38	5.18	2.39
K2O	3.33	0.19	0.32	0.74	0.48	0.33	0.09	0.20	0.08	0.50	0.16	0.42
P2O5	0.10	0.23	0.08	0.12	0.26	0.14	0.16	0.43	0.17	0.10	0.41	0.11
LOI	7.19	9.16	2.88	11.62	5.25	4.25	1.94	2.65	5.54	5.58	1.86	2.53
Total	100.24	100.57	100.39	100.89	100.62	100.66	100.81	100.18	100.52	100.03	99.49	100.36
Nb	1	2	2	3	2	3	3	2	3	1	5	1
U	<1	<1	<1	<1	<1	3	2	<1	<1	4	<1	1
Ga	16	11	14	12	18	16	14	13	23	12	15	16
Hf	<3	<3	<3	<3	<3	<3	<3	<3	<3	3	<3	<3
Ta	<10	<10	<10	<10	<10	<10	<10	<10	<10	<10	<10	<10
Sc	14	25	26	27	33	40	35	30	33	36	55	41
Y	23	34	17	21	40	35	33	39	33	60	28	30
Zr	62	94	50	47	87	89	91	102	77	114	68	83
Sr	176	499	159	183	168	103	162	148	363	199	177	214
Rb	121	8	12	34	18	16	3	7	6	8	23	25
Th	1	<1	<1	<1	<1	<1	<1	3	3	<1	3	<1
Bi	5	<2	5	5	4	6	5	5	<2	5	3	9
species	MB	MB	MD (III)	MB	MB	MD (II)	MB	MB	MB	MD (II)	MB	MD (II)

Table 5.2. Continued (3)

	Boshy Tank area		Wilandra area									
	25	26	27	28	29	30	31	32	33	34	35	36
	762706	762803	861203	861205	861209	861211	861302	861304	861305	861307	861311	861314
SiO2	44.57	46.56	46.06	47.20	73.32	45.98	46.28	46.24	44.46	53.74	46.50	51.21
TiO2	1.29	1.25	1.21	1.70	0.55	2.32	0.75	1.28	1.15	2.48	1.18	1.03
Al2O3	16.09	20.77	19.49	15.29	11.46	14.90	23.62	17.07	16.96	14.00	20.92	15.45
Fe2O3	10.88	7.97	9.67	11.55	5.46	12.72	5.37	9.77	9.45	16.74	7.83	8.72
MnO	0.18	0.13	0.15	0.19	0.05	0.41	0.10	0.17	0.15	0.09	0.13	0.16
MgO	7.74	5.45	6.13	7.50	1.19	7.12	5.22	6.52	6.49	0.96	4.62	7.20
CaO	9.79	12.86	10.43	10.96	0.82	9.20	10.74	10.93	8.49	3.78	12.24	10.69
Na2O	1.87	2.39	3.19	3.39	5.08	3.96	1.78	2.34	1.78	6.29	2.74	3.21
K2O	0.22	0.07	0.30	0.42	0.16	0.31	2.64	0.75	1.45	1.22	1.12	0.25
P2O5	0.13	0.15	0.12	0.18	0.11	0.26	0.11	0.14	0.12	0.32	0.14	0.23
LOI	7.76	3.26	3.69	2.45	1.79	3.53	3.53	4.91	9.53	0.70	2.71	2.38
Total	100.52	100.86	100.44	100.83	99.99	100.71	100.14	100.12	100.03	100.32	100.13	100.53
Nb	3	6	3	8	35	7	2	6	5	7	6	5
U	<1	4	1	4	8	<1	2	2	<1	4	2	<1
Ga	16	16	16	15	15	19	15	15	14	12	16	16
Hf	<3	<3	3	3	6	6	<3	3	<3	5	<3	<3
Ta	<10	<10	<10	<10	<10	<10	<10	<10	<10	<10	<10	<10
Sc	39	34	35	37	13	46	24	38	33	37	31	40
Y	27	23	24	35	83	45	14	24	22	78	20	42
Zr	95	100	84	144	583	190	49	77	67	199	93	148
Sr	411	320	243	243	108	116	333	233	111	89	297	193
Rb	14	4	7	12	3	6	54	41	57	33	13	11
Th	3	1	<1	5	14	2	3	<1	3	1	4	5
Bi	4	4	4	3	3	4	5	3	2	4	5	4
species	MD (III)	MD (II)	MB	MB	FT	MD (II)	MD(III)	MB	MB	MB	MD (I)	MD (I)

Table 5.2. Continued (4)

	Wilandra area						Cymbric Vale area					
	37	38	39	40	41	42	43	44	45	46	47	48
	861315	861316	861407	861601	861604	861605	861705	861707	861713	861714	861806	861906
SiO2	46.85	44.71	45.91	48.25	46.14	47.81	48.17	47.89	49.57	48.29	51.10	71.94
TiO2	1.29	1.52	2.22	1.69	1.67	1.07	1.21	1.12	1.41	1.47	1.35	0.56
Al2O3	15.50	13.65	13.66	14.29	15.87	17.94	12.45	17.16	15.00	15.21	15.57	12.17
Fe2O3	10.86	11.35	12.74	12.71	10.54	9.02	9.56	8.87	10.67	11.60	11.64	5.23
MnO	0.16	0.17	0.21	0.21	0.16	0.17	0.32	0.16	0.18	0.18	0.18	0.03
MgO	8.01	6.86	6.38	6.24	8.28	6.71	5.05	5.34	5.26	6.37	5.43	2.12
CaO	10.59	9.25	8.30	11.02	11.94	10.36	5.96	11.88	13.16	12.02	6.72	0.26
Na2O	2.18	3.28	3.08	2.12	2.24	3.57	5.46	2.66	3.37	3.12	3.78	1.89
K2O	0.12	0.19	0.05	0.24	0.65	0.75	0.22	0.05	0.10	0.16	0.10	1.84
P2O5	0.14	0.14	0.27	0.17	0.21	0.11	0.12	0.15	0.13	0.14	0.14	0.09
LOI	3.75	9.38	7.23	3.94	3.12	3.17	11.87	5.64	2.14	2.42	3.88	3.13
Total	99.45	100.50	100.05	100.88	100.82	100.68	100.39	100.92	100.99	100.98	99.89	99.26
Nb	3	3	9	4	6	2	2	<1	<1	3	2	11
U	<1	3	5	1	6	<1	5	<1	2	<1	<1	1
Ga	15	15	18	17	16	17	9	14	16	16	20	14
Hf	3	4	<3	3	<3	<3	<3	5	5	<3	5	<3
Ta	<10	<10	<10	<10	<10	<10	<10	<10	<10	<10	<10	<10
Sc	45	41	47	49	44	37	41	35	44	48	46	11
Y	28	33	34	39	29	32	88	25	30	32	32	19
Zr	82	94	157	108	141	127	95	80	101	106	91	113
Sr	115	180	144	261	247	268	281	116	111	120	267	117
Rb	5	2	1	9	14	16	7	2	3	4	5	68
Th	3	2	2	1	3	2	3	1	3	2	3	17
Bi	<2	3	<2	<2	3	4	<2	<2	4	3	<2	<2
species	MD (I)	MB	MD (II)	MB	MB	MB	MB	MB	AM	AM	MB	FT

Table 5.2. Continued

Cymbric Vale area				
	49	50	51	52
	861909	861911	861913	861915
SiO2	49.16	54.09	69.20	48.86
TiO2	1.26	1.27	0.64	1.41
Al2O3	14.78	16.14	13.35	15.61
Fe2O3	11.39	12.06	5.98	10.42
MnO	0.26	0.12	0.07	0.15
MgO	7.61	4.56	1.88	6.18
CaO	7.95	0.82	0.13	10.82
Na2O	2.87	2.91	1.92	3.91
K2O	2.00	1.33	3.05	0.23
P2O5	0.11	0.18	0.11	0.15
LOI	3.02	6.45	2.90	2.77
Total	100.41	99.93	99.23	100.51
Nb	2	2	14	3
U	3	3	2	<1
Ga	17	17	15	14
Hf	<3	<3	<3	<3
Ta	<10	<10	<10	<10
Sc	42	35	17	46
Y	31	30	27	29
Zr	87	85	143	97
Sr	350	126	38	111
Rb	80	59	132	8
Th	4	5	21	5
Bi	3	<2	3	<2
species	MD(II)	MB	schist	AM

Note: AM, amphibolite
FT, felsic tuff
MD, metadolerite (three types)
MB, metabasite, metabasalt

Table 6.2. Major and Trace Element Compositions of Selected Samples from the late Proterozoic Sequence.

	Packsaddle area							Nundora							
	1	2	3	4	5	6	7	8	9	10	11	12	13	14	15
	760801	760805	760806	761001	761203	761204	761301	761503	761505	761512	761602	761603	761801	761809	761901
SiO2	47.84	43.65	47.62	48.61	47.68	58.38	43.21	44.66	38.82	47.96	43.95	58.28	38.18	39.94	46.00
TiO2	1.55	2.75	3.53	1.64	1.53	0.44	3.74	3.01	2.93	4.34	3.82	0.27	0.96	3.14	2.18
Al2O3	18.90	13.85	15.84	14.92	14.66	16.72	15.38	14.45	12.72	16.88	17.52	18.98	5.07	13.27	16.23
Fe2O3	9.02	12.89	12.42	11.82	11.40	12.11	11.70	13.59	11.73	12.73	15.96	7.20	14.88	12.24	14.28
MnO	0.11	0.31	0.19	0.19	0.18	0.13	0.17	0.21	0.17	0.13	0.12	0.14	0.20	0.13	0.15
MgO	5.86	2.65	4.82	6.98	7.31	0.00	4.03	6.89	3.20	3.73	4.35	0.22	25.39	3.55	4.83
CaO	7.16	9.41	4.48	8.84	9.74	0.25	7.32	10.26	13.70	3.53	3.76	0.56	4.29	10.20	4.06
Na2O	4.27	6.03	6.32	2.95	2.88	6.61	6.41	3.62	5.14	5.26	5.29	7.98	0.17	5.98	3.92
K2O	1.86	0.78	0.58	0.71	0.55	4.88	1.04	0.71	1.38	1.80	1.37	3.23	0.05	1.19	2.24
P2O5	0.21	0.68	0.50	0.21	0.21	0.12	0.63	0.41	0.46	0.77	0.79	0.39	0.13	0.96	1.71
LOI	3.17	6.93	3.97	4.10	3.79	0.86	7.35	3.04	10.55	3.69	3.88	2.53	11.05	9.33	4.78
Total	99.95	99.93	100.27	100.97	99.93	100.50	100.98	100.85	100.80	100.82	100.81	99.78	100.37	99.93	100.38
Nb	11	47	40	4	4	137	47	33	34	46	61	168	9	47	72
U	<1	2	4	2	1	6	<1	3	2	2	4	3	3	<1	6
Ga	20	16	27	18	18	31	20	23	20	20	29	29	9	21	21
Hf	<3	7	5	4	7	4	5	<3	<3	4	5	10	<3	<3	5
Ta	<10	<10	<10	<10	<10	13	<10	<10	<10	<10	<10	11	<10	<10	<10
Sc	12	8	17	43	43	<2	15	25	6	12	10	<2	9	9	4
Y	9	34	37	34	32	49	32	30	26	35	34	34	9	37	41
Zr	72	320	273	115	109	815	303	223	224	301	371	1106	67	322	467
Sr	1280	407	208	303	395	174	355	450	356	543	294	426	49	506	814
Rb	22	13	8	16	20	71	33	16	31	26	31	64	5	34	51
Th	2	6	4	3	2	15	5	3	8	4	7	19	3	4	9
Bi	6	6	4	5	<2	3	<2	3	4	4	<2	4	5	4	4
species	MD(I)	MB	MB	MD(II)	MD(II)	syenite	MB	MB	MB	MB	MB	syenite	peridotite	MB	MB

Table 6.2. Continued (2)

Nundora area

	16	17	18	19	20	21	22	23	24	25	26	27
	761906	761907	761908	762401	762402	762403	762404	762405	762406	762407	762408	762409
SiO2	48.75	41.11	45.32	59.22	54.82	54.36	53.56	61.01	54.33	53.80	60.40	60.58
TiO2	1.80	2.75	2.70	0.03	0.02	0.02	0.02	0.02	0.02	0.02	0.04	0.02
Al2O3	11.64	13.48	14.18	23.15	20.20	20.62	20.88	23.28	20.86	21.37	20.88	21.54
Fe2O3	8.65	12.92	7.91	2.52	3.52	3.60	3.90	0.90	3.73	3.52	3.66	3.60
MnO	0.16	0.23	0.24	0.01	0.24	0.25	0.25	0.01	0.24	0.23	0.10	0.19
MgO	2.12	6.09	2.54	0.00	0.28	0.00	0.00	0.00	0.00	0.00	0.58	0.00
CaO	19.24	15.21	9.62	0.10	0.18	0.36	0.54	0.07	0.47	0.41	0.05	0.17
Na2O	0.48	2.08	6.77	5.42	11.00	11.18	10.75	6.71	10.66	10.47	6.69	8.00
K2O	0.13	0.34	0.80	6.51	4.10	4.63	4.42	5.30	4.62	4.72	5.60	3.60
P2O5	0.32	0.40	1.15	0.08	0.02	0.00	0.02	0.07	0.02	0.00	0.04	0.04
LOI	7.44	5.53	8.14	2.00	5.33	4.40	5.40	2.03	5.42	5.23	1.44	1.55
Total	100.73	100.14	99.37	99.04	99.71	99.42	99.74	99.40	100.37	99.77	99.48	99.29
Nb	18	29	55	236	242	270	274	287	272	259	259	282
U	<1	5	1	12	15	11	14	12	14	10	11	10
Ga	25	23	20	55	45	46	48	52	49	48	39	48
Hf	<3	<3	8	29	28	28	28	26	30	26	28	31
Ta	<10	<10	<10	28	23	28	26	19	21	19	24	21
Sc	6	24	9	<2	<2	<2	<2	<2	<2	<2	<2	<2
Y	14	25	41	59	105	104	96	100	111	91	99	102
Zr	110	202	382	2752	2505	2526	2377	2379	2713	2349	2543	2687
Sr	3891	1580	265	54	63	3	66	40	41	75	240	532
Rb	6	10	10	236	165	172	130	170	141	145	156	106
Th	3	8	5	40	36	35	38	39	41	38	36	42
Bi	5	2	4	<2	3	5	<2	<2	<2	3	4	<2
species	MB	MB	MB	nundorite	nundorite	nundorite	nundorite	nundorite	nundorite	nundorite	nundorite	nundorite

Table 7.2. Major and Trace Element Compositions of Selected from the Cambrian Sequences in the Wonominta Block

	Comarto area											
	1	2	3	4	5	6	7	8	9	10	11	12
	860901	860904	860909	861002	861003	861010	861011	861013	861014	861015	861016	862101
SiO2	42.69	49.70	41.15	48.45	49.11	47.45	47.45	52.56	51.21	41.57	47.16	59.41
TiO2	1.44	1.52	2.63	1.22	1.32	1.43	1.76	1.64	1.39	0.99	1.41	0.82
Al2O3	15.67	13.65	12.30	16.63	15.05	15.80	14.78	12.88	14.69	15.97	16.06	15.29
Fe2O3	8.77	11.71	11.95	8.37	9.62	11.26	11.80	11.05	9.17	6.94	11.18	6.33
MnO	0.15	0.17	0.19	0.12	0.14	0.17	0.17	0.18	0.18	0.15	0.17	0.14
MgO	4.75	6.85	3.58	5.56	6.02	6.92	6.82	6.96	4.86	3.57	6.63	2.29
CaO	14.73	10.38	12.13	11.35	10.96	11.79	13.25	8.47	12.50	20.50	12.01	3.31
Na2O	4.11	4.04	4.56	4.36	4.46	3.23	1.81	5.19	4.41	3.76	3.24	5.79
K2O	0.41	0.22	0.13	0.81	0.42	0.27	0.12	0.10	0.06	0.03	0.35	0.96
P2O5	0.18	0.16	0.65	0.15	0.15	0.16	0.19	0.17	0.16	0.13	0.14	0.23
LOI	8.33	1.64	11.48	3.34	3.19	2.28	2.73	1.08	2.03	7.10	1.83	4.81
Total	101.23	100.04	100.75	100.36	100.44	100.76	100.88	100.28	100.66	100.71	100.18	99.38
Nb	6	7	13	7	7	6	9	10	9	5	4	10
U	4	<1	5	2	<1	<1	3	2	4	5	<1	1
Ga	16	15	18	14	13	16	17	14	16	12	17	16
Hf	<3	<3	<3	<3	<3	4	<3	6	<3	<3	<3	<3
Ta	<10	<10	<10	<10	<10	<10	<10	<10	<10	<10	<10	<10
Sc	23	36	28	29	30	38	33	41	29	13	36	21
Y	28	29	41	24	26	27	32	29	25	19	29	24
Zr	107	119	226	102	113	103	132	126	104	75	95	171
Sr	282	301	139	403	358	363	271	156	249	145	192	383
Rb	9	4	3	8	4	8	5	3	2	2	8	35
Th	6	2	2	<1	<1	2	<1	4	5	4	5	14
Bi	4	6	5	3	4	5	4	3	2	2	5	3
species	MB	MB	MB	MB	MB	MD(I)	MD(I)	MB	MB	MB	MB	porphyry

Table 7.2. Continued (2)

	Comarto	Mt. Wright area										
	13	14	15	16	17	18	19	20	21	22	23	24
	862103	862110	862112	862205	862206	862214	862217	862218	862221	862222	862225	862304
SiO2	67.61	72.90	39.20	46.47	67.97	71.24	50.37	66.55	55.29	65.41	43.32	56.40
TiO2	0.71	0.32	2.29	3.10	0.66	0.67	2.20	0.45	2.50	0.50	1.80	1.38
Al2O3	14.47	12.35	13.09	12.98	14.29	7.68	13.54	15.97	14.50	15.01	13.91	15.19
Fe2O3	5.48	2.32	11.95	13.52	4.71	2.87	14.02	5.16	15.21	7.91	11.06	6.09
MnO	0.06	0.05	0.16	0.18	0.08	0.10	0.16	0.02	0.05	0.03	0.17	0.13
MgO	0.20	0.65	4.51	3.06	1.54	2.11	1.95	0.13	0.12	0.00	3.58	0.88
CaO	0.57	1.40	15.42	6.56	2.80	4.72	6.27	0.16	1.80	0.28	15.14	5.60
Na2O	7.81	5.61	4.18	6.00	1.34	4.43	7.56	6.94	8.77	7.45	4.90	7.02
K2O	0.39	0.95	0.07	0.17	4.16	0.04	0.14	2.91	0.44	1.79	0.50	0.78
P2O5	0.09	0.07	0.32	0.68	0.16	0.14	0.89	0.04	1.19	0.09	0.31	0.28
LOI	2.20	3.37	9.43	8.11	2.24	6.43	3.88	1.58	0.97	1.34	6.49	6.56
Total	99.59	99.99	100.62	100.83	99.95	100.43	100.98	99.91	100.84	99.81	101.18	100.31
Nb	10	7	17	39	13	8	48	92	61	89	23	10
U	1	6	<1	2	3	2	1	4	<1	<1	<1	3
Ga	11	9	23	17	16	4	23	26	14	27	17	17
Hf	<3	4	<3	4	<3	4	<3	13	6	13	<3	<3
Ta	<10	<10	<10	<10	<10	<10	<10	<10	11	<10	<10	<10
Sc	17	7	24	21	13	8	13	<2	13	<2	23	24
Y	15	25	22	30	44	18	52	91	64	80	20	38
Zr	174	159	165	239	233	315	385	1018	517	927	168	181
Sr	223	134	77	219	143	85	266	120	119	165	323	198
Rb	16	47	2	5	223	2	2	56	8	29	10	27
Th	13	16	2	4	20	12	5	18	8	17	7	8
Bi	3	<2	<2	4	4	2	<2	<2	3	<2	<2	4
species	porphyry	porphyry	MB	MB	FT	FT	MB	trachyte	trachytic andesite	trachyte	MB	porphyry

Table 7.2. Continued (3)

	Mt. Wright area								Bilpa			
	25	26	27	28	29	30	31	32	33	34	35	36
	862402	862405	862501	862504	862506	MW-1	MW-2	MW-3	862901	862902	862909	862914
SiO2	46.68	35.46	75.73	68.33	72.36	75.09	82.82	68.72	57.45	68.05	41.40	44.98
TiO2	2.86	1.30	0.33	0.47	0.42	0.70	0.33	1.01	1.09	0.67	1.79	1.64
Al2O3	13.51	10.41	13.06	12.98	11.66	7.36	8.67	14.28	11.72	13.95	14.35	16.28
Fe2O3	12.38	9.15	1.96	2.28	2.74	0.85	2.14	1.36	8.91	4.29	12.03	11.58
MnO	0.23	0.13	0.03	0.10	0.06	0.00	0.01	0.00	0.12	0.07	0.19	0.18
MgO	2.95	7.96	0.00	0.12	0.67	0.15	0.46	0.57	1.75	1.87	4.92	7.12
CaO	7.26	14.54	0.17	2.88	2.23	0.17	0.16	0.19	10.68	2.77	10.81	8.58
Na2O	7.09	2.41	4.98	4.11	4.34	0.41	0.31	0.29	2.25	2.38	4.40	2.47
K2O	0.16	0.32	1.07	1.72	0.98	1.26	2.64	3.78	0.07	1.96	0.30	1.18
P2O5	0.55	0.21	0.01	0.10	0.00	0.11	0.05	0.09	0.35	0.15	0.18	0.18
LOI	6.99	18.86	2.56	4.76	3.76	4.35	2.60	4.87	5.54	3.30	10.09	5.69
Total	100.66	100.75	99.90	97.85	99.22	90.45	100.19	95.16	99.93	99.46	100.46	99.88
Nb	38	13	5	8	8	4	7	20	10	11	6	6
U	1	<1	1	3	<1	13	4	63	<1	2	<1	<1
Ga	24	13	10	13	11	24	12	20	31	17	17	17
Hf	10	<3	<3	<3	<3	9	3	8	14	<3	6	5
Ta	<10	<10	<10	10	<10	84	<10	20	<10	<10	<10	<10
Sc	15	26	4	11	7	7	5	10	26	13	46	50
Y	33	15	11	26	33	7	15	25	84	49	44	31
Zr	320	110	122	140	162	98	93	237	984	212	141	133
Sr	203	232	186	132	214	303	43	263	415	128	225	204
Rb	4	10	42	62	49	42	119	148	4	116	18	65
Th	6	2	13	12	12	124	11	29	14	16	<1	2
Bi	2	4	<2	<2	3	<2	3	<2	2	3	2	2
species	MB	MB	porphyry	porphyry	porphyry	mineralised felsic tuff samples			andesite	FT	MB	MB
											basement	basement

Table 7.2. Continued (4)

	Bilpa				Ponto Mine	Kayrunnera	Wonnaminta			Boshy Tank
	37	38	39	40	41	42	43	44	45	46
	863004	863009	863011	863012	752110	762904	762410	762412	762413	762602
SiO2	65.70	71.52	69.66	50.10	46.05	45.33	47.47	49.56	41.93	43.50
TiO2	0.64	0.20	0.60	1.15	2.86	1.27	2.88	1.96	0.54	2.90
Al2O3	13.58	15.93	13.65	21.72	14.12	16.99	15.20	15.60	20.62	14.21
Fe2O3	7.09	1.36	4.27	5.18	15.52	10.38	10.70	8.94	12.23	13.29
MnO	0.15	0.03	0.07	0.09	0.23	0.16	0.16	0.13	0.19	0.20
MgO	2.67	0.23	1.46	2.55	5.40	7.44	5.88	5.68	1.28	9.95
CaO	0.51	2.23	1.67	8.78	9.16	11.24	7.29	7.65	18.31	7.84
Na2O	1.17	5.41	4.22	5.59	3.88	2.73	4.64	4.48	0.68	3.53
K2O	4.03	1.56	2.08	0.75	0.41	0.71	1.64	1.33	2.27	1.22
P2O5	0.16	0.05	0.12	0.13	0.26	0.15	1.24	0.83	0.23	0.61
LOI	4.28	0.98	1.96	3.96	2.54	3.06	2.68	3.34	1.97	3.02
Total	99.98	99.50	99.76	100.00	100.43	99.46	99.78	99.50	100.25	100.27
Nb	11	6	14	11	12	7	71	54	57	27
U	3	<1	<1	2	<1	1	<1	2	<1	<1
Ga	17	15	18	15	23	17	20	19	36	16
Hf	4	<3	<3	4	<3	<3	9	6	5	3
Ta	<10	<10	<10	<10	<10	<10	<10	<10	<10	<10
Sc	15	30	3	15	34	28	14	14	<2	30
Y	32	27	12	37	29	22	30	25	18	29
Zr	162	90	89	209	158	84	503	424	634	252
Sr	55	272	578	106	449	381	1410	1470	13047	609
Rb	161	19	69	116	14	22	55	43	56	58
Th	19	2	9	19	2	<1	6	9	16	3
Bi	4	<2	2	3	3	3	<2	5	<2	5
species	FT	granite	FT	MB	MD (I)	gabbro	lamprophyre		Ep nodule	lamprophyre

Appendix 6.
Analytical Parameters of Isotope Studies

A6.1. MASS SPECTROMETRY

Mass spectrometry (MS) is one of the most important technical developments in modern science and has many applications in geosciences, particularly in geochronology and isotope geochemistry. Theoretically, the technique is based on a very simple, yet elegant principle, which can be briefly described as follows. After emission, the ionised sample particles are introduced in a magnetic field by means of electronic charges. In this field, ions travel in curved orbits and the radii of the curves are proportional to the mass to charge ratios of the ions. Thus, isotopes of an element travel in various orbits due to different mass to charge ratios and by measuring the relative intensity of these ion signals with characteristic orbits, the isotope ratios, the relative abundance, can be obtained.

There are several ways of generating the ion emissions, which lead to various apparatuses in mass spectrometry. For conventional MS, ions are generated by the process of thermal ionisation over a hot filament; thus the apparatus is named a thermal ion mass spectrometer (TIMS). In contrast, the SHRIMP uses an oxygen ion beam to bombard target samples to obtain the secondary samples ions. In the ICP-MS techniques (Appendix A8), the sample ions are generated by plasma.

A6.1.1. Thermal Ion Mass Spectrometer (TIMS)

As mentioned above, sample ions for the TIMS analysis are generated in the source by thermal ionisation. There are two different processes of thermal ionisation, which correspond two different kinds of filaments, single and triple ones. The filament techniques are presented in Appendix A6.3. The ionised samples are then focussed by various elements of the source collimator onto the entrance slit of the analyser tube, and then split up in the magnetic analyser according to the mass to charge ratio of the particles and ions of chosen mass to mass ratio are focussed onto the collector slit by selecting the appropriate value of the magnetic field. Isotope ratios for the samples are then calculated by measuring the ion beams arriving at the collector.

In this project, Sr, Nd and Sm were analysed on the VG© Sector 54 using a fully automated multi-collector dynamic mode. The Pb isotope compositions were analysed on VG© 54E with a fully automated single-collector mode

A6.1.2 SHRIMP

Sensitive high-resolution ion micro-probe, hence SHRIMP, is one of the state-of-the-art mass spectrometers of modern technology. It brings together the techniques of the mass spectrometer and microprobe, and this combination enables not only the avoidance of tedious chemical processes required for conventional mass spectrometry, but also the analysis on a microscopic scale (20 μm across), thus isotopic heterogeneity within single mineral grains.

A6.1.2.1. Analytical Preamble

Unlike the TIMS, the SHRIMP uses a micro-beam of oxygen ions to bombard the polished surface of samples to generate secondary ion signals. Then, the ion beams are introduced into powerful electronic and magnetic fields sequentially to filter out most of the unwanted signals before reaching the collector slit. One of the most difficult aspects of the SHRIMP technique is the fact that ion emission signals of the samples under bombardment are extremely complex and the analysed ions (U and Pb in this case) are extremely low in abundance compared with those from the major components of the samples. Thus, the physical processes are much more complicated than those of the TIMS. It is due to these difficulties that only a single collector mode has been achieved at the present.

Understandably, the high analytical sensitivity is accompanied by the high instability and this requires constant calibration by analysing standard materials. In practice, the analyses on samples and on the standard were carried out sequentially for Phanerozoic samples to monitor the behaviour of the machine, which is crucial for estimation of the analytical errors and other correction parameters, such as common lead.

The analytical processes are described briefly as follows. Upon the bombardment of the primary ion beam, a tiny proportion of the ejected material is ionised and is accelerated down the mass spectrometer by a high voltage. After the powerful filtering, the target ions are counted for set times on a single collector by cyclically

stepping the magnet through the atomic masses. The analysed masses are presented in the following table:

Table A6.1.1. Ions measured on SHRIMP for the U-Th-Pb work

Mass	196	204	204.1	206	207	208	238	248	254
Species	Zr_2O^+	$^{204}Pb^+$	back-ground	$^{206}Pb^+$	$^{207}Pb^+$	$^{208}Pb^+$	$^{238}U^+$	ThO^+	UO^+
Time (s)	2	10	10	10	40	10	5	5	2

A set of 7 such scans through the mass range is carried out to form a single analysis after the removal of outliers. The raw data set comprises the measured counts for each mass and the time elapsed. From these raw data, the required isotopic ratios, such as $^{207}Pb^*/^{206}Pb^*$, $^{206}Pb^*/^{238}U$ and $^{207}Pb^*/^{235}U$ ($^{206}Pb^*$ and $^{207}Pb^*$ denote the radiogenic lead isotopic contents, which means common lead correction has to apply) can be obtained after a series of calculations.

In practice, it is generally found that the ion beam counts vary over the time of analysis even though the target material has a homogeneous composition. This is due to the differential yields of various ions as the bombardment proceeds and the crater depth increases. Therefore, this variation of the ionisation processes has to be considered for calibration.

During the counting process, the signals of $^{206}Pb^+$, $^{207}Pb^+$, and $^{208}Pb^+$ show a correlated change while the Pb-Pb ratios remain constant. Furthermore, the mass fractionation effect during the ionisation is negligible compared with the analytical precision, therefore, the Pb/Pb ratios do not require calibration and are taken as exactly the ratios of the measured counts.

However, the inter-element ratios vary as a function of time during analysis due to the differential yield of Pb, Th and U ions from the sputtered crater, and this is where much of the endeavour of the data reduction has been devoted. In the case of Th/U, it has been found empirically that there is a fixed correlation that:

$$^{232}Th/^{238}U = 1.11\ \{ThO^+/UO^+\} \qquad (A6.1)$$

where $\{ThO^+/UO^+\}$ denotes the measured ratios of the respective ions yielded by the ionisation process.

In the case of Pb/U, the machine bias varies from day to day as a function of machine conditions and spot shape, which to some extent, are beyond human control at the present technical level. This is corrected by calibrating the measured $^{206}Pb^+/^{238}U^+$ ratios to the known $^{206}Pb/^{238}U$ of a standard zircon using the relationship:

$$[^{206}Pb/^{238}U]_{sample}/[^{206}Pb^+/^{238}U^+]_{sample} = [^{206}Pb/^{238}U]_{std}/[^{206}Pb^+/^{238}U^+]_{std} \quad (A6.2)$$

In this equation, the $[^{206}Pb/^{238}U]_{standard}$ is 0.0928, which corresponds to an age of 572 Ma, the $[^{206}Pb^+/^{238}U^+]_{sample}$ is taken as the measured value, and the $[^{206}Pb^+/^{238}U^+]_{standard}$, which theoretically should be constant but varies during the machine analysis, has been found to have an empirical correlation with the measured UO^+/U^+ ratios with a quadratic relationship:

$$[^{206}Pb^+/^{238}U^+]_{standard} = A\{UO^+/U^+\}^2_{standard} + B\{UO^+/U^+\}_{standard} + C \quad (A6.3)$$

This is the equation for the actual calibration curve which is required during every session of analysis. After repeated analysis on the standard, quadratic regression should produce the values for A, B, and C. After obtaining these parameters, the $[^{206}Pb^+/^{238}U^+]_{standard}$ ratio can be calculated; Then the ratio is used to calculate the $^{206}Pb/^{238}U$ ratio of the real samples and thereafter the other inter-element ratios such as $^{207}Pb/^{235}U$ and $^{208}Pb/^{232}Th$.

As mentioned earlier, what is useful in the geochronological calculation is the radiogenic isotopic compositions (generated after the formation of the mineral, thus bearing the age information) such as, $^{206}Pb^*/^{238}U^*$, $^{207}Pb^*/^{235}U^*$ and $^{208}Pb^*/^{232}Th^*$, not the "measured" compositions. This means initial (or common) lead correlation has to apply to deduce those isotopes already existing when the mineral was formed. There are two ways to carry out the correction; one using the observed ^{204}Pb and the other using $^{208}Pb/^{206}Pb$ and Th/U ratios. All the ^{204}Pb is of common lead origin since there is no radiogenic process producing this isotope. Thus this is a direct method of correction but is relatively imprecise due to the low ^{204}Pb content (<30 ppb in zircons). The other method may be more precise due to the fact that all the ratios can be easily measured but the correction relies on an assumption of no relative movement of Th and U in the zircon crystals after crystallisation, which may not be true in many practical cases. Therefore, a further regression test between $^{208}Pb/^{206}Pb$ and Th/U has to be carried out to verify this assumption.

A6.2. SAMPLE PROCESSING PROCEDURES FOR Sr-Nd-Sm ISOTOPE ANALYSES

For the hand-specimen-sized bulk samples, weathered surfaces were removed using a diamond saw and the fresh interior parts were then crushed by a hydrostatic hammer. Small fragments were hand-picked between 50 and 100 grams to avoid any obvious carbonate veins and amygdales and then powdered in a cleaned (using alcohol plus distilled water) tungsten carbide mortar. The powdered samples were homogenised thoroughly on clean kraft paper before being stored in cleaned plastic bottles. The powdered samples have also been used for the XRF analysis for major and trace element compositions of the samples (*cf.* Chapters Five to Seven). Approximately 0.2 gram powders for each sample were accurately weighed and then digested in HF + $HClO_4$ using a "Teflon© bomb" method (Krogh, 1973). Details of the digestion procedures are as follows:

A6.2.1. Sample Dissolution

The first step of the digestion is to let the sample dissolve in 2 ml HF acid (distilled three times before usage; concentration about 50 weight percent) in open beakers. After several hours reaction at room temperature (preferably over night), 10 drops $HClO_4$ are added to the beakers. Sample solutions are evaporated at about 120 ^{0}C till dryness and then at 210 ^{0}C to fume out all reagents.

For the metamorphosed mafic samples, many minerals, such as epidote, clinozoisite are difficult to digest, thus an extended period of digestion at high temperature in sealed containers (thus the high pressure of reagent) has to be carried out. After adding 2 ml HF reagent, the containers are then sealed in a steel device with bomb-like shape (hence the name bomb method); then, the whole device is heated in an oven at 180 ^{o}C for five days.

After dismantling the bombs, the samples in HF solution are slowly heated, adding another 10 drops $HClO_4$ to oxidise the components in the sample.

When the solutions are dried, another 10 drops $HClO_4$ acid are added to each sample to ensure that all components are digested without fluorides. Samples are then dried at 210 ^{o}C.

The next step is to transform various components into chlorides. The samples are dissolved in 3 ml 6 M HCl solution in bombs at 180 ^{0}C overnight.

After digestion, the samples are then taken up by 9 ml 6 M HCl and split evenly into three parts. Each part is accurately weighed. The three parts are used for **ID** (isotope dilution analysis) analyses (see 7.2), **IR**, (isotope ratio measurements) and **REE** (REE analyses).

For the **ID** fractions, about 200 mg spike solution are accurately weighed and added to the samples; they are then dried for column-separation treatment.

The **IR** samples are dried directly after splitting for column-separation treatment.

The **REE** samples are spiked with 100 mg of REE spike solution, and then dried for separation processes.

A6.2.2. Sample Separation

The dried samples are dissolved in 2 ml 2.5 M HCl acid; and then centrifuged to get rid of undissolved residues. In this exercise, it was noted that an extended period of dissolution (over a weekend) helped to take up the samples more efficiently.

A. Primary Separation.

The clear sample solution are then run through resin columns to separate Sr, Nd and Sm from rest of the components. The operation procedures are as follows:

LOAD	2 ml 2.5 M HCl sample solution (centrifuged).
WASH	1 ml 2.5 M HCl.
WASH	1 ml 2.5 M HCl.
WASH	1 +12.5 ml 2.5 M HCl
COLLECT Rb	7.5 ml 2.5 M HCl (Rb off)
FLUSH	9 ml 2.5 M HCl.
COLLECT Sr	10 ml 2.5 M HCl (Sr samples then dried for analyses)
COLLECT REE	20 ml 6 M HCl (Nd and Sm fraction).
WASH	25 ml 6 M HCl (wash out all others in the columns)

CONDITION 25 ml 2.5 M HCl

CONDITION 5 ml 2.5 M HCl and the process is accomplished..

B. Separation of REE fractions for Nd and Sm.

PRESERVE 10.5 ml 0.22 M HCl; then the REE samples taken up by 3 drops acid from the reserve.

LOAD the 3 drop 0.22 M HCl samples on to the top of the resin.

WASH with 3 drop 0.22 M HCl from the reserve 3 times

FLUSH with the remainder of the acid reserve through the columns

COLLECT Nd with 4 ml 0.22 M HCl

The collection are then dried and ready for analyses.

FLUSH with 5 ml 0.45 M HCl

COLLECT Sm with 5.5 ml 0.45 M HCl

The collections are carried out only for the ID samples.

FLUSH with 10 ml 6 M HCl to clean the columns

CONDITION the columns with 5 ml 0.22 M HCl twice.

And the process is accomplished.

C. REE Separation

REE fractions of REE-spiked samples are required to be further separated into LREE and HREE fractions for the ICP-MS analysis (Appendix 10). This was carried out using anion columns and the procedures for column work are as follows:

CONDITION 10 ml 5M HNO_3.

CONDITION 10 ml S_1* solution.

LOAD 5 ml S_1 sample solution.

WASH 1 ml S_1.

WASH 1 ml S_1.

WASH/FLUSH 1 + 47 ml S_1.

FLUSH 7 ml S_2**solution

COLLECT HREE 15 ml S_2.

COLLECT LREE 10 ml 0.5 M HNO_3

WASH 10 ml H_2O.

CONDITION 2 ml H_2O.

* S_1, 90% HAC + 10% 5 M HNO_3.

** S_2, 75% HAC + 10% 5 M HNO_3 + 15% H_2O.

A6.3. SAMPLE PROCESSING PROCEDURES FOR Pb ISOTOPE ANALYSES.

A6.3.1. Sample Washings

Pyrrhotite. Samples are washed in 1 M HCl acid quickly; rinsed several times with purified water until no observable reactions; dried.

Chalcopyrite. Samples are washed in 6 M HCl acid, heating up to 50 ^{0}C for three minutes; rinsed with purified water several times; boiled in the water; dried.

Pyrite. Samples are washed quickly in cold 6 M HCl, rinsed with purified water several times, boiled in the water and then dried.

Chemical Separation of Sphalerite/Chalcopyrite Mixture

The separation of mixed sphalerite/chalcopyrite sample is proceeded by means of chemical method, described as follows.

Firstly add 3 ml 1 M HCl acid to the mixed sample in an open beaker; Warm up the sample solution slightly for about ten minutes. Then drain the solution into another beaker; dry the solution on a hotplate. The materials left in the beaker is the sphalerite fraction of the mixture. The residue in the first beaker is also dried out on the hotplate and is the chalcopyrite fraction.

Since there is no washing step proceeding the separation, it is obvious that the surface contaminates, likely including variable lead, will be in the sphalerite part of the sample.

A6.3.2. Sample Digestions

1. Weigh accurately about 100 mg cleaned samples into a clean teflon® beaker.

2. Dissolutions.

For chalcopyrite, sphalerite and pyrite, the reagents are 1:1, 7 M HCl: 7 M HNO_3 plus 3 drops 4M HBr.

For pyrrhotite, the reagents are 7 M HCl plus 3 drops 4 M HBr acid.

(The purpose of adding HBr is to retain S as anion status; however, during digestion of the second batch of GR8 samples, excessive free sulphur was noted in the beakers; thus once evaporated, approximately one millilitre of concentrated HNO_3 was added to each of the beakers to get rid of the free S.)

Cover the reacting beakers and stand overnight in a clean hood.

Evaporate to dryness on a hot plate at about 150 ^{0}C in a clean laminar flow fume hood.

Convert the samples to a bromide using 3 to 5 drops 4 M HBr, evaporate to dryness.

A6.3.3. Ion Exchange Separations

A. Samples are taken up in 3 - 5 ml 1 M HBr. Stand overnight before loading.
B. Prepare 0.5 ml of *AG 1-8x* resin in heat shrinkable teflon columns with approximately 2.5 ml reservoir capacity. In practice, these columns are washed with a full column 7 M HCl and then rinsed with water before loading the resins.
C. Wash the resins twice with full column 7 M HCl respectively (thus about 5 ml acid).
D. Wash the resins with 1 full column purified water.
E. Condition the resins with 1 column wash of 1 M HBr
F. Load the sample solutions.
G. Flush the resins twice with full columns 1 M HBr.
H. Flush the resins three times with full columns 0.5 M HBr. And
I. Collect Pb fraction with a full column 7 M HCl and using tall teflon beakers.

The sample solutions are then dried in a clean hood for further purification with ED technique.

A6.3.4. Electronic Deposition (ED) Technique.

The dried Pb fraction samples are then processed further with a technique known as the electronic deposition (ED) method.

The samples are dissolved in freshly made solution with 0.1 M HCl : H2O of 1: 9 (In practice, 4 drops HCl and 36 drops water were added. The amount of solution required was determined by the abundance of Pb estimated in the beakers.)

A teflon-wrapped clean magnet rod is also placed in each of the beakers to speed up the process.

Two platinum electrodes connected to a power source are placed in the solution. Place the beakers on a magnetic stirrer and connect the terminals to the potentiometer with voltage set-up at 1.8 V. When the power is on, the current indicator is normally between 0.2 - 1.0 mA and drops to less than 1 mA after about 5 minutes.

The Pb atoms will be gradually deposited on the surface of the anode (specially marked with an ink pen).

Check the anode regularly (approximately 5 to 10 minute intervals). When the Pt anode appears to be light brown in colour due to the Pb deposition (this particular colour indicates one to two microgram Pb deposits), the process is terminated so that the amount of Pb collected each time is approximately at the same level regardless of the original concentration. (The ID technique discussed below helped to obtain the answer not only Pb isotope ratios, but also the concentration of total Pb in the samples)

The collected Pb is then dissolved in a small 1 ml teflon beaker with three drops 3 M HNO_3 by placing the platinum anodes into the acid. The solutions are then dried out on a hotplate. When the samples are dried, one drop of concentrated HNO_3 is added to each of the beakers and fumed out at 210 ^{0}C.

In each batch of the samples, a blank sample is processed simultaneously, starting with nothing, but all reagents used in the whole process are added together with special spike solution so that interferences from the processes can be monitored. Because of the generally low level of Pb, the ED time is set up to be 120 minutes; and when dried, one drop of H_3PO_4 is also added to the particular sample. In this way, the tiny amount of Pb can be easily picked up in the loading processes.

A6.4. THE FILAMENT TECHNIQUE

The purified samples are loaded on a metal filament to carry out analyses in the mass spectrometer. For the thermal ionisation mass spectrometer (TIMS), the analysed element must be firstly ionised by thermal heating. Obviously, it is the easiest way to load the sample elements on to a filament device, which is charged with strong electrical current to generate the high temperature. Under this environment, the samples will be ionised so that analyses can be proceeded. However in practice, it is usually found that the temperature of the filament must be substantially lower (approximately 1200 ^{0}C typically for Sr and Pb compared with 2300 ^{0}C needed for proper ionisation) in order not to evaporate all the samples too rapidly, unless some sort of activator or special loading process is used. To overcome this problem, special filaments have been designed, that is the double and triple filament techniques, which separate the sample filament(s) and ionising filament. In both cases, sample is distilled onto the ionising surface from a further (sample) filament placed nearby, and the processes of ionisation and sample evaporation are separated. For the triple device, the samples are loaded on both side-filaments while the centre one used as ionising filament; In contrast, there is only one "side-filament" for the double filament device, which is loaded with samples.

Both single and triple filaments are used in this project. The single filaments were used for Sr (using Ta filament), and Pb (using Re filament), and the special activators used include silica gel and phosphoric acid for Pb and U, and phosphoric acid for Sr. The analyses for Rb, Nd and Sm were carried out on triple filaments, which is actually used as "double-filament" since only one side filament is loaded with samples. The filament preparation involves welding of the filaments onto the holder devices (beads) and clean them before loading the samples.

Construction of the sample filaments involves two steps, making the filament and loading the samples on to the filament.

A6.4.1. Construction of Filament

Construction of filaments technically involves welding of the metal (Ta or Re) filaments onto the commercially available holder devices (beads) with a special electrical welder. After the welding, the filaments are rinsed in purified water three times and washed in a ultrasound bath. However, the major step of the cleaning

involves a degassing process, which uses electric current to heat the filament in a vacuum environment, locally known as outgassing processes.

A6.4.2. Loading Samples on to the Filament

A. Sr samples

1. Zone refined Ta single filaments are used and placed in a holder device through which electrical current can be charged.

2. Install syringe tips. The plastic disposal tips are stored in conc. nitrate acid. When loading, the tips are fitted to the rubber end of syringes. Rinse the tips thoroughly with purified water (both inside and outside).

3. Take a small drop of purified water (half to a third of the normal drop depend on the amount of samples available) to dissolved the samples.

4. Load the sample solution neatly onto the central part of the filaments with a small drop. Normally, a quarter to a third of the sample is loaded; when the amount of sample is low, repeat this procedure to have half to all of the sample loaded depending the amount of sample. In the present project, one third to half of the collected Sr samples are ample for analysis.

After the first loading, turn on the power to add current through the filaments with the indicator set at 2nd division. And when solutions dry, repeat loading if necessary.

5. When finally all sample solutions are dried, add a tiny drop of 0.75 M H_3PO_5 on top of the samples on the filaments.

Use a separate cleaned syringe to take a big drop of phosphoric acid and to divide the acid into several small drops on a piece of Parafilm®. Use the 'sample' syringe to pick up the small drops of acid and load for each sample. The ideal amount of the acid is to just cover the sample surface.

6. After the phosphoric acid has dried, slowly increase the current through the filament until the filament becomes red in colour, carefully leave there for a few seconds, to fume out all the volatiles and potential organic materials. Then turn off the power. The sample filaments are ready for machine analysis.

B. Nd and Sm samples

1. Zone refined Re triple filaments are used.

2. Operation of the device, syringe cleaning and sample loading are essentially the same as those for loading Sr samples, except that samples are loaded onto one of side filaments, which is previously bent outwards to provide enough space for loading.

3. When the sample solutions are dried, gradually turn up the current directly without using the phosphoric acid as the activator.

4. After the fuming, the current is turned off and the filament cooled rapidly in the cleaned-air hood. Then the outwardly bent filament is moved back to the straight-up position and all three filaments in the bead are parallel to each other in all three dimensions.

The sample filaments are thus ready for machine analysis.

C. Pb samples.

1. Add two drops water to each sample beaker (the Pb contents in the present sulphide samples are generally high). For blank sample, 1 drop is used. Use the 'tips' to scratch the bottom edge of the beakers to ensure all Pb is dissolved; then use the tip to suck and squeeze the solution several times to homogenise the sample solution
2. When dissolved, use the 1 mm-diameter tube to suck about one-centimetre-long solution and preserve them by dropping on the other side of the beaker away from the main reservoir.
3. Prepare silicon gel. Take a large drop of silicon gel and spilt it into approximately equal-sized small drops for each sample with 'tips'.
4. Mix the samples with prepared gels. Use the tip to take up spilt gel and drop them in the preserved samples in Step 2; mix up by suck-and-squeeze processes.
5. Loading. Use the tip to take up mixed samples and carefully load the samples in the centre of the filament (see next section). Generally, it takes four steps to load the whole sample fraction.
6. Step-heating. Turn on the heating power and set the intensity at unit two initially. When samples appear to be dried, slowly increase the current intensity by one unit each time and stand for at least 10 minutes at each intensity level. And finally, when filament become dark red, carefully increase the current intensity to bright red to burn off all volatile components. Turn off the current and when cool, the sample devices are ready to be loaded in the mass spectrometer.

A6.5. ISOTOPE DILUTION (ID) TECHNIQUES

The isotopic dilution technique is used in the mass spectrometer analysis to determine not only the concentration of the element(s), but also ratios of isotopes of an element or inter-elements, such as $^{87}Rb/^{87}Sr$ (Moore *et al.*, 1973).

The spike used in this study are diluted acid solutions, containing particular elements (Sr/Rb or Nd/Sm) whose concentrations and isotope compositions are known accurately. Thus, when a known amount of sample is mixed evenly with a known amount of spike, and the isotope compositions of the spiked samples are measured by the mass spectrometer, the isotope compositions and the concentration of the elements can be calculated. Unfortunately, the isotope composition of the Nd spike used in this study is relatively poorly known; thus, an unspiked sample has to be analysed in parallel to monitor the calculated Nd isotope ratios from the spiked analyses.

From the start, there is an invariable relationship that the compositions of the spiked samples (M) are the sum of natural samples (S) and spike solutions (T), that is

$$\mathbf{M} = \mathbf{S} + \mathbf{T} \qquad \text{(A6.1)}$$

The bold letters in the formulae represent the vectors of the parameters.

For elements with only two isotopes, such as Rb (^{85}Rb and ^{87}Rb), the data reduction is relatively simple, that the measured isotopic ratio (R_m) of an element in the spiked samples is given by:

$$Rm = \frac{N_s C_s^a + N_k C_k^a}{N_s C_s^b + N_k C_k^b} \qquad \text{(A6.2)}$$

where substitute s for samples and k for spike; C for proportion of isotopes in the element;

N for number of atoms of the element; and a and b for the two isotopes of the element.

To obtain the elemental concentration in samples, solving equation A6.2 yields:

$$N_s = N_k \frac{C_k^a - R_m C_k^b}{R_m C_s^b - C_s^a} \qquad \text{(A6.3)}$$

And transforming into mass (M) formulae yields:

$$M_s = M_k \frac{W_s(C_k^a - R_m C_k^b)}{W_k(R_m C_s^b - C_s^a)} \qquad \text{(A6.4)}$$

where, W_s and W_k stand for the atomic weight of sample and spike respectively. Since the isotope compositions in natural samples and in spikes are different, their atomic weights are different too. And the concentration of the element in natural samples can be easily obtained by dividing the Ms with total mass of the sample used for analysis.

For Rb analyses, C_s^{Rb87} is 27.83% and C_s^{Rb85} is 72.17% respectively; this composition gives the atomic weight as 85.4677. When using the CIS1 solution (Rb/Sr mixed spike) to carry out the spiking, C_k^{Rb85} is 2.02%, C_k^{Rb87} is 97.98%; and the atomic weight for the spike is 86.9596. Apparently, given the measured $^{85}Rb/^{87}Rb$ from mass spectrometer analyses (with zero mass fractionation; see discussion below), the concentration of Rb in the samples can be accurately obtained, and hence the $^{87}Rb/^{87}Sr$ ratio together with Sr isotope dilution analyses discussed below.

When the analysed elements have more than two isotopes, the algebra become relatively complex. Russell (1971 & 1977) developed the mathematical systematics of the double spiking technique. For Sr, the solution is:

$$S_{\frac{87Sr}{86Sr}} = \frac{\Delta 1}{\Delta 3} M_{\frac{87Sr}{86Sr}} - \frac{\Delta 1}{\Delta 3} T_{\frac{87Sr}{86Sr}} \qquad \text{(A6.5)}$$

where $\Delta 1 = [(S_{84/86} - 3M_{84/86})(S_{88/86} - T_{88/86}) - (S_{84/86} - T_{84/86})(S_{88/86} - M_{88/86})]/2$

$\Delta 2 = M_{84/86}(M_{88/86} - S_{88/86}) - M_{88/86}(S_{84/86} - M_{84/86})$ and

$\Delta 3 = M_{84/86}(T_{88/86} - M_{88/86}) - M_{88/86}(M_{84/86} - T_{84/86})$

However, in practice, there is always a problem of mass fractionation during the analysis by thermal ion mass spectrometer. In simple words, the mass fractionation refers to the phenomena that atoms with lighter mass are more easily ionised than those with heavier mass. Since the mass spectrometer analyses the ratios of isotopes of the element in samples, the difference in the ionisation of different isotopes over the period of time of analysis will result in the variation of the ratios of the isotope, though in theory the ratios should be constant. Because of the mass fractionation problem in

the measurement, the measured $^{84}Sr/^{86}Sr$ and $^{87}Sr/^{86}Sr$ are always normalised to a standard $^{86}Sr/^{88}Sr$ ratio, 0.1194, which represent the true ratio in natural materials. This arbitrary normalisation process is carried out automatically for the spiked samples (their $^{86}Sr/^{88}Sr$ ratio is somewhere between that of the natural samples (0.1194) and that of the spike (1.51281 for CIS spike 1), and unfortunately the 'the print-out' results do not represent the true ratios of the spiked samples. Thus, corrections have to be carried out further to obtain the true $^{84}Sr/^{86}Sr$ and $^{87}Sr/^{86}Sr$ ratios corresponding to the real spiked $^{86}Sr/^{88}Sr$ values.

The data reduction process in the CIS Laboratory is based on a solution proposed by Krogh and Hurley (1968), later improved by Hofman (1971). The solutions for corrected $^{86}Sr/^{88}Sr$ and $^{84}Sr/^{88}Sr$ (note a different denominator used here from the one used above) were obtained by inserting the line of zero fractionation (equation A6.6) with a fractionation line for a given mixture (equation A6.7):

$$\{\frac{84Sr}{88Sr}\}_{true} = [\frac{86Sr}{88Sr}]_{true} C_1 - C_2 \qquad \text{(A6.6)}$$

$$\{\frac{84Sr}{88Sr}\}_{true} = 2\frac{[\frac{84Sr}{88Sr}]_m}{[\frac{86Sr}{88Sr}]_m} [\frac{86Sr}{88Sr}]_{true} - [\frac{84Sr}{88Sr}]_m \qquad \text{(A6.7)}$$

where m stands for measured ratios. C_1 and C_2 can be resolved by inserting the $^{84}Sr/^{88}Sr$ and $^{86}Sr/^{88}Sr$ ratios of natural samples and spikes respectively in equation A6.6.

From these two equations, the corrected isotopic ratio can be obtained as:

$$\{\frac{86Sr}{88Sr}\}_{true} = \frac{[\frac{84Sr}{88Sr}] - C_2}{2\frac{[\frac{84Sr}{88Sr}]_m}{[\frac{86Sr}{88Sr}]_m} - C_1} \qquad \text{(A6.8)}$$

and

$$\{\frac{84Sr}{88Sr}\}_{true} = \frac{[\frac{86Sr}{88Sr}]_m - \frac{2C_2}{C_1}}{\frac{2}{C_1} - \frac{[\frac{86Sr}{88Sr}]_m}{[\frac{84Sr}{88Sr}]_m}} \qquad \text{(A6.9)}$$

Another related issue, firstly pointed out by Long (1965), is that under certain circumstances, a critical mixture of spike and sample exists, where the two equations have no solution. This happens when both numerator and denominator equal to zero, that:

$$\left[\frac{84Sr}{88Sr}\right]_m^{crit} = C_2 \qquad \text{(A6.10)}$$

$$\left[\frac{86Sr}{88Sr}\right]_m^{crit} = \frac{2C_2}{C_1} \qquad \text{(A6.11)}$$

It is quite easy to demonstrate that at this critical mixed composition, the tie lines represented by equations A6.6 and A6.7 coincide, which means a new mixing line defined by the critical mixture and natural samples is free of fractionation effects. In return, this new mixing line can be used to determine spike compositions accurately and hence improve the quality of data reduction. Apparently, the practical reduction will involve some looping calculations until certain criteria are reached. Hofmann (1971) proposed a three-step solution to determine the isotopic compositions of spiked samples, and this is used in the practical exercises.

For the Nd systematics, the algebra can be developed in an identical way in order to obtain the $^{143}Nd/^{144}Nd$ ratios and Nd concentration in samples. A particular advantage, however, using the critical mixture solution for the Nd systematics is that since the isotope composition of the Nd spikes are poorly defined compared with that of Sr, the practice can precisely calibrate the spike compositions as suggested by Roddick *et al* (in press).

In the present project, all data reductions were carried out using the CIS1 computer program developed by M. J. Korsch (1989, CIS unpublished program).

A6.6. ANALYTICAL PRECISIONS

There are generally two ways to determine the analytical precisions, namely the internal and external precisions. For the Mass spectrometer analysis, the internal precision refers the one derived from a single machine run and is defined by:

$$1\sigma\% = 100\{\Sigma(X_m - X_i)^2/n(n-1)\}^{1/2}/X_m \qquad \text{(A6.12)}$$

where X_m stands for the mean of the individual analyses (X_i), and n is the number of analysis

The external precision is derived from many machine runs at different time and different status of the machine. Most of the analytical precisions in mass spectrometry are quoted for the external precision, which provides a way of monitoring the consistence of the machine behaviour. The external precision is usually quoted with 95% confidence (2σ) and is defined by the same equation as above.

During the period of the present project, the quoted precisions for both Sr and Nd standards is about 0.0020%. This is equivalent to ± 0.00001 for Nd and ±0.000015 for Sr isotopic compositions.

As shown in Table 9.3.1 and 9.4.1, the internal precisions for most of the sample runs are less than the quoted precision on standard. Therefore, the external precisions of the standard runs are used for individual samples analysis for both Sr and Nd.

Both duplicate and replicate analyses of some of the selected samples were also carried out during the laboratory activities to monitor the quality of various exercises.

The duplicate analysis refers that the concentrated Sr samples from a single chemical process were analysed twice at different times (from one week to five months apart). The comparison of the results should provide a test of the external precision of the mass spectrometer during this period. And the replicate analysis is that the Sr concentrate run on the machine were obtained from separate chemical processes of the same sample. In this case, the analytical error is the combination of those from chemical processes and machine runs.

For the Sr analysis the average of the six duplicate runs is 0.0014%, and this results is well within external precision of the standard runs (Table A6.1). The replicate runs

Table A6.1. Comparison of duplicate/replicate analysis of 87Sr/86Sr ratios of the selected samples.

		87Sr/86Sr					
	sample	first run	date	second run	date	mean	2 sigma%
duplicate runs	861209	0.705571	5/2/90	0.705581	5/24/90	0.705576	0.0007
	762705	0.712023	5/2/90	0.711973	6/12/90	0.711998	0.0035
	861211	0.708503	5/2/90	0.708486	6/12/90	0.708495	0.0012
	861314	0.709395	5/2/90	0.709363	10/29/90	0.709379	0.0023
	861713	0.703726	5/2/90	0.703726	10/29/90	0.703726	0.0000
	861909	0.719416	5/2/90	0.719395	10/29/90	0.719406	0.0015
						average	0.0015
replicate runs	760801	0.703840	8/9/89	0.703843	8/21/89	0.703842	0.0002
	760805	0.704277	8/9/89	0.704298	8/21/89	0.704288	0.0015
	761301	0.705531	8/9/89	0.705576	8/21/89	0.705554	0.0032
	761809	0.704134	8/9/89	0.704210	8/21/89	0.704172	0.0054
	761901	0.704483	8/9/89	0.704443	8/21/89	0.704463	0.0028
	862205	0.705920	8/9/89	0.705926	8/23/89	0.705923	0.0004
	862221	0.705267	8/9/89	0.705286	8/23/89	0.705277	0.0013
	862225	0.703946	8/9/89	0.703984	8/23/89	0.703965	0.0027
	862402	0.704452	8/9/89	0.704508	8/23/89	0.704480	0.0040
						average	0.0024

Note: 2sigma% =50 [difference]/mean

yielded an average 2σ% error of 0.0024%, marginally higher than the quoted external precision of the standard runs (Table A6.2). This results clearly indicate that the analytical errors introduced from the chemical processes, such as the blank contribution, is insignificant compared with that from machine runs.

The Nd replicate runs of some of the samples yielded the same conclusion. (Table A6.3).

A comparison is also made for the Nd and Sm contents obtained by two isotope dilution (ID) analyses by MS and ICP-MS respectively (Table A6.4). On average, the difference of the two methods is about 7% for the elemental concentrations, but this error is largely due to very high errors from the basement samples. The relatively large elemental difference of the samples from the basement sequences is partly due to the fact that most of the samples has very low Nd and Sm contents. The absolute difference ranges from 0.37 ppm to 1.1 ppm for Nd and 0.06 to 0.91 ppm for Sm, and only marginally larger than those of the younger samples (0.1 to 1.1 ppm for Nd and 0.06 to 0.52 ppm for Sm). In comparison, precision on Nd/Sm ratios is significantly higher about 2.6%. This comparison would also provide a minimum external precision for ICP-MS analysis, considering that Sm/Nd analysis by MS yields a much better precision about 0.1% (Whitford, CIS unpublished data).

Table A6.2. Replicate analysis of Nd isotope compositions					
sample	first run	date	replicate	date	2 sigma%
752001	0.512913	6/30/90	0.512898	12/1/91	0.0015
752302	0.512921	6/30/90	0.512886	12/1/91	0.0034
760402	0.513020	6/30/90	0.513032	12/1/91	0.0012
760806	0.512616	11/13/91	0.512609	12/1/91	0.0007
762501	0.513092	6/30/90	0.513100	12/1/91	0.0008
861314	0.512896	6/30/90	0.512836	12/1/91	0.0058
861713	0.513110	6/30/90	0.513047	12/1/91	0.0061
861915	0.513083	6/30/90	0.513089	12/1/91	0.0006
				mean	0.0025

Note 2sigma% = 50*(difference)/mean

Table A6.3. Comparison of Nd and Sm contents analysed by ICP-MS and MS.

	Nd			Sm			Nd/Sm		
sample	ICP-MS	MS	error%	ICP-MS	MS	error%	ICP-MS	MS	error%
752110	18.3	14.2	28.9	4.67	3.76	24.2	3.92	3.78	1.85
752302	7.29	6.31	15.5	2.21	2.04	8.3	3.30	3.09	3.22
753001	6.33	5.02	26.1	1.93	1.62	19.1	3.28	3.10	2.84
762501	10.3	9.13	12.5	3.35	3.24	3.4	3.07	2.82	4.21
861314	15.0	14.4	4.3	4.55	4.49	1.3	3.30	3.21	1.44
861713	8.81	8.09	8.9	2.83	2.75	2.9	3.11	2.94	2.83
861909	10.3	10.9	5.8	3.12	3.48	10.3	3.29	3.13	2.48
861915	8.99	8.47	6.1	2.89	2.95	2.0	3.11	2.87	4.00
760801	9.71	10.5	7.9	2.22	2.58	14.0	4.37	4.09	3.41
760806	31.5	31.5	0.1	6.59	7.02	6.1	4.77	4.49	3.10
761301	36.3	36.8	1.5	8.13	8.11	0.2	4.46	4.54	0.86
761503	30.2	29.3	3.0	6.35	6.55	3.1	4.75	4.47	3.05
761809	39.6	40.4	1.9	8.37	8.59	2.6	4.73	4.70	0.32
761901	52.1	51.2	1.7	10.7	10.7	0.1	4.88	4.79	0.91
862112	18.4	18.7	1.9	4.14	4.47	7.4	4.43	4.19	2.86
862205	34.6	35.6	2.7	6.84	7.36	7.1	5.06	4.83	2.29
862221	58.8	58.2	1.2	12.59	12.9	2.4	4.67	4.51	1.79
862225	11.5	10.9	5.5	2.27	2.39	5.0	5.07	4.56	5.25
862402	36.6	37.0	0.9	7.53	7.99	5.8	4.87	4.63	2.49
		average	7.2			6.6			2.59

Appendix 7
Notation of Nd Isotope Systematics

Unlike other radiogenic isotope systems, variations of the Nd isotopic ratio (principally $^{143}Nd/^{144}$ Nd) due to the ^{147}Sm decay (see Chapter Nine) is rather small in nature, so their representation in terms of deviation from a 'standard' value is mostly used in practice. This standard value has been referred as the CHUR value (Chondritic Uniform Reservoir, DePaolo and Wasserburg, 1976a), and its $^{143}Nd/^{144}$ Nd ratio at any time (T) in the pass is given by:

$$[\frac{143Nd}{144Nd}]^{T}_{CHUR} = [\frac{143Nd}{144Nd}]^{0}_{CHUR} - [\frac{147Sm}{144Nd}]^{0}_{CHUR}[e^{\lambda SmT} - 1] \qquad (A7.1)$$

where $[\frac{143Nd}{144Nd}]^{0}_{CHUR}$ and $[\frac{147Sm}{144Nd}]^{0}_{CHUR}$ represent the values in CHUR today (0.511847 and 0.1967 respectively).

The $^{143}Nd/^{144}$ Nd of actual rock samples at time T is usually represented by a parameter $\varepsilon_{Nd}(T)$, which is defined as:

$$\varepsilon^{T}_{Nd} = 10^{4}\frac{[\frac{143Nd}{144Nd}]^{T}_{sample} - [\frac{143Nd}{144Nd}]^{T}_{CHUR}}{[\frac{143Nd}{144Nd}]^{T}_{CHUR}} \qquad (A7.2)$$

By this definition, $\varepsilon_{Nd}(T)$ indicates the deviation of the $^{143}Nd/^{144}$ Nd of the samples from that of CHUR in units of parts in ten thousand. Since T = 0 is used to represent the present time, the $\varepsilon_{Nd}(0)$ of analysed samples refers to the $^{143}Nd/^{144}$ Nd ratio measured in the laboratory; and thus $\varepsilon_{Nd}(T_x)$ is referred to as the 'initial ε_{Nd} value' of the rock, where Tx is the crystallisation age of the rock. Apparently, the initial values of rocks are more useful in characterisation of the primary isotopic features of the rocks, and this initial value can be obtained by:

$$\varepsilon^{Tx}_{Nd} = \{\varepsilon^{0}_{Nd} - \frac{10^{4} f_{Sm/Nd}[\frac{147Sm}{144Nd}]^{0}_{CHUR}[e^{\lambda SmT} - 1]}{[\frac{143Nd}{144Nd}]^{0}_{CHUR}}\}\frac{[\frac{143Nd}{144Nd}]^{0}_{CHUR}}{[\frac{143Nd}{144Nd}]^{T}_{CHUR}} \qquad (A7.3)$$

$$\text{where } f_{Sm/Nd} = \frac{[\frac{147Sm}{144Nd}]^{T}_{sample} - [\frac{147Sm}{144Nd}]^{T}_{CHUR}}{[\frac{147Sm}{144Nd}]^{T}_{CHUR}}$$

Details can be obtained in DePaolo (1988).

Another useful concept adopted in this thesis is the model age. The model age of a certain rock refers to the 'age' of the source of the rock (invariably from the mantle) segregated from the upper mantle (see Figure 9.1.2). An empirical model age can be constructed using the average 'depleted mantle' ε_{Nd} evolution instead of the chondritic evolution (*i.e.* CHUR) (DePaolo, 1981). The mantle ε_{Nd} evolution curves used by different proposals vary slightly, but most of them lie between the upper two curves shown in Figure 9.1.2. The model age data presented in the present project are calculated from the following equation proposed by McCulloch (1987):

$$T_{Nd} = 1.529 \times 10^5 \ln\{1+\frac{[\frac{143Nd}{144Nd}]_{sample} - 0.51235}{[\frac{147Sm}{144Nd}]_{sample} - 0.225}\} \quad (Ma) \qquad (A7.4)$$

if the samples are post-Archaean in age.

Appendix 8
ICP-MS Techniques

The ICP-MS is a new mass spectrometric technique. It combines the inductively coupled plasma (ICP) and mass spectrometric (MS) techniques and enables measurement of isotopic compositions at very fast rates compared with the conventional MS method. At the present time, the new method is still not capable of producing high precision measurements of isotopic ratios, and thus is only used for ID analysis (*cf.* Appendix 6). This technique has, nonetheless, been rapidly improved recently and a new model of the equipment is going to be available in the foreseeable future, when the conventional TIMS technique can be replaced for high precision isotope studies.

In the present project, the rare earth element (REE) compositions of some of the samples from the Wonominta Block were measured using the ICP-MS techniques at CSIRO's Lucas Heights laboratories in Sydney.

When carrying out the analyses, the ICP-MS uses a high-temperature argon plasma as an atmospheric pressure ionisation source for a quadruple mass spectrometer. The aqueous sample solutions were sprayed as an aerosol of fine droplets into the plasma, where solvent is evaporated, the sample molecules are broken down into their constituent atoms and the atoms ionised with a high degree of efficiency. Ions are then extracted through an interface into the high vacuum of the quadruple mass spectrometer. Each sample is run three times on the ICP-MS, scanning over the mass range from 133 to 180 for 200 sweeps with a dwell time of 320 μsec/channel. Solutions are nebulised for 15 second prior to data collection to allow the system to equilibrate. The nebulising system is washed with 1% HNO_3 for 1 minute between samples.

The chemical preparation of the samples for ICP-MS analysis is described in Appendix A6, and in Chapter 5. The full description of the working conditions of the machine is presented in Table A8.1.

Table A8.1.ICP-MS operating parameters
(From Eames, 1991; CSIRO unpublished report).

1. ICP settings			
Incident power	1.5 kW		
Reflected power	<10 W		
Load coil	3 turns		
Argon gas flow rates	Cooling	15	l/min
	Auxiliary	0.7	l/min
	Nebuliser	0.8	l/min
2. Sample Injection			
Nebuliser type:	Meinhard Type C		
Sample uptake rate	0.7 ml/min		
3. Interface			
Sampler diameter	1 mm		
Skimmer diameter	0.75 mm		
Load coil-aperture spacing	10 mm		
4. Measurement parameters			
Dwell time	320 µs/channel		
No. of channels	2048 channels		
No. of scans	200 scans		

MAP 1. PONTO MINE AREA

NUNDORA

1:10 000

762001
762202/05
762401/09
761601
762002/04
761807/08
761602
761809/10
761801/06
761603/04
761901/4
761905
761508/12
761507
761505
761506
762201
761504
761908
761907
761503
761502
761906
761501
TO WONNAMINTA 16km
TO NUNDORA 9km
MO
T1
T2
M1
M2
T3
Fe
6 608N
6 607N
6 606N
6 605N
6 604N
6603N
606 E
607 E
608 E
609 E

Legend

late Proterozoic

- T1 — Cleaved metabasite
- M1 — Massive metabasite
- Slate
- Alluvium
- Silcrete
- Fault breccia

Palaeozoic

- Syenite
- Peridotite
- Nundorite
- 762401 — Sample locality
- Fault
- Geological boundary (dashed line, inferred)

Cenozoic

- Fe — Ferricrete
- Fence
- strike and dip of cleavage/bedding

200 400 600 800 1000 m

B.D. 9106

MAP 6. NUNDORA AREA

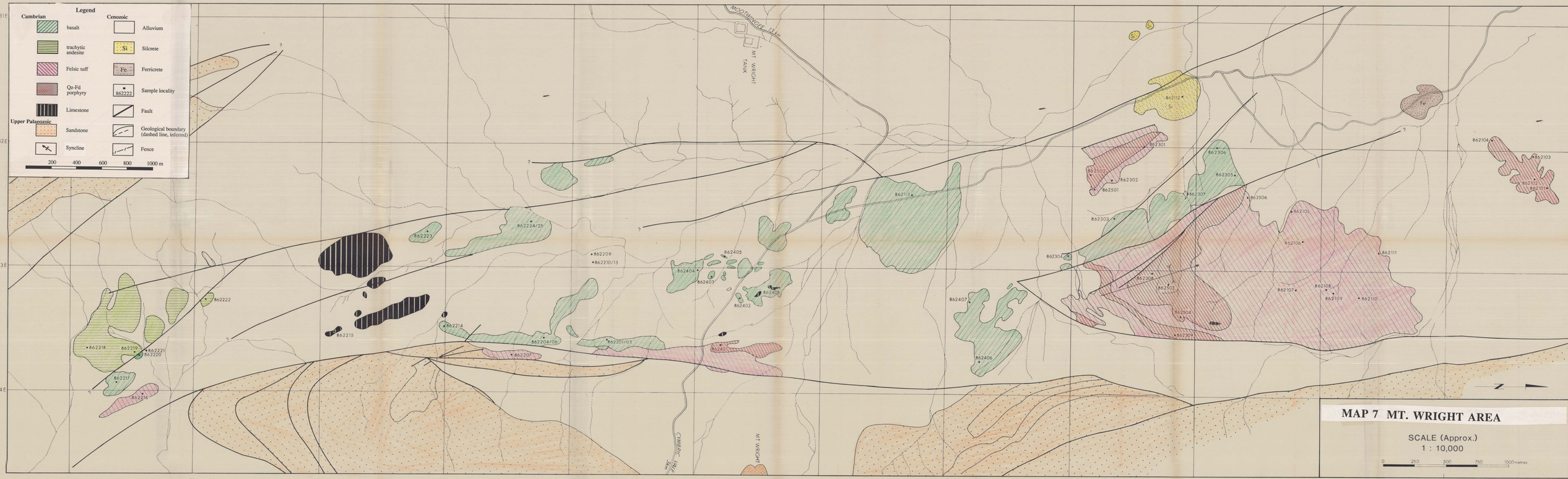
Legend
Cambrian
basalt
trachytic andesite
Felsic tuff
Qz-Fd porphyry
Limestone
Upper Palaeozoic
Sandstone
Syncline
Cenozoic
Alluvium
Silcrete
Ferricrete
Sample locality
Fault
Geological boundary (dashed line, inferred)
Fence
200 400 600 800 1000 m
MOOTWINGEE 19 Mi
MT WRIGHT TANK
CYMBERIC WELL
MT WRIGHT
862222
862223
862224/25
862209
862210/13
862405
862404
862403
862402
862408
862214
862215
862204/06
862207
862201/03
862240
862218
862219
862221
862220
862217
862216
862113
862407
862406
862112
862301
862502
862302
862501
862306
862305
862307
862506
862303
862304
862105
862106
862111
862308
862503
862504
862309
862107
862108
862109
862110
862104
862103
862102
862101
Si
Fe
MAP 7 MT. WRIGHT AREA
SCALE (Approx.)
1 : 10,000
0 250 500 750 1000 metres
631E
632E
633E
634E
540N
541N
542N
543N
544N
545N
546N
547N
548N
549N
550N
551N

MAP 7. MT. WRIGHT AREA

COMARTO

1:10 000

B.D. 9201

MAP 8. COMARTO AREA

BILPA

1:29 000

B.D. 9201

MAP 9. BILPA AREA

1:10 000

762601
762602
762603
762604
BELT 4
762605
WONNAMINTA
7km
Koonenberry
Fault
762804
762805
762607
762608
762606
762803
762502/3
762802
762806
762280
BELT 3
BELT 1
762701
762504/05
2609
762710
762709
762708
762707
762706
762705
762703/4
762501
762710
BELT 2
J K Creek
BOSHY TANK
KAYRUNNERA
6.5km
N
610N
609N
608N
607N
606N
605N
604N
603N
602N
633E
634E
635E
636E
637E
638E
639E
640E
641E

Legend

Basement
- Cleaved metabasite
- Metadolerite III
- Metadolerite II
- P, G, P+G — Undifferentiated phyllite(P) and meta-greywacke (G)

Cambrian
- Sandstone
- Metadolerite I

Cenozoic
- Alluvium

Others
- Ironstone rocks
- Quartize
- Fault breccia
- 762501 — Sample locality
- Fault (dashed line, inferred)
- Geological boundary (dashed line, inferred)
- Fence
- strike and dip of cleavage/bedding

200 400 600 800 1000 m

B.D. 9201

MAP 2. BOSHY TANK AREA

WILANDRA

1:10 000

B.D. 9201

MAP 3. WILANDRA AREA

CYMBRIC VALE

1:10 000

200 400 600 800 m

BLUE TANK 3km

861709 861710 861711 861712 861713/15 861716/17 861701 861702 861703 861704 861705 861706 861707 861708 861801 861802/03 861804 861805 861806 861807 861808 861809 861810/11 861811 861901 861902 861903/06 861907 861908 861909 861912 861913 861914 861915

550 N 549 N 548 N 547 N 546 N 545 N

635 E 636 E 637 E 638 E

CYMBRIC VALE 2km

Legend

Basement

- Amphibolite
- Mica schist

Palaeozoic

- Sandstone
- Chert

Cenozoic

- Alluvium

Others

- 861901 — Sample locality
- Fault
- Geological boundary
- Fence
- strike and dip of cleavage/bedding

B.D. 9201

MAP 4. CYMBRIC VALE AREA

PACKSADDLE

1:10 000

761307/2
760805
760806
TIBOOBURRA 154 km
N
621 N
UNIT 1
761001
761003/5
761002
761002B
UNIT 2
761303
760807
M2 T2 M1 T1
HIGHWAY
M2 T2 M1 T1
760808
761305
761306
760904/A
761307/08
620 N
761009
761206
CITY
761006
760801–760804
761008–761010
761207
619 N
Dam
SILVER
UNIT 3
761203
760901
760902
760903
618 N
761201/02
UNIT 4
761204/05
Airstrip
140–90
617 N
BROKEN HILL 178 km
616 N

Legend

late Proterozoic

- T — Cleaved metabasite
- M — Massive metabasite
- Metadoleirte(IIA)
- Slate
- Carbonate
- strike and dip of cleavage/bedding

Palaeozoic

- Syenite

Cenozoic

- Alluvium

Others

- 761001 — Sample locality
- Fault
- Geological boundary (dashed line, inferred)
- Fence

200 400 600 800 1000 m

593 E 594 E 595 E 596 E 597 E

B.D. 9105

MAP 5. PACKSADDLE AREA

PONTO MINE AREA

1:10 000

BELT H
752201/05
760503
752109/14
BLUFF TANK
Koonenberry Fault
760502
753102
753105
760501
MILPA 10km
752107
752106
752108
753106
Boundary of mapped area
752102
760103
PONTO MINE
752001
760601
MORDEN 17km
760413
760401/11
760701/3
752902/11
760414
BELT G
760301
760302
752801/02
760412
752803/04
ROCKY TANK
760201
BELT D
BELT B
753001/02
752805/07
752809/08
752810/1
753006
BELT E
BELT A
753007/8
75013/14
753009/10
753011/12
BELT C
BELT F
752001/02
752501
STEVENS TANK
752301/12

637 N
636 N
635 N
634 N
633 N
632 N
631 N
630 N

612 E
613 E
614 E
615 E
616 E
617 E
618 E
619 E
620 E

Legend

Basement
- Cleaved metabasite
- Massive metabasite
- Metadolerite II
- Metadolerite (III)
- Phyllite
- Schist
- Meta-greywacke

Cambrian
- Metadolerite I

Cenozoic
- Alluvium

Others
- Ironstone rocks
- Quartize
- Sample locality (752001)
- Fault (dashed line, inferred)
- Geological boundary (dashed line, inferred)
- Fence
- strike and dip of cleavage/bedding

200 400 600 800 1000 m

B.D. 9112